CHALMERS UNIVERSITY OF TECHNOLOGY
Gothenburg, Sweden
www.chalmers.se

A tiny superconducting microparticle floating in a magnetic field can be used as a new type of quantum sensor. When cooled close to extremely low temperatures, it enters a superconducting state in which it strongly reshapes magnetic fields, allowing it to be stably levitated in vacuum without touching any surface. If its motion is reduced to the quantum limit, it would become sensitive to extremely tiny forces. This paves the way to building a sensor that detects forces with a precision approaching the fundamental limits set by quantum mechanics.

This thesis first demonstrates the levitation of a micrometer-sized particle on a chip. Then, a superconducting microwave circuit is developed for precisely reading out the motion of the levitated particle. Such a circuit responds strongly to tiny magnetic signals from the particle and converts its motion into a measurable electrical signal. A new chip-to-chip assembly technique is developed using microscopic indium bonds. This allows the microwave circuit to be positioned very close to the particle so that weak motion signals can be detected.

Together, these advances establish the platform needed to levitate a microparticle on a chip and precisely measure its motion. In the future, such a quantum system could have applications in navigation and gravitational sensing. The beauty of this experiment is that the particle is far larger than the objects usually studied in quantum experiments, being closer in size to a speck of dust. Therefore, creating quantum effects in such a particle could one day help answer some of the deepest questions in physics: where the limits of quantum mechanics lie and how quantum objects interact with gravity.

CHALMERS
UNIVERSITY OF TECHNOLOGY

ACHINTYA PARADKAR • Coupling a Flux-Tunable Resonator to a Magnetically Levitated Superconducting Microparticle • 2026

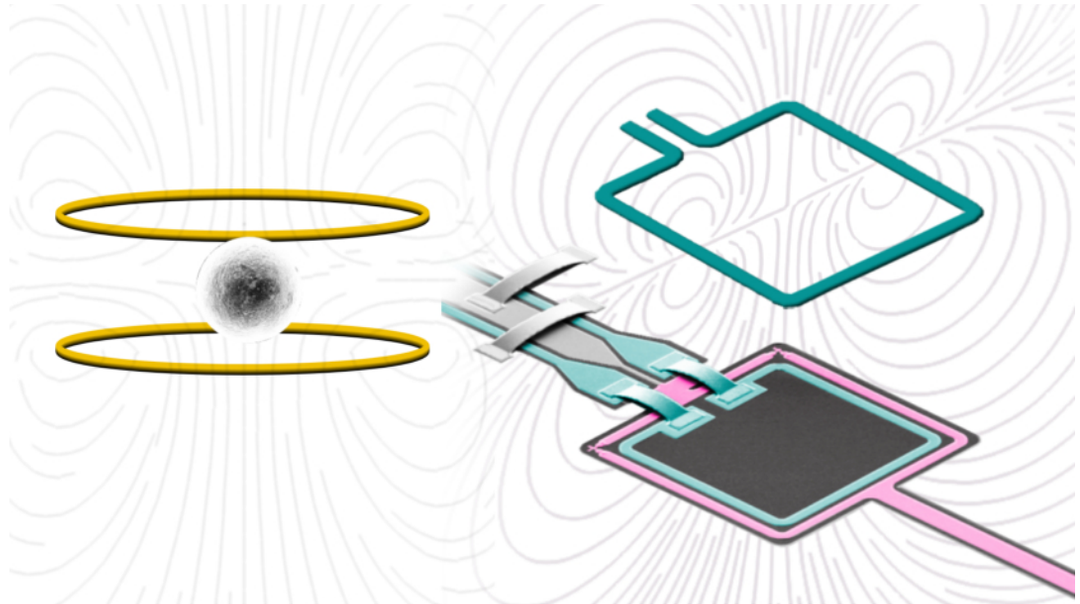

Coupling a Flux-Tunable Resonator to a Magnetically Levitated Superconducting Microparticle

ACHINTYA PARADKAR
DEPARTMENT OF MICROTECHNOLOGY AND NANOSCIENCE (MC2)

CHALMERS UNIVERSITY OF TECHNOLOGY
Gothenburg, Sweden 2026
www.chalmers.se

THESIS FOR THE DEGREE OF DOCTOR OF PHILOSOPHY

Coupling a Flux-Tunable Resonator to a Magnetically Levitated Superconducting Microparticle

Achintya Paradkar

Department of Microtechnology and Nanoscience (MC2)
Chalmers University of Technology
Gothenburg, Sweden, 2026

Coupling a Flux-Tunable Resonator to a Magnetically Levitated Superconducting Microparticle

Achintya Paradkar

ISBN 978-91-8103-391-5
DOI 10.63959/chalmers.dt/5848

Copyright © Achintya Paradkar 2026
All rights reserved.

Technical Report No. 5848
ISSN 0346-718X

Department of Microtechnology and Nanoscience (MC2)

Under the supervision of:
Witlef Wieczorek, Professor (1)
Thilo Bauch, Docent (2)

Examined by:
Per Delsing, Professor (1)

(1) Quantum Technology division, Department of Microtechnology and Nanoscience
(2) Quantum Devices division, Department of Microtechnology and Nanoscience

Chalmers University of Technology
SE-412 96 Gothenburg, Sweden
Phone: +46 (0)31 772 1000
www.chalmers.se

Printed by Chalmers Reproservice
Gothenburg, Sweden, March 2026

Dedicated to my loving parents who constantly supported my career ambitions and encouraged me to believe in myself and pursue science.

Abstract

Magnetically levitated superconducting microparticles provide a promising platform for fundamental quantum experiments and quantum-limited sensing. In the Meissner state, the levitated particle is trapped without mechanical clamping, allowing its center-of-mass motion to exhibit ultralow dissipation. The particle's displacement can be read out dispersively via magnetic flux coupling to superconducting resonators. A challenge for magnetomechanical coupling is to realize a flux-tunable microwave circuit that provides strong flux-to-frequency transduction, low dissipation, and a sufficiently large linear operating range for readout and cooling. This thesis develops and characterizes a chip-based superconducting platform for realizing this transduction.

Chip-based levitation of a superconducting microparticle is demonstrated at 40 mK. Passive cryogenic vibration isolation is developed to increase the mechanical quality factors of the levitated particle. For coupling to a microwave circuit, a superconducting flip-chip process based on indium microspheres was developed. The need for Au passivation of Nb or NbN under-bump metallization is demonstrated, and indium-based superconducting interconnects are shown to carry ampere-scale currents. Flux-tunable resonators with 100-200 µm SQUID loops and integrated input coils are designed, fabricated, and characterized. A peak flux responsivity of $20\,\mathrm{GHz}/\Phi_0$ is achieved, with one flux quantum modulation requiring only 10-20 µA of input-coil current. Two integrated flux-biasing architectures are developed with flip-chip and on-chip input coils, achieving a total flux transfer efficiency of 1.6%. Junction asymmetry is shown to suppress branch-switching behavior associated with finite SQUID screening.

Together, these results establish the superconducting subsystems required for dispersive microwave readout of the center-of-mass motion of a levitated microparticle. Such a magnetomechanical coupling provides a route toward cooling the center-of-mass motion to the ground state, paving the way for the preparation of nonclassical motional states. More broadly, such systems are well-suited for quantum-limited force and acceleration sensing, as well as for probing quantum physics in a previously unexplored mass regime.

Keywords: Chip-based trap, Magnetic levitation, Coplanar waveguides, Superconducting flux-tunable resonators, SQUID-based microwave cavity, Asymmetric SQUIDs, Superconducting flip-chip interconnect, Passive vibration isolation, Magnetomechanical coupling.

List of Publications

Publications included in the thesis:

1. Gutierrez, M., **Paradkar, A.**, Hambraeus, D., Higgins, G., & Wieczorek, W.
   A Chip-Based Superconducting Magnetic Trap for Levitating Superconducting Microparticles.
   IEEE Transactions on Applied Superconductivity **32**, 1-5 (2022).
   Contributions:
   - Installed the dilution refrigerator and the full cryogenic setup, including the SQUID magnetometer, cryogenic cables, and magnetic shields.
   - Developed the cryogenic optical readout setup inside the cryostat (focusing and collimation lenses, holders, and optical windows) and outside the cryostat (optical table, camera, illumination LED, and beam splitter).
   - Optimized thermalization and minimized mass loading.
   - Contributed to experiment setup, measurements, and methodology.

2. **Paradkar, A.**, Nicaise, P., Dakroury, K., Resare, F., & Wieczorek, W.
   Superconducting flip-chip devices using indium microspheres on Au-passivated Nb or NbN as under-bump metallization layer.
   Applied Physics Letters **126**, 022601 (2025).
   Contributions:
   - Led the design and conceptual development of the flip-chip bonding technique using indium microspheres.
   - Planned the fabrication process, material selection, and parameter optimization together with co-authors; led the initial cleanroom fabrication, after which co-authors further improved the recipes and process.
   - Developed the setup and planned and performed all experiments.
   - Processed and interpreted the data and developed analytical models.
   - Conducted the literature review and prepared the manuscript.

3. **Paradkar, A.**, Nicaise, P., Dakroury, K., Resare, F., Dejaco, C., Deeg, L., Kirchmair, G., & Wieczorek, W.
   Efficient flip-chip and on-chip-based modulation of flux-tunable superconducting resonators.

arXiv:2512.23119 (2025).

Contributions:

- Developed expertise in superconducting microwave circuits in the lab.
- Designed, fabricated, and characterized flux-tunable resonators.
- Developed 1 µm Josephson junctions to reduce Kerr nonlinearity.
- Designed a flux transformer with analytic model and FEM simulations to maximize efficiency.
- Designed and fabricated flip-chip and on-chip input coils.
- Characterized integrated flux modulation and flux-transfer efficiency.
- Developed the setup and planned and performed all experiments.
- Processed and interpreted the data and developed analytical models.
- Conducted the literature review and prepared the manuscript.

Publications not included in the thesis:

1. Gutierrez Latorre, M., Higgins, G., **Paradkar, A.**, Bauch, T., & Wieczorek, W.
Superconducting Microsphere Magnetically Levitated in an Anharmonic Potential with Integrated Magnetic Readout.
Physical Review Applied **19**, 054047 (2023).

Acknowledgments

Many people have contributed, directly and indirectly, to the work presented in this thesis, and I would like to express my sincere gratitude to all of them.

First and foremost, I am deeply grateful to my supervisor, Witlef Wieczorek, for his guidance, trust, and continued support throughout my PhD. Witlef, I have always admired your scientific acumen and rigor, as well as the seriousness and care with which you approach both research and supervision. I am especially thankful for the support and advice you gave me in my early years when I was still struggling to find my footing. Thank you for not giving up on me during that time and for helping me grow into a more confident researcher.

I have also been incredibly lucky to share this PhD with a team that has changed over the years, and yet it has always felt like a constant. Martí, you were my first companion in this project, and I owe you a great deal for everything you taught me in those early days, not only about the project itself but also about the persistence and resilience needed for this PhD. Fabian and Paul, thank you for the laughter, the inside jokes, shared frustrations, and for being amazing buddies. From sharing the lab load to challenging norms, I could always count on you, at the very least for solidarity, bad ideas, and the occasional good one. Alireza, Aditi, Joram, and Rishabh, thank you for bringing a fresh perspective. You all broadened the project's horizon, and I'm excited to see how you will shape it in the coming years. Alex, although we worked on different projects, you always took an interest in my work. I appreciate the discussions that seemed to open up new ways of thinking about it. I would also like to acknowledge Gerard and Paul for helping set up homodyne readout, Tom for teaching me about dark matter, Anastasiia for helping me navigate chemistry and the cleanroom, and Hannes for the many interesting conversations over coffee. Christian and Lukas, thank you for the collaboration, for sharing your insights so generously, and for the endless discussions on the potato fitting, which somehow always managed to be both useful and entertaining. I would also like to thank my master students, Avan, Anton, Karim, and Anant, for their enthusiasm and curiosity, and for keeping the student in me alive. Somewhere along the way, this group became more than a workplace and, in many ways, my second family in Gothenburg.

Aside from science, I also gained a great deal from my time in the PhD student council. Ariadna, thank you for welcoming me so openly, and Isak and Nuria, thank you for being such great companions in that work. This part

would be incomplete without mentioning DrGENIE, which gave an added sense of purpose to my PhD years and strongly influenced how I think about gender equity in academia. Georgia, thank you for making it so easy to feel at home and speak openly. Vi, Malin, and Kelsey, thank you for the energy, team spirit, and care with which you made WG4 such a success. I still look back on that time very fondly. Thank you, Emma, for connecting on this journey and for your friendship. Your conviction and passion for equality are truly contagious. I also want to thank Maria Saline, Maria Messing, and Lauri for being a real support system and for listening to us with seriousness and generosity, even when we did not yet have the broader perspective that comes with experience. You showed me what good leadership can look like in practice.

My sincere thanks to my co-supervisor Thilo Bauch and my examiner Per Delsing for always being available for me with their expertise. Linda for being my go-to person throughout these years. You've made my life in Gothenburg a smooth journey. Many thanks to Lars for his amazing talent in making the impossible happen and for always accommodating my needs. I would like to thank all my collaborators and colleagues at MC2 for making this a stimulating and enjoyable place to work. I am grateful for the many discussions, suggestions, practical help, and shared pain and successes in the lab, cleanroom, and office. I also thank the cleanroom NFL staff for being so supportive and for being available for troubleshooting. I gratefully acknowledge the funding from the Wallenberg Foundation and from EU Horizon that supported this work and made the underlying experiments and collaborations possible.

I am deeply indebted to all the teachers who recognized potential in me and encouraged me to find my own niche. Finally, I would like to thank my family. My parents, to whom this thesis is dedicated, have always put my interests and dreams before their own comfort, despite all the struggles and sacrifices that came with it. Whatever I have achieved rests on that foundation. I owe them more than I can ever properly express. I would also like to thank my wife, Santoshi, for her love, patience, and understanding throughout these years. You endured my absence, stood beside me through difficult times, and made the hardest phases of this journey easier to get through. For that, I am deeply grateful.

To all of you, a big thank you!

Contents

Abstract **i**

Acknowledgments **v**

List of Figures **xiii**

List of Tables **xvii**

Acronyms **xviii**

Symbols **xix**

1 Introduction **1**

2 Theory **9**

2.1 Superconductivity 9

2.1.1 Meissner-Ochsenfeld effect 10

2.1.2 Two-fluid model 11

2.1.3 Ginzburg-Landau theory 13

2.1.4 BCS theory and Cooper pairing 14

2.1.5 Fluxoid quantization 16

2.1.6 Kinetic inductance 18

2.1.7 Proximity effect 20
2.2 Magnetic levitation of superconductors 21
2.2.1 Earnshaw's theorem 22
2.2.2 Meissner-state trapping 23
2.2.3 On-chip magnetic trap 24
2.3 Josephson junction 28
2.3.1 Josephson effect 28
2.3.2 Ambegaokar-Baratoff relation 29
2.3.3 Josephson inductance and energy 30
2.4 Superconducting Quantum Interference Device 31
2.4.1 Phase and current definitions 33
2.4.2 RCSJ model and equations of motion 34
2.4.3 Current-phase relations in the zero-voltage state 36
2.4.4 Fluxoid quantization and screening 36
2.4.5 Effective critical current 38
2.4.6 Circulating current 40
2.4.7 Potential energy landscape 41
2.5 Coplanar waveguide resonators 46
2.5.1 CPW geometry and field distribution 46
2.5.2 Conformal mapping analysis 46
2.5.3 CPW kinetic inductance 49
2.5.4 Characteristic impedance 50
2.5.5 Quarter-wave resonator 51
2.5.6 Coupling capacitance 53
2.5.7 Coupling quality factor 54
2.5.8 Intrinsic quality factor 56
2.6 Flux-tunable resonator 58
2.6.1 Circuit model and Lagrangian 59
2.6.2 Eigenmode equation 61
2.6.3 Linearized SQUID inductance 65
2.6.4 Flux responsivity 69
2.6.5 Effective mode parameters 71
2.6.6 Single-mode quantization 72
2.6.7 Kerr nonlinearity 73
2.6.8 Driven Kerr response and bistability 76
2.6.9 Circle fitting 78

2.7 Flux noise 81
2.7.1 Flux noise spectrum 81
2.7.2 Frequency jitter 82
2.7.3 Lorentzian and Voigt profiles 82
2.8 Flux transformer 85
2.8.1 Mutual inductance 85
2.8.2 Flux transfer efficiency 86
2.9 Magnetomechanical coupling 87
2.9.1 System Hamiltonian 87

3 Methods **91**
3.1 Finite element methods 92
3.1.1 Magnetostatic simulations 92
3.1.2 Microwave simulations 97
3.2 Design and fabrication 100
3.2.1 Design principle 102
3.2.2 FTR layer stack 104
3.2.3 Wiring layer 105
3.2.4 Under-bump metallization (UBM) 106
3.2.5 Josephson junctions 108
3.2.6 Patch layer 111
3.2.7 Air-bridges 113
3.2.8 Input coils 114
3.3 Cryogenic setup for levitation 116
3.3.1 Optical readout setup 117
3.3.2 Magnetic shielding 119
3.3.3 Passive vibration isolation 120
3.4 Flip-chip bonding 124
3.4.1 Bonding technique 125
3.4.2 Four-wire measurement 127
3.5 Resonator characterization 129
3.5.1 Sample holder and chip mounting 129
3.5.2 Magnetic and thermal environment 130
3.5.3 Cryogenic microwave wiring 131
3.5.4 Data acquisition and fitting 138

4 Results **141**
4.1 Optical readout of levitated microparticle 142
4.2 Passive vibration isolation system 144
4.2.1 Transfer function and stage noise 144
4.2.2 SQUID-based readout of particle motion 145
4.2.3 Thermalization 148
4.2.4 Two-stage system 149
4.3 Magnetic Shielding 149
4.4 Flip-chip characterization 152
4.4.1 UBM thin-film characterization 152
4.4.2 Flip-chip device characterization 155
4.4.3 Indium interconnect 158
4.5 CPW resonators 160
4.5.1 Device A: resonance and coupling benchmark 160
4.5.2 Device A: power sweep 162
4.5.3 Device B: temperature sweep 163
4.6 Flux-tunable resonators 165
4.6.1 Microwave line characterization 165
4.6.2 Junction characterization 166
4.6.3 Reference FTR: uncoupled 10 µm SQUID loop 171
4.6.4 Coupled FTRs: 100 µm and 200 µm SQUID loops 177
4.7 Integrated flux transformer 187
4.7.1 Coil-to-SQUID efficiency 187
4.7.2 FEM simulations 187
4.7.3 Flux transformer demonstration 190
4.8 Flux-noise characterization 191
4.8.1 Flux noise at sweet spot 192
4.8.2 Flux-noise fit of $Q_i^{eff}(\Phi_e)$ 193
4.8.3 Flux noise from fast S_{21} measurements 195
4.8.4 Spectral flux-noise analysis 196
4.9 Magnetomechanical coupling estimates 199
4.9.1 Cooperativity 201

5 Conclusion and outlook **203**

6 Appendix **211**
6.1 SQUID and Kerr nonlinearity 211
6.1.1 Quadratic and higher-orders of the SQUID potential . . 211
6.1.2 Perturbative derivation of the Kerr contributions 215
6.2 Single-stage vibration isolation model 220
6.2.1 Linearized vertical equation of motion 220
6.2.2 Frequency-domain transmissibility 222
6.2.3 Limiting regimes and design implications 223
6.2.4 Propagation of vibration spectra 224
6.2.5 Parasitic modes and validity of the reduced model . . . 224
6.2.6 Relevance to a levitated-particle experiment 225
6.3 Fabrication recipes 225
6.3.1 Wafer cleaning 226
6.3.2 Wiring layer (ground plane) 226
6.3.3 Under-bump metallization 228
6.3.4 Josephson junctions 229
6.3.5 Patch layer 230
6.3.6 Air-bridges 231
6.4 Supplementary results 233
6.4.1 Parasitic mode engineering 233
6.5 Homodyne readout 235
6.5.1 Homodyne principle 235
6.5.2 Transduction chain 237
6.5.3 Homodyne setup 238

7 Summary of included papers **241**

References **243**

1 Paper A **A1**

2 Paper B **B1**

3 Paper C **C1**

List of Figures

1.1 Concept of the magnetomechanical readout platform 4

2.1 Meissner-Ochsenfeld effect and magnetic screening 10
2.2 Superfluid and normal fractions in the two-fluid model 12
2.3 Phonon-mediated Cooper pair formation 15
2.4 Kinetic inductance in thin superconducting films 18
2.5 Quadrupole fields from anti-Helmholtz coil traps 24
2.6 Structure and phase difference of a Josephson junction 28
2.7 dc SQUID in the RCSJ representation 32
2.8 Flux screening and branch following in a dc SQUID 38
2.9 Effective critical current of symmetric and asymmetric dc SQUIDs 39
2.10 Potential landscapes of a symmetric screened dc SQUID 42
2.11 Potential landscapes of an asymmetric screened dc SQUID . . . 43
2.12 Coplanar waveguide geometry and field profiles 47
2.13 Quarter-wave CPW resonator and mode profiles 52
2.14 Flux-tunable resonator circuit and mode schematic 59
2.15 Closed-form approximations for the FTR resonance frequency . 64
2.16 Flux tuning of an FTR with and without screening 70
2.17 Kerr response and Kerr cancelation in an FTR 76
2.18 Kerr-induced hysteresis in the complex transmission plane . . . 80
2.19 Voigt broadening of resonator line shapes 84

2.20 Flux transformer circuit and mutual-inductance geometry . . . 85

3.1 FEM meshes for the coupled SQUID-input-coil geometries . . . 94
3.2 COMSOL model for magnetic-shielding simulations 95
3.3 HFSS eigenmode model of a quarter-wave CPW resonator . . . 98
3.4 HFSS model of a flux-tunable resonator 99
3.5 Chip layout with bare and flux-tunable resonators 101
3.6 Wiring-layer fabrication process for the FTR chips 105
3.7 Fabricated aluminum wiring layer and coupler region 106
3.8 UBM fabrication process on the FTR bonding pads 107
3.9 Fabricated UBM on the FTR bonding pads 107
3.10 Josephson-junction fabrication process 108
3.11 Fabricated Josephson junctions and junction asymmetry 110
3.12 Aluminum patch-layer fabrication process 111
3.13 Fabricated aluminum patch layer around the SQUID junctions 112
3.14 Aluminum air-bridge fabrication process 113
3.15 Fabricated air bridges for crossovers and ground stitching . . . 114
3.16 Input-coil layouts for on-chip and flip-chip flux biasing 115
3.17 Two-chip magnetic trap and fabricated lead microparticles . . . 117
3.18 Optical setup for readout of levitated microparticle 118
3.19 Magnetic shielding for the levitation experiment 119
3.20 CAD design of the vibration isolation stage 122
3.21 Photograph of the vibration isolation stage 123
3.22 Superconducting flip-chip concept using indium microspheres . 125
3.23 Flip-chip assembly tools and alignment procedure 126
3.24 Indium microsphere before and after bonding 126
3.25 Cryogenic four-wire setup for flip-chip measurements 128
3.26 Sample holder and chip mounting for resonator spectroscopy . 130
3.27 Experimental shielding and cabling for the FTR devices 132
3.28 Microwave and dc wiring for FTR control and readout 133
3.29 dc flux-line transfer and noise analysis 134
3.30 Microwave drive thermalization and readout noise budget . . . 136
3.31 Resonator line shape and circle fit for a bare CPW resonator . 139

4.1 Optical levitation of a SnPb microsphere in the chip trap . . . 142
4.2 Optical tracking and mode spectra of a levitated microsphere . 143
4.3 Vibration transfer and noise spectra of the isolation stage . . . 146

4.4 SQUID readout and ringdown with vibration isolation 147
4.5 Cooldown-warmup plots with and without isolation stage . . . 148
4.6 Simulated magnetic shielding of a single shield geometry 150
4.7 Simulated magnetic shielding of the full experimental setup . . 150
4.8 TOF-SIMS depth profiles of the UBM thin films 153
4.9 Critical temperature and current of the UBM thin films 154
4.10 Critical temperature and current of the flip-chip devices 155
4.11 Current-dependent resistance of NbN flip-chip devices 157
4.12 Current-carrying capacity of the indium interconnect 159
4.13 HFSS simulation of the bare quarter-wave CPW resonator . . . 161
4.14 Measured transmission and circle fit of bare CPW Device A . . 162
4.15 Power dependence of the bare CPW resonator 163
4.16 Temperature dependence of the bare CPW resonator 164
4.17 Room-temperature verification of line attenuation 166
4.18 SEM images of symmetric and asymmetric Josephson junctions 167
4.19 Resistance scaling in the symmetric junction regime 167
4.20 Resistance scaling in the asymmetric junction regime 168
4.21 HFSS simulation of the 10 µm loop FTR 173
4.22 Measured transmission and circle fits of the 10 µm loop FTR . 174
4.23 Power dependence of the 10 µm loop FTR 175
4.24 Flux modulation of the 10 µm loop FTR 177
4.25 Near-single-photon transmission of the coupled FTRs 179
4.26 Temperature dependence of the 200 µm flip-chip FTR 180
4.27 Kerr nonlinearity of the coupled FTRs 182
4.28 Multiple-Φ_0 modulation of the 200 μm FTR 183
4.29 External-coil flux modulation of the coupled FTRs 184
4.30 Input-coil flux modulation of the coupled FTRs 186
4.31 Geometry dependence of the input-coil flux-transfer efficiency . 188
4.32 FEM magnetic fields for flip-chip and on-chip input coils 189
4.33 Tandem sample holder for integrated flux transfer 190
4.34 Flux-transformer demonstration with the 200 µm FTR 192
4.35 Flux-noise fits to the effective quality factor 194
4.36 Fast-trace resonance fluctuations 196
4.37 Direct repeated-trace estimate of flux noise 197
4.38 CW time-trace noise spectroscopy 198

5.1 Proposed magnetomechanical trap-FTR integration 205

5.2 Next-generation SQUID geometries 207
5.3 Flux-transfer efficiency versus SQUID screening 208
5.4 Cooperativity and feedback-cooling scaling 209

6.1 SEM images of the four UBM thin-film stacks 234
6.2 Eigenmode simulation of parasitic modes 234
6.3 Frequency-to-amplitude transduction in an FTR 236
6.4 Homodyne interferometric readout of the FTR 238

List of Tables

2.1 Superconducting parameters of materials used in this thesis . . 14
2.2 Representative parameters of the chip-based microsphere trap . 27
2.3 Analytic CPW parameters for bare and flux-tunable resonators 51

3.1 Key design parameters of the resonators 102

4.1 Simulated shielding factors and residual flux in the FTR loop . 151
4.2 Superconducting properties of the UBM thin films 154
4.3 Low-temperature properties of the flip-chip devices 158
4.4 Bare CPW resonator parameters for Device A 161
4.5 Average parameters extracted from the SQUID test-junction resistance 171
4.6 Design parameters of the three flux-tunable resonators 172
4.7 Extracted SQUID parameters of the three FTRs 178
4.8 Input-coil-to-SQUID flux-transfer efficiency 188
4.9 Flux-noise fit parameters for the three FTRs 193
4.10 Magnetomechanical coupling estimates 201

5.1 Present metrics and near-term targets for the 200 µm FTR . . 206

Acronyms

AHC	Anti-Helmholtz Coil
ASD	Amplitude Spectral Density
ATS	Asymmetrically Threaded SQUID
BCS	Bardeen-Cooper-Schrieffer
COM	Center-of-Mass
CPW	Coplanar Waveguide
CW	Continuous Wave
FEM	Finite Element Method
FTR	Flux-Tunable Resonator
FWHM	Full Width at Half Maximum
GL	Ginzburg-Landau
HEMT	High Electron Mobility Transistor
HFSS	High Frequency Structure Simulator
IQ	In-phase and Quadrature
JJ	Josephson Junction
JTWPA	Josephson Travelling-Wave Parametric Amplifier
LO	Local Oscillator
MXC	Mixing Chamber
OFHC	Oxygen-Free High-Conductivity
PEC	Perfect Electric Conductor
PSD	Power Spectral Density
RCSJ	Resistively and Capacitively Shunted Junction
RF	Radio Frequency
SEM	Scanning Electron Microscopy
SIS	Superconductor-Insulator-Superconductor

SNAIL	Superconducting Nonlinear Asymmetric Inductive eLement
SQUID	Superconducting Quantum Interference Device
TEM	Transverse Electromagnetic
TLS	Two-Level System
TOF-SIMS	Time-of-Flight Secondary Ion Mass Spectrometry
UBM	Under-Bump Metallization
VIS	Vibration Isolation System
VNA	Vector Network Analyzer

Symbols

e	Elementary charge
$\hbar$	Reduced Planck constant
k_B	Boltzmann constant
μ_0	Vacuum permeability
ε_0	Vacuum permittivity
Φ_0	Magnetic flux quantum, $h/(2e)$
Δ	Superconducting energy gap
κ_{GL}	Ginzburg-Landau parameter, λ_L/ξ
λ_L	London penetration depth
$L_{k,\square}$	Kinetic inductance per square
n_n	Normal-fluid carrier density
n_s	Superfluid carrier density
σ_1	Real part of the complex conductivity
σ_2	Imaginary part of the complex conductivity
T_c	Superconducting critical temperature

ξ	Superconducting coherence length
β_c	Stewart-McCumber parameter
C_J	Junction capacitance
E_C	Charging energy
E_J	Josephson energy
I_c	Critical current (single junction)
L_J	Josephson inductance
R_n	Normal-state resistance
α	Junction asymmetry parameter
β_L	Screening parameter, $2L_g I_0/\Phi_0$
I_0	Mean critical current of the dc SQUID
I_{circ}	Circulating current
L_g	Geometric SQUID loop inductance
$L_{g,\mathrm{cm}}$	Common-mode loop-arm inductance
L_S	Total SQUID termination inductance
$L_{S,\mathrm{core}}$	SQUID core inductance
ϕ_l	Common-mode (terminal) phase
Φ_e	Externally applied magnetic flux
Φ_s	Screened magnetic flux
φ	Differential (loop) phase
α_k	Kinetic inductance fraction
C_c	Coupling capacitance
C_l	Capacitance per unit length
C_r	Effective modal capacitance
$\varepsilon_{\mathrm{eff}}$	Effective dielectric permittivity
ε_r	Relative permittivity
κ	Total loaded linewidth, ω_r/Q_l
κ_c	Coupling linewidth, ω_r/Q_c

κ_i	Intrinsic linewidth, ω_r/Q_i
l	Resonator physical length
L_l	Inductance per unit length
L_r	Effective modal inductance
ω_r	Resonator angular frequency
Q_c	Coupling quality factor
Q_i	Intrinsic quality factor
Q_l	Loaded quality factor
S_{21}	Forward transmission coefficient
v_{ph}	Phase velocity
w	Center conductor width
Z_0	CPW characteristic impedance
Z_r	Modal characteristic impedance
γ	SQUID participation ratio
λ	Termination factor, $\cos\theta$
$\mathcal{K}$	Kerr coefficient
n_c	Intracavity photon number
n_{crit}	Critical photon number at bifurcation onset
$\mathcal{R}_\Phi$	Flux responsivity, $\partial\omega_r/\partial\Phi_e$
θ	Electrical length of resonator at operating frequency
η_1	Pickup-to-Input flux transfer efficiency
η_2	Input-to-SQUID flux transfer efficiency
η	Total flux transfer efficiency
I_{Φ_0}	Coil current per flux quantum through the SQUID loop
L_i	Input coil self-inductance
L_p	Pickup coil self-inductance
L_{wire}	Parasitic wire inductance
M	Mutual inductance (input coil to SQUID)

Φ_i	Flux in the input coil
Φ_p	Flux in the pickup coil
χ_{eff}	Effective magnetic susceptibility
N_d	Demagnetisation factor
ω_i	Trap frequency along principal direction i
R_p	Particle radius
ρ	Mass density
$\bar{n}$	Mean intracavity photon number
$\bar{n}_{\text{th}}$	Thermal phonon occupancy
C_q	Quantum cooperativity
C_0	Single-photon cooperativity
g_0	Single-photon coupling rate
G	Frequency-pull coefficient, $\partial\omega_r/\partial x$
Γ_m	Mechanical damping rate
m_{eff}	Effective mass of the mechanical mode
Ω_m	Mechanical oscillation frequency
Q_m	Mechanical quality factor
x_{zpf}	Zero-point fluctuation amplitude
n_{add}	Added noise quanta referred to device output
σ_f	Root-mean-square frequency jitter
σ_Φ	Root-mean-square flux fluctuation

CHAPTER 1

Introduction

To chase the quantum limit is to live Zeno's paradox.

Quantum mechanics is one of the most extensively tested theories in modern physics. Experimental demonstrations of the quantum superposition principle now span an extraordinary range of object sizes. They extend from single electrons [1] and atoms [2], through matter-wave interference of molecules ranging from fullerene C_{60} [3] to tailored organics beyond 25 kDa [4] and metal nanoparticles exceeding 170 kDa [5]. At the macroscopic end, superposition has also been demonstrated in superconducting circuits with distinct persistent-current states [6, 7] and, more recently, in microgram-scale mechanical resonators prepared in Schrödinger-cat states of motion [8]. Realizing and preserving such states becomes progressively more demanding with increasing size and mass of the object, even though the linear Schrödinger dynamics itself has no preferred mass or size scale. This is because coupling to the environment generally increases with system size and rapidly decoheres spatial eigenstates [9–12]. Environmental decoherence, therefore, explains why macroscopic superpositions are so difficult to observe. However, it does not, by itself, explain why measurements yield one definite outcome, which is known as the measurement

problem of quantum mechanics [11].

To address the measurement problem, several phenomenological modifications to the standard quantum theory are proposed, which introduce an intrinsic suppression of macroscopic superpositions [13–16]. In continuous spontaneous localization (CSL), the Schrödinger equation is augmented with nonlinear stochastic terms that force localization at a rate increasing with the number of constituents [14, 15]. In Diosi-Penrose-type models, the gravitational self-energy associated with different mass distributions in a superposition sets an intrinsic decoherence (or collapse) rate [15, 17, 18].

Testing these models requires massive, weakly damped mechanics operated in regimes where conventional decoherence channels are reduced below the predicted intrinsic effect [12, 15, 16]. Such an isolated system is also extremely sensitive to ultra-weak forces, making it suitable for quantum-limited inertial sensing, ranging from superconducting gravimeters to opto- and electromechanical devices approaching quantum noise limits [19–24].

Traditionally, cavity optomechanics and electromechanics couple a clamped mechanical resonator, such as a beam, membrane, or bulk-acoustic mode, to an optical or microwave cavity field [21, 22]. These platforms have enabled motional ground-state preparation by sideband cooling in both the microwave [25] and optical domains [26, 27]. Clamped resonators have also been utilized in displacement sensing near the standard quantum limit [28–30], and in nonclassical mechanical state preparation, including single-phonon control, electromechanical entanglement, and Schrödinger-cat states of motion [8, 31, 32]. At the same time, specially engineered clamped devices have reached extraordinary coherence: dissipation-diluted strained silicon nanostrings have exceeded mechanical quality factors of 10^{10} in cryogenic experiments [33], while centimeter-scale dissipation-diluted Si_3N_4 strings have reached the 10^9 range at room temperature and are projected to improve further at cryogenic temperatures [34].

Nevertheless, levitation remains compelling for reasons that go beyond the mechanical quality factor alone. By removing the physical support entirely, levitated systems eliminate clamping loss at the architectural level, thereby shifting the dominant limitations to gas collisions and blackbody-related radiative processes [35, 36]. They also permit modes such as rotational or librational modes that are not naturally available in substrate-bound resonators. Furthermore, the trap can be weakened or switched off for a certain time, allowing

free evolution of the center-of-mass motion. This is central to free-fall force sensing, wave-packet expansion, and matter-wave interferometry protocols, and is therefore attractive for macroscopic-superposition experiments [27, 37, 38]. Lastly, because the confinement is generated externally rather than by a fabricated support, the trapping landscape can be reconfigured in situ without changing the mechanical element itself. Depending on the platform, the trap frequencies and potential shape can be tuned by optical control, magnetic fields, or applied currents [37, 39, 40].

This flexibility is particularly powerful in magnetic levitation, where higher-order magnetic traps provide direct access to strongly nonharmonic potentials. In such traps, the dominant confinement can arise from hexapolar and higher multipolar fields, enabling anharmonic and double-well potentials generated by static coil arrangements with switchable currents only [40]. This makes levitated magnetomechanics attractive for preparing nonclassical motional states without requiring an additional nonlinear element coupled to the mechanics.

Optical levitation has already demonstrated motional ground-state cooling for nanoparticles [27]. However, the optical fields required for trapping introduce photon-recoil backaction and absorption-related internal heating, both of which can limit coherence. Larger particle sizes require larger optical powers for levitation, which increases these decoherence channels and effectively constrains the maximum particle size for a given dielectric material [36, 41, 42]. Similar limitations exist in electrodynamic traps such as Paul traps, which create stable confinement of charged particles [43, 44]. There, the net charge makes the motion sensitive to stray electric fields and electrode-related noise sources, both of which become increasingly problematic for larger particles [44, 45].

Magnetic levitation provides static or persistent-current trapping without photons or net charge [38, 46]. Ferromagnetic levitation above superconductors is possible, but it remains susceptible to dissipation and instability arising from magnetization dynamics, eddy-current loss, hysteresis, and moment drift [47]. Meissner-state superconductors are preferable because they closely approach the ideal diamagnetic limit and generate the restoring force through dissipationless screening currents, enabling strong passive levitation with very low intrinsic loss [38]. Quality factors above 10^9 have been projected for superconducting microspheres in such traps [38, 48], and quality factors of up to 2.6×10^7 have been demonstrated experimentally at millikelvin temperatures [49].

At Chalmers, superconducting levitation has been developed in a chip-based geometry in which patterned superconducting coils generate an anti-Helmholtz trap for Pb microspheres, and an integrated pickup coil connected to a SQUID magnetometer enables motion readout [39]. Once stable levitation is achieved, the primary challenge becomes the efficient transport and transduction of motion-induced flux signals to a superconducting detector [21, 38].

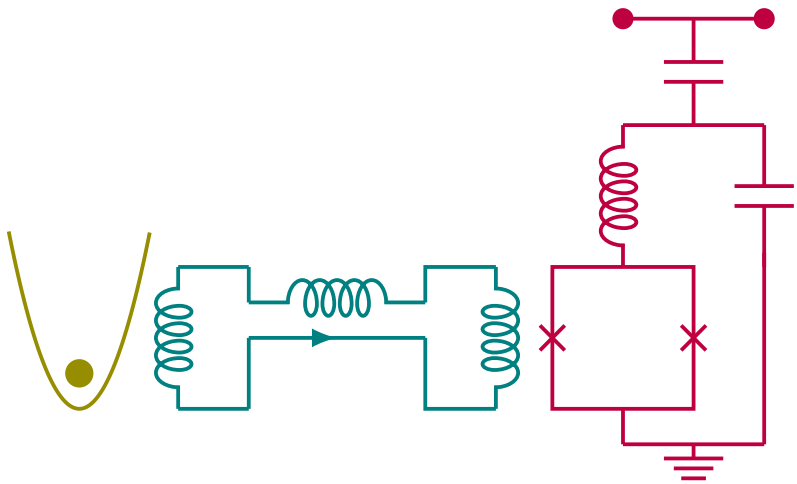

Figure 1.1: Schematic of a magnetomechanical system. Left: a superconducting microparticle levitated in a magnetic trap potential. Middle: a flux-transformer circuit that picks up the magnetic flux signal induced by particle motion and routes it to the readout circuit. Right: a superconducting LC resonator circuit with a flux-tunable inductance for readout.

For a Meissner-state superconducting particle, a displacement modifies the distribution of screening currents and thereby changes the magnetic flux coupled into a nearby pickup loop, making inductive coupling preferable in superconducting magnetomechanics [38, 46] as shown in Fig. 1.1. This contrasts with optically levitated or clamped platforms, where motion is commonly transduced via electric fields or optical scattering [22, 27, 35, 44].

Two flux-based readout strategies are particularly relevant. Direct detection with a dc-SQUID magnetometer is a standard approach for ultrasensitive flux measurement [50], and it enabled the first chip-based tracking and in-

tegrated magnetic readout of levitated superconducting microspheres [39]. However, for low-frequency mechanics, slow drifts and $1/f$-like flux noise become important [50, 51]. This motivates an alternative approach in which the same low-frequency flux signal is encoded dispersively as a phase or frequency modulation of a coherent microwave carrier.

In dispersive readout, a flux-tunable microwave resonator (FTR) converts changes in flux into a corresponding shift in resonance frequency using a flux-tunable nonlinear inductance [52, 53], for example, a superconducting quantum interference device (SQUID). A motion-induced flux modulation is then detected as phase (or frequency) modulation of a microwave probe tone. Thus, the mechanical signal is upconverted onto a gigahertz carrier [21, 54]. Operating at microwave frequencies enables homodyne detection with near-quantum-limited amplification [21, 55–57]. Therefore, microwave resonators enable a broader measurement toolbox of circuit quantum electrodynamics, including calibrated noise thermometry, measurement-based feedback control, and engineered measurement backaction [21, 22, 58]. This dispersive, cavity-based approach is the route pursued in this thesis.

Flux-tunable resonators have already been implemented in superconducting electromechanics with clamped oscillators. Rodrigues *et al.* incorporated a suspended mechanical beam into the loop of a SQUID-based microwave resonator for magnetic-flux-mediated coupling and microwave readout [59]. Zöpfl *et al.* demonstrated microwave magnetomechanical cooling of a cantilever and later exploited intrinsic cavity Kerr nonlinearity to enhance backaction cooling [60, 61]. Schmidt *et al.* implemented inductive coupling using a partly suspended SQUID integrated into a coplanar-waveguide resonator and operating in the sideband-resolved regime [62, 63]. In all of these platforms, the mechanical element is integrated into or placed in immediate proximity to the flux-tunable resonator, so the coupling is largely determined by on-chip geometry [59, 60, 62].

The present platform differs qualitatively because the levitated particle and the microwave circuit are spatially separated. The magnetic trap requires strong static fields and gradients, whereas superconducting microwave resonators are susceptible to magnetic-field-induced loss and therefore typically require careful shielding to maintain low loss [64, 65]. The motion-induced flux must therefore be transported from a pickup loop in the trap to the SQUID loop of the FTR through an external superconducting flux transformer [39, 49, 50] as

shown in Fig. 1.1. Recently, Schmidt *et al.* demonstrated such a remote magnetomechanical coupling of a levitated microparticle to an FTR [66] using macroscopic coils for trapping and flux transfer. The present system uses an on-chip trap for an integrated coupling to the readout circuit, which merits a chip-based flux transformer. The need for separating the two subsystems is further motivated by the use of aluminum-based Josephson junctions intended for low-loss microwave operation. An integrated flux-transfer interface thus becomes an essential part of the transducer itself. To this end, a flip-chip-based integration is developed in this thesis to improve flux-transfer efficiency while enabling a compact assembly in a common shielded environment.

The dispersive coupling of a magnetomechanical system is quantified by a single-photon coupling rate

$$g_0 = \frac{\partial \omega_r}{\partial \Phi} \frac{\partial \Phi}{\partial x} x_{\mathrm{zpf}},$$

where $x_{\mathrm{zpf}} = \sqrt{\hbar/(2m_{\mathrm{eff}}\Omega_m)}$ is the zero-point motional amplitude of the mechanical mode [22]. Here $\partial\omega_r/\partial\Phi$ is set by the FTR's flux responsivity at the bias point, $\partial\Phi/\partial x$ by the trap and pickup geometry, and x_{zpf} by the particle mass and trap frequency. Thus, a strong coupling requires both a large flux sensitivity and an efficient transfer to the SQUID.

In our platform, the mechanical linewidth is on the order of $\Gamma_m/2\pi \sim 1 \times 10^{-4}\,\mathrm{Hz}$ for a $\sim 100\,\mathrm{Hz}$ mode, corresponding to a mechanical quality factor of $Q_m \sim 10^6$. At millikelvin temperatures, however, the thermal occupation of such a low-frequency mode remains high, $n_{\mathrm{th}} \sim 10^7$ due to mechanical vibrations. A necessary condition for coherent quantum dynamics is that the thermal decoherence rate remains below the mechanical frequency, $\Gamma_m n_{\mathrm{th}} < \Omega_m$, or, equivalently, $Q_m > n_{\mathrm{th}}$. Thus, the relevant challenge is to suppress the thermal decoherence rate by increasing Q_m and reducing n_{th}.

On the microwave side, the single-photon coupling rate is only $g_0/2\pi \sim \mathrm{mHz}$, while the cavity linewidth is $\kappa/2\pi \sim 10\,\mathrm{MHz}$. Since $\Omega_m \ll \kappa$, the system lies deep in the unresolved-sideband regime, such that conventional sideband cooling is not available, and measurement-based feedback cooling must instead be employed [21]. Because g_0 is small, the interaction must be enhanced by driving the resonator to a large intracavity photon number n_c, which provides

a single-photon cooperativity

$$C_0 = \frac{4g_0^2}{\kappa\,\Gamma_m}.$$

Including the thermal bath occupation and the intra-cavity photon number defines quantum cooperativity

$$C_q = \frac{C}{n_{\mathrm{th}}} = \frac{4g_0^2 n_c}{\kappa\,\Gamma_m\,n_{\mathrm{th}}},$$

which should exceed unity for quantum-limited control and ground-state cooling [21, 22]. However, in a SQUID-terminated resonator, the maximum intracavity photon number is limited by the Josephson nonlinearity, which induces a Kerr shift and eventually bifurcation at high drive powers. The SQUID and junction parameters must therefore be chosen to maximize flux responsivity, and hence g_0, while keeping the Kerr nonlinearity sufficiently small to preserve a usable linear readout regime.

Thesis objectives Realizing a chip-based magnetomechanical system poses several engineering challenges, which this thesis aims to address: stable levitation, suppression of vibration and field noise, efficient flux transfer, and a readout circuit with large responsivity, low loss, and weak nonlinearity. Therefore, the goal of this thesis is to develop and characterize the superconducting subsystems required for a chip-based magnetomechanical readout of a levitated superconducting microsphere using a superconducting flux-tunable microwave resonator and a superconducting flux transformer.

Chapter 2 develops the theoretical framework for Meissner-state levitation, SQUID-terminated microwave resonators, flux-mediated coupling, and homodyne readout. **Chapter 3** describes the methods used in this thesis: finite-element modeling, nanofabrication, flip-chip assembly, vibration isolation, cryogenic wiring, and data analysis. **Chapter 4** presents the experimental results of chip-based levitation and optical characterization (Paper I), establishes the need for and characterizes vibration isolation and magnetic shielding, develops a superconducting flip-chip bonding technique (Paper II), and characterizes bare and flux-tunable resonators with on-chip and flip-chip input coils, including tunability, Kerr effects, flux noise, and coupling efficiency (Paper III). **Chapter 5** summarizes the results and identifies the steps toward

full magnetomechanical readout and cooling: reducing parasitic inductance, suppressing flux noise, reducing Kerr effects, and upgrading the readout chain.

CHAPTER 2

Theory

First assume a harmonic oscillator.
Then apologize to the SQUID.

This chapter presents the theory required to describe a magnetomechanical experiment where a levitated superconducting microsphere is read out with a flux-tunable microwave resonator (FTR). The chapter first reviews the superconducting theory needed to describe magnetic levitation and the microwave circuit. In particular, the Josephson junction and the dc SQUID model are presented, including junction asymmetry and finite screening. This description is then used to obtain the FTR mode equation, flux tuning, and Kerr nonlinearity. The chapter ends by introducing flux noise and magnetomechanical coupling.

2.1 Superconductivity

Superconductivity is a macroscopic quantum state characterized by (i) vanishing dc resistivity in the superconducting phase below a material-specific critical temperature T_c, and (ii) magnetic field expulsion in the Meissner state below the relevant critical field scale. It was discovered by Kamerlingh Onnes in 1911

in mercury at 4.2 K [67]. In the Meissner state, superconductors support persistent currents and exhibit an ideal diamagnetic response. The superconducting state breaks down when temperature, magnetic field, or current exceed their critical values due to pair breaking.

2.1.1 Meissner-Ochsenfeld effect

The Meissner-Ochsenfeld effect is the active expulsion of magnetic fields from the bulk of a superconductor upon cooling below T_c, discovered in 1933 [68]. This effect distinguishes a superconductor from a hypothetical perfect conductor, which would retain whatever field was present when its resistivity vanished (Fig. 2.1).

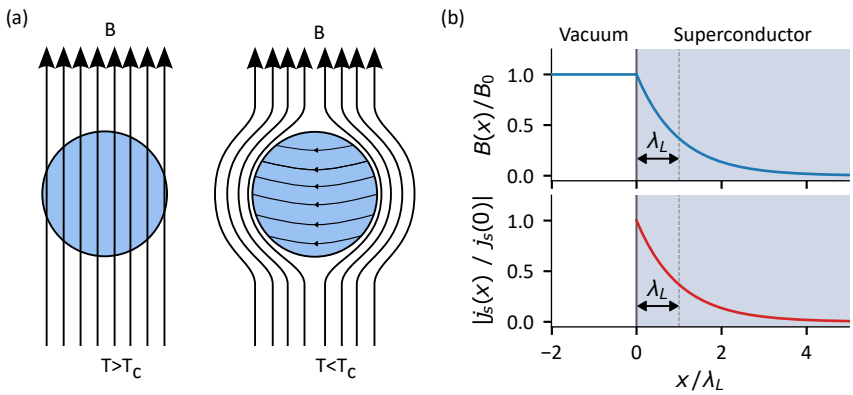

Figure 2.1: Meissner-Ochsenfeld effect. (a) Above T_c, the field fully penetrates the material. Below T_c, it is expelled by screening currents in a thin surface layer. (b) Normalized magnetic field $B(x)/B_0$ (top) and screening current density $|j_s(x)|/|j_s(0)|$ (bottom) versus depth, showing exponential decay over λ_L.

Fritz and Heinz London provided a phenomenological description of this behavior in 1935 [69, 70]. They proposed two equations relating the supercurrent density $\mathbf{j}_s$ to the electromagnetic fields:

$$\frac{\partial \mathbf{j}_s}{\partial t} = \frac{n_s e^2}{m_e}\,\mathbf{E}, \tag{2.1}$$

$$\nabla \times \mathbf{j}_s = -\frac{n_s e^2}{m_e}\,\mathbf{B}, \tag{2.2}$$

where n_s is the density of superconducting charge carriers, e is the magnitude of the elementary charge, and m_e is the electron mass. Eq. (2.1) describes dissipationless current flow, while Eq. (2.2) implies that any magnetic field induces a screening supercurrent, giving rise to the Meissner-Ochsenfeld effect.

In the magnetostatic limit, Ampère's law reduces to $\nabla \times \mathbf{B} = \mu_0 \mathbf{j}_s$. Combining this with Eq. (2.2) yields

$$\nabla^2 \mathbf{B} = \frac{1}{\lambda_L^2}\,\mathbf{B}, \tag{2.3}$$

$$\lambda_L = \sqrt{\frac{m_e}{\mu_0 n_s e^2}}, \tag{2.4}$$

where λ_L is the London penetration depth.

For a planar superconductor surface at $x = 0$, the one-dimensional solution to Eq. (2.3) gives the B-field decay as

$$B(x) = B_0\, e^{-x/\lambda_L}, \tag{2.5}$$

Then, using Ampère's law, we obtain the screening current density

$$j_s(x) = \frac{B_0}{\mu_0 \lambda_L}\, e^{-x/\lambda_L}, \tag{2.6}$$

The equations show exponential attenuation of both field and current into the bulk over a length scale $\sim \lambda_L$ (Fig. 2.1(b)). The screening current cancels the applied field in the interior.

2.1.2 Two-fluid model

The London equations treat the supercarrier density n_s as a constant, leaving its temperature dependence unspecified. Gorter and Casimir [71] addressed this

in 1934 by modeling a superconductor as containing two interpenetrating fluids: a superfluid component with density n_s that carries current without dissipation, and a normal component with density n_n that scatters and contributes to resistive losses. The total carrier density n is fixed, and the two fractions obey $n = n_s(T) + n_n(T)$. At $T = 0$, all carriers are in the superfluid. On the other hand, at $T = T_c$, the superfluid fraction vanishes, and the material becomes normal-conducting.

By fitting the thermodynamic data available at the time (in particular, the parabolic temperature dependence of the critical field), Gorter and Casimir obtained [70, 71]

$$\frac{n_s(T)}{n} = 1 - \tau^4, \qquad \frac{n_n(T)}{n} = \tau^4, \qquad \tau \equiv \frac{T}{T_c}. \tag{2.7}$$

This quartic power law is empirical. BCS theory later provided a microscopic justification that agrees with Eq. (2.7) to within a few percent over most of the temperature range [70]. Eq. (2.7) is plotted in Fig. 2.2.

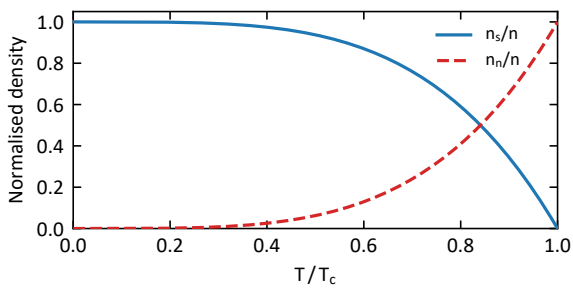

Figure 2.2: Temperature dependence of the superfluid fraction n_s/n and the normal fraction n_n/n according to the two-fluid model (Eq. (2.7)).

Temperature-dependent penetration depth. Substituting Eq. (2.7) into the London penetration depth (Eq. (2.4)) gives its temperature dependence:

$$\lambda_L(T) = \frac{\lambda_L(0)}{\sqrt{1 - \tau^4}}, \tag{2.8}$$

where $\lambda_L(0) = \sqrt{m_e/(\mu_0 n e^2)}$ is the zero-temperature value. As $T \to T_c$ the superfluid density vanishes and the penetration depth diverges, reflecting the

loss of screening. This divergence marks the breakdown of the Meissner state. Near $T = 0$, $\lambda_L(T)$ is nearly constant because the normal fraction is negligibly small. The temperature-dependent penetration depth enters directly into the kinetic inductance (Sec. 2.1.6) and, through it, into the resonance frequency of superconducting microwave circuits [72].

Temperature-dependent critical current. The two-fluid model also provides the temperature dependence of the critical current in a superconducting thin film or wire. The critical (depairing) current density is proportional to the superfluid density and the maximum drift velocity of the condensate. Within the Ginzburg-Landau framework, the depairing current density scales as $j_d \propto n_s(T)^{3/2}$ [70]. A simpler and widely used approximation follows from the assumption that the critical current is proportional to the superfluid fraction:

$$I_c(T) = I_{c0}\left(1 - \tau^4\right), \tag{2.9}$$

where I_{c0} is the zero-temperature critical current. This expression does not capture the exact GL depairing scaling near T_c, but it agrees well with measured data for thin-film superconductors such as Nb, NbN, and Al studied in Paper II and in the literature [73, 74]. In Sec. 4.4, Eq. (2.9) is used to fit the measured critical currents of the UBM thin films and flip-chip devices.

2.1.3 Ginzburg-Landau theory

Ginzburg and Landau [75] introduced a complex order parameter $\Psi(\mathbf{r})$, whose squared magnitude $|\Psi|^2$ gives the local density of superconducting carriers:

$$\Psi(\mathbf{r}) = |\Psi(\mathbf{r})|\, e^{i\theta(\mathbf{r})}, \tag{2.10}$$

where $\theta(\mathbf{r})$ is the macroscopic quantum phase. A second characteristic length scale is the coherence length

$$\xi = \sqrt{\frac{\hbar^2}{2m^*|\alpha_{\mathrm{GL}}|}}, \tag{2.11}$$

where α_{GL} is the temperature-dependent coefficient of the Ginzburg-Landau free energy. The coherence length ξ sets the distance over which the Cooper

pair density recovers from a local suppression, e.g., near a vortex core or a superconductor-normal conductor interface [70]. The ratio $\kappa_{\mathrm{GL}} = \lambda_L/\xi$ (Ginzburg-Landau parameter) determines whether a superconductor is Type-I ($\kappa_{\mathrm{GL}} < 1/\sqrt{2}$) or Type-II ($\kappa_{\mathrm{GL}} > 1/\sqrt{2}$) [76]. Type-I superconductors exhibit a single critical field H_c, above which superconductivity is destroyed. Type-II superconductors remain in the Meissner state below a lower critical field H_{c1} but enter a mixed state for $H_{c1} < H < H_{c2}$, where magnetic flux penetrates as quantized Abrikosov vortices, each carrying a single flux quantum. The critical fields are approximately $\mu_0 H_{c1} \approx (\Phi_0/4\pi\lambda_L^2)\ln\kappa_{\mathrm{GL}}$ and $\mu_0 H_{c2} = \Phi_0/(2\pi\xi^2)$ [70]. Table 2.1 lists typical bulk superconducting parameters for the materials used in this thesis.

Table 2.1: Typical bulk superconducting parameters at zero temperature for the materials used in this thesis. Al is used for the resonator wiring and junction electrode material, In is used for superconducting microbump interconnects, Pb is the levitated microsphere, and Nb and NbN are used as UBM. Elemental values are compiled from Tinkham [70] unless otherwise noted.

Material	T_c (K)	$\lambda(0)$ (nm)	ξ_0 (nm)	κ_{GL}	Type	$\mu_0 H_c(0)$ (mT)	$\Delta(0)$ (meV)
Al	1.18	50-100	1600	0.03	I	10.5	0.18
In	3.41	65	360	0.18	I	23.0	0.54
Pb	7.20	39	83	0.47	I	80.3	1.35
Pb-Sn[a]	7.0-7.2	40-50	50-80	0.5-1	I/II	70-80	1.2-1.4
Nb	9.25	85	40	2.1	II[b]	198[c]	1.50
NbN[d]	10-16	200-400	3-5	>50	II	–	∼2.5

[a]Pb-Sn properties depend on composition. Stated values are for Pb-rich solder (>60% Pb) [77].
[b]Type-II in the dirty limit but intrinsically Type-I in the clean limit, where $\kappa_{\mathrm{GL}}(T_c) = 0.123$ and $\kappa_{\mathrm{GL}}(0) = 0.355$ [78].
[c]The upper critical field is $\mu_0 H_{c2}(0) \approx 440\,\mathrm{mT}$ [79].
[d]NbN properties depend strongly on stoichiometry [80] and $\mu_0 H_{c2}(0)$ can exceed 20 T [81].

2.1.4 BCS theory and Cooper pairing

Bardeen, Cooper, and Schrieffer (BCS) explained the microscopic origin of superconductivity in 1957 [82]. Electrons near the Fermi surface form bound

pairs (Cooper pairs) through a retarded phonon-mediated interaction. This means that the relaxation of the lattice polarization left by one electron is slow enough to attract a second electron, producing a net attractive interaction despite the Coulomb repulsion (Fig. 2.3).

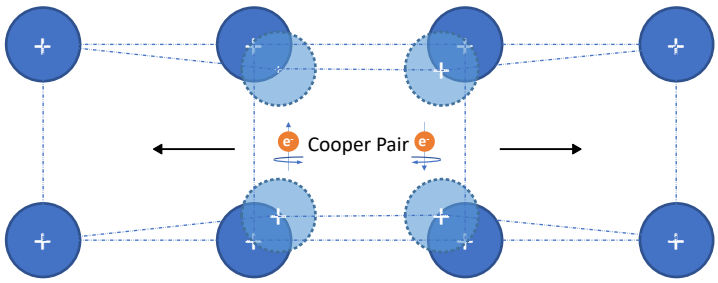

Figure 2.3: Phonon-mediated Cooper pair formation. An electron distorts the lattice, creating a region of increased positive charge density that attracts a second electron. The paired electrons have opposite spin and momentum.

The resulting Cooper pairs have opposite spin and momentum ($\mathbf{k}\uparrow, -\mathbf{k}\downarrow$) and behave as composite bosons that condense into a macroscopic ground state below T_c. Breaking a pair requires an energy exceeding the superconducting gap Δ, creating quasiparticle excitations. At zero temperature, BCS theory predicts [70]

$$\Delta(0) = 1.764\, k_B T_c, \tag{2.12}$$

where k_B is the Boltzmann constant. This BCS weak-coupling relation is approximately satisfied by Al, In, and Nb [70, 83].

The gap also determines the microwave electrodynamic response. Mattis and Bardeen [84] derived the complex conductivity $\sigma(\omega) = \sigma_1(\omega, T) - i\sigma_2(\omega, T)$, where σ_1 describes quasiparticle dissipation and σ_2 the reactive condensate response. For $\hbar\omega < 2\Delta$ and $k_B T \ll \Delta$, σ_1 is exponentially suppressed, while σ_2 grows roughly as $\sigma_2(\omega, T) \sim (\pi\Delta/\hbar\omega)\,\sigma_n$ in the local dirty limit, where σ_n is the normal-state conductivity scale [70, 72]. The reactive response can be expressed through an effective penetration depth via

$$\lambda_{\text{eff}}^{-2}(\omega, T) = \mu_0\, \omega\, \sigma_2(\omega, T), \tag{2.13}$$

which approaches the London penetration depth at low temperatures and for frequencies well below the gap. The ratio σ_1/σ_2 sets the quasiparticle-limited intrinsic quality factor of a superconducting resonator through $Q_i^{-1} \propto \sigma_1/\sigma_2$ [72].

2.1.5 Fluxoid quantization

Macroscopic phase coherence requires the condensate phase to be single-valued around any closed superconducting path, leading to the quantization of the fluxoid in units of the magnetic flux quantum $\Phi_0 = h/(2e) \approx 2.068 \times 10^{-15}$ Wb.

Consider a closed contour $\mathcal{C}$ lying entirely within a superconductor and enclosing a surface $\mathcal{S}$. In Ginzburg-Landau theory, the supercurrent density $\mathbf{j}_s$ is related to the order-parameter phase θ and the magnetic vector potential $\mathbf{A}$ via

$$\mathbf{j}_s = \frac{e\, n_s}{2m_e}\big(\hbar\, \nabla\theta - 2e\, \mathbf{A}\big), \tag{2.14}$$

with n_s as defined in Sec. 2.1.1.

Rearranging Eq. (2.14) and integrating around $\mathcal{C}$ yields

$$\hbar \oint_{\mathcal{C}} \nabla\theta \cdot d\boldsymbol{\ell} = \frac{2m_e}{e\, n_s} \oint_{\mathcal{C}} \mathbf{j}_s \cdot d\boldsymbol{\ell} + 2e \oint_{\mathcal{C}} \mathbf{A} \cdot d\boldsymbol{\ell}. \tag{2.15}$$

By Stokes' theorem, $\oint_{\mathcal{C}} \mathbf{A} \cdot d\boldsymbol{\ell} = \iint_{\mathcal{S}} \mathbf{B} \cdot d\mathbf{S} \equiv \Phi_s$, where Φ_s is the total magnetic flux through the loop. The single-valuedness of the order parameter enforces $\oint_{\mathcal{C}} \nabla\theta \cdot d\boldsymbol{\ell} = 2\pi n$ with $n \in \mathbb{Z}$. Substituting into Eq. (2.15) gives the fluxoid quantization

$$\Phi_s + \frac{m_e}{e^2\, n_s} \oint_{\mathcal{C}} \mathbf{j}_s \cdot d\boldsymbol{\ell} = n\, \Phi_0, \qquad \Phi_0 = \frac{h}{2e}. \tag{2.16}$$

The second term is the condensate-momentum contribution associated with the loop supercurrent. In the thin-wire limit discussed below, it becomes the kinetic-inductance term $L_k I_s$. This term distinguishes fluxoid quantization from pure flux quantization.

Inductance-based formulation. For a thin-wire loop carrying a screening current I_s and having a local cross-section $S(s)$,

$$\mathbf{j}_s(s) \cdot d\boldsymbol{\ell} \approx \frac{I_s}{S(s)}\, ds, \tag{2.17}$$

so that the supercurrent contribution in Eq. (2.16) becomes

$$\frac{m_e}{e^2 n_s} \oint_{\mathcal{C}} \mathbf{j}_s \cdot d\boldsymbol{\ell} \approx \frac{m_e}{e^2 n_s} \oint_{\mathcal{C}} \frac{I_s}{S(s)}\, ds = L_k I_s. \tag{2.18}$$

This defines the loop kinetic inductance L_k for a uniform wire of length ℓ and cross-section S as

$$L_k \equiv \frac{m_e}{e^2 n_s} \oint_{\mathcal{C}} \frac{ds}{S(s)} = \frac{m_e}{e^2 n_s} \frac{\ell}{S}. \tag{2.19}$$

The loop flux Φ_s consists of the externally applied flux Φ_e and the self-flux generated by the loop supercurrent. Defining the geometric (magnetostatic) inductance L_g by $\Phi_{\text{self}} = L_g I_s$ gives

$$\Phi_s = \Phi_e + L_g I_s. \tag{2.20}$$

With this sign convention, a screening current corresponds to $I_s < 0$ when $\Phi_e > 0$.

Substituting Eq. (2.20) and the kinetic inductance contribution into Eq. (2.16) yields

$$\Phi_e + (L_g + L_k)\, I_s = n\, \Phi_0. \tag{2.21}$$

Thus, Φ_e sets the applied bias, and the loop current adjusts to satisfy the fluxoid constraint. In later sections on dc SQUIDs, the circulating current is defined with a different sign convention, so the screening relation is written with a different sign for the self-flux term. In addition, the kinetic-inductance contribution is neglected.

Flux quantization as a limiting case. If the contour $\mathcal{C}$ is chosen deep within the bulk of a thick superconductor, farther than λ_{L} from any surface, Meissner screening implies $\mathbf{j}_s = 0$ along $\mathcal{C}$. The supercurrent term then vanishes, and

Eq. (2.16) reduces to pure flux quantization

$$\Phi_s = n\,\Phi_0. \tag{2.22}$$

2.1.6 Kinetic inductance

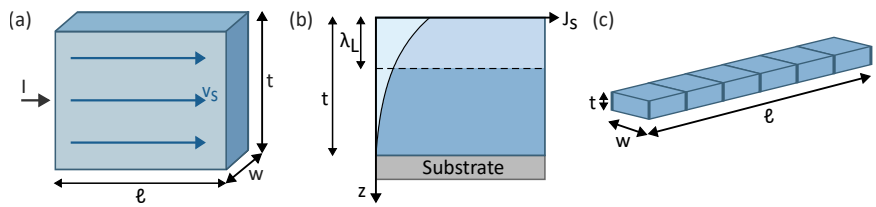

Figure 2.4: Kinetic inductance in thin films. (a) Uniform superconducting wire of length ℓ and cross-sectional area $A = w \cdot t$, carrying current I via Cooper-pair drift at velocity v_s. The kinetic energy $E_{\text{kin}} = \frac{1}{2} L_k I^2$ defines $L_k = \mu_0 \lambda_L^2\, \ell/A$, which grows with λ_L^2 and diverges for narrow, thin traces. (b) Cross-section of a superconducting film of thickness t on a substrate, illustrating the role of the penetration depth λ_L. In thick films, magnetic field and current density are concentrated near the surfaces over a distance of order λ_L, whereas in thin films with $t \lesssim \lambda_L$ the current distribution extends across the full thickness. The two hues distinguish the near-surface screening region from the interior. (c) A long thin-film strip of total length ℓ and width w tiled into ℓ/w square sections in series, each contributing one sheet inductance $L_{k,\square} = \mu_0 \lambda_L^2/t$ ($t \ll \lambda_L$), and the total kinetic inductance is $L_k = L_{k,\square}\, \ell/w$.

The kinetic inductance L_k introduced in Eq. (2.21) quantifies the energy stored in superfluid inertia, as opposed to the geometric inductance L_g derived from the energy stored in the magnetic field.

Uniform-current limit. For a uniform superconducting wire of length ℓ, cross-sectional area A, and condensate drift velocity v_s (Fig. 2.4(a)), the kinetic energy of the Cooper pairs is

$$E_{\text{kin}} = \frac{1}{2}\left(\frac{n_s}{2}\right) m^* v_s^2\, A\ell = \frac{1}{2}\, n_s\, m_e\, v_s^2\, A\ell, \tag{2.23}$$

where n_s is the superconducting electron density and $m^* = 2m_e$ is the Cooper-pair mass. The supercurrent is $I = 2e\,(n_s/2)\,A\,v_s = e\,n_s\,A\,v_s$. Eliminating v_s gives

$$E_{\text{kin}} = \frac{1}{2}\,L_k\,I^2, \tag{2.24}$$

with

$$L_k = \frac{m_e}{e^2 n_s}\,\frac{\ell}{A}, \tag{2.25}$$

$$= \mu_0 \lambda_L^2\,\frac{\ell}{A}, \tag{2.26}$$

where $\lambda_L^2 = m_e/(\mu_0 e^2 n_s)$. Hence, L_k scales as λ_L^2/A and becomes significant in narrow, thin traces or high-λ_L materials [85].

Thin-film limit and sheet inductance. For a superconducting film of thickness t, the sheet, or per-square, kinetic inductance is more useful than the bulk form in Eq. (2.26). Since "per square" refers to a dimensionless geometric ratio, $L_{k,\square}$ still carries units of henry. The thin-film enhancement of $L_{k,\square}$ arises because reducing the film thickness lowers the sheet superfluid density $n_s t$, so the same current requires a larger condensate velocity and, therefore, a larger kinetic-energy cost. Equivalently, since $L_k \propto 1/A$, reducing the available cross-sectional area enhances the kinetic inductance. A strip of length ℓ and width w can be viewed as ℓ/w squares in series (Fig. 2.4(c)), so that the total kinetic inductance is $L_k = L_{k,\square}\,\ell/w$. Within local London electrodynamics, the sheet kinetic inductance is

$$L_{k,\square} = \mu_0 \lambda_L \coth\!\left(\frac{t}{\lambda_L}\right), \tag{2.27}$$

which reduces in the thin-film limit to

$$L_{k,\square} \approx \frac{\mu_0 \lambda_L^2}{t}, \qquad (t \ll \lambda_L), \tag{2.28}$$

and approaches $L_{k,\square} \approx \mu_0 \lambda_L$ for $t \gg \lambda_L$. Here λ_L should be understood as the effective penetration depth of the film, which can be modified by disorder, temperature, and proximity effects. For a strip of width w, the

kinetic inductance is then $L_k = (L_{k,\square}\,\ell)/w$, which is relevant for designing microwave elements, as discussed in Sec. 2.5.2. In high-λ_L superconductors such as granular aluminum or NbN, kinetic inductance can dominate over geometric inductance [86].

Because $L_k \propto \lambda_L^2$, any mechanism that reduces the superfluid density, including disorder or the inverse proximity effect from adjacent normal-metal layers, increases the kinetic inductance of the film.

2.1.7 Proximity effect

Certain thin-film devices in this thesis employ normal-metal (N) as a capping layer in direct contact with a superconducting layer (S). Such S-N heterostructures can exhibit the superconducting proximity effect, which modifies the effective superconducting properties of the stack, including the superconducting gap Δ, the transition temperature T_c, and the electrodynamic response [87–89].

At an S-N interface, Andreev reflection transfers superconducting pair correlations from the superconductor into the normal metal [90, 91]. These correlations decay in the normal metal over a characteristic coherence length

$$\xi_N = \frac{\hbar v_F}{2\pi k_B T} \tag{2.29}$$

in the clean limit, and

$$\xi_N = \sqrt{\frac{\hbar \mathcal{D}}{2\pi k_B T}} \tag{2.30}$$

in the dirty limit [70], where v_F is the Fermi velocity, $\mathcal{D}$ is the diffusion constant, k_B is Boltzmann's constant, and T is the temperature of the film. In the dirty limit, $\mathcal{D} \approx v_F l_e/3$, with l_e the elastic mean free path. If the normal-metal thickness is smaller than ξ_N, the induced pair correlations extend across the full N layer, so the N layer acquires a superconducting-like electrodynamic response through its contact with S. This induced order in N is the superconducting proximity effect.

Since N cannot sustain a superconducting gap in the bulk far beyond ξ_N, the leakage of pair correlations into N reduces the pair amplitude available in S near the interface, causing an inverse proximity effect. This means a suppression of $\Delta(\mathbf{r})$ in S over a distance of the order of ξ_S, where ξ_S is the superconducting coherence length.

When the superconducting film thickness d_S becomes comparable to or smaller than ξ_S, this suppression is no longer confined to a narrow interfacial region but extends across much of the entire film thickness. The thickness-averaged superconducting gap is then reduced, which in turn lowers the transition temperature T_c. In the weak-coupling BCS limit, this follows from the approximate proportionality $\Delta(0) \propto k_B T_c$ [70].

This effect plays a role in the thin Au capping layer in the UBM stack, which induces an inverse proximity effect and thereby slightly reduces the effective superconducting properties of Nb- or NbN-based films.

2.2 Magnetic levitation of superconductors

This section shows that the Meissner-state diamagnetic response enables stable levitation of a superconducting particle in a quadrupole-like magnetic field. Stable levitation in a potential U requires an equilibrium point $\mathbf{r}_{\mathrm{eq}}$ satisfying

$$\nabla U(\mathbf{r}_{\mathrm{eq}}) = 0, \tag{2.31}$$

together with a positive-definite Hessian at $\mathbf{r}_{\mathrm{eq}}$, that is,

$$\delta\mathbf{r}^{\mathsf{T}}\, H(\mathbf{r}_{\mathrm{eq}})\, \delta\mathbf{r} > 0 \qquad \text{for } \delta\mathbf{r} \neq 0, \tag{2.32}$$

where the Hessian matrix is defined by

$$H_{ij}(\mathbf{r}_{\mathrm{eq}}) = \left.\frac{\partial^2 U}{\partial r_i \partial r_j}\right|_{\mathbf{r}_{\mathrm{eq}}}. \tag{2.33}$$

This means that the potential energy increases for any sufficiently small displacement away from the equilibrium point, so that $\mathbf{r}_{\mathrm{eq}}$ is a local minimum.

Since the Hessian is real and symmetric, it can always be diagonalized at $\mathbf{r}_{\mathrm{eq}}$. In the corresponding principal-axis basis, the mixed second derivatives vanish, and the stability condition reduces to requiring positive curvature along each principal direction:

$$\left.\frac{\partial^2 U}{\partial x^2}\right|_{\mathbf{r}_{\mathrm{eq}}} > 0, \qquad \left.\frac{\partial^2 U}{\partial y^2}\right|_{\mathbf{r}_{\mathrm{eq}}} > 0, \qquad \left.\frac{\partial^2 U}{\partial z^2}\right|_{\mathbf{r}_{\mathrm{eq}}} > 0. \tag{2.34}$$

2.2.1 Earnshaw's theorem

In the vacuum region occupied by the particle, and away from conductors and magnetic materials, $J_{\text{free}} = 0$ and $\mathbf{M} = 0$. Magnetostatics is then governed by $\nabla \times \mathbf{B} = 0$ and $\nabla \cdot \mathbf{B} = 0$. A magnetic scalar potential $\phi_m(\mathbf{r})$ may therefore be introduced such that $\mathbf{B}(\mathbf{r}) = -\nabla\phi_m(\mathbf{r})$. The absence of magnetic charge implies that the scalar potential satisfies Laplace's equation

$$\nabla^2\phi_m(\mathbf{r}) = 0, \tag{2.35}$$

that is, $\phi_m(\mathbf{r})$ is a harmonic function in the source-free region. Here, "harmonic" refers to satisfying Laplace's equation, not to a quadratic confining potential.

Earnshaw's theorem states that stable three-dimensional static equilibrium cannot be obtained for a body whose interaction energy in a source-free static field is determined by fixed magnetic multipole moments [92]. For a permanent magnetic dipole with a fixed moment $\mathbf{m}$, the potential energy is

$$U_{\text{dip}}(\mathbf{r}) = -\mathbf{m} \cdot \mathbf{B}(\mathbf{r}) = \mathbf{m} \cdot \nabla\phi_m(\mathbf{r}). \tag{2.36}$$

Since ϕ_m is harmonic, U_{dip} is harmonic as well and obeys $\nabla^2 U_{\text{dip}} = 0$, and therefore cannot exhibit a strict local minimum in the interior of a source-free region. Stationary points satisfying $\nabla U_{\text{dip}} = 0$ can therefore only be saddles, implying instability along at least one direction. For a free permanent magnet, the magnetic moment aligns with the local field, so the potential energy is minimized by moving toward regions of larger field magnitude. It is therefore a high-field seeker. Stable levitation would then require a point where the field magnitude has a local maximum. However, such a maximum cannot exist inside a source-free static magnetic field. Therefore, a permanent magnet cannot be stably levitated in free space using static magnetic fields alone.

In contrast, diamagnets are not excluded by Earnshaw's theorem in this form because their magnetic moment is induced by the applied field rather than being a fixed multipole moment. For a diamagnetic body in the linear-response regime, the magnetic potential energy is proportional to B^2:

$$U_{\text{dia}}(\mathbf{r}) = -\frac{\chi_{\text{eff}} V}{2\mu_0} B^2(\mathbf{r}), \tag{2.37}$$

where $\chi_{\text{eff}} < 0$ for a diamagnet. In contrast to the field components, $B^2(\mathbf{r})$

is generally not a harmonic function. In a current-free region, it satisfies

$$\nabla^2\left(B^2\right) = 2\sum_{i,j}\left(\frac{\partial B_i}{\partial x_j}\right)^2 \geq 0, \tag{2.38}$$

so local minima of B^2 are permitted. For $\chi_{\text{eff}} < 0$, Eq. (2.37) implies $U_{\text{dia}} \propto +B^2$, and confinement may therefore be provided by a local minimum of B^2. This possibility was established experimentally and theoretically by Braunbeck [93, 94].

A Meissner-state superconductor approaches the ideal bulk diamagnetic limit $\chi \to -1$. For particles much larger than the London penetration depth, the magnetic field is expelled from the interior, so the superconductor behaves as a strong low-field seeker and is therefore well suited for levitation in a static magnetic field.

2.2.2 Meissner-state trapping

For a spherical particle of radius a with $a \gg \lambda_L$, the magnetic potential energy is [95]

$$U_{\text{mag}}(\mathbf{r}) = -\frac{\chi_{\text{eff}}}{2\mu_0}\int_V \left|\mathbf{B}_{\text{ext}}(\mathbf{r}+\boldsymbol{\rho})\right|^2 \, d^3\boldsymbol{\rho}, \tag{2.39}$$

where $\mathbf{r}$ is the center-of-mass position of the particle, $\boldsymbol{\rho}$ is the integration coordinate within the particle volume V, a is the particle radius, λ_L is the London penetration depth, and $\mathbf{B}_{\text{ext}}$ is the externally applied magnetic field.

In the point-particle limit, where the field varies negligibly across the particle volume, the total potential energy, including gravity, becomes

$$U(\mathbf{r}) = -\frac{\chi_{\text{eff}}V}{2\mu_0}\left|\mathbf{B}_{\text{ext}}(\mathbf{r})\right|^2 + Mgz, \tag{2.40}$$

where χ_{eff} is the effective susceptibility that accounts for the demagnetizing effect of the particle shape (see Eq. (2.46)), M is the particle mass, g is the gravitational acceleration, and z is the height above the chip surface. The magnetic force is

$$\mathbf{F}_{\text{mag}} = -\nabla U_{\text{mag}} = \frac{\chi_{\text{eff}}V}{2\mu_0}\nabla\left(B_{\text{ext}}^2\right) = \frac{\chi_{\text{eff}}V}{\mu_0}\left(\mathbf{B}_{\text{ext}}\cdot\nabla\right)\mathbf{B}_{\text{ext}}. \tag{2.41}$$

At equilibrium, the magnetic force balances gravity,

$$\mathbf{F}_{\mathrm{mag}}(\mathbf{r}_{\mathrm{eq}}) = -Mg\,\hat{\mathbf{z}}. \tag{2.42}$$

2.2.3 On-chip magnetic trap

The magnetic field generated by a circular current loop of radius a carrying current I follows from the Biot-Savart law [95]:

$$\mathbf{B}(\mathbf{r}) = \frac{\mu_0 I}{4\pi} \oint \frac{d\boldsymbol{\ell}' \times (\mathbf{r} - \mathbf{r}')}{|\mathbf{r} - \mathbf{r}'|^3}, \tag{2.43}$$

where $\mathbf{r}'$ traces the current path and $d\boldsymbol{\ell}'$ is the differential line element. For a loop centered at the origin in the xy-plane, the field components can be written analytically in terms of complete elliptic integrals of the first and second kinds.

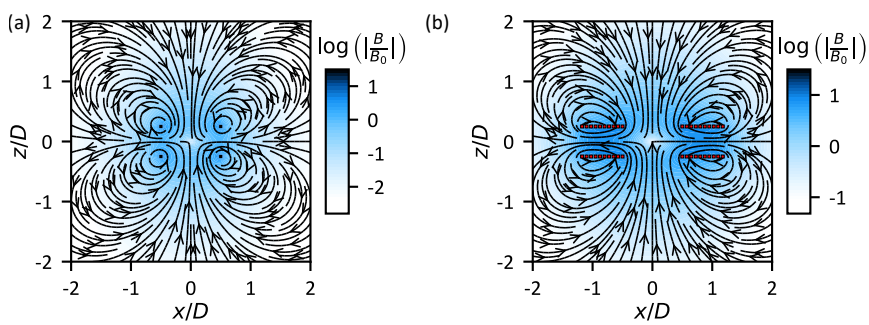

Figure 2.5: Magnetic field $\log(|B/B_0|)$ in the xz-plane for an anti-Helmholtz coil (AHC) configuration with (a) a single-turn pair and (b) a multi-turn pair ($N = 10$), where $B_0 = \mu_0 I/d$ and d is the coil spacing. Square dots represent the cross-section of the coils at $z = \pm d/4$ that carry opposite currents, producing a quadrupole field that vanishes at the origin. Black lines indicate the magnetic field direction, while the coil cross-sections are shown in red.

Anti-Helmholtz coil (AHC) trap. Two planar coils with N turns are arranged in an anti-Helmholtz configuration with opposite current directions; see Fig. 2.5. The single-turn case (Fig. 2.5(a)) produces the basic quadrupole structure, while additional windings (Fig. 2.5(b)) steepen the field gradient and increase

the trap frequencies. The coil separation is set by the chip thickness. Near the trap center, Maxwell's equation $\nabla \cdot \mathbf{B} = 0$ requires the principal gradients to satisfy $G_x + G_y + G_z = 0$. For an ideal axially symmetric anti-Helmholtz geometry, this reduces to

$$G_x = G_y = -\frac{G_z}{2}, \tag{2.44}$$

so that $|G_z| = 2|G_x| = 2|G_y|$ and therefore $\omega_z = 2\omega_x = 2\omega_y$ [96].

Trap frequencies and stability

Returning to the superconducting sphere with $R \gg \lambda_L$ and $\chi = -1$ as introduced above, the potential energy in a magnetic field is [95]

$$U = -\frac{\chi_{\text{eff}}}{2\mu_0} B^2 V + mgz. \tag{2.45}$$

For a finite-sized object, the demagnetizing field modifies the effective susceptibility [39, 95]:

$$\chi_{\text{eff}} = \frac{\chi}{1 + N_d \chi}. \tag{2.46}$$

For a sphere, $N_d = 1/3$ [97], which, together with $\chi = -1$, yields $\chi_{\text{eff}} = -3/2$.

Near the magnetic field minimum of an anti-Helmholtz trap, the field vanishes and increases linearly with displacement. In the principal-axis basis, the field may be written as

$$B_i \approx \left.\frac{\partial B_i}{\partial r_i}\right|_{\mathbf{r}=0} r_i, \tag{2.47}$$

For a superconducting sphere with $\chi_{\text{eff}} = -3/2$, the magnetic potential is therefore harmonic near the trap center, with spring constants

$$k_i = \left.\frac{\partial^2 U}{\partial r_i^2}\right|_{\mathbf{r}=0} = \frac{3V}{2\mu_0} \left(\left.\frac{\partial B_i}{\partial r_i}\right|_{\mathbf{r}=0} \right)^2. \tag{2.48}$$

Using $V = m/\rho$, the trap frequency along the direction i becomes

$$\omega_i = \left| \left.\frac{\partial B_i}{\partial r_i}\right|_{\mathbf{r}=0} \right| \sqrt{\frac{3}{2\mu_0 \rho}}, \tag{2.49}$$

where ρ is the particle mass density. For a realistic anti-Helmholtz configuration, the field gradient at the trap center may be written as [39]

$$\left.\frac{\partial B_i}{\partial r_i}\right|_{\mathbf{r}=0} = \zeta_i \frac{\mu_0 N I}{R_{\text{coil}}^2}, \tag{2.50}$$

so that the trap frequencies become

$$\omega_i = \zeta_i \frac{\mu_0 N I}{R_{\text{coil}}^2} \sqrt{\frac{3}{2\mu_0 \rho}}, \tag{2.51}$$

where N is the number of coil windings, I is the trap current, R_{coil} is the inner coil radius, and ζ_i is a geometric factor. In practice, deviations from the ideal geometry, such as finite coil extent, wire openings, and chip asymmetry, are accounted by ζ_i.

(2.51) is the ideal point-particle result, where the trap frequency depends on density but not explicitly on mass. In the realized chip trap, however, finite particle size, gravity-induced sag, and geometric asymmetries such as the coil openings shift the equilibrium position and modify the local field curvature. Consequently, larger particles of the same material can exhibit different trap frequencies even at a fixed density. [96, 98]

In a radially symmetric trap, the equilibrium position is centered laterally at $x = 0$ and $y = 0$. Along the vertical direction, however, gravity shifts the equilibrium position downward by

$$z_0 = -\frac{g}{\omega_z^2} \approx 25\,\mu\text{m}, \tag{2.52}$$

for a trapping frequency of 100 Hz. Since this displacement is not negligible compared with the trap dimensions, it places an additional constraint on the maximum particle size that can be levitated for a given trap geometry.

Table 2.2 lists typical parameters for the levitation experiments. The effective London penetration depth of 80 nm quoted for the commercial Pb-Sn microspheres exceeds the bulk Pb value of 39 nm because impurities and grain boundaries place the material in the dirty limit, where $\lambda_{\text{eff}} \approx \lambda_L \sqrt{\xi_0 / l_e}$ with l_e the electronic mean free path [70]. The resulting trap frequencies are approximately 43, 64, and 125 Hz along the three principal axes [39].

Table 2.2: Typical parameters for a levitated lead-based microsphere in the chip-based AHC trap. Values from Refs. [39, 98].

Parameter	Symbol	Value
Particle material		Lead-based microsphere
Particle radius	R_p	$48\,\mu$m
Mass density	ρ	$11\,340\,\mathrm{kg/m^3}$
London penetration depth	λ_L	80 nm[a]
Critical temperature	T_c	7.2 K
Coil inner radius	R_{coil}	$125\,\mu$m
Coil separation		$280\,\mu$m
Trap current	I	0.5 A
Trap frequency (x)	$\omega_x/2\pi$	43 Hz
Trap frequency (y)	$\omega_y/2\pi$	64 Hz
Trap frequency (z)	$\omega_z/2\pi$	125 Hz

[a]Effective value for commercial Pb-Sn microspheres. It exceeds the bulk Pb value of 39 nm in Table 2.1 due to impurities and dirty-limit effects.

Flux-based position readout

The center-of-mass motion of the levitated particle is detected through the time-varying magnetic flux that it induces in a pickup loop placed near the trap. This flux signal is transported via a superconducting flux transformer (Sec. 2.8) to a flux-tunable resonator (Sec. 2.6), which converts the flux into a resonance-frequency modulation. The corresponding frequency-to-voltage conversion by homodyne detection is derived in Appendix 6.5.

The pickup transduction coefficient is defined as the change in pickup-loop flux per unit displacement,

$$\Lambda_i = \frac{\partial \Phi_p}{\partial r_i}, \tag{2.53}$$

where Φ_p is the flux through the pickup loop and r_i is the particle position along the direction i. The transduction coefficient Λ_i depends on the pickup-loop size, position, and orientation relative to the trap, and is computed numerically for the trap geometries used in this work (see Sec. 2.9).

2.3 Josephson junction

Josephson junctions provide the nonlinear, flux-sensitive inductance used for frequency tuning of superconducting resonators. The treatment here follows Refs. [70, 99–102].

2.3.1 Josephson effect

A Josephson junction consists of two superconducting electrodes separated by a weak link, typically a thin insulating barrier (Fig. 2.6), which allows Cooper pairs to tunnel coherently [70, 99, 103].

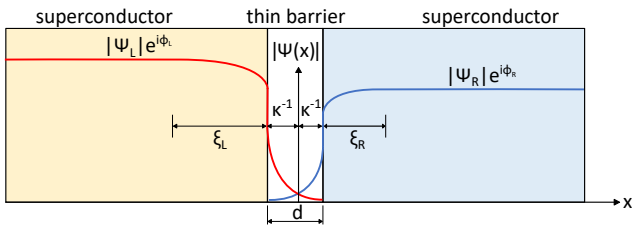

Figure 2.6: Josephson junction: two superconducting electrodes separated by an insulating barrier of thickness d. The superconducting order parameter Ψ recovers to its bulk value inside the electrodes over the coherence lengths ξ_L and ξ_R, while its amplitude decays into the barrier over the characteristic tunneling length κ^{-1}. For a sufficiently thin barrier, the decaying tails overlap, enabling coherent Cooper-pair tunneling. The gauge-invariant phase difference δ determines the supercurrent.

Figure 2.6 schematically illustrates the spatial variation of the complex superconducting order parameter $\Psi = |\Psi|e^{i\phi}$ across a tunnel junction. In each superconducting electrode, the order-parameter magnitude recovers to its bulk value over a coherence length $\xi_{L,R}$ near the interface, whereas inside the insulating barrier it decays evanescently over the characteristic tunneling length κ^{-1}. If the barrier thickness d is sufficiently small, the decaying condensate tails from the two electrodes overlap across the barrier, so that the two superconductors remain phase coupled despite the absence of a metallic connection. This overlap underlies coherent Cooper-pair tunneling and therefore the dependence of the supercurrent on the gauge-invariant phase difference δ.

Let ϕ_L and ϕ_R denote the macroscopic phases of the superconducting order

parameter on either side of the junction. The gauge-invariant phase difference is defined as

$$\delta = \phi_R - \phi_L - \frac{2\pi}{\Phi_0} \int_L^R \mathbf{A} \cdot d\boldsymbol{\ell}, \tag{2.54}$$

where $\mathbf{A}$ is the magnetic vector potential, and the integral is taken across the junction along the direction of the supercurrent flow [70, 103]. The two Josephson relations are:

DC Josephson effect. A supercurrent flows through the junction without any applied voltage, its magnitude being determined by the phase difference:

$$I = I_c \sin \delta, \tag{2.55}$$

where I_c is the critical current of the junction [70, 99].

AC Josephson effect. When a voltage V is applied across the junction, the phase difference evolves according to

$$\frac{d\delta}{dt} = \frac{2\pi}{\Phi_0} V = \frac{2e}{\hbar} V, \tag{2.56}$$

where Φ_0 is the magnetic flux quantum defined in Sec. 2.1.5. A constant voltage therefore produces an oscillating supercurrent at frequency $f = V/\Phi_0 = 2eV/h$ [70, 99].

2.3.2 Ambegaokar-Baratoff relation

The critical current I_c depends on the junction transparency, the superconducting gap, and the junction area. For two identical superconducting electrodes with gap $\Delta(T)$, the tunnel Hamiltonian theory [70, 104] gives a sinusoidal current-phase relation $I(\delta) = I_c \sin \delta$, with the critical current obtained from a Matsubara sum:

$$I_c = \frac{2\pi k_B T}{eR_N} \sum_{n=0}^{\infty} \frac{\Delta^2(T)}{\omega_n^2 + \Delta^2(T)}, \qquad \omega_n = (2n+1)\pi k_B T. \tag{2.57}$$

Evaluating the sum yields the Ambegaokar-Baratoff relation [70, 104]

$$I_c R_N = \frac{\pi\Delta(T)}{2e} \tanh\left(\frac{\Delta(T)}{2k_B T}\right), \tag{2.58}$$

which reduces to $I_c R_N \approx \pi\Delta(0)/(2e)$ for $T \ll T_c$.

Eq. (2.58) is the form used throughout this thesis to estimate the critical current of Al/AlO$_x$/Al tunnel junctions from their measured normal-state resistance. For junctions with dissimilar superconducting electrodes, the corresponding expression is more general and is best written as a Matsubara sum with $\Delta_1(T)$ and $\Delta_2(T)$ on the two sides of the barrier [70, 104, 105]. In the unequal-gap case, the low-temperature limit involves a complete elliptic integral rather than a simple geometric-mean substitution [104, 105]. This situation can become relevant for unintended SIS interfaces between dissimilar superconductors, such as the oxide-mediated interconnects discussed in Sec. 4.4.

2.3.3 Josephson inductance and energy

The current-phase relation in Eq. (2.55) implies that a Josephson junction behaves as a nonlinear inductor. Using the flux-phase relation

$$\Phi = \frac{\Phi_0}{2\pi}\,\delta, \tag{2.59}$$

the differential Josephson inductance is defined as

$$L_J(\delta) \equiv \frac{\partial\Phi}{\partial I}. \tag{2.60}$$

With $I = I_c \sin\delta$, this gives

$$L_J(\delta) = \frac{\Phi_0}{2\pi}\left(\frac{\partial I}{\partial\delta}\right)^{-1} = \frac{\Phi_0}{2\pi I_c \cos\delta}, \tag{2.61}$$

$$L_{J0} \equiv L_J(0) = \frac{\Phi_0}{2\pi I_c}. \tag{2.62}$$

Equivalently, using $\frac{dI}{dt} = I_c \cos\delta\,\frac{d\delta}{dt}$ together with Eq. (2.56), one obtains

$$V = L_J(\delta)\,\frac{dI}{dt}. \tag{2.63}$$

The inductance is therefore nonlinear in δ and diverges as $\delta \to \pm\pi/2$. For the junctions used in this work, with $I_c \sim 400\,\mathrm{nA}$, the zero-bias Josephson inductance is $L_{J0} \sim 800\,\mathrm{pH}$.

The associated Josephson energy scale is

$$E_{J0} = \frac{\Phi_0 I_c}{2\pi} = \frac{\hbar I_c}{2e}. \tag{2.64}$$

The junction potential energy then follows from

$$U_J(\delta) = \int I\, d\Phi = \frac{\Phi_0 I_c}{2\pi} \int \sin\delta\, d\delta = E_{J0}(1 - \cos\delta), \tag{2.65}$$

In the presence of a dc bias current I_b, the potential is tilted to

$$U(\delta) = E_{J0}(1 - \cos\delta) - \frac{\Phi_0 I_b}{2\pi}\,\delta, \tag{2.66}$$

which is the familiar washboard potential of a single Josephson junction.

2.4 Superconducting Quantum Interference Device

A dc superconducting quantum interference device (dc SQUID) consists of a superconducting loop interrupted by two Josephson junctions, as shown in Fig. 2.7. An applied external flux Φ_e constrains the allowed combinations of junction phases through fluxoid quantization, while finite loop inductance introduces self-flux screening. The resulting loop-phase operating point $\bar{\varphi}$ is therefore determined self-consistently on a chosen branch, which modifies the interference between the two junction supercurrents. As a result, both the effective critical current and linearized inductance become flux dependent, while the individual junction relations Eq. (2.55) and Eq. (2.56) remain unchanged. This flux dependence provides the tunable termination element for the FTRs in this thesis.

This section develops the dc SQUID model used throughout the thesis as the flux-sensitive termination element of the flux-tunable resonator. The treatment includes both junction critical-current asymmetry and screening by finite loop inductance, which are necessary for quantitative comparison with the measured tuning curves, and follows Ref. [100] and Paper III. The aim is to establish the ingredients that will later determine the FTR tuning,

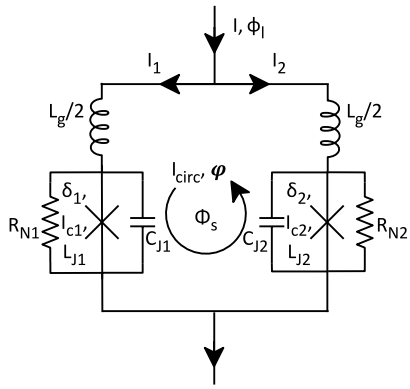

Figure 2.7: Equivalent-circuit model of a dc SQUID in the RCSJ representation, showing the two junction branches with phase drops δ_1 and δ_2, branch parameters (I_{c1}, R_{N1}, C_{J1}) and (I_{c2}, R_{N2}, C_{J2}), the loop inductance split as $L_g/2$ in each arm, and the current and flux conventions used in the text: transport current I, branch currents I_1 and I_2, circulating current I_{circ}, and screened flux Φ_s.

flux responsivity, and nonlinearity. In particular, the section focuses on (i) screening and fluxoid branch structure caused by finite loop inductance, (ii) suppression of abrupt branch switching by junction asymmetry, and (iii) the effective one-port inductance presented to the FTR.

Throughout this section, the applied flux and transport current are decomposed as $\Phi_e(t) = \Phi_e^{\mathrm{dc}} + \delta\Phi_e(t)$ and $I(t) = I_{\mathrm{dc}} + \delta I(t)$, where the dc components define a dc operating point on the zero-voltage branch. The SQUID phases are correspondingly written as $\phi_l(t) = \bar{\phi}_l + \delta\phi_l(t)$ and $\varphi(t) = \bar{\varphi} + \delta\varphi(t)$, where $(\bar{\phi}_l, \bar{\varphi})$ denotes the dc operating point and the δ terms denote small perturbations about it. Unless stated otherwise, Φ_e and I appearing in stationary screening, stability, and potential-energy equations denote the dc components Φ_e^{dc} and I_{dc}. Microwave or rf excitation is treated as a small perturbation about the dc operating point. The term steady state is reserved for the periodic response under continuous driving, while switching denotes the loss of local stability of a zero-voltage solution under parameter variation, possibly followed by phase slips into a finite-voltage running state.

The section begins by defining the common-mode and loop-phase coordinates and the associated transport and circulating currents (Sec. 2.4.1). The RCSJ

description is then introduced, reduced to the dc operating point, and linearized response on the zero-voltage branch relevant for the present devices (Sec. 2.4.2). From the current-phase relations on that branch and fluxoid quantization, the screening equation, the parameter β_L, and the resulting fluxoid branch structure are obtained (Sec. 2.4.3, Sec. 2.4.4). These results are used to derive the effective critical current and circulating current, showing how junction asymmetry both lifts the half-integer flux nodes of the symmetric modulation and breaks the symmetry between competing stationary branches, thereby suppressing abrupt branch switching (Sec. 2.4.5, Sec. 2.4.6). The analysis is then recast in terms of the SQUID potential landscape, whose minima define the stable operating points and whose Hessian gives the stability criterion and the onset of branch switching (Sec. 2.4.7). Finally, the local curvature of this potential is reduced to the one-port inductance that enters the FTR boundary condition.

2.4.1 Phase and current definitions

The gauge-invariant phase drops across the junctions are expressed in terms of a terminal (common-mode) phase ϕ_l and a loop (differential-mode) phase φ:

$$\delta_1 = \phi_l + \varphi, \qquad \delta_2 = \phi_l - \varphi. \tag{2.67}$$

Fabrication variations lead to different critical currents I_{c1}, I_{c2}. The asymmetry parameter α and mean critical current I_0 are defined as

$$\alpha = \frac{I_{c1} - I_{c2}}{I_{c1} + I_{c2}}, \qquad I_0 = \frac{I_{c1} + I_{c2}}{2}, \tag{2.68}$$

$$I_{c1} = I_0(1+\alpha), \qquad I_{c2} = I_0(1-\alpha), \tag{2.69}$$

with $\alpha \in (-1, 1)$ and $\alpha = 0$ corresponding to a symmetric SQUID.

The transport current, circulating current (positive for counterclockwise

flow), and screened flux are

$$I(t) = I_1(t) + I_2(t), \tag{2.70}$$

$$I_{\mathrm{circ}}(t) \equiv \frac{I_1(t) - I_2(t)}{2}, \tag{2.71}$$

$$\Phi_s(t) = \Phi_e(t) - L_g I_{\mathrm{circ}}(t), \tag{2.72}$$

where the last expression accounts for screening by the finite loop inductance L_g.

2.4.2 RCSJ model and equations of motion

Each junction $k \in \{1, 2\}$ is modeled by the Resistively and Capacitively Shunted Junction (RCSJ) model [106, 107], in which an ideal Josephson element is placed in parallel with a normal-state resistance R_k and junction capacitance C_k.

Current relations The total current through junction k is

$$I_k(t) = I_{ck} \sin \delta_k(t) + \frac{V_k(t)}{R_k} + C_k \dot{V}_k(t) \tag{2.73}$$

$$= I_{ck} \sin \delta_k(t) + \frac{\Phi_0}{2\pi R_k} \dot{\delta}_k(t) + \frac{\Phi_0 C_k}{2\pi} \ddot{\delta}_k(t), \tag{2.74}$$

where the second form follows from the ac Josephson relation $V_k = (\Phi_0/2\pi)\dot{\delta}_k$; see Eq. (2.56).

Voltage relations In the SQUID parametrization $\delta_{1,2} = \phi_l \pm \varphi$, the terminal (common-mode) and loop (differential-mode) voltages are

$$V(t) \equiv \frac{V_1(t) + V_2(t)}{2} = \frac{\Phi_0}{2\pi} \dot{\phi}_l(t), \tag{2.75}$$

$$V_1(t) - V_2(t) = \frac{\Phi_0}{2\pi} \left(\dot{\delta}_1 - \dot{\delta}_2\right) = \frac{\Phi_0}{\pi} \dot{\varphi}(t). \tag{2.76}$$

The voltage relations become relevant whenever the junction phases vary in time, for example, under microwave excitation or after switching to a finite-voltage running state. For the FTRs in this work, the question is whether the

resistive and capacitive RCSJ terms can be neglected at the resonator frequency, so that the SQUID can be treated to leading order as a flux-dependent nonlinear inductive termination on the zero-voltage branch. This is assessed using two figures of merit: the plasma frequency, which sets the size of the capacitive correction, and the Stewart-McCumber parameter, which characterizes the damping of the junction mode from the resistive term.

Typical parameters The Al/AlO$_x$/Al junctions used throughout this work have dimensions of $1.0 \times 1.0\,\mu\text{m}^2$ or $0.5 \times 1.0\,\mu\text{m}^2$, with a nominal oxide thickness of $d \approx 2\,\text{nm}$ and $\epsilon_r \approx 9$. A parallel-plate estimate then gives $C_J \approx$ 20-40 fF. With a normal resistance $R_n \approx$ 450-1200 Ω, the critical current is $I_c \approx$ 230-600 nA, which corresponds to a linearized Josephson inductance of $L_J(0) \approx$ 540-1400 pH.

Stewart-McCumber parameter Using the typical Al/AlO$_x$/Al junction parameters above, the Stewart-McCumber parameter is estimated as [106, 107]

$$\beta_c = \frac{2\pi}{\Phi_0} I_c R_n^2 C_J. \tag{2.77}$$

Using $(R_n, C_J) \approx (450\,\Omega, 40\,\text{fF})$ and $(1200\,\Omega, 20\,\text{fF})$ gives $\beta_c \approx 15$ and 21, respectively. The junctions are therefore moderately underdamped, $\beta_c \gg 1$, with a damping factor

$$Q = \omega_p R_n C_J = \sqrt{\beta_c} \approx 3.9\text{–}4.5. \tag{2.78}$$

Plasma frequency The plasma frequency,

$$\omega_p = \frac{1}{\sqrt{L_J C_J}} = \sqrt{\frac{2\pi I_c}{\Phi_0 C_J}}, \tag{2.79}$$

lies in the range $\omega_p/2\pi \approx$ 30-35 GHz and the characteristic frequency $f_c = (I_c R_n)/\Phi_0 \approx 137$ GHz.

Implications Two conclusions follow for the devices used throughout this thesis. First, the junctions are deep in the phase regime: with $E_J/h = \Phi_0 I_c/(2\pi h)$ in the range 120 to 300 GHz and $E_C/h = e^2/(2C_J h)$ of order 0.5 to 1 GHz, $E_J/E_C \gg 1$ for both junctions, which allows a classical phase

description for the operating conditions considered here. Second, for microwave operation well below the plasma frequency and while the SQUID remains on the zero-voltage branch, the RCSJ equations reduce to a predominantly inductive response with a small capacitive correction. In practice, for resonator frequencies in the few GHz range, $\omega/\omega_p \ll 1$ is well satisfied. The microwave response is therefore treated as a perturbation about a dc operating point: the resistive term is negligible in the zero-voltage state, the capacitive term gives only a small correction, and the current is dominated by the Josephson term, $I_k \simeq I_{ck} \sin \delta_k$. Time-dependent effects beyond this picture become important mainly during switching events, phase slips, or large-amplitude driven motion near bifurcation.

2.4.3 Current-phase relations in the zero-voltage state

On the zero-voltage branch defined above,

$$I_1 = I_{c1} \sin(\phi_l + \varphi), \qquad I_2 = I_{c2} \sin(\phi_l - \varphi). \tag{2.80}$$

The transport and circulating currents are

$$I = I_{c1} \sin(\phi_l + \varphi) + I_{c2} \sin(\phi_l - \varphi), \tag{2.81}$$

$$I_{\text{circ}} = \frac{I_{c1} \sin(\phi_l + \varphi) - I_{c2} \sin(\phi_l - \varphi)}{2}. \tag{2.82}$$

Expanding with Eq. (2.69) gives

$$I = 2I_0 \cos\varphi \, \sin\phi_l + 2\alpha I_0 \sin\varphi \, \cos\phi_l, \tag{2.83}$$

$$I_{\text{circ}} = I_0 \big[\alpha \cos\varphi \, \sin\phi_l + \sin\varphi \, \cos\phi_l\big]. \tag{2.84}$$

2.4.4 Fluxoid quantization and screening

The general fluxoid quantization condition from Sec. 2.1.5 is now specialized to the dc SQUID loop. For a SQUID with gauge-invariant junction phase drops $\delta_1 = \phi_l + \varphi$ and $\delta_2 = \phi_l - \varphi$, the gauge-invariant phase winding around the loop is $\delta_1 - \delta_2 = 2\varphi$. In the lumped SQUID model used here, the loop kinetic-inductance contribution is assumed to be negligible, so the fluxoid constraint is written only in terms of the screened flux Φ_s and an integer

fluxoid branch index $m \in \mathbb{Z}$ as

$$2\varphi = 2\pi \left(\frac{\Phi_s}{\Phi_0} + m \right). \tag{2.85}$$

Using Eq. (2.72), this becomes

$$2\varphi + \frac{2\pi}{\Phi_0} L_g I_{\text{circ}} = 2\pi \left(\frac{\Phi_e}{\Phi_0} + m \right). \tag{2.86}$$

A dimensionless screening parameter is defined as

$$\beta_L \equiv \frac{2L_g I_0}{\Phi_0}. \tag{2.87}$$

Note that an alternative convention of $\beta_L = 2\pi L_g I_0/\Phi_0$ exists in the literature. In terms of Eq. (2.87), Eq. (2.86) becomes

$$2\varphi + \pi\beta_L \frac{I_{\text{circ}}}{I_0} = 2\pi \left(\frac{\Phi_e}{\Phi_0} + m \right). \tag{2.88}$$

For $\beta_L \ll 1$, screening is weak, and $\varphi \simeq \pi(\Phi_e/\Phi_0 + m)$. For larger β_L, the relationship becomes nonlinear and potentially multivalued, leading to hysteresis and inter-branch jumps.

Fluxoid branch structure. For a given applied flux Φ_e, Eq. (2.88) can admit more than one self-consistent solution for the loop phase φ and screened flux Φ_s. These solution families are referred to here as *fluxoid branches* and are indexed by the integer m, which labels different allowed phase windings around the SQUID loop. When screening is weak, a single branch is typically followed over the relevant flux range. For larger β_L, however, different fluxoid branches can coexist, and the SQUID may remain on one locally stable branch until that branch loses stability, at which point it switches to another. This multivalued fluxoid-branch structure is the origin of the hysteresis and branch-switching behavior discussed below.

Fig. 2.8 shows how finite loop inductance modifies the SQUID screening relation. The black curve denotes the $\beta_L = 0$ limit, while the blue solid and dashed curves show the two available branches for $\beta_L = 0.3$. The red and green dots mark the branches followed under forward and reverse flux sweeps, respectively. In the symmetric case in Fig. 2.8(a), the forward and

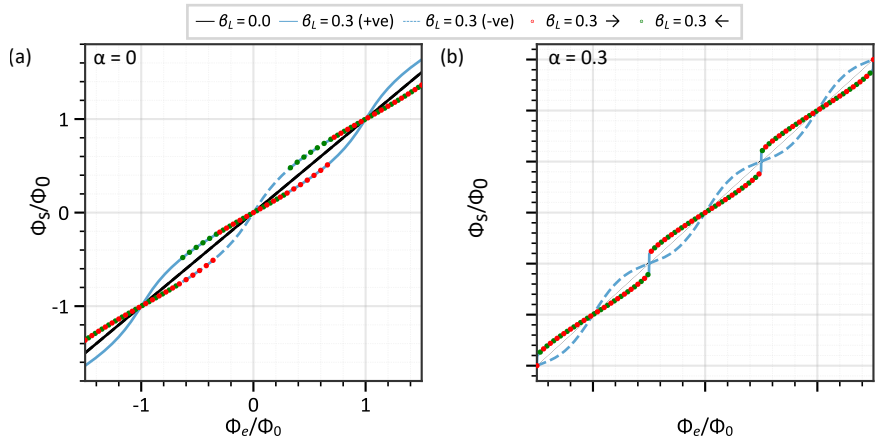

Figure 2.8: Screened flux Φ_s/Φ_0 versus external flux Φ_e/Φ_0 for a dc SQUID, comparing the $\beta_L = 0$ case (black) with the $\beta_L = 0.3$ case (blue). For $\beta_L = 0.3$, the blue solid and dashed curves show the positive and negative branches, while the red and green points indicate the branches followed under forward and reverse flux sweeps, respectively. Panel (a) shows the symmetric case ($\alpha = 0$), for which the sweep-followed branch depends on sweep direction and exhibits abrupt branch switching, whereas Panel (b) shows the asymmetric case ($\alpha = 0.3$), for which the forward and reverse sweeps follow the same smooth branch. Adapted from Paper III.

reverse sweep traces separate, indicating hysteretic branch switching between the two blue branches. In the asymmetric case in Fig. 2.8(b), the red and green dots instead follow the same smooth branch, showing that junction critical-current asymmetry suppresses abrupt switching. The shift of the blue $\beta_L = 0.3$ branches away from the black $\beta_L = 0$ curve also shows the partial screening of the applied flux by the circulating current.

2.4.5 Effective critical current

Since Eq. (2.83) has the form $A \sin\phi_l + B \cos\phi_l$, it can be written as

$$I = R(\varphi)\, \sin\big(\phi_l + \psi_0(\varphi)\big), \qquad |I| \leq R(\varphi), \tag{2.89}$$

with amplitude

$$R(\varphi) = 2I_0 D(\varphi), \qquad D(\varphi) \equiv \sqrt{\cos^2\varphi + \alpha^2 \sin^2\varphi}, \tag{2.90}$$

and phase

$$\psi_0(\varphi) = \operatorname{atan2}\big(\alpha \sin\varphi, \cos\varphi\big), \tag{2.91}$$

where the two-argument arctangent instead uses the signs of both arguments separately and therefore selects the appropriate branch of ψ_0 uniquely, while the ordinary arctangent would determine ψ_0 only up to integer multiples of π.

For fixed φ, the maximum transport current is the effective critical-current

$$I_c^{\text{eff}}(\varphi) = R(\varphi). \tag{2.92}$$

For finite screening, this is the local envelope at fixed φ; the actual switching current at fixed external flux must be obtained self-consistently together with the screening relation, since φ generally depends on I.

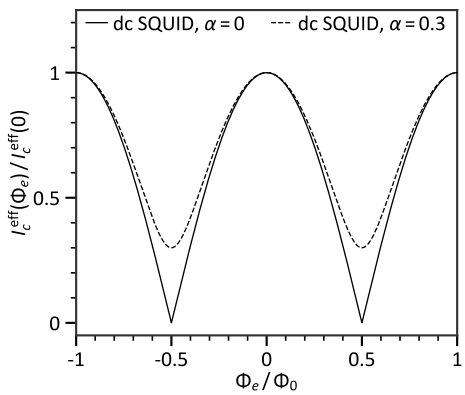

Figure 2.9: Normalized effective critical current of a dc SQUID versus external flux for symmetric ($\alpha = 0$, solid) and asymmetric ($\alpha = 0.3$, dashed) junctions.

In the weak-screening limit, $\varphi \simeq \pi(\Phi_e/\Phi_0 + m)$ and $I_c^{\text{eff}}(\Phi_e)$ follow directly from Eq. (2.92). The resulting modulation pattern is shown in Fig. 2.9: for a symmetric SQUID ($\alpha = 0$), the envelope reaches zero at half-integer flux quanta, whereas junction asymmetry ($\alpha = 0.3$) lifts the nodes and reduces the modulation depth.

For $|I| < R(\varphi)$, Eq. (2.89) admits two stationary points in ϕ_l, given by

$$\cos\left(\phi_l + \psi_0\right) = s\sqrt{1 - \left(\frac{I}{R}\right)^2}, \qquad s \in \{+1, -1\}. \tag{2.93}$$

Here s labels the two local stationary points at fixed φ and should not be confused with the fluxoid branch index m introduced in Sec. 2.4.4. The local slope at a fixed φ is

$$\frac{\partial I}{\partial \phi_l} = R(\varphi)\cos\left(\phi_l + \psi_0\right) = R(\varphi)\, s\sqrt{1 - \left(\frac{I}{R(\varphi)}\right)^2}. \tag{2.94}$$

For a current-biased stationary point at fixed φ, local stability requires $\partial I/\partial\phi_l > 0$ and selects $s = +1$. At zero transport current, energy minimization selects $\phi_l = -\psi_0(\varphi) \pmod{2\pi}$, which also yields $\cos(\phi_l + \psi_0) = +1$ and therefore corresponds to $s = +1$ on the stable branch.

2.4.6 Circulating current

Using Eq. (2.93) and the identities

$$\cos\psi_0 = \frac{\cos\varphi}{D(\varphi)}, \qquad \sin\psi_0 = \frac{\alpha\sin\varphi}{D(\varphi)}, \tag{2.95}$$

the circulating current Eq. (2.84) can be expressed without explicit dependence on ϕ_l as

$$\boxed{I_{\mathrm{circ}}(I,\varphi;s) = I_0\, s\,\frac{(1-\alpha^2)\cos\varphi\,\sin\varphi}{D(\varphi)}\sqrt{1 - \left(\frac{I}{2I_0 D(\varphi)}\right)^2} + \frac{\alpha}{2}\,\frac{I}{D^2(\varphi)}.} \tag{2.96}$$

This expression is defined for $|I| \leq R(\varphi) = 2I_0 D(\varphi)$.
At zero transport current, Eq. (2.96) reduces to

$$I_{\mathrm{circ}}(\varphi) = I_0\,\frac{(1-\alpha^2)\cos\varphi\,\sin\varphi}{D(\varphi)}, \tag{2.97}$$

on the stable branch ($s = +1$). For a symmetric SQUID ($\alpha = 0$) $D(\varphi) =$

$|\cos\varphi|$, and thus Eq. (2.97) becomes

$$I_{\text{circ}} = I_0 \ \text{sgn}(\cos\varphi) \ \sin\varphi, \tag{2.98}$$

which is equivalent to the standard expression $I_{\text{circ}} = I_0 \sin\varphi$, together with the energy-minimizing choice of ϕ_l that flips by π when $\cos\varphi$ changes sign.

Combining Eq. (2.88) with Eq. (2.96) yields an implicit screening equation for φ at fixed (I, Φ_e, m):

$$\boxed{\begin{aligned} 2\varphi + \pi\beta_L \Bigg[s\,\frac{(1-\alpha^2)\cos\varphi\,\sin\varphi}{D(\varphi)} \sqrt{1 - \left(\frac{I}{2I_0 D(\varphi)}\right)^2} \\ + \frac{\alpha}{2}\,\frac{I/I_0}{D^2(\varphi)} \Bigg] = 2\pi \left(\frac{\Phi_e}{\Phi_0} + m\right). \end{aligned}} \tag{2.99}$$

In the devices used in this thesis, $I_{\text{dc}} = 0$. Therefore, the microwave drive produces only a small ac transport current.

2.4.7 Potential energy landscape

The numerical code used to generate the dc-SQUID potential-landscape plots in this subsection is publicly archived at 10.5281/zenodo.19341957.

At a fixed dc bias on the zero-voltage branch, the SQUID operating point is determined by minimizing the total potential energy with respect to the two coordinates ϕ_l and φ.

Josephson terms. As derived in Sec. 2.3.3, the Josephson potential of junction k is

$$U_{Jk}(\delta_k) = E_{Jk}\big(1 - \cos\delta_k\big), \qquad E_{Jk} \equiv \frac{\Phi_0 I_{ck}}{2\pi}, \tag{2.100}$$

with junction phase drops $\delta_{1,2} = \phi_l \pm \varphi$.

Magnetic (screening) term. A circulating current in the SQUID loop produces a self-flux $\Phi_{\text{self}} = \Phi_s - \Phi_e$. The magnetic energy stored in the loop inductance is

$$U_L = \frac{\Phi_{\text{self}}^2}{2L_g} = \frac{(\Phi_s - \Phi_e)^2}{2L_g} = \frac{L_g I_{\text{circ}}^2}{2}, \tag{2.101}$$

where $\Phi_s = \Phi_e - L_g I_{\text{circ}}$ follows from the sign convention used in Eq. (2.72).

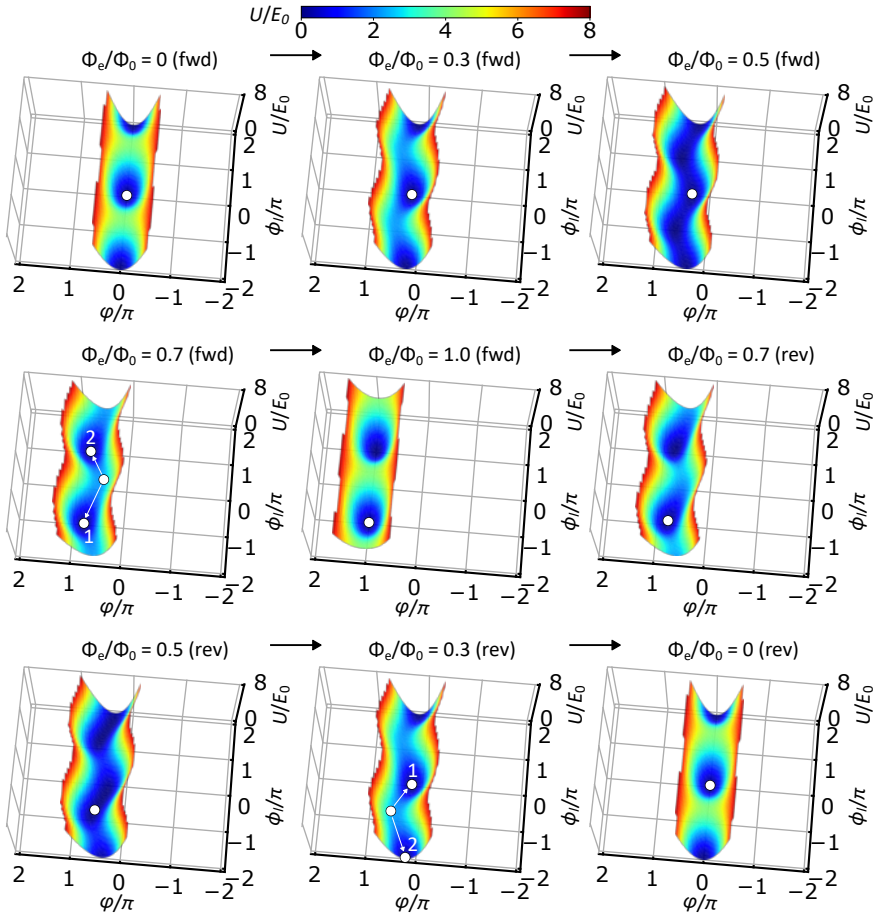

Figure 2.10: SQUID potential landscapes $U(\phi_l, \varphi)/E_0$ for a symmetric dc SQUID ($\alpha = 0$) with finite screening ($\beta_L = 0.3$) during a forward sweep of the applied flux from $\Phi_e/\Phi_0 = 0$ to 1 and a reverse sweep back to $\Phi_e/\Phi_0 = 0$. The white marker denotes the SQUID phase particle at the stable equilibrium point. At the switching points, arrows indicate the two symmetric routes available when the occupied minimum loses stability. On the forward sweep, branch switching occurs near $\Phi_e/\Phi_0 = 0.7$, whereas on the reverse sweep it occurs near $\Phi_e/\Phi_0 = 0.3$, demonstrating hysteretic branch following caused by finite loop screening. Adapted from Paper III.

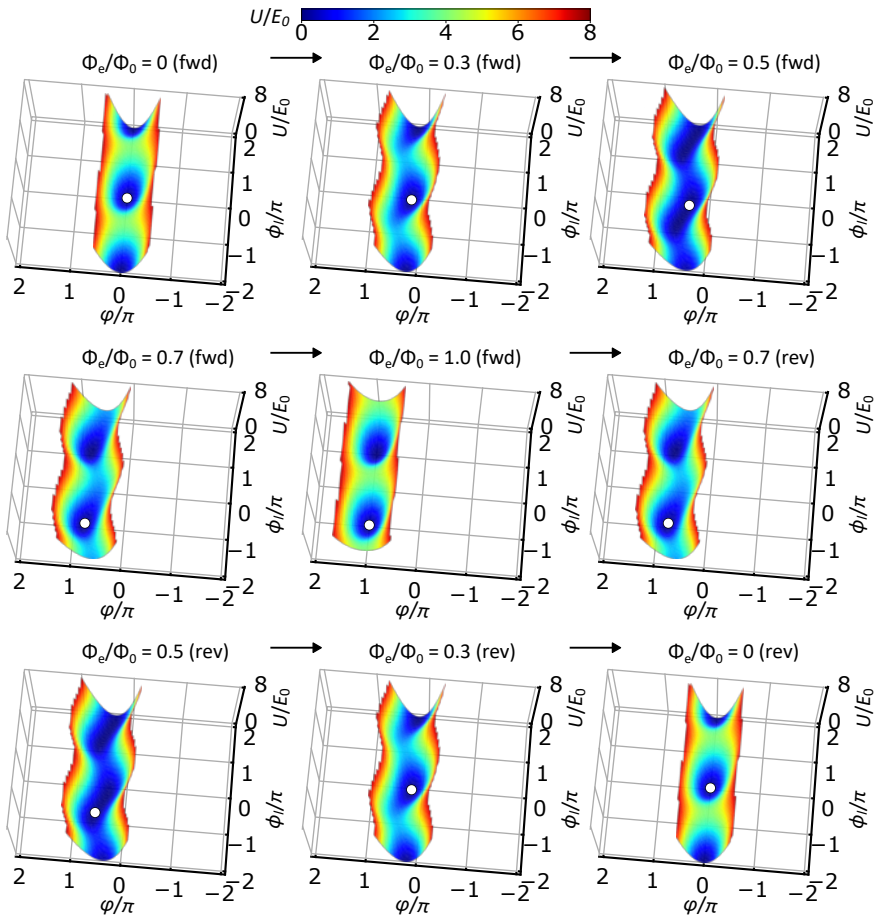

Figure 2.11: SQUID potential landscapes $U(\phi_l, \varphi)/E_0$ for an asymmetric dc SQUID ($\alpha = 0.3$) with finite screening ($\beta_L = 0.3$) during a forward sweep of the applied flux from $\Phi_e/\Phi_0 = 0$ to 1 and a reverse sweep back to $\Phi_e/\Phi_0 = 0$. The plotting conventions are the same as in Fig. 2.10. Junction critical-current asymmetry skews the potential landscape and breaks the exact symmetry between competing minima, so the forward and reverse sweeps remain on the same smooth branch and no hysteretic jump in SQUID inductance or FTR frequency appears. Adapted from Paper III.

Current-bias work term. For a current-biased SQUID, when the terminal flux $\Phi_l = (\Phi_0/2\pi)\phi_l$ changes, work is done on the phase by the current source. This contributes the term $-I\Phi_l = -(\Phi_0/2\pi)I\,\phi_l$. Here I denotes the dc transport current that sets the operating point.

Total SQUID potential energy. Combining these contributions gives the SQUID potential

$$U(\phi_l,\varphi) = E_{J1}\big[1-\cos(\phi_l+\varphi)\big]+E_{J2}\big[1-\cos(\phi_l-\varphi)\big]+\frac{\big(\Phi_s-\Phi_e\big)^2}{2L_g}-\frac{\Phi_0}{2\pi}I\,\phi_l. \tag{2.102}$$

Here Φ_s is related to φ and m by Eq. (2.85). Using $E_0 = \Phi_0 I_0/2\pi$ and $u = U/E_0$ yields

$$\begin{aligned} u(\phi_l,\varphi) &= 2-(1+\alpha)\cos(\phi_l+\varphi)-(1-\alpha)\cos(\phi_l-\varphi) \\ &\quad + \frac{2\pi}{\beta_L}\left(\frac{\varphi}{\pi}-\frac{\Phi_e}{\Phi_0}-m\right)^2-\frac{I}{I_0}\phi_l. \end{aligned} \tag{2.103}$$

In the limit $\beta_L \to 0$, the magnetic term becomes infinitely stiff and enforces the constraint $\varphi = \pi(\Phi_e/\Phi_0 + m)$. After imposing this constraint, the SQUID potential reduces to a one-dimensional landscape in ϕ_l, so the remaining minimization is governed by the Josephson terms alone.

The panel sequences in Fig. 2.10 and Fig. 2.11 visualize how the SQUID phase particle, represented by the white marker, moves through the potential landscape as the external flux is swept forward from 0 to Φ_0 and then backward to 0. In the symmetric case in Fig. 2.10, finite screening ($\beta_L = 0.3$) produces a hysteretic branch following: the phase particle remains trapped in a metastable minimum up to about $\Phi_e/\Phi_0 = 0.7$ on the forward sweep, but switches already near $\Phi_e/\Phi_0 = 0.3$ on the reverse sweep. The arrows indicate the two symmetry-related escape routes available once the occupied minimum loses stability. In contrast, the asymmetric case in Fig. 2.11 shows a slightly skewed landscape in which the exact symmetry between competing minima is broken. As a result, the phase particle stays on the same smooth branch in both sweep directions, so no hysteretic jump in SQUID inductance or FTR frequency appears.

Stationary points satisfy

$$\frac{\partial U}{\partial \phi_l} = 0, \qquad \frac{\partial U}{\partial \varphi} = 0. \tag{2.104}$$

Using the shorthand notation

$$U_\phi \equiv \frac{\partial U}{\partial \phi_l}, \qquad U_\varphi \equiv \frac{\partial U}{\partial \varphi}, \tag{2.105}$$

$$U_{\phi\phi} \equiv \frac{\partial^2 U}{\partial \phi_l^2}, \qquad U_{\phi\varphi} \equiv \frac{\partial^2 U}{\partial \phi_l \, \partial \varphi}, \qquad U_{\varphi\varphi} \equiv \frac{\partial^2 U}{\partial \varphi^2}, \tag{2.106}$$

the Hessian matrix at a stationary point $(\bar{\phi}_l, \bar{\varphi})$ is

$$H(\bar{\phi}_l, \bar{\varphi}) \equiv \begin{pmatrix} U_{\phi\phi} & U_{\phi\varphi} \\ U_{\phi\varphi} & U_{\varphi\varphi} \end{pmatrix}_{(\bar{\phi}_l, \bar{\varphi})}. \tag{2.107}$$

A stationary point is a stable operating point if H is positive definite. For a 2×2 symmetric matrix, this requires

$$U_{\phi\phi} > 0, \qquad \det H > 0, \tag{2.108}$$

or equivalently

$$U_{\varphi\varphi} > 0, \qquad \det H > 0. \tag{2.109}$$

These conditions are equivalent to both eigenvalues of H being positive.

Branch switching criterion. Loss of stability of a locally stable minimum during an adiabatic dc-flux sweep occurs when the smallest eigenvalue of the Hessian reaches zero. For a stationary point that is initially a stable minimum, a convenient scalar criterion for this loss of stability is

$$\det H = U_{\phi\phi} U_{\varphi\varphi} - U_{\phi\varphi}^2 = 0, \tag{2.110}$$

evaluated at the stationary point. Under adiabatic dc-flux sweeps, reaching Eq. (2.110) causes the local minimum occupied by the SQUID to lose stability, so the SQUID switches to a different locally stable minimum. This corresponds to branch switching in the screening relation and may involve a change of the fluxoid branch index m. In the symmetric, zero-transport limit ($\alpha = 0$, $I = 0$), the onset of multivalued screening solutions occurs at $\beta_L \geq 2/\pi$.

The dc SQUID has been described here as a flux-sensitive nonlinear termination whose behavior is governed by fluxoid quantization, loop screening, and junction critical-current asymmetry. Finite screening produces multivalued fluxoid branches, and in the symmetric case, hysteretic branch switching. Junction asymmetry breaks the exact symmetry between competing minima, lifts the zero-critical-current nodes of the symmetric modulation, and suppresses abrupt jumps. In the linearized zero-voltage regime, the local curvature of the SQUID potential determines the effective one-port inductance seen by the resonator. This provides the basis for the FTR tuning, responsivity, and nonlinearity developed in the next section.

2.5 Coplanar waveguide resonators

The coplanar waveguide (CPW) is a planar transmission line used as the distributed element in the resonators of this thesis [108, 109].

2.5.1 CPW geometry and field distribution

A CPW consists of a center conductor of width w separated from two semi-infinite ground planes by gaps of width g, as shown in Fig. 2.12. In Fig. 2.12(a), the concentration of electric field in the gaps explains why dielectric and interface participation is dominated by the CPW edges. In Fig. 2.12(b), the magnetic-field loops around the conductors motivate the inductive description used in the conformal-mapping formulas below. The structure lies on a dielectric substrate of thickness h and relative permittivity ε_r. For high-resistivity silicon, $\varepsilon_r = 11.45$ is used, which is commonly assumed in superconducting circuit work [110, 111], consistent with cryogenic measurements of float-zone high-resistivity silicon [112, 113].

Because the dielectric environment is inhomogeneous, the propagating mode is not exactly TEM. However, for CPW dimensions much smaller than the wavelength, it is well described by a quasi-TEM mode, with the field distribution shown in Fig. 2.12.

2.5.2 Conformal mapping analysis

The CPW line parameters are calculated using conformal mapping, and derivations of the following expressions can be found in Refs. [108, 114, 115]. For

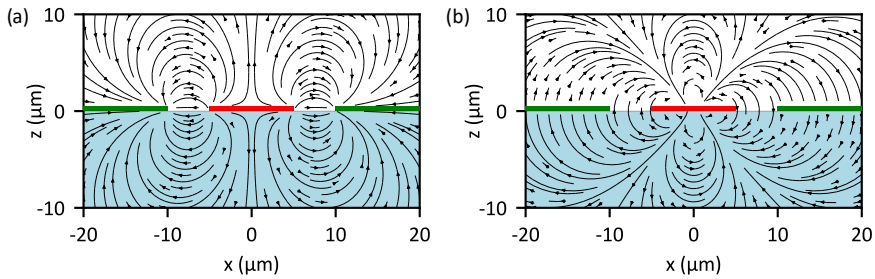

Figure 2.12: Coplanar waveguide geometry. Cross-section showing the center conductor (width w), gaps (width g), ground planes, and substrate (thickness h, permittivity ε_r). (a) The electric field concentrates in the gaps, while (b) the magnetic field encircles the conductors.

the geometries used in this thesis, the substrate is thick compared with the lateral CPW dimensions, $h \gg w + 2g$, so the thick-substrate approximation is adequate and is used throughout unless stated otherwise.

Modulus parameter. In the thick-substrate limit, the elliptic-integral modulus is

$$k = \frac{w}{w + 2g}. \tag{2.111}$$

The complementary modulus is defined as

$$k' = \sqrt{1 - k^2}. \tag{2.112}$$

For completeness, a finite-substrate correction can be written as [115]

$$k_h = \frac{\sinh\left(\dfrac{\pi w}{4h}\right)}{\sinh\left(\dfrac{\pi(w + 2g)}{4h}\right)}, \tag{2.113}$$

with complementary modulus $k'_h = \sqrt{1 - k_h^2}$. In the present devices, $k_h \approx k$, so this correction is negligible and is not used further.

Complete elliptic integrals. The CPW parameters are expressed in terms of the complete elliptic integral of the first kind,

$$K(k) = \int_0^{\pi/2} \frac{d\theta}{\sqrt{1 - k^2 \sin^2 \theta}}. \tag{2.114}$$

The elliptic-integral ratios enter the expressions for the capacitance, geometric inductance, and characteristic impedance.

Capacitance per unit length. The capacitance per unit length of a CPW on a substrate is [108, 115]

$$C_l = 4\varepsilon_0 \varepsilon_{\text{eff}} \frac{K(k)}{K(k')}, \tag{2.115}$$

where the effective permittivity is approximated by

$$\varepsilon_{\text{eff}} = \frac{\varepsilon_r + 1}{2}. \tag{2.116}$$

For high-resistivity silicon with $\varepsilon_r = 11.45$, this gives $\varepsilon_{\text{eff}} = 6.225$.

A more complete finite-thickness correction is [115]

$$\varepsilon_{\text{eff}} = 1 + \frac{\varepsilon_r - 1}{2} \cdot \frac{K(k')}{K(k)} \cdot \frac{K(k_h)}{K(k_h')}. \tag{2.117}$$

For the present geometries on a 280 μm silicon substrate, *Eq.* (2.117) differs from *Eq.* (2.116) by less than 0.1%, so *Eq.* (2.116) is used throughout this section.

Geometric inductance per unit length. For a lossless quasi-TEM CPW, the per-unit-length inductance and capacitance satisfy

$$L_l C_l = \frac{1}{v_{\text{ph}}^2}. \tag{2.118}$$

Evaluating the same CPW cross-section in air gives $v_{\text{ph}} = c$, and therefore

$$L_{l,\text{geo}}\, C_{\text{air}} = \mu_0 \varepsilon_0. \tag{2.119}$$

With

$$C_{\text{air}} = 4\varepsilon_0 \frac{K(k)}{K(k')}, \tag{2.120}$$

this yields

$$L_{l,\text{geo}} = \frac{\mu_0}{4} \frac{K(k')}{K(k)}. \tag{2.121}$$

For superconducting films, a kinetic inductance contribution is added, as derived next.

2.5.3 CPW kinetic inductance

Using $L_{k,\square}$ from Eq. (2.28) and accounting for the non-uniform current distribution in the CPW [116, 117], the kinetic-inductance contribution can be written in a thin-film approximation. The expressions below assume $t \ll w, g$, and the approximation $L_{k,\square} \approx \mu_0 \lambda_L^2 / t$ is valid for $t \ll \lambda_L$. The kinetic inductance per unit length is

$$L_{l,\text{kin}} = L_{k,\square}\,(g_c + g_g) \approx \frac{\mu_0 \lambda_L^2}{t}\,(g_c + g_g) \qquad (t \ll \lambda_L). \tag{2.122}$$

where g_c and g_g are geometric factors that account for the current distribution in the center conductor and ground planes, respectively [116, 117]:

$$g_c = \frac{1}{2w(1-k^2)K^2(k)} \left[\pi + \ln\left(\frac{2\pi w}{t}\right) - k \ln\left(\frac{1+k}{1-k}\right)\right], \tag{2.123}$$

$$g_g = \frac{k}{2w(1-k^2)K^2(k)} \left[\pi + \ln\left(\frac{4\pi(w+2g)}{t}\right) - \frac{1}{k} \ln\left(\frac{1+k}{1-k}\right)\right]. \tag{2.124}$$

For typical CPW geometries with $w = 10\,\mu\text{m}$, $g = 5\,\mu\text{m}$, and $t = 100\,\text{nm}$, $g_c \sim 0.1\text{-}0.2\,\mu\text{m}^{-1}$ and $g_g \sim 0.05\text{-}0.1\,\mu\text{m}^{-1}$ [116].

The total inductance per unit length is

$$L_l = L_{l,\text{geo}} + L_{l,\text{kin}}, \tag{2.125}$$

and the kinetic inductance fraction is defined as $\alpha_k \equiv L_{l,\text{kin}}/L_l$. Here α_k is defined with respect to the total line inductance, not the geometric inductance alone. For the aluminum CPWs used in this thesis, α_k is typically at the percent level or below, so kinetic inductance provides only a small correction

to v_{ph} and Z_0. For materials with larger penetration depths, such as NbTiN or granular aluminum, α_k can approach unity [72].

Temperature dependence from the Gorter-Casimir model. Combining the Gorter-Casimir result $\lambda_L(T) = \lambda_L(0)/\sqrt{1-\tau^4}$ from Sec. 2.1.2 with Eq. (2.122) gives a temperature-dependent CPW kinetic inductance per unit length

$$L_{l,\mathrm{kin}}(T) = L_{l,\mathrm{kin}}(0)\frac{1}{1-\tau^4}, \qquad \tau \equiv \frac{T}{T_c}, \tag{2.126}$$

since $L_{l,\mathrm{kin}} \propto \lambda_L^2$. The total line inductance therefore becomes

$$L_l(T) = L_{l,\mathrm{geo}} + \frac{L_{l,\mathrm{kin}}(0)}{1-\tau^4}. \tag{2.127}$$

For a fixed distributed capacitance C_l, the phase velocity and resonance frequency decrease as the kinetic inductance increases with temperature. Writing the zero-temperature kinetic-inductance fraction as

$$\alpha_k \equiv \frac{L_{l,\mathrm{kin}}(0)}{L_{l,\mathrm{geo}} + L_{l,\mathrm{kin}}(0)}, \tag{2.128}$$

the resonance frequency of a CPW mode can be written as

$$f_r(T) = f_{r0}\sqrt{\frac{1-\tau^4}{(1-\alpha_k)(1-\tau^4)+\alpha_k}}, \tag{2.129}$$

where f_{r0} is the zero-temperature resonance frequency. This expression is the form used later to analyze the temperature-dependent frequency shift of the bare CPW resonator in Sec. 4.5.3. It describes a temperature-dependent resonance shift arising from the increase of kinetic inductance with temperature, not a Kerr-type microwave nonlinearity.

2.5.4 Characteristic impedance

The CPW supports quasi-TEM wave propagation characterized by the distributed inductance L_l and capacitance C_l. The phase velocity is

$$v_{\mathrm{ph}} = \frac{1}{\sqrt{L_l C_l}} = \frac{c}{\sqrt{\varepsilon_{\mathrm{eff}}}}\sqrt{1-\alpha_k}, \tag{2.130}$$

where c is the speed of light in vacuum and $\alpha_k = L_{l,\mathrm{kin}}/L_l$. For $\alpha_k \ll 1$, this reduces to $v_{\mathrm{ph}} \simeq c/\sqrt{\varepsilon_{\mathrm{eff}}}\,(1-\alpha_k/2)$.

The characteristic impedance is $Z_0 = \sqrt{L_l/C_l}$. Using Eq. (2.115) and Eq. (2.121), the impedance in the absence of kinetic inductance is

$$Z_0 = \frac{1}{4\sqrt{\varepsilon_0\varepsilon_{\mathrm{eff}}}}\sqrt{\frac{\mu_0}{\varepsilon_0}}\frac{K(k')}{K(k)} = \frac{30\pi}{\sqrt{\varepsilon_{\mathrm{eff}}}}\frac{K(k')}{K(k)}\,\Omega. \tag{2.131}$$

Table 2.3: Analytic CPW parameters for the two CPW geometries used in this thesis, evaluated for high-resistivity silicon with $\varepsilon_r = 11.45$. The tabulated values use the thick-substrate approximation and neglect the small kinetic-inductance correction.

Parameter	Bare CPW	FTR
Conductor width w	$10\,\mu$m	$10\,\mu$m
Gap width g	$5\,\mu$m	$2\,\mu$m
Effective permittivity $\varepsilon_{\mathrm{eff}}$	6.23	6.23
Characteristic impedance Z_0	$48\,\Omega$	$37\,\Omega$
Phase velocity v_{ph}	$0.40c$	$0.40c$
Capacitance per unit length C_l	172 pF/m	223 pF/m
Inductance per unit length L_l	402 nH/m	311 nH/m

Two CPW geometries are used in this thesis (Table 2.3). Bare (non-tunable) resonators serve as fixed-frequency reference devices for loss characterization. They use $w = 10\,\mu$m and $g = 5\,\mu$m, corresponding to a standard near-$50\,\Omega$ CPW geometry compatible with the $50\,\Omega$ feedline. In the FTR devices, the SQUID termination adds inductive loading and thereby increases the effective mode impedance of the resonator. To compensate for this, the CPW gap is reduced to $g = 2\,\mu$m while keeping $w = 10\,\mu$m, which increases the per-unit-length capacitance C_l and lowers the CPW section impedance. This keeps the overall SQUID-loaded resonator closer to the desired impedance range while also increasing the SQUID participation ratio γ (Sec. 2.6.2).

2.5.5 Quarter-wave resonator

A section of CPW terminated at both ends forms a resonator whose mode frequencies depend on the boundary conditions. All resonators in this thesis are quarter-wave ($\lambda/4$) resonators.

Quarter-wave resonator. A $\lambda/4$ resonator has one end shorted (grounded) and one end open, as shown in Fig. 2.13(a). The voltage node occurs at the shorted end and the voltage antinode at the open end. In practice, the open end is only approximately open because of the coupling capacitor and fringing fields, but the ideal open-short boundary conditions provide an accurate starting point for the fundamental mode. The fundamental mode satisfies $l = \lambda/4$, giving a resonance frequency

$$f_0 = \frac{v_{\mathrm{ph}}}{4l} = \frac{c}{4l\sqrt{\varepsilon_{\mathrm{eff}}}}\sqrt{1-\alpha_k}. \tag{2.132}$$

Higher harmonics occur at $f_n = (2n+1)f_0$ for $n = 0, 1, 2, \ldots$. The corresponding voltage and current standing-wave profiles for the fundamental mode are shown in Fig. 2.13(b).

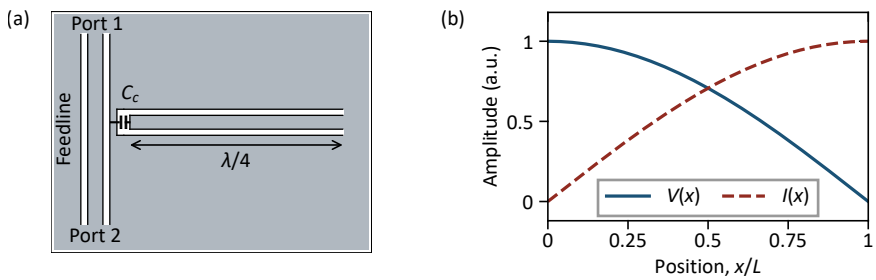

Figure 2.13: Quarter-wave CPW resonator. (a) Schematic with shorted termination and capacitive coupling. (b) Voltage (solid) and current (dashed) standing-wave profiles for the fundamental mode.

Equivalent lumped-element model. A distributed resonator can be equated to a lumped LC circuit by energy matching. For a quarter-wave resonator with the open end at $x = 0$, the shorted end at $x = l$, and V_0 denoting the voltage amplitude at the open end,

$$V(x) = V_0 \cos\left(\frac{\pi x}{2l}\right), \qquad I(x) = \frac{V_0}{Z_0}\sin\left(\frac{\pi x}{2l}\right), \tag{2.133}$$

The time-averaged electric energy stored in the distributed capacitance is

$$\langle E_C \rangle = \frac{1}{4}\int_0^l C_l V_0^2 \cos^2\left(\frac{\pi x}{2l}\right) dx = \frac{l C_l V_0^2}{8}. \tag{2.134}$$

Equating this to $\langle E_C \rangle = \frac{1}{4} C_r V_0^2$ for a lumped capacitor yields C_r, and from $\omega_0 = 1/\sqrt{L_r C_r}$ the effective inductance follows:

$$C_r = \frac{l C_l}{2}, \tag{2.135}$$

$$\omega_0 = \frac{\pi v_{\mathrm{ph}}}{2l} = \frac{1}{\sqrt{L_r C_r}}, \tag{2.136}$$

$$L_r = \frac{1}{\omega_0^2 C_r} = \frac{8 l L_l}{\pi^2}. \tag{2.137}$$

The factor $8/\pi^2 \approx 0.81$ comes from the sinusoidal current distribution along the resonator, which reduces the effective inductance below the total distributed inductance lL_l.

The modal characteristic impedance is

$$Z_r = \sqrt{\frac{L_r}{C_r}} = \sqrt{\frac{8 l L_l/\pi^2}{l C_l/2}} = \frac{4}{\pi}\sqrt{\frac{L_l}{C_l}} = \frac{4}{\pi} Z_0 \approx 1.27 Z_0. \tag{2.138}$$

For a $50\,\Omega$ CPW, $Z_r \approx 64\,\Omega$. Here Z_0 denotes the distributed transmission-line characteristic impedance of the CPW, whereas Z_r denotes the effective lumped impedance of the fundamental resonant mode.

2.5.6 Coupling capacitance

The resonator is coupled to the feedline through a finite side-coupled section near the open end. The corresponding mutual capacitance is denoted by C_c. For planar electrodes defined by cuts in a continuous ground plane, Martinis and Megrant give the general electrostatic expression [118]

$$C_{12} = \frac{\varepsilon}{\pi} \iint \frac{dA_1\, dA_2}{|\mathbf{r}_1 - \mathbf{r}_2|^3}, \tag{2.139}$$

where ε is the effective permittivity of the media above and below the metallization, and the integrals are taken over the two coupled electrodes. In the present context, this expression is used to estimate the feedline-resonator cou-

pling capacitance C_c from the device geometry. For fixed transverse geometry, Eq. (2.139) implies that C_c increases approximately linearly with the coupler length l_c.

For the bare-resonator geometry considered here, the coupler length is $l_c = 100\,\mu\text{m}$ and the feedline-to-resonator spacing is $d_g = 21\,\mu\text{m}$, defined as the gap between the outer edge of the feedline center conductor and the outer edge of the resonator center conductor. The coupling capacitance per unit length is estimated using [119]

$$\frac{C_c}{l_c} = -\frac{2\varepsilon_0\,\varepsilon_{\text{eff}}}{\pi}\ln\left[1-\left(\frac{w+g-g/4}{d_g+w-2g}\right)^2\right], \tag{2.140}$$

giving $C_c = 2.02\,\text{fF}$ for the bare-resonator coupler geometry. In the weak-coupling limit, the corresponding external quality factor is approximately

$$Q_c \approx \frac{1}{2(\omega_r C_c)^2 Z_{\text{FL}} Z_r}, \tag{2.141}$$

where Z_{FL} is the local characteristic impedance of the feedline and $Z_r = \sqrt{L_r/C_r}$ is the modal impedance of the $\lambda/4$ resonator from Sec. 2.5.5. A more general expression beyond the weak-coupling limit is derived in Sec. 2.5.7.

2.5.7 Coupling quality factor

The coupling strength is quantified by the external quality factor

$$Q_c = \frac{\omega_r U}{P_{\text{ext}}}, \tag{2.142}$$

where U is the energy stored in the resonator mode and P_{ext} is the power lost from that mode into the external circuit [109]. Near resonance, Göppl *et al.* model the coupling capacitor in series with the feedline load and transform this series combination into a Norton-equivalent parallel load [119]. For one propagation direction of the feedline with characteristic impedance Z_{FL}, the equivalent resistance and capacitance are [119]

$$R^*_{\text{env}} = \frac{1+(\omega_r C_c Z_{\text{FL}})^2}{(\omega_r C_c)^2 Z_{\text{FL}}}, \qquad C^*_c = \frac{C_c}{1+(\omega_r C_c Z_{\text{FL}})^2}. \tag{2.143}$$

Here Z_{FL} denotes the local feedline characteristic impedance, distinguishing it from the resonator line impedance Z_0. The quantity R^*_{env} is not a physical dissipative element on chip. Rather, it is the effective parallel resistance that represents photon leakage from the resonator into the external environment through the coupling capacitor [119, 120].

The extra capacitance C_c^* produces a small downward shift of the resonance frequency [119]. For a quarter-wave resonator coupled symmetrically to the two propagation directions of the feedline [119]

$$Q_c = \frac{\omega_r R^*_{\mathrm{env}} C_r}{2}, \tag{2.144}$$

where C_r is the effective modal capacitance [119]. Using the quarter-wave modal relation,

$$C_r = \frac{1}{\omega_r Z_r}, \tag{2.145}$$

this becomes

$$Q_c = \frac{R^*_{\mathrm{env}}}{2Z_r} = \frac{1 + (\omega_r C_c Z_{\mathrm{FL}})^2}{2(\omega_r C_c)^2 Z_{\mathrm{FL}} Z_r}. \tag{2.146}$$

In the weak-coupling limit $\omega_r C_c Z_0 \ll 1$, this reduces to

$$Q_c \approx \frac{1}{2(\omega_r C_c)^2 Z_{\mathrm{FL}} Z_r}. \tag{2.147}$$

For the bare resonators, the short coupler of 100 µm and the large gap of 21 µm produce weak coupling, so a lumped C_c model provides a reasonable first estimate. By contrast, the FTRs use a 1 mm-long coupler with only a 2 µm-wide ground strip between the feedline and the coupler, which produces much stronger and more distributed coupling. In that regime, the capacitance estimate combined with the external-loading model is useful only as a first-order approximation, whereas a distributed coupled-line treatment is physically more appropriate [120]. Thus, the long FTR couplers should ultimately be analyzed with a dedicated transmission-line model rather than reduced to a single lumped coupling capacitor.

2.5.8 Intrinsic quality factor

The intrinsic quality factor Q_i characterizes intrinsic loss processes such as dielectric, conductor, radiation, and TLS loss. The total loaded quality factor is then

$$Q_l^{-1} = Q_i^{-1} + Q_c^{-1}, \tag{2.148}$$

with the corresponding linewidth

$$\kappa = \frac{\omega_r}{Q_l}, \tag{2.149}$$

and contributions

$$\kappa_i = \frac{\omega_r}{Q_i}, \qquad \kappa_c = \frac{\omega_r}{Q_c}. \tag{2.150}$$

Typical coupling capacitances in superconducting microwave resonators lie in the femtofarad range and can produce external quality factors spanning from strongly overcoupled values of order 10^2 to weakly coupled values above 10^6, depending on the coupler geometry and operating frequency. In the present device set, the FTRs are designed to be comparatively strongly coupled in transmission in order to enhance readout contrast, whereas the bare reference resonators are coupled more weakly so that intrinsic loss can be characterized with less external loading.

Two-level system loss

Amorphous dielectrics at material interfaces and in oxide layers contain two-level systems (TLS), described by the tunneling model [121, 122]. These defects couple to the resonator electric field and absorb microwave power [123–125]. In superconducting CPW resonators, the dominant TLS contributions arise from the metal-substrate interface, the native oxide on the superconductor surface, and the substrate-air interface within the capacitive gaps where the electric field is concentrated [86, 126].

TLS defects have a spread of energy splittings and relaxation rates. At low temperatures ($k_B T \ll \hbar\omega_r$), the thermal factor $\tanh(\hbar\omega_r/2k_B T)$ is approximately unity. The TLS-induced loss can then be written as

$$\delta_{\mathrm{TLS}}(n_c) = \frac{\delta_{\mathrm{TLS},0}}{1 + (n_c/n_c^*)^{\beta'}}, \tag{2.151}$$

where $\delta_{\mathrm{TLS},0} = pF \tan\delta_{\mathrm{TLS}}$ is the low-power TLS loss contribution, p is the filling factor (fraction of mode energy in the lossy regions), F is a geometric factor of order unity, $\tan\delta_{\mathrm{TLS}}$ is the intrinsic loss tangent of the TLS-hosting material, n_c is the intracavity photon number, n_c^* is a characteristic saturation photon number, and β' is the saturation exponent [124, 126]. At high photon numbers ($n_c \gg n_c^*$), the TLS saturate and the associated loss decreases.

The intrinsic quality factor of the resonator is related to the total loss tangent by $Q_i^{-1} = \delta_{\mathrm{res}} + \delta_{\mathrm{TLS}}$, where δ_{res} accounts for residual non-TLS loss mechanisms. The power-dependent intrinsic quality factor is then given by [126, 127]

$$Q_i^{-1}(n_c) = \delta_{\mathrm{res}} + \frac{\delta_{\mathrm{TLS},0}}{(1 + n_c/n_c^*)^{\beta'}}, \tag{2.152}$$

where $\delta_{\mathrm{TLS},0}$ is the unsaturated TLS loss contribution at $n_c \ll n_c^*$. This model predicts a low-power quality factor $Q_{i,0} = 1/(\delta_{\mathrm{res}} + \delta_{\mathrm{TLS},0})$ and a high-power saturation value $Q_{i,\infty} = 1/\delta_{\mathrm{res}}$. At high powers, the remaining loss is set by excess quasiparticles ($n_{\mathrm{qp}} \sim$ 1-100 $\mu\mathrm{m}^{-3}$ at $T \lesssim 50\,\mathrm{mK}$ [128, 129]), orders of magnitude above the thermal prediction [70], which is attributed to stray infrared photons, cosmic rays, and phonon-mediated pair breaking [130]. Further contributions arise from coupling to spurious modes, vortex-induced dissipation at film edges or constrictions where residual fields exceed H_{c1} locally.

Thermally activated quasiparticle loss

At finite temperature, a superconductor contains a thermally activated quasiparticle population set by the superconducting energy gap Δ. These excitations add a dissipative component to the complex conductivity and thereby reduce the internal quality factor of a microwave resonator. In the sub-gap and low-temperature limit, $\hbar\omega_r \ll 2\Delta$ and $k_B T \ll \Delta$, the Mattis-Bardeen response gives an approximately activated contribution to the microwave loss [72, 84, 116]

$$Q_i^{-1}(T) = Q_{i,\mathrm{bg}}^{-1} + A\sqrt{\frac{\Delta}{k_B T}} \exp\left(-\frac{\Delta}{k_B T}\right), \tag{2.153}$$

where $Q_{i,\mathrm{bg}}^{-1}$ is a temperature-independent background loss, Δ is the superconducting energy gap, and A is a dimensionless prefactor that absorbs the

coupling of the resonator mode to the film conductivity, along with the relevant geometric factors. The exponential factor reflects the Boltzmann activation of quasiparticles across the gap, while the prefactor $\sqrt{\Delta/k_B T}$ originates from the BCS density of states near the gap edge [84]. In weak-coupling BCS theory, the zero-temperature gap satisfies $\Delta(0) = 1.764\, k_B T_c$ [70]. Eq. (2.153) is therefore useful for identifying the onset temperature of quasiparticle-limited loss and for extracting an effective gap from temperature-dependent Q_i data. Far below T_c, the activated term is exponentially suppressed, so thermally excited quasiparticles make a negligible contribution to the resonator loss.

2.6 Flux-tunable resonator

A flux-tunable resonator (FTR), also called a SQUID cavity, is a half-wave or quarter-wave coplanar-waveguide (CPW) resonator with a dc SQUID placed at a current antinode. The FTRs developed in this thesis are quarter-wave CPW resonators whose grounded end is replaced by a dc SQUID shunt [60]. The SQUID provides a flux-dependent boundary condition, so the resonator eigenfrequency and its self-Kerr nonlinearity depend on the applied flux. The formulation developed in this section follows Refs. [102, 131, 132].

For the fundamental mode, this section derives the resonance condition $\omega_r(\Phi_e)$, a single-mode quantization with the mapping from the resonator mode coordinate to the SQUID flux, and the resulting self-Kerr coefficient $\mathcal{K}(\Phi_e)$. The CPW and SQUID termination are described using a flux-coordinate Lagrangian, including the boundary term (Sec. 2.6.1). First, the distributed mode problem relates the termination inductance L_S to the electrical length θ and the eigenfrequency ω_r (Sec. 2.6.2). Then, the mode shape relates the resonator mode coordinate to the SQUID terminal phase through $\phi_l/\phi_0 = \cos\theta$ (Sec. 2.6.5).

The control parameter is the applied flux Φ_e. For each applied flux, the SQUID dc operating point $(\bar{\phi}_l, \bar{\varphi})$ and the screened flux Φ_s are defined as stable dc solutions on the zero-voltage branch of the SQUID equations from Sec. 2.4.4 and Sec. 2.4.7. The microwave response is then treated as a perturbation about that operating point. Unless stated otherwise, all SQUID derivatives entering the termination inductance and Kerr coefficients are evaluated at this dc operating point.

2.6.1 Circuit model and Lagrangian

The circuit is shown in Fig. 2.14(a): a CPW of length l terminated at $x = l$ by a dc SQUID and capacitively coupled to a feedline at $x = 0$. Panels (b) and (c) show why the SQUID termination cannot always be treated as a point-like short. The mode current remains finite over the geometrical extent of the SQUID loop, so part of the phase drop occurs over the loop arms before the junction phase drop is reached. This is represented by the finite SQUID length d_s and the equivalent junction extension d'. Physically, these lengths capture the boundary softening produced by the SQUID termination and explain why the resonance frequency is reduced relative to the ideal short-terminated quarter-wave limit.

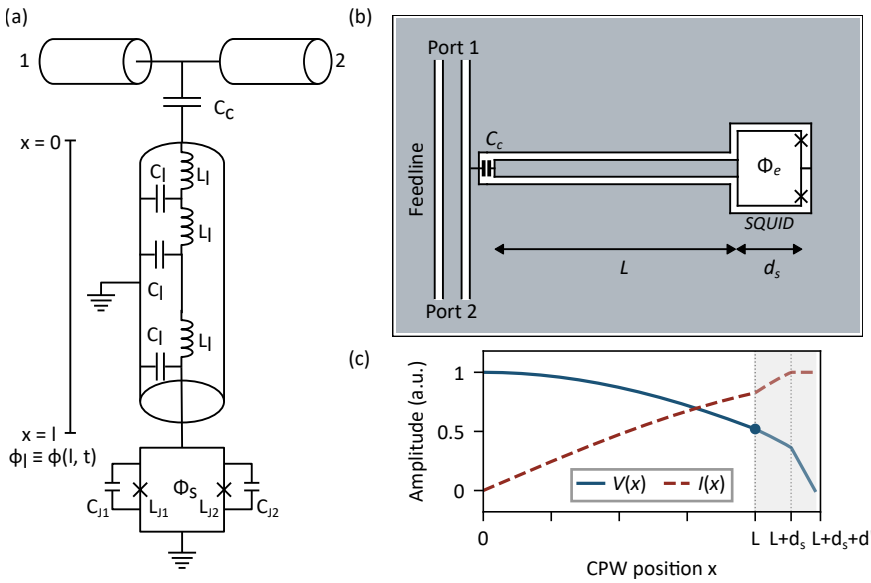

Figure 2.14: Flux-tunable resonator circuit model. (a) CPW of length l (L_l, C_l) terminated by a dc SQUID ($L_{J1,2}$, L_g, $C_{J1,2}$) and coupled to a feedline via C_c. (b) Schematic of the FTR with one end of the CPW terminated by a SQUID loop of finite geometrical extent d_s and shunted to ground through the junctions. (c) Voltage (solid) and current (dashed) standing-wave profiles. The mode effectively extends beyond $x = l$ over the SQUID-loop length d_s, followed by an additional equivalent junction extension d'.

The Lagrangian of the distributed CPW line is [131, 132]

$$\mathcal{L}_{\text{cpw}} = \int_0^l \left[\frac{C_l}{2} \dot{\Phi}^2 - \frac{1}{2L_l} (\partial_x \Phi)^2 \right] dx, \tag{2.154}$$

where $\Phi(x,t)$ is the node-flux field of the CPW, defined as the time integral of the local node voltage, $\Phi(x,t) = \int^t V(x,t')\,dt'$. It is therefore a circuit coordinate and should not be confused with the magnetic fluxes Φ_e and Φ_s that thread the SQUID loop. In this section, $\Phi(x,t)$ denotes the small perturbation of the CPW node flux about its dc operating point set by the applied flux bias. The dc part is absorbed into that operating point and does not appear explicitly in the linearized dynamics. Introducing the corresponding dimensionless phase perturbation $\phi(x,t) = 2\pi\Phi(x,t)/\Phi_0$, this becomes

$$\mathcal{L}_{\text{cpw}}[\phi] = \left(\frac{\Phi_0}{2\pi} \right)^2 \int_0^l \frac{C_l}{2} \left[\dot{\phi}^2 - v_{\text{ph}}^2 (\phi')^2 \right] dx, \tag{2.155}$$

with the phase velocity $v_{\text{ph}} = 1/\sqrt{L_l C_l}$.

At the SQUID termination ($x = l$), the two Josephson junctions and the loop inductance are treated for simplicity as a lumped termination for the distributed line. At fixed dc flux bias, the SQUID is biased at an operating point $(\bar{\phi}_l, \bar{\varphi})$ on the zero-voltage branch. Thus, for now, we neglect the Kerr nonlinearity arising at high amplitudes. Small microwave excitations are then treated as perturbations about that operating point, so the termination can be represented by a linear one-port inductance $L_S(\Phi_e)$ in parallel with an effective junction capacitance $C_S = C_{J1} + C_{J2}$. For the eigenmode calculation, the weak input coupling capacitor C_c is neglected because it perturbs the boundary condition only weakly compared to the SQUID termination.

The SQUID contribution to the Lagrangian is [131, 132]

$$\mathcal{L}_S[\phi_l] = \left(\frac{\Phi_0}{2\pi} \right)^2 \left[\frac{C_S}{2} \dot{\phi}_l^2 - \frac{\phi_l^2}{2L_S} \right], \tag{2.156}$$

where the full terminal phase is written as

$$\phi_l^{\text{tot}}(t) = \bar{\phi}_l + \delta\phi_l(t), \tag{2.157}$$

where $\bar{\phi}_l$ is the dc operating point and $\delta\phi_l(t)$ is the small microwave perturbation. In this section, $\phi(x,t)$ denotes only the small phase perturbation of the

mode, with the dc part omitted, so

$$\phi_l(t) \equiv \phi(l,t) = \delta\phi_l(t). \tag{2.158}$$

The SQUID Lagrangian is, therefore, the quadratic expansion about the dc operating point. The constant term is irrelevant for the resonator eigenmode, and the linear term vanishes because the expansion is taken about a stationary operating point. Therefore, only the quadratic capacitive and inductive terms remain, giving Eq. (2.156).

The termination inductance L_S appearing in Eq. (2.156) is derived by first obtaining the SQUID inductance from the SQUID potential (Sec. 2.6.3). The total FTR Lagrangian is

$$\mathcal{L}_{\mathrm{FTR}}[\phi, \phi_l] = \mathcal{L}_{\mathrm{cpw}}[\phi] + \mathcal{L}_S[\phi_l]. \tag{2.159}$$

2.6.2 Eigenmode equation

Given the linearized one-port termination inductance L_S between the resonator end node and ground, evaluated at the SQUID dc operating point, the eigenmode of the FTR is obtained from the Lagrangian Eq. (2.159). Varying the action with respect to $\phi(x,t)$ yields the bulk Euler-Lagrange equation for the CPW, [131, 132]

$$\ddot{\phi}(x,t) - v_{\mathrm{ph}}^2 \phi''(x,t) = 0. \tag{2.160}$$

In the flux-coordinate formulation, the line current is

$$I(x,t) = -\frac{1}{L_l}\,\partial_x \Phi(x,t) = -\left(\frac{\Phi_0}{2\pi}\right)\frac{1}{L_l}\,\partial_x \phi(x,t), \tag{2.161}$$

so the open-end boundary condition of vanishing current is

$$\phi'(0,t) = 0. \tag{2.162}$$

At the SQUID end ($x = l$), the CPW is terminated to ground through the SQUID. Therefore, the current arriving through the CPW is also the current flowing through the SQUID termination. With the flux coordinate $\Phi(x,t)$, the

CPW current at the end is

$$I_{\mathrm{cpw}}(l,t) = -\frac{1}{L_l}\,\partial_x\Phi(l,t). \tag{2.163}$$

In the linearized termination model, the SQUID is represented by an inductor L_S in parallel with a capacitance C_S, so the termination current is

$$I_S(t) = \frac{\Phi_l(t)}{L_S} + C_S\,\ddot{\Phi}_l(t), \qquad \Phi_l(t) \equiv \Phi(l,t). \tag{2.164}$$

Enforcing $I_{\mathrm{cpw}}(l,t) = I_S(t)$ gives

$$\partial_x\Phi(l,t) = -L_l\left[\frac{\Phi_l(t)}{L_S} + C_S\,\ddot{\Phi}_l(t)\right]. \tag{2.165}$$

Using $\Phi = (\Phi_0/2\pi)\phi$ and $\Phi_l = (\Phi_0/2\pi)\phi_l$ yields the boundary condition in the phase coordinate,

$$\phi'(l,t) = -L_l\left[\frac{\phi_l(t)}{L_S} + C_S\ddot{\phi}_l(t)\right]. \tag{2.166}$$

As stated in Sec. 2.4.2, the junction plasma frequency is well above the FTR fundamental mode. The SQUID also has an internal loop mode. If that loop mode is likewise far above ω_r, the linearized termination response at the resonator frequency is predominantly inductive. The term proportional to C_S can then be neglected to leading order in the eigenfrequency boundary condition. Its effect is retained later only as a small correction to the effective mode capacitance $C_r(\theta)$ in Sec. 2.6.5 [131, 132]. The eigenfrequency boundary condition, therefore, reduces to

$$\phi'(l,t) = -\frac{L_l}{L_S}\phi_l(t). \tag{2.167}$$

Mode ansatz and eigenfrequency. The wave equation Eq. (2.160) and the boundary conditions Eq. (2.162) and Eq. (2.167) are linear and time independent. Without a drive, the solutions can be written as eigenmodes with a definite angular frequency ω. For a single eigenmode,

$$\phi(x,t) = \psi(x)e^{-i\omega t}. \tag{2.168}$$

Substituting into Eq. (2.160) gives the ordinary differential equation

$$\psi''(x) + k^2\psi(x) = 0, \qquad k \equiv \omega\sqrt{L_l C_l}. \tag{2.169}$$

The general solution is $\psi(x) = A\cos(kx) + B\sin(kx)$. The open-end condition Eq. (2.162) requires $\psi'(0) = 0$, which sets $B = 0$, so

$$\psi(x) = A\cos(kx). \tag{2.170}$$

Applying the SQUID boundary condition Eq. (2.167) at $x = l$ gives

$$\psi'(l) = -\frac{L_l}{L_S}\psi(l). \tag{2.171}$$

With $\psi'(x) = -Ak\sin(kx)$, the ratio becomes

$$\frac{\psi'(l)}{\psi(l)} = -k\tan(kl), \tag{2.172}$$

and eliminating the overall amplitude A yields the transcendental eigenfrequency equation

$$\tan(kl) = \frac{L_l}{kL_S}. \tag{2.173}$$

Inductance participation ratio. The resonance condition Eq. (2.173) can be expressed in a simple, dimensionless form in terms of the electrical length

$$\theta \equiv kl = \omega\, l\sqrt{L_l C_l}, \tag{2.174}$$

and the inductance participation ratio

$$\gamma \equiv \frac{L_S}{lL_l}. \tag{2.175}$$

The quantity γ compares the termination inductance to the total distributed inductance of the CPW section. Then Eq. (2.173) becomes

$$\tan\theta = \frac{1}{\gamma\theta}. \tag{2.176}$$

The fundamental mode is the lowest-frequency solution of Eq. (2.176) that

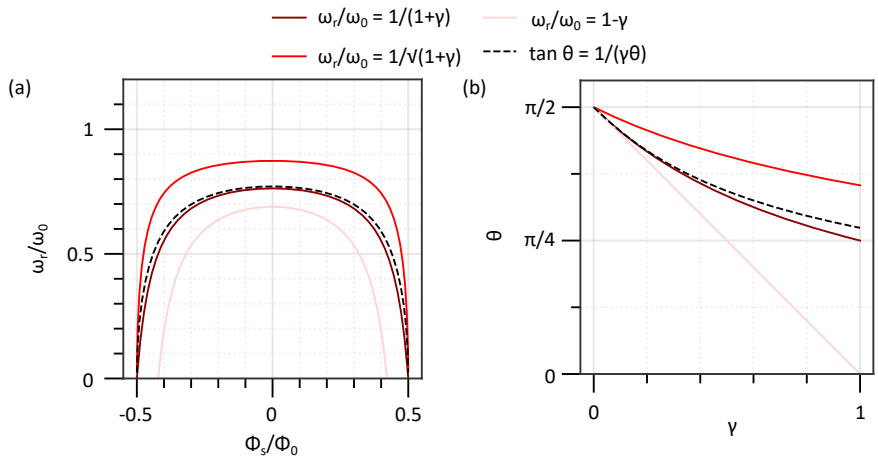

Figure 2.15: Comparison of three closed-form approximations with the exact transcendental solution Eq. (2.176) for a representative large-loop FTR with $\gamma_{\Phi=0} \approx 0.3$. (a) Normalized resonance frequency ω_r/ω_0 versus screened flux Φ_s/Φ_0, showing how the different approximations propagate into the tuning curve. (b) Electrical length θ versus the dimensionless termination parameter γ, comparing the exact relation $\tan\theta = 1/(\gamma\theta)$ with the commonly used approximations.

approaches the usual short-terminated quarter-wave resonance when the termination inductance becomes small. In the limit $L_S \to 0$ the boundary condition becomes an ideal short, and the solution satisfies $\theta \to \pi/2$. Increasing L_S softens the termination, increases the electrical length of the mode, and lowers the eigenfrequency relative to the ideal short, which leads to flux-tuning of the resonance frequency.

Closed-form approximation. For $\gamma \ll 1$, the solution satisfies $\theta = \pi/2 - \epsilon$ with $0 < \epsilon \ll 1$. Using $\tan(\pi/2 - \epsilon) \simeq 1/\epsilon$, Eq. (2.176) gives

$$\frac{1}{\epsilon} \simeq \frac{1}{\gamma\theta} \qquad \Rightarrow \qquad \epsilon \simeq \gamma\theta. \tag{2.177}$$

With $\theta = \pi/2 - \epsilon$, this becomes $\epsilon \simeq \gamma(\pi/2 - \epsilon)$, so $\epsilon(1+\gamma) \simeq (\pi/2)\gamma$ and therefore

$$\theta \approx \frac{\pi}{2} \cdot \frac{1}{1+\gamma}. \tag{2.178}$$

Since $\omega_r/\omega_0 = \theta/(\pi/2)$ with $\omega_0 = \pi v_{\mathrm{ph}}/(2l)$, this yields the expression

$$\boxed{\omega_r \approx \frac{\omega_0}{1+\gamma} = \frac{\omega_0}{1+L_S/(lL_l)}.} \tag{2.179}$$

For the present devices, $\gamma(\Phi_e = 0) \approx 0.4$ to 0.6, so the different closed-form expressions for $\theta(\gamma)$ used in the literature [133, 134] are no longer quantitatively equivalent. Figure Fig. 2.15 benchmarks these approximations against the exact transcendental relation Eq. (2.176) for the large-loop regime relevant here. Panel (b) compares the approximations directly at the level of $\theta(\gamma)$, while panel (a) shows the corresponding differences in the normalized tuning curve ω_r/ω_0 versus Φ_s/Φ_0. This comparison justifies using Eq. (2.176) for quantitative modeling while retaining Eq. (2.179) only as an approximate expression.

2.6.3 Linearized SQUID inductance

For microwave operation, the SQUID enters the resonator boundary condition through an effective one-port inductance determined by the linearized SQUID response about its dc operating point. Writing the SQUID coordinates as

$$\phi_l^{\mathrm{tot}} = \bar{\phi}_l + \delta\phi_l, \qquad \varphi^{\mathrm{tot}} = \bar{\varphi} + \delta\varphi, \tag{2.180}$$

where $(\bar{\phi}_l, \bar{\varphi})$ is the dc operating point and $(\delta\phi_l, \delta\varphi)$ are small perturbations about it, the SQUID potential from Sec. 2.4.7 may be expanded to second order as

$$\delta U^{(2)} = \frac{1}{2} \begin{pmatrix} \delta\phi_l & \delta\varphi \end{pmatrix} H(\bar{\phi}_l, \bar{\varphi}) \begin{pmatrix} \delta\phi_l \\ \delta\varphi \end{pmatrix}, \tag{2.181}$$

where $\delta U^{(2)}$ is the quadratic part of the change in potential energy and $H(\bar{\phi}_l, \bar{\varphi})$ is the Hessian matrix of $U(\phi_l, \varphi)$ evaluated at the operating point. Writing out Eq. (2.181) gives

$$\delta U^{(2)} = \frac{1}{2}\Big(U_{\phi\phi}\, \delta\phi_l^2 + 2U_{\phi\varphi}\, \delta\phi_l\, \delta\varphi + U_{\varphi\varphi}\, \delta\varphi^2 \Big). \tag{2.182}$$

One-port reduction and Schur complement

In the one-port configuration relevant here, the resonator drives the SQUID only through the terminal phase ϕ_l, while the loop coordinate φ is internal and not independently driven. In the quasistatic limit relevant for the linearized boundary condition, φ relaxes to the local minimum corresponding to each imposed ϕ_l. This defines the minimizing path

$$\frac{\partial U}{\partial \varphi}\big(\phi_l, \varphi^\star(\phi_l)\big) = 0, \qquad \varphi^\star(\bar{\phi}_l) = \bar{\varphi}. \tag{2.183}$$

The SQUID therefore behaves as an effective one-port element described by the reduced potential

$$U_{\text{eff}}(\phi_l) = U\big(\phi_l, \varphi^\star(\phi_l)\big). \tag{2.184}$$

For the linearized inductance, only the local curvature of U_{eff} at the operating point is required. Eliminating the internal coordinate gives the effective quadratic energy

$$\delta U_{\text{eff}}^{(2)} = \frac{1}{2}\left(U_{\phi\phi} - \frac{U_{\phi\varphi}^2}{U_{\varphi\varphi}}\right)\delta\phi_l^2, \tag{2.185}$$

with all derivatives evaluated at $(\bar{\phi}_l, \bar{\varphi})$. This is the Schur-complement reduction of the Hessian of $U(\phi_l, \varphi)$. Physically, the coupling term $U_{\phi\varphi}$ allows the internal coordinate to relax as the terminal phase is displaced, which reduces the effective one-port stiffness seen by the resonator. A detailed derivation of the reduced-potential expansion is given in App. 6.1.1.

Inductance from curvature

Define the terminal flux coordinate

$$\Phi_l \equiv \frac{\Phi_0}{2\pi}\phi_l, \qquad \bar{\Phi}_l \equiv \frac{\Phi_0}{2\pi}\bar{\phi}_l. \tag{2.186}$$

Expanding the effective SQUID potential U_{eff} around $\bar{\Phi}_l$ gives

$$U_{\text{eff}}(\Phi_l) = U_{\text{eff}}(\bar{\Phi}_l) + \sum_{n\geq 1}\frac{c_n}{n!}\left(\Phi_l - \bar{\Phi}_l\right)^n, \qquad c_n \equiv \left.\frac{d^n U_{\text{eff}}}{d\Phi_l^n}\right|_{\Phi_l=\bar{\Phi}_l}. \tag{2.187}$$

At a stationary operating point, $c_1 = 0$, and the quadratic coefficient defines

the linearized inductance through

$$c_2 = \frac{1}{L_S}. \tag{2.188}$$

This can be seen as a linear one-port element described by an effective potential $U_{\text{eff}}(\Phi_l)$, for which the terminal current is

$$I_l = \frac{\partial U_{\text{eff}}}{\partial \Phi_l}. \tag{2.189}$$

Linearizing about the operating point gives

$$\delta I_l = \left.\frac{\partial^2 U_{\text{eff}}}{\partial \Phi_l^2}\right|_{\bar{\Phi}_l} \delta\Phi_l. \tag{2.190}$$

The linearized inductance is defined by $\delta\Phi_l = L_S\,\delta I_l$, so

$$\frac{1}{L_S} = \left.\frac{\partial^2 U_{\text{eff}}}{\partial \Phi_l^2}\right|_{\bar{\Phi}_l}. \tag{2.191}$$

Eq. (2.185) gives this curvature in terms of the derivatives of $U(\phi_l, \varphi)$ evaluated at $(\bar{\phi}_l, \bar{\varphi})$. The corresponding linearized one-port inductance of the SQUID is therefore

$$\frac{1}{L_S} \equiv \left(\frac{2\pi}{\Phi_0}\right)^2 \left(U_{\phi\phi} - \frac{U_{\phi\varphi}^2}{U_{\varphi\varphi}}\right)_{(\bar{\phi}_l, \bar{\varphi})}. \tag{2.192}$$

Expressed in terms of the linearized Josephson inductances

$$L_{Jk}(\delta_k) = \frac{\Phi_0}{2\pi I_{ck} \cos\delta_k}, \qquad k \in \{1, 2\}, \tag{2.193}$$

evaluated at the operating point, i.e. at $\bar{\delta}_1 = \bar{\phi}_l + \bar{\varphi}$ and $\bar{\delta}_2 = \bar{\phi}_l - \bar{\varphi}$, one obtains

$$\frac{1}{L_S} = \left(\frac{1}{L_{J1}} + \frac{1}{L_{J2}}\right) - \frac{\left(\frac{1}{L_{J1}} - \frac{1}{L_{J2}}\right)^2}{\left(\frac{1}{L_{J1}} + \frac{1}{L_{J2}} + \frac{4}{L_g}\right)}. \tag{2.194}$$

L_g in Eq. (2.194) accounts for the stiffness of the differential (loop) mode

arising from the magnetic energy term. In the weak-screening limit ($\beta_L \to 0$) with symmetric junctions ($\alpha = 0$), the result reduces to the usual symmetric dc SQUID inductance,

$$L_S = \frac{L_{J0}}{2|\cos\bar{\varphi}|}, \tag{2.195}$$

which diverges at half-integer flux quanta.

The factor $4/L_g$ arises because the loop flux couples to the differential phase 2φ. In the quadratic expansion, the magnetic energy therefore contributes a curvature proportional to $(2\varphi)^2/(2L_g)$, which appears in $U_{\varphi\varphi}$ as the term $4/L_g$.

Loop inductance model. Let the geometric inductances of the two loop arms be $L_{g,1}$ and $L_{g,2}$. In a one-port excitation, the drive current enters the SQUID and splits between the two arms on its way to ground. If the two arms are identical, then the loop arms can be treated as two linear inductors in parallel as seen from the terminals. Under this approximation, the loop-arm contribution to the terminal inductance is

$$L_{g,\mathrm{cm}} = \frac{L_{g,1}L_{g,2}}{L_{g,1} + L_{g,2}}. \tag{2.196}$$

For symmetric arms, $L_{g,1} = L_{g,2} = L_g/2$, and therefore

$$L_{g,\mathrm{cm}} \simeq \frac{L_g}{4}. \tag{2.197}$$

This is an approximation. If the arms are not symmetric, or if the branch impedances are strongly flux dependent, $L_{g,\mathrm{cm}}$ should instead be treated as an effective linear contribution extracted from the linearized one-port impedance seen at the CPW end node.

Further, the finite size of the SQUID loop will cause an additional drop in the terminal mode phase ϕ_l, which is not captured in the current model. The exact treatment of this effect merits treating the loop as a distributed inductance with an effective reactance at microwave frequencies. To keep the model simple, a phenomenological factor A is introduced to account for the finite size of the SQUID loop relative to the CPW length.

2.6.4 Flux responsivity

The flux dependence of the FTR frequency enters through the termination inductance $L_S(\Phi_e)$ that appears in the eigenmode condition Eq. (2.173). Using the SQUID inductance from Eq. (2.194) and the participation ratio Eq. (2.175), the resonance frequency becomes a function of the external flux:

$$\omega_r(\Phi_e) = \frac{\omega_0}{1 + L_S(\Phi_e)/(lL_l)}. \tag{2.198}$$

Eq. (2.198) is obtained from Eq. (2.179) as a closed-form approximation. The exact resonance condition is Eq. (2.173) with $L_S \to L_{S,\mathrm{eff}}(\omega_r)$ for large-loop devices.

The flux tuning characteristics for asymmetric and symmetric SQUID terminations are shown in Fig. 2.16. Panel (a) shows the symmetric case, $\alpha = 0$, for which the singular half-integer flux limit is recovered. For $\beta_L \to 0$, the SQUID inductance diverges at $\Phi_e = (n + 1/2)\Phi_0$, which increases the effective electrical length and strongly pulls the resonance frequency downward. This trend should not be extrapolated to $\omega_r \to 0$ because the closed-form inductive approximation in Eq. (2.198) fails for large L_S as it only applies to the short-terminated quarter-wave limit, $\theta \approx \pi/2$. For finite screening, $\beta_L = 0.3$, the two stationary branches remain degenerate in the symmetric case, and the system switches between them at different flux values for increasing and decreasing sweeps. This produces the hysteretic tuning visible in panel (a).

Panel (a) considers the asymmetric case, $\alpha = 0.3$. Even for negligible screening, $\beta_L \to 0$, the resonance minimum near $\Phi_e = (n + 1/2)\Phi_0$ remains finite because junction asymmetry removes the exact cancelation responsible for the divergence of the symmetric SQUID inductance. When finite screening is included, $\beta_L = 0.3$, two stationary branches exist in principle, but the asymmetry lifts their degeneracy so that the forward and reverse sweeps nearly coincide.

The sensitivity of the resonance frequency to external flux is characterized by the flux responsivity

$$\mathcal{R}_\Phi = \frac{\partial \omega_r}{\partial \Phi_e}. \tag{2.199}$$

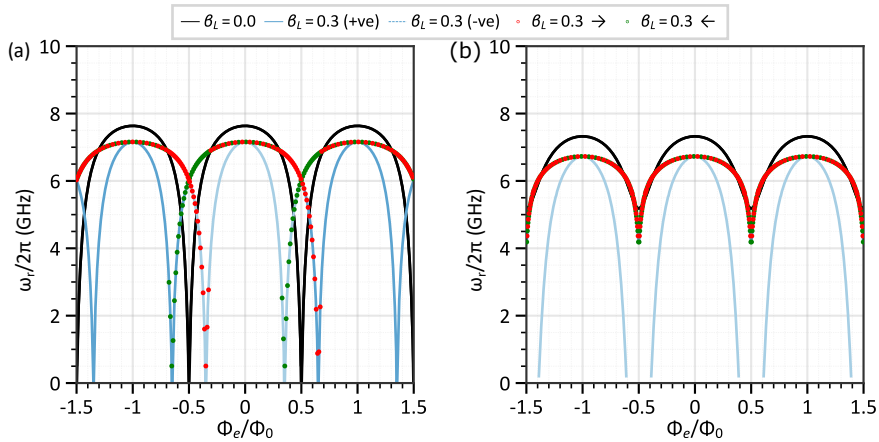

Figure 2.16: Flux tuning of the FTR resonance frequency for (a) a symmetric SQUID ($\alpha = 0$) and (b) an asymmetric SQUID ($\alpha = 0.3$). The resonance frequency $\omega_r/2\pi$ is plotted versus applied flux Φ_e/Φ_0 for negligible screening ($\beta_L = 0$, black) and finite screening ($\beta_L = 0.3$). For $\beta_L = 0.3$, the blue solid and dashed curves denote the two stationary branches, while the red and green markers show the branches followed for increasing and decreasing flux sweeps, respectively. In the symmetric case, finite screening produces branch switching and a clear hysteretic response near half-integer flux. In the asymmetric case, junction asymmetry lifts the branch degeneracy, smooths the half-integer-flux minima, and strongly suppresses hysteresis. Parameters: $\omega_0/2\pi = 9\,\mathrm{GHz}$ and $\gamma(0) = 0.5$.

Using the closed-form approximation Eq. (2.198) and the chain rule,

$$\mathcal{R}_\Phi = -\frac{\omega_0}{(1+\gamma)^2} \cdot \frac{1}{lL_l} \cdot \frac{\partial L_S}{\partial \Phi_e}. \tag{2.200}$$

The derivative $\partial L_S/\partial \Phi_e$ is obtained from Eq. (2.194) through the screened flux,

$$\frac{\partial L_S}{\partial \Phi_e} = \frac{\partial L_S}{\partial \Phi_s} \cdot \frac{\partial \Phi_s}{\partial \Phi_e}, \tag{2.201}$$

where $\partial L_S/\partial \Phi_s$ follows from the flux dependence of the linearized junction inductances $L_{Jk}(\Phi_s) = \Phi_0/[2\pi I_{ck} \cos \bar{\delta}_k(\Phi_s)]$ entering Eq. (2.194), while $\partial \Phi_s/\partial \Phi_e$ is set by the static screening equations on the chosen stable branch.

In the limit $\beta_L \to 0$ and $\alpha = 0$, one has $\Phi_s = \Phi_e$ and

$$L_S = \frac{L_{J0}}{2\cos\varphi}, \qquad \varphi = \pi\frac{\Phi_e}{\Phi_0}. \tag{2.202}$$

This gives

$$\frac{\partial L_S}{\partial \Phi_e} = \frac{\pi}{\Phi_0}\frac{L_{J0}}{2}\frac{\sin\varphi}{\cos^2\varphi}, \tag{2.203}$$

and therefore

$$\mathcal{R}_\Phi = -\frac{\omega_0}{\left(1+\dfrac{L_{J0}}{2lL_l\cos\varphi}\right)^2}\frac{\pi L_{J0}}{2\Phi_0 l L_l}\frac{\sin\varphi}{\cos^2\varphi} = -\frac{\pi\omega_0}{\Phi_0}\frac{\gamma_0\sin\varphi}{(\cos\varphi+\gamma_0)^2}, \tag{2.204}$$

where $\gamma_0 = L_{J0}/(2lL_l)$. For the FTR devices in this work, $|\mathcal{R}_\Phi|/2\pi$ reaches the tens of GHz/Φ_0.

2.6.5 Effective mode parameters

For quantization, the FTR is written as a single-mode oscillator with effective capacitance C_r and inductance L_r. Using the mode ansatz $\phi(x,t) = \phi_0(t)\cos(kx)$, the quadratic Lagrangian becomes

$$\mathcal{L} = \left(\frac{\Phi_0}{2\pi}\right)^2\left[\frac{C_r(\theta)}{2}\dot{\phi}_0^2 - \frac{\phi_0^2}{2L_r(\theta)}\right]. \tag{2.205}$$

The effective modal capacitance is [102, 119]

$$C_r(\theta) = \frac{lC_l}{2}\left[1+\frac{\sin(2\theta)}{2\theta}\right] + C_S\cos^2\theta, \tag{2.206}$$

and the effective modal inductance is [119, 131, 132]

$$\frac{1}{L_r(\theta)} = \frac{\theta^2}{2lL_l}\left[1-\frac{\sin(2\theta)}{2\theta}\right] + \frac{\cos^2\theta}{L_S}. \tag{2.207}$$

In Eq. (2.207), L_S denotes the total one-port termination inductance that enters the linear eigenmode boundary condition (Sec. 2.6.2). In the short-terminated quarter-wave limit, $L_S \to 0$ together with $\theta \to \pi/2$, and Eq. (2.206) and Eq. (2.207) reduce to the standard quarter-wave values $C_r^{(0)} = lC_l/2$ and $L_r^{(0)} = 8lL_l/\pi^2$ from Eq. (2.135) and Eq. (2.137).

The modal characteristic impedance is

$$Z_r(\theta) = \sqrt{\frac{L_r(\theta)}{C_r(\theta)}}. \tag{2.208}$$

Neglecting the shunt capacitance C_S, this reduces to the closed form [119, 131]

$$Z_r(\theta) = \frac{4Z_0}{2\theta + \sin(2\theta)}, \tag{2.209}$$

where $Z_0 = \sqrt{L_l/C_l}$ is the CPW characteristic impedance. In the short-terminated quarter-wave limit $\theta \to \pi/2$, this gives $Z_r^{(0)} = 4Z_0/\pi \approx 1.27Z_0$.

In the short-termination limit $L_S/(lL_l) \ll 1$, equivalently $\theta \to \pi/2$, a series expansion of Eq. (2.209) gives

$$Z_r \simeq \frac{4}{\pi}\sqrt{\frac{L_l}{C_l}}\left[1 + \frac{\pi^2}{6}\left(\frac{L_S}{lL_l}\right)^3\right]. \tag{2.210}$$

2.6.6 Single-mode quantization

The quantization proceeds by the standard circuit-QED procedure for a single linear mode in flux and charge variables [131, 132]. The quadratic single-mode Lagrangian Eq. (2.205) defines a harmonic oscillator with canonical flux and charge coordinates

$$\hat{\Phi} \equiv \left(\frac{\Phi_0}{2\pi}\right)\hat{\phi}_0, \qquad \hat{Q} \equiv \frac{\partial \mathcal{L}}{\partial \dot{\Phi}} = C_r(\theta)\,\dot{\hat{\Phi}}, \qquad [\hat{\Phi}, \hat{Q}] = i\hbar, \tag{2.211}$$

and resonance frequency $\omega_r(\Phi_e) = 1/\sqrt{L_r(\theta)C_r(\theta)}$. The zero-point fluctuations are

$$\Phi_{\text{zpf}} = \sqrt{\frac{\hbar}{2C_r\omega_r}} = \sqrt{\frac{\hbar Z_r}{2}}, \qquad Q_{\text{zpf}} = \sqrt{\frac{\hbar C_r\omega_r}{2}} = \sqrt{\frac{\hbar}{2Z_r}}, \tag{2.212}$$

with $Z_r(\Phi_s) = \sqrt{L_r/C_r}$ from Eq. (2.209), evaluated at the operating point corresponding to Φ_e.

Introducing the annihilation operator $\hat{a}$ by

$$\hat{\Phi} = \Phi_{\mathrm{zpf}}(\hat{a} + \hat{a}^\dagger), \qquad \hat{Q} = -iQ_{\mathrm{zpf}}(\hat{a} - \hat{a}^\dagger), \qquad [\hat{a}, \hat{a}^\dagger] = 1, \tag{2.213}$$

the Hamiltonian becomes

$$\hat{\mathcal{H}}_0 = \frac{\hat{Q}^2}{2C_r} + \frac{\hat{\Phi}^2}{2L_r} = \hbar\omega_r \left(\hat{a}^\dagger \hat{a} + \frac{1}{2}\right). \tag{2.214}$$

2.6.7 Kerr nonlinearity

The linearized inductance from Sec. 2.6.3 captures only the quadratic curvature of the reduced SQUID potential at the operating point. Higher-order terms of the reduced potential make the resonator frequency depend on the amplitude. Keeping only the leading nonlinear correction for the fundamental mode gives the effective Hamiltonian

$$\hat{\mathcal{H}} \simeq \hbar\omega_r \hat{a}^\dagger \hat{a} - \frac{\hbar\mathcal{K}}{2} \hat{a}^\dagger \hat{a}^\dagger \hat{a}\hat{a}, \tag{2.215}$$

where $\omega_r(\Phi_e)$ is the linear resonance frequency at the chosen bias point and $\mathcal{K}(\Phi_e)$ is the self-Kerr coefficient of the fundamental mode.

With the sign convention in Eq. (2.215), the transition frequency between $|n\rangle$ and $|n+1\rangle$ is

$$\omega_r(n) = \omega_r(0) - \mathcal{K}n, \tag{2.216}$$

so $\mathcal{K} > 0$ means that the transition frequency decreases with photon number.

Nonlinear expansion of the SQUID potential

The same one-port reduction can be extended beyond quadratic order by expanding the reduced SQUID potential

$$U_{\mathrm{eff}}(\phi_l) = U\big(\phi_l, \varphi^\star(\phi_l)\big), \tag{2.217}$$

about the dc operating point.

At a stationary operating point, $c_1 = 0$ and $c_2 = 1/L_S$. The coefficients c_3 and c_4 are the leading nonlinear coefficients of the reduced one-port SQUID potential: c_3 sets the cubic nonlinearity, while c_4 sets the quartic nonlinearity

that gives the direct Kerr contribution in the single-mode description. Their explicit expressions follow from differentiating along the minimizing path $\varphi^\star(\phi_l)$ and are derived in App. 6.1.1. Only the resulting coefficients are needed in the main text.

Mode-to-SQUID flux mapping

The nonlinear SQUID response is driven by the SQUID-flux perturbation. This perturbation is reduced from the full resonator mode flux by the ratio $\phi_l/\phi_0 = \cos\theta$. The resulting SQUID-flux perturbation is therefore

$$\delta\hat{\Phi}_S = \left(\frac{\phi_l}{\phi_0}\right)\Phi_{\mathrm{zpf}}(\hat{a}+\hat{a}^\dagger), \tag{2.218}$$

with

$$\delta\hat{\Phi}_l \equiv \hat{\Phi}_l - \bar{\Phi}_l. \tag{2.219}$$

Perturbative Kerr contributions

Expanding the reduced one-port SQUID potential about the operating point as in Eq. (2.187), the nonlinear part of the Hamiltonian is

$$\hat{\mathcal{H}}_{\mathrm{nl}} = \sum_{n\geq 3}\frac{c_n}{n!}(\delta\hat{\Phi}_s)^n, \qquad \delta\hat{\Phi}_s = \left(\frac{\phi_l}{\phi_0}\right)\Phi_{\mathrm{zpf}}(\hat{a}+\hat{a}^\dagger), \tag{2.220}$$

where the mode-to-SQUID flux mapping from Sec. 2.6.7 has been used. Keeping only the leading cubic and quartic terms gives

$$\hat{\mathcal{H}}_3 = \frac{c_3}{3!}\left(\frac{\phi_l}{\phi_0}\right)^3\Phi_{\mathrm{zpf}}^3(\hat{a}+\hat{a}^\dagger)^3, \tag{2.221}$$

$$\hat{\mathcal{H}}_4 = \frac{c_4}{4!}\left(\frac{\phi_l}{\phi_0}\right)^4\Phi_{\mathrm{zpf}}^4(\hat{a}+\hat{a}^\dagger)^4. \tag{2.222}$$

Perturbation theory then gives two leading Kerr contributions. The quartic term produces the direct first-order Kerr contribution

$$\mathcal{K}_4(\Phi_s) = -\frac{c_4(\Phi_s)}{2\hbar}\left(\frac{\phi_l}{\phi_0}\right)^4\Phi_{\mathrm{zpf}}^4, \tag{2.223}$$

while the cubic term produces an additional Kerr contribution at second order,

$$\mathcal{K}_3(\Phi_s) = \frac{5}{3}\frac{c_3(\Phi_s)^2}{\hbar^2\omega_r(\Phi_s)}\left(\frac{\phi_l}{\phi_0}\right)^6 \Phi_{\mathrm{zpf}}^6. \tag{2.224}$$

The full perturbative derivation, including the vanishing first-order cubic term and the selection-rule argument for the absence of the mixed second-order contribution, is given in App. 6.1.2.

In the Kerr-only approximation, the total Kerr coefficient is taken as

$$\mathcal{K}_{\mathrm{tot}}(\Phi_s) \simeq \mathcal{K}_4(\Phi_s) + \mathcal{K}_3(\Phi_s). \tag{2.225}$$

Kerr at zero flux. The Kerr shift per photon at zero flux is

$$\boxed{\begin{aligned}\frac{\mathcal{K}_{\mathrm{tot}}(0)}{2\pi} &= \frac{\hbar\pi Z_r(0)^2}{4\Phi_0^2}\left(\frac{\phi_l}{\phi_0}\right)^4 \\ &\times\left[\left(\frac{1}{L_{J1}}+\frac{1}{L_{J2}}\right)(1+6r_0^2+r_0^4)+4\left(\frac{1}{L_{J1}}-\frac{1}{L_{J2}}\right)(r_0+r_0^3)\right].\end{aligned}} \tag{2.226}$$

For symmetric junctions ($L_{J1} = L_{J2} \equiv L_J$), one has $r_0 = 0$ and

$$\frac{\mathcal{K}_{\mathrm{tot}}(0)}{2\pi} = \frac{\hbar\pi Z_r(0)^2}{2\Phi_0^2 L_J}\left(\frac{\phi_l}{\phi_0}\right)^4. \tag{2.227}$$

A detailed derivation is given in the App. 6.1.2.

Kerr-free operation. The total Kerr coefficient can be tuned to zero by balancing the quartic and cubic contributions. Setting $\mathcal{K}_{\mathrm{tot}} = 0$ gives the Kerr-free condition

$$c_4(\Phi_s) \approx \frac{5}{3}\left(\frac{\phi_l}{\phi_0}\right)^2 \frac{Z_r(\Phi_s)}{\omega_r(\Phi_s)} c_3(\Phi_s)^2. \tag{2.228}$$

At bias points where symmetry enforces $c_3 = 0$ (such as $\Phi_e = 0$ or $\Phi_e = \Phi_0/2$ for symmetric junctions), the Kerr-free condition reduces to $c_4 = 0$, which cannot be satisfied for finite Josephson energy. A Kerr-free point, therefore, exists only away from these symmetric bias points, where both c_3 and c_4 are

nonzero and can cancel. The flux dependence of the Kerr contributions is shown in Fig. 2.17(b).

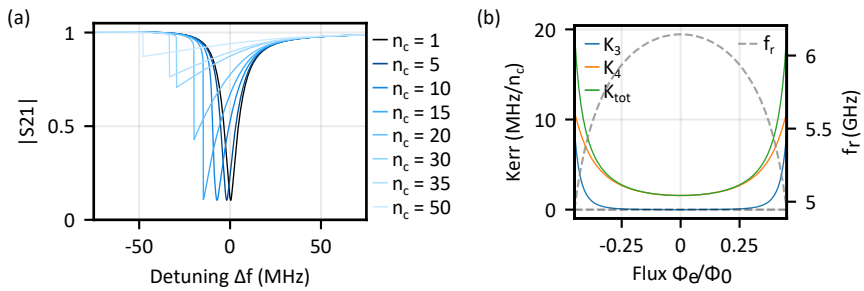

Figure 2.17: (a) $|S_{21}|$ versus detuning at increasing photon number n for a notch-type Kerr resonator ($Q_l = 450$, $Q_c = 500$, $\mathcal{K}/2\pi = 0.5\,\mathrm{MHz/photon}$). The Kerr shift tilts the lineshape and produces bistability above the bifurcation threshold. (b) Kerr contributions $\mathcal{K}_3$ (Eq. (2.224)), $\mathcal{K}_4$ (Eq. (2.223)), and $\mathcal{K}_{\mathrm{tot}}$ (Eq. (2.225)) versus external flux for the 200 μm loop FTR, with f_r on the right axis (dashed gray).

2.6.8 Driven Kerr response and bistability

When the FTR is driven by a coherent tone, the Kerr nonlinearity produces a Duffing response: the resonance frequency shifts with the intracavity photon number, leading to power-dependent frequency pulling, lineshape distortion, and bistability [135–137].

Steady-state equation

The steady-state intracavity amplitude under a coherent drive at frequency ω is [138]

$$a = \frac{\sqrt{\kappa_c}}{\kappa/2 - i(\Delta + \mathcal{K}n)}\, s_{\mathrm{in}}, \qquad n = |a|^2, \tag{2.229}$$

where $\Delta = \omega - \omega_r$ is the detuning from the bare resonance frequency and s_{in} is the input field amplitude normalized such that $|s_{\mathrm{in}}|^2$ is the incident photon flux. Using $n = |a|^2$ yields

$$n\left[\left(\frac{\kappa}{2}\right)^2 + (\Delta + \mathcal{K}n)^2\right] = \kappa_c\,|s_{\rm in}|^2 = \kappa_c\,\frac{P_{\rm in}}{\hbar\omega}, \tag{2.230}$$

where $P_{\rm in}$ is the incident power to the device. Eq. (2.230) is a real cubic equation in n. For weak drive, the cubic has a single positive real root, and the resonance has a Lorentzian lineshape. As the drive power increases, the Kerr shift changes the effective detuning through the term $(\Delta + \mathcal{K}n)$. For $\mathcal{K} > 0$, the resonance frequency decreases with photon number, tilting the lineshape toward lower frequencies and, for sufficiently negative detuning ($\Delta \leq -\sqrt{3}\kappa/2$), producing bistability [135, 136].

Onset of bistability

At sufficiently high drive power and detuning, Eq. (2.230) acquires three positive real roots: two stable roots and one unstable root. As the detuning sweeps through the bistable region, the system follows one branch until a turning point, and then jumps to the other, producing hysteresis [135, 136] as shown in Fig. 2.17(a).

The turning points are found by determining the extremum of Eq. (2.230). Defining $F(n) \equiv n[(\kappa/2)^2 + (\Delta + \mathcal{K}n)^2]$, the condition $F'(n) = 0$ yields, with the substitution $x \equiv \Delta + \mathcal{K}n$,

$$3x^2 - 2\Delta x + \left(\frac{\kappa}{2}\right)^2 = 0. \tag{2.231}$$

This quadratic equation has real solutions only when $|\Delta| \geq \sqrt{3}\,\kappa/2$. $\omega_r(n) = \omega_r(0) - \mathcal{K}n$, a positive Kerr coefficient ($\mathcal{K} > 0$) corresponds to a softening nonlinearity, and bistability occurs for drive frequencies below resonance, $\Delta \leq -\sqrt{3}\,\kappa/2$.

Using Eq. (2.231), it is seen that the onset of bistability starts at $|\Delta| = \sqrt{3}\,\kappa/2$ and $x = \Delta/3$. The critical intracavity photon number at this point is

$$n_{\rm crit} = \frac{\kappa}{\sqrt{3}\,|\mathcal{K}|}. \tag{2.232}$$

The corresponding critical input power follows from Eq. (2.230):

$$P_{\rm crit} = \frac{\hbar\omega\,\kappa^3}{3\sqrt{3}\,\kappa_c\,|\mathcal{K}|}. \tag{2.233}$$

Since $P_{\text{crit}} \propto \kappa^3/\mathcal{K}$, resonators with larger linewidths and smaller Kerr coefficients sustain higher photon numbers before bifurcation. For the FTRs in this thesis, $\mathcal{K}/2\pi \sim 200\,\text{kHz}$ and $\kappa/2\pi \sim 10\,\text{MHz}$ at zero flux bias (Sec. 2.6.7), giving $n_{\text{crit}} \sim 30$ and $P_{\text{crit}} \sim -120\,\text{dBm}$ at the device.

In experiments, the onset of bistability is observed as a hysteretic jump in VNA sweeps at a power P_b. Equating P_b with Eq. (2.233) provides an initial estimate of the Kerr coefficient [137]:

$$|\mathcal{K}|_{\text{init}} \simeq \frac{\kappa^3}{3\sqrt{3}\,\kappa_c}\,\frac{\hbar\omega_r}{P_b}. \tag{2.234}$$

Eq. (2.234) is an initial estimate, refined by fitting the full nonlinear S_{21} model (Sec. 2.6.9).

2.6.9 Circle fitting

The resonance frequency and quality factors of a notch-coupled microwave resonator are extracted from the complex transmission coefficient S_{21} [137, 139, 140].

Linear transmission model

In a notch (hanger) geometry, the resonator is side-coupled to a through feedline, and the transmission coefficient S_{21} exhibits a dip near the resonance frequency. In the linear regime ($\mathcal{K} = 0$), input-output theory [21, 140–142] gives

$$S_{21}(\omega) = 1 - \frac{\kappa_c}{(\kappa/2) - i\Delta}, \tag{2.235}$$

with $\Delta = \omega - \omega_r$.

Including impedance mismatch via a phase angle ϕ and converting to quality-factor notation yields the working model [139, 140]

$$S_{21}(f) = a\,e^{i\alpha}\left(1 - \frac{(Q_L/Q_c)\,e^{i\phi}}{1 + 2iQ_L(f - f_r)/f_r}\right), \tag{2.236}$$

where $f_r = \omega_r/2\pi$, Q_L is the loaded quality factor, Q_c is the coupling quality factor, ϕ captures mismatch, and $a\,e^{i\alpha}$ is the cable background. When mismatch is described by $Q_c^{\text{complex}} = Q_c\,e^{-i\phi}$, the effective real coupling is [139]

$$Q_c^{\text{eff}} = \text{Re}\left(Q_c^{\text{complex}}\right), \qquad \frac{1}{Q_L} = \frac{1}{Q_i} + \frac{1}{Q_c^{\text{eff}}}. \tag{2.237}$$

Complex circle representation

Setting $\phi = 0$ and a dimensionless detuning $x \equiv 2\Delta/\kappa$, Eq. (2.235) reduces to

$$S_{21}(x) = 1 - \frac{Q_L}{Q_c}\frac{1}{1 - ix}. \tag{2.238}$$

The transformation $x \mapsto (1 - ix)^{-1}$ sends the real detuning axis to a circle in the complex plane [139], so a single-pole notch response traces a circle in the I-Q plane as the frequency is swept. In the matched case ($\phi = 0$), the circle has radius

$$r_0 = \frac{Q_L}{2\,Q_c} = \frac{\kappa_c}{2\kappa} \tag{2.239}$$

and is centered on the real axis at $1 - r_0$. The off-resonance point lies at $1 + 0i$, the on-resonance point at $1 - Q_L/Q_c$, and the circle diameter $2r_0 = Q_L/Q_c$ gives the coupling ratio directly. When $\phi \neq 0$, the coupling term acquires a phase rotation $e^{i\phi}$ that shifts the circle center off the real axis but preserves the radius. Rotating the normalized circle about $1 + 0i$ by ϕ and scaling by $\cos\phi$ recovers the identity Eq. (2.239).

Background correction

A finite cable length adds a propagation phase $-\omega\tau$ that turns the closed circle into a spiral, and frequency-dependent gain imposes a magnitude tilt. Both effects vary smoothly over the narrow measurement bandwidth and are removed by estimating τ from the off-resonance phase slope and flattening the magnitude trend [139].

The position on the circle is described by the polar angle ϑ, measured from the center. From Eq. (2.238), the relation is

$$\vartheta(\omega) = \vartheta_0 + 2\arctan\left(2Q_L\,\frac{\omega_r - \omega}{\omega_r}\right), \tag{2.240}$$

where ϑ_0 is a constant offset. The loaded quality factor determines the sweep rate of ϑ per unit frequency, and ω_r corresponds to the midpoint.

Nonlinear circle model

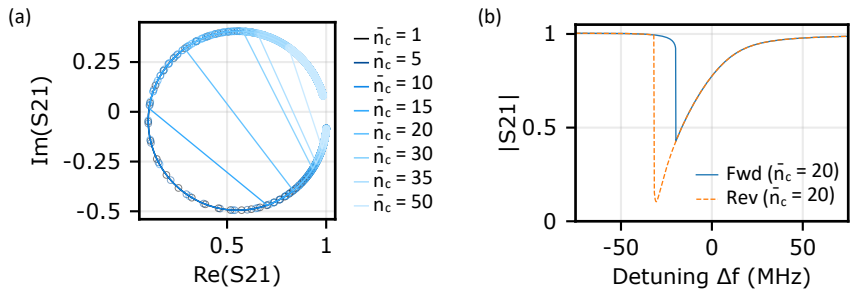

Figure 2.18: (a) Complex S_{21} traces at increasing photon number n (same parameters as Fig. 2.17(a)) plotted for forward sweep. Open circles mark equally spaced frequency points. The Kerr effect distorts the circle at higher powers. (b) Forward (solid) and reverse (dashed) $|S_{21}|$ sweeps at $n = 20 > n_{\text{crit}} = 12$ (Eq. (2.232)), showing the bistable behavior between the two stable branches.

The nonlinear transmission is Eq. (2.235) evaluated at the Kerr-shifted resonance [102, 137]:

$$S_{21}^{(\text{nl})}(\omega, n) = 1 - \frac{\kappa_c}{(\kappa/2) - i[\omega - (\omega_r - \mathcal{K}n)]}, \tag{2.241}$$

where n is the branch-specific root of the photon-number cubic equation (Eq. (2.230)) at each ω. In quality-factor notation,

$$S_{21}^{(\text{nl})}(f, n) = 1 - \frac{Q_L}{Q_c^{\text{eff}}} \frac{1}{1 + 2iQ_L \dfrac{f - (f_r - \mathcal{K}n/2\pi)}{f_r}}. \tag{2.242}$$

Since Eq. (2.241) has the same form as Eq. (2.235) with $\omega_r \to \omega_r - \mathcal{K}n$, each stable branch still traces the same circle in the complex plane. This assumes the response remains single-pole and that κ and κ_c do not change much over the fitted power range. What changes is the frequency-to-angle relation: the angle ϑ is reparameterized by $n(\omega)$, so that data points cluster near the resonance dip and spread apart off resonance. This uneven sweep along the circle produces the asymmetric lineshape in $|S_{21}|$ and the S-shaped phase response characteristic of the Duffing regime.

The radius identity Eq. (2.239) remains valid because Q_c is set by the coupling capacitor geometry and is power-independent. The nonlinear effects from the resonator and the readout chain determine how frequency corresponds to angle along the circle. This separation is the basis of the nonlinear circle fit: the circle parameters (r_0, center, ϕ) are extracted as in the linear case, while $\mathcal{K}$ is obtained from the power-dependent distortion of the frequency-to-angle relation. At each power, the fit yields an effective resonance frequency $f_r^{\text{eff}}(P) = f_r - (\mathcal{K}/2\pi)\, n(P)$, and the linear dependence of f_r^{eff} on n gives $\mathcal{K}$ directly [102]. Below the bifurcation threshold (Eq. (2.233)), the response is single-valued, and the linear circle fit is applied to each trace independently. Above bifurcation, the cubic (Eq. (2.230)) has three real roots, and branch selection must be accounted for. The fitting procedure is described in Sec. 3.5.4.

2.7 Flux noise

External flux fluctuations couple to the FTR resonance frequency through the flux responsivity (Sec. 2.6.4) and produce both frequency jitter and inhomogeneous linewidth broadening.

2.7.1 Flux noise spectrum

Superconducting devices exhibit flux noise with a characteristic $1/f$ spectrum at low frequencies [51, 143]. The one-sided power spectral density (PSD) of flux fluctuations is modeled as

$$S_{\Phi\Phi}(f) = A_\Phi f^{-\mu} \quad [\Phi_0^2/\text{Hz}], \tag{2.243}$$

where A_Φ is the noise amplitude at 1 Hz and $\mu \approx 0.8$-1.2 is the spectral exponent. Typical values for aluminum SQUIDs are $\sqrt{A_\Phi} \sim 1$-$10\,\mu\Phi_0/\sqrt{\text{Hz}}$ at 1 Hz [51, 144]. The main sources of $1/f$ flux noise are fluctuating surface spins at superconductor-substrate interfaces [143], paramagnetic adsorbates [145], and defect states in the junction barrier oxide [125].

Over a measurement bandwidth $[f_{\min}, f_{\max}]$, the integrated flux variance is

$$\sigma_\Phi^2 = \int_{f_{\min}}^{f_{\max}} S_{\Phi\Phi}(f)\, df = \begin{cases} A_\Phi \ln(f_{\max}/f_{\min}), & \mu = 1, \\ \dfrac{A_\Phi}{1-\mu}\left(f_{\max}^{1-\mu} - f_{\min}^{1-\mu}\right), & \mu \neq 1. \end{cases} \tag{2.244}$$

2.7.2 Frequency jitter

Flux noise is mapped into frequency noise. Writing the resonance frequency as a Taylor expansion about the bias point Φ_e,

$$f_r(\Phi_e + \delta\Phi) = f_r(\Phi_e) + f_r'\delta\Phi + \frac{1}{2}f_r''\delta\Phi^2 + \frac{1}{6}f_r'''\delta\Phi^3 + \cdots, \tag{2.245}$$

with derivatives evaluated at Φ_e, it shows that even when $f_r' = 0$, curvature still converts flux noise into finite frequency broadening. For Gaussian flux noise with variance σ_Φ^2, the leading mean shift is

$$\langle \delta f_r \rangle \approx \frac{1}{2}f_r''\sigma_\Phi^2, \tag{2.246}$$

and the leading variance is

$$\mathrm{Var}(f_r) \approx (f_r')^2\sigma_\Phi^2 + \left(f_r' f_r''' + \frac{1}{2}(f_r'')^2\right)\sigma_\Phi^4 + \cdots. \tag{2.247}$$

At a symmetry point where $f_r' = 0$, this reduces to

$$\mathrm{Var}(f_r) \approx \frac{1}{2}(f_r'')^2\sigma_\Phi^4, \tag{2.248}$$

so the linewidth is broadened even though the first-order responsivity vanishes.

2.7.3 Lorentzian and Voigt profiles

Without flux noise, the measured resonance line is Lorentzian. Writing the loaded full width at half maximum as

$$\Delta f_L = \frac{f_r}{Q_l}, \tag{2.249}$$

the corresponding normalized Lorentzian line shape may be written as

$$\mathcal{L}(f; f_r, \Delta f_L) = \frac{1}{\pi} \frac{\Delta f_L/2}{(f - f_r)^2 + (\Delta f_L/2)^2}. \tag{2.250}$$

Here Δf_L is the loaded linewidth, that is, the linewidth set by intrinsic dissipation together with external coupling.

A white-noise flux produces an approximately Gaussian spread in resonance frequency. In that regime, the frequency-jitter distribution is

$$\mathcal{G}(f; f_r, \sigma_f) = \frac{1}{\sqrt{2\pi}\sigma_f} \exp\left[-\frac{(f - f_r)^2}{2\sigma_f^2}\right], \tag{2.251}$$

with full width at half maximum

$$\Delta f_G = 2\sqrt{2\ln 2}\,\sigma_f \approx 2.355\,\sigma_f, \tag{2.252}$$

where σ_f is given by the linearized relation

$$\sigma_f(\Phi_e) \approx \left|\frac{\partial f_r}{\partial \Phi_e}\right| \sigma_\Phi \tag{2.253}$$

The observed line is then the convolution of the unbroadened loaded Lorentzian response and the Gaussian inhomogeneous broadening, known as the Voigt profile,

$$\mathcal{V}(f; f_r, \Delta f_L, \sigma_f) = \int_{-\infty}^{\infty} df'\, \mathcal{G}(f'; 0, \sigma_f)\, \mathcal{L}(f - f'; f_r, \Delta f_L). \tag{2.254}$$

Its full width at half maximum can be approximated by [146]

$$\Delta f_V \approx 0.5346\,\Delta f_L + \sqrt{\Delta f_G^2 + 0.2166\,\Delta f_L^2}. \tag{2.255}$$

Eq. (2.255) is accurate to better than 0.02% for a true Voigt profile [146].

The different line-shape contributions are illustrated in Fig. 2.19(a). The Lorentzian curve represents the resonator linewidth in the absence of flux noise, the Gaussian curve represents pure inhomogeneous frequency spreading, and the Voigt curve shows the combined response when both mechanisms are present.

Figure 2.19(b) shows the same idea at the level of the complex microwave response. In the absence of inhomogeneous broadening, a driven Kerr resonator traces the distorted resonance circle discussed in Sec. 2.6.7 and described by Eq. (2.241). Averaging over resonance frequency fluctuations smears this response because each realization of the slow flux offset shifts the instantaneous resonance frequency. The measured S_{21} is therefore the ensemble average of many slightly displaced nonlinear resonance circles. This broadens the magnitude response and compresses the circle nonuniformly in the complex plane, showing that flux noise modifies not only the scalar linewidth but also the full measured microwave line shape.

Near a sweet spot, however, the flux-to-frequency map becomes nonlinear, as discussed in Sec. 2.7.2. Then the instantaneous resonance-frequency distribution is generally not Gaussian, and the broadened line is not strictly Voigt, even for Gaussian flux noise.

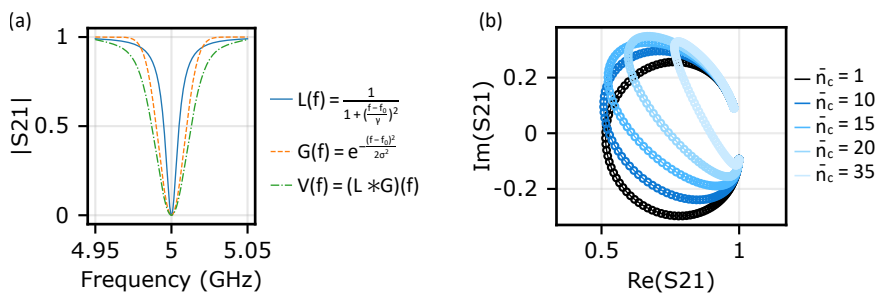

Figure 2.19: Flux-noise broadening of resonator line shapes. (a) Lorentzian, Gaussian, and Voigt profiles normalized to equal peak amplitude for $\Delta f_G/\Delta f_L = 2$. (b) Complex S_{21} traces at increasing photon number n for a Kerr resonator ($Q_l = 450$, $Q_c = 500$, $\mathcal{K}/2\pi = 0.5\,\mathrm{MHz/photon}$) with resonance-frequency fluctuations ($\sigma_f = 10\,\mathrm{MHz}$). The panel illustrates how inhomogeneous broadening modifies the full complex microwave response.

An effective internal quality factor, including inhomogeneous broadening, can then be defined by

$$\frac{1}{Q_i^{\mathrm{eff}}} = \frac{\Delta f_{\mathrm{eff}}}{f_r} - \frac{1}{Q_c}, \tag{2.256}$$

where Δf_{eff} denotes the frequency-noise broadened linewidth.

When flux-noise broadening dominates, the apparent Q_i^{eff} decreases even

though the intrinsic Q_i^{int} could remain high.

2.8 Flux transformer

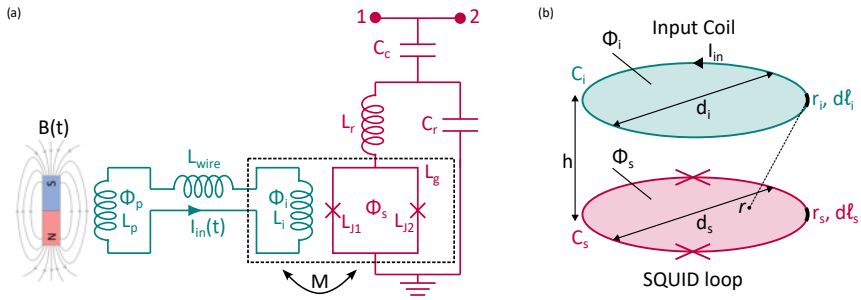

Figure 2.20: (a) Flux transformer circuit. A pickup coil (L_p) captures flux (Φ_p) from an external source. The screening current (I_{in}) flows through parasitic wire inductance (L_{wire}) and input coil (L_i) of the flux transformer (green), thereby delivering $\Phi_e = MI_{\text{in}}$ to the SQUID loop of the FTR (red). (b) Flux transfer schematic. Mutual inductance geometry between the input coil (contour C_i, green) carrying current I_{in} and the SQUID loop (contour C_s, red). The differential line elements $d\boldsymbol{\ell}_i$ and $d\boldsymbol{\ell}_s$ are located at positions $\mathbf{r}_i$ and $\mathbf{r}_s$, respectively for integration in the Neumann formula Eq. (2.259) to compute flux through the SQUID loop generated by I_{in} in the input coil.

Figure 2.20 summarizes the two ingredients of the transformer model. Panel (a) shows the full superconducting loop that converts pickup-loop flux Φ_p into the screening current I_{in} and hence into applied SQUID flux Φ_e. Panel (b) isolates the geometric mutual-inductance problem between the input coil and the SQUID loop, which is quantified by the Neumann formula given below.

2.8.1 Mutual inductance

When a current I_{in} flows through the input coil, it generates a magnetic vector potential at any point in space. In the Coulomb gauge, the vector potential is given by the Biot-Savart law [97]:

$$\mathbf{A}(\mathbf{r}) = \frac{\mu_0 I_{\text{in}}}{4\pi} \oint_{C_i} \frac{d\boldsymbol{\ell}'}{|\mathbf{r} - \mathbf{r}'|}, \tag{2.257}$$

where the integral is taken over the input coil contour C_i. The flux through the SQUID loop is the line integral of $\mathbf{A}$ along the SQUID contour C_s:

$$\Phi_e = \oint_{C_s} \mathbf{A}(\mathbf{r}) \cdot d\boldsymbol{\ell}. \tag{2.258}$$

Substituting Eq. (2.257) into Eq. (2.258) yields the Neumann formula for mutual inductance [147]:

$$M = \frac{\mu_0}{4\pi} \oint_{C_s} \oint_{C_i} \frac{d\boldsymbol{\ell}_s \cdot d\boldsymbol{\ell}_i}{|\mathbf{r}_s - \mathbf{r}_i|}, \tag{2.259}$$

which relates the input current to the coupled flux via $\Phi_e = M I_{\text{in}}$. The self-inductance of the input coil follows from the same approach, with both integrals taken over the same contour ($\Phi_i = L_i I_{\text{in}}$).

2.8.2 Flux transfer efficiency

For a pickup coil that captures flux from an external source (e.g., a levitated particle or external bias coil) and is connected in series with the input coil, the flux transfer to the SQUID occurs in two stages.

Stage 1: Pickup to input coil. Consider a superconducting loop formed by a pickup coil (self-inductance L_p), connecting wires (parasitic inductance L_{wire}), and the input coil (L_i). When external flux Φ_p threads the pickup, fluxoid quantization drives a screening current

$$I_{\text{in}} = \frac{\Phi_p}{L_p + L_{\text{wire}} + L_i} \tag{2.260}$$

through the loop (assuming no trapped fluxoids). The self-flux in the input coil is $\Phi_i = L_i I_{\text{in}}$, so the first-stage efficiency is

$$\eta_1 = \frac{\Phi_i}{\Phi_p} = \frac{L_i}{L_p + L_{\text{wire}} + L_i}. \tag{2.261}$$

This efficiency approaches unity when the input coil dominates the total loop inductance ($L_i \gg L_p + L_{\text{wire}}$).

Stage 2: Input coil to SQUID. The mutual inductance M between the input coil and the SQUID loop couples flux $\Phi_e = M I_{\text{in}}$ into the SQUID. The

second-stage efficiency is defined as

$$\eta_2 = \frac{\Phi_e}{\Phi_i} = \frac{M}{L_i}. \tag{2.262}$$

This ratio depends only on the geometry of the input coil and the SQUID loop, not on the current or the pickup circuit.

Total efficiency. The total flux transfer efficiency from the pickup to the SQUID is the product of the two stages:

$$\eta = \eta_1 \eta_2 = \frac{\Phi_e}{\Phi_p} = \frac{M}{L_p + L_{\text{wire}} + L_i}. \tag{2.263}$$

Maximizing η therefore requires large mutual inductance M, which is achieved by optimizing the geometry of the input coil and the SQUID loop, as well as minimizing parasitic inductance in the connecting wires.

2.9 Magnetomechanical coupling

The magnetomechanical interaction considered here is the standard cavity frequency-pulling coupling, in which mechanical displacement changes the resonator frequency through a flux-mediated boundary condition. The treatment follows the cavity optomechanics approach [22], adapted to flux-mediated coupling following the proposal of Romero-Isart *et al.* [38] and the implementation in Ref. [66].

2.9.1 System Hamiltonian

The displacement x of the levitated particle perturbs the magnetic flux threading the SQUID by an amount $\delta\Phi(x)$, such that the cavity parameters become position dependent, $\omega_r = \omega_r(\Phi_e + \delta\Phi(x))$ and $\mathcal{K} = \mathcal{K}(\Phi_e + \delta\Phi(x))$. Expanding about the equilibrium position $x = 0$ allows the Hamiltonian to be decomposed into an x-independent part and an interaction term linear in $\hat{x}$:

$$\hat{H} = \hat{H}_{\text{cav}} + \hat{H}_{\text{mech}} + \hat{H}_{\text{int}}. \tag{2.264}$$

Here $\hat{H}_{\text{cav}}$ is the cavity Hamiltonian at the equilibrium position ($x = 0$, static bias Φ_e), and $\hat{H}_{\text{int}}$ contains the terms that arise from expanding $\omega_r(\Phi_e + \delta\Phi(x))$

and $\mathcal{K}(\Phi_e + \delta\Phi(x))$ in powers of x.

Cavity Hamiltonian. Evaluated at the static bias point ($x = 0$), the FTR is a nonlinear cavity with Kerr interaction:

$$\hat{H}_{\text{cav}} = \hbar\omega_r(\Phi_e)\hat{a}^\dagger\hat{a} - \frac{\hbar\mathcal{K}(\Phi_e)}{2}\hat{a}^\dagger\hat{a}^\dagger\hat{a}\hat{a}, \tag{2.265}$$

where $\omega_r(\Phi_e)$ is the flux-dependent resonance frequency from Eq. (2.198) and $\mathcal{K}(\Phi_e)$ is the Kerr coefficient from Eq. (2.225), both of which depend on the external flux bias point.

Mechanical Hamiltonian. The magnetic trap potential is harmonic near equilibrium but contains higher-order nonlinearities for large displacements [39, 95]:

$$\hat{H}_{\text{mech}} = \hbar\Omega_m\hat{b}^\dagger\hat{b} + \hbar\chi_m^{(3)}(\hat{b} + \hat{b}^\dagger)^3 + \hbar\chi_m^{(4)}(\hat{b} + \hat{b}^\dagger)^4 + \cdots, \tag{2.266}$$

where Ω_m is the linearized trap frequency, and $\chi_m^{(3)}$, $\chi_m^{(4)}$ are the cubic and quartic anharmonicity coefficients determined by the trap geometry and field gradients. For small oscillation amplitudes ($x \ll R_{\text{coil}}$), the anharmonic terms can be neglected.

Interaction Hamiltonian. The coupling originates from the position dependence of the cavity term $\hbar\omega_r(\Phi_e + \delta\Phi(x))\,\hat{a}^\dagger\hat{a}$, where the particle displacement changes the flux threading the SQUID by an amount $\delta\Phi(x)$. Expanding to first order about the equilibrium position $x = 0$ yields

$$\omega_r(x) \simeq \omega_r(0) + \left.\frac{\partial\omega_r}{\partial x}\right|_0 x \equiv \omega_r(0) + Gx, \tag{2.267}$$

with

$$G = \left.\frac{\partial\omega_r}{\partial\Phi_e}\right|_0 \left.\frac{\partial\Phi_e}{\partial x}\right|_0 \equiv \mathcal{R}_\Phi \left.\frac{\partial\Phi_e}{\partial x}\right|_0. \tag{2.268}$$

An analogous expansion applies to the Kerr coefficient,

$$\mathcal{K}(x) \simeq \mathcal{K}(0) + \left.\frac{\partial\mathcal{K}}{\partial x}\right|_0 x \equiv \mathcal{K}(0) + K_x x, \tag{2.269}$$

with

$$K_x = \left.\frac{\partial \mathcal{K}}{\partial \Phi_e}\right|_0 \left.\frac{\partial \Phi_e}{\partial x}\right|_0 \equiv \mathcal{R}_{\mathcal{K}} \left.\frac{\partial \Phi_e}{\partial x}\right|_0, \tag{2.270}$$

where $\mathcal{R}_{\mathcal{K}} \equiv \partial \mathcal{K}/\partial \Phi_e|_0$ is the flux responsivity of the Kerr coefficient. Upon quantization, $\hat{x} = x_{\text{zpf}}(\hat{b} + \hat{b}^\dagger)$ with

$$x_{\text{zpf}} = \sqrt{\frac{\hbar}{2m_{\text{eff}}\Omega_m}},$$

the interaction Hamiltonian becomes

$$\hat{H}_{\text{int}} = \hbar G\, \hat{x}\, \hat{a}^\dagger \hat{a} - \frac{\hbar K_x}{2}\, \hat{x}\, \hat{a}^\dagger \hat{a}^\dagger \hat{a}\hat{a} \equiv \hbar g_0\, \hat{a}^\dagger \hat{a}(\hat{b} + \hat{b}^\dagger) - \hbar g_{0,\mathcal{K}}\, \hat{a}^\dagger \hat{a}^\dagger \hat{a}\hat{a}\, (\hat{b} + \hat{b}^\dagger), \tag{2.271}$$

where $g_0 \equiv G x_{\text{zpf}}$ and

$$g_{0,\mathcal{K}} \equiv \frac{K_x x_{\text{zpf}}}{2}. \tag{2.272}$$

The total Hamiltonian is written as

$$\hat{H}_{\text{eff}} \simeq \hbar\omega_r \hat{a}^\dagger \hat{a} - \frac{\hbar \mathcal{K}(\Phi_e)}{2} \hat{a}^\dagger \hat{a}^\dagger \hat{a}\hat{a} + \hbar\Omega_m \hat{b}^\dagger \hat{b} \tag{2.273}$$

$$+ \hbar g_0 \hat{a}^\dagger \hat{a}(\hat{b} + \hat{b}^\dagger) - \hbar g_{0,\mathcal{K}}\, \hat{a}^\dagger \hat{a}^\dagger \hat{a}\hat{a}\, (\hat{b} + \hat{b}^\dagger). \tag{2.274}$$

The first interaction term is the usual radiation-pressure-like coupling in which mechanical displacement modulates the cavity frequency. The second interaction term describes a displacement-induced modulation of the Kerr nonlinearity (a position-dependent photon-photon interaction). For larger oscillation amplitudes, higher-order terms in $\omega_r(x)$ and $\mathcal{K}(x)$, as well as the trap anharmonicities, become relevant, and the full nonlinear dynamics must be retained; see Refs. [61, 137].

Single-photon coupling rate The single-photon coupling rate is defined as the cavity frequency shift per zero-point displacement of the mechanical oscillator:

$$g_0 = G\, x_{\text{zpf}} = \frac{\partial \omega_r}{\partial x} \sqrt{\frac{\hbar}{2m_{\text{eff}}\Omega_m}}, \tag{2.275}$$

where m_{eff} is the effective mass of the mechanical mode.

Using Eq. (2.268), the single-photon coupling rate can be expressed as

$$g_0 = \frac{\partial \omega_r}{\partial \Phi_e} \cdot \frac{\partial \Phi_e}{\partial x} \cdot x_{\mathrm{zpf}}. \tag{2.276}$$

Photon enhancement. The Kerr nonlinearity constrains the maximum usable intracavity photon number before the onset of bifurcation (Sec. 2.6.8), and limits the largest achievable photon-enhanced coupling $g = g_0\sqrt{\bar{n}}$ in driven operation.

CHAPTER 3

Methods

"Never touch a working system."

- my supervisor, repeatedly

This chapter presents the methods used to design, simulate, fabricate, and characterize SQUID-terminated superconducting microwave resonators with integrated flux-modulation for magnetomechanical readout. Finite element simulations in COMSOL and ANSYS HFSS are described for magnetostatic flux coupling and microwave mode analysis, respectively. The fabrication section covers the process steps detailing the fabrication of aluminum wiring, Josephson junctions, air-bridges, under-bump metallization, and integrated input coils, followed by a section on the flip-chip bonding technique developed for integrated flux transformers. Finally, the experimental setup is described, which includes magnetic shielding, vibration isolation, and the optical setup for observing particle levitation. The chapter ends with the cryogenic measurement techniques for resonator spectroscopy and homodyne readout for the magnetomechanical system.

3.1 Finite element methods

Finite element method (FEM) simulations are used throughout this thesis to estimate device parameters prior to fabrication and to compare analytical models against realistic designs. Two simulation platforms are used:

- **COMSOL Multiphysics** (AC/DC Module) for magnetostatic studies, including flux coupling and shielding.
- **ANSYS HFSS** (High Frequency Structure Simulator) for microwave eigenmode and frequency-domain scattering analysis of superconducting coplanar structures.

All simulations use full three-dimensional models without exploiting geometric symmetries, since the coil openings and corner roundings lead to significant deviations from analytical models [95].

3.1.1 Magnetostatic simulations

Magnetostatic simulations are performed using the AC/DC Module of COMSOL Multiphysics to characterize magnetic flux coupling and magnetic shielding in the experimental setup.

Physical model

Depending on whether applied currents are present, two related physics interfaces are used:

- *Magnetic Fields* (mf): a vector-potential formulation that supports applied currents and is used for flux coupling calculations.
- *Magnetic Fields, No Currents* (mfnc): a scalar-potential formulation valid in regions without applied currents, used for dc shielding calculations under a uniform background field.

The magnetostatic equations used in these simulations are:

$$\nabla \times \mathbf{B} = \mu_0 \mu_r \mathbf{J}, \qquad \nabla \cdot \mathbf{B} = 0, \qquad \mathbf{B} = \mu_0 \mu_r \mathbf{H}. \tag{3.1}$$

High-permeability shielding alloys are approximated as linear in the low-field regime using an effective constant μ_r.

In the mf interface, the coil current is explicitly imposed. Thus, the magnetic flux density is expressed in terms of the magnetic vector potential as $\mathbf{B} = \nabla \times \mathbf{A}$, where the coil current generates the magnetic vector potential A via Ampère's law

$$\nabla \times (\nabla \times \mathbf{A}) = \mu_0 \mu_r \mathbf{J}. \tag{3.2}$$

In the mfnc interface, $\mathbf{J} = \mathbf{0}$, therefore the magnetic scalar potential (ϕ_m) [148] is solved instead:

$$\mathbf{H} = -\nabla \phi_m \tag{3.3}$$

Since solving for scalar fields is computationally cheaper compared to vector fields, the mfnc interface is preferred when no applied currents are present in the simulation domain.

Flux transfer

Magnetostatic simulations are used to estimate the flux transfer efficiency η_2 between an input coil and the SQUID loop of an FTR; see Sec. 2.8.

Because free currents are explicitly applied to the input coil, these calculations employ the mf interface. The current-carrying coil generates a magnetic vector potential $\mathbf{A}(\mathbf{r})$, and the magnetic flux through a closed contour C_k is obtained from the line integral

$$\Phi_k = \oint_{C_k} \mathbf{A} \cdot \mathrm{d}\boldsymbol{\ell}, \qquad k \in \{i, s\}, \tag{3.4}$$

where $k = i$ denotes the input-coil contour and $k = s$ denotes the SQUID-loop contour. The self-inductance L_i is obtained from the total magnetic energy E_m stored in the simulation domain using the energy method:

$$L_i = \frac{2E_m}{I_{\mathrm{in}}^2} = \frac{1}{\mu_0 \mu_r I_{\mathrm{in}}^2} \int_V \mathbf{B} \cdot \mathbf{B} \, \mathrm{d}V, \tag{3.5}$$

where I_{in} is the current through the input coil, and the integral extends over the entire simulation volume V. This definition is used instead of $L_i = \Phi_i / I_{\mathrm{in}}$ because it is numerically more stable and is directly available from the FEM solution. Fig. 3.1 shows the mesh distribution with free tetrahedral elements for (a) flip-chip and (b) on-chip configurations, with denser meshing for the coils and flux integration surfaces, and coarser meshing for the surrounding

"air" sphere.

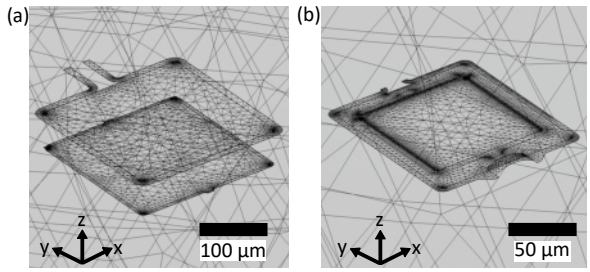

Figure 3.1: FEM mesh distributions for (a) a 200 µm-wide SQUID loop coupled to a flip-chip input coil with ∼50 μm gap, and (b) a 100 µm-wide SQUID loop coupled to an on-chip input coil.

Magnetic shielding

Magnetostatic simulations are also used to determine the attenuation of ambient magnetic fields by the superconducting and high-permeability shields used in the experimental setup. Here, the shielding factor is defined as the ratio B_0/B_{in}, where B_0 is the externally applied uniform field, and B_{in} is the residual field magnitude at the sample location inside the shield. Here, the external field is taken as the Earth field at Göteborg, Sweden, with $B_0 = 51.2\,\mu\text{T}$ and an inclination of $71°37'$ from the horizontal xy plane. In practice, this inclination of the field immediately outside the shield will be modified by other shields, metals, and superconductors. To account for this uncertainty, the field is simultaneously applied in both horizontal (y) and vertical (z) directions to obtain a conservative estimate of the shielding factor along both directions. The effective applied field B_{in} is evaluated as a volume average of B_z. The averaging is performed over a small measurement volume centered at the sample position, rather than at a single point, to reduce sensitivity to local numerical noise and mesh discretization:

$$B_{\text{in}} = |\langle B_{y,z}\rangle| \equiv \left| \frac{1}{V_{\text{meas}}} \int_{V_{\text{meas}}} B_{y,z}(\mathbf{r})\,\mathrm{d}V \right|. \tag{3.6}$$

Shielding calculations are performed in the mfnc interface since no free currents are present, and the applied ambient field is static. The uniform

background field is prescribed as a known field $\mathbf{H}_0$, and the scalar potential is solved only for the perturbation generated by the shielding structures. In COMSOL, this is implemented using the reduced-field formulation, in which the total field is decomposed as

$$\mathbf{H}(\mathbf{r}) = \mathbf{H}_0(\mathbf{r}) + \mathbf{H}_r(\mathbf{r}), \qquad \mathbf{H}_r(\mathbf{r}) = -\nabla\phi_r(\mathbf{r}), \tag{3.7}$$

so that only the reduced scalar potential ϕ_r is obtained from the FEM solution. For a uniform background field, an associated background potential $\phi_0(\mathbf{r}) = -\mathbf{H}_0 \cdot \mathbf{r}$ may be defined such that $\mathbf{H}_0 = -\nabla\phi_0$, and the total scalar potential becomes $\phi_m = \phi_0 + \phi_r$. The far-field boundary condition is then imposed on the reduced potential (typically $\phi_r = 0$ on the outer boundary), while the background field $\mathbf{H}_0$ is added analytically. This improves numerical conditioning because the mesh is required to resolve only the perturbation to the uniform field rather than the uniform field itself. A full view and zoom-in of the simulation geometry are shown in Fig. 3.2(a,b) along with the measurement sphere for B_{in}.

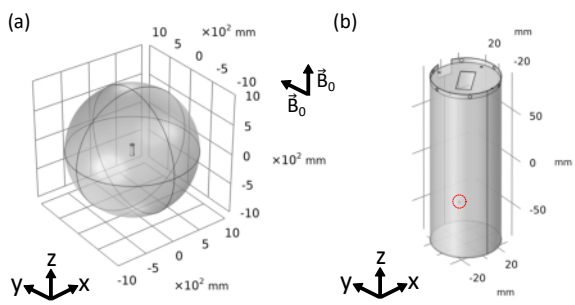

Figure 3.2: COMSOL shielding-factor model for a uniform external field of $B_0 = 51.2\,\mu\text{T}$ along both y and z axes. (a) A full view showing the outer air domain enforces a uniform background field and fixes the scalar potential reference. (b) A zoom-in showing the shield with cable opening and end cap on the top, and a measurement sphere (dotted circle), centered at the sample location, used to evaluate the residual field B_{in}.

Superconducting shield. Superconducting materials can be employed for shielding ambient magnetic fields; see Sec. 3.5.2. In the ideal Meissner limit, a superconductor behaves as a perfect diamagnet that expels magnetic flux from

its interior when cooled below T_c; see Sec. 2.1.1. In FEM magnetostatics, this behavior may be modeled either (i) by assigning a very small effective relative permeability $\mu_r \ll 1$ to the superconducting material or (ii) by excluding the superconducting domains from the simulation and applying a zero-normal-flux boundary condition ($\mathbf{B} \cdot \hat{n} = 0$) at the resulting surfaces. The latter approach is numerically stable for the ideal Meissner limit (perfect diamagnetism) and is used here to obtain an idealized shielding factor for the superconducting shield. This approach forces a vanishing magnetic flux density in the superconducting bulk, but it does not set the surface screening-current distribution, nor does it capture the finite London penetration depth, trapped flux, or type-II vortex physics. However, a more physical description of Meissner screening in COMSOL can be obtained by incorporating the London equation, which expresses the supercurrent density in terms of the vector potential as $\mathbf{J}_s = -(\mu_0 \lambda_L^2)^{-1}\mathbf{A}$ (see Sec. 2.1.1) within the superconducting domains, as demonstrated by Latorre [95].

High-permeability shield. High-permeability shields attenuate ambient magnetic fields by providing a low-reluctance path that guides field lines through the shield material and reduces flux density in the interior. At low field amplitudes, the material response is approximately linear, so a constant $\mu_r \gg 1$ is sufficient. At higher fields, the permeability decreases as the material saturates, requiring a nonlinear $\mathbf{B}(\mathbf{H})$ curve for accurate modeling. In the mfnc interface, *Free Space* is restricted to the air domains only, and a *Magnetic Flux Conservation* domain feature is added to the shield and end-cap domains to apply the prescribed μ_r (or B-H curve).

Frequency dependence. The two shielding mechanisms have complementary frequency responses. The superconducting shield expels static and varying fields through the Meissner effect and remains effective from dc up to the superconducting gap frequency ($\sim$100 GHz). However, superconducting shields are ineffective above T_c or in regions where flux has already been trapped. This is where the high-permeability shield becomes important, as it shields from room temperature down to millikelvin. In addition to its static permeability-based attenuation, it also provides increasing attenuation at higher frequencies because time-varying fields induce eddy currents in the conductive shield wall. As frequency increases, the skin depth in the shield wall decreases, and once

it becomes comparable to or smaller than the wall thickness, the oscillating field is exponentially attenuated across the wall, reducing the flux that reaches the interior. However, the magnetostatic solvers (mf and mfnc), being time-independent, do not capture eddy current shielding and, therefore, provide conservative estimates of the shielding factors.

3.1.2 Microwave simulations

Microwave simulations are performed using ANSYS HFSS to model eigenmodes and scattering response of superconducting resonators along with their coupling to the readout feedline. HFSS solves Maxwell's equations in the frequency domain using FEM. Two HFSS solver types are used in this thesis:

- **Eigenmode simulations** to obtain the resonance frequency and coupling quality factors Q_c.
- **Driven frequency-domain simulations** to compute the transmission S_{21} and the impedance mismatch with the feedline.

Geometry and boundaries

All microwave structures are imported as 2D structures from a GDS layout file. The substrate is modeled as a 3D box, the metallization is represented as zero-thickness sheets, and the surrounding region is defined as a vacuum. The resonators are capacitively coupled to a CPW feedline, where a 50Ω impedance termination is applied at the input and output ports of the feedline.

Since measurements are performed in a copper sample box, this packaging is approximated by enclosing the chip in a finite radiation region with absorbing boundary conditions at the outer boundary. All superconducting structures are modeled as perfect electrical conductors (PEC), which ignores TLS and surface losses, as well as kinetic inductance. Therefore, HFSS predictions of quality factors only represent coupling loss, while the resonance frequency ignores L_k contribution. This approach is based on the work of Hang-Xi Li [149].

CPW resonator modeling

The eigenmode solver computes the resonance frequencies and field distributions. Fig. 3.3(a) shows the model geometry of a GDS-imported CPW

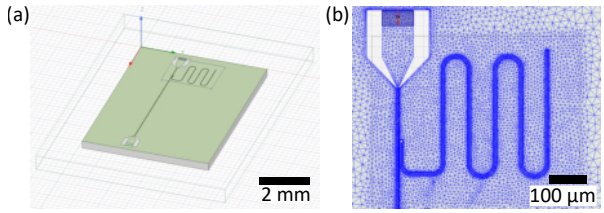

Figure 3.3: HFSS eigenmode simulation of a $\lambda/4$ CPW resonator. (a) Model geometry showing a GDS-derived CPW structure ($w = 10\,\mu\text{m}$, $g = 2\,\mu\text{m}$) on a 300 µm silicon substrate. (b) Adaptive tetrahedral mesh with refinement near the CPW gaps where the electric field is concentrated. The red arrow at the feedline input indicates a $50\,\Omega$ lumped port, with the arrow showing the reference direction for current flow.

structure on a silicon substrate, and (b) shows the adaptive tetrahedral mesh used by the solver, with denser elements near the CPW gaps where the fields are concentrated. The eigenmode solver finds solutions to the source-free Maxwell's equations by discretizing the electromagnetic fields and solving the generalized eigenvalue problem

$$\nabla \times \left(\mu^{-1} \nabla \times \mathbf{E}\right) = \omega^2 \varepsilon \mathbf{E}. \tag{3.8}$$

The eigenvalues yield the resonance frequencies $\tilde{\omega}_i$, and the eigenvectors yield the corresponding field distributions. For a single resonator, the lowest-frequency mode is the fundamental, while higher modes include harmonics and spurious box resonances.

At the feedline ports, a $50\,\Omega$ lumped termination imposes a matched (non-reflecting) boundary condition. Mathematically, this introduces loss into the eigenvalue problem, making the eigenfrequency complex: $\tilde{\omega} = \omega_r - i\kappa/2$, where ω_r is the resonance frequency and κ is the loss rate. The coupling quality factor is extracted from the eigenmode solution as

$$Q_c = \frac{\omega_r}{\kappa} = \frac{\mathrm{Re}(\tilde{\omega})}{2\,|\mathrm{Im}(\tilde{\omega})|}. \tag{3.9}$$

The intrinsic quality factor Q_i is not captured because superconductors are modeled as perfect electrical conductors with zero surface resistance. Compared to the analytical expression in Eq. (2.130), HFSS captures geometric effects

not included in the uniform-cross-section approximation, such as the capacitive coupling gap, bends in the meander, and fringing fields at the open end, making it more accurate than analytical estimates.

Flux-tunable resonator modeling

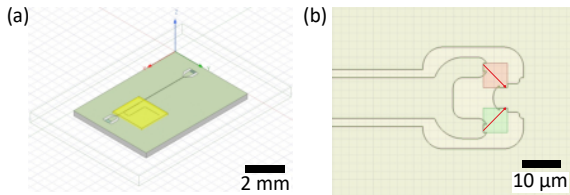

Figure 3.4: HFSS model of a flux-tunable resonator. (a) Model geometry showing a CPW resonator terminated by a SQUID loop. (b) Linearized Josephson junctions represented as lumped elements (colored boxes) with L_J in parallel with C_J. Different values can be assigned to each junction to model asymmetry. The arrows define the direction for current flow.

An FTR layout coupled to a feedline and placed on a silicon substrate with a surrounding "air" box is shown in Fig. 3.4(a). Each junction is represented by a linearized lumped element consisting of a Josephson inductance L_J in parallel with a junction capacitance C_J, as indicated in (b). Junction asymmetry is incorporated by assigning different inductance ($L_{J1} \neq L_{J2}$) and capacitance values to each junction.

The SQUID loop geometry is included in the 3D model, so the geometric inductance L_g and its contribution to the total SQUID inductance L_S, and therefore the resonator eigenfrequency, are captured directly by the field solution. In the theoretical model developed in Sec. 2.6, the effective SQUID inductance seen by the resonator includes the inductance of the linearized junctions and the common-mode geometric inductance, both of which are captured by the eigenmode solver.

However, HFSS FTR simulations are restricted to the linear regime at a fixed flux operating point. Flux-dependent frequencies can be calculated by sweeping the assigned L_J values calculated at different Φ_e using the theoretical screening relation Eq. (2.86). Nonlinear dynamics and multi-photon effects require analytical or numerical circuit-model approaches beyond the scope of linear eigenmode analysis.

Driven frequency-domain simulations

While eigenmode simulations yield resonance frequencies and Q_c, driven simulations produce the transmission response $S_{21}(f)$ of the resonator. Power is injected through one port, and the transmitted and reflected fields are computed as a function of frequency, allowing direct comparison with VNA measurements.

The solver uses sinusoidal fields ($e^{i\omega t}$) and solves the wave equation at each frequency point. At the ports, the field solution is split into incident and outgoing wave amplitudes, from which the scattering parameters S_{ij} and port impedance are extracted. These simulations are used to identify slotline modes, which arise from asymmetric excitation or imperfect ground continuity, and to detect Fano-like lineshape asymmetry caused by impedance mismatch or interference with parasitic modes.

Parasitic modes in packaging

Cavity resonances in the sample box can couple to the CPW feedline and appear as spurious dips in measurements [150, 151]. Therefore, the sample box, excluding the chip and wirebonds, is simulated for eigenmodes within 4-8 GHz. The box material is assigned as copper, while the surrounding empty region is assigned as air. A box design is accepted when no eigenmodes are present in the measurement band and when modes immediately outside this band exhibit minimal field concentration at the chip location.

3.2 Design and fabrication

This thesis uses two types of superconducting microwave resonators: (i) a bare CPW resonator used as a non-tunable reference and (ii) an FTR obtained by terminating a CPW with a dc-SQUID. All resonators are designed to lie in the 4 GHz to 8 GHz frequency range, constrained by the readout components (see Sec. 3.5.3). This is achieved by varying the resonator length for a defined CPW cross-section and SQUID geometry (in the case of the FTR). The film thickness of all resonators and ground wiring is fixed at 150 nm, following the fabrication process developed by Biznarová et al. [152, 153]. This thickness satisfies $t \ll w, g$ and therefore allows modeling with the conformal mapping technique used to derive the CPW parameters (Sec. 2.5.2). Because $t > \lambda_{\text{eff}}$

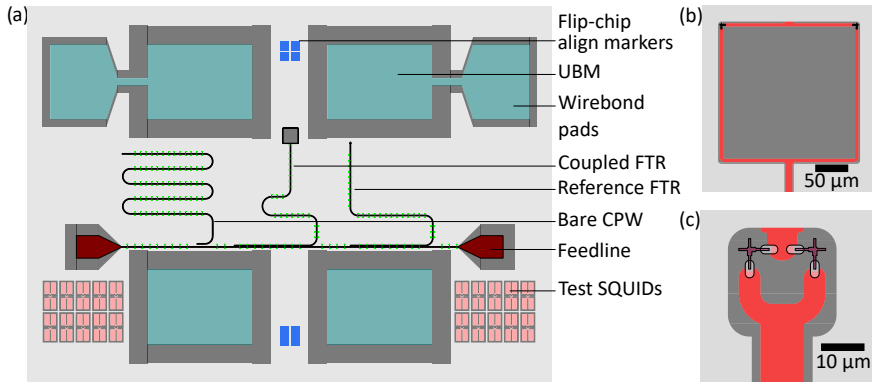

Figure 3.5: Layout of a representative resonator chip used in this thesis. (a) Chip overview showing a through feedline capacitively coupled to three resonators (left to right): a bare CPW resonator, a coupled FTR, and a reference FTR. Flip-chip bonding pads provide galvanic connection to top chip (not shown; see Fig. 3.16(d)). The ground plane has 2 µm-wide square flux trapping holes in a 10×10 µm grid (hidden for clarity). Zoom-in of (b) the coupled FTR with SQUID 200 µm and (c) the reference FTR SQUID with 10 µm SQUID.

for evaporated aluminum ($\lambda_{\text{eff}} \approx 50$ nm-100 nm in the dirty limit), kinetic inductance contributes less than 10% of the total line inductance (Sec. 2.5.3), so the resonance frequency and the effective mode impedance are dominated by geometry and can be well-predicted from conformal mapping alone. At the same time, 150 nm is thick enough to preserve bulk-like superconducting properties. Subsequent work by Biznarová et al. demonstrated that thicker films ($t \geq$ 300 nm) reduce TLS loss at the substrate-metal interface by increasing grain size and reducing oxide along grain boundaries [153].

Fig. 3.5(a) shows a chip layout with a through feedline capacitively coupled to three resonators: a bare CPW resonator, a coupled FTR, and a reference FTR. Zoom-ins of the coupled FTR with a 200 µm SQUID loop and the reference FTR with a 10 µm SQUID loop are shown in (b) and (c), respectively. Arrays of test SQUIDs are included for room-temperature resistance measurements and microscopy inspection. The design and microfabrication processes are described below, while the detailed parameters and recipes are provided in App. 6.3.

Table 3.1: Key parameters for the resonators used in this thesis: CPW width w, gap g, SQUID loop width d_s, junction width w_J, resonance frequency $\omega_r/2\pi$, and coupling quality factor Q_c.

Device	w (µm)	g (µm)	d_s (µm)	w_J (µm)	$\omega_r/2\pi$ (GHz)	Q_c
Bare CPW	10	5	-	-	4.3	$\sim 5 \times 10^5$
Coupled FTR	10	2	100–200	1	~ 6	500–1000
Reference FTR	10	2	10	1	~ 6.5	500–1000

3.2.1 Design principle

CPW resonators

Bare resonators are implemented as hanger-type $\lambda/4$ CPWs capacitively coupled to a through feedline. The cross-section is fixed at a thickness $t = 150\,\text{nm}$, width $w = 10\,\mu\text{m}$, and gap $g = 5\,\mu\text{m}$, designed for $50\,\Omega$ mode impedance (see Sec. 2.5).

The bare resonators are designed with weak external loading ($Q_c \sim 5 \times 10^5$), close to their intrinsic quality factors, keeping them near critical coupling. This allows for the accurate extraction of internal loss rates using circle-fitting routines without being dominated by feedline-loading [139, 154], and provides a narrower loaded linewidth to avoid parasitic coupling to nearby modes.

In an ideal CPW, both ground planes remain at the same potential, supporting the intended quasi-TEM mode. However, voltage imbalance can excite slotline-like modes that appear as spurious transmission features [155]. These are mitigated with ground stitching [156] using air bridges with dense packing, since the slotline mode can be re-formed further along the line if only a single connection is used [157].

Flux-tunable resonators

FTRs are realized by terminating a $\lambda/4$ CPW with a dc-SQUID at the grounded end. The CPW cross-section is fixed at $t = 150\,\text{nm}$, $w = 10\,\mu\text{m}$, and $g = 2\,\mu\text{m}$. Given the added SQUID inductance, the reduced gap increases capacitance to avoid strong mismatch between the effective mode impedance and the line impedance.

Compared to bare CPWs, FTRs introduce additional interfaces near the

SQUID termination (junction electrodes, resist residues, native oxides, patch interfaces) that can contribute to dissipation [152, 158, 159], reducing Q_i to $\sim 10^3$-10^4. The coupling quality factor is therefore set to 500-1000 to keep FTRs overcoupled across the measurable flux range, providing a broader linewidth for fast spectroscopy in the presence of flux noise and slow drifts. The larger loops are more susceptible to flux noise, which causes linewidth broadening in the FTR, thereby lowering its effective Q_i Sec. 2.7. Nonetheless, larger loops increase flux-transfer efficiency at the cost of lower Q_i, while remaining within the non-hysteretic limit (Sec. 2.4.4). Even though square loop geometry was chosen for all devices, circular loops would be preferred as they minimize geometric inductance for the same effective area. The reference FTRs have a 10 µm-wide SQUID loop, which minimizes flux-induced linewidth broadening and serves as a benchmark for the coupled FTRs with 100 µm and 200 µm loops. Josephson junctions of all FTRs are 1 µm wide to reduce the Kerr coefficient $\mathcal{K}$ (Sec. 2.6.7), with critical currents extracted from the resistances of test SQUIDs (see Sec. 4.6.2).

Flux trapping holes

Residual perpendicular fields at the chip cannot be completely eliminated due to finite shielding, the remanent magnetization of nearby parts, and flux focusing by the chip geometry. Therefore, during cooldown through T_c in this residual perpendicular magnetic field, quantized flux can become trapped in the aluminum ground plane as vortices. This can introduce excess dissipation and frequency noise through driven vortex dynamics under microwave currents when located in regions of high rf current density [160, 161], which can limit the high power Q_i; see Sec. 2.5.8. A dense array of engineered pinning sites was therefore patterned so that trapped flux was preferentially captured at predefined locations in the ground plane rather than at random defects or conductor edges, thereby mitigating vortex-induced loss [160, 162]. This was implemented as square antidots of width 2 µm on a 10 µm pitch across the ground plane; see Fig. 3.7.

A 2 µm square opening was chosen as it is sufficiently larger than the characteristic vortex-core scale ($\xi \sim$ 100-200 nm), providing a strong energetic preference for vortex occupation while keeping the additional dielectric participation from the etched perimeter small. The 10 µm pitch yields an 8 µm superconducting strip between neighboring holes, which preserves ground-

plane continuity while providing a high areal density of pinning sites. For a superconducting thin-film strip of width w, Stan et al. showed that a critical perpendicular field $B_{\text{exp}} \propto \Phi_0/w^2$ exists below which all vortices are expelled from the strip [163]. For the 8 µm inter-hole strips in the present design, B_{exp} is of the order of 10 µT, which exceeds the residual field expected at the chip inside the nested magnetic shielding described in Sec. 3.5.2. The corresponding unit-cell area of 100 µm^2 implies one flux quantum per cell at a field scale of $\sim$ 20 µT, so that for typical residual fields in the µT range, the available hole density exceeds the expected vortex density. To avoid increased TLS loss from the added etched perimeter in high electric field regions, the hole lattice was avoided near the CPW, SQUIDs, and air bridges, where the electric field energy density is concentrated. Instead, the array was confined to the ground-plane regions where the quasi-TEM mode stores negligible electric energy, such that the mitigation of vortex-induced loss is achieved without measurable degradation of Q_i from additional dielectric participation [164].

Input coils

Two configurations of integrated input coils are used in this thesis: flip-chip and on-chip input coils. In the flip-chip configuration, a square input coil on a separate sapphire chip (see Fig. 3.16) is positioned above the square SQUID loop on a silicon bottom chip, connected via flip-chip interconnects (Sec. 3.4). In the on-chip configuration, the input coil is patterned concentrically around the SQUID loop using air-bridge interconnects, with $h = 0$ but constrained to $d_i > d_s$ due to routing. The input coil width d_i is optimized for a non-zero axial separation h; see Sec. 2.8.

3.2.2 FTR layer stack

All resonators are fabricated on 2-inch high-resistivity undoped ⟨111⟩ Si wafers to reduce substrate losses [152, 153]. The FTR stack is fabricated in the following order:

- 150 nm evaporated Al wiring layer defining the CPW, SQUID loop, feedline, ground plane with flux-trapping holes, and on-chip input coil.
- 50 nm sputtered Nb or NbN UBM for flip-chip interconnects with optional Au passivation.

- Shadow-evaporated Al/AlO_x/Al Josephson junctions.
- 200 nm Al patch layer for galvanic connection.
- 500 nm air-bridges for ground stitching and input-coil crossovers.

The UBM is deposited after the Al wiring layer and before the Josephson junctions are patterned to avoid any unwanted effects of the Nb/NbN process on the junctions, including interdiffusion into the Al junction electrodes, plasma-induced damage, or charging effects that could degrade the tunnel barrier, and particulate or chemical contamination of the junction interfaces. The air bridges are fabricated last since they do not tolerate the sonicated solvent cleaning steps used during junction processing to remove resist residues and minimize excess microwave loss.

3.2.3 Wiring layer

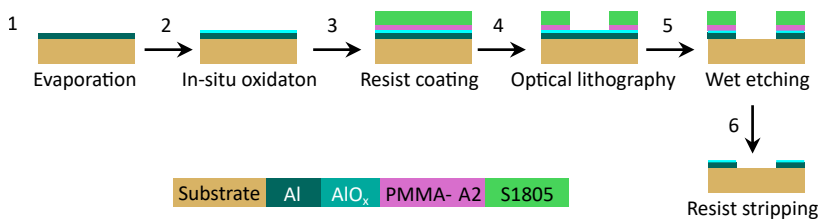

Figure 3.6: Fabrication process for the FTR wiring layer. A 150 nm Al film is deposited and patterned by optical lithography and wet etching to define the CPW, feedline, ground plane, and on-chip input coil.

The wiring layer defines the resonators, feedline, on-chip input coil, and flux-trapping holes. Surface cleanliness and oxide control are needed in the fabrication process, as oxygen-containing interfacial layers increase dielectric participation and contribute to TLS loss [152, 153, 156, 165, 166].

Process flow. The entire wiring layer is defined in 150 nm-thick evaporated aluminum. Prior to deposition, the wafer undergoes solvent cleaning, a standard cleaning procedure (App. 6.3), and a short HF dip to remove the native oxide and reduce TLS loss [152, 153]. HF strips surface SiO_x and leaves a temporarily passivated surface, which reduces dielectric participation at the metal-substrate

interface if the wafer is immediately loaded into the vacuum chamber. After loading, the wafer is pumped to high vacuum, baked for degassing, and the Al is deposited at a controlled rate (App. 6.3).

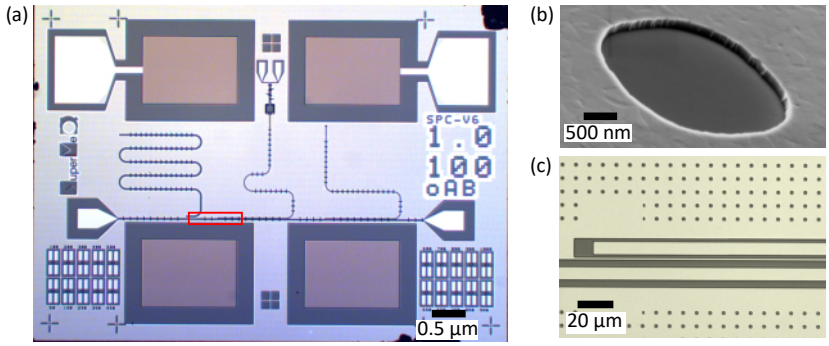

Figure 3.7: Fabricated Al wiring layer. (a) Optical image of the full chip showing the resonator layout. The red box indicates the coupler region shown in (c). (b) SEM image of a single flux-trapping hole. (c) Coupler region where the CPW resonator is separated from the feedline by a narrow ground strip, with flux-trapping holes in the surrounding ground plane.

A thin sacrificial PMMA-A2 layer is coated beneath the S1805 photoresist to protect the Al during development. After optical lithography and development, this layer is removed by oxygen plasma ash, followed by wet etching in a temperature-controlled Al-etchant bath and resist stripping. Fig. 3.6 summarizes the process flow, and Fig. 3.7 shows an optical image of the feedline and coupler region with surrounding flux-trapping holes, as well as an SEM image of a single flux-trapping hole.

3.2.4 Under-bump metallization (UBM)

Flip-chip interconnects require clean metal contact at bonding pads. However, native oxides and intermetallic compounds (IMC) can prevent fully superconducting galvanic contact. For indium interconnects, direct In-Al contact can form non-superconducting IMC, requiring a diffusion barrier [167]. A UBM layer is therefore patterned on bonding pads with Nb or NbN, while other studies have also implemented Ti or TiN [168–171]. Since Nb and NbN readily oxidize upon air exposure [172], the UBM is optionally passivated in situ with

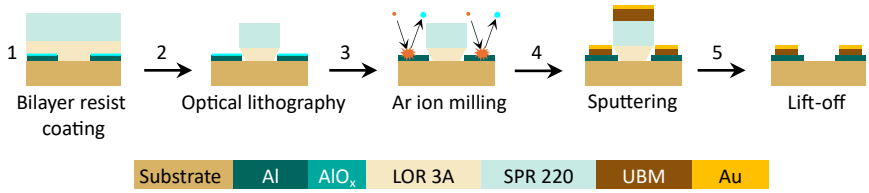

Figure 3.8: Fabrication process for the UBM on FTR bonding pads. In-situ Ar ion mill removes native AlO_x prior to depositing 50 nm Nb or NbN with optional in-vacuo 5 nm Au passivation.

sputtered 5 nm Au without breaking vacuum. Au passivation suppresses oxide formation prior to bonding, and Au-In interfaces remain superconducting at low temperatures [173, 174].

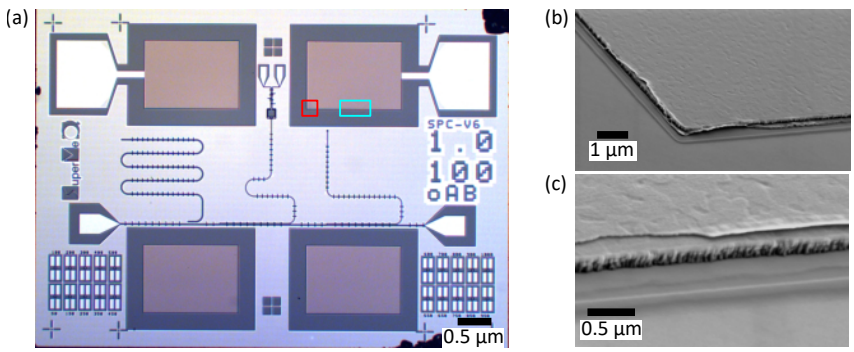

Figure 3.9: Fabricated UBM on FTR bonding pads. (a) Optical image of the full chip; the red and cyan boxes indicate the regions shown in (b) and (c), respectively. (b) SEM image of the NbN UBM edge on the Al pad. (c) Higher-magnification SEM image of the same UBM stack indicating peeling of the top surface of NbN.

Process flow. First, an optical bilayer resist stack is coated for lift-off prior to deposition. Native AlO_x on the Al pads is removed by in-vacuo Ar ion milling immediately before UBM sputtering. A 5 nm Au, if desired, is sputtered in-vacuo, followed by lift-off and resist stripping.

In Paper II, the UBM pads and the top-chip input coil were defined in a single lithography layer, allowing all four UBM combinations (Nb and NbN, each

with and without Au) to be fabricated with a single lithography process and deposition. The FTR devices in Paper III used NbN without Au passivation. Fig. 3.8 summarizes the process flow, and Fig. 3.9(a) shows an optical image of the full device with four UBM pads on each corner of the chip for flip-chip bonding. The optical image shows that the NbN is golden in color, which indicates a cubic δ phase. This phase is preferred over the hexagonal β and γ phases for superconducting applications, given its high critical current and temperatures [175, 176]. Fig. 3.9 (b,c) shows SEM images of the fabricated NbN UBM on an Al flip-chip pad. The top surface of NbN appears to be peeling off. This could likely be due to considerable oxidation over time, as the SEM images were taken two years after the devices were fabricated and stored in the atmosphere. Oxidation is known to induce local stress in Nb and NbN based thin films, which can possibly lead to peeling [177, 178].

3.2.5 Josephson junctions

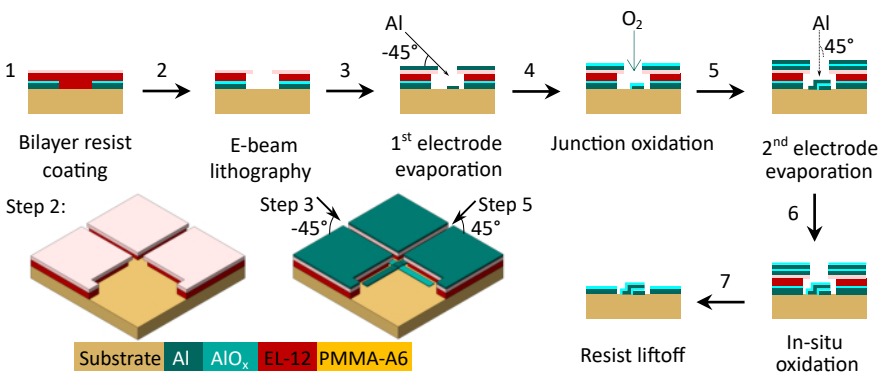

Figure 3.10: Fabrication process for Al/AlO$_x$/Al Josephson junctions in the dc-SQUID termination. A bilayer resist (EL-12/PMMA-A6) is patterned by e-beam lithography, followed by double-angle Al evaporation at 45° from two perpendicular directions with intermediate controlled O_2 oxidation to form the tunnel barrier, and final lift-off. The dotted line in Step 5 indicates evaporation direction is tilted by 45° into the plane. 3D schematics illustrate the bilayer resist trench after e-beam patterning (Step 2) and after the second electrode evaporation (Step 5) for a 500 nm junction.

The effective junction critical current depends on the fabricated area, barrier growth during oxidation, and processing-induced geometry variations. Hence, junction inductance is extracted from measurements rather than taken as a design value.

The devices in this thesis use Manhattan-style (cross-type) shadow-evaporated $Al/AlO_x/Al$ junctions [159], although other bridge-free techniques exist [179]. Unlike the Niemeyer-Dolan bridge approach [180], where junction overlap is set by a fragile suspended resist bridge, the Manhattan geometry defines overlap solely through the intersection of patterned electrodes, eliminating bridge collapse as a failure mode and improving yield and reproducibility [159].

Design. The width of these shadow-evaporated Manhattan JJs cannot reliably exceed 800 nm, as it is limited by the total resist height and the length of the undercut region. Therefore, a new technique was developed in this thesis as a design variant of the standard Manhattan approach to fabricate Josephson junctions of arbitrarily large sizes. The 1 µm JJs were fabricated by designing the electrodes to be 500 nm-wide and making only the junction area 1 µm-wide, with an additional 0.8 µm×1 µm offset on each electrode to compensate for the resist shadow (see Fig. 3.10). This increases the effective overlapping area of the junction, despite some side appendages created as an artifact of the shadow evaporation and resist undercut. In the design of the two JJs of the dc SQUID, these additional offsets were unintentionally mirrored along with the electrodes. Since the evaporation angles are identical (unmirrored) for both junctions in the fabricated devices, one junction was patterned smaller than the other junction, resulting in an asymmetric dc SQUID, as seen in the hatched regions of the junction schematic in Fig. 3.10. The side appendage on the right junction (see Fig. 3.11(c)) overlaps on the electrode, again due to the incorrect mirroring. However, it only potentially adds to an effective junction overlap but does not create any galvanic contact, as the entire surface of the first (bottom) electrode is oxidized before the second (top) electrode is evaporated.

It is important to note that alternative techniques for fabricating large junctions have been developed by Lecocq et al. at Ion Pop's group [179], called "Cliff junctions", and independently by Raftery at Andrew Houck's group at Princeton, which they aptly call "Princeton junction" [181]. This approach circumvents the limitation of resist stack height by making use of the strongly

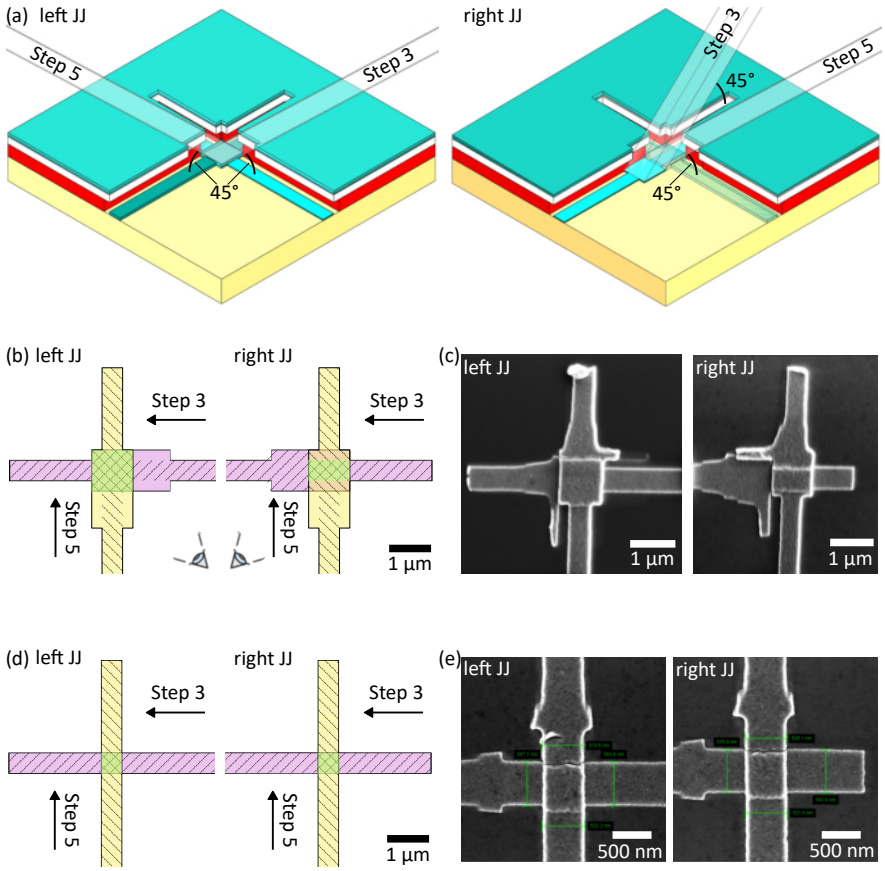

Figure 3.11: Fabricated Al/AlO$_x$/Al Josephson junctions. (a) 3D schematics of the left and right 1 µm junctions in the bilayer resist trench, showing the electrode geometry after double-angle evaporation. (b) Top-view designs of both 1 µm junctions; left and right hatched regions indicate material deposited in Steps 3 and 5, respectively (see Fig. 3.10). The unintentional mirroring of the electrode offsets results in asymmetric junction areas. The electrode overlap is highlighted in green. (c) SEM images of the fabricated left and right 1 µm junctions. The side appendages are artefacts of shadow evaporation in the undercut region. (d) Top-view designs and (e) SEM images of the corresponding 500 nm junctions showing symmetry between left and right junction areas.

asymmetric undercuts in the Cliff junction design. Both approaches are design variants of the standard Manhattan design that similarly allow for junctions of arbitrary size, similar to the one developed in this thesis. However, it leaves a large oxidized region in the vicinity of the junction, which may affect the quality factors of the resonator.

Process flow. The junctions are patterned using electron-beam lithography and liftoff, with an e-beam bilayer resist stack of EL-12 and PMMA-A6 providing an undercut for double-angle evaporation. After exposure, the resist is developed in MIBK:IPA (1:1) and cleaned with a short oxygen plasma. Junction electrodes are deposited at $\pm 45°$ angles using e-beam evaporation at approximately $1\,\mathrm{nm\,s^{-1}}$, with 50 nm for the first electrode (JJ1), followed by controlled oxidation in static oxygen to form a 2 nm thick tunnel barrier, and then 110 nm for the second electrode (JJ2). Proper liftoff and thorough stripping are crucial since dielectrics and resist residues near the junctions can significantly impact FTR quality factors [158, 182, 183]. Oxide thickness varies between fabrication runs due to chamber contamination, pressure variations, and changes in resist undercuts. Therefore, four-wire test structures are used to extract junction inductance. Fig. 3.10 illustrates the fabrication process, and Fig. 3.11 shows the junction designs and SEM images.

3.2.6 Patch layer

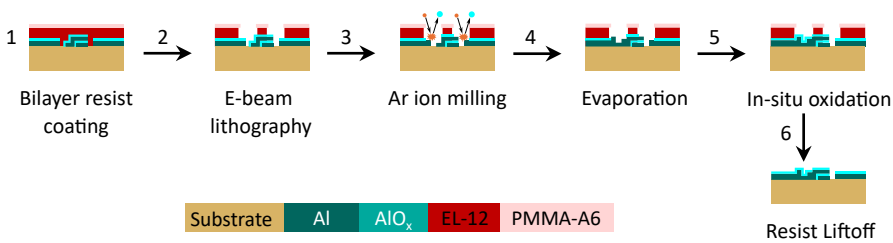

Figure 3.12: Fabrication process for the Al patch layer. After lithography of the patch regions, the exposed Al surface is cleaned by an in-situ Ar ion mill and immediately followed by Al deposition and then lifted-off.

Patch layers are fabricated to create galvanic contact between junction electrodes and the resonator circuit. Since Al forms a native oxide rapidly

in air, galvanic contacts between separately deposited junction electrodes and ground layers require a dedicated oxide removal step. For a microwave resonator, a partially oxidized Al-to-Al overlap can introduce excess resistance, parasitic junctions, and additional lossy dielectric participation, all of which can increase resonator dissipation or add parasitic nonlinearities. This becomes important near high-current and high-field regions of the junctions, where uncontrolled interfaces can dominate resonator loss rates [152, 159].

Process flow. After the lithography of the patch regions with an e-beam bilayer resist stack, the exposed Al is ion-milled with Ar to remove AlO_x, followed immediately by Al deposition without breaking vacuum, and then the resist is lifted-off. Fig. 3.12 summarizes the fabrication process. Fig. 3.13 shows SEM images of the fabricated patches connecting junction electrodes to the circuit for two SQUID geometries.

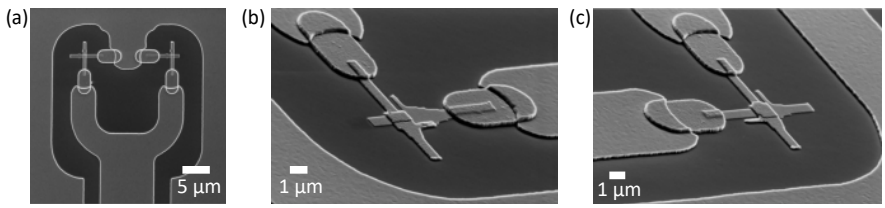

Figure 3.13: Fabricated Al patch layer. (a) SEM image of a 10 µm-wide SQUID loop with 500 nm-wide junctions and patches. (b, c) SEM images of the left and right 1 µm-wide junctions of a 200 µm-wide SQUID loop, showing the patch connections to either side of the circuit.

A simplified alternative to patch layers is the patch-integrated cross-type (PICT) junction process developed by A. Osman [159], which forms both junction electrodes and the galvanic patch connection within the same lithography step and vacuum cycle. This can reduce fabrication steps and the number of potentially lossy interfaces [158, 184]. However, the PICT flow relies on a three-angle shadow-evaporation sequence and therefore imposes a tighter geometry constraint on the junction electrodes. In particular, for the process parameters reported by Osman, the junction electrode width must be below 300 nm to avoid unintended shorts in the three-angle deposition geometry [159]. In this thesis, the junction electrode width is 500 nm (with a junction overlap length of 1 µm), which motivates the need for a dedicated patch layer.

3.2.7 Air-bridges

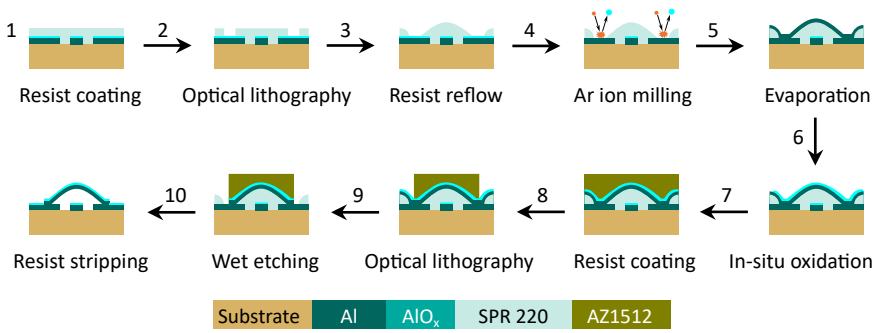

Figure 3.14: Fabrication process for Al air-bridges. The process uses a two-layer optical lithography sequence: a reflow mask to form the arched scaffold, followed by in-situ Ar ion milling, Al evaporation, and a second mask to protect the bridge geometry during wet etching.

Air-bridges serve two purposes in this thesis. First, they periodically connect the two CPW ground planes across the gaps, suppressing slotline-like modes that would otherwise arise from ground-voltage variations and packaging imperfections. Second, they act as superconducting crossovers, for example, to connect the on-chip input coil to the flux-bias lines without needing additional dielectric layers. Compared to wirebonds, air-bridges are more compact, mechanically robust, and add lower losses.

Process flow. The air-bridge process used here is a two-layer lithography process. In the first lithography, SPR220 is patterned and reflown to form an arched scaffold that defines the height of the bridge and ensures a sturdy and smooth structure after metallization. After reflow, the wafer is loaded into the evaporator, and an in-situ Ar ion mill is performed to remove native AlO_x from the contact surface. Then, a 500 nm thick bridge metal is deposited at a controlled rate. In the second lithography, AZ1512 defines an etch protection mask so that Al is removed everywhere except where the bridge arch and feet are intended. Wet etching is performed in an Al etchant under temperature control, followed by resist stripping. The final stripping is done without sonication to avoid mechanically damaging the released bridges. Fig. 3.14 summarizes the fabrication process. Fig. 3.15 shows optical and SEM images

of fabricated air-bridges used for ground stitching and input-coil crossovers.

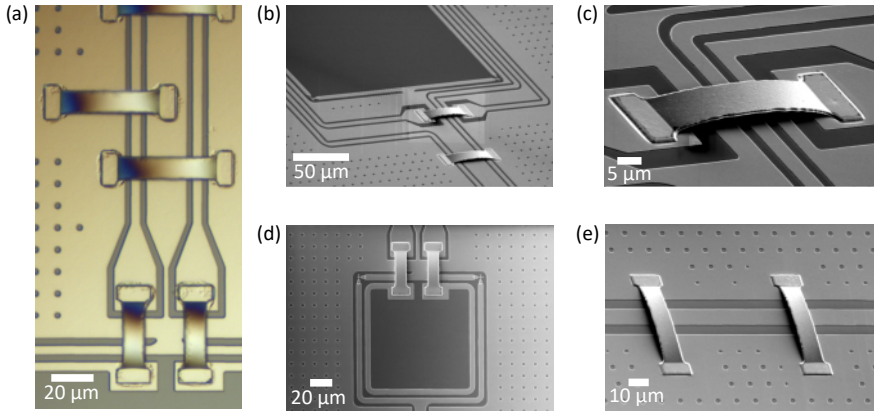

Figure 3.15: Fabricated Al air-bridges. (a) Optical image showing air-bridges used for ground stitching and as crossovers connecting the input coil to the flux line. (b) Titled SEM image of air-bridge crossovers in a multi-winding input coil (Fig. 3.16(c)). (c) Higher-magnification titled SEM image of the airbridge shown in (b). (d) SEM image of two air-bridges connecting the flux line to an inner on-chip input coil (Fig. 3.16(a)). (e) Titled SEM image of ground-stitching air-bridges across the feedline.

Design constraints. The design constraints for the length L and width W of the air-bridge are set by mechanical yield and reliability. Empirically, yields exceed 99% for $L \leq 50\,\mu\text{m}$ with $W \geq 8\,\mu\text{m}$, and for $50\,\mu\text{m} < L \leq 70\,\mu\text{m}$ with $W \geq 12\,\mu\text{m}$ [159]. Shorter bridges risk leaving residual residue, while those longer than 70 µm show decreased mechanical yield and increased sensitivity to processing variation.

3.2.8 Input coils

Local flux biasing is implemented using integrated input coils coupled to the SQUID loop, achieved in this thesis through two different approaches.

On-chip coil. The on-chip coil is patterned in the same 150 nm Al wiring layer as the CPW and ground plane described in Sec. 3.2.3, and it uses air-bridges

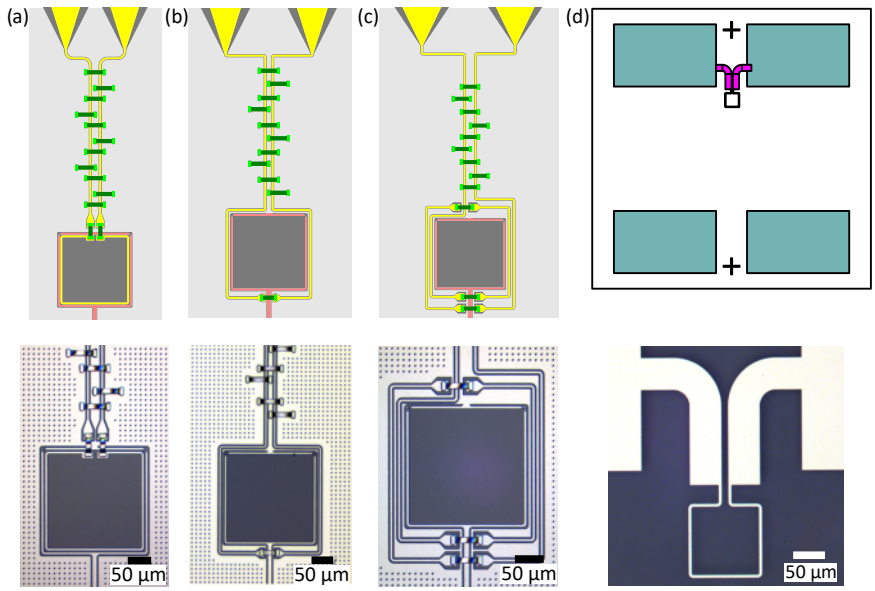

Figure 3.16: Top panels: designs of input-coil layouts used for flux biasing a 200 µm-loop FTR SQUID (red) patterned on an Al ground layer (light grey) with silicon subtrate (dark grey). On-chip single-turn input coils patterned (a) inside and (b) outside the SQUID loop. (c) On-chip multi-winding input coil with two turns patterned outside the SQUID loop. In (a)-(c), the on-chip coils are routed to the flux-bias lines (yellow) using air-bridge crossovers (green). Additional air-bridges are for ground stitching. (d) Flip-chip input coil (magenta) on a sapphire chip (white), galvanically connected to the bottom chip through UBM pads (light blue). Bottom panels: optical images of corresponding fabricated devices.

for crossovers. This layout minimizes axial separation between the coil and the SQUID loop and allows for compact routing with multiwindings.

Flip-chip coil. In the flip-chip implementation, the coil is fabricated on a sapphire chip and galvanically connected to the resonator chip via indium interconnects on UBM pads (see Sec. 3.4.1). Separating the coil from the resonator chip allows denser multi-winding geometries that enhance flux transfer efficiency at a fixed drive current. In the Paper II process, both lift-off-based

and etch-based patterning routes were developed for the top-chip coil and UBM layer. However, the flip-device in Paper III used lift-off-based UBM patterning discussed in Sec. 3.2.4.

Fig. 3.16 shows the designs and optical images of all four types of fabricated input coils: (a) inner on-chip coil, (b) outer on-chip coil, (c) multi-winding on-chip coil, and (d) flip-chip coil.

3.3 Cryogenic setup for levitation

Chip-based magnetic levitation of superconducting microparticles was first demonstrated in a 4 K cryostat using optical readout [95]. Extending these experiments to millikelvin temperatures provides two main advantages: reduced thermal occupation of the mechanical modes and the ability to couple to Al-based superconducting circuits. However, operating in a dilution refrigerator introduces new experimental constraints that are addressed by developing three key subsystems. First, an optical readout system was installed to verify levitation and extract initial motion spectra before moving to SQUID-based detection. This work resulted in the first demonstration of millikelvin levitation of a magnetically trapped superconducting microparticle (Paper I). Second, magnetic shielding was implemented to reduce ambient flux noise to the order of $100\,\mu\Phi_0$ for SQUID-based detection. Third, after initial measurements revealed that the particle motion was strongly driven by vibrations from the cryostat pulse tube, a passive vibration isolation stage was developed to attenuate this mechanical noise in the frequency range of the trap modes.

Fig. 3.17 summarizes earlier work on the design, fabrication, and implementation of a chip-based superconducting magnetic trap for levitating superconducting microparticles [96, 98]. Panel (a) shows a COMSOL simulation of the magnetic field generated by the two-chip trap geometry. The two stacked chips generate a three-dimensional magnetic-field minimum near the trap center and a field gradient on the order of $10\,\mathrm{m}\Phi_0\,\mu\mathrm{m}^{-1}$.

Panel (b) shows a top-view image of the assembled two-chip trap. The trap consists of two stacked silicon chips, each patterned with a planar multi-winding niobium coil. The vertical separation between the two coils is set by the substrate thickness of 280 µm. Each coil contains ten windings with a width of 30 µm, a spacing of 2 µm, and a niobium thickness of 1 µm. For a 50 µm-diameter superconducting sphere in the Meissner state, simulations predict a

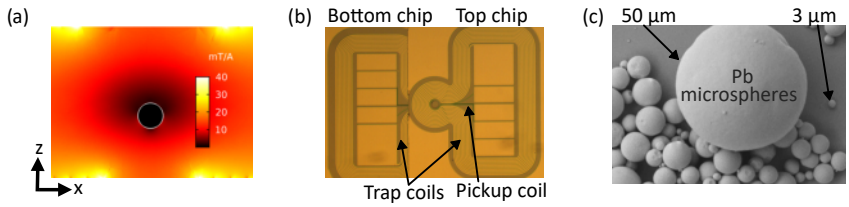

Figure 3.17: Chip-based magnetic trap and superconducting microparticles. (a) COMSOL simulation of the magnetic field generated by the two-chip trap geometry. (b) Top-view microscope image of the assembled two-chip trap showing the superconducting coils and the central trapping region. (c) Scanning electron microscope image of in-house-fabricated lead microparticles. Adapted from [96, 98].

lift force of 19 nN at a coil current of 0.5 A, which exceeds the particle weight and can be sufficient to overcome adhesion to the chip surface [98]. Parallel efforts are being made to reduce particle-surface adhesion through engineered silicon surface treatments, which may lower the trap current required for lift-off [185].

Panel (c) shows lead microparticles fabricated in house by ultrasonic cavitation [98]. This method yields near-spherical particles over a broad diameter distribution, allowing particles of different sizes to be selected for different measurement regimes. In general, smaller particles are favorable for force sensing because of their lower mass, whereas larger particles can be advantageous for acceleration sensing because they provide a larger inertial signal.

3.3.1 Optical readout setup

Optical imaging is used in Paper I to verify particle levitation and to extract the particle's center-of-mass motion [95, 98].

Optical path. The imaging system employs a custom microscope using Köhler illumination for uniform field coverage (Fig. 3.18). A white LED source is collimated ($f = 30$ mm), passed through a chromatic filter, and focused ($f = 200$ mm) onto the back focal plane of a lens ($f = 21$ mm) mounted inside the cryostat. This lens collimates illumination onto the trap plane and collects the particle image. A tilted mirror redirects the beam through viewports in the thermal and vacuum shields. Outside the cryostat, a tube lens ($f = 30$ mm)

focuses the image onto a CMOS camera (Teledyne FLIR Chameleon3, CM3-U3-31S4C-CS) operating at 600 Hz, exceeding twice the largest expected trap frequency to satisfy the Nyquist criterion [98]. Fig. 3.18(a) shows a schematic of the illumination and imaging paths, while (b) shows a photograph of the assembled setup with the cryostat open.

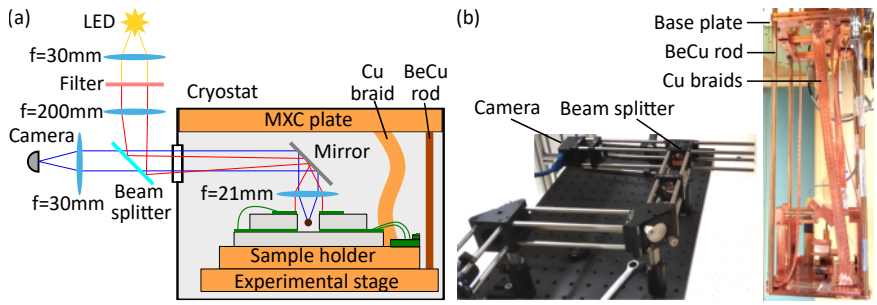

Figure 3.18: Optical readout setup. (a) Schematic showing illumination (red) and imaging (blue) paths with Köhler illumination. The plano-convex lens ($f = 21$ mm) and tilted mirror are mounted above the chip trap. (b) Photograph of the setup outside (left) and inside (right) the cryostat. Adapted from [98].

Design constraints. The optical assembly had four constraints: (i) limited vertical space below the mixing chamber plate (set by the magnetic shielding) and the position of the optical access ports, (ii) the need to minimize added mass for cooldown time and thermalization, (iii) mechanical rigidity requirements for stable alignment during cooldown, and (iv) cable routing for the trap.

Calibration and tracking. Pixel-to-micrometer conversion is calibrated using the ∼180 µm diameter deep-reactive-ion-etched hole in the top chip as an in-situ reference. The CMOS sensor (Sony IMX265) has a pixel size of 3.45 µm, which, combined with the effective magnification $f_{\mathrm{tube}}/f_{\mathrm{obj}} = 30/21 \approx 1.4\times$, gives a pixel scale of ∼2.4 µm per pixel on the sample plane. The effective spatial resolution is further degraded beyond this pixel-limited value by edge detection uncertainty and motion blur. The particle position is extracted offline by fitting an ellipse to the particle contour in each frame. A Fourier transform of the time-dependent position yields the COM frequencies. The

vertical (z) motion is not resolvable because the amplitude of motion blur is smaller than the depth of field of the imaging system [95].

3.3.2 Magnetic shielding

To detect particle motion in a magnetic trap, ambient fields and low-frequency magnetic noise must be suppressed to reach SQUID-limited sensitivity [95, 98], which requires effective magnetic shielding.

Shield configuration. Unlike the closed cylindrical shield used for the FTR experiments (Sec. 3.5.2), the levitation setup employs open-top baskets to permit optical access (Fig. 3.19). A schematic overview of all shielding layers of the optical detection setup is provided in Fig. 3.19(a). The sample is enclosed by multiple nested layers [95, 98]:

1. **Inner stack layers:** nested niobium and Cryoperm basket around the sample holder; see Fig. 3.19(b).
2. **Outer shield layers:** Lead, mu-metal, and aluminum foil wrapping the entire sample stage; see Fig. 3.19(c).

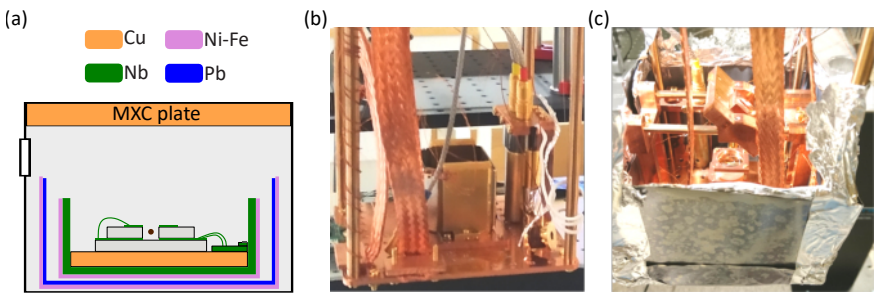

Figure 3.19: Magnetic shielding for the levitation experiment. (a) Schematic of all shielding layers in the dilution refrigerator. (b) Inner shield of niobium and Cryoperm baskets at the sample stage. (c) Outer shield of lead with mu-metal and aluminum tapes with sample and optical parts. Adapted from [98].

Open-top geometry. The open-top configuration limits the achievable shielding factor, particularly for horizontal fields where flux leaks through the opening. FEM simulations predict shielding factors on the order of 10^3 for vertical fields and 10^1 for horizontal fields [95]. Deeper shields with smaller openings would improve attenuation but would conflict with optical access requirements.

3.3.3 Passive vibration isolation

A single-stage mass-spring isolator suspended from the 4 K plate was designed to attenuate pulse-tube and building vibrations at the sample stage. In pulse-tube-operated dilution refrigerators, vibrational noise dominates over thermal motion, yielding an effective phonon occupation that far exceeds the thermal equilibrium value. For a 50 µm lead particle with a vertical trap mode near 120 Hz, the thermal displacement amplitude at 50 mK is approximately 60 pm, whereas the measured center-of-mass amplitude on a rigid stage reaches approximately 10 µm, corresponding to an effective temperature of $T_{\text{eff}} \sim 10^9$ K and an effective phonon occupation $n_{\text{eff}} \sim 10^{17}$ [95]. Reaching the quantum coherent regime requires $Q_m > n_{\text{eff}}$ [22], which motivates the need for vibration isolation. Pulse-tube vibrations at 1.4 Hz are the dominant noise source at the MXC stage, with building vibrations contributing in the 10-100 Hz range [186]. Since particle trap modes are near 100 Hz, the isolation system must attenuate this range without amplifying the 1.4 Hz pulse-tube disturbance. The pulse tube also generates noise at kHz frequencies, but it is situated far above the trap modes and thus is not considered in the vibration isolator design.

Physical model

The vibration isolation system (VIS) is a single-stage passive mass-spring isolator suspended from the 4 K plate [187]. A mass m suspended by a spring of stiffness k acts as a mechanical low-pass filter with a resonance frequency

$$f_0 = \frac{1}{2\pi}\sqrt{\frac{k}{m}}. \tag{3.10}$$

For a linear damped system with a single degree-of-freedom subjected to

harmonic base excitation, the displacement transmissibility is given by [186]

$$T(f) = \frac{X_{\text{stage}}}{X_{\text{base}}} = \sqrt{\frac{1 + (2\zeta r)^2}{(1 - r^2)^2 + (2\zeta r)^2}}, \tag{3.11}$$

where $r = f/f_0$ is the frequency ratio and $\zeta = c/(2m\omega_0)$ is the damping ratio, with c being the viscous damping coefficient [186]. For lightly damped systems, $\zeta \approx 1/(2Q_m)$. For $f \gg f_0$ and light damping, transmissibility decreases as $T \propto (f_0/f)^2$, corresponding to 40 dB attenuation per decade. Attenuation occurs only for $r > \sqrt{2}$. Below this threshold, the system amplifies base motion, with peak amplification near resonance.

The resonant frequency depends on the static deflection under gravity (with g as the local acceleration due to gravity):

$$\delta_{\text{static}} = \frac{mg}{k} = \frac{g}{(2\pi f_0)^2}, \tag{3.12}$$

which depends only on f_0. Lower resonant frequencies provide greater high-frequency attenuation, and $f_0 < 1.4\,\text{Hz}$ would additionally isolate the stage from the pulse-tube fundamental. However, achieving $f_0 = 1\,\text{Hz}$ requires $\delta_{\text{static}} \approx 250\,\text{mm}$, which is challenging within the limited space below the MXC plate. The design, therefore, targets $f_0 \approx 3\,\text{Hz}$, providing approximately 20 dB attenuation at 100 Hz. The suspended stage also exhibits a lateral pendulum mode with

$$f_{\text{pend}} = \frac{1}{2\pi}\sqrt{\frac{g}{L}}, \tag{3.13}$$

where L is the length of the pendulum. For $L = 0.82\,\text{m}$, the pendulum mode is $f_{\text{pend}} \approx 0.55\,\text{Hz}$, which is below the pulse-tube frequency.

Mechanical design

Fig. 3.20 shows the mechanical design of the single-stage VIS. The experimental stage is built around a copper bulk plate to which all other components are fixed, including thermal links, SQUID sensors, and electrical connectors. The stage is suspended from a support fixed to the 4 K plate using three polyamide monofilaments (nylon fishing wire) of 0.55 mm diameter and three music-wire springs, each with $k = 140\,\text{N}\,\text{m}^{-1}$, arranged in a 120° pattern. The total

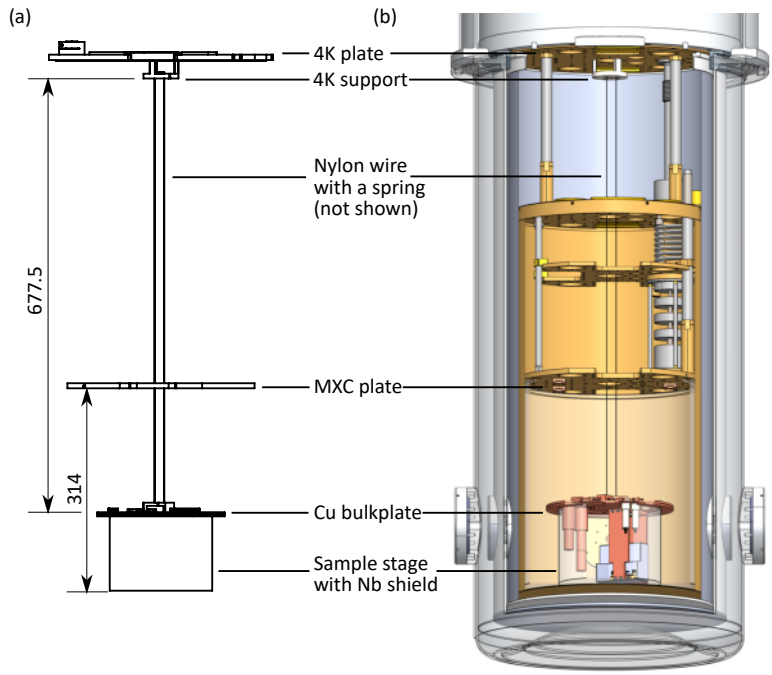

Figure 3.20: (a) 2D drawing and (b) 3D CAD model of the single-stage vibration isolation system inside the BlueFors LD-250 dilution refrigerator. The experimental stage is suspended from a support at the 4 K plate via nylon wires and springs. Dimensions are in millimeters.

suspended mass is approximately 1.35 kg without the niobium magnetic shield and approximately 2 kg with it, comprising the copper bulk plate, sapphire sample wafer, sample holder, SQUID sensor, and thermal link clamps. For a 1.35 kg stage with a combined spring stiffness of 420 $\mathrm{N\,m^{-1}}$ and an additional 31 $\mathrm{N\,m^{-1}}$ from three slacked copper thermal links, the design elongation-mode frequency is 2.9 Hz [187]. The spring-wire connections pass through the line-of-sight KF ports of the cryostat, and the assembly is rotationally symmetric to suppress torsional modes. The maximum available space below the MXC is 320 mm.

Nylon wire is used for the suspension because of its low thermal conductivity (0.012 $\mathrm{W\,m^{-1}\,K^{-1}}$ at 4 K [188]), which minimizes heat load from the 4 K plate

to the suspended stage. Thermalization to the MXC is instead provided by dedicated copper links, as described below. Fig. 3.21 shows the photo of the implementation inside the cryostat.

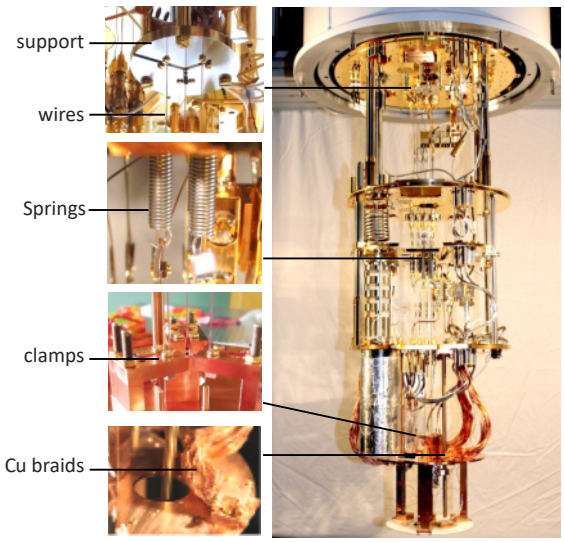

Figure 3.21: Photo of the single-stage passive vibration isolation system with zoom-in insets of key components.

Thermal links and damping. Mechanical decoupling reduces thermal contact between the suspended stage and the MXC cold finger. To restore thermalization, flexible braided OFHC copper links connect the stage to the MXC plate, which was chosen for its high thermal conductivity ($630\,\mathrm{W\,m^{-1}\,K^{-1}}$ at $4\,\mathrm{K}$ [188]) and mechanical flexibility [189]. However, these links also add stiffness and damping to the suspension.

Proof-of-concept measurements on a $0.4\,\mathrm{kg}$ test mass suspended from a cantilever showed that a single slack copper braid contributes an effective stiffness of approximately $10.5\,\mathrm{N\,m^{-1}}$ and decreases the quality factor Q from approximately 25 (no braids) to 11 (three braids), corresponding to an increase in the damping ratio from $\zeta \approx 0.02$ to $\zeta \approx 0.045$ [187]. While increased damping reduces the resonance peak amplitude, it also degrades high-frequency attenuation per Eq. (3.11). Additionally, the rectangular cross-section of the

original braids produced a torque that rotated the stage out of alignment. Therefore, in the final design, the braids were unbraided into bunched wires and annealed at 700 °C in argon for 7 hours to recrystallize the grain structure for improved thermal conductivity and mechanical flexibility [187].

Transfer function measurement. Vibration isolation performance is characterized at room temperature using a vertical geophone velocimeter (Siestech ST2A) on the suspended stage. The geophone operates as an inertial sensor, where the casing moves with the surface while an internal mass-spring system remains approximately stationary above its resonant frequency. A coil attached to the mass moves through the magnetic field of a permanent magnet fixed to the casing. By Faraday's law, the relative motion induces a voltage

$$V = \dot{\Phi} = Bl\dot{z}, \tag{3.14}$$

where B is the radial magnetic flux density, l is the coil length, and $\dot{z}$ is the relative velocity between the mass and the casing. For frequencies well above the geophone resonance, the internal proof mass remains approximately stationary, so the induced voltage is proportional to the absolute velocity of the surface under test. The voltage output is recorded with an oscilloscope and converted to displacement power spectral density (PSD) using the sensitivity curve from the datasheet.

The transfer function $T(f)$ is obtained by comparing the displacement PSD at the suspended stage to that at the 4 K plate under identical excitation. Measurements are performed with the pulse tube on and off to separate the isolator response from pulse-tube-driven motion. The measured transmissibility curves and the comparison with theory are presented in Sec. 4.2.

3.4 Flip-chip bonding

This section describes a superconducting flip-chip interconnect method based on indium microspheres presented in Paper II. This method allows for efficient chip-based flux transport to the FTR.

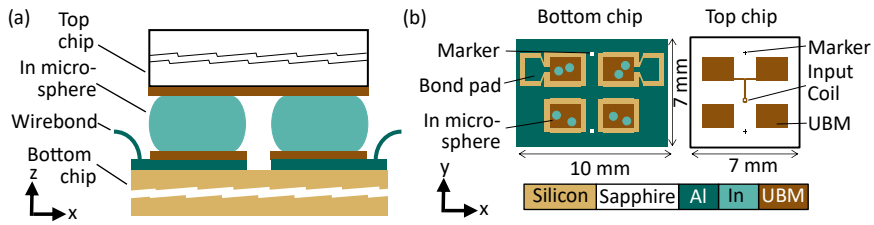

Figure 3.22: Schematic representation of a superconducting flip-chip device using indium microspheres, showing (a) the side view after assembly and (b) the top view before assembly (adapted from Paper II).

3.4.1 Bonding technique

Superconducting flip-chip interconnects provide vertical routing and compact chip-to-chip integration, as illustrated schematically in Fig. 3.22. Flip-chip interconnects are commonly used in superconducting quantum processors for packaging and high-density wiring [169, 190–193], and in cryogenic detectors and sensors for galvanic contact and thermalization [194, 195]. In this thesis, flip-chip integration decouples microwave-device fabrication from coil geometry and routing constraints, allowing for efficient flux coupling while minimizing parasitic capacitive coupling to the resonator. The approach also provides precise control over alignment and tilt, reducing errors in flux calibrations across devices and cooldowns [169, 193].

Concept and material choice. A widely used material for galvanic superconducting interconnect is indium [190, 196]. Indium becomes superconducting below 3.4 K [197], and its ductility and mechanical compliance make it resilient under thermal cycling [190, 195]. Typical indium interconnect fabrication is an involved process requiring optical patterning, deposition via electroplating or evaporation, and a well-calibrated flip-chip bonder [169, 170, 190, 193, 196, 198, 199]. Therefore, a simplified process was developed for applications that require only a limited number of superconducting interconnects. Commercially available 300 µm indium microspheres with 99.99% purity[200] are used as the interconnects (Fig. 3.24(b)), and are pressed onto UBM pads to form indium bumps (Fig. 3.22). Although indium forms a native oxide, it passivates at only a few nanometers in thickness and is typically ruptured during bonding, as indium is malleable and deforms substantially under compression [201]. With

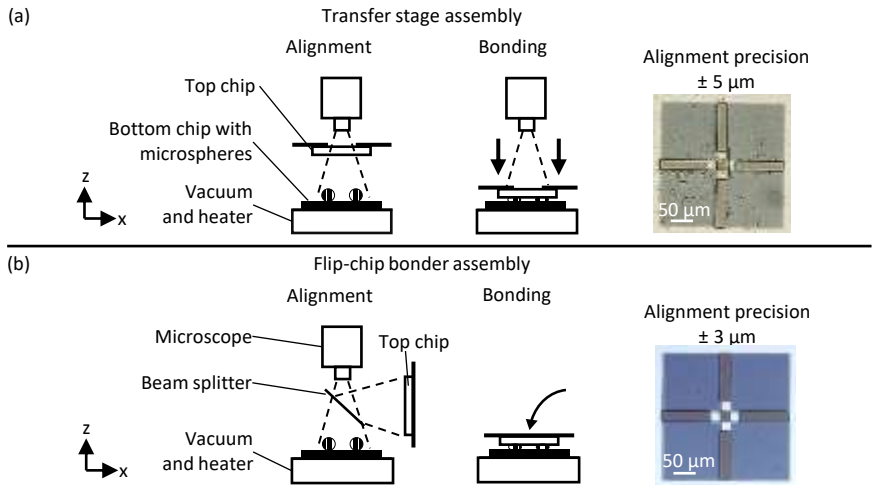

Figure 3.23: Schematic of the flip-chip assembly method and picture of the alignment crosses after successful bonding for (a) the transfer stage that allows continuous visual alignment and dynamic correction during pressing, and (b) the flip-chip bonder that provides a calibrated bonding force (adapted from Paper II).

a reasonable bonding force, we achieve lateral alignments within a few microns; see Fig. 3.23 and chip separation of 20-50 µm, as shown in Fig. 3.24(a). The indium microspheres used for bonding are shown in Fig. 3.24(b).

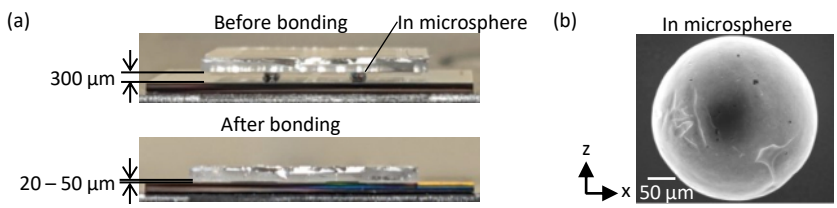

Figure 3.24: (a) Side-view photographs of a flip-chip device before and after bonding. (b) SEM image of a commercially purchased indium microsphere used for flip-chip bonding. Adapted from Paper II.

Transfer-stage bonding. In Papers II and III, the flip-chip devices were bonded using an xyz micro-manipulator transfer stage similar to those used

for 2D material transfer [202]. Fig. 3.23(a) shows the transfer stage setup along with a photograph of the alignment crosses after successful bonding. The bottom chip is held by a vacuum, two indium microspheres are placed on each UBM pad, and the top chip is mounted on a glass slide using PDMS tape. The chips are aligned optically via alignment markers viewed through the transparent substrate of the top chip. The bottom chip may be heated to 110 °C to improve mechanical and thermal contact while remaining well below the melting point of indium (156 °C). The pressing is performed slowly while correcting for drifts. Since the applied force is uncalibrated in this method, pressing is terminated once the top chip begins to drift laterally due to shearing.

Commercial flip-chip bonder. As a benchmark, a commercial flip-chip bonder (Fineplacer 96 Lambda) can be used to provide a calibrated bonding force. Fig. 3.23(b) shows this tool along with the resulting alignment after bonding. Calibrated compression bonding is the standard route in many indium microbump-based superconducting packaging approaches [169, 170, 190, 193]. In this tool, a beam-splitter optical path is used to view both chips simultaneously for alignment. After alignment, the microscope is retracted, and a pre-calibrated lever applies a controlled force to press the top chip onto the bottom chip, with a typical calibrated bonding force in the range 50 N to 65 N (corresponding to 60 MPa to 80 MPa) at room temperature.

3.4.2 Four-wire measurement

dc I-V measurements are required to infer sub-ohmic resistances by measuring voltage drops in flip-chip devices. For this, four wire measurements are preferred, as parasitic contact and lead resistances dominate in two-wire configurations. The resistances are obtained by assuming a linear I-V relation (Ohmic regime) for simplicity. A more accurate method would involve small AC current modulation to infer the resistance. Sharp transitions in the resistances of the samples define the critical currents and temperatures of the thin films. The measurement schematic is shown in Fig. 3.25(a). The flip-chip is glued onto a copper sample holder with BF-6 and is mounted on the mixing-chamber plate of the cryostat. Bond pads are connected via 25 µm-diameter aluminum wirebonds to Nb screw terminals, which clamp twisted copper-clad NbTi wires thermalized at each plate from the MXC stage to the 4 K stage where the

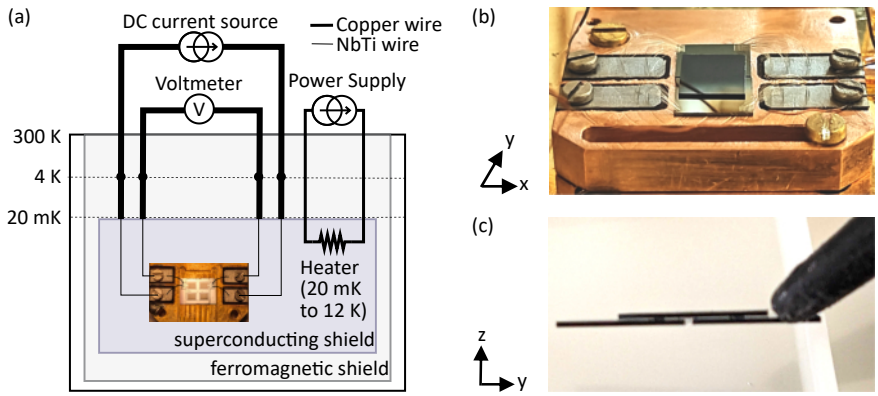

Figure 3.25: (a) Schematic of the cryogenic four-wire measurement setup for superconducting flip-chip devices including a local heater (adapted from Paper II supplementary). (b) Photo of an unpatterned three-chip flip-chip device assembled and wire-bonded for measuring the critical current of the indium interconnect. (c) Side view showing indium interconnects connecting the three chips.

wiring transitions to normal-metal connections.

A resistive heater on the mixing-chamber plate is used to vary the sample temperature from base to above 10 K. From base temperature up to 300 mK, the mixture is circulated with the turbo pump running. From 300 mK to 1 K, the turbo is turned off to reduce the cooling power. Beyond the phase separation of the mixture, there is no further condensation, and all the mixture rapidly begins to evaporate, and is therefore collected back into the tank. From this point onward, the fridge is held in thermal equilibrium at different temperatures solely with pulse-tube cooling and varying heater power. A sufficient waiting time is provided for the temperatures to stabilize at each set point. A Keithley 2450 SourceMeter supplies low-noise current bias, and a Rohde & Schwarz HMC8012 voltmeter records the voltage drop. The critical current of the indium interconnect was measured using an unpatterned three-chip assembly (Fig. 3.25(b,c)) with 24 superconducting Al wirebonds per pad, ensuring the interconnect was the limiting element rather than thin-film or wire bond resistances.

3.5 Resonator characterization

Device characterization requires a photon number calibrated microwave chain for a power-dependent extraction of ω_r, Q_i, and Q_c from complex transmission data [139, 203, 204]. For flux-tunable resonators, the flux modulation and Kerr nonlinearity can also be experimentally determined from this calibration [137]. Reliable magnetic shielding is needed because trapped flux and low-frequency flux noise can cause frequency jumps and linewidth broadening [52, 53, 135, 136, 205].

Three device types are characterized using the same experimental setup: a bare $\lambda/4$ CPW resonator, a coupled FTR with an integrated input coil, and an uncoupled reference FTR. The bare CPW and reference FTR serve as reference structures for isolating the effects of shielding, materials, and readout-chain contributions.

3.5.1 Sample holder and chip mounting

All microwave devices are measured in an oxygen-free high-conductivity (OFHC) copper (99.99%) sample holder designed for low microwave loss, ground continuity, and suppression of parasitic cavity and slotline modes (see Sec. 3.1.2), which can otherwise add spurious modes [151, 154, 156]. Although not performed in this thesis, gold-plating the copper box can further improve thermalization and reduce quasiparticle generation by reflecting stray infrared radiation.

A recessed pocket below the chip area (Fig. 3.26(a)) reduces chip-to-box cavity resonances and mitigates slotline excitation by lowering the parasitic capacitance to the box. The chip is glued to the rim of this recess using cryogenic-compatible BF-6 glue for thermal contact, and dense wire bonding around the chip perimeter connects the ground plane to the copper holder to equalize ground potential and suppress slotline modes [151, 156]. Microwave access is provided by two 50 Ω SMA ports at opposite ends, with flat-milled beryllium-copper pins and a feedline-pad transition geometry for impedance matching. Each SMA-to-feedline connection uses three 1 mm-long wirebonds to reduce series inductance [151]. The bonding wire is 25 µm-diameter aluminum with 1% silicon doping, which remains superconducting at millikelvin temperatures [206].

The sample holder includes two DC feedthroughs (Fig. 3.26(b)) with alu-

minum pins for superconducting contact, insulated by PEEK plastic. Copper-clad 250 µm NbTi wires are soldered to these pins and routed as a twisted pair to SMA adapters on the microwave lines. Soldered SnPb joints are preferred over mechanical clamps because they are superconducting at cryogenic temperatures, thereby minimizing dissipation [207]. A ∼1000-turn external bias coil, wound from copper-clad 100 µm NbTi wire on a 10 mm copper bobbin, is mounted on the sample-holder lid for static tuning of the FTR with a dc magnetic field.

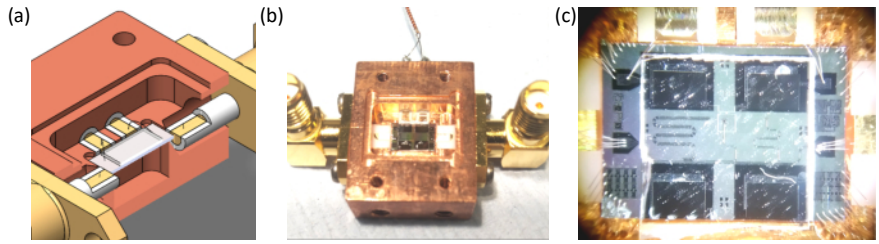

Figure 3.26: Sample holder and chip mounting for resonator spectroscopy. (a) CAD cross-section showing the recessed pocket below the chip to suppress chip-to-box resonances and slotline excitation. (b) Photograph of the OFHC copper holder with DC feedthroughs. (c) Assembled chip showing the perimeter ground-bond fence and microwave launch with three wirebonds for impedance-matched termination, and single bonds from fluxline to the DC pins.

3.5.2 Magnetic and thermal environment

Measurements are performed in a BlueFors LD250 dilution refrigerator with a base temperature of approximately 20 mK. Parallel experiments in the cryostat may cause the temperature to rise but remain below 50 mK, which is sufficient to suppress thermal quasiparticles in aluminum films. With proper attenuation, residual thermal photon occupation in the microwave lines is also negligible [203, 208].

Magnetic shielding for the microwave setup is implemented in nested stages (Fig. 3.27). The outermost layer is a room-temperature mu-metal shield that reduces the ambient field entering the cryostat. At the MXC stage, a tin-plated copper shield attenuates residual static fields and low-frequency fluctuations. The innermost shield, around the sample stage, is a supercon-

ducting niobium cylinder wrapped with high-permeability tape (Fig. 3.27(b,c)). The nesting order reflects the complementary frequency response of the two shielding mechanisms. Superconducting shields expel magnetic flux through the Meissner effect after transitioning below T_c. Any ambient field present during cooldown can become permanently trapped as flux vortices, producing a static residual field inside the shield that the superconductor cannot remove. High-permeability shields, by contrast, provide a finite DC shielding factor set by the geometry and permeability of the material, and their attenuation increases at higher frequencies as the skin depth in the shield wall decreases below the wall thickness, where eddy currents additionally attenuate the ac magnetic field. Thus, the outer high-permeability layers attenuate the ambient field that the superconductor sees during cooldown, minimizing trapped flux, as well as providing additional high-frequency attenuation through eddy currents once the system is cold. Niobium is chosen for the superconducting shield because its T_c (9.3 K) is well above that of the aluminum devices [209]. Alternative superconducting shield materials include tin or niobium-tin alloys [210]. The high-permeability tape wrapped around the niobium cylinder improves shielding against field leakage through openings and seams [211, 212] and aids thermalization during cooldown. Nickel-based mu-metal (∼80% Ni, ∼15% Fe, ∼5% Mo) is widely used for low-frequency shielding. For cryogenic applications, Cryoperm-10 is preferred over standard mu-metal for its high permeability ($> 10^5$) at millikelvin temperatures [213]. To mitigate trapped flux, a local heater (20 kΩ resistor) near the sample holder allows controlled warm-up above T_c and re-cooling in low fields when hysteresis or flux jumps are observed.

3.5.3 Cryogenic microwave wiring

Resonator spectroscopy in a hanger configuration supports multiplexed readout while keeping the device layout compact, and it is widely used in superconducting resonator and circuit-QED characterization [119, 204]. Compared to reflection (S_{11}), the off-resonance response in a hanger measurement is dominated by the approximately 50 Ω transmission line, along with the smooth wiring background (electrical delay and ripple), while the resonator only adds a local notch close to resonance. This separation between a slowly varying baseline and a localized notch enables the background to be recorded separately and subtracted offline from the resonator trace, where the resonator contribu-

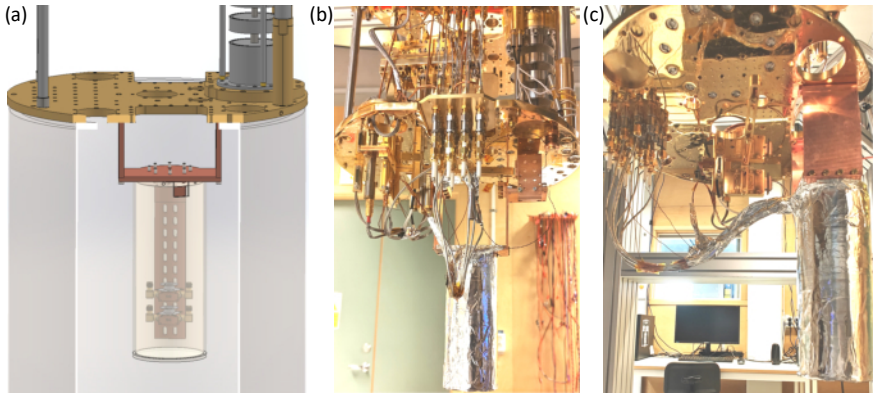

Figure 3.27: Experimental setup showing magnetic shielding and cabling. (a) 3D CAD model showing two sample holders clamped to a copper plate, along with external bias coils, shrouded inside a superconducting niobium shield with cable opening at the top. The setup is clamped below the MXC plate of the cryostat with OFHC brackets for thermalization. There is an additional tin-plated copper shield (with a cut section for visibility) for the entire MXC stage. (b,c) Photographs of the experimental setup showing the niobium shield wrapped with soft ferromagnetic tapes, which in turn are wrapped with aluminum tapes on the outside, along with the SMA cables, for magnetic and RF shielding. The DC breakout box has an RC filter at the MXC and 4 K stages.

tion appears primarily as a shift of the notch frequency and linewidth [139, 154].

DC wiring and filtering. External flux bias is applied using a multi-turn NbTi coil glued on top of the sample-holder and driven by a programmable current source (Keithley 2450). In addition, an integrated input coil is biased through an attenuated coaxial line to provide local flux tuning and modulation of the resonators. The external-coil dc lines are low-pass filtered at 4 K and mK stages to suppress broadband current noise that would otherwise convert into flux noise at the SQUID [51, 204, 214]. For the integrated input-coil line, the dominant low-frequency attenuation arises from the resistive attenuator network, quantified by the dc transfer factor η_{dc} (Eq. (3.15)). Furthermore, long DC wires can pick up electrical noise through vibrations, which can

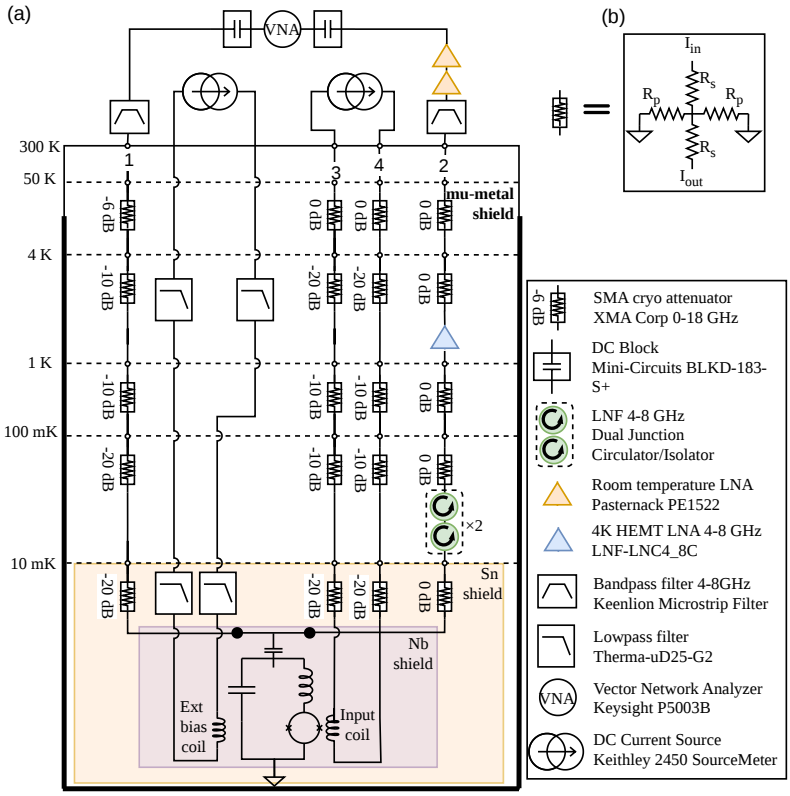

Figure 3.28: Cryogenic microwave and dc wiring for resonator spectroscopy and flux biasing. (a) Wiring schematic of the microwave measurement chain including staged attenuation, base-temperature isolation, 4 K HEMT amplification, room-temperature readout, and external-coil bias line including cold low-pass filtering. (b) Circuit model of the XMA cryogenic attenuators used for the integrated input-coil line, represented as an equivalent unbalanced symmetric resistive attenuator consisting of two shunt resistors R_p to ground and a series resistor R_s.

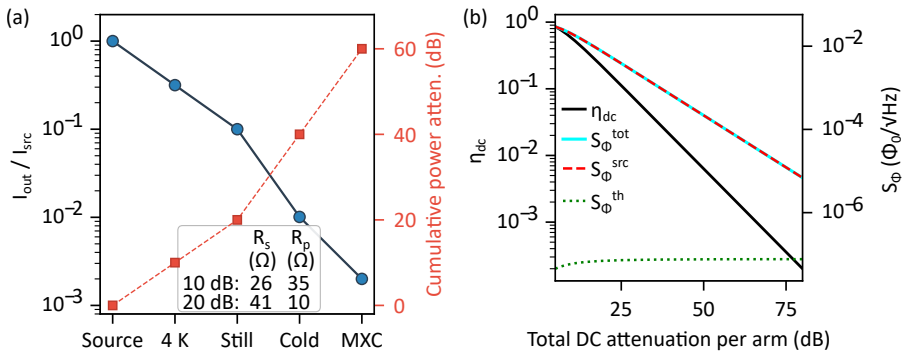

Figure 3.29: Flux line characterization for dc biasing of the integrated input coil. (a) Current transfer through the attenuated coax line obtained from nodal analysis. The stage markers show the output current ratio $I_{\mathrm{out}}/I_{\mathrm{src}}$ after each attenuator. The terminal value defines the dc transfer factor $\eta_{\mathrm{dc}} \equiv I_{\mathrm{coil}}/I_{\mathrm{src}}$. The cumulative attenuation along the down-line is shown on the secondary axis. (b) Predicted equivalent flux-noise amplitude spectral density $S_\Phi^{1/2}$ at the device due to the flux line, evaluated at $M = 150\,\mathrm{pH}$ and shown as a function of total dc attenuation per arm. The total curve (solid blue) is the sum of source current-noise (dashed red) propagated by η_{dc} and an attenuator thermal (Johnson-Nyquist) noise (dotted green) of the attenuator resistors at their stage temperatures.

appear as phase and frequency fluctuations. The wiring inside the cryostat is therefore wrapped with aluminum tape for electrostatic and RF shielding and clamped to the fridge chassis with slack to reduce motion-induced magnetic flux pickup. Aside from the low-pass filters (Therma-uD25-G2), the densely wound coil itself acts as a low-pass filter with a cutoff frequency below 10 Hz, which further suppresses flux noise.

DC current attenuation. The integrated input coil is biased with dc current routed through a coaxial line with 60 dB of distributed cryogenic attenuation. The attenuators provide thermalization and dissipate stray RF and low-frequency voltage noise from room-temperature electronics before reaching the device [203, 204]. At dc, each attenuator is modeled as a resistive attenuator (Fig. 3.28(b)) that leaks current to ground through shunt resistors. The dc transfer factor is defined as

$$\eta_{\mathrm{dc}} \equiv \frac{I_{\mathrm{coil}}}{I_{\mathrm{src}}} \tag{3.15}$$

and is obtained by nodal analysis of the full two-arm resistive network. For the nominal 10-10-20-20 dB per-arm configuration, this yields $\eta_{\mathrm{dc}} \approx 2 \times 10^{-3}$.

Each XMA attenuator is represented by an equivalent symmetric resistive attenuator with a series resistor R_s and two equal shunt resistors R_p to ground. At dc, the two shunts from Eq. (3.16) act in parallel, giving an effective shunt $R_{p,\mathrm{eff}} = R_p/2$. For attenuation A at $Z_0 = 50\,\Omega$, the resistor values are

$$R_s = Z_0 \frac{\sqrt{G}-1}{\sqrt{G}+1}, \qquad R_p = Z_0 \frac{4\sqrt{G}}{G-1}, \qquad G = 10^{A/10}. \tag{3.16}$$

The coil current is sourced and returned through two attenuated lines (10-10-20-20 dB staging), with the superconducting integrated coil acting as a short at the mixing-chamber stage. Solving the full two-arm resistive network defined by Eq. (3.16) yields $\eta_{\mathrm{dc}} \approx 2 \times 10^{-3}$ for the nominal 60 dB configuration. The stage-resolved transfer and the cumulative down-line attenuation are shown in Fig. 3.29(a). This calibration is used to convert programmed source currents to integrated coil currents and to perform flux calibration via $\Phi = M I_{\mathrm{coil}}$.

Additionally, η_{dc} was measured at room temperature by applying dc currents at the top flange of the cryostat and measuring the transmitted dc current at the MXC stage, after which the results were compared with the analytical estimates. For this measurement, a single microwave line was connected to a dc current source at the top flange such that the current flowed through the center conductor of the coaxial line, with the return through the outer conductor. At the MXC stage, an ammeter was connected between the center and outer conductors to close the circuit and measure the attenuated current. The ratio of the measured output current to the applied input current was then taken as the dc current transfer factor, η_{dc}.

The corresponding low-frequency flux-noise contribution of the flux line is shown in Fig. 3.29(b). In this model, the source current noise amplitude spectral density is propagated to the coil using η_{dc}, while the attenuator thermal noise is obtained from the Johnson-Nyquist current noise power spectral density [109, 215]

$$S_I(f) = \frac{4k_{\mathrm{B}}T}{R} \qquad [\mathrm{A}^2/\mathrm{Hz}] \tag{3.17}$$

of the resistors in Eq. (3.16) at their respective stage temperatures. Each resistor's current-noise contribution is propagated through the two-arm network to the coil terminal and converted to flux-noise spectral density via $S_\Phi = M^2 S_I$. The plotted quantity in Fig. 3.29(b) is therefore the amplitude spectral density $S_\Phi^{1/2}$. The curves show source noise with increasing attenuation and the small noise generated by the resistive network itself.

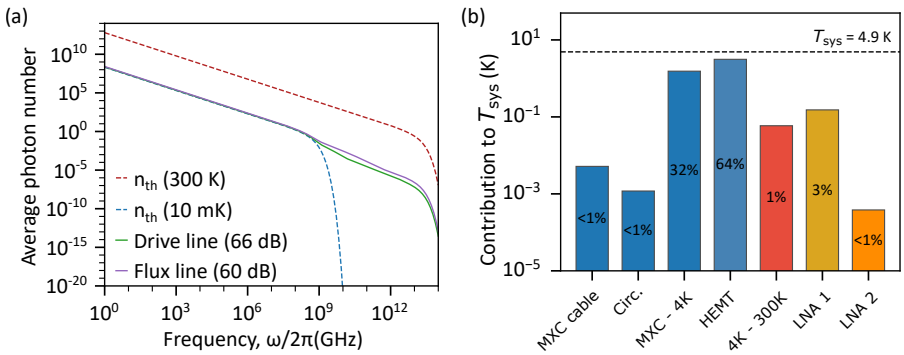

Figure 3.30: Microwave drive line and readout noise. (a) Mean thermal photon occupation $\bar{n}(f)$ versus frequency for the room-temperature source, the base-temperature limit, and the effective occupations at the device port after staged cryogenic attenuation of the drive line (66 dB) and flux line (60 dB). The staged attenuators progressively thermalize the incoming field to colder stages and suppress room-temperature Johnson-Nyquist noise incident on the device. (b) Readout-chain noise temperature budget referred to the device output, computed using the Friis cascade of the uplink components (cables, isolators, 4 K HEMT, and room-temperature amplification). The dashed line indicates the total system noise temperature $T_{\rm sys}$, which sets the technical noise floor of the measured microwave quadratures.

Microwave attenuation. The resonator drive line and the integrated-coil line include discrete cryogenic attenuator chains with total nominal attenuations of 66 dB and 60 dB, respectively. In addition, the CuNi coaxial cables between cryostat stages contribute a small but non-negligible distributed attenuation of approximately 6-7 dB m^{-1} at 5-6 GHz. Together, these losses progressively re-thermalize the propagating microwave field to colder stages and suppress room-temperature Johnson-Nyquist noise incident on the device [203, 208,

216]. For an attenuator at stage k with physical temperature T_k and power transmission $\eta_k = 10^{-A_k/10}$, the output occupation at angular frequency ω is given by [208]

$$n_k^{(\mathrm{out})}(\omega) = \eta_k \, n_{k-1}^{(\mathrm{out})}(\omega) + (1 - \eta_k) \, n_{\mathrm{th}}(T_k, \omega), \tag{3.18}$$

where

$$n_{\mathrm{th}}(T, \omega) = \frac{1}{e^{\hbar\omega/k_{\mathrm{B}}T} - 1}. \tag{3.19}$$

Iterating Eq. (3.18) over the full attenuation chain shows that noise added at a given stage is further suppressed by all subsequent attenuation between that stage and the device. The integrated coil was therefore driven through an attenuated coaxial line in order to thermalize the injected microwave field stage by stage and to suppress thermal noise from warmer stages. This photon-occupation description applies to microwave-frequency signals. In the low-frequency or dc limit relevant for flux-bias noise, the corresponding noise at the device is instead set by η_{dc} (Eq. (3.15)), together with the current-source noise.

This staged thermalization is summarized in Fig. 3.30(a), which shows the effective mean occupation at the device port for the nominal 66 dB drive-line and 60 dB flux-line attenuation chains. The low-frequency asymptote follows the Rayleigh-Jeans limit of Eq. (3.19), $\bar{n} \approx k_{\mathrm{B}}T/hf$, whereas the high-frequency roll-off marks the onset of the quantum regime, $\bar{n} \ll 1$, at the device port after staged attenuation. At 5 GHz, the effective thermal occupation incident on the device is reduced to $\bar{n}_{\mathrm{drive}} \approx 1.9 \times 10^{-3}$ for the 66 dB drive line and $\bar{n}_{\mathrm{coil}} \approx 7.1 \times 10^{-3}$ for the 60 dB integrated-coil line, compared with $\bar{n}_{\mathrm{th}}(300\,\mathrm{K}) \approx 1.25 \times 10^{3}$ at the room-temperature source. A stage-by-stage evaluation at 5 GHz further shows that the residual occupation at the device port is dominated by the Cold-stage attenuator at approximately 100 mK, while the room-temperature contribution is strongly suppressed by the full downstream attenuation chain.

Readout chain. The readout chain is designed to preserve the transmitted microwave signal while adding minimal noise. The wiring schematic is shown in Fig. 3.28(a), and the attenuator circuit model used for the dc analysis is shown in Fig. 3.28(b). The corresponding input-referred system noise temperature is $T_{\mathrm{sys}} \approx 4.9\,\mathrm{K}$ for the nominal readout chain, dominated by the first cryogenic

gain stage (HEMT contribution ∼64 %) and by loss between MXC and the 4 K stage (contribution ∼32 %). The cryogenic interconnects are non-magnetic to reduce flux noise and are hand-formable to reroute easily and minimize strain-induced variations in impedance. On the output, two LNF dual-junction 4-8 GHz circulator/isolators at base temperature provide reverse isolation from the 4 K amplifier [204]. Since ferrite non-reciprocal components contain internal bias magnets, they are enclosed in dedicated magnetic shields positioned farther from the experiments. An LNF HEMT amplifier at 4 K provides the first low-noise gain, followed by two room-temperature LNAs. 4-8 GHz band-pass filters suppress out-of-band noise and reduce the risk of amplifier saturation. The resulting system noise temperature sets the device-referred technical noise floor of the readout chain [21, 72]. The corresponding input-referred noise temperature budget is shown in Fig. 3.30(b). The cumulative contribution is dominated by the first cryogenic gain stage, while subsequent room-temperature amplification is strongly suppressed when referred to the device port by the preceding gain.

3.5.4 Data acquisition and fitting

Spectroscopy is performed by measuring $S_{21}(f)$ around the resonance and fitting the complex response. The flux dependence is characterized by sweeping the external-coil current and acquiring a resonance trace at each bias point, from which the flux responsivity $\partial\omega_r/\partial\Phi$ is obtained, which is relevant for the single-photon coupling rate [133, 134, 217, 218]. Flux sweeps are performed at fixed power to separate flux-dependent nonlinearity from power-dependent effects. The same flux responsivity also determines the transduction from flux noise to frequency noise [51, 214, 219]. The power dependence is measured at fixed flux bias by sweeping the generator power and recording the resonance trace at each step. For bare CPW resonators, this primarily probes TLS saturation and residual non-equilibrium loss channels [124, 140], whereas for FTRs, it additionally reveals Kerr-induced frequency pulling and the onset of Duffing distortion and bifurcation, which set the maximum usable photon number for linear readout [135–137]. While the exact parameters vary slightly across cooldowns and devices, flux sweeps are typically acquired with an applied VNA power of −65 dBm, an IF bandwidth of 20 Hz, and 10k points without averaging, whereas power sweeps are performed over an applied VNA power range of −80 to −10 dBm using about 10 averages at low powers and 2,000

points.

For bare CPW resonators, a linear S_{21} model is accurate at all power levels. For FTRs, the response becomes amplitude-dependent due to Josephson nonlinearity, leading to Kerr-induced frequency pulling and Duffing bistability. The fitting routine uses (i) a linear complex-plane circle fit where the response remains Lorentzian[139] and (ii) an extended nonlinear model below bifurcation to extract ω_r, Q_i, and the Kerr coefficient [135–137] (see Sec. 2.6.9). This defines the maximum photon number for linear readout [101, 137]. Fig. 3.31 illustrates the fitting routine for a bare CPW resonator. The circle fitting routine yields ω_r, Q_i, Q_c, photon-number calibration, flux calibration, and responsivity $\partial\omega_r/\partial\Phi$ for FTRs, as well as Kerr/bifurcation limits.

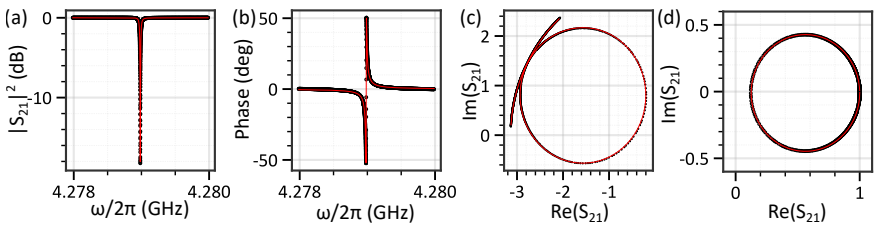

Figure 3.31: Example spectroscopy trace and complex-plane fit for a bare CPW resonator. (a) Measured magnitude $|S_{21}|$ and (b) phase $\arg(S_{21})$ near resonance with fitted hanger model. (c) Complex-plane representation and (d) normalized circle used for parameter extraction [139].

CHAPTER 4

Results

It's not a bug, it's a feature.

This chapter presents the experimental characterization of the subsystems developed for magnetomechanical coupling between a flux-tunable resonator and a levitated superconducting microparticle. First, chip-based magnetic levitation is demonstrated using optical readout of the particle motion (Sec. 4.1). A passive vibration isolation stage is characterized, and its effect on the motion of the particle is assessed (Sec. 4.2). The magnetic shielding enclosing the FTR devices is evaluated through finite-element simulations (Sec. 4.3). The superconducting flip-chip interconnect, developed to integrate a flux-bias coil onto the resonator chip, is validated through material analysis and transport measurements (Sec. 4.4). On the microwave side, bare CPW resonators are measured to determine their quality factors (Sec. 4.5), followed by flux-tunable resonators whose tunability, quality factors, and Kerr nonlinearity are characterized for both on-chip and flip-chip input coil configurations (Sec. 4.6). The integrated flux transformer that couples the pickup loop to the resonator is then characterized (Sec. 4.7). The sensitivity of the large-loop FTR to flux noise and its effect on the extracted effective intrinsic quality factor are

analyzed in Sec. 4.8. Finally, the measured device parameters are combined with simulated flux gradients to estimate the single-photon magnetomechanical coupling strength and to project the displacement sensitivity and cooperativity of the full system (Sec. 4.9).

4.1 Optical readout of levitated microparticle

The optical readout measurements are detailed in Paper I. A 50 µm-diameter tin-lead (Sn63Pb37) microsphere was loaded into the two-chip magnetic trap described in Sec. 3.3 and cooled in the dilution refrigerator. The particle was imaged using the optical setup detailed in Sec. 3.3.1. When a current of 0.5 A was applied to the trap coils, the particle lifted off the substrate and oscillated about the trap center. A sudden displacement of the particle from its rest position marked the onset of levitation, followed by a visible blur caused by the oscillatory motion within the camera exposure time (Fig. 4.1(a-b)). The motional amplitude decreased over approximately one second, after which the particle appeared stationary at its equilibrium position (Fig. 4.1(c)). Under continuous illumination, the particle fell back onto the substrate after approximately 10 s (Fig. 4.1(d)), because the visible-light photons exceeded the superconducting gap energy of the particle material, breaking Cooper pairs and heating the particle above its critical temperature.

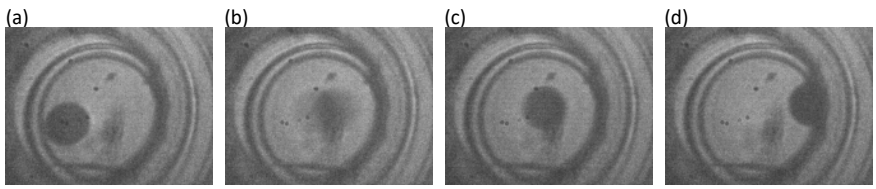

Figure 4.1: Optical images of a 50 µm-diameter SnPb microsphere in the chip trap at 4 K. (a) The particle rests on the substrate with no trap current applied. (b) At $t = 0.1$ s after applying 0.5 A, the particle levitates and appears blurred due to its oscillatory motion. (c) At $t = 1$ s, the motional amplitude has decreased and the particle appears stationary at its equilibrium position. (d) At $t = 11$ s, continuous illumination has caused the particle to lose superconductivity and fall. Adapted from Paper I.

The center-of-mass (COM) frequencies were extracted by tracking the particle

position frame-by-frame (see Sec. 3.3.1 for calibration details) and computing the Fourier transform of the resulting time-dependent displacement. The frequency spectrum (Fig. 4.2) shows two peaks corresponding to the in-plane COM modes at $(\omega_x, \omega_y) = 2\pi \times (32 \pm 1.6,\ 60 \pm 1.8)$ Hz for a trap current of 0.5 A. The vertical mode (ω_z) was not resolved optically because its motional amplitude is smaller than the depth of field of the imaging system. Finite-element simulations of the trap predict $(\omega_x, \omega_y, \omega_z) = 2\pi \times (43 \pm 4,\ 64 \pm 19,\ 125 \pm 3)$ Hz at the same current. The measured in-plane frequencies agree well with the simulations. The remaining discrepancy is attributed to spatial misalignment between the top and bottom trap chips, which was visible in the optical images.

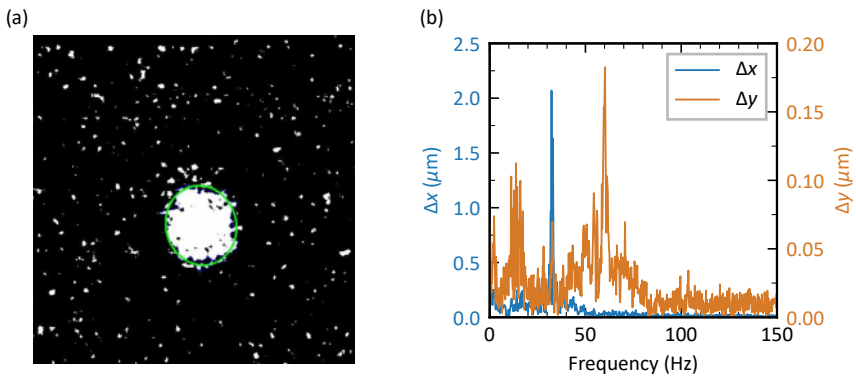

Figure 4.2: Optical tracking of a levitated 50 µm diameter SnPb microparticle at 4 K with a trap current of 0.5 A. (a) Single frame from the 600 Hz camera recording showing the levitated particle inside the chip trap. The blue dots mark the detected edge pixels and the green curve is the fitted ellipse contour, the center of which defines the particle position in each frame. (b) FFT amplitude spectrum of the particle's center-of-mass motion in the x (blue, left axis) and y (orange, right axis) directions. The in-plane COM frequencies are $f_x = 32$ Hz and $f_y = 60$ Hz, in agreement with FEM simulations shown in Paper I. The x-mode amplitude is roughly ten times larger than the y-mode amplitude because the coil openings, aligned with the x direction, provide weaker trap confinement. Adapted from Paper I.

Without illumination, the particle remained stably levitated for several hours, with no upper time limit observed. This was later confirmed by SQUID-based

detection over measurement periods exceeding 48 hours. Similar levitation was observed when using pure lead microspheres. The expected scaling of the COM frequencies with particle density, $\omega_i \propto 1/\sqrt{\rho}$ (see Eq. (2.51) in Sec. 2.1.1), was confirmed in subsequent measurements by comparing lead and tin-lead particles under identical trap conditions. Levitation was also demonstrated at a base temperature of 40 mK, with no measurable difference in the COM frequencies compared to 4 K operation. These results demonstrated chip-based magnetic levitation at millikelvin temperatures as a working platform and motivated the development of non-invasive SQUID-based readout and, ultimately, the flux-tunable resonator approach pursued in this thesis.

4.2 Passive vibration isolation system

This section evaluates the single-stage vibration isolation system (VIS) described in Sec. 3.3.3. The evaluation covers room-temperature measurements of the VIS mechanical response (Sec. 4.2.1), cryogenic measurements of the levitated particle motion obtained with a SQUID magnetometer (Sec. 4.2.2), and thermalization limitations of the current design (Sec. 4.2.3).

4.2.1 Transfer function and stage noise

The mechanical response of the VIS was first characterized at room temperature by measuring vibrations at the 4 K plate and the suspended stage with a geophone (Seis Tech ST-2A, sensitivity 260 V/(m/s), resonance frequency 2 Hz) while raw voltage time traces were recorded with a PicoScope at a 20 kHz sampling rate. The voltage traces were then converted into displacement amplitude spectral densities by correcting for the geophone frequency response and dividing by $2\pi f$ to convert velocity to displacement [187]. The stage-to-plate displacement transmissibility was then obtained from the ratio of the corresponding displacement amplitude spectral densities. It should be noted that a ratio of power spectral densities would instead yield the squared magnitude of the transfer function.

Fig. 4.3(a) shows the measured transmissibility from the 4 K plate to the suspended stage. The pendulum mode appears at 0.55 Hz (peak 1) and the elongation mode at 3.2 Hz (peak 2), the latter close to the design value of 2.9 Hz [187]. The slight increase in the measured elongation-mode frequency is

attributed to additional stiffness from the copper thermal braids [187]. Two theoretical curves are overlaid: a single-stage transfer function following the model developed in App. 6.2 (solid red), and a two-stage transfer function for the proposed upgrade (dashed blue). Above the elongation resonance, the measured single-stage transmissibility decreases overall, consistent with passive isolation. However, the measured curve does not exhibit a clean f^{-2} asymptote over the full plotted range, but instead shows substantial residual structure and flattening. The pulse-tube fundamental at 1.4 Hz lies between the pendulum and elongation resonances. Correspondingly, no strong enhancement is observed at that frequency in the measured transfer curve.

Fig. 4.3(b–e) shows the displacement amplitude spectral density recorded at five cryostat stages (top flange, 50 K, 4 K, still, and MXC plates) with the pulse tube turned off (solid lines) and on (dashed lines). These measurements were performed at room temperature with the cryostat closed but not cooled, following the procedure used by Söderqvist [187]. The geophone was placed sequentially on each stage, and the displacement spectra were extracted as described above. With the pulse tube off, all stages show comparable vibration levels dominated by building and laboratory noise. With the pulse tube on, a pronounced increase is visible at the 50 K and 4 K stages at frequencies below 10 Hz, consistent with the pulse tube operating frequency and its harmonics. The still and MXC stages show progressively lower vibration levels above 10 Hz, consistent with partial mechanical filtering by the cryostat structure and wiring between successive stages.

4.2.2 SQUID-based readout of particle motion

With the VIS installed in the dilution refrigerator, the effect of vibration isolation on the levitated particle motion was assessed using SQUID magnetometry [39, 95]. Two measurements were compared: a 48 µm diameter lead particle levitated on a stage rigidly bolted to the mixing chamber and a 62 µm diameter lead particle levitated in a similar magnetic trap mounted on the vibration-isolated stage [95, 187]. Both measurements used a trap current of 0.5 A.

Fig. 4.4(a) compares the SQUID signal PSD for the two configurations. On the rigid stage, the z-mode COM peak appears at 118 Hz. On the isolated stage, it shifts to 107 Hz, as the larger particle (and therefore larger mass) changes the equilibrium position and mechanical frequency in a non-ideal

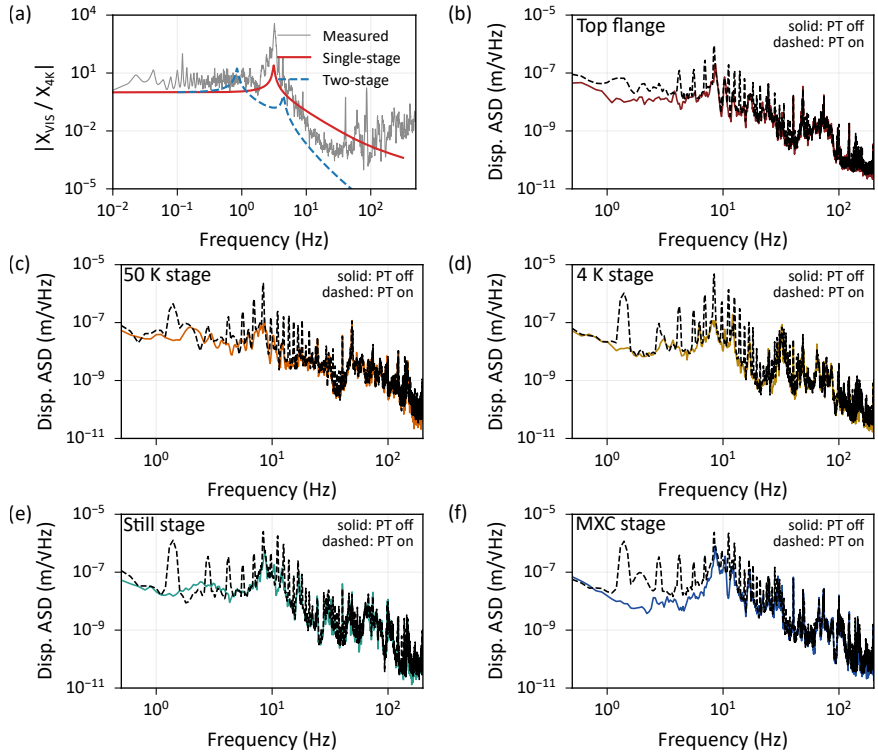

Figure 4.3: Room-temperature characterization of the vibration isolation system. (a) Measured displacement transmissibility from the 4 K plate to the suspended stage (gray), together with theoretical single-stage (solid red) and two-stage (dashed blue) transfer functions. The pendulum mode (peak 1, 0.55 Hz) and elongation mode (peak 2, 3.2 Hz) are visible. Above the elongation resonance the measured transfer approaches the expected f^{-2} rolloff. (b-f) Displacement amplitude spectral density measured at all fives stages of the cryostat with a geophone. Solid lines correspond to pulse-tube off, dashed lines to pulse-tube on. The pulse-tube-on spectra show increased vibrations at the 50 K and 4 K stages, particularly below 10 Hz.

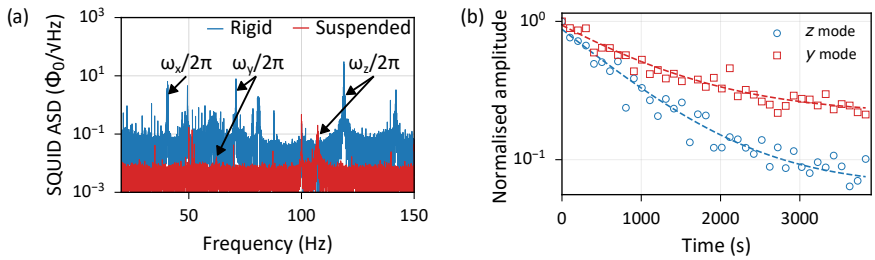

Figure 4.4: SQUID measurements of levitated particle motion with and without vibration isolation. (a) SQUID amplitude spectral density for a lead particle on a rigid stage (blue) and a lead particle on the vibration-isolated stage (red), both measured at a trap current of 0.5 A. The mode frequencies $\omega_x/2\pi$, $\omega_y/2\pi$, and $\omega_z/2\pi$ are indicated. (b) Ringdown measurements of the z and y COM modes on the vibration-isolated stage. Open symbols are the measured normalized amplitudes and dashed lines are exponential fits.

trap. The isolated-stage spectrum also exhibits both a substantially reduced z-mode peak and a lower broadband noise floor. Comparing the measured spectra gives a peak reduction of approximately 50 dB in V^2, corresponding to about 25 dB in displacement amplitude, which lies well in agreement with the room temperature transfer function 20 dB at 100 Hz. A strict quantitative comparison remains uncertain because the two measurements were performed in different cooldowns with different particles.

The reduced vibrational drive on the isolated stage enabled the first observation of free ringdowns of the COM modes, as shown in Fig. 4.4(b). On the rigid stage, the motion remains continuously driven, and no clear ringdown can be observed. For an amplitude decay $A(t) = A_0 \exp(-t/\tau)$, the corresponding quality factor is

$$Q = \pi f_0 \tau, \tag{4.1}$$

where f_0 is the mode frequency and τ is the amplitude $1/e$ ringdown time. From the fits in Fig. 4.4(b), the z-mode gives $\tau_z \approx 1350\,\mathrm{s}$ at $f_z = 107\,\mathrm{Hz}$, corresponding to $Q_z \approx 4.5 \times 10^5$, while the y-mode gives $\tau_y \approx 2240\,\mathrm{s}$ at $f_y = 60\,\mathrm{Hz}$, corresponding to $Q_y \approx 4.2 \times 10^5$. These values remain well below the gas-damping limit [95] and below those reported for related experiments with improved radiation shielding [49], indicating that additional dissipation still dominates in the present setup.

4.2.3 Thermalization

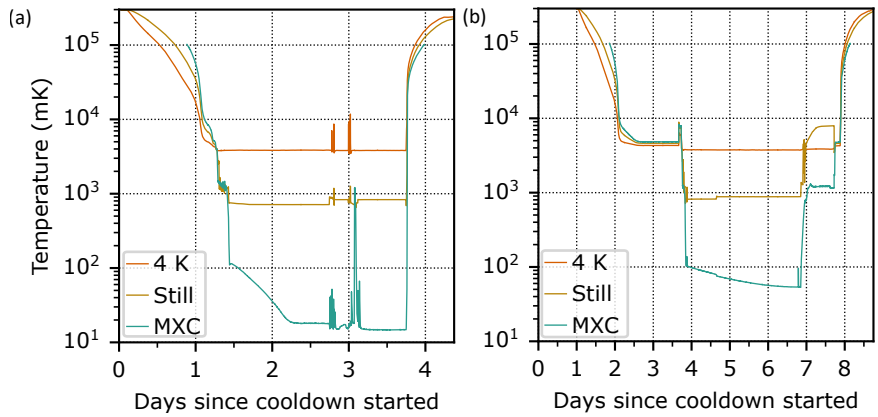

Figure 4.5: Temperature logs for two representative cooldown-warmup cycles of the cryostat (a) without VIS and (b) with VIS. Curves show temperatures of the 4 K plate, Still plate, MXC plate, and the sample stage, plotted versus days since cooldown start on a logarithmic scale.

The main limitation of the present single-stage vibration isolation system is the poor thermalization of the suspended setup. This is shown directly in Fig. 4.5, which compares representative cooldown and warmup temperature logs of the cryostat for (a) the rigid configuration without VIS and (b) the suspended configuration with VIS. In both cases, the cryostat stages cool in the expected hierarchy, and the refrigerator reaches its millikelvin operating regime. However, when the VIS is installed, both the cooldown time and the apparent MXC base temperature are substantially degraded.

In the rigid configuration without VIS [Fig. 4.5(a)], the MXC temperature drops to approximately 20 mK after about two days. This is already longer than expected for a standard BlueFors LD250 refrigerator, which is attributed here to the additional experimental mass of roughly 2 kg that must be cooled. In contrast, the suspended configuration with VIS [Fig. 4.5(b)] exhibits a substantially longer cooldown. Even after about one week from the start of the cooldown, the MXC temperature remains above 50 mK. The marked increase in both cooldown time and apparent base temperature when VIS is installed shows that the suspended assembly introduces a significant thermal bottleneck.

Despite these limitations, the achieved temperatures were still sufficient for the present levitation experiments, since they remain far below the superconducting transition temperature of lead. However, the installation of VIS increases the apparent MXC base temperature by more than 30 mK and extends the cooldown time to roughly one week because of the suspended mass and its weak thermal anchoring. The present VIS should therefore be regarded as mechanically functional but thermally unoptimized. Further improvement will require a redesigned thermalization path that increases the effective thermal conductance of the suspended assembly while preserving the low mechanical stiffness needed for vibration isolation.

4.2.4 Two-stage system

The single-stage VIS provides approximately 20 dB displacement attenuation at 100 Hz, which falls short of the estimated 50 dB target required to suppress vibration-driven motion to the thermally limited level. A two-stage system with an intermediate mass between the 4 K plate and the experimental stage would improve the asymptotic high-frequency rolloff from f^{-2} to f^{-4}, corresponding to 80 dB per decade in amplitude. A proposed design with a 1 kg upper mass ($f_1 \approx 0.84$ Hz) and a 2 kg lower mass ($f_2 \approx 4.4$ Hz) predicts approximately 60 dB attenuation at 100 Hz [187]. The corresponding theoretical transmissibility is overlaid in Fig. 4.3(a) for comparison.

4.3 Magnetic Shielding

This section discusses the magnetic environment of the FTR and trap assemblies using magnetostatic finite-element simulations. The objective is not to model the full cooldown history of the shields but to quantify the residual internal field expected from a uniform ambient background field for the geometries used in the experiment. The relevant metric for the FTR is the volume-averaged internal field component normal to the SQUID loop plane, since this component sets the residual flux offset through the loop.

Table 4.1 summarizes the shielding factors and residual normalized flux for the four simulated configurations. Under the Nb-only shield, the transverse and axial shielding factors reach $SF_y \approx 7 \times 10^3$ and $SF_z \approx 1 \times 10^4$, respectively, reducing the residual flux threading a 200 µm FTR loop to $|\Phi_{\mathrm{res}}|/\Phi_0 \approx 9 \times 10^{-2}$.

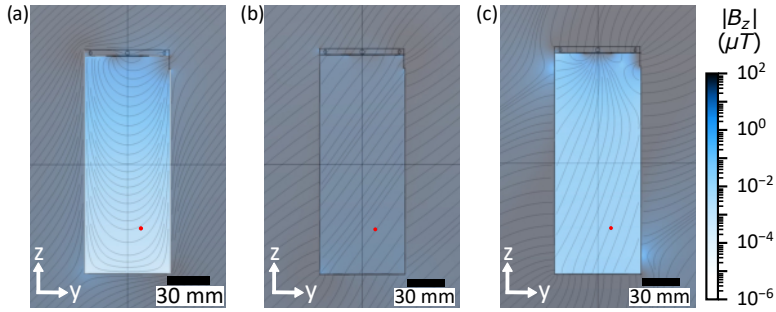

Figure 4.6: Magnetic shielding under a uniform applied field of 51.2 µT along both the y and the z direction. (a) Ideal perfect-diamagnetic shield (Meissner limit) excluding magnetic flux from the interior. (b,c) High-permeability shields redirecting magnetic flux into the shield walls, thereby reducing the residual field inside the cavity for (b) $\mu_r = 10^2$ and (c) $\mu_r = 10^5$. The cable opening at the top-right provides a leakage path for magnetic flux and introduces lateral asymmetry in the field distribution.

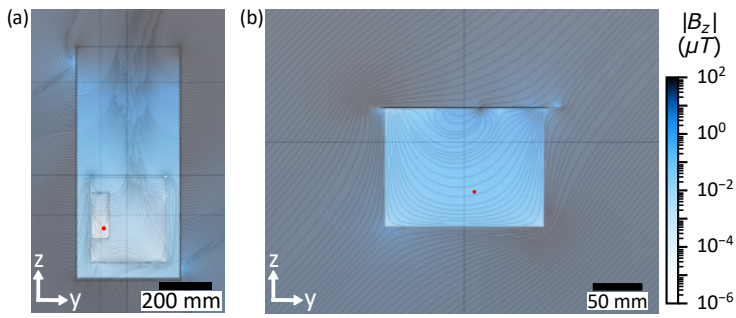

Figure 4.7: Magnetic shielding under a uniform applied field of 51.2 µT along both the y and the z direction. (a) Magnetic shielding of the entire experimental setup with room temperature mu-metal shield around the vacuum can, intermediate superconducting tin-plated copper shield at the MXC stage, and innermost superconducting niobium shield (same as in Fig. 4.6(a)). (b) Magnetic shielding of the superconducting niobium shield used in the vibration isolation stage for magnetic trap and for coupling the levitated particle to the FTR. The cable opening at the top-right provides a leakage path for magnetic flux and introduces lateral asymmetry in the field distribution.

Table 4.1: Magnetic shielding factor simulations for different shielding configurations. The shielding factor is defined as $SF_i = B_0/B_{i,\mathrm{in}}$ with $B_0 = 5 \times 10^1$ μT for $i \in \{y, z\}$. The last two columns give the magnitude of the residual normalized flux through square FTR loops, calculated from the simulated z-component as $\Phi_{\mathrm{res}} = B_{z,\mathrm{in}} A$.

Shield config	Field inside shield		Shielding factor		$\lvert\Phi_{\mathrm{res}}\rvert/\Phi_0$	
	B_y (μT)	B_z (μT)	SF_y	SF_z	10 μm	200 μm
FTR shields						
Nb	8×10^{-3}	5×10^{-3}	7×10^3	1×10^4	2×10^{-4}	9×10^{-2}
Mu-metal $\mu_r = 10^2$	3×10^1	4×10^1	2×10^0	1×10^0	2×10^0	8×10^2
Mu-metal $\mu_r = 10^5$	6×10^{-2}	2×10^{-1}	8×10^2	3×10^2	8×10^{-3}	3×10^0
Nb+Sn+Mu-metal	3×10^{-6}	6×10^{-6}	2×10^7	8×10^6	3×10^{-7}	1×10^{-4}
Trap shield						
Nb	8×10^{-1}	2×10^{-1}	6×10^1	3×10^2	–	–

This is sufficient to prevent a static flux offset from biasing the SQUID far from its sweet spot during field-cooled operation, provided the cooldown is performed in the pre-screened residual field. The stacked Nb+Sn+mu-metal configuration suppresses the residual flux through the same loop to $|\Phi_{\mathrm{res}}|/\Phi_0 \approx 1 \times 10^{-4}$, nearly three orders of magnitude below the Nb-only result. For the 10 µm FTR loop, the corresponding flux under the Nb-only shield is $|\Phi_{\mathrm{res}}|/\Phi_0 \approx 2 \times 10^{-4}$, negligible in comparison. The cable opening at the top of the shield introduces a leakage path that reduces the shielding factor below the ideal closed-cylinder limit of Thomasson and Ginsberg [220] and is visible as lateral field asymmetry in Fig. 4.6 and Fig. 4.7. The trap Nb shield, listed separately in Table 4.1, achieves substantially lower shielding factors ($SF_y = 6 \times 10^1$, $SF_z = 3 \times 10^2$) because the trap geometry requires a more open structure than the FTR shield.

4.4 Flip-chip characterization

The electrical performance of the UBM thin films and flip-chip test structures is discussed here. The central result is that Au-passivated Nb/Au and NbN/Au stacks show behavior consistent with superconducting end-to-end transport through the bonded device at millikelvin temperatures, whereas non-passivated Nb does not, and non-passivated NbN is limited by an oxide interface.

4.4.1 UBM thin-film characterization

Material composition

Fig. 4.8 compares the TOF-SIMS depth profiles of the four UBM stacks. The non-passivated Nb and NbN films show clear near-surface signals from niobium oxides with multiple stoichiometries, indicating that both materials oxidize during ambient exposure. In the Nb film, the oxide signal decreases rapidly near the surface and then more gradually throughout the film, whereas the NbN film shows smaller intermediate oxide peaks at later sputtering times. By contrast, the Au-passivated Nb/Au and NbN/Au films show a strong Au signal at the surface and strongly suppressed niobium-oxide signals, demonstrating that the 5 nm Au cap effectively inhibits oxidation of the underlying superconducting film. The metallic Nb and NbN signals remain approximately constant throughout the film thickness, while the increase in the Al signal identifies the UBM-Al interface for the bottom-chip samples. These measurements, therefore, support the interpretation that the dominant difference between the passivated and non-passivated stacks is the presence or absence of an oxidized bonding surface.

This interpretation is qualitatively consistent with the SEM images of the non-passivated thin film discussed in App. 6.4, which show peeling on the surface of the thin film, likely due to oxide-induced stress. In contrast, no such peeling is observed for Au-passivated thin films.

Superconducting properties

Fig. 4.9(a) shows the superconducting transitions of the four standalone UBM stacks. The measured transition temperatures are 8.0 K for Nb and 10.4 K for NbN, consistent with reported values for films of similar thickness and deposition conditions [73, 86]. The Au-passivated bilayers show slightly reduced

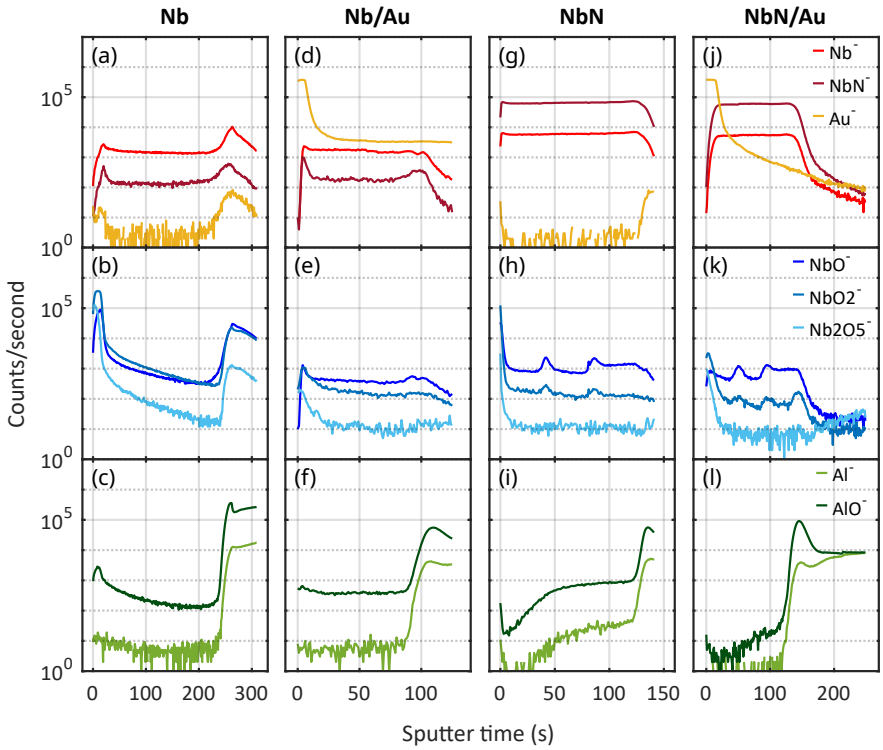

Figure 4.8: TOF-SIMS depth profiles of UBM thin films acquired with Cs^+ primary ions at 1 keV. Each column corresponds to a different UBM stack (Nb, Nb/Au, NbN, NbN/Au). Top row: metallic secondary ions of the UBM layer. Middle row: niobium oxide secondary ions (NbO^-, NbO_2^-, $Nb_2O_5^-$). Bottom row: Al^- ions from the Al ground plane (for Nb/Au, NbN, NbN/Au) or sapphire substrate (for Nb). Adapted from Paper II.

transition temperatures of 7.7 K for Nb/Au and 9.9 K for NbN/Au, consistent with a proximity-effect-induced suppression by the normal-metal Au cap [172, 221].

Fig. 4.9(b) shows the corresponding critical currents. The data are well described by the two-fluid expression introduced in Sec. 2.1.2,

$$I_c(T) = I_{c0}(1 - t^4), \qquad t = T/T_c, \tag{4.2}$$

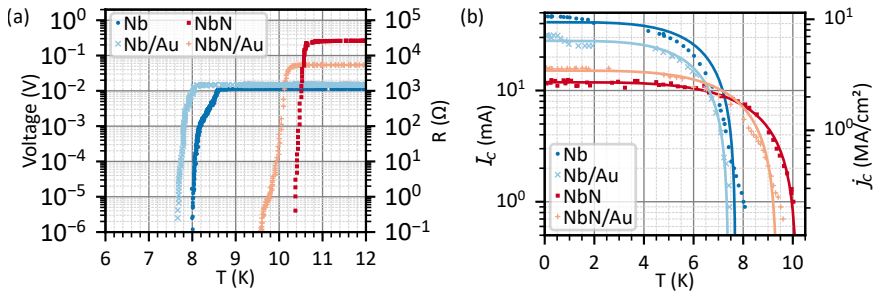

Figure 4.9: Superconducting characterization of UBM thin films. (a) Voltage and resistance as a function of temperature at 10 µA bias current. Below the respective T_c, the measured voltage drops to the noise floor of the voltmeter, which has been subtracted. (b) Critical current and critical current density as a function of temperature. The solid lines are fits to the two-fluid model (Eq. (2.9)). Adapted from Paper II.

using Eq. (2.9). At 100 mK, the extracted critical current densities are 9.3 MA cm^{-2} for Nb, 6.3 MA cm^{-2} for Nb/Au, 2.5 MA cm^{-2} for NbN, and 3.2 MA cm^{-2} for NbN/Au. These values are summarized in Table 4.2 and are consistent with the literature for comparable films [73, 74, 86, 222]. Thus, Au passivation causes only a modest reduction in T_c (see Sec. 2.1.7), and leaves the low-temperature critical current density in the same order as that of the corresponding non-passivated film.

Table 4.2: Measured superconducting properties of the UBM thin films. The reported j_c values correspond to the low-temperature measurements near 100 mK. Literature values are taken from works using similar deposition techniques and film thicknesses [73, 74, 86, 222].

Thin film	j_c (MA/cm^2)		T_c (K)	
	Exp.	Lit.	Exp.	Lit.
Nb [50 nm]	9.3	4 [73]	8.0	8.1 [73]
Nb [50 nm] / Au [5 nm]	6.3	–	7.7	7.3 [222]
NbN [50 nm]	2.5	2.5 [74]	10.4	10.6 [86]
NbN [50 nm] / Au [5 nm]	3.2	–	9.9	10.2 [172]

A separate control measurement on a nominally identical 150 nm sputtered Al wiring film gave $j_{c0} \approx 1.3 \times 10^4$ A cm^{-2} at approximately 20-50 mK. This

value is far below that of the Nb-based UBM films, but still far above the microampere-level flux-bias currents used later in the FTR experiments of Sec. 4.6, so the Al wiring does not limit that application.

4.4.2 Flip-chip device characterization

The assembled flip-chip devices then test whether the characterized UBM stacks yield end-to-end transport consistent with superconducting bonded contacts.

Temperature-dependent resistance

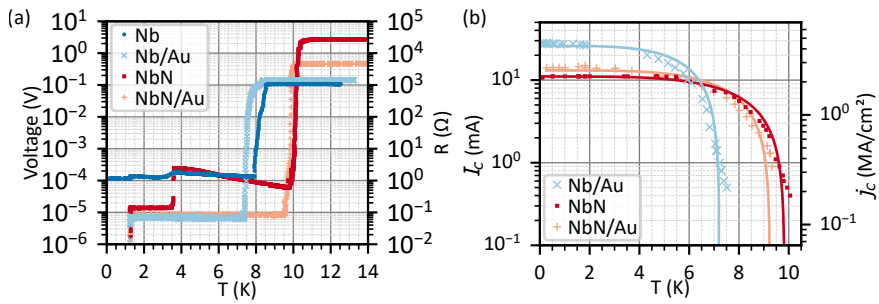

Figure 4.10: Measurements of assembled flip-chip devices. (a) Voltage and resistance as a function of temperature at 100 µA bias current for all four device types. The voltage noise floor has been subtracted. (b) Critical current and critical current density as a function of temperature for the three devices that show no detectable low-temperature voltage within the resolution of the setup. The solid lines are fits to Eq. (2.9). Adapted from Paper II.

Fig. 4.10(a) compares the temperature-dependent resistance of the four assembled device types. Two stacks, Nb/Au and NbN/Au, show behavior consistent with superconducting end-to-end transport through the bonded device within the resolution of the setup. Both devices first exhibit the transition of the Al wiring layer at 1.25 K, followed by a second transition associated with the UBM layer at 7.4 K for Nb/Au and near 10 K for NbN/Au. The corresponding normal-state resistivity of the Al wiring layer is estimated to lie between 0.68 µΩ cm and 1.6 µΩ cm, consistent with reported values [223].

These transition temperatures closely follow the standalone thin-film data of Fig. 4.9(a), with the slight downward shift in the bonded devices attributed to the proximity effect (see Sec. 2.1.7) from the underlying Al on the bottom chip that is resistive at these temperatures [221]. Above their respective UBM transition temperatures, the devices recover normal-state resistances consistent with the corresponding standalone thin films. Because the expected normal-state resistance of the pressed indium microspheres is many orders of magnitude below the voltage resolution of the setup, these data do not directly resolve the intrinsic Indium bump resistance.

The non-passivated Nb device does not reach the low-voltage state observed in the passivated devices and retains a resistance of several ohms at base temperature. The curve in Fig. 4.10(a) nevertheless still shows the Al and Nb transitions near 1.25 K and 8 K, indicating that the constituent films become superconducting while the bonded interface remains resistive. Together with the oxide signal in Fig. 4.8, this indicates that the native Nb oxide forms an insulating barrier at the Nb-In interface.

The non-passivated NbN device behaves differently. It shows no detectable low-temperature voltage only below the superconducting transition of indium, and a resistance step of about 2.5 Ω appears near 3.5 K. Since the normal-state resistance expected from the pressed indium geometry is only on the order of 30 nΩ, the observed step cannot originate from the indium itself. It is instead attributed to an oxide barrier at the NbN surface. Using a pressed contact diameter of approximately 500 µm and an oxide thickness of about 0.5 nm estimated from the TOF-SIMS sputtering rate gives an oxide resistivity on the order of 10^6 Ω cm, which is reasonable for NbO_2 [224]. NbO_2 has also been identified as a relevant oxide species on superconducting NbN thin films [225].

For the present bonding geometry, the measured device resistance corresponds to an effective per-interface normal-state resistance

$$R_N = \frac{R}{2} = 1.25\,\Omega, \tag{4.3}$$

where $R = 2.5\,\Omega$ is the measured total resistance. Using the asymmetric Ambegaokar-Baratoff expression for an $NbN/NbO_x/In$ interface,

$$I_{c,\mathrm{int}} = \frac{\pi\sqrt{\Delta_{\mathrm{In}}\Delta_{\mathrm{NbN}}}}{2eR_N}\tanh\left(\frac{\sqrt{\Delta_{\mathrm{In}}\Delta_{\mathrm{NbN}}}}{2k_BT}\right), \tag{4.4}$$

with $\Delta_{\mathrm{In}} = 1.05\,\mathrm{meV}$ [226] and $\Delta_{\mathrm{NbN}} = 4.16\,\mathrm{meV}$ [81], an order-of-magnitude estimate of $I_{c,\mathrm{int}} \approx 2.6\,\mathrm{mA}$ is obtained at 100 mK. This estimate is used only to set the current scale expected for the oxide-limited interface.

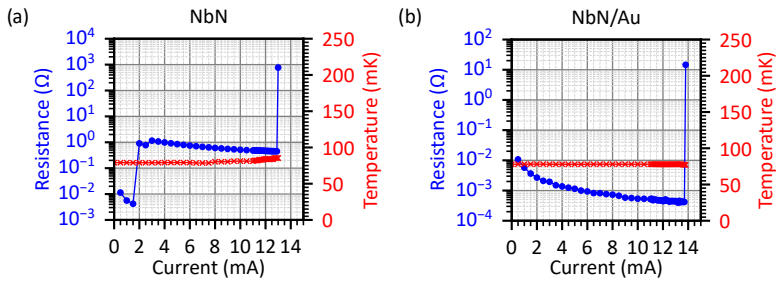

Figure 4.11: Current-dependent measurements of the (a) non-passivated NbN and (b) Au-passivated NbN flip-chip devices at base temperature. The plots show resistance (blue circles, left axis) and mixing-chamber temperature (red crosses, right axis) as a function of bias current. The apparent decrease in resistance at the lowest currents is an artifact caused by the finite voltage resolution of the setup. For the non-passivated device, an additional resistance step near 2 mA is attributed to oxide interfaces in the NbN/NbO$_x$/In junctions exceeding their critical current. Adapted from Paper II supplementary.

This interpretation is supported by Fig. 4.11. In Fig. 4.11(a), the non-passivated NbN device shows an additional resistance step near 2 mA, of the same order as the estimate from Eq. (4.4), before the higher-current transition of the NbN test structure. The corresponding low-current feature is absent in the Au-passivated device shown in Fig. 4.11(b). Both devices show the higher-current transition of the NbN test structure near 12-13 mA. The broadened onset of the low-current step in the non-passivated device indicates that the individual oxide interfaces are not identical. The mixing-chamber temperature remains close to base temperature through this low-current step and rises more strongly only as the higher-current transition is approached, so simple global heating is unlikely to be its primary origin. Above the indium transition, the same interface would be expected to behave as a normal-metal-insulator-superconductor contact rather than an SIS junction [227–229]. Consistent with this picture, the thermal sweep in Fig. 4.10(a) shows a decrease in voltage and resistance with increasing temperature above the indium transition. However, additional nonlinear current-voltage or voltage-temperature measurements at

different bias points would be required to verify the SIS or NIS interpretation conclusively, and this was not pursued here.

Critical current of flip-chip devices

Fig. 4.10(b) shows the temperature-dependent critical currents of the assembled devices that show no detectable low-temperature voltage within the resolution of the setup. For the Au-passivated Nb/Au and NbN/Au devices, the data follow the two-fluid model and yield low-temperature values of 28 mA and 15 mA, corresponding to 5.6 MA cm^{-2} and 3.0 MA cm^{-2}, respectively. These values are close to those of the corresponding standalone films, which indicates that the measured current limit is set by the patterned thin-film section on the top chip rather than by any detected transition of the bonded indium interface.

The non-passivated NbN device requires separate interpretation. The higher-current branch corresponds to the NbN test structure and gives about 2.2 MA cm^{-2}, while Fig. 4.11(a) shows an additional lower-current step near 2 mA that corresponds to the oxide-limited interconnect and gives about 0.4 MA cm^{-2}. Since Table 4.3 is intended to summarize the performance of the bonded interconnects, the lower value is listed for non-passivated NbN.

Table 4.3: Low-temperature superconducting properties of the assembled flip-chip devices. The reported j_c values correspond to measurements near 100 mK. *The non-passivated NbN device exhibits 2.2 MA cm^{-2} when limited by the NbN test structure, and 0.4 MA cm^{-2} when limited by the oxide interface in the bonded interconnect.

UBM material [thickness]	j_c (MA/cm^2)	T_c (K)
Nb [50 nm] / Au [5 nm]	5.6	7.4
NbN [50 nm]	0.4*	10.0
NbN [50 nm] / Au [5 nm]	3.0	9.7

4.4.3 Indium interconnect

The current-carrying capacity of the indium microsphere interconnect was measured separately using the unpatterned three-chip structure described in Sec. 3.4.2. Nb/Au was chosen for this test because it combines a high critical

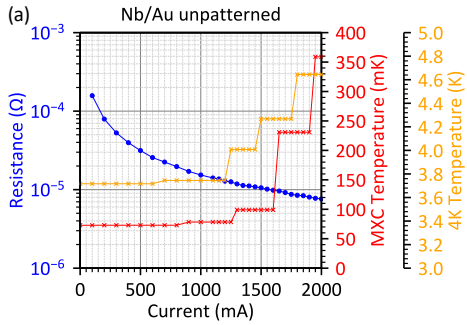

Figure 4.12: Current-carrying measurement of the indium microsphere interconnect. Resistance (blue, left axis), mixing-chamber temperature (red, right axis), and 4 K stage temperature (orange, right axis) as a function of bias current for an unpatterned Nb/Au flip-chip device. No voltage onset attributable to the sample is detected up to 2 A, the maximum output of the current source. The 4 K stage temperature rises before the mixing-chamber temperature, consistent with Joule heating at the normal-metal connection at the 4 K stage rather than a transition of the indium interconnect. Adapted from Paper II supplementary.

current density with an oxidation-resistant bonding surface. Fig. 3.25(b,c) shows the device geometry and the use of 24 Al wirebonds per pad to ensure that neither the wirebonds nor a patterned thin-film section limited the measurement.

The resulting current sweep is shown in Fig. 4.12(a). No voltage onset attributable to the sample was detected up to 2 A, which was the maximum output of the current source. Thus, the measurement was source-limited rather than limited by an observed transition of the device. The increase in mixing-chamber temperature above about 1.2 A is attributed to Joule heating at the normal-metal connection at the 4 K stage and does not provide evidence for a transition of the indium interconnect. This interpretation is supported by Fig. 4.12(a), where the 4 K stage temperature rises before the mixing-chamber temperature. Taking current flow within the London penetration depth of indium, $\lambda_{\mathrm{In}} = 40\,\mathrm{nm}$ [230], over a pressed contact diameter of approximately 500 µm gives a lower bound of $j_c > 1.6\,\mathrm{MA\,cm^{-2}}$. A simple Silsbee estimate, $I_c = \pi d H_c$, with the bulk critical field of indium $H_c = 2.75 \times 10^{-2}\,\mathrm{T}$ [231], gives $I_c \sim 34\,\mathrm{A}$, well above the available measurement range. Using the bulk

resistivity of indium at 4 K, $\rho = 1.2\,\mathrm{n\Omega\,cm}$ [232], and approximating the pressed microsphere as a cylinder with a diameter of 500 µm and a height of 50 µm gives a normal-state resistance of approximately 30 nΩ.

This resistance scale is far below the voltage resolution of the present setup, so the measurement does not directly resolve the intrinsic resistance of the indium interconnect. Further, the heating produced by a supposedly resistive interconnect would be on the order of 100 nW for 2 A current. Given the cooling power of 250 µW, this heating would cause no resolvable increase in the base temperature. Thus, this measurement constrains the indium interconnect only indirectly, as no voltage increase was detected up to the 2 A source limit that could be attributed to the same. However, neither the intrinsic resistance nor the true critical current of a single indium interconnect was directly resolved.

4.5 CPW resonators

This section characterizes the bare CPW resonators to establish the microwave loss and drive-dependent baseline of the aluminum film before the SQUID termination is introduced. Device A, measured on the same chip platform as the flux-tunable resonators of Paper III, is used to benchmark resonance frequency, external coupling, and power dependence. Device B, measured in a separate cooldown and fabrication run, is used to extract the thermal frequency shift and an approximate kinetic inductance fraction of the Al film.

4.5.1 Device A: resonance and coupling benchmark

Device A was measured on a chip containing one bare CPW resonator and three flux-tunable resonators coupled to a common through-line feedline. Parasitic modes of the feedline and sample box are discussed separately in App. 6.4.1.

The simulated field pattern in Fig. 4.13(a) follows the expected quarter-wave profile, and Fig. 4.13(b,c) shows the corresponding notch response in transmission.

The measured magnitude, phase, and complex-plane data are shown in Fig. 4.14. After background normalization, the response collapses onto a nearly ideal circle, indicating that the resonance is well described by the linear circle-fit model of Sec. 3.5.4. The extracted parameters are summarized in Table 4.4.

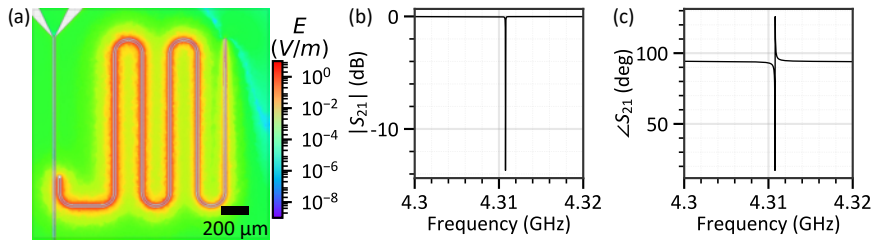

Figure 4.13: HFSS simulation of the $\lambda/4$ CPW resonator. (a) Electric-field magnitude of the fundamental eigenmode, showing the expected quarter-wave voltage profile, with a field minimum at the shorted end and a maximum near the coupling end. The corresponding current antinode is located at the shorted end. The simulated eigenfrequency is $f_{r,\mathrm{sim}} = 4310.4\,\mathrm{MHz}$ under the PEC approximation. (b) Simulated transmission magnitude $|S_{21}(f)|$ showing the resonant notch. (c) Simulated transmission phase $\angle S_{21}(f)$.

Table 4.4: Bare CPW resonator parameters for Device A from the analytical model, HFSS, and measurement. The measured values are from Paper III.

Parameter	Analytical	HFSS	Measured
Z_0 (Ω)	48.0	48.5	48.8
f_r (GHz)	4.245	4.310	4.279
Q_c	1.6×10^5	1.6×10^5	2.9×10^5

The analytical, simulated, and measured resonance frequencies agree within 1.5 %, and the distributed line impedance remains close to 50 Ω, consistent with Table 2.3. The PEC HFSS value overestimates f_r because kinetic inductance is excluded. Using the value $\alpha_k = 0.60\%$ extracted from Device B shifts the simulated frequency from 4.310 GHz to 4.297 GHz, leaving a residual offset of 18.5 MHz (0.4 %). The remaining difference is attributed to uncertainty in the substrate permittivity, lithographic length, and end corrections.

The measured coupling quality factor is $Q_c \approx 2.9 \times 10^5$, whereas the finite-length conformal estimate from Eq. (2.141) gives 1.6×10^5. This weaker experimental coupling is plausibly due to fringing fields, three-dimensional current return, and lithographic uncertainty in the short side-coupled section.

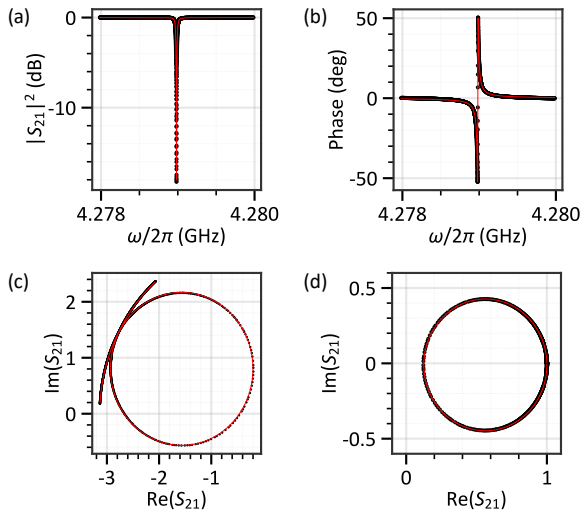

Figure 4.14: Microwave transmission measurement of Device A at a VNA output power of $-40\,\mathrm{dBm}$ ($P_{\mathrm{dev}} = -114\,\mathrm{dBm}$, $n_c \approx 49\,000$). (a) Measured $|S_{21}(f)|$ centered at $f_r = 4278.98\,\mathrm{MHz}$, with the fitted response overlaid. (b) Measured $\angle S_{21}(f)$, with the fitted response overlaid. (c) Raw complex S_{21} data in the IQ plane prior to background normalization. (d) Background-normalized resonance circle used for quality-factor extraction by the circle-fit method described in Sec. 3.5.4. Data from Paper III.

4.5.2 Device A: power sweep

The power dependence of Device A is shown in Fig. 4.15. Quality factors were extracted from the measured $S_{21}(f)$ using the circle-fit procedure of Sec. 3.5.4. Over the full range from $n_c \approx 0.04$ to 2×10^7, the coupling quality factor remains constant at $Q_c \approx 2.92 \times 10^5$, as expected for a geometrically fixed coupling capacitor. The dominant power dependence is therefore in Q_i, and the corresponding increase in Q_L reflects the gradual approach to the coupling-limited regime.

The increase of Q_i with photon number is consistent with TLS saturation, as discussed in Sec. 2.5.8. Using the empirical fit form of Paper III gives $\delta_0 = 3.43 \times 10^{-7}$, $\delta_{\mathrm{TLS}} = 2.55 \times 10^{-6}$, $\beta = 0.296$, and $n_c^* = 3.3$, corresponding to $Q_{i,0} \approx 3.45 \times 10^5$ and $Q_{i,\infty} \approx 2.91 \times 10^6$. These values are consistent with

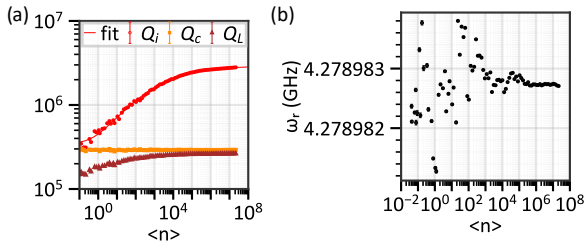

Figure 4.15: Power-dependent quality factors and resonance frequency of Device A. (a) Intrinsic quality factor Q_i (filled circles), coupling quality factor Q_c (open squares), and loaded quality factor Q_L (open triangles) as a function of intracavity photon number n_c. The solid curve is a fit of Eq. (2.152), yielding $\delta_0 = 3.43 \times 10^{-7}$, $\delta_{\mathrm{TLS}} = 2.55 \times 10^{-6}$, $\beta = 0.296$, and $n_c^* = 3.3$. The corresponding asymptotic quality factors are $Q_{i,0} \approx 3.45 \times 10^5$ and $Q_{i,\infty} \approx 2.91 \times 10^6$. (b) Resonance frequency f_r as a function of n_c. Despite larger point-to-point scatter at the lowest photon numbers, no monotonic frequency shift is resolved across the full range, consistent with a negligible film-induced nonlinearity. Data from Paper III.

TLS-limited loss in standard evaporated Al-on-Si CPW resonators [125, 127, 153, 156, 233].

The resonance frequency shows no systematic dependence on photon number. Across eight decades in n_c, the total variation remains below 600 Hz. The bare Al CPW therefore contributes negligibly to the nonlinear response observed in the FTR devices.

4.5.3 Device B: temperature sweep

Device B was measured to determine the thermal frequency shift and the onset of quasiparticle-related loss in the Al film. The resonator has $f_r = 5.367\,\mathrm{GHz}$ and $Q_c \approx 4.88 \times 10^5$. The sweep was taken at a fixed device input power of approximately $-136\,\mathrm{dBm}$, corresponding to $n_c \approx 36$, and therefore above the nominal TLS-saturation scale inferred from Device A. The low-temperature Q_i plateau should accordingly be interpreted as a power-dependent floor rather than the true single-photon limit. Measurements were taken between 27 mK and 486 mK.

As shown in Fig. 4.16(b,c), the resonance frequency is nearly constant

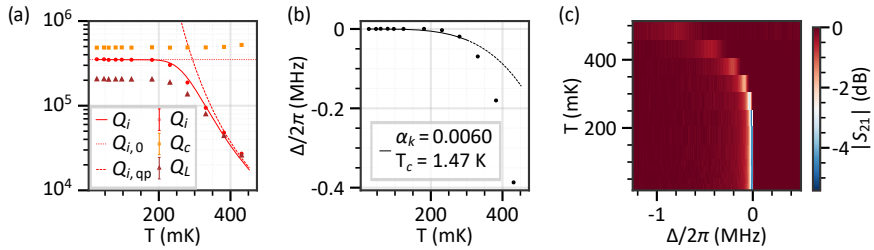

Figure 4.16: Temperature dependence of the bare CPW resonator Device B ($f_r \approx 5.37\,\mathrm{GHz}$, from a separate fabrication run and cooldown). (a) Internal (Q_i, red circles), coupling (Q_c, orange squares), and loaded (Q_L, brown triangles) quality factors versus temperature. The solid red curve is a fit to the thermally activated quasiparticle-loss model of Eq. (2.153). The dashed red curve shows the extracted quasiparticle contribution $Q_{i,\mathrm{qp}}^{-1}(T) = Q_i^{-1}(T) - Q_{i,\mathrm{bg}}^{-1}$. The dotted horizontal line marks the fitted background floor $Q_{i,\mathrm{bg}} = 3.51 \times 10^5$. (b) Resonance-frequency shift $\delta f_r(T) = f_r(T) - f_r(27\,\mathrm{mK})$ versus temperature. The solid curve is the kinetic-inductance model of Eq. (2.129) fitted to data at $T \leq 280\,\mathrm{mK}$. The dashed extension is an extrapolation beyond the reliable fit range. (c) Baseline-normalized $|S_{21}|$ versus detuning from $f_r(27\,\mathrm{mK})$ and temperature, showing the downward shift and progressive broadening of the resonance with increasing temperature. The colorbar is clipped at $-4\,\mathrm{dB}$. The true base-temperature notch depth is $-15.7\,\mathrm{dB}$.

below approximately 150 mK and then shifts downward monotonically with increasing temperature. The same trend is visible directly in Fig. 4.16(c), where the resonance notch moves to negative detuning and broadens as the temperature increases. The low-temperature data were fitted with the two-fluid kinetic-inductance model described in Sec. 2.1.2 and Sec. 2.5.3. Fitting the data for $T \leq 280\,\mathrm{mK}$ gives $f_{r0} = 5366.870\,\mathrm{MHz}$, $\alpha_k = 0.60 \pm 0.07\%$, and $T_c = 1.47 \pm 0.5\,\mathrm{K}$.

The extracted α_k is typical for a 150 nm Al CPW on Si and confirms that the resonator remains in the geometric-inductance-dominated regime [70, 72, 116, 117]. This is consistent with the absence of any measurable power-dependent frequency pulling in Device A. The fitted T_c should be interpreted only as an effective fit parameter, since the frequency shift remains small over most of the fitted range.

The temperature dependence of Q_i in Fig. 4.16(a) shows a pronounced drop above approximately 200 mK. Fitting Eq. (2.153), as introduced in Sec. 2.5.8, gives $Q_{i,\mathrm{bg}} = 3.51 \times 10^5$, $A = 9.01 \times 10^{-3}$, and $\Delta/k_B \approx 2.716\,\mathrm{K}$, corresponding to $\Delta = 234\,\mu\mathrm{eV}$. The activated term in Eq. (2.153) is exponentially suppressed at the FTR operating temperature near 20 mK, so thermally generated quasiparticles in the Al film are not expected to set the loss floor in Sec. 4.6.

The coupling quality factor remains constant at $Q_c \approx 4.88 \times 10^5$ over the full temperature range, which serves as a consistency check on the extraction procedure. Since the sweep was taken at $n_c \approx 36 \approx 11\,n_c^*$, TLS loss is already partially saturated, so $Q_{i,\mathrm{bg}}$ is a power-dependent floor internal quality factor of Device B.

4.6 Flux-tunable resonators

This section characterizes the three flux-tunable resonators presented in Paper III: a 10 µm reference device without an integrated input coil, a 100 µm device with an on-chip input coil, and a 200 µm device with a flip-chip input coil. The reference device is first used to benchmark the negligible-screening regime. The two large-loop devices are then compared in terms of zero-flux response, Kerr nonlinearity, flux tuning, and chip-based flux transfer.

4.6.1 Microwave line characterization

Figure 4.17 provides a room-temperature consistency check of the dc and microwave calibrations used later. Panel (a) tests the dc transfer model of Sec. 3.5.3. Panel (b) shows RF transmission traces from the attenuated microwave lines.

The integrated input-coil lines show a linear relation between sourced current and current delivered to MXC over the full measured range. The fitted slopes lie between 1.74 and 1.93 µA mA^{-1}, corresponding to $\eta_{\mathrm{dc}} = (1.74-1.93)\times 10^{-3}$, and the offsets remain below 0.33 µA. This is consistent with the resistive-network estimate of order 2×10^{-3} from Sec. 3.5.3, validating the dc transfer model used in the later flux-bias analysis.

Figure 4.17(b) shows three 66 dB traces. The trace remains smooth across the measured 4 to 8 GHz band, and at 4 GHz, the nominal 66 dB lines yield -73.7 ± 0.1 dB. The additional attenuation of about 7 dB arises from the

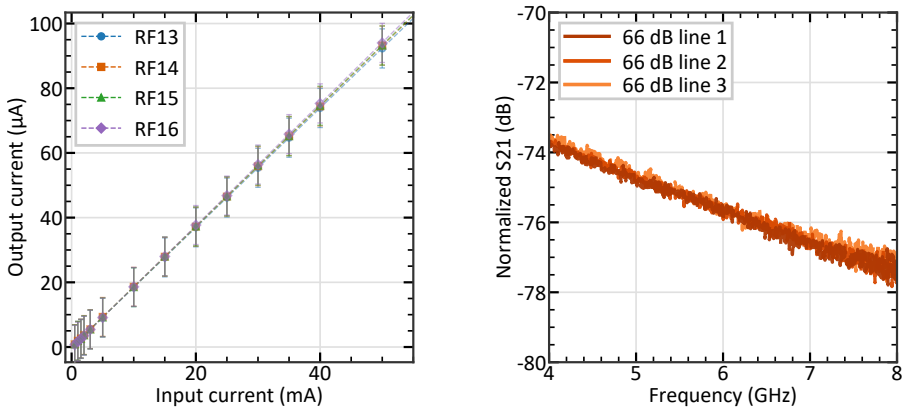

Figure 4.17: Room-temperature verification of the bias and microwave lines. (a) DC current-transfer measurements for the integrated input-coil lines, showing the current delivered to the MXC stage as a function of sourced current together with linear fits. (b) Background-subtracted room-temperature RF transmission traces of three nominal 66 dB lines, showing attenuation across the 4 to 8 GHz band.

coaxial lines connecting the discrete attenuators between each stage.

4.6.2 Junction characterization

Figure 4.18 shows the two junction-layout regimes used in the dc-SQUID test structures. Below 700 nm, the junctions are nominally symmetric. At 700 nm and above, the mirrored-offset geometry fixes one electrode at 500 nm, producing the asymmetry. This deliberate asymmetry sets a nonzero α and prevents the effective critical current from vanishing at $\Phi_e = \Phi_0/2$, as discussed in Sec. 3.2.5. The purpose of the room-temperature resistance analysis below is to estimate the Josephson scale of the fabricated SQUID terminations before comparison with the cryogenic FTR fits.

All measurements were performed on room-temperature four-point dc-SQUID test structures fabricated in the same run as the resonator terminations. The measured quantity is the normal-state SQUID resistance R_{sq}, namely the parallel combination of the two junction resistances. For the 1000 nm structures relevant here, the two junctions are intentionally asymmetric, with approximate areas $1.0 \times 1.0\,\mu\mathrm{m}^2$ and $1.0 \times 0.5\,\mu\mathrm{m}^2$.

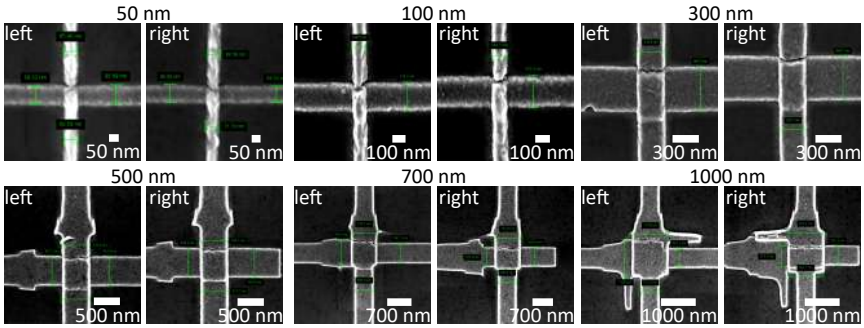

Figure 4.18: SEM images of the left and right Josephson junctions in the dc-SQUID test structures from 50 nm to 1000 nm. Junctions below 700 nm are nominally symmetric. Junctions with nominal width 700 nm and above use a mirrored offset geometry in which one electrode remains fixed at 500 nm, producing a visible asymmetry in the left and right junction areas.

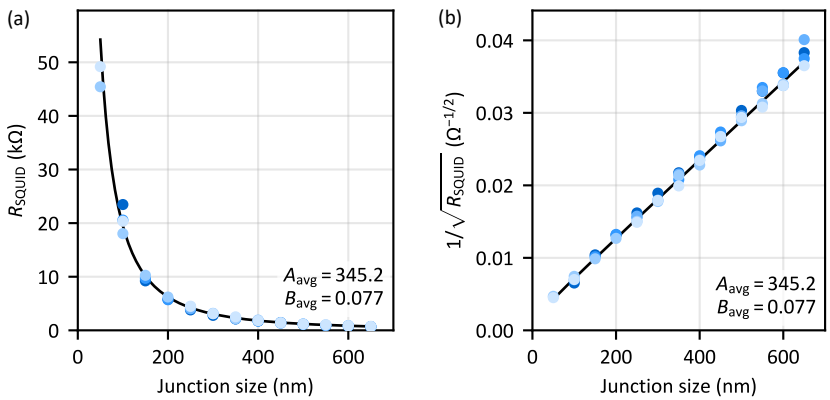

Figure 4.19: Room-temperature resistance scaling in the symmetric junction regime of the SPC V7 dc-SQUID test structures. (a) Measured SQUID resistance R_{sq} as a function of nominal junction width d for 50-650 nm, together with the chip-averaged fit to Eq. (4.5). (b) Corresponding $1/\sqrt{R_{\mathrm{sq}}}$ representation. The extracted chip-averaged parameters are $A_{\mathrm{avg}} = 345.2\ \Omega\,\mu\mathrm{m}^2$ and $B_{\mathrm{avg}} = 0.077\ \mu\mathrm{m}$.

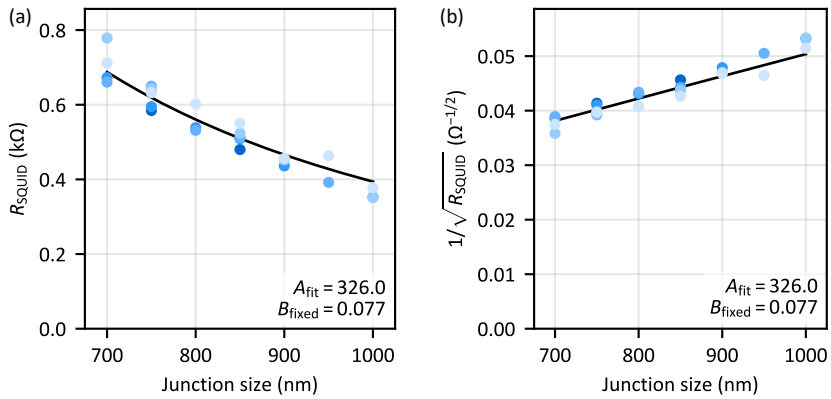

Figure 4.20: Room-temperature resistance scaling in the asymmetric junction regime of the SPC V7 dc-SQUID test structures. (a) Measured SQUID resistance R_{sq} as a function of nominal junction width d for 700-1000 nm, together with the global asymmetry-aware fit of Eq. (4.10). In this fit, the width offset is fixed to the symmetric-regime value $B_{\mathrm{fixed}} = 0.077$ µm and only A is fitted, yielding $A_{\mathrm{fit}} = 326.0\ \Omega\,\mu\mathrm{m}^2$. (b) Corresponding $1/\sqrt{R_{\mathrm{sq}}}$ representation.

For the symmetric regime, the measured SQUID resistance is described empirically by

$$R_{\mathrm{sq,sym}}(d) = \frac{A}{d(d+B)}, \tag{4.5}$$

where d is the nominal junction width in µm, A has units of $\Omega\,\mu\mathrm{m}^2$, and B is an effective width offset that captures lithography bias and the geometric effects of shadow evaporation [152, 159]. Since Eq. (4.5) is fitted to the resistance of a symmetric dc SQUID rather than that of a single junction, the corresponding single-junction resistance is

$$R_j(d) = 2R_{\mathrm{sq,sym}}(d) = \frac{2A}{d(d+B)}. \tag{4.6}$$

The symmetric-regime data in Fig. 4.19 follow the expected decrease in resistance with increasing junction size. The fit captures the overall trend well, with the largest scatter confined to the smallest nominal widths, where

lithographic bias is most significant. The chip-averaged fit parameters are

$$A_{\mathrm{avg}} = 345.2\ \Omega\,\mu\mathrm{m}^2, \qquad B_{\mathrm{avg}} = 0.077\ \mu\mathrm{m}. \tag{4.7}$$

The positive offset B_{avg} reflects an empirical correction to the nominal junction area that captures lithographic bias and shadow-evaporation geometry, as discussed in Sec. 3.2.5. These symmetric-regime fits provide the primary process calibration used below.

The asymmetric-regime data are shown in Fig. 4.20. As expected, the resistance still decreases with increasing nominal size, but more weakly than in the symmetric regime because only one junction dimension continues to scale. To capture this, the asymmetric SQUID resistance was modeled as the parallel combination of a larger junction with resistance

$$R_{j1}(d) = \frac{2A}{d(d+B)} \tag{4.8}$$

and a smaller junction with resistance

$$R_{j2}(d) = \frac{2A}{d(d_s+B)}, \tag{4.9}$$

where $d_s = 0.5\,\mu\mathrm{m}$ is the fixed smaller junction dimension. This gives

$$R_{\mathrm{sq,asym}}(d) = \frac{R_{j1}R_{j2}}{R_{j1}+R_{j2}} = \frac{2A}{d(d+d_s+2B)}. \tag{4.10}$$

Because the asymmetric size window is too narrow to determine both A and B robustly, the width offset was fixed to the symmetric-regime value, $B = B_{\mathrm{avg}}$, and only A was fitted. The resulting fit, shown by the black curve in Fig. 4.20(a), yields

$$A_{\mathrm{fit}} = 326.0\ \Omega\,\mu\mathrm{m}^2, \tag{4.11}$$

which is lower than A_{avg} by only about 6%. This agreement indicates that the large-sized asymmetric devices remain broadly compatible with the same junction-process calibration developed for the symmetric junctions.

This calibration is then applied directly to the 1000 nm SQUIDs that correspond to the FTR terminations. For each chip, the larger-junction resistance is obtained by extrapolating the symmetric fit to $d = 1\,\mu\mathrm{m}$ and converting the

symmetric SQUID resistance to a single-junction resistance,

$$R_{j1} = 2R_{\mathrm{sq,sym}}(1\,\mu\mathrm{m}). \tag{4.12}$$

The smaller-junction resistance is then inferred from the measured asymmetric SQUID resistance through the parallel-combination relation

$$R_{j2} = \frac{R_{j1}R_{\mathrm{sq}}}{R_{j1} - R_{\mathrm{sq}}}. \tag{4.13}$$

For the tested 1000 nm devices, the average value of the extracted larger-junction resistance is $R_{j1} = 536.9\,\Omega$, while the inferred smaller-junction resistance is $R_{j2} = 1027.8\,\Omega$. These values are of the expected order for the asymmetric termination geometry.

To convert the room-temperature resistances into critical currents, the normal-state resistance just above the superconducting transition was taken as

$$R_{n,4\mathrm{K}} = 1.10\,R_{n,\mathrm{RT}}, \tag{4.14}$$

following Ref. [234]. Using the Ambegaokar-Baratoff relation introduced in Sec. 2.3.2,

$$I_0 = \frac{\pi\Delta}{4eR_{\mathrm{sq},4\mathrm{K}}}, \tag{4.15}$$

with $\Delta = 180\,\mu\mathrm{eV}$ for Al, the mean critical current is estimated to be 364 nA. Using the zero-phase Josephson inductance relation from Sec. 2.3.3,

$$L_J(I_0) = \frac{\Phi_0}{2\pi I_0}, \tag{4.16}$$

the corresponding inductance is 903 pH. These values are also summarized in Table 4.5 and agree well with the cryogenic estimate $I_0 \approx 375\,\mathrm{nA}$ extracted later from the flux-dependent FTR resonance-frequency data. This agreement shows that the room-temperature resistance calibration captures the correct overall Josephson scale of the FTR terminations.

A rough estimate of the asymmetry parameter may also be obtained from the inferred individual critical currents using the definition introduced in Sec. 2.3.1.

Table 4.5: Average parameters extracted from room-temperature resistance of the 1000 nm dc-SQUIDs. R_{j1} is obtained from the symmetric-regime extrapolation using Eq. (4.12); $R_{\mathrm{sq,RT}}$ is the measured room-temperature SQUID resistance. R_{j2} is inferred from Eq. (4.13). I_0 and $L_J(I_0)$ are calculated from Eq. (4.15) using $\Delta = 180\,\mu\mathrm{eV}$ and $R_{4\mathrm{K}} = 1.10\,R_{\mathrm{RT}}$.

R_{j1} (Ω)	$R_{\mathrm{sq,RT}}$ (Ω)	R_{j2} (Ω)	α	I_0 (nA)	$L_J(I_0)$ (pH)
536.9	352.7	1027.8	0.31 ± 0.12	364 ± 11	903 ± 26

4.6.3 Reference FTR: uncoupled 10 µm SQUID loop

This 10 µm device serves as fabrication and modeling benchmark in the negligible-screening regime. The analytical design values are $L_g = 10.8\,\mathrm{pH}$, $\beta_L = 0.005$, and $\gamma = 0.33$, while the external-coil fit to the measured flux sweep yields $L_g = 13.0\,\mathrm{pH}$, $\beta_L = 0.006$, $\gamma = 0.34$, $\alpha = 0.35$, and $I_0 = 444\,\mathrm{nA}$. Because β_L is effectively zero on the scale relevant here, the flux tuning of this device is well described by the asymmetric-SQUID model without the large-loop screening that arises for the 100 µm and 200 µm devices.

Device design and analytical parameters

Table 4.6 collects the corresponding analytical, HFSS, and measured zero-flux parameters used here for comparison.

For the 10 µm FTR, the simplified analytical estimate gives 6.649 GHz, about 2.2 % above the measured sweet-spot value. In Paper III, this residual offset is absorbed by the phenomenological factor $A = 0.98$, which accounts for the finite size of the SQUID loop. Across the full device set, the analytical estimates reproduce the overall resonance-frequency scale, but the agreement is not uniform. The 10 µm reference device is reproduced to within a few percent, whereas the 200 µm device shows a substantially larger discrepancy between the PEC-based HFSS eigenfrequency and the measured zero-flux value. The larger-loop devices have correspondingly larger γ, consistent with stronger SQUID loading of the CPW mode.

HFSS eigenmode simulation

Electromagnetic simulations of the 10 µm FTR were performed in ANSYS HFSS using the same PEC eigenmode approach described for the bare CPW

Table 4.6: CPW and resonator design parameters for the three FTRs. All three devices share the cross-section $w = 10\,\mu\text{m}$, $g = 2\,\mu\text{m}$, $t = 150\,\text{nm}$ (Al on $\langle 111 \rangle$ Si). The analytical resonance frequency uses the simplified closed-form estimate $f_r = \omega_0/[2\pi(1+\gamma)]$ with $\omega_0/2\pi = 1/(2\pi\sqrt{L_r C_r})$. The HFSS eigenfrequency is obtained under the PEC approximation with junction inductances set to their analytical zero-flux values. The analytical Q_c uses the Martinis formula [119]. Measured f_r and Q_c for the coupled FTRs are the zero-flux values extracted from the near-single-photon and flux-modulation characterizations reported in Sec. 4.6.4.

Parameter	Symbol	Unit	10 µm FTR	100 µm FTR	200 µm FTR
Resonator geometry and bare-mode parameters					
Length	l_r	µm	3320	3440	3259
Mode inductance	L_r	pH	897.7	930.1	881.2
Mode capacitance	C_r	fF	360.9	373.9	354.2
Participation ratio	γ	–	0.33	0.43	0.55
Mode impedance	Z_r	Ω	53.26	55.55	58.18
Bare frequency	$\omega_0/2\pi$	GHz	8.84	8.53	9.01
Resonance frequency comparison					
Analytical	$f_r^{(\text{an})}$	GHz	6.65	5.97	5.81
HFSS (PEC)	$f_r^{(\text{sim})}$	GHz	6.76	6.38	5.36
Measured	$f_r^{(\text{meas})}$	GHz	6.51	5.82	6.17
Coupling quality factor comparison					
Analytical	$Q_c^{(\text{an})}$	–	995	1082	1045
HFSS	$Q_c^{(\text{sim})}$	–	878	975	1318
Measured	$Q_c^{(\text{meas})}$	–	416	1232	536

(Sec. 4.5.1). The two Josephson junctions are represented as lumped inductive elements in parallel, with inductances $L_{J1} = 682\,\text{pH}$ and $L_{J2} = 1355\,\text{pH}$, inferred from Chip 2 of Table 4.5 using $I_0 = 364\,\text{nA}$ and $\alpha = 0.31$ (see Sec. 4.6.2 and Eq. (2.61)). Junction capacitances are included using $C_{J1} \approx 40\,\text{fF}$ and $C_{J2} \approx 20\,\text{fF}$, estimated from the respective junction areas ($1.0 \times 1.0\,\mu\text{m}^2$ and $1.0 \times 0.5\,\mu\text{m}^2$) and a specific capacitance of approximately $40\,\text{fF}\,\mu\text{m}^{-2}$, giving a total SQUID shunt capacitance $C_S = C_{J1} + C_{J2} \approx 60\,\text{fF}$. The SQUID loop geometry is imported directly from the GDS layout, so the geometric loop inductance $L_g = 10.8\,\text{pH}$ and the spatial distribution of the SQUID

current are captured by the field solution without further approximation (see Sec. 3.1.2). Fig. 4.21 shows the simulated electric field distribution, $|S_{21}(f)|$, and $\angle S_{21}(f)$ at zero-flux bias. Panel (a) confirms the intended quarter-wave mode structure: the field is concentrated toward the capacitive coupling end, while the SQUID termination sits at the current antinode, where its inductive loading has maximal influence on the mode frequency and nonlinearity.

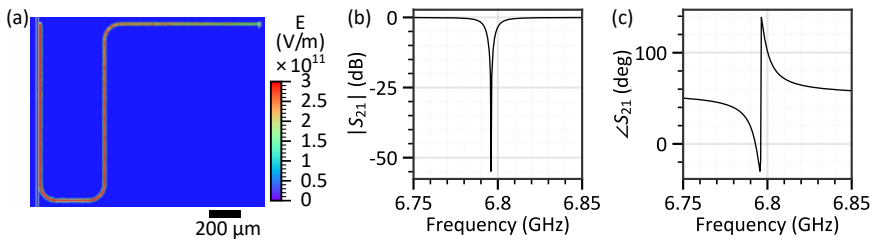

Figure 4.21: HFSS eigenmode simulation of the 10 µm SQUID-loop FTR at zero-flux bias ($L_{J1} = 682$ pH, $L_{J2} = 1355$ pH, PEC approximation). (a) Electric field magnitude of the fundamental eigenmode showing the quarter-wave profile with a current antinode at the SQUID end and a voltage maximum at the coupling capacitor. The electric field magnitude is clipped to a narrow range to make the field distribution prominent. The SQUID loop and junction elements are visible at the short-circuit end. The simulated eigenfrequency is $f_r^{(\mathrm{sim})} = 6.76$ GHz. (b) Simulated transmission magnitude $|S_{21}(f)|$ showing the resonant notch. (c) Simulated transmission phase $\angle S_{21}(f)$. The driven simulation yields $Q_c^{(\mathrm{sim})} = 878$.

The HFSS eigenfrequency, 6.76 GHz, lies above the measured value mainly because the PEC model omits kinetic inductance. For the FTR cross-section, the corresponding correction is about 220 MHz, which accounts for most of the offset. The driven response in Fig. 4.21(b,c) shows the expected notch in $|S_{21}|$ and the accompanying phase winding of a hanger-type resonator. The extracted simulated coupling quality factor remains larger than the measured value, so the simple electromagnetic model captures the qualitative response while still underestimating the realized coupling strength.

Near-single-photon response

The complex transmission $S_{21}(f)$ was measured at the zero-flux sweet spot and compared at two drive powers, $n_c \approx 1$ and $n_c \approx 10$. The circle-fit procedure of Sec. 3.5.4 was applied to the normalized complex data to extract the resonance frequency and quality factors. The resulting traces are shown in Fig. 4.22. In all three representations, the response remains single-valued between $n_c = 1$ and $n_c = 10$, so the device is still below bifurcation, but the phase and complex-plane traces already show the first visible signatures of nonlinear distortion.

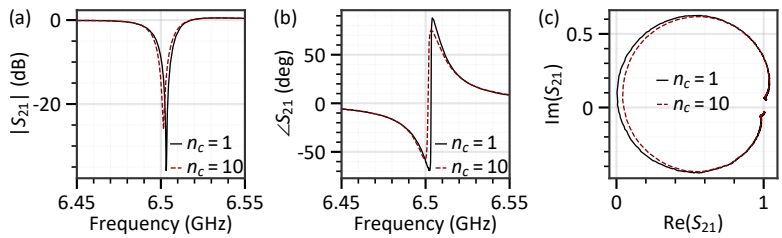

Figure 4.22: Microwave response of the 10 µm loop FTR at the zero-flux sweet spot for two drive powers. Solid black traces show $n_c = 1$ and dashed red traces show $n_c = 10$. (a) Transmission magnitude. (b) Transmission phase. (c) Background-normalized resonance circle used for the circle fit. The response remains single-valued, while a small power-dependent distortion is already visible in the phase and complex-plane traces.

At the sweet spot, the 10 µm device resonates at 6.5048 GHz. This is 2.2 % below the simplified analytical estimate and below the PEC-based HFSS value of 6.76 GHz. The measured coupling quality factor, $Q_c = 416$, is also smaller than the analytical design value of 995, which is consistent with the simple coupling estimate underestimating the effective fringing contribution for the 2 µm coupling gap.

Power sweep and Kerr nonlinearity

Fig. 4.23 shows a power sweep at the zero-flux bias point. At low photon numbers, the quality factors remain close to their weak-drive values. Above $n_c \sim 1$, Q_i increases due to TLS saturation, while the resonance frequency

shifts monotonically downward, indicating the onset of Kerr nonlinearity. The photon number calibration assumes a linear relation between input photons and intracavity photons below the bifurcation limit.

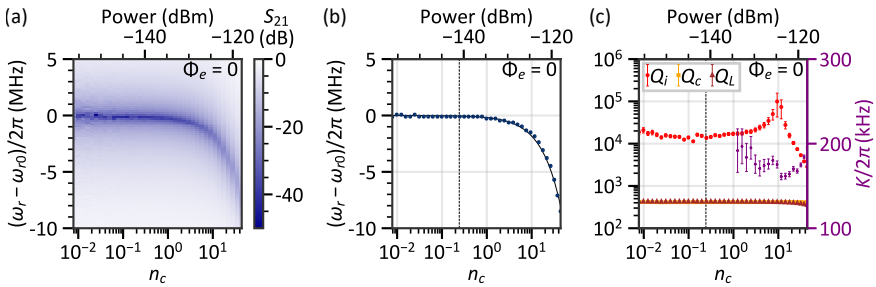

Figure 4.23: Power dependence of the 10 µm loop FTR at the zero-flux sweet spot. (a) Measured $|S_{21}|$ as a function of photon number and detuning. (b) Extracted resonance-frequency shift versus n_c with a linear Kerr fit. (c) Extracted Q_i, Q_c, Q_L, and $K/2\pi$ versus n_c. The onset of measurable Kerr shift occurs above $n_c \sim 1$, while Q_c remains nearly constant and Q_i rises with drive due to TLS saturation.

Panel (a) shows the background-subtracted colormap of the power sweep, while Panel (b) shows the circle-fit-extracted resonance frequency as a function of intra-cavity photon number. Fitting the measured frequency shift to $\omega_r = \omega_{r,0} - \mathcal{K} n_c$ yields a Kerr coefficient of $\mathcal{K}/2\pi = 187\,\text{kHz}$. This agrees with the analytical value derived in Sec. 2.6.7 using the junction parameters extracted in Sec. 4.6.2.

Panel (c) shows the quality factors and Kerr coefficient extracted from the circle-fit routine; see Sec. 2.6.9. At the lowest powers, the fitted Kerr coefficient remains close to the initial fit guess of 10^4 MHz and is therefore not physically meaningful, since the Kerr-induced frequency shift is still too small compared to the resonance linewidth and fit uncertainty. As the nonlinearity becomes more pronounced, the fitted value converges to approximately 200 kHz, in good agreement with the value extracted independently from Panel (b). The intrinsic quality factor increases for photon numbers above unity, consistent with the saturation of parasitic two-level-system loss channels in dielectric interfaces and surface oxides [124, 166]. At still higher powers, however, the extracted Q_i decreases again. Such a turnover is consistent with previously reported power-dependent internal loss in Josephson nonlinear resonators and

SQUID-based microwave circuits [235, 236]. A plausible interpretation is that a strong microwave drive activates additional dissipation channels in the Josephson element or SQUID termination, for example, through enhanced subgap conductance or nonequilibrium quasiparticle processes, which increase the internal loss and thereby reduce the measured Q_i [235]. It should nevertheless be noted that, in strongly nonlinear Josephson resonators, part of the observed high-power broadening can also appear as an effective nonlinear damping of the response rather than as a purely microscopic increase in dissipation [237].

Flux sweep with external bias coil

Flux tuning was measured by sweeping the external bias-coil current. The observed periodicity was first used to calibrate the current-to-flux conversion, after which a high-resolution one-period scan was taken for circle fitting. The results are shown in Fig. 4.24.

The calibrated coil sensitivity is $I_{\Phi_0} = 83.0\,\mu\text{A}\,{\Phi_0}^{-1}$, obtained from the observed flux periodicity seen in Fig. 4.24(a). In that panel, the slower modulation corresponds to the 10 µm reference device, while the faster modulation arises from the 200 µm device present on the same chip. Panel (b) shows part of a single period of the 10 µm device at a higher resolution for the circle-fit analysis used in panels (c,d). Fitting the analytical flux-tuning model to the circle-fit resonance-frequency data yields $A = 0.98$, $\alpha = 0.35$, and $I_0 = 444\,\text{nA}$. The fitted I_0 is somewhat higher than the room-temperature resistance estimate $I_0 = 372$ nA from Sec. 4.6.2. The fitted asymmetry and mean critical current imply individual critical currents $I_{c1} = I_0(1+\alpha) \approx 600\,\text{nA}$ and $I_{c2} = I_0(1-\alpha) \approx 290\,\text{nA}$ for the 10 µm reference device.

The minimum frequency remains finite because the junction asymmetry, $\alpha = 0.35$, prevents the effective critical current from vanishing at $\Phi_e = \Phi_0/2$. For this device, $\beta_L = 0.005$, screening is negligible, and the tuning curve is well described by the asymmetric-SQUID model without large-loop corrections.

Q_c varies only weakly with flux, as expected for a fixed coupling geometry. By contrast, the fitted internal quality factor varies significantly with no clear trend and, therefore, should be read as an effective value. As discussed in Sec. 2.7.3, the nonzero flux responsivity converts slow flux fluctuations into frequency jitter, which broadens the line without requiring a change in the underlying dissipation. For the 10 µm reference device, this effect is weaker than in the 100 µm and 200 µm devices.

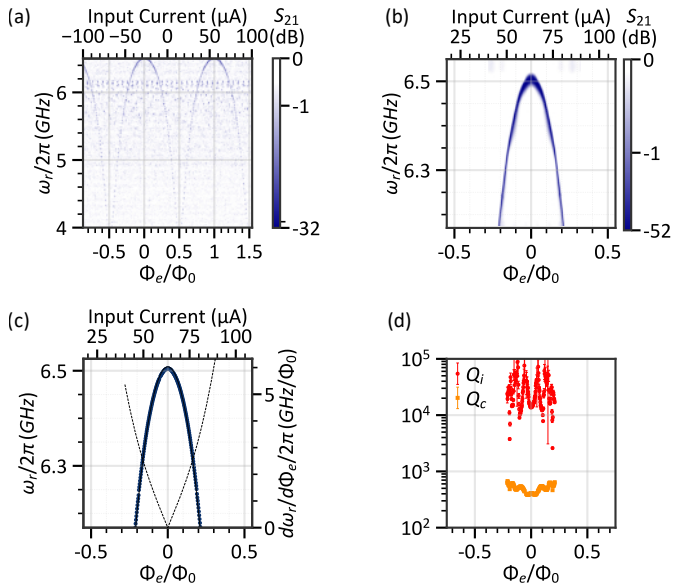

Figure 4.24: Flux modulation of the 10 µm loop FTR via the external bias coil. (a) Multiple Φ_0 modulations showing the slower periodicity of the 10 µm reference FTR near 6.5 GHz. The faster modulation arises from the 200 µm loop FTR present on the same chip. (b) High-resolution measurement of one flux period of the 10 µm FTR. (c) Resonance frequency f_r versus reduced external flux Φ_e/Φ_0, extracted by circle fitting at $n_c \approx 0.76$ photons. The solid curve is the analytical model of Eq. (2.198) fitted with $\alpha = 0.35$, $I_0 = 444\,\mathrm{nA}$, and $I_{\Phi_0} = 83.0\,\mu\mathrm{A}\,{\Phi_0}^{-1}$. (d) Extracted Q_i^{eff} and Q_c as a function of reduced external flux. Adapted from Paper III.

4.6.4 Coupled FTRs: 100 µm and 200 µm SQUID loops

The two coupled FTRs extend the characterization of the 10 µm reference device (Sec. 4.6.3) into the finite-screening regime. The 200 µm loop FTR employs a flip-chip input coil: a NbN superconducting coil patterned on a separate sapphire top chip and galvanically connected to the FTR chip via indium microsphere bump bonds (Sec. 3.4.1). The 100 µm loop FTR employs an on-chip input coil: an aluminum coil concentric with the SQUID loop, routed over the CPW center conductor via an aluminum air bridge.

Input coil architectures and SQUID design

The two coil architectures make different trade-offs. The flip-chip geometry offers lower loss in the FTR, likely due to suppressed parasitic coil-resonator capacitance at the cost of reduced mutual inductance due to the 50 µm chip separation. The on-chip geometry removes this separation but forces $d_i/d_s > 1$ and places the coil close to the resonator. The realized layouts use $d_i/d_s = 1.05$ for the flip-chip device and $d_i/d_s = 1.25$ for the on-chip device.

The main consequence of increasing the SQUID loop size is the onset of finite screening. The analytical design values $L_g = 697$ pH and 331 pH correspond to $\beta_L = 0.28$ and 0.13 for the 200 µm and 100 µm devices, respectively. Both remain below the symmetric branch-switching threshold. The finite asymmetry $\alpha \approx 0.33$ keeps the measured tuning curves single-valued in this regime.

Table 4.7: SQUID parameters for all three FTRs determined from the analytical model and from fitting the flux-tuning data acquired with the chip-based input coil and with the external bias coil independently. The junction asymmetry parameter is defined as $\alpha = (I_{c1} - I_{c2})/(I_{c1} + I_{c2})$; the screening parameter as $\beta_L = 2L_g I_0/\Phi_0$; and the SQUID participation ratio as $\gamma = L_S(0)/(l_r L_l)$ at zero flux. The average critical current I_0 and average junction inductance L_J are defined in Eq. (2.68) and Eq. (2.61). The current per flux quantum I_{Φ_0} is the applied coil current required to thread one flux quantum through the SQUID loop.

			200 µm FTR (flip-chip)			100 µm FTR (on-chip)		
Qty	Unit	Model	Input	Ext.	Model	Input	Ext.	Ext.
I_{Φ_0}	µA/Φ_0	–	17.8	5.8	–	30.8	20	83.0
A	–	–	1.1	1.06	–	0.98	0.98	0.98
α	–	0.33	0.30	0.35	0.33	0.35	0.33	0.35
I_0	nA	400	361	405	400	394	400	444
L_J	pH	823	913	812	823	836	823	740
L_S	pH	600	663	605	492	509	502	380
L_g	pH	697	776	723	331	331	332	13.0
β_L	–	0.27	0.27	0.28	0.11	0.13	0.13	0.006
γ	–	0.55	0.61	0.56	0.43	0.44	0.44	0.34

The fitted parameters from the input-coil and external-coil modulations are in good mutual agreement for both coupled devices (see Table 4.7).

Zero-flux response and quality factors

The zero-flux response of both coupled FTRs was measured at $n_c \approx 1$ and compared with a representative higher-power trace at $n_c \approx 10$. The 200 µm flip-chip device and the 100 µm on-chip device are shown in Fig. 4.25.

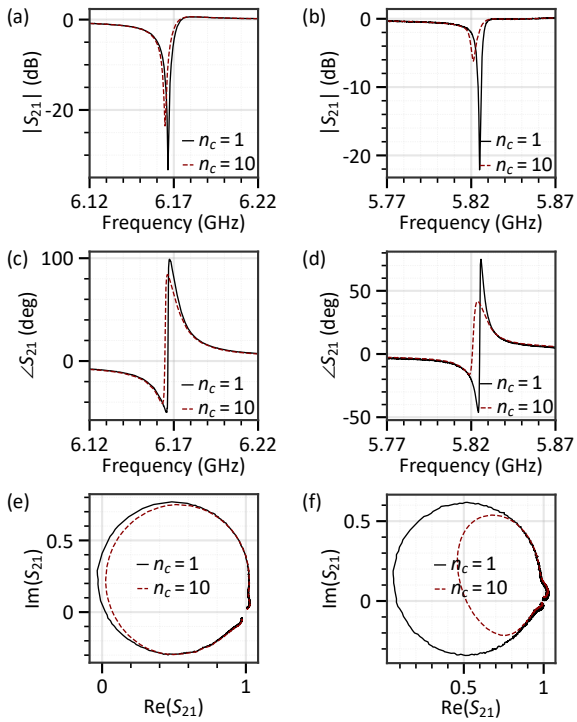

Figure 4.25: Zero-flux microwave response of the coupled FTRs at two drive powers. Left column: 200 µm flip-chip FTR. Right column: 100 µm on-chip FTR. Solid black traces show $n_c = 1$ and dashed red traces show $n_c = 10$. (a,b) Transmission magnitude. (c,d) Transmission phase. (e,f) Background-normalized resonance circles. The on-chip device already shows a stronger power-dependent distortion in the phase and complex-plane response, consistent with its larger Kerr coefficient and lower Q_i.

At the sweet spot, the flip-chip and on-chip devices resonate at 6.17 GHz and 5.82 GHz, respectively. Their coupling quality factors, $Q_c = 490$ and 1170,

are close to the design values. Both devices are strongly overcoupled, which is deliberate for flux-sweep spectroscopy.

The flip-chip device changes only weakly between $n_c \approx 1$ and $n_c \approx 10$, whereas the on-chip device shows a visibly stronger deformation in phase and in the complex plane, consistent with its larger Kerr coefficient and lower intrinsic quality factor. The flip-chip device reaches $Q_i \approx 3 \times 10^4$, whereas the on-chip device reaches only $Q_i \approx 0.7 \times 10^4$. Since both devices share the same CPW film and junction process, this difference is most naturally attributed to the coil architecture rather than the resonator itself. The lower Q_i of the on-chip device is attributed to parasitic capacitive coupling between the on-chip coil and the resonator, which is strongly reduced in the flip-chip geometry by the vertical separation between the coil and the resonator chip.

Temperature sweep at zero-flux sweet spot

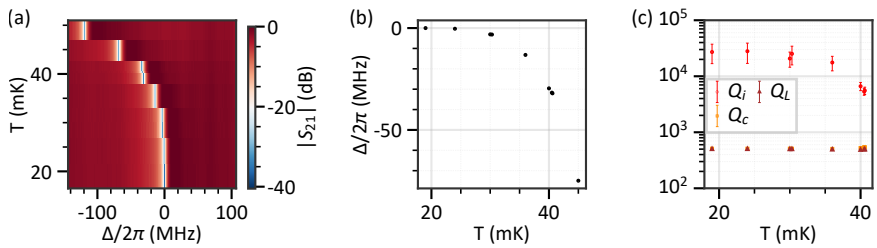

Figure 4.26: Temperature dependence of the 200 µm flip-chip FTR measured at the nominal zero-flux sweet spot, with both the external bias coil and the flip-chip input coil set to zero current. (a) Baseline-normalized $|S_{21}|$ as a function of detuning. (b) Resonance frequency shift $\delta f_r(T) = f_r(T) - f_r(19\,\mathrm{mK})$ as a function of temperature. (c) Internal (Q_i), coupling (Q_c), and loaded (Q_L) quality factors as a function of temperature.

A temperature sweep was performed on the 200 µm flip-chip FTR at nominal zero flux. In panel (a) of Fig. 4.26, the resonance remains close to the sweet spot frequency at lower temperatures and then shifts downward as the temperature increases, while panel (b) shows the extracted resonance frequencies at each temperature. Panel (c) indicates that this degradation is primarily due to the internal response, since Q_c changes only weakly compared with the clear reduction in Q_i. Up to about 30 mK, the resonance remains comparatively stable, with only a few-megahertz frequency shift and Q_c close to its zero-flux

value. Above 30 mK, however, a pronounced downward frequency pull and a clear reduction in Q_i develop, unlike the much weaker low-temperature response of the bare CPW control in Sec. 4.5.3. The large-loop FTR, therefore, shows an additional temperature-dependent effect not visible in the bare CPW control and is possibly associated with the SQUID termination or with drift of the effective flux bias. A separation between true dissipation and temperature-induced flux drift would require re-centering the sweet spot at each temperature or repeating the sweep at several fixed flux biases, which was not done here.

Power sweep and Kerr nonlinearity

Power sweeps were performed at the zero-flux sweet spot of both coupled FTRs, stepping the drive tone from the single-photon regime toward the bifurcation threshold. The resonance frequency shift $\omega_r(n_c) - \omega_r(0)$ and quality factors as a function of intracavity photon number are shown in Fig. 4.27.

Panels (a,b) of Fig. 4.27 show that the measured Kerr coefficients are $\mathcal{K}/2\pi$ = 216 kHz for the 200 µm device and 381 kHz for the 100 µm device, compared with analytical values of 184 kHz and 371 kHz, respectively, from Sec. 2.6.7. Panels (e,f) further show that Q_c stays approximately constant, while the internal and loaded quality factors evolve with power. On the other hand, Q_i remains constant below a single photon and then monotonically decreases at higher powers. This trend contrasts with that seen in the uncoupled FTR (see Fig. 4.23), as no increase in Q_i due to TLS saturation is observed. This could potentially be explained if Josephson loss channels and power broadening effects are more dominant than the effect of TLS saturation. Further investigation is needed to understand and quantify these effects clearly. The values of Kerr obtained from circle fitting are on the order of 100 kHz but show opposite trends for increasing power. For the flip-chip device, similar to the uncoupled FTR, the Kerr values start close to the guessed value of 10^4 and, with increasing power, saturate close to 200 kHz, which aligns with the value obtained from frequency fitting. For the on-chip FTR, the raw data has some additional features which distorts the circle fit results.

Flux modulation

Flux tuning of both devices was measured using two independent methods: modulation with the external bias coil alone or with the chip-based input coil.

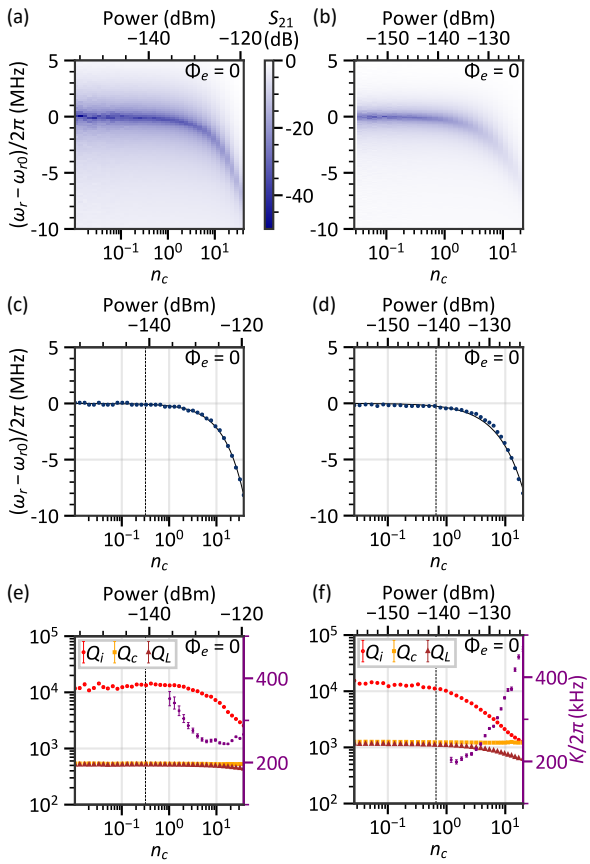

Figure 4.27: Kerr nonlinearity of the coupled FTRs at zero-flux bias. (a,b) Resonance frequency as a function of intracavity photon number n_c for the 200 µm flip-chip FTR (a) and the 100 µm on-chip FTR (b). (c,d) Circle-fit-based extraction of the Kerr coefficient from the power sweeps for the flip-chip (c) and on-chip (d) devices using $\omega_r(n_c) = \omega_r(0) - \mathcal{K}n_c$ (Eq. (2.229)). (e,f) Intrinsic, coupling, and loaded quality factors together with the extracted Kerr coefficient as a function of intracavity photon number for the flip-chip (e) and on-chip (f) devices. The dashed lines indicate the photon numbers used in the flux-modulation measurements. Adapted from Paper III.

The external-coil and input coil results are compared to test whether chip-based modulation produces tuning behavior consistent with the external-coil measurements. The photon numbers used in the flux sweeps are given in the corresponding figure captions and in Fig. 4.27(e,f).

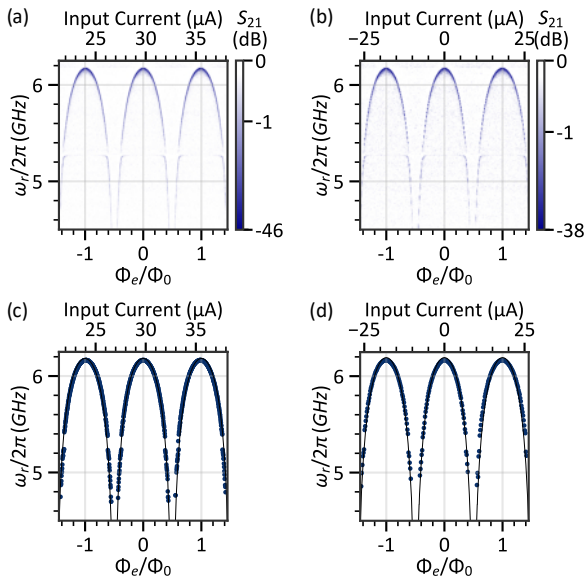

Figure 4.28: Multiple Φ_0 modulations of an FTR with a 200 µm-wide SQUID modulated at 0.33 intra-cavity photons via (a,c) an external bias coil and (b,d) via a flip-chip-based input coil. (a,b) show the background-subtracted FTR modulation in dependence of coil current and applied flux. (c,d) show the extracted resonance frequency of the FTR (dots), the solid line is the model accounting for finite screening and junction asymmetry.

External coil modulation. Figure 4.29 shows the external-coil tuning of both coupled devices. The current per flux quantum is reduced from 83.0 µA ${\Phi_0}^{-1}$ in the 10 µm reference device to 20 µA ${\Phi_0}^{-1}$ and 5.8 µA ${\Phi_0}^{-1}$ in the 100 µm and 200 µm devices, respectively. This reduction follows directly from the larger loop area. The fitted parameters agree with the input-coil fits in Table 4.7, which shows that the same SQUID model describes both biasing methods. In the 200 µm device, the avoided crossing near 5.3 GHz is attributed

to hybridization with a parasitic slotline mode. Panels (e,f) show that the quality-factor degradation is strongest away from the sweet spot, where the flux responsivity is largest, while Q_c varies only moderately over the same range.

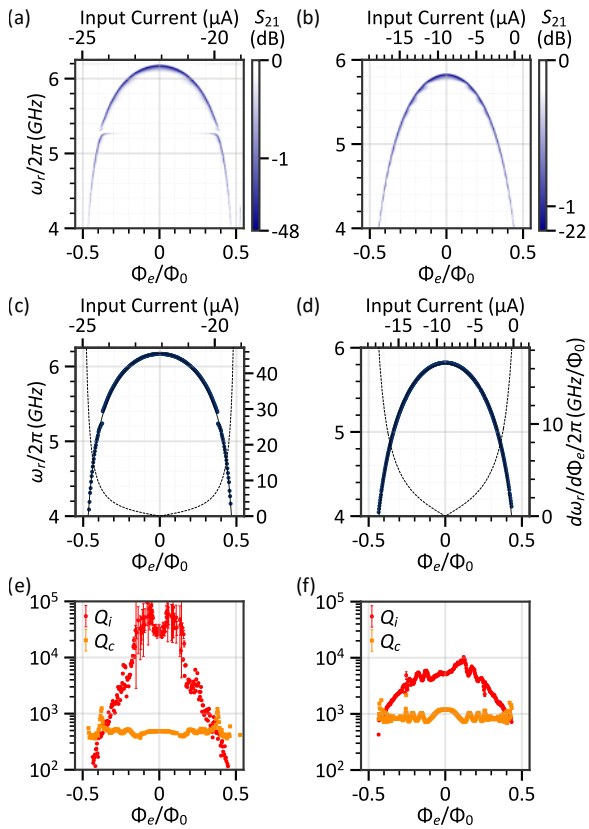

Figure 4.29: Flux modulation of the coupled FTRs using the external bias coil. Left column: 200 µm flip-chip FTR. Right column: 100 µm on-chip FTR. (a,b) Background-subtracted $|S_{21}|$ as a function of external-coil current and frequency. (c,d) Resonance frequency extracted by circle fitting together with fits to Eq. (2.198). (e,f) Extracted Q_i^{eff}, Q_c, and Q_L as a function of reduced external flux Φ_e/Φ_0. The avoided crossing in the 200 µm device is visible near 5.3 GHz. Adapted from Paper III.

Input coil modulation. Figure 4.30 shows the high-resolution flux modulation achieved via the chip-based input coils. The input coil current required for one flux quantum is $I^{\text{in}}_{\Phi_0} = 17.8\,\mu\text{A}\,{\Phi_0}^{-1}$ (200 µm flip-chip) and $30.8\,\mu\text{A}\,{\Phi_0}^{-1}$ (100 µm on-chip). Both values are in the range of tens of microamperes, demonstrating that the chip-based input coils allow full Φ_0 modulation at experimentally modest current levels. The raw maps in panels (a,b) make this directly visible: full periodic tuning is achieved in both devices without large applied current, with the flip-chip device requiring the smaller current because of its larger loop area and stronger mutual coupling.

The input-coil sweeps reach peak responsivities of up to approximately $2\pi \times 20\,\text{GHz}\,{\Phi_0}^{-1}$. This is the main gain of the large-loop design, as small flux changes are converted into clearly resolvable frequency shifts. The cost is that away from the sweet spot, the extracted internal quality factor must be read as an effective value, because flux-noise broadening adds to the true dissipative linewidth. No additional degradation specific to chip-based modulation is observed when the input-coil and external-coil sweeps are compared.

The effective Q_i decreases with increasing $|\Phi_e|$ in both devices (Fig. 4.30(e,f)), consistent with flux-noise-induced Voigt linewidth broadening (Sec. 2.7.3): away from $\Phi_e = 0$, the non-zero responsivity converts flux-noise into frequency jitters, reducing Q_i^{eff} below the intrinsic value. This degradation is more pronounced for the 200 µm device because its flux responsivity becomes larger away from the sweet spot. A comparison of the Q_i^{eff} versus flux curves obtained from the external-coil and input coil measurements shows no discernible additional degradation associated with chip-based modulation. The Q_c varies mildly with flux for both devices, following the expected frequency- and impedance-dependent scaling discussed in Sec. 4.6.3 [119].

Flux transfer efficiency

The flux transfer efficiency η_2 from the input coil to the SQUID loop is a key figure of merit for the chip-based modulation scheme. It is defined as $\eta_2 = M/L_i$, where M is the mutual inductance between the input coil and the SQUID loop and L_i is the input coil self-inductance (Sec. 2.8). The experimental value is extracted from the measured current per flux quantum $I^{\text{in}}_{\Phi_0}$ and the total input coil inductance L_i estimated analytically and by FEM simulation. The measured, simulated, and analytically calculated values are summarized in Table 4.8.

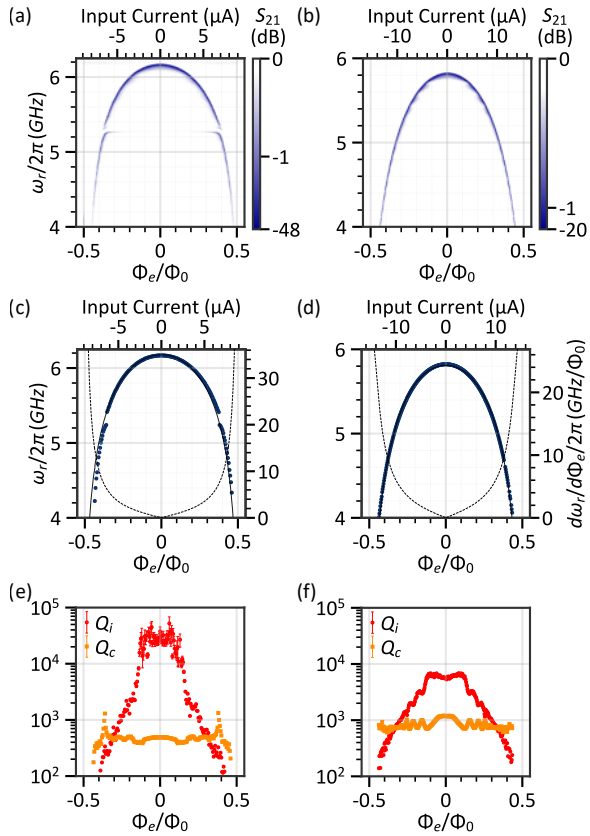

Figure 4.30: Flux modulation of the coupled FTRs using the chip-based input coil. Left column: 200 µm flip-chip FTR (flip-chip input coil, $n_c \approx 0.33$ photons). Right column: 100 µm on-chip FTR (on-chip input coil, $n_c \approx 0.83$ photons). (a,b) Background-subtracted $|S_{21}|$ as a function of input coil current and resonance frequency. (c,d) Resonance frequency (dots) extracted by circle fitting and fitted tuning curve (solid line). The dotted line shows the corresponding flux responsivity $|\partial\omega_r/\partial\Phi_e|$ on the right axis. Across the coupled-device dataset, the maximum responsivity reaches up to approximately $2\pi \times 20\,\mathrm{GHz}\,\Phi_0{}^{-1}$. (e,f) Effective internal (Q_i^{eff}) and coupling (Q_c) quality factors as a function of input flux. Adapted from Paper III.

4.7 Integrated flux transformer

The flux transformer provides the inductive link between the pickup loop and the SQUID of the FTR, converting flux produced by an external magnetic source into a resonance-frequency shift. Its performance is set by two sequential efficiencies: the coil-to-SQUID efficiency $\eta_2 = M/L_i$ and the pickup-to-coil efficiency $\eta_1 = L_i/(L_p + L_{\text{wire}} + L_i)$. This section first analyzes η_2 using analytical and FEM results, then examines the corresponding field distributions, and finally demonstrates the full transformer chain experimentally.

4.7.1 Coil-to-SQUID efficiency

Figure 4.31(a) shows η_2 as a function of d_i/d_s for both the flip-chip ($h = 50\,\mu\text{m}$) and on-chip ($h = 0$) configurations. The analytical curves peak sharply at $d_i/d_s = 1$ for both cases, where the input coil and SQUID loop are exactly concentric, and the mutual inductance M is maximized relative to the coil self-inductance L_i. For the flip-chip geometry, the axial separation broadens and suppresses the peak: at $h = 50\,\mu\text{m}$ and $d_i/d_s = 1$, the analytical η_2 is of order 75 % and is substantially reduced relative to the coplanar case. Moving the operating point to $d_i/d_s = 1.05$, which is the value achieved in the fabricated flip-chip device (a 215 µm coil above a 200 µm SQUID loop), yields an analytical $\eta_2 \approx 30\%$.

For the on-chip configuration, the input coil surrounds the SQUID loop from the outside and is therefore constrained to $d_i > d_s$, since placing it inside would require an additional air bridge and would increase the parasitic coupling loss to the CPW center conductor (Sec. 4.6.4). The fabricated on-chip device uses $d_i/d_s = 1.25$ (a 125 µm coil surrounding a 100 µm SQUID loop), which falls on the descending side of the $d_i/d_s = 1$ peak. The red simulation markers in Fig. 4.31(a) lie slightly below the idealized analytical curves, consistent with finite trace width and routing details that are absent from the one-dimensional loop model.

4.7.2 FEM simulations

Figure 4.31(b) shows η_2 as a function of axial separation h for the flip-chip coil ($d_i/d_s = 1.05$). The efficiency decreases monotonically with h as the fringing field produced by the input coil current spreads laterally before reaching the

Table 4.8: Flux transfer efficiency $\eta_2 = M/L_i$ from the input coil to the SQUID loop for the flip-chip and on-chip geometries, determined analytically, from FEM simulation, and from the experimental measurement. The input coil self-inductance L_i is computed analytically using Eq. (2.259). The experimental M is extracted via $M = \Phi_0/I_{\Phi_0}$ (see Table 4.7).

		Flip-chip device			On-chip device		
Parameter	Unit	Calc.	Sim.	Exp.	Calc.	Sim.	Exp.
L_i	pH	565	567	–	315	348	–
M	pH	153	169	116	121	116	67
η_2	%	29.3	29.8	20.8	38.4	33.1	19.3

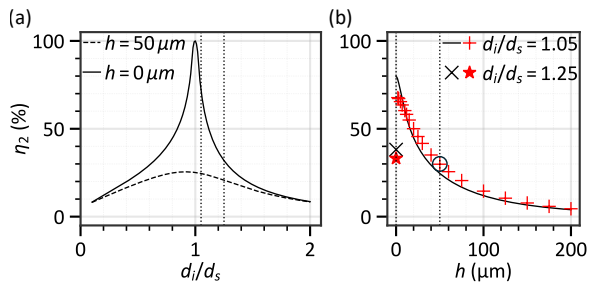

Figure 4.31: Flux transfer efficiency η_2 between the input coil and the SQUID loop as a function of geometry. (a) Efficiency versus the ratio of input coil loop width to SQUID loop width, d_i/d_s, for the flip-chip ($h = 50\,\mu$m) and on-chip ($h = 0$) configurations. (b) Efficiency versus axial loop separation h for the flip-chip geometry ($d_i/d_s = 1.05$). Black lines: analytical Neumann formula results for idealized one-dimensional square loops. Red markers: FEM simulation results for the realistic device geometries, with the star indicating the on-chip geometry ($d_i/d_s = 1.25$) and the cross indicating the flip-chip geometry ($d_i/d_s = 1.05$, $h = 50\,\mu$m). The dotted vertical lines in (a) mark $d_i/d_s = 1.05$ and 1.25, while the dotted vertical lines in (b) mark $h = 0$ and $50\,\mu$m. Adapted from Paper III.

SQUID loop plane. The FEM simulation again follows the analytical trend but remains slightly below it at small separations, where finite trace width effects are most significant. At $h = 50\,\mu$m, corresponding to the bonded indium-microsphere assembly described in Sec. 3.4.1, the simulated $\eta_2 \approx 30\%$. The analytical and FEM results are summarized alongside the experimental

values in Table 4.8.

The spatial distribution of the magnetic flux density produced by the input coil provides an intuitive picture of the coupling geometry and identifies the field regions that contribute to or detract from η_2. Figure 4.32 shows FEM-simulated field maps at an input coil current of 100 µA for the flip-chip (Fig. 4.32(a)) and on-chip (Fig. 4.32(b)) configurations.

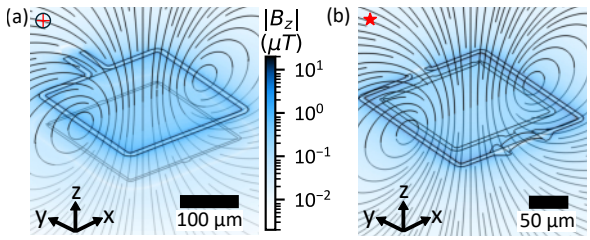

Figure 4.32: FEM-simulated magnetic flux density $|B_z|$ for an input-coil current of 100 µA. (a) Flip-chip configuration with a 215 µm NbN coil above a 200 µm SQUID loop at $h \approx 50$ µm. The axial separation spreads the field laterally before it reaches the SQUID plane. (b) On-chip configuration with a 125 µm aluminum coil surrounding a 100 µm SQUID loop in the same plane. The field is more concentrated, but only the flux threading the SQUID area contributes constructively to the coupling. Color scale: $|B_z|$ in µT on a logarithmic scale. Adapted from Paper III.

In the flip-chip geometry, the field spreads across the chip separation before reaching the SQUID plane, which reduces the fraction of the coil flux captured by the SQUID area. In the on-chip geometry, the field is more localized, but the coil encloses area outside the SQUID loop. Once $d_i/d_s > 1$, part of the field generated by the coil threads regions that do not contribute to the flux through the SQUID area itself. That geometric mismatch reduces η_2 even without axial separation.

The experimentally realized coil-to-SQUID efficiencies are similar for the two architectures, 20.8 % for the flip-chip device and 19.3 % for the on-chip device. The FEM simulation for the same geometry gives a slightly lower value than the analytical idealized-loop result because the one-dimensional analytical model assumes an infinitesimally thin wire and no coil openings, whereas the fabricated geometry has finite trace widths and wire crossings that redirect flux away from the SQUID loop area. Both configurations achieve similar

values of $\eta_2 \approx 30\%$ from the FEM simulations. Achieving significantly higher η_2 would require reducing h in the flip-chip case (for example, by using smaller indium bumps to decrease the chip separation below 50 µm) or switching to a washer-type SQUID design in which the SQUID loop encloses a smaller area for the same effective coupling, thereby relaxing the $d_i > d_s$ routing constraint.

The gap between the experiment and the ∼30% FEM values should not be attributed to screening alone. Additional contributions are likely to come from geometric idealization in the simulations, uncertainty in the current calibration, and, for the flip-chip device, lateral misalignment between the coil and the SQUID loop. For the present application, the flip-chip architecture is the better compromise because it preserves coherence while retaining a similar measured η_2.

4.7.3 Flux transformer demonstration

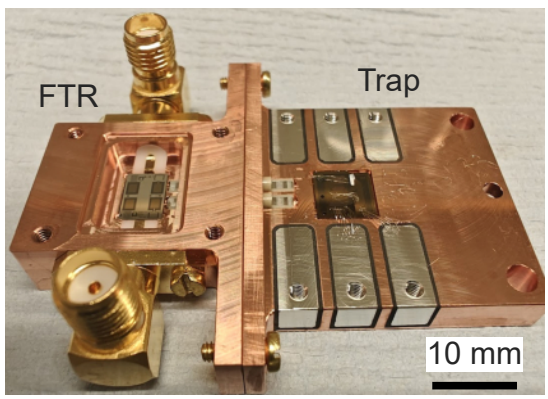

Figure 4.33: Tandem sample holder showing FTR packaging with SMA ports on the left and the trap mounting and dc pads on the right. The two sides are screwed together and an aluminum dc pin connects the input coil pads in the FTR box to the pickup coil pads in the trap holder.

The input coil to SQUID transfer efficiency η_2 characterizes the local inductive coupling stage, but the practical figure of merit for remote magnetic sensing is the total efficiency $\eta = \Phi_e/\Phi_p$ from the pickup coil to the SQUID (Eq. (2.263)). To characterize η and validate the full circuit model, a proof-of-principle flux transformer was assembled and tested using a separate 200 µm

SQUID-loop FTR with an on-chip 210 µm input coil. This is therefore not the same device as the flip-chip FTR characterized above in Sec. 4.6.4.

The transformer circuit comprised a superconducting pickup loop on a separate source chip connected to the FTR input coil through dc pins and aluminum wirebonds, as shown in Fig. 4.33. The magnetic source was a multi-winding coil patterned on the same chip as the pickup loop, with a FEM-simulated current-to-flux transduction of $0.27\,\Phi_0/\mu\mathrm{A}$ at the pickup loop. The series inductance is dominated by the interconnect parasitics, with $L_{\mathrm{wire}} = 28.6\,\mathrm{nH}$ compared with $L_p = 2.02\,\mathrm{nH}$ and $L_i = 485\,\mathrm{pH}$. The full circuit topology is described in Sec. 2.8.

The mutual inductance between the 210 µm on-chip input coil and the 200 µm SQUID loop, obtained from the FEM simulation, is $M = 469\,\mathrm{pH}$, giving a calculated total efficiency of

$$\eta = \frac{M}{L_p + L_{\mathrm{wire}} + L_i} = 1.5\%. \tag{4.17}$$

Figure 4.34 shows the measured FTR transmission as a function of source-coil current, together with the extracted resonance frequency and responsivity. One flux period at the SQUID required 230 µA through the source coil. Using the FEM transduction of $0.27\,\Phi_0/\mu\mathrm{A}$ from source current to pickup-loop flux, this gives

$$\eta^{\mathrm{exp}} = \frac{1\,\Phi_0}{62.1\,\Phi_0} = 1.6\%, \tag{4.18}$$

in close agreement with the calculated value of 1.5%. The dominant inefficiency in the demonstrated circuit is the parasitic wire inductance. This represents an order-of-magnitude improvement over the flux transformer efficiency of approximately 0.16% reported in Ref. [66] for a similar circuit architecture with a smaller SQUID loop and a less geometrically optimized coil arrangement.

4.8 Flux-noise characterization

This section analyzes flux-noise broadening in the large-loop FTRs using three complementary methods: linewidth fits, fast S_{21} sweeps, and the PSD of the time traces.

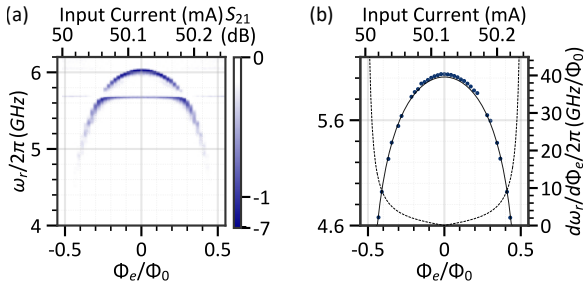

Figure 4.34: Flux transformer demonstration using the 200 µm SQUID-loop FTR with an on-chip input coil, measured at $n_c \approx 1.45$ intracavity photons. (a) Measured transmission $|S_{21}|$ (color scale, dB) as a function of source chip current through the multi-winding coil, showing periodic modulation by one flux quantum per 230 µA. (b) Resonance frequency f_r (dots, left axis) extracted by circle fitting, and flux responsivity $|\partial\omega_r/\partial\Phi_e|/2\pi$ (dashed line, right axis) as a function of the flux Φ_e/Φ_0 delivered to the SQUID through the transformer. Adapted from Paper III.

4.8.1 Flux noise at sweet spot

The resonance frequency of the FTR may be expanded about a chosen static bias field $B_{n,\text{bias}}$ as

$$f_r(B_{n,\text{bias}} + \delta B_n) = f_r(B_{n,\text{bias}}) + \left.\frac{\partial f_r}{\partial B_n}\right|_{B_{n,\text{bias}}} \delta B_n \tag{4.19}$$

$$+ \frac{1}{2}\left.\frac{\partial^2 f_r}{\partial B_n^2}\right|_{B_{n,\text{bias}}} \delta B_n^2 + \mathcal{O}(\delta B_n^3). \tag{4.20}$$

This magnetic field noise is then converted to flux noise for a given SQUID loop area. At the zero-flux sweet spot,

$$\left.\frac{\partial f_r}{\partial B_n}\right|_{B_n=0} = 0, \tag{4.21}$$

such that the leading frequency shift is no longer linear but quadratic:

$$\delta f_r \simeq \frac{1}{2}\left.\frac{\partial^2 f_r}{\partial B_n^2}\right|_{B_n=0} \delta B_n^2. \tag{4.22}$$

Therefore, the sweet spot suppresses the linear flux responsivity, but it does not eliminate flux-noise-induced broadening.

For a zero mean Gaussian field noise with rms amplitude σ_B, Eq. (4.22) implies a nonzero mean frequency shift and finite inhomogeneous broadening.

$$\langle \delta f_r \rangle = \frac{1}{2} \left. \frac{\partial^2 f_r}{\partial B_n^2} \right|_{B_n=0} \sigma_B^2, \tag{4.23}$$

$$\sigma_f = \sqrt{\left\langle (\delta f_r - \langle \delta f_r \rangle)^2 \right\rangle} = \frac{\sqrt{5} \left| \frac{\partial^2 f_r}{\partial B_n^2} \right|_{B_n=0}}{2} \sigma_B^2. \tag{4.24}$$

Thus, even at the sweet spot, the fitted linewidth can still contain a non-dissipative contribution from second-order flux broadening.

4.8.2 Flux-noise fit of $Q_i^{eff}(\Phi_e)$

The first flux-noise estimate is based on the linewidth-broadening model of Sec. 2.7. It is important to note that this model assumes colored flux noise ($1/f^\alpha$), which conflicts with the Gaussian noise model developed in Sec. 4.8.3. Additionally, the flux noise spectrum measured in Sec. 4.8.4 does not show a $1/f$-like trend for all flux biases. Therefore, this model must be seen as a preliminary approach developed independently and before other measurement and modeling techniques were pursued. The fitted parameters are summarized in Table 4.9. Throughout this analysis, the spectral exponent was fixed to $\mu = 1$, and $Q_{i,\text{fit}}$ denotes the dissipative quality factor before inhomogeneous broadening is added.

Table 4.9: Effective flux-noise fit parameters extracted from the flux sweeps of the three FTRs using the nonlinear broadening model described in Sec. 2.7.3. The spectral exponent was fixed to $\mu = 1$. The parameter $Q_{i,\text{fit}}$ denotes the underlying dissipative quality factor entering Eq. (2.249). The parameter C_c^{eff} is an effective coupling-capacitance parameter.

Device	Bias	n_c	C_c^{eff} (fF)	A_Φ ($\mu\Phi_0^2$/Hz)	$Q_{i,\text{fit}}$
200 µm FTR	Input	0.05	26.49	2.42×10^5	4.83×10^5
200 µm FTR	Ext.	0.05	26.11	8.84×10^4	1.43×10^6
10 µm FTR	Ext.	0.12	26.17	9.77×10^2	3.54×10^4
100 µm FTR	Input	0.13	21.66	3.70×10^4	6.85×10^3
100 µm FTR	Ext.	0.13	21.26	5.66×10^3	5.79×10^3

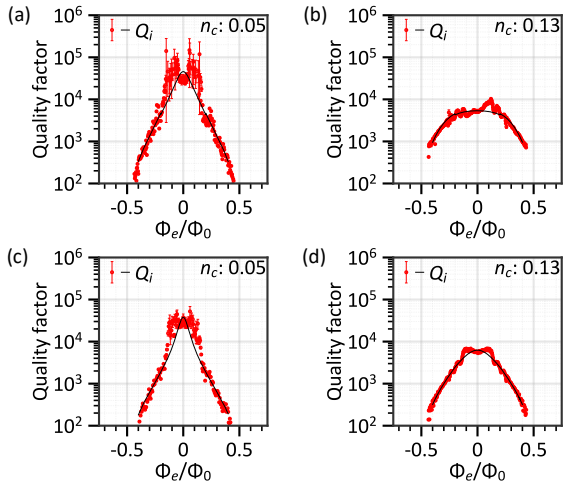

Figure 4.35: Effective intrinsic quality factor Q_i^{eff} as a function of reduced external flux Φ_e/Φ_0 for the two coupled FTRs, together with the flux-noise fits described in Sec. 2.7.3. Panels (a,c) show the 200 µm flip-chip FTR, and panels (b,d) show the 100 µm on-chip FTR. Panels (a,b) correspond to external-coil modulation, while panels (c,d) correspond to input coil modulation. Red markers show the circle-fit-extracted Q_i^{eff}, and the black curve shows the fitted flux-noise model. The flip-chip device shows a much stronger flux-dependent decrease of Q_i^{eff} than the on-chip device, consistent with its larger flux responsivity.

The extracted C_c^{eff} values are consistent between the two biasing methods for each coupled device.

The fitted $Q_i^{\text{eff}}(\Phi_e)$ curves are shown in Fig. 4.35. In both devices, the measured Q_i^{eff} is maximal near the zero-flux sweet spot and falls rapidly with increasing $|\Phi_e|$, consistent with the flux-noise broadening mechanism discussed in Sec. 2.7. A purely first-order treatment would predict too sharp a peak at $\Phi_e = 0$, because $\partial f_r/\partial \Phi_e$ vanishes there.

Panels Fig. 4.35(a) and (c) show that the 200 µm flip-chip FTR has the strongest flux-dependent linewidth degradation in the dataset. In both biasing methods, Q_i^{eff} falls by more than two orders of magnitude away from the sweet spot, consistent with the large flux responsivity of this device. The two datasets have nearly the same overall shape, indicating that the broadening is set by the device response rather than by the choice of bias coil.

Panels Fig. 4.35(b) and (d) show the same mechanism in the 100 µm on-chip FTR, but with a smaller dynamic range because the baseline dissipative loss is already much larger. In this device, flux noise broadens the line, but it does not dominate the measured linewidth to the same degree.

The extracted A_Φ values should be read only as effective low-frequency broadening parameters. In the present fit, they absorb not only intrinsic SQUID flux noise but also slow technical current noise, field drift, trapped-flux rearrangement, and other offsets during the measurement.

4.8.3 Flux noise from fast S_{21} measurements

As a second approach, the 200 µm flip-chip FTR was measured by taking fast (IFBW of 50-100 kHz) VNA sweeps repeated 100 times at each of 55 fixed external-flux bias points, similar to the work in Ref. [238]. This directly probes trace-to-trace resonance jitter on the sweep timescale. A representative dataset is shown in Fig. 4.36. The repeated magnitude, phase, and complex-plane traces broaden visibly instead of collapsing onto a single curve. At the bias point shown, near $\Phi_e/\Phi_0 \approx 0.18$ to 0.19, the rms frequency jitter is on the order of 2 MHz. The broadened annulus in the complex plane shows that this variation is already visible in the raw microwave response.

The flux dependence of the averaged linewidth and frequency jitter is shown in Fig. 4.37(b-d). The linewidth stays in the 7-10 MHz range, while the frequency jitter shows the expected U-shaped dependence on flux. It is smallest near the sweet spot and increases away from it, consistent with the local flux responsivity. The remaining jitter at $\Phi_e = 0$ is consistent with the finite curvature of the tuning curve.

Using the local slope of the tuning curve, the measured σ_f was converted into an effective rms flux fluctuation away from the sweet spot. The resulting $\sigma_{\Phi,\mathrm{eff}}$, shown in Fig. 4.37(f), is approximately constant over the valid flux range, with a mean of about $1.1\,\mathrm{m}\Phi_0$.

The repeated-trace analysis, therefore, provides a direct cross-check of the linewidth-based result. The extracted rms fluctuation of order $10^{-3}\Phi_0$ is consistent with the scale implied by the model-based broadening in Sec. 4.8.2.

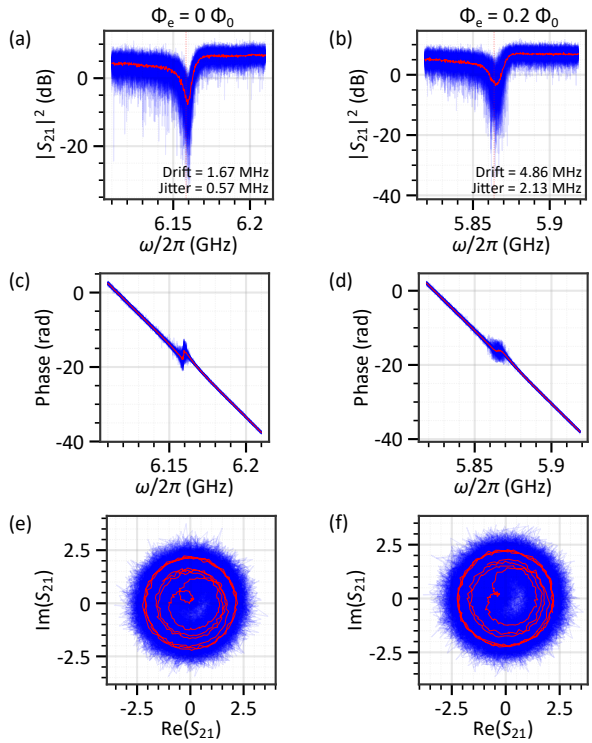

Figure 4.36: Fast-sweep resonance fluctuations of the 200 µm flip-chip FTR at a fixed external-flux bias near $\Phi_e/\Phi_0 = 0$ and $\Phi_e/\Phi_0 = 0.2$. Blue curves show 100 repeated VNA traces acquired at the same nominal bias point, and the red curve shows the mean response. (a,b) Transmission magnitude, showing a resonance-frequency drift of several MHz across the repeated sweeps and an rms frequency jitter of order 2 MHz. (c,d) Transmission phase, showing the corresponding phase broadening around the resonance. (e,f) complex S_{21} plane, where the repeated traces form a broadened annulus rather than a single sharp resonance circle.

4.8.4 Spectral flux-noise analysis

As a third approach to the flux-noise characterization, the 200 µm flip-chip coupled FTR was measured in the VNA CW time-trace mode at several fixed external-flux bias points. In contrast to the linewidth-based analysis

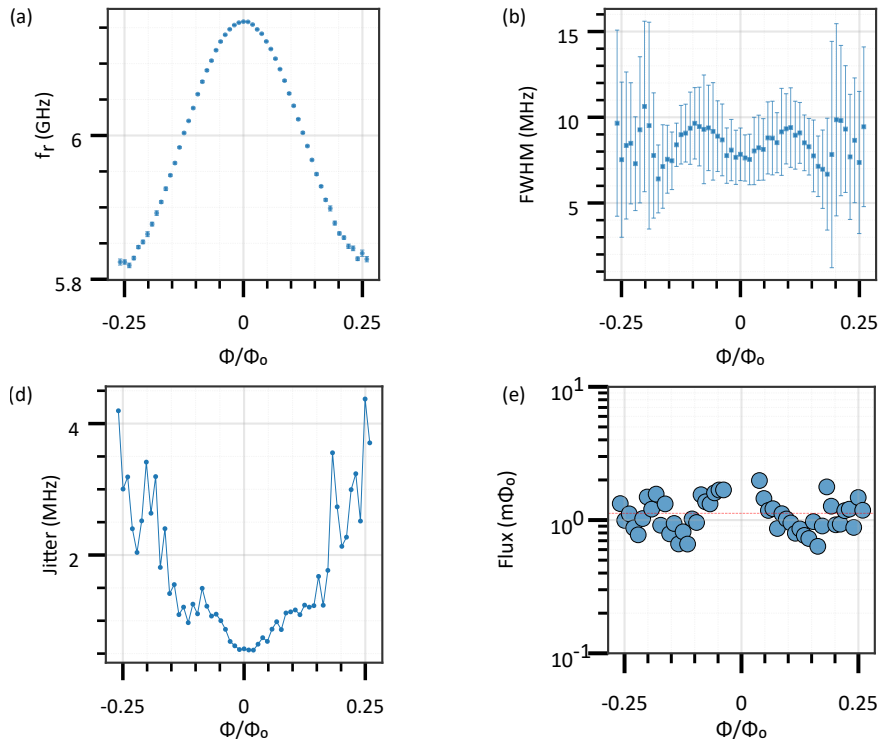

Figure 4.37: Average flux-noise values estimates from fast S_{21} traces of the 200 µm flip-chip FTR under external-coil bias. (a) Mean resonance frequency f_r as a function of reduced external flux Φ_e/Φ_0, extracted from 100 repeated traces at each of 55 flux points. (b) Mean resonance FWHM versus flux. (c) Resonance-frequency jitter. (d) rms flux fluctuation obtained by dividing the measured frequency jitter by the local flux responsivity away from the sweet spot.

above and the repeated-sweep analysis of the previous subsection, the present method resolves the noise directly in the Fourier domain. The resulting spectra, therefore, provide bias-dependent information on the distribution of the resonator noise over Fourier frequency, rather than only an effective broadening or integrated trace-to-trace jitter.

The measurement and processing workflow follows Sec. 3.5.4. At each bias point, CW time traces were acquired at several IF bandwidths, converted to

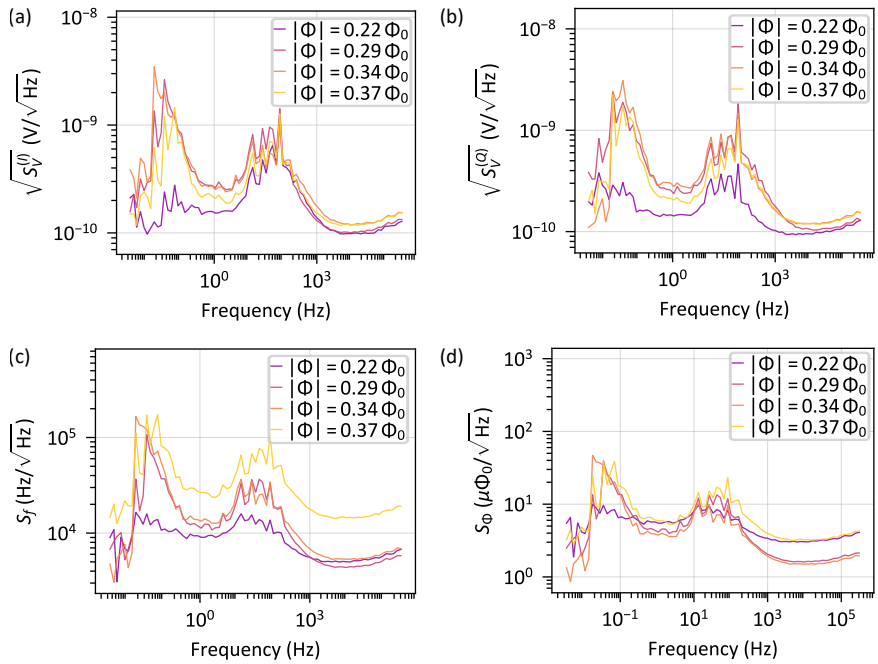

Figure 4.38: CW time-trace noise spectroscopy of the 200 µm flip-chip FTR under external-coil bias at five selected flux points. (a,b) Raw voltage ASD of the in-phase and quadrature channels, referred to the chip output plane. The off-resonance cable reference and amplifier noise floors are overlaid. (c) Frequency-noise ASD obtained from the full complex transduction factor after reference subtraction in PSD units. (d) Equivalent input flux-noise ASD obtained by dividing $\sqrt{S_f}$ by the local flux responsivity.

voltage at the chip output plane, stitched in Fourier space, and combined using the full complex transduction factor to obtain S_f and the equivalent input flux-noise ASD.

The raw voltage ASDs in Fig. 4.38(a,b) lie above the off-resonance cable reference at low Fourier frequencies, confirming an on-resonance excess noise contribution. The ordering of the traces changes between the two quadratures, which shows that the transduction vector rotates with bias and that no single quadrature can represent the frequency noise over the full tuning curve.

Fig. 4.38(c) shows the corresponding frequency-noise ASD after combining the two quadratures with the full complex transduction factor and subtracting the off-resonance reference in PSD units. The spectra-integrated average flux noise magnitude lies in the range of 4-8 $\mu\Phi_0$. This value is significantly smaller than the one obtained in Sec. 4.8.3, likely due to improvements in the shielding of the setup.

4.9 Magnetomechanical coupling estimates

No direct magnetomechanical signal was measured in this thesis. This section therefore gives order-of-magnitude estimates based on the measured 200 µm flip-chip FTR parameters and previously simulated trap gradients.

Transduction chain The mechanically induced frequency shift of the FTR follows the three-stage transduction chain

$$g_0 = \frac{\partial \omega_r}{\partial \Phi_e} \cdot \frac{\partial \Phi_e}{\partial \Phi_p} \cdot \frac{\partial \Phi_p}{\partial x} \cdot x_{\mathrm{zpf}}, \tag{4.25}$$

where the three factors correspond to: (i) the flux to-frequency responsivity of the FTR at the chosen operating point; (ii) the total transformer efficiency $\eta = \Phi_e/\Phi_p = M/(L_p + L_{\mathrm{wire}} + L_i)$ from the pickup loop flux to SQUID flux (Eq. (2.263)); and (iii) the pickup flux gradient per unit particle displacement, which depends on the trap geometry and pickup loop design. The zero-point fluctuation amplitude is defined as $x_{\mathrm{zpf}} = \sqrt{\hbar/(2m_{\mathrm{eff}}\Omega_m)}$ of the targeted mechanical mode.

Mechanical mode The estimates use a 48 µm-diameter lead sphere, consistent with the order of magnitude of the trapped particles discussed in Sec. 4.2.2. For $m \approx 6.6 \times 10^{-10}$ kg and the FEM-predicted trap frequencies $\Omega_z/2\pi = 125$ Hz, $\Omega_y/2\pi = 64$ Hz, and $\Omega_x/2\pi = 43$ Hz, the zero-point amplitudes are $x_{\mathrm{zpf},z} \approx 10.1$ fm, $x_{\mathrm{zpf},y} \approx 14.1$ fm, and $x_{\mathrm{zpf},x} \approx 17.2$ fm. The estimates below focus on the z mode, which has the largest pickup-loop flux response. Using the measured ringdown value $Q_z \approx 4.5 \times 10^5$, the corresponding mechanical damping rate is $\Gamma_m/2\pi \approx 2.8 \times 10^{-4}$ Hz.

Flux responsivity The coupling must be evaluated away from the sweet spot, where the flux responsivity is finite. For the 200 µm flip-chip FTR, the measured input-coil sweep in Fig. 4.30 gives a maximum responsivity of about $2\pi \times 20\,\mathrm{GHz}\,{\Phi_0}^{-1}$ near $|\Phi_e/\Phi_0| \approx 0.15$ and 0.25. At the same bias, the fitted internal quality factor is reduced by flux-noise broadening, and the Kerr coefficient is larger than at zero flux. To keep the estimate conservative, the calculations below use $n_{\mathrm{crit}} = 25$ as a representative upper photon number at the high-responsivity operating point.

Pickup flux gradient The pickup-loop flux gradient was taken from the FEM results discussed in Sec. 4.2.2 and in Ref. [95]. For a practical baseline geometry with a 100 µm-diameter pickup loop placed 50 µm above the trap center, $\partial\Phi_p/\partial z \approx 15\,\mathrm{m}\Phi_0/\mu\mathrm{m}$. This baseline value is used below.

Single-photon coupling rate Combining the measured FTR responsivity with the baseline pickup gradient gives two useful reference cases. For the demonstrated transformer efficiency $\eta = 1.6\%$ from Sec. 4.7.3, the estimated coupling is

$$g_0^{(A)}/2\pi \approx 48\,\mathrm{mHz}. \tag{4.26}$$

If the same circuit is evaluated in the wire-free limit of Sec. 4.7.3, $\eta = 18.7\%$, the corresponding estimate becomes

$$g_0^{(B)}/2\pi \approx 0.57\,\mathrm{Hz}. \tag{4.27}$$

These numbers should be read as order-of-magnitude benchmarks for the present platform.

Kerr and flux noise The usable drive is limited by Kerr nonlinearity and by flux-noise broadening at the high-responsivity bias point. Using the measured zero-flux Kerr coefficient of the 200 µm FTR and a conservative operating value $n_{\mathrm{crit}} \approx 25$, the maximum linearized coupling rates are

$$g_{\mathrm{max}}^{(A)}/2\pi \approx 0.24\,\mathrm{Hz}, \tag{4.28}$$

$$g_{\mathrm{max}}^{(B)}/2\pi \approx 2.9\,\mathrm{Hz}. \tag{4.29}$$

The estimates below therefore use $n_{\mathrm{crit}} = 25$ throughout.

4.9.1 Cooperativity

The cooperativity is estimated using $\kappa/2\pi = 12.8\,\mathrm{MHz}$, $\Gamma_m/2\pi \approx 2.8\times10^{-4}\,\mathrm{Hz}$, and the two g_0 estimates above gives

$$C_0^{(i)} = \frac{4(g_0^{(i)})^2}{\kappa\Gamma_m}, \qquad C^{(i)} = C_0^{(i)}\, n_{\mathrm{crit}}. \tag{4.30}$$

The resulting values are listed in Table 4.10.

Table 4.10: Order-of-magnitude magnetomechanical coupling estimates for the 200 µm flip-chip FTR. Scenario A uses the demonstrated transformer efficiency $\eta = 1.6\%$. Scenario B uses the wire-free reference value $\eta = 18.7\%$. The photon number is conservatively limited to $n_{\mathrm{crit}} = 25$.

Scenario	η (%)	$g_0/2\pi$ (Hz)	$g_{\max}/2\pi$ (Hz)	C_0	$C_{\max}$
A	1.6	0.048	0.24	1.9×10^{-6}	4.7×10^{-5}
B	18.7	0.57	2.9	2.7×10^{-4}	6.7×10^{-3}

Even in the wire-free reference case, the estimated cooperativity remains well below unity. Within the present parameter set, the dominant limitation is therefore the critical photon number of the FTR rather than the microwave readout or flux transfer efficiency.

CHAPTER 5

Conclusion and outlook

The goal is reached. You just can't see it... yet.

Conclusion

This thesis has developed and characterized the key superconducting subsystems required for a microwave circuit-based magnetomechanical readout of the levitated microparticle. The work addresses three connected building blocks: a chip-based magnetic trap, flip-chip-based superconducting interconnects for flux transfer, and a flux-tunable microwave resonator. Together, these results demonstrate the microwave and integration platform needed for a future experiment in which a levitated superconducting microsphere is read out through a flux-tunable resonator and a superconducting flux-transfer chain.

Paper I [98] demonstrated chip-based magnetic levitation of superconducting microspheres at temperatures down to 40 mK. In-plane COM frequencies of $(f_x, f_y) = (32, 60)$ Hz were resolved optically and agreed with FEM trap simulations. With the passive vibration-isolation stage installed (not included in Paper I), ringdowns of low-frequency COM modes were measured, yielding

mechanical quality factors of up to $Q \sim 4 \times 10^5$ [187]. This work established a chip-based levitation platform for coupling to a microwave readout circuit.

Paper II developed the flip-chip interconnect needed to position a superconducting input coil directly above the SQUID loop of an FTR. Indium microsphere bonds provided galvanic and mechanical interconnects at chip separations of 20 to 50 µm, with lateral alignment better than 5 µm. The key materials result was that Au-passivated Nb or NbN under-bump metallization enables reliable superconducting interconnects at millikelvin temperatures, whereas native oxides on non-passivated films degrade the interface.

Paper III characterized FTRs with a 200 µm SQUID loop coupled to a flip-chip input coil and a 100 µm SQUID loop coupled to an on-chip input coil, together with a 10 µm reference device without an input coil. Full Φ_0 modulation was achieved with tens of microamperes, resulting in a peak flux responsivity of $|\partial\omega_r/\partial\Phi_e|_{\max}/2\pi = 20\,\mathrm{GHz}\,{\Phi_0}^{-1}$. A central result of this work was that large SQUID loops can be used to improve flux transfer, while asymmetric Josephson junctions mitigate the branch-switching effect associated with finite SQUID loop inductance and thereby suppress jumps in the FTR tuning curve. The input coil-to-SQUID flux-transfer efficiencies of $\eta_2 \approx 20\%$ were realized in both flip-chip and on-chip input coil architectures. In the flip-chip geometry, the flux-transfer efficiency is mainly limited by the finite chip separation. In the on-chip geometry, the lower intrinsic quality factor was attributed to a possible parasitic capacitive coupling between the resonator and the nearby input coil. A proof-of-principle remote flux-transfer experiment further demonstrated a total efficiency of 1.6%, close to the estimated 1.5% based on the circuit inductances.

For the present platform, a suitable operating bias of $0.15\,\Phi_0$ is preferred, where the flux responsivity is $|\partial\omega_r/\partial\Phi_e|/2\pi \approx 2\,\mathrm{GHz}\,{\Phi_0}^{-1}$ and the flux noise is on the order of $\delta\Phi_{\mathrm{rms}} \sim 1\,\mathrm{m}\Phi_0$. For the 200 µm FTR, the effective Q_i at this bias point is above 10^4, while for larger bias points, the linewidth is significantly broadened by flux noise. At this bias point, the single-photon coupling rate is estimated to be $g_0/2\pi \sim 5\,\mathrm{mHz}$ and the single-photon cooperativity is $C_0 \sim 2 \times 10^{-8}$, with a maximum photon-enhanced value of $C_{\max} = C_0\, n_{\mathrm{crit}} \sim 5 \times 10^{-7}$ at the Kerr-limited critical photon number $n_{\mathrm{crit}} = 25$. The present platform is therefore limited simultaneously by weak total flux transfer through the flux transformer, flux-noise broadening away from the sweet spot, the small Kerr-limited operating photon number, and the limited detection efficiency of

the current cryogenic amplifiers. The main outlook of this thesis is to improve these four bottlenecks in parallel.

Outlook

The main challenges ahead are reliable trapping, improved flux transfer, reduced flux noise, lower nonlinearity, and demonstration of magnetomechanical coupling. Table 5.1 summarizes the current flip-chip baseline together with rounded next-generation target values.

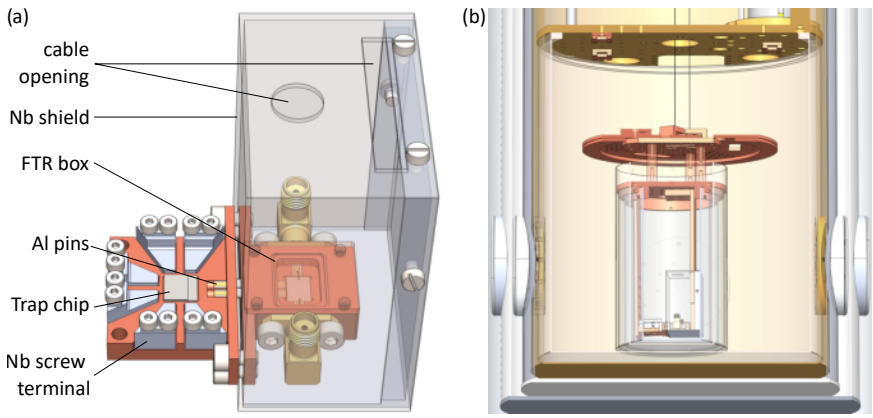

Figure 5.1: Magnetomechanical setup: (a) CAD model of a modified sample holder housing the trap and the FTR chips. A Nb shield is placed between the trap and the FTR in order to suppress stray trap fields at the resonator location and thereby protect the FTR from excessive magnetic-field exposure. (b) Vibration isolation stage with magnetic shields that houses the modified sample holder.

Platform stabilization Immediate experimental priorities are to mount the trap and resonator onto a single holder, reduce low-frequency vibration of the sample stage, and reduce magnetic-field fluctuations at the FTR. A two-stage vibration-isolation scheme is particularly useful for suppressing both pulse-tube-induced motion and other vibrations near trap modes by 40 dB compared to the 20 dB provided by the present single passive stage. In parallel, improved magnetic shielding of the sample region, together with persistent-current

operation of the trap and bias structures, would reduce cavity-frequency jitter due to flux noise. These improvements do not increase the magnetomechanical coupling, but they are prerequisites for operating at a stronger flux-sensitive bias point.

Magnetomechanical coupling Magnetomechanical coupling experiments are currently being pursued with the integrated setup shown in Fig. 5.1, in which the trap chip and the FTR chip are co-mounted on a common sample holder, and the magnetic signal from the trap pickup coil is routed to the SQUID input coil through aluminum dc pins, using the same sample holder that was employed to demonstrate the total flux-transfer efficiency in Paper III, as described in Sec. 4.7.3. This eliminates the need for a twisted-pair NbTi wire. The full shielding stack surrounding the assembly is expected to exceed that of the current FTR setup. The integrated sample holder is mounted inside the passive stage described in Sec. 3.3.3. Flexible cryogenic microwave cables are used to reduce mechanical coupling between the refrigerator and the suspended stage. This setup is intended to provide a reliable route toward demonstrating magnetomechanical coupling with the current devices, and experiments toward this goal are ongoing.

Table 5.1: Present metrics from Paper III and near-term goals for the 200 µm flip-chip FTR platform. The coupling quantities g_0 and C_0 refer to the operating bias point $0.15\,\Phi_0$, where $|\partial\omega_r/\partial\Phi_e|/2\pi \approx 2\,\mathrm{GHz}\,{\Phi_0}^{-1}$.

Parameter	Present	Goal	Main lever
η_2	20%	30%	Lower β_L, multiwinding coil
η	2%	10%	Lower parasitic inductance
$g_0/2\pi$	5 mHz	100 mHz	Improved full flux-transfer chain
C_0	2×10^{-8}	10^{-5}	Larger g_0
$\lvert\mathcal{K}\rvert/2\pi$	200 kHz	50 kHz	SNAIL / ATS
n_{crit}	30	10^2	Lower $\lvert\mathcal{K}\rvert$
$\delta\Phi_{\mathrm{rms}}$	$1\,\mathrm{m}\Phi_0$	$30\,\mu\Phi_0$	Shielding, gradiometry, persistent current, active locking
Q_i^{eff}	3×10^3	10^5	Lower flux-noise broadening
η_{det}	0.03	0.3	JTWPA-enabled low-loss chain

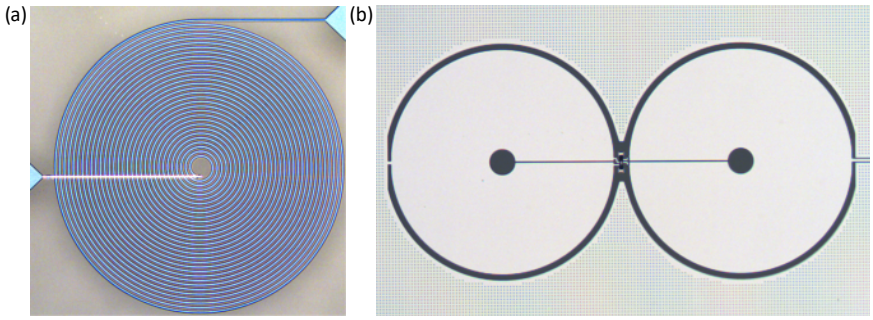

Figure 5.2: Optical microscope images of fabricated devices for the next generation FTRs. (a) An integrated multiwinding input coil to increase input coil inductance (bottom). This reduces β_L while preserving a large effective flux-collection area. (b) Gradiometrically connected two washer-type dc SQUID loops combining washer-based screening reduction with gradiometric common-mode rejection.

Washer-type and gradiometric SQUIDs The dominant source of the local η_2 shortfall in the 200 µm flip-chip device is flux screening, quantified by $\beta_L \sim 0.3$ (Sec. 4.6.4). A washer-type SQUID concentrates much of the loop inductance into a narrow slit and a smaller effective inductive core, thereby reducing β_L while retaining a large magnetic collection area. Schmidt et al. [66] demonstrated this design with a washer SQUID of $\beta_L \approx 0.06$, which is a useful benchmark for the present platform.

The washer geometries shown in Fig. 5.2 are designed primarily to reduce the SQUID-loop inductance and thereby provide more design margin to increase I_c at fixed β_L, which helps reduce the Kerr nonlinearity. Even though the washer preserves nearly the same flux-collection area as the original open-square loops, the smaller loop inductance reduces screening, which increases the fraction of coupled flux that reaches the SQUID and thereby improves the effective flux-transfer efficiency.

Reduction of parasitic inductance must be pursued along with washer-type SQUID geometry. This can, in principle, be achieved by extending the bottom trap chip above the FTR chip, with the pickup coil and input coil patterned in a single lithography.

A gradiometric SQUID geometry, in which two loops are connected in series with opposite orientation, is an attractive solution for rejecting spatially

uniform ambient field fluctuations while remaining sensitive to differential or localized flux signals. The main design challenges are achieving sufficiently well-matched loop inductances and coupling for strong common-mode cancelation and minimizing cross-coupling of the input-coil flux into the nominally compensating loop.

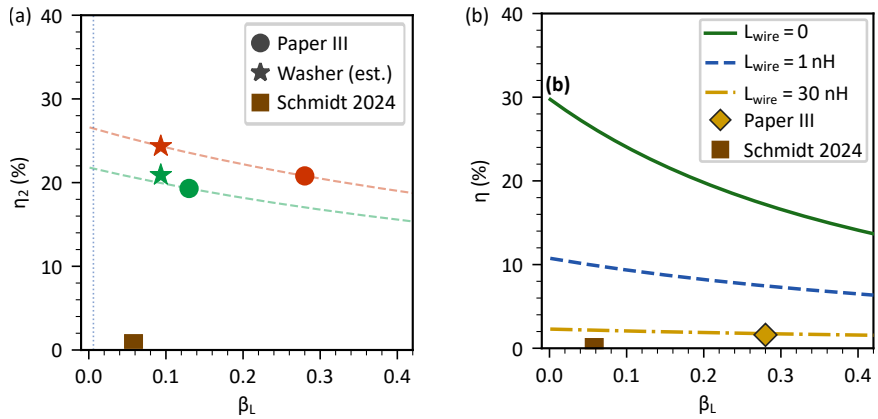

Figure 5.3: Input and total flux-transfer efficiencies versus screening parameter $\beta_L = 2L_{\mathrm{geo}}I_c/\Phi_0$ for square loops and the washer-type designs. (a) Input-coil-to-SQUID flux-transfer efficiency η_2. Circle markers show measured η_2 for the 100 µm (green) and 200 µm (red) devices in Paper III. Star markers: projected η_2 for the corresponding washer-type designs. The square marks the washer-SQUID geometry from Ref. [66]. (b) Total flux-transfer efficiency η, for the 200 µm loop while varying the SQUID screening and the total parasitic inductance L_{par}. The diamond marks the measured total efficiency $\eta = 1.6\%$ of the present flux transformer.

Kerr-free operation: SNAILs and ATS The Kerr nonlinearity limits the intracavity photon number to the order of 10 in the coupled devices (Sec. 4.6.4). For the 200 µm flip-chip FTR at the $0.15\,\Phi_0$ operating bias, the photon number required to reach $C = 1$ is on the order of 10^7. Kerr reduction is therefore necessary but not sufficient on its own: improving g_0 and increasing the usable photon number must be pursued simultaneously. This is illustrated in Fig. 5.4(a), which shows that even with a Kerr-reduced resonator operating at $n_c = 10^3$, the present g_0 gives only $C = 2 \times 10^{-5}$.

SNAILs [239, 240] and asymmetrically threaded SQUIDs (ATS) [241] can cancel the fourth-order Josephson nonlinearity at a specific flux bias, thereby extending the practical photon-number ceiling. For $n_{\mathrm{crit}} \geq 100$ with the present loaded linewidth ($\kappa/2\pi = 12.8\,\mathrm{MHz}$), the required Kerr coefficient is $|\mathcal{K}|/2\pi \lesssim 75\,\mathrm{kHz}$, which is approximately a factor of three below the current flip-chip value. However, at very large photon numbers, the effects of higher order terms and second-order perturbations can ultimately make the resonator nonlinear. This limitation is present for any Josephson junction based resonator, and therefore, it demands increasing g_0 by about two orders of magnitude.

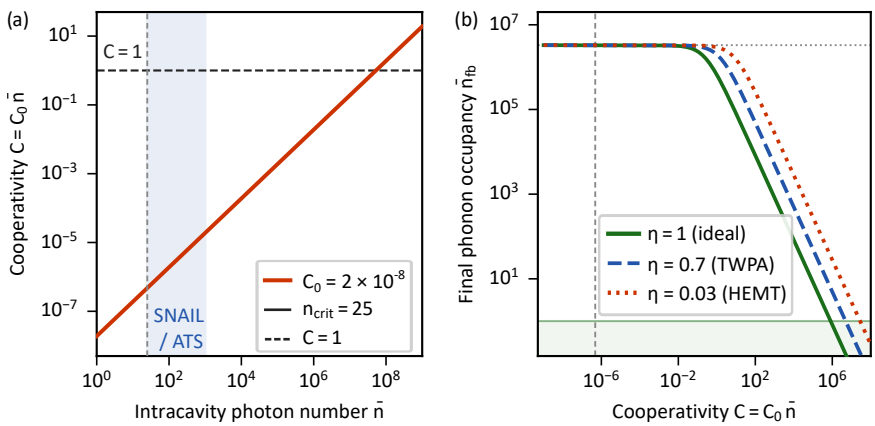

Figure 5.4: Cooperativity and feedback-cooling scaling for the current device, evaluated at the operating bias $0.15\,\Phi_0$ ($g_0/2\pi = 4.8\,\mathrm{mHz}$, $C_0 = 2 \times 10^{-8}$). (a) Photon-enhanced cooperativity $C = C_0\,\bar{n}$ versus intracavity photon number. The dashed vertical line marks the Kerr-limited $n_{\mathrm{crit}} = 25$ of present devices. The shaded region indicates the extended range accessible with a Kerr-reduced SNAIL or ATS resonator ($\bar{n} \lesssim 10^3$ [239, 241]), and the dashed horizontal line marks $C = 1$. (b) Illustrative scaling estimate of the final phonon occupancy under cold-damping feedback versus cooperativity, using $\bar{n}_{\mathrm{fb}} \approx \bar{n}_{\mathrm{th}}/(1 + 4\eta C)$ at 20 mK ($\bar{n}_{\mathrm{th}} = 3.3 \times 10^6$). The plot shows that improving η is ineffective while $C \ll 1$. The three curves correspond to $\eta = 1$ (ideal reference), $\eta = 0.7$ (optimistic near-quantum-limited benchmark), and $\eta = 0.03$ (present HEMT-dominated chain). The green shading indicates $\bar{n}_{\mathrm{fb}} < 1$. The vertical dashed line marks the current $C_{\max} = 5 \times 10^{-7}$.

Flux noise suppression Recovering the present intrinsic sweet-spot performance of order 3×10^4 at the same responsivity requires a reduction of flux noise to about $\delta\Phi_{\mathrm{rms}} \lesssim 0.1\,\mathrm{m}\Phi_0$. Beyond the passive solutions discussed earlier, active stabilization via a feedback loop is required, which monitors the FTR detuning at the chosen operating point and applies corrections through the input coil. This can be achieved either via Pound-Drever-Hall lock [86] or a PID controlled cavity-lock as implemented by Schmidt et al. [66].

Readout efficiency and feedback cooling At 20 mK and $\Omega_m/2\pi = 125\,\mathrm{Hz}$, the thermal phonon occupancy is $\bar{n}_{\mathrm{th}} \approx 3.3 \times 10^6$.

The readout chain is characterized using the total detection efficiency, which limits the achievable phonon occupancy [242]:

$$\bar{n}_{\mathrm{fb,min}} = \frac{1}{2}\left(\frac{1}{\sqrt{\eta_{\mathrm{det}}}} - 1\right). \tag{5.1}$$

For the present HEMT-dominated chain ($\eta_{\mathrm{det}} = 0.03$), this gives $\bar{n}_{\mathrm{fb,min}} \approx 2.4$. For an optimistic target of $\eta_{\mathrm{det}} = 0.4$, consistent with the path discussed by Schmidt et al. [66], the lower bound becomes $\bar{n}_{\mathrm{fb,min}} \approx 0.29$. Ground-state cooling, therefore, requires a substantial simultaneous increase of g_0 and C. A relatively straightforward improvement to η_{det} is replacing HEMT with a Josephson traveling-wave parametric amplifier (JTWPA) as the first amplifier.

CHAPTER 6

Appendix

For the meticulous souls.

This chapter includes the detailed derivation relevant to the FTR, the circle-fitting analysis routine, fabrication recipes for the flux-tunable resonator devices, and the homodyne-readout derivation and measurement setup.

6.1 SQUID and Kerr nonlinearity

6.1.1 Quadratic and higher-orders of the SQUID potential

This Appendix provides the detailed derivation behind the reduced one-port SQUID description used in the main text. It first shows how the internal loop coordinate is eliminated along the minimizing path, which reproduces the Schur-complement expression for the quadratic one-port stiffness used in Sec. 2.6.3. It then extends the same reduction to higher order to obtain the coefficients used in Sec. 2.6.7. The starting point is the reduced potential

$$U_{\text{eff}}(\phi_l) = U\big(\phi_l, \varphi^\star(\phi_l)\big), \tag{6.1}$$

where the minimizing path $\varphi^\star(\phi_l)$ is defined by the stationarity condition

$$\left.\frac{\partial U(\phi_l,\varphi)}{\partial\varphi}\right|_{\varphi=\varphi^\star(\phi_l)} = 0. \tag{6.2}$$

All partial derivatives of $U(\phi_l,\varphi)$ are evaluated at the dc operating point $(\bar{\phi}_l,\bar{\varphi})$.

For compactness, the total derivative along the minimizing path is written as

$$\frac{d}{d\phi_l} = \frac{\partial}{\partial\phi_l} + \frac{d\varphi^\star}{d\phi_l}\frac{\partial}{\partial\varphi}. \tag{6.3}$$

Derivatives of the minimizing path

Differentiating Eq. (6.2) once with respect to ϕ_l gives

$$0 = \frac{d}{d\phi_l}\left(\frac{\partial U}{\partial\varphi}\right) = U_{\phi\varphi} + U_{\varphi\varphi}\frac{d\varphi^\star}{d\phi_l}. \tag{6.4}$$

Evaluated at the operating point, this yields

$$r \equiv \left.\frac{d\varphi^\star}{d\phi_l}\right|_{\bar{\phi}_l} = -\frac{U_{\phi\varphi}}{U_{\varphi\varphi}}. \tag{6.5}$$

Differentiating the same stationarity condition a second time gives

$$0 = \frac{d^2}{d\phi_l^2}\left(\frac{\partial U}{\partial\varphi}\right) = U_{\phi\phi\varphi} + 2U_{\phi\varphi\varphi}\frac{d\varphi^\star}{d\phi_l} + U_{\varphi\varphi\varphi}\left(\frac{d\varphi^\star}{d\phi_l}\right)^2 + U_{\varphi\varphi}\frac{d^2\varphi^\star}{d\phi_l^2}. \tag{6.6}$$

Evaluated at the operating point, this gives

$$s \equiv \left.\frac{d^2\varphi^\star}{d\phi_l^2}\right|_{\bar{\phi}_l} = -\frac{U_{\phi\phi\varphi} + 2U_{\phi\varphi\varphi}r + U_{\varphi\varphi\varphi}r^2}{U_{\varphi\varphi}}. \tag{6.7}$$

Second and third derivatives of the reduced potential

Along the minimizing path, the stationarity condition implies $U_\varphi = 0$, so the first derivative of the reduced potential is simply

$$U'_{\text{eff}} = \frac{dU_{\text{eff}}}{d\phi_l} = \frac{d}{d\phi_l}U\big(\phi_l,\varphi^\star(\phi_l)\big) = U_\phi. \tag{6.8}$$

Differentiating once more gives

$$U''_{\text{eff}} = \frac{dU_\phi}{d\phi_l} = U_{\phi\phi} + r\,U_{\phi\varphi}. \tag{6.9}$$

Using $r = -U_{\phi\varphi}/U_{\varphi\varphi}$ yields

$$U''_{\text{eff}} = U_{\phi\phi} - \frac{U_{\phi\varphi}^2}{U_{\varphi\varphi}}. \tag{6.10}$$

The third derivative follows from differentiating the previous line:

$$U'''_{\text{eff}} = \frac{d}{d\phi_l}\left(U_{\phi\phi} + rU_{\phi\varphi}\right) \tag{6.11}$$

$$= U_{\phi\phi\phi} + 2rU_{\phi\phi\varphi} + r^2U_{\phi\varphi\varphi} + sU_{\phi\varphi} + r\left(U_{\phi\phi\varphi} + rU_{\phi\varphi\varphi}\right). \tag{6.12}$$

Collecting terms gives

$$U'''_{\text{eff}} = U_{\phi\phi\phi} + 3rU_{\phi\phi\varphi} + 2r^2U_{\phi\varphi\varphi} + sU_{\phi\varphi}. \tag{6.13}$$

From the second derivative of the stationarity condition,

$$U_{\phi\phi\varphi} + 2rU_{\phi\varphi\varphi} + r^2U_{\varphi\varphi\varphi} + sU_{\varphi\varphi} = 0, \tag{6.14}$$

and from the first derivative,

$$U_{\phi\varphi} + rU_{\varphi\varphi} = 0. \tag{6.15}$$

Combining these two relations gives

$$sU_{\phi\varphi} = rU_{\phi\phi\varphi} + 2r^2U_{\phi\varphi\varphi} + r^3U_{\varphi\varphi\varphi}, \tag{6.16}$$

so that

$$U'''_{\text{eff}} = U_{\phi\phi\phi} + 3U_{\phi\phi\varphi}r + 3U_{\phi\varphi\varphi}r^2 + U_{\varphi\varphi\varphi}r^3. \tag{6.17}$$

Fourth derivative of the reduced potential

Differentiating the third derivative gives

$$\begin{aligned} U''''_{\text{eff}} &= \frac{d}{d\phi_l}\left(U_{\phi\phi\phi} + 3U_{\phi\phi\varphi}r + 3U_{\phi\varphi\varphi}r^2 + U_{\varphi\varphi\varphi}r^3\right) \\ &= U_{\phi\phi\phi\phi} + 4U_{\phi\phi\phi\varphi}r + 6U_{\phi\phi\varphi\varphi}r^2 + 4U_{\phi\varphi\varphi\varphi}r^3 + U_{\varphi\varphi\varphi\varphi}r^4 \\ &\quad + 3s\left(U_{\phi\phi\varphi} + 2U_{\phi\varphi\varphi}r + U_{\varphi\varphi\varphi}r^2\right). \end{aligned} \tag{6.18}$$

The first five terms are the fourth derivative of $U(\phi_l, \varphi)$ along the local tangent direction $(1, r)$ of the minimizing path.

The bracket in the last line is eliminated using the second derivative of the stationarity condition,

$$U_{\phi\phi\varphi} + 2U_{\phi\varphi\varphi}r + U_{\varphi\varphi\varphi}r^2 = -U_{\varphi\varphi}s. \tag{6.19}$$

Substituting this identity gives

$$U''''_{\text{eff}} = U_{\phi\phi\phi\phi} + 4U_{\phi\phi\phi\varphi}r + 6U_{\phi\phi\varphi\varphi}r^2 + 4U_{\phi\varphi\varphi\varphi}r^3 + U_{\varphi\varphi\varphi\varphi}r^4 - 3U_{\varphi\varphi}s^2. \tag{6.20}$$

The additional term $-3U_{\varphi\varphi}s^2$ therefore arises from the curvature of the minimizing path itself. It is absent if only the local tangent direction $(1, r)$ is retained.

Conversion to flux derivatives

The reduced one-port SQUID potential is later expanded in the terminal flux coordinate

$$\Phi_l = \frac{\Phi_0}{2\pi}\phi_l. \tag{6.21}$$

Therefore,

$$\frac{d}{d\Phi_l} = \left(\frac{2\pi}{\Phi_0}\right)\frac{d}{d\phi_l}, \tag{6.22}$$

so the flux-derivative coefficients used in the Kerr expansion are

$$c_n = \left(\frac{2\pi}{\Phi_0}\right)^n U_{\text{eff}}^{(n)}. \tag{6.23}$$

In particular,

$$c_2 = \left(\frac{2\pi}{\Phi_0}\right)^2 U''_{\text{eff}}, \qquad c_3 = \left(\frac{2\pi}{\Phi_0}\right)^3 U'''_{\text{eff}}, \qquad c_4 = \left(\frac{2\pi}{\Phi_0}\right)^4 U''''_{\text{eff}}. \tag{6.24}$$

These are the coefficients used in Sec. 2.6.7.

6.1.2 Perturbative derivation of the Kerr contributions

This Appendix derives the perturbative Kerr contributions quoted in Sec. 2.6.7. In the main text, only the first-order quartic contribution and the second-order cubic contribution are retained since these define the Kerr-only approximation used throughout the thesis. The additional second-order quartic correction is included here only to show why it is omitted from the main text: it generates a higher-order dependence on photon number rather than a pure Kerr shift. The reduced one-port SQUID potential is expanded about the operating point $\bar{\Phi}_l$ as

$$U_{\text{eff}}(\Phi_l) = U_0 + \sum_{n\geq 1} \frac{c_n}{n!} (\Phi_l - \bar{\Phi}_l)^n. \tag{6.25}$$

Promoting the perturbation $(\Phi_l - \bar{\Phi}_l)$ to an operator gives the nonlinear contribution to the Hamiltonian,

$$\hat{\mathcal{H}}_{\text{nl}} = \sum_{n\geq 3} \frac{c_n}{n!} (\delta\hat{\Phi}_s)^n, \qquad \delta\hat{\Phi}_s \equiv \hat{\Phi}_s - \bar{\Phi}_s. \tag{6.26}$$

Using the mode-to-SQUID flux mapping,

$$\delta\hat{\Phi}_s = \left(\frac{\phi_l}{\phi_0}\right) \Phi_{\text{zpf}}(\hat{a} + \hat{a}^\dagger), \tag{6.27}$$

the cubic and quartic perturbation Hamiltonians are

$$\hat{\mathcal{H}}_3 = \frac{c_3}{3!} \left(\frac{\phi_l}{\phi_0}\right)^3 \Phi^3_{\text{zpf}}(\hat{a} + \hat{a}^\dagger)^3, \tag{6.28}$$

$$\hat{\mathcal{H}}_4 = \frac{c_4}{4!} \left(\frac{\phi_l}{\phi_0}\right)^4 \Phi^4_{\text{zpf}}(\hat{a} + \hat{a}^\dagger)^4. \tag{6.29}$$

The unperturbed harmonic Hamiltonian is

$$\hat{\mathcal{H}}_0 = \hbar\omega_r \left(\hat{a}^\dagger \hat{a} + \frac{1}{2}\right), \qquad E_n^{(0)} = \hbar\omega_r \left(n + \frac{1}{2}\right). \tag{6.30}$$

For a perturbation $\hat{V}$, the first-order and second-order energy corrections are

$$\delta E_n^{(1)} = \langle n|\hat{V}|n\rangle, \tag{6.31}$$

$$\delta E_n^{(2)} = \sum_{m\neq n} \frac{|\langle m|\hat{V}|n\rangle|^2}{E_n^{(0)} - E_m^{(0)}}. \tag{6.32}$$

Here $\hat{V} = \hat{\mathcal{H}}_3 + \hat{\mathcal{H}}_4$. At second order there is no mixed contribution proportional to $\hat{\mathcal{H}}_3\hat{\mathcal{H}}_4$, because $(\hat{a}+\hat{a}^\dagger)^3$ connects number states with odd Δn whereas $(\hat{a}+\hat{a}^\dagger)^4$ connects only even Δn. The mixed term therefore vanishes by selection rules.

First-order perturbation

Cubic term The cubic perturbation has no diagonal matrix elements at first order:

$$\delta E_{n,3}^{(1)} = \langle n|\hat{\mathcal{H}}_3|n\rangle = \frac{c_3}{3!}\left(\frac{\phi_l}{\phi_0}\right)^3 \Phi_{\text{zpf}}^3 \langle n|(\hat{a}+\hat{a}^\dagger)^3|n\rangle = 0. \tag{6.33}$$

This vanishes because $(\hat{a}+\hat{a}^\dagger)^3$ is odd in the oscillator quadrature. Therefore, the cubic term produces no first-order frequency shift and no first-order Kerr contribution.

Quartic term The first-order energy shift from the quartic perturbation is

$$\delta E_{n,4}^{(1)} = \langle n|\hat{\mathcal{H}}_4|n\rangle. \tag{6.34}$$

Using

$$\langle n|(\hat{a}+\hat{a}^\dagger)^4|n\rangle = 6n^2 + 6n + 3, \tag{6.35}$$

one obtains

$$\delta E_{n,4}^{(1)} = \frac{c_4}{24}\left(\frac{\phi_l}{\phi_0}\right)^4 \Phi_{\text{zpf}}^4 (6n^2 + 6n + 3). \tag{6.36}$$

The corresponding shift of the adjacent transition frequency is

$$\delta\omega^{(4,1)}_{n\to n+1} = \frac{\delta E^{(1)}_{n+1,4} - \delta E^{(1)}_{n,4}}{\hbar} = \frac{c_4}{2\hbar}\left(\frac{\phi_l}{\phi_0}\right)^4 \Phi^4_{\mathrm{zpf}}(n+1). \tag{6.37}$$

The term proportional to n gives the direct Kerr contribution,

$$\mathcal{K}_4(\Phi_s) = -\frac{c_4(\Phi_s)}{2\hbar}\left(\frac{\phi_l}{\phi_0}\right)^4 \Phi^4_{\mathrm{zpf}}. \tag{6.38}$$

The constant part renormalizes the zero-photon resonance frequency. Physically, this is the direct quartic Kerr shift of the reduced SQUID potential.

Second-order perturbation

Cubic term At second order, the cubic perturbation couples $|n\rangle$ to $|n\pm 1\rangle$ and $|n\pm 3\rangle$. The required matrix elements are

$$\begin{aligned}
|\langle n{-}3|(\hat{a}+\hat{a}^\dagger)^3|n\rangle|^2 &= n(n{-}1)(n{-}2),\\
|\langle n{-}1|(\hat{a}+\hat{a}^\dagger)^3|n\rangle|^2 &= 9n^3,\\
|\langle n{+}1|(\hat{a}+\hat{a}^\dagger)^3|n\rangle|^2 &= 9(n{+}1)^3,\\
|\langle n{+}3|(\hat{a}+\hat{a}^\dagger)^3|n\rangle|^2 &= (n{+}1)(n{+}2)(n{+}3).
\end{aligned} \tag{6.39}$$

Using $E^{(0)}_n - E^{(0)}_{n\pm1} = \mp\hbar\omega_r$ and $E^{(0)}_n - E^{(0)}_{n\pm3} = \mp 3\hbar\omega_r$, the second-order energy shift is

$$\begin{aligned}
\delta E^{(2)}_{n,3} = \frac{c_3^2}{36\hbar\omega_r}\left(\frac{\phi_l}{\phi_0}\right)^6 \Phi^6_{\mathrm{zpf}}\Bigg[&\frac{n(n-1)(n-2)}{3} + 9n^3\\
&- 9(n+1)^3 - \frac{(n+1)(n+2)(n+3)}{3}\Bigg].
\end{aligned} \tag{6.40}$$

The polynomial in brackets simplifies to

$$-30n^2 - 30n - 11, \tag{6.41}$$

so

$$\delta E_{n,3}^{(2)} = -\frac{c_3^2}{36\hbar\omega_r}\left(\frac{\phi_l}{\phi_0}\right)^6 \Phi_{\mathrm{zpf}}^6(30n^2+30n+11). \tag{6.42}$$

The transition-frequency shift contains a term proportional to n, which defines the cubic-induced Kerr contribution,

$$\mathcal{K}_3(\Phi_s) = \frac{5}{3}\frac{c_3(\Phi_s)^2}{\hbar^2\omega_r(\Phi_s)}\left(\frac{\phi_l}{\phi_0}\right)^6 \Phi_{\mathrm{zpf}}^6. \tag{6.43}$$

Physically, this term comes from virtual transitions generated by the cubic nonlinearity. It is absent at first order but appears at second order and contributes directly to the Kerr coefficient.

Quartic term At second order, the quartic perturbation couples $|n\rangle$ to $|n\pm 2\rangle$ and $|n\pm 4\rangle$. The required matrix elements are

$$\langle n+2|(\hat{a}+\hat{a}^\dagger)^4|n\rangle = 2(2n+3)\sqrt{(n+1)(n+2)}, \tag{6.44}$$

$$\langle n+4|(\hat{a}+\hat{a}^\dagger)^4|n\rangle = \sqrt{(n+1)(n+2)(n+3)(n+4)}, \tag{6.45}$$

with the corresponding downward matrix elements obtained by Hermitian conjugation.

Using $E_n^{(0)} - E_{n\pm 2}^{(0)} = \mp 2\hbar\omega_r$ and $E_n^{(0)} - E_{n\pm 4}^{(0)} = \mp 4\hbar\omega_r$, the second-order energy shift is

$$\begin{aligned}\delta E_{n,4}^{(2)} = g_4^2\Bigg[&\frac{|\langle n-2|(\hat{a}+\hat{a}^\dagger)^4|n\rangle|^2}{2\hbar\omega_r} + \frac{|\langle n-4|(\hat{a}+\hat{a}^\dagger)^4|n\rangle|^2}{4\hbar\omega_r} \\ &- \frac{|\langle n+2|(\hat{a}+\hat{a}^\dagger)^4|n\rangle|^2}{2\hbar\omega_r} - \frac{|\langle n+4|(\hat{a}+\hat{a}^\dagger)^4|n\rangle|^2}{4\hbar\omega_r}\Bigg],\end{aligned} \tag{6.46}$$

where

$$g_4 \equiv \frac{c_4}{4!}\left(\frac{\phi_l}{\phi_0}\right)^4 \Phi_{\mathrm{zpf}}^4. \tag{6.47}$$

After simplification,

$$\delta E_{n,4}^{(2)} = -\frac{2g_4^2}{\hbar\omega_r}(2n+1)(17n^2+17n+21). \tag{6.48}$$

The corresponding shift of adjacent level spacings is

$$\delta\omega^{(4,2)}_{n\to n+1} = \frac{\delta E^{(2)}_{n+1,4} - \delta E^{(2)}_{n,4}}{\hbar} = -\frac{g_4^2}{\hbar^2\omega_r}\left(204n^2 + 408n + 288\right). \tag{6.49}$$

This term does not simply renormalize the Kerr coefficient. It produces an additional nonlinear dependence beyond a Kerr model because the transition frequencies acquire terms beyond linear order in n. It is also of higher order in the SQUID-flux perturbation than the terms kept in the main text. In the Kerr-only treatment used in this thesis, the quartic contribution is therefore kept only at first order, whereas the cubic contribution is kept at second order.

Kerr at zero flux.

At zero external flux and zero transport bias ($\Phi_e = 0$, $I = 0$), the stable operating point is $(\bar{\phi}_l, \bar{\varphi}) = (0, 0)$ on the $m = 0$ branch. Expanding the SQUID potential $U(\phi_l, \varphi)$ to second order in the phases and enforcing the stationarity condition $\partial U/\partial\varphi = 0$ gives

$$(E_{J1} - E_{J2})\,\phi_l + \left(E_{J1} + E_{J2} + \frac{\Phi_0^2}{\pi^2 L_g}\right)\varphi = 0, \tag{6.50}$$

which determines the perturbative elimination $\varphi^\star(\phi_l) \simeq r_0\,\phi_l$ with

$$r_0 = -\frac{E_{J1} - E_{J2}}{E_{J1} + E_{J2} + \Phi_0^2/(\pi^2 L_g)}. \tag{6.51}$$

Substituting $\varphi = r_0\,\phi_l$ into the fourth-order expansion and converting to flux coordinates via $c_4 = (2\pi/\Phi_0)^4 U^{(4)}_{\text{eff}}$ yields

$$c_4(0) = -\frac{4\pi^2}{\Phi_0^2}\left[\left(\frac{1}{L_{J1}} + \frac{1}{L_{J2}}\right)(1 + 6r_0^2 + r_0^4) + 4\left(\frac{1}{L_{J1}} - \frac{1}{L_{J2}}\right)(r_0 + r_0^3)\right], \tag{6.52}$$

where $E_{Jk} = \Phi_0^2/(4\pi^2 L_{Jk})$ has been used. Since K_3 is zero at zero-flux bias, the total Kerr is given by K_4 to the first order. Substituting Eq. (6.52) into Eq. (2.223) gives the Kerr shift per photon at zero flux

$$\boxed{\begin{aligned}\frac{\mathcal{K}_{\text{tot}}}{2\pi} &= \frac{\hbar\pi Z_r(0)^2}{4\Phi_0^2}\left(\frac{\phi_l}{\phi_0}\right)^4 \\ &\times\left[\left(\frac{1}{L_{J1}}+\frac{1}{L_{J2}}\right)(1+6r_0^2+r_0^4)+4\left(\frac{1}{L_{J1}}-\frac{1}{L_{J2}}\right)(r_0+r_0^3)\right].\end{aligned}} \tag{6.53}$$

For symmetric junctions ($L_{J1} = L_{J2} \equiv L_J$), one has $r_0 = 0$ and

$$\frac{\mathcal{K}_{\text{tot}}}{2\pi} = \frac{\hbar\pi Z_r(0)^2}{2\Phi_0^2 L_J}\left(\frac{\phi_l}{\phi_0}\right)^4. \tag{6.54}$$

6.2 Single-stage vibration isolation model

This Appendix derives a compact model for the vertical vibration isolation obtained by suspending an experimental stage from a cryostat plate through a compliant support. The purpose of the model is to quantify how vertical base motion is transferred to the suspended stage in the frequency domain and to make explicit the trade-off between low resonance frequency, static sag, and parasitic stiffness from thermalization links and wiring. Only the dominant vertical translational coordinate is retained here. Lateral pendulum motion and internal suspension resonances are discussed separately at the end as corrections to the reduced model.

6.2.1 Linearized vertical equation of motion

Let $y(t)$ denote the vertical displacement of the support point and $x(t)$ the vertical displacement of the suspended stage of mass m. The load-bearing suspension element is modeled by a spring of stiffness k_s, while dissipation is represented by an effective viscous coefficient c. In addition, thermalization links, wiring, and other flexible connections can contribute an incremental vertical stiffness. Their combined linearized contribution is denoted by k_{par}. The total linearized vertical stiffness is therefore

$$k_{\text{eff}} = k_s + k_{\text{par}}. \tag{6.55}$$

If the auxiliary connections are installed with slack, they need not carry the

static load even though they can still contribute to the local dynamic stiffness once the stage oscillates. In that case the static sag is determined primarily by the load-bearing spring,

$$z_0 \simeq \frac{mg}{k_s}, \tag{6.56}$$

whereas the resonance frequency is governed by k_{eff}, not by k_s alone.

Linearizing the motion about the static equilibrium position gives

$$m\ddot{x} + c(\dot{x} - \dot{y}) + k_{\text{eff}}(x - y) = 0. \tag{6.57}$$

It is often convenient to introduce the relative suspension extension

$$u(t) \equiv x(t) - y(t), \tag{6.58}$$

in terms of which Eq. (6.57) becomes

$$m\ddot{u} + c\dot{u} + k_{\text{eff}}u = -m\ddot{y}. \tag{6.59}$$

The corresponding vertical isolation resonance is

$$\omega_{\text{iso}} = \sqrt{\frac{k_{\text{eff}}}{m}}, \qquad f_{\text{iso}} = \frac{\omega_{\text{iso}}}{2\pi}, \tag{6.60}$$

and the damping ratio and quality factor are

$$\zeta = \frac{c}{2m\omega_{\text{iso}}}, \qquad Q_{\text{iso}} = \frac{1}{2\zeta}. \tag{6.61}$$

A useful special case follows if all elastic elements that determine the dynamics also carry the static load. Then Eq. (6.56) and Eq. (6.60) combine to

$$\omega_{\text{iso}} = \sqrt{\frac{g}{z_0}}. \tag{6.62}$$

This identity is no longer exact once slack thermal links or wiring contribute to k_{par} without contributing to the static sag. For cryogenic suspensions this distinction is often essential.

6.2.2 Frequency-domain transmissibility

Assume harmonic base motion at angular frequency ω,

$$y(t) = Y e^{i\omega t}, \qquad x(t) = X e^{i\omega t}. \tag{6.63}$$

Substituting into Eq. (6.57) gives

$$\left(-m\omega^2 + ic\omega + k_{\text{eff}}\right) X = \left(ic\omega + k_{\text{eff}}\right) Y. \tag{6.64}$$

Introducing the frequency ratio

$$r \equiv \frac{\omega}{\omega_{\text{iso}}}, \tag{6.65}$$

one obtains the displacement transfer function from support to suspended stage,

$$H_x(\omega) \equiv \frac{X}{Y} = \frac{1 + i\,2\zeta r}{1 - r^2 + i\,2\zeta r}. \tag{6.66}$$

Its magnitude,

$$T_x(r) \equiv \left|\frac{X}{Y}\right| = \sqrt{\frac{1 + (2\zeta r)^2}{(1 - r^2)^2 + (2\zeta r)^2}}, \tag{6.67}$$

is the absolute displacement transmissibility.

Likewise, using $u = x - y$, the transfer function for relative suspension extension is

$$H_u(\omega) \equiv \frac{U}{Y} = \frac{r^2}{1 - r^2 + i\,2\zeta r}, \tag{6.68}$$

with magnitude

$$T_u(r) \equiv \left|\frac{U}{Y}\right| = \frac{r^2}{\sqrt{(1 - r^2)^2 + (2\zeta r)^2}}. \tag{6.69}$$

For harmonic motion, acceleration obeys the same transfer factor as displacement, since

$$\frac{\ddot{X}}{\ddot{Y}} = \frac{X}{Y}. \tag{6.70}$$

Therefore Eq. (6.67) also describes the transmissibility of acceleration amplitudes.

6.2.3 Limiting regimes and design implications

The reduced model admits three important asymptotic regimes.

For $r \ll 1$,

$$T_x(r) \to 1, \qquad T_u(r) \to 0. \tag{6.71}$$

At low frequencies the stage follows the support almost rigidly, while the suspension element carries very little dynamic extension.

At resonance, $r \simeq 1$, the response is amplified. In the weak-damping limit,

$$T_x(1) \simeq \frac{1}{2\zeta}, \qquad T_u(1) \simeq \frac{1}{2\zeta}. \tag{6.72}$$

Hence a cryogenic suspension with large Q_{iso} exhibits a strong resonance peak unless additional damping or active control is introduced.

For $r \gg 1$,

$$T_x(r) \approx \frac{\sqrt{1 + (2\zeta r)^2}}{r^2}. \tag{6.73}$$

If damping is very small, then $T_x(r) \sim r^{-2}$ and the stage approaches an inertial reference. If damping is appreciable, the asymptote crosses over to $T_x(r) \sim 2\zeta/r$, which reduces the resonance peak but worsens deep isolation at high frequency. This is the usual trade-off of passive isolation: damping is beneficial near resonance and detrimental far above resonance.

From Eq. (6.67) it follows that attenuation of support displacement begins only when

$$r > \sqrt{2}, \tag{6.74}$$

that is,

$$f > \sqrt{2}\, f_{\mathrm{iso}}. \tag{6.75}$$

Therefore, if a disturbance at frequency f_d is itself to be attenuated rather than merely not strongly amplified, the isolation resonance must satisfy

$$f_{\mathrm{iso}} < \frac{f_d}{\sqrt{2}}. \tag{6.76}$$

This simple inequality often conflicts with available refrigerator height, allowable spring extension, and the load capacity of low-stiffness springs. When that occurs, a single-stage suspension cannot simultaneously provide strong attenuation at low frequency and compact mechanical implementation, which

is one of the main motivations for moving to a multi-stage architecture.

6.2.4 Propagation of vibration spectra

In practice, the cryostat plate motion is measured as a displacement power spectral density. The single-stage model then predicts the suspended-stage spectrum directly. If $S_{yy}(\omega)$ is the displacement PSD of the support, then

$$S_{xx}(\omega) = |H_x(\omega)|^2 S_{yy}(\omega), \tag{6.77}$$

and for the relative extension of the suspension,

$$S_{uu}(\omega) = |H_u(\omega)|^2 S_{yy}(\omega). \tag{6.78}$$

Equivalently, in amplitude spectral density form,

$$\sqrt{S_{xx}(\omega)} = T_x(\omega)\sqrt{S_{yy}(\omega)}, \qquad \sqrt{S_{uu}(\omega)} = T_u(\omega)\sqrt{S_{yy}(\omega)}. \tag{6.79}$$

The band-limited rms displacement of the suspended stage is then

$$x_{\mathrm{rms}}^2 = \int_{\omega_1}^{\omega_2} S_{xx}(\omega)\,\frac{d\omega}{2\pi}, \tag{6.80}$$

with an analogous expression for u_{rms}. These relations make the model directly usable for cryostat vibration budgeting once the support spectrum has been measured.

6.2.5 Parasitic modes and validity of the reduced model

The model above captures only the dominant vertical isolation mode. A real suspended cryogenic stage also supports lateral pendulum motion, torsional motion, and internal resonances of the spring, thermal links, and mechanical frame.

For a suspension of length L, the lateral pendulum frequency is approximately

$$\omega_{\mathrm{p}} \simeq \sqrt{\frac{g}{L}}, \qquad f_{\mathrm{p}} \simeq \frac{1}{2\pi}\sqrt{\frac{g}{L}}. \tag{6.81}$$

If the stage is not perfectly symmetric, or if the suspension points are misaligned,

vertical and lateral motion can mix. Likewise, if the spring mass is not negligible, or if the spring is driven close to its own internal resonances, additional peaks can appear that are not described by the single-degree-of-freedom model. Flexible thermal links can also contribute both damping and parasitic stiffness in a configuration-dependent manner.

Accordingly, Eq. (6.67) should be interpreted as the leading-order envelope for the vertical base-to-stage transfer. It is quantitatively reliable only when the motion remains in the linear regime, the measurement frequency is sufficiently far from pendulum and internal suspension resonances, and the stage behaves approximately as a rigid body. For quantitative comparison with cryogenic data, the experimentally measured values of f_{iso} and Q_{iso} should therefore be used in place of room-temperature design values, since both stiffness and dissipation can change after cooldown.

6.2.6 Relevance to a levitated-particle experiment

If the trap chip and pickup structure are rigidly mounted to the suspended stage, then the relevant vibrational input seen by the levitation experiment is the suspended-stage motion $x(t)$ rather than the cryostat-plate motion $y(t)$. Any spurious signal that is linear in the stage displacement, such as vibration-induced modulation of pickup-loop flux or motion of the trap relative to the refrigerator frame, is therefore suppressed by the same transfer factor $H_x(\omega)$ derived above. The single-stage suspension thus reduces the vibrational background presented to the levitated particle only insofar as the support spectrum is filtered through Eq. (6.66). The residual background is then set by the combination of the cryostat support spectrum, the isolation resonance, the damping, and any parasitic modes not captured by the reduced model.

6.3 Fabrication recipes

This section lists the process parameters for each fabrication step of the flux-tunable resonator (FTR) devices. The layer stack and process flow are described in Sec. 3.2.2. All fabrication is performed on 2-inch undoped high-resistivity $\langle 111 \rangle$ Si wafers with a measured bow $\leq 10\,\mu\mathrm{m}$. Optical lithography

steps use the Heidelberg MLA 150 direct-write system unless noted otherwise.[1] Reactive ion etching (RIE) for oxygen plasma ashing is performed in tool #419 with the wafer placed on an 8-inch Si carrier to prevent aluminum re-sputtering from the chamber.

6.3.1 Wafer cleaning

Only the SC1 step of the standard RCA cleaning procedure is used since the primary concern before ground-plane deposition is the removal of organic contamination rather than the metallic impurities targeted by SC2.

Solvent cleaning.

- Acetone bath at 40 °C for 5 min, followed by ultrasonic agitation at 40 °C, 40% power, sweep mode, 35 kHz for 5 min.
- IPA bath with identical heating and sonication parameters.

Standard Clean 1 (SC1).

- Solution: 5 L DI water + 1 L NH_4OH (29 wt%) + 1 L H_2O_2 (aqueous).
- Heat to 80 °C, immerse the wafer for 10 min.
- Rinse in QDR bath and blow dry with N_2.

Native oxide removal (2% HF).

- Immerse the wafer in 2% HF for 1 min.
- Rinse in QDR and blow dry with N_2.
- Load it into the evaporator immediately to prevent re-oxidation.

6.3.2 Wiring layer (ground plane)

The Al wiring layer defines the CPW resonators, feedline, ground plane with flux-trapping holes, and on-chip input coil. The process flow is shown in Fig. 3.6.

[1] The Heidelberg DWL 2000 can be used as an alternative exposure tool for all optical lithography steps, with different parameters that are calibrated separately.

Al deposition (Plassys 521 e-beam evaporator).

- Pump load lock to $< 5 \times 10^{-8}$ mbar (target: 2.5 to 3×10^{-8} mbar); bake at 300 °C during pumping for degassing (minimum 6 h, overnight preferred).
- Deposit 150 nm Al at $\sim 1\,\mathrm{nm\,s^{-1}}$.
- Passivation oxidation: 10 mbar O_2, 500 sccm static MFC, 10 min.

Resist mask.

- Sacrificial layer: spin 950k PMMA-A2 ($\sim$ 50 nm) at 4000 rpm, 2000 rpm/s, bake at 180 °C for 5 min, cool on cold plate for 30 s.
- Photoresist: spin S1805 ($\sim$ 600 nm) at 4000 rpm, 2000 rpm/s, bake at 115 °C for 2 min.

Optical lithography (MLA).

- Exposure mode: Standard, High-Quality.
- Dose: $120\,\mathrm{mJ\,cm^{-2}}$, defocus: 0.
- Expose without substrate angle correction.

Developing and etching.

- Develop S1805 in MF319 for 60 s with paddle agitation; rinse in water for 30 s; rinse in QDR.
- Ash sacrificial PMMA in O_2 plasma (RIE #419): 50 W, 70 s.
- Inspect under optical microscope.
- Wet etch in Al Etchant Type A (77% H_3PO_4 + 3.5% CH_3COOH + 3% HNO_3) at 40 °C for 80 to 90 s (stop $\sim$ 10 s after Si becomes visible).
- Rinse in QDR and blow dry with N_2.

Resist stripping.

- Remover 1165 at 80 °C for 10 min; fresh 1165 with sonication (40%, sweep, 35 kHz) at 80 °C for 10 min.
- Acetone with identical sonication at 40 °C for 5 min.
- IPA with identical sonication at 40 °C for 5 min.

6.3.3 Under-bump metallization

The UBM layer is deposited on the flip-chip bonding pads to serve as a diffusion barrier between the indium interconnects and the Al wiring layer. The process flow is shown in Fig. 3.8.

Resist mask (bilayer for lift-off).

- Sacrificial layer: spin 950k PMMA-A2 ($\sim$ 50 nm) at 4000 rpm, 2000 rpm/s, bake at 180 °C for 5 min, cool on cold plate for 30 s.
- LOR-3A: spin at 2000 rpm, 1000 rpm/s, bake at 180 °C for 5 min, cool on cold plate for 30 s.
- SPR220-3.0: spin at 3000 rpm, 1500 rpm/s, bake at 115 °C for 90 s, cool on cold plate for 30 s.

Optical lithography (MLA).

- Dose: 220 mJ cm^{-2}, defocus: +2.
- Expose with substrate angle correction for global alignment.

Developing.

- Develop SPR220-3.0 in MF-24A for 60 s with paddle agitation; rinse in water for 30 s; rinse in QDR. Inspect optically.
- UV flood exposure (SUSS MJB3 UV 400): 45 s, to prevent bubble formation in the resist.
- Ash sacrificial PMMA and clean resist residue in O_2 plasma (RIE #419): 50 W, 90 s.

NbN sputtering (DCA metal cluster).

- Verify chamber pressure $P_{\mathrm{MC}} \lesssim 1 \times 10^{-8}$ Torr before opening the Ar valve.
- Ar ion mill: 30 s stabilization + 50 s milling to remove native AlO_x.
- Verify P_{MC} recovery to $\sim 1 \times 10^{-8}$ Torr after milling.
- Deposit NbN: 3× 17 nm ($\sim$ 51 nm total).

Lift-off and cleaning.

- Remover 1165 at 80 °C for at least 8 h; fresh 1165 rinse.
- Fresh 1165 with sonication (40%, sweep, 35 kHz) for 3 min.
- Acetone with identical sonication for 3 min.
- IPA with identical sonication for 3 min.
- Blow dry with N_2; inspect optically.

6.3.4 Josephson junctions

The $Al/AlO_x/Al$ junctions are fabricated by shadow evaporation through a bilayer e-beam resist providing the undercut for double-angle deposition. The process flow is shown in Fig. 3.10.

Resist mask (bilayer for lift-off).

- Copolymer EL-12 (MMA 8.5% MAA, 12% ethyl lactate, $\sim$ 600 nm): spin at 3000 rpm, 1500 rpm/s, bake at 180 °C for 5 min.
- PMMA-A6 950k ($\sim$ 300 nm): spin at 6000 rpm, 3000 rpm/s, bake at 180 °C for 5 min.

Electron-beam lithography (Raith EBPG 5200).

- Beam current: 2 nA, acceleration voltage: 100 kV, dose: 800 µC cm^{-2}.

Developing.

- Develop in MIBK:IPA (1:1) for 90 s with paddle agitation. The 1:1 ratio (rather than the standard 1:3 for single-layer PMMA) provides sufficient clearing of the copolymer underlayer to form the undercut required for double-angle evaporation through the ~ 900 nm-thick bilayer.
- Rinse in IPA for 30 s; blow dry with N_2.
- Ash resist residue in O_2 plasma (RIE #419): 50 W, 15 s.

Junction deposition (Plassys 521 e-beam evaporator).

- Pump to $< 5 \times 10^{-8}$ mbar (minimum 6 h, overnight preferred).
- Rotate stage to $\theta_1 = \theta_i + 90°$, where θ_i is the initial wafer-flat angle. Deposit JJ1: 50 nm Al at $\sim 1\,\mathrm{nm\,s^{-1}}$.
- Tunnel barrier oxidation: 2 mbar O_2, 100 sccm static MFC, 20 min. Wait 3 min for the wafer to cool.
- Rotate stage to $\theta_2 = \theta_i + 180°$. Deposit JJ2: 110 nm Al at $\sim 1\,\mathrm{nm\,s^{-1}}$.
- Passivation oxidation: 0.5 nm oxide layer.

Lift-off and cleaning.

- Remove 1165 at 80 °C for at least 6 h (overnight preferred) with the wafer face-down.
- Same stripping and solvent cleaning as the wiring layer (Sec. 6.3.2).

6.3.5 Patch layer

The patch layer provides galvanic contact between junction electrodes and the ground plane by removing the native AlO_x in situ before Al deposition. The process flow is shown in Fig. 3.12.

Resist mask. Same bilayer stack as for junctions (Sec. 6.3.4).

Electron-beam lithography (Raith EBPG 5200). Same as for junctions except the beam current is set to 30 nA.

Developing. Same as for junctions (Sec. 6.3.4).

Deposition (Plassys 521 e-beam evaporator).

- Ar ion mill for 10 min to remove native AlO_x. The stage is rotated during milling to ensure a uniform etch rate across the wafer.
- Deposit 200 nm Al without breaking vacuum.

Lift-off and cleaning. Same as for junctions (Sec. 6.3.4).

6.3.6 Air-bridges

The air-bridge process uses two optical lithography steps: the first defines a reflown resist scaffold for the arched bridge profile, and the second defines an etch mask to protect the bridge geometry during wet etching. The process flow is shown in Fig. 3.14.

First layer: air-bridge pads and scaffold

Resist mask.

- SPR220 ($\sim$2.6 µm): spin at 3000 rpm, 1500 rpm/s, bake at 115 °C for 90 s.

Optical lithography (MLA).

- Dose: 460 mJ cm^{-2}, defocus: -3.
- Expose with substrate angle correction for global alignment.

Developing.

- Develop in AZ Developer : DI water (1:1) for 60 s with paddle agitation; rinse in water for 60 s; rinse in QDR; blow dry with N_2.
- Ash in O_2 plasma (RIE #419): 50 W, 30 s.

Resist reflow.

- Hard-bake on hotplate at 160 °C for 4 min to reflow the unexposed resist into an arched scaffold.
- Post-reflow ash in O_2 plasma (RIE #419): 50 W, 30 s.

Al deposition (Plassys 521 e-beam evaporator).

- Cover wafer alignment marks with scrap Si pieces to preserve them for the second lithography step.
- In-situ Ar ion mill for 1 min with the neutralizer filament turned off to prevent resist hardening.
- Deposit 500 nm Al.

Second layer: etch protection mask

Resist mask.

- AZ 1512 ($\sim$1.3 µm): spin at 4000 rpm, 2000 rpm/s, bake at 100 °C for 50 s.

Optical lithography (MLA).

- Dose: 220 mJ cm^{-2}, defocus: -2.
- Polarity: inverted pattern.
- Expose with substrate angle correction for global alignment.

Developing.

- Develop in AZ Developer: DI water (1:1) for 45 s with paddle agitation; rinse in water for 60 s; rinse in QDR; blow dry with N_2.
- Ash in O_2 plasma (RIE #419): 50 W, 30 s.

Etching.

- Wet etch in Al Etchant Type A at 32 °C for 5 to 5.5 min with gentle manual agitation; continue for 20 to 30 s after the ground plane becomes visible. The lower etch temperature compared to the wiring layer (40 °C) gives a slower, more controllable etch rate for the thin bridge metal.
- Rinse in QDR and blow dry with N_2.

Resist stripping.

- Ash in O_2 plasma (RIE #419): 50 W, 3 min.
- Clean in 1165, acetone, and IPA without ultrasonic agitation to avoid damaging the released bridges.

6.4 Supplementary results

UBM thin-film SEM imaging The SEM images of the UBM thin films in Fig. 6.1 show that all four material stacks form continuous patterned pads without visible cracks or large-scale film breakup. Non-passivated Nb exhibits pronounced edge thickening and appears to have some peeling at the top surface, likely due to oxide induced stress. After Au passivation, both films show a relatively uniform thickness with a well-defined edge. However, the Au passivated films exhibit a markedly coarser, nodular surface texture. Despite the morphological differences between Nb/Au and NbN/Au, both passivated systems yielded functioning superconducting flip-chip devices, whereas non-passivated Nb did not.

6.4.1 Parasitic mode engineering

The most likely sources of parasitic spectral features are standing-wave resonances in the CPW-like lines on the chip, for example, the feedline, the fluxline, and the sample enclosure. Fig. 6.2(a) shows the simulated electric field distribution of the on-chip input-coil structure along with the flux line. The simulated electric-field distribution is concentrated mainly around the coil and air-bridge region, which indicates that the finite input-coil structure can support a high-frequency electromagnetic mode. The lowest simulated

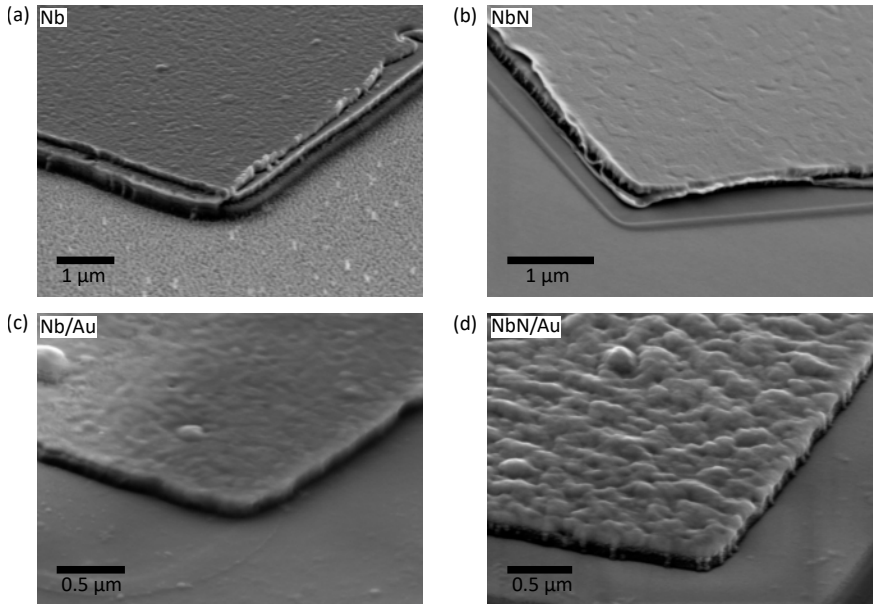

Figure 6.1: SEM images of all four UBM thin films characterized in Paper II.

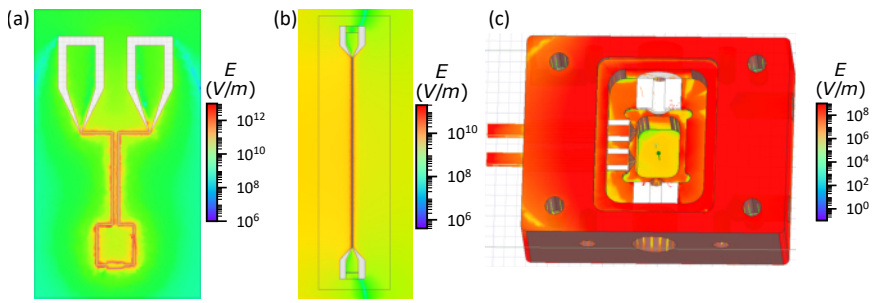

Figure 6.2: Eigenmode simulation of parasitic excitations in (a) on-chip input coil and flux line geometry, (b) feedline geometry, and (c) sample box.

mode appears near 18 GHz. Since the fundamental FTR resonance is close to 6 GHz, this frequency lies near the third harmonic of the resonator. A coupling between the input-coil mode and higher-order resonator modes is therefore plausible. However, this remains speculative because the simulation

does not include the full FTR, in particular, the SQUID loop and the complete resonator structure. At present, this result should therefore be regarded only as an indication that the on-chip coil can introduce an additional parasitic electromagnetic channel, which may contribute to the reduced Q_i observed in the on-chip-coupled FTR.

Fig. 6.2(b) shows the simulated electric field distribution of the feedline, which obtained an eigenfrequency of 8.6 GHz and a coupling quality factor below 1000. This indicates a strong coupling of the standing mode to the nearby structures, including the resonators and the rest of the transmission line. In practice, such a standing mode can be excited due to port impedance mismatch caused by a non-optimized wirebond geometry. Nevertheless, such a spurious mode ideally should not show up in the measurements as it is outside of the measurement window of $4 - 8$ GHz. A similar conclusion can be drawn for the sample box spurious modes, which too lie above 10 GHz for the mode distribution shown in Fig. 6.2(c).

6.5 Homodyne readout

Homodyne detection [109] converts the FTR frequency fluctuations into a baseband voltage, enabling continuous measurement of the mechanical motion.

A small flux modulation $\delta\Phi$ about a dc bias point corresponds to a frequency modulation δf_{res} via the local slope of the tuning curve (Fig. 6.3, upper panel). When a fixed-frequency drive tone is placed on the steep slope of the $|S_{21}|^2$ resonance dip (lower left panel, red line), the resulting frequency shift converts into an amplitude modulation of the transmitted signal. Alternatively, when the drive tone is placed exactly on resonance, small frequency shifts convert into a phase modulation of the signal. The time-domain output (lower right panel) then oscillates at the modulation frequency with an amplitude set by the product of the flux responsivity and the slope of the resonance.

6.5.1 Homodyne principle

In homodyne detection, the transmitted microwave signal is mixed with a local oscillator (LO) at the same frequency to produce a baseband output. Consider a probe signal at frequency ω_p that has passed through the FTR:

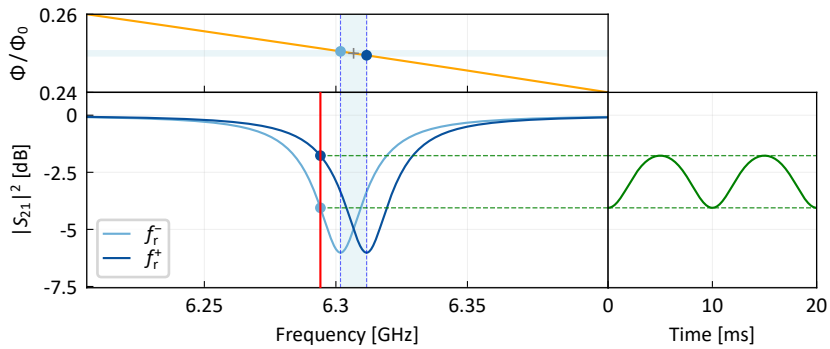

Figure 6.3: FTR transduction mechanism. Upper panel: $f_{\mathrm{res}}(\Phi)$ (orange) near the bias point $\Phi_{\mathrm{bias}} = 0.25\,\Phi_0$. Flux modulation $\delta\Phi$ corresponds to δf_{res} via the local slope. Lower left: $|S_{21}|^2$ dip at the two modulation extremes (blue). Fixed-frequency drive (red) on the resonance slope converts the frequency modulation into amplitude modulation. Lower right: time-domain output with modulation envelope (green).

$$V_{\mathrm{RF}}(t) = A_{\mathrm{RF}} \cos(\omega_p t + \phi), \tag{6.82}$$

$$V_{\mathrm{LO}}(t) = A_{\mathrm{LO}} \cos(\omega_p t), \tag{6.83}$$

where A_{RF} is the transmitted amplitude, ϕ is the phase shift from the resonator, and A_{LO} is the local oscillator amplitude.

An IQ mixer multiplies the microwave signal with in-phase and quadrature LO components, producing

$$I(t) = V_{\mathrm{RF}}(t) \times A_{\mathrm{LO}} \cos(\omega_p t), \tag{6.84}$$

$$Q(t) = -V_{\mathrm{RF}}(t) \times A_{\mathrm{LO}} \sin(\omega_p t). \tag{6.85}$$

Expanding using product-to-sum identities and low-pass filtering to remove the $2\omega_p$ components yields the baseband quadratures:

$$I = \frac{A_{\mathrm{RF}} A_{\mathrm{LO}}}{2} \cos\phi, \tag{6.86}$$

$$Q = \frac{A_{\mathrm{RF}} A_{\mathrm{LO}}}{2} \sin\phi. \tag{6.87}$$

The complex transmission is obtained as $S_{21} = I + iQ$, with amplitude $|S_{21}| = \sqrt{I^2 + Q^2}$ and phase $\arg(S_{21}) = \arctan(Q/I)$.

6.5.2 Transduction chain

The measurement chain converts displacement into a voltage through four stages: (i) displacement to applied flux at the SQUID, $\Phi_e(x) = \Phi_{e,\mathrm{bias}} + (\partial\Phi_e/\partial x)\, x(t)$, (ii) applied flux to resonator frequency via the responsivity, (iii) frequency to complex transmission via the slope of the resonance response, and (iv) transmission to baseband voltage via the homodyne detector. The corresponding transfer relations are

$$\delta\omega_r(t) = \left.\frac{\partial\omega_r}{\partial\Phi_e}\right|_{\Phi_{e,\mathrm{bias}}} \cdot \left.\frac{\partial\Phi_e}{\partial x}\right|_0 \cdot x(t) \equiv G\, x(t), \tag{6.88}$$

$$\delta S_{21}(t) = -\left.\frac{\partial S_{21}}{\partial\omega}\right|_{\omega_p} \delta\omega_r(t), \quad \text{with} \quad \left|\frac{\partial S_{21}}{\partial\omega}\right|_{\omega_p} = \frac{\kappa_c}{(\omega_p - \omega_r)^2 + (\kappa/2)^2}, \tag{6.89}$$

$$V_{\mathrm{out}}(t) = K_{\mathrm{IF}} \cdot \delta S_{21}(t), \tag{6.90}$$

where K_{IF} incorporates the mixer conversion loss, IF amplifier gain, and LO power. The total displacement-to-voltage gain magnitude is

$$K_{\mathrm{total}} = K_{\mathrm{IF}} \cdot \left|\frac{\partial S_{21}}{\partial\omega}\right| \cdot \left|\frac{\partial\omega_r}{\partial\Phi_e}\right| \cdot \left|\frac{\partial\Phi_e}{\partial x}\right|. \tag{6.91}$$

This gain is calibrated experimentally by applying a known modulation of Φ_e with the input coil. The displacement imprecision scales as $\sqrt{S_{xx}^{\mathrm{imp}}} \propto 1/(K_{\mathrm{total}}\sqrt{P_{\mathrm{probe}}})$, with the usable probe power limited by the bifurcation point (Sec. 2.6.8).

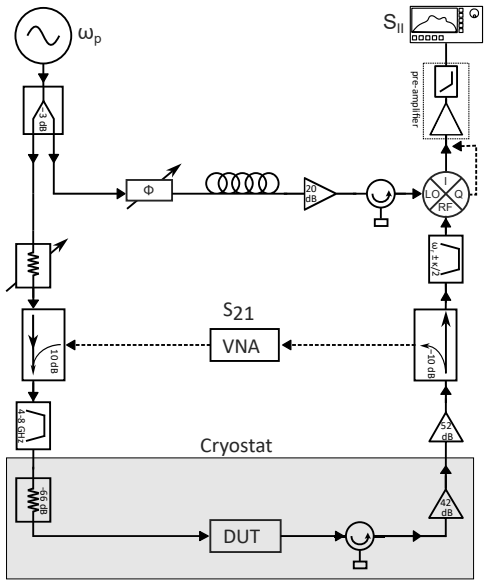

Figure 6.4: Homodyne measurement schematic based on microwave interferometry. A probe tone at ω_p is split into two paths. The RF path is attenuated to the device and amplified to the output. The LO path provides a phase-reference for IQ demodulation, with an adjustable phase shift φ to rotate the complex plane. The in-phase (I) and quadrature (Q) outputs are filtered and amplified before computing the voltage power spectral density.

6.5.3 Homodyne setup

The homodyne chain is shown in Fig. 6.4. A fixed probe tone is placed on the steepest slope of the complex transmission circle, where small resonance-frequency fluctuations appear primarily as phase fluctuations of the transmitted signal [243]. The working point is defined by a flux bias Φ_b and a probe detuning $\Delta = \omega_p - \omega_c(\Phi_b)$, chosen so that the response remains linear and the device operates below the Kerr-induced bifurcation threshold. The LO phase φ_{LO} is adjusted so that the recorded quadrature is maximally frequency-sensitive rather than amplitude-sensitive.

The transfer function from resonance-frequency fluctuations to baseband voltage is calibrated by applying a known current modulation δI through

the input coil at Φ_b and recording the voltage response δV in the frequency-sensitive quadrature. The corresponding frequency shift $\delta\omega = (\partial\omega_r/\partial\Phi) \cdot M\delta I$ is computed from the mutual inductance M and the flux responsivity $\partial\omega_r/\partial\Phi$ obtained independently from spectroscopy, yielding the homodyne transfer function dV/df. The conversion from baseband voltage PSD to frequency-noise PSD and subsequently to flux-noise PSD follows the procedure outlined in Sec. 2.7.

The homodyne readout serves two purposes. First, it quantifies SQUID flux noise in the FTRs under the same wiring and shielding conditions used for device operation. Second, the same readout chain detects the frequency modulation produced by the motion of a levitated microparticle that is flux-coupled to the FTR. Particle motion appears as a narrowband peak in the baseband spectrum, from which the mechanical mode frequency and displacement amplitude can be extracted using a dedicated calibration procedure [101].

CHAPTER 7

Summary of included papers

This thesis is based on three papers that develop the experimental platform needed for magnetomechanical coupling.

Paper A establishes the superconducting levitation platform by demonstrating a chip-based magnetic trap for superconducting microparticles [98]. It provides the trapping architecture on which the later readout and coupling concepts rely.

Paper B develops the superconducting flip-chip integration method used to connect separate chips through reliable galvanic interconnects at millikelvin temperatures [244]. This provides the technological basis for modular device integration in the thesis.

Paper C demonstrates efficient chip-based flux control of flux-tunable superconducting resonators using integrated input coils in both flip-chip and on-chip implementations [102]. This provides the microwave control and readout element required for the long-term magnetomechanical goal of the thesis.

Together, these papers establish the trap, the interconnect, and the flux-tunable microwave resonator platform developed in the thesis.

References

[1] A. Tonomura, J. Endo, T. Matsuda, T. Kawasaki, and H. Ezawa, "Demonstration of single-electron buildup of an interference pattern," *American Journal of Physics*, vol. 57, no. 2, pp. 117–120, 1989. DOI: 10.1119/1.16104.

[2] O. Carnal and J. Mlynek, "Young's double-slit experiment with atoms: A simple atom interferometer," *Physical Review Letters*, vol. 66, no. 21, pp. 2689–2692, 1991. DOI: 10.1103/PhysRevLett.66.2689.

[3] M. Arndt, O. Nairz, J. Vos-Andreae, C. Keller, G. van der Zouw, and A. Zeilinger, "Wave-particle duality of c_{60} molecules," *Nature*, vol. 401, no. 6754, pp. 680–682, 1999. DOI: 10.1038/44348.

[4] Y. Y. Fein et al., "Quantum superposition of molecules beyond 25 kda," *Nature Physics*, vol. 15, no. 12, pp. 1242–1245, 2019. DOI: 10.1038/s41567-019-0663-9.

[5] S. Pedalino, B. E. Ramírez-Galindo, R. Ferstl, K. Hornberger, M. Arndt, and S. Gerlich, "Probing quantum mechanics with nanoparticle matter-wave interferometry," *Nature*, vol. 649, pp. 866–870, 2026. DOI: 10.1038/s41586-025-09917-9.

[6] J. R. Friedman, V. Patel, W. Chen, S. K. Tolpygo, and J. E. Lukens, "Quantum superposition of distinct macroscopic states," *Nature*, vol. 406, no. 6791, pp. 43–46, 2000. DOI: 10.1038/35017505.

[7] C. H. van der Wal et al., "Quantum superposition of macroscopic persistent-current states," *Science*, vol. 290, no. 5492, pp. 773–777, 2000. DOI: 10.1126/science.290.5492.773.

[8] M. Bild et al., "Schrödinger cat states of a 16-microgram mechanical oscillator," *Science*, vol. 380, no. 6642, pp. 274–278, 2023. DOI: 10.1126/science.adf7553.

[9] E. Joos and H. D. Zeh, "The emergence of classical properties through interaction with the environment," *Zeitschrift für Physik B Condensed Matter*, vol. 59, pp. 223–243, 1985. DOI: 10.1007/BF01725541.

[10] W. H. Zurek, "Decoherence, einselection, and the quantum origins of the classical," *Reviews of Modern Physics*, vol. 75, pp. 715–775, 2003. DOI: 10.1103/RevModPhys.75.715.

[11] M. Schlosshauer, "Decoherence, the measurement problem, and interpretations of quantum mechanics," *Reviews of Modern Physics*, vol. 76, pp. 1267–1305, 2004. DOI: 10.1103/RevModPhys.76.1267.

[12] M. Arndt and K. Hornberger, "Testing the limits of quantum mechanical superpositions," *Nature Physics*, vol. 10, pp. 271–277, 2014. DOI: 10.1038/nphys2863.

[13] G. C. Ghirardi, A. Rimini, and T. Weber, "Unified dynamics for microscopic and macroscopic systems," *Physical Review D*, vol. 34, pp. 470–491, 1986. DOI: 10.1103/PhysRevD.34.470.

[14] G. C. Ghirardi, P. Pearle, and A. Rimini, "Markov processes in hilbert space and continuous spontaneous localization of systems of identical particles," *Physical Review A*, vol. 42, no. 1, pp. 78–89, 1990. DOI: 10.1103/PhysRevA.42.78.

[15] A. Bassi, K. Lochan, S. Satin, T. P. Singh, and H. Ulbricht, "Models of wave-function collapse, underlying theories, and experimental tests," *Reviews of Modern Physics*, vol. 85, pp. 471–527, 2013. DOI: 10.1103/RevModPhys.85.471.

[16] M. Carlesso, S. Donadi, L. Ferialdi, M. Paternostro, H. Ulbricht, and A. Bassi, "Present status and future challenges of non-interferometric tests of collapse models," *Nature Physics*, vol. 18, pp. 243–250, 2022. DOI: 10.1038/s41567-021-01489-5.

[17] L. Diósi, "Models for universal reduction of macroscopic quantum fluctuations," *Physical Review A*, vol. 40, no. 3, pp. 1165–1174, 1989. DOI: 10.1103/PhysRevA.40.1165.

[18] R. Penrose, "On gravity's role in quantum state reduction," *General Relativity and Gravitation*, vol. 28, pp. 581–600, 1996. DOI: 10.1007/BF02105068.

[19] J. M. Goodkind, "The superconducting gravimeter," *Review of Scientific Instruments*, vol. 70, no. 11, pp. 4131–4152, Nov. 1999. DOI: 10.1063/1.1150092.

[20] C. M. Caves, "Quantum-mechanical radiation-pressure fluctuations in an interferometer," *Physical Review Letters*, vol. 45, pp. 75–79, 1980. DOI: 10.1103/PhysRevLett.45.75.

[21] A. A. Clerk, M. H. Devoret, S. M. Girvin, F. Marquardt, and R. J. Schoelkopf, "Introduction to quantum noise, measurement, and amplification," *Rev. Mod. Phys.*, vol. 82, pp. 1155–1208, 2 Apr. 2010. DOI: 10.1103/RevModPhys.82.1155. [Online]. Available: https://link.aps.org/doi/10.1103/RevModPhys.82.1155.

[22] M. Aspelmeyer, T. J. Kippenberg, and F. Marquardt, "Cavity optomechanics," *Reviews of Modern Physics*, vol. 86, no. 4, pp. 1391–1452, Dec. 2014. DOI: 10.1103/revmodphys.86.1391.

[23] C. Timberlake, G. Gasbarri, A. Vinante, A. Setter, and H. Ulbricht, "Acceleration sensing with magnetically levitated oscillators above a superconductor," *Applied Physics Letters*, vol. 115, no. 22, p. 224 101, 2019. DOI: 10.1063/1.5129145.

[24] D. Carney, G. Krnjaic, D. C. Moore, C. A. Regal, G. Afek, S. Bhave, et al., "Mechanical quantum sensing in the search for dark matter," *Quantum Science and Technology*, vol. 6, p. 024 002, 2021. DOI: 10.1088/2058-9565/abcfcd.

[25] J. D. Teufel et al., "Sideband cooling of micromechanical motion to the quantum ground state," *Nature*, vol. 475, pp. 359–363, 2011. DOI: 10.1038/nature10261.

[26] J. Chan et al., "Laser cooling of a nanomechanical oscillator into its quantum ground state," *Nature*, vol. 478, pp. 89–92, 2011. DOI: 10.1038/nature10461.

[27] U. Delić et al., "Cooling of a levitated nanoparticle to the motional quantum ground state," *Science*, vol. 367, no. 6480, pp. 892–895, 2020. DOI: 10.1126/science.aba3993.

[28] J. D. Teufel, T. Donner, M. A. Castellanos-Beltran, J. W. Harlow, and K. W. Lehnert, "Nanomechanical motion measured with an imprecision below that at the standard quantum limit," *Nature Nanotechnology*, vol. 4, no. 12, pp. 820–823, 2009. DOI: 10.1038/nnano.2009.343.

[29] G. Anetsberger et al., "Measuring nanomechanical motion with an imprecision below the standard quantum limit," *Physical Review A*, vol. 82, 061804(R), 2010. DOI: 10.1103/PhysRevA.82.061804.

[30] T. P. Purdy, R. W. Peterson, and C. A. Regal, "Observation of radiation pressure shot noise on a macroscopic object," *Science*, vol. 339, no. 6121, pp. 801–804, 2013. DOI: 10.1126/science.1231282.

[31] A. D. O'Connell et al., "Quantum ground state and single-phonon control of a mechanical resonator," *Nature*, vol. 464, no. 7289, pp. 697–703, 2010. DOI: 10.1038/nature08967.

[32] T. A. Palomaki, J. D. Teufel, R. W. Simmonds, and K. W. Lehnert, "Entangling mechanical motion with microwave fields," *Science*, vol. 342, no. 6159, pp. 710–713, 2013. DOI: 10.1126/science.1244563.

[33] A. Beccari et al., "Strained crystalline nanomechanical resonators with quality factors above 10 billion," *Nature Physics*, vol. 18, no. 4, pp. 436–441, Feb. 2022, ISSN: 1745-2481. DOI: 10.1038/s41567-021-01498-4. [Online]. Available: http://dx.doi.org/10.1038/s41567-021-01498-4.

[34] A. Cupertino, D. Shin, L. Guo, P. G. Steeneken, M. A. Bessa, and R. A. Norte, "Centimeter-scale nanomechanical resonators with low dissipation," *Nature Communications*, vol. 15, no. 1, May 2024, ISSN: 2041-1723. DOI: 10.1038/s41467-024-48183-7. [Online]. Available: http://dx.doi.org/10.1038/s41467-024-48183-7.

[35] C. Gonzalez-Ballestero, M. Aspelmeyer, L. Novotny, R. Quidant, and O. Romero-Isart, "Levitodynamics: Levitation and control of microscopic objects in vacuum," *Science*, vol. 374, no. 6564, Oct. 2021. DOI: 10.1126/science.abg3027.

[36] J. Millen, T. S. Monteiro, R. Pettit, and A. N. Vamivakas, "Optomechanics with levitated particles," *Reports on Progress in Physics*, vol. 83, no. 2, p. 026 401, 2020. DOI: 10.1088/1361-6633/ab6100.

[37] U. Delić et al., "Levitated cavity optomechanics in high vacuum," *Quantum Science and Technology*, vol. 5, no. 2, p. 025 006, Mar. 2020, ISSN: 2058-9565. DOI: 10.1088/2058-9565/ab7989. [Online]. Available: http://dx.doi.org/10.1088/2058-9565/ab7989.

[38] O. Romero-Isart, L. Clemente, C. Navau, A. Sánchez, and J. I. Cirac, "Quantum magnetomechanics with levitating superconducting microspheres," *Physical Review Letters*, vol. 109, p. 147 205, 2012. DOI: 10.1103/PhysRevLett.109.147205.

[39] M. Gutierrez Latorre, G. Higgins, A. Paradkar, T. Bauch, and W. Wieczorek, "Superconducting microsphere magnetically levitated in an anharmonic potential with integrated magnetic readout," *Physical Review Applied*, vol. 19, p. 054 047, 2023. DOI: 10.1103/PhysRevApplied.19.054047.

[40] J. Cunill-Subiranas et al., "Macroscopic quantum interference of levitated superconducting microparticles in magnetic higher-order traps," Manuscript in preparation, 2026.

[41] V. Jain, J. Gieseler, C. Moritz, C. Dellago, R. Quidant, and L. Novotny, "Direct measurement of photon recoil from a levitated nanoparticle," *Physical Review Letters*, vol. 116, p. 243 601, 2016. DOI: 10.1103/PhysRevLett.116.243601.

[42] E. Hebestreit, R. Reimann, M. Frimmer, and L. Novotny, "Measuring the internal temperature of an optically levitated nanoparticle in high vacuum," *Physical Review A*, vol. 97, p. 043 803, 2018. DOI: 10.1103/PhysRevA.97.043803.

[43] G. P. Conangla, F. Ricci, M. T. Cuairan, A. W. Schell, N. Meyer, and R. Quidant, "Optimal feedback cooling of a charged levitated nanoparticle with adaptive control," *Physical Review Letters*, vol. 122, p. 223 602, 2019. DOI: 10.1103/PhysRevLett.122.223602.

[44] L. Dania, D. S. Bykov, C. Knoll, P. Mestres, and T. E. Northup, "Optical and electrical feedback cooling of a silica nanoparticle levitated in a paul trap," *Physical Review Research*, vol. 3, p. 013 018, 2021. DOI: 10.1103/PhysRevResearch.3.013018.

[45] M. Brownnutt, M. Kumph, P. Rabl, and R. Blatt, "Ion-trap measurements of electric-field noise near surfaces," *Reviews of Modern Physics*, vol. 87, pp. 1419–1482, 2015. DOI: 10.1103/RevModPhys.87.1419.

[46] J. Prat-Camps, C. Teo, C. Rusconi, W. Wieczorek, and O. Romero-Isart, "Ultrasensitive inertial and force sensors with diamagnetically levitated magnets," *Physical Review Applied*, vol. 8, no. 3, p. 034 002, Sep. 2017. DOI: 10.1103/PhysRevApplied.8.034002.

[47] A. Vinante, P. Falferi, G. Gasbarri, A. Setter, C. Timberlake, and H. Ulbricht, "Ultralow mechanical damping with meissner-levitated ferromagnetic microparticles," *Phys. Rev. Applied*, vol. 13, p. 064 027, 6 Jun. 2020. DOI: 10.1103/PhysRevApplied.13.064027.

[48] M. T. Johnsson, G. K. Brennen, and J. Twamley, "Macroscopic superpositions and gravimetry with quantum magnetomechanics," *Scientific Reports*, vol. 6, no. 1, Nov. 2016. DOI: 10.1038/srep37495.

[49] J. Hofer et al., "High-Q magnetic levitation and control of superconducting microspheres at millikelvin temperatures," *Physical Review Letters*, vol. 131, p. 043 603, 2023. DOI: 10.1103/PhysRevLett.131.043603.

[50] R. L. Fagaly, "Superconducting quantum interference device instruments and applications," *Review of Scientific Instruments*, vol. 77, p. 101 101, 2006. DOI: 10.1063/1.2337091.

[51] F. C. Wellstood, C. Urbina, and J. Clarke, "Low-frequency noise in dc superconducting quantum interference devices below 1 K," *Appl. Phys. Lett.*, vol. 50, no. 12, pp. 772–774, Mar. 1987. DOI: 10.1063/1.98041. [Online]. Available: https://doi.org/10.1063/1.98041.

[52] A. Palacios-Laloy, F. Nguyen, F. Mallet, P. Bertet, D. Vion, and D. Esteve, "Tunable resonators for quantum circuits," *Journal of Low Temperature Physics*, vol. 151, no. 3–4, pp. 1034–1042, Jan. 2008. DOI: 10.1007/s10909-008-9774-x.

[53] M. Sandberg et al., "Tuning the field in a microwave resonator faster than the photon lifetime," *Applied Physics Letters*, vol. 92, no. 20, p. 203 501, May 2008. DOI: 10.1063/1.2929367.

[54] M. Hatridge, R. Vijay, D. H. Slichter, J. Clarke, and I. Siddiqi, "Dispersive magnetometry with a quantum limited squid parametric amplifier," *Physical Review B*, vol. 83, p. 134 501, 2011. DOI: 10.1103/PhysRevB.83.134501.

[55] C. M. Caves, "Quantum limits on noise in linear amplifiers," *Phys. Rev. D*, vol. 26, pp. 1817–1839, 8 Oct. 1982. DOI: 10.1103/PhysRevD.26.1817.

[56] N. Bergeal et al., "Phase-preserving amplification near the quantum limit with a josephson ring modulator," *Nature*, vol. 465, pp. 64–68, 2010. DOI: 10.1038/nature09035.

[57] C. Macklin, K. O'Brien, D. Hover, M. E. Schwartz, I. Siddiqi, and R. McDermott, "A near–quantum-limited josephson traveling-wave parametric amplifier," *Science*, vol. 350, pp. 307–310, 2015. DOI: 10.1126/science.aaa8525.

[58] M. H. Devoret and R. J. Schoelkopf, "Superconducting circuits for quantum information: An outlook," *Science*, vol. 339, no. 6124, pp. 1169–1174, Mar. 2013. DOI: 10.1126/science.1231930.

[59] I. C. Rodrigues, D. Bothner, and G. A. Steele, "Coupling microwave photons to a mechanical resonator using quantum interference," *Nat. Commun.*, vol. 10, pp. 1–7, 1 Nov. 2019, ISSN: 2041-1723. DOI: 10.1038/s41467-019-12964-2.

[60] D. Zoepfl, M. L. Juan, C. M. Schneider, and G. Kirchmair, "Single-photon cooling in microwave magnetomechanics," *Phys. Rev. Lett.*, vol. 125, p. 023 601, 2 Jul. 2020, ISSN: 10797114. DOI: 10.1103/PHYSREVLETT.125.023601.

[61] D. Zoepfl et al., "Kerr enhanced backaction cooling in magnetomechanics," *Phys. Rev. Lett.*, vol. 130, p. 033 601, 3 Jan. 2023. DOI: 10.1103/PhysRevLett.130.033601.

[62] P. Schmidt et al., "Sideband-resolved resonator electromechanics based on a nonlinear josephson inductance probed on the single-photon level," *Communications Physics*, vol. 3, p. 233, Dec. 2020. DOI: 10.1038/s42005-020-00501-3.

[63] T. Luschmann et al., "Mechanical frequency control in inductively coupled electromechanical systems," *Sci. Rep.*, vol. 12, pp. 1–7, 1 Jan. 2022, ISSN: 2045-2322. DOI: 10.1038/s41598-022-05438-x.

[64] D. Bothner, T. Gaber, M. Kemmler, D. Koelle, and R. Kleiner, "Improving the performance of superconducting microwave resonators in magnetic fields," *arXiv:1101.3185*, 2011.

[65] J. G. Kroll et al., "Magnetic-field-resilient superconducting coplanar waveguide resonators for hybrid circuit quantum electrodynamics experiments," *Physical Review Applied*, vol. 11, p. 064 053, 2019. DOI: 10.1103/PhysRevApplied.11.064053.

[66] P. Schmidt et al., "Remote sensing of a levitated superconductor with a flux-tunable microwave cavity," *Phys. Rev. Appl.*, vol. 22, p. 014 078, 1 Jul. 2024. DOI: 10.1103/PhysRevApplied.22.014078.

[67] H. K. Onnes, "Further experiments with liquid helium. c. on the change of electric resistance of pure metals at very low temperatures etc. iv. the resistance of pure mercury at helium temperatures," in *KNAW, Proceedings*, vol. 13, 1911, pp. 1910–1911.

[68] R. Ochsenfeld and W. Meissner, "Ein neuer effekt bei eintritt der supraleitfhigkeit," *Naturwissenschaften*, vol. 21, pp. 787–788, 1933.

[69] F. London and H. London, "The electromagnetic equations of the supraconductor," *Proceedings of the Royal Society of London. Series A-Mathematical and Physical Sciences*, vol. 149, no. 866, pp. 71–88, 1935.

[70] M. Tinkham, *Introduction to Superconductivity*, 2nd. Mineola, New York: Dover Publications, 2004, ISBN: 978-0-486-13472-7.

[71] C. J. Gorter and H. Casimir, "On supraconductivity I," *Physica*, vol. 1, no. 1–6, pp. 306–320, 1934. DOI: 10.1016/S0031-8914(34)90037-9.

[72] J. Zmuidzinas, "Superconducting microresonators: Physics and applications," *Annu. Rev. Condens. Matter Phys.*, vol. 3, no. 1, pp. 169–214, Mar. 2012. DOI: 10.1146/annurev-conmatphys-020911-125022. [Online]. Available: https://doi.org/10.1146/annurev-conmatphys-020911-125022.

[73] Y. W. Kim, Y. H. Kahng, J.-H. Choi, and S.-G. Lee, "Critical properties of submicrometer-patterned Nb thin film," *IEEE Transactions on Applied Superconductivity*, vol. 19, no. 3, pp. 2649–2652, Jun. 2009. DOI: 10.1109/tasc.2009.2019099.

[74] K. Il'in, M. Siegel, A. Semenov, A. Engel, and H. Hubers, "Critical current of Nb and NbN thin-film structures: The cross-section dependence," *Physica Status Solidi (c)*, vol. 2, no. 5, pp. 1680–1687, Mar. 2005. DOI: 10.1002/pssc.200460811.

[75] V. Ginzburg and L. Landau, "Phenomenological theory," *J. Exp. Theor. Phys. USSR*, vol. 20, no. 1064, p. 17, 1950.

[76] A. A. Abrikosov, "Magnetic properties of superconductors of the second group," *Journal of Experimental and Theoretical Physics*, vol. 5, no. 6, p. 1442, Jan. 1957.

[77] R. Meservey and B. B. Schwartz, "Equilibrium properties: Comparison of experimental results with predictions of the bcs theory," *Superconductivity*, vol. 1, R. D. Parks, Ed., pp. 117–191, 1969.

[78] R. Prozorov, M. Zarea, and J. A. Sauls, "Niobium in the clean limit: An intrinsic type-i superconductor," *Phys. Rev. B*, vol. 106, p. L180505, 18 Nov. 2022. DOI: 10.1103/PhysRevB.106.L180505.

[79] D. K. Finnemore, T. F. Stromberg, and C. A. Swenson, "Superconducting properties of high-purity niobium," *Phys. Rev.*, vol. 149, pp. 231–243, 1 Sep. 1966. DOI: 10.1103/PhysRev.149.231.

[80] D. M. Glowacka, D. J. Goldie, S. Withington, H. Muhammad, G. Yassin, and B. K. Tan, "Development of a NbN deposition process for superconducting quantum sensors," *arXiv*, no. arXiv:1401.2292, 2014. DOI: 10.48550/arXiv.1401.2292.

[81] K. Komenou, T. Yamashita, and Y. Onodera, "Energy gap measurement of niobium nitride," *Physics Letters A*, vol. 28, no. 5, pp. 335–336, Dec. 1968. DOI: 10.1016/0375-9601(68)90319-8.

[82] J. Bardeen, L. N. Cooper, and J. R. Schrieffer, "Theory of superconductivity," *Physical Review*, vol. 108, no. 5, pp. 1175–1204, Dec. 1957. DOI: 10.1103/PhysRev.108.1175.

[83] R. Gross, A. Marx, and F. Deppe, *Applied superconductivity: Josephson effect and Superconducting Electronics*. De Gruyter, 2016.

[84] D. C. Mattis and J. Bardeen, "Theory of the anomalous skin effect in normal and superconducting metals," *Phys. Rev.*, vol. 111, no. 2, pp. 412–417, 1958. DOI: 10.1103/PhysRev.111.412.

[85] A. J. Annunziata et al., "Tunable superconducting nanoinductors," *Nanotechnology*, vol. 21, no. 44, p. 445 202, 2010.

[86] D. Niepce, "Superinductance and fluctuating two-level systems loss and noise in disordered and non-disordered superconducting quantum devices," PhD Thesis, Chalmers University of Technology, Aug. 2020. [Online]. Available: https://research.chalmers.se/en/publication/?id=518627.

[87] P. G. DE GENNES, "Boundary effects in superconductors," *Rev. Mod. Phys.*, vol. 36, pp. 225–237, 1 Jan. 1964. DOI: 10.1103/RevModPhys.36.225. [Online]. Available: https://link.aps.org/doi/10.1103/RevModPhys.36.225.

[88] G. Deutscher and P. G. de Gennes, "Proximity effects.," *Superconductivity. Parks, R. D. (ed.). New York, Marcel Dekker, Inc., 1969.*, vol. 1, Oct. 1969. [Online]. Available: https://www.osti.gov/biblio/4842932.

[89] J. CLARKE, "The proximity effect between superconducting and normal thin films in zero field," *Le Journal de Physique Colloques*, vol. 29, no. C2, Feb. 1968. DOI: 10.1051/jphyscol:1968201.

[90] A. F. Andreev, "The thermal conductivity of the intermediate state in superconductors," *Sov. Phys. JETP*, vol. 19, pp. 1228–1231, 1964.

[91] C. W. Beenakker, "Quantum transport in semiconductor-superconductor microjunctions," *Physical Review B*, vol. 46, no. 19, pp. 12 841–12 844, Nov. 1992. DOI: 10.1103/physrevb.46.12841.

[92] S. Earnshaw, "On the Nature of the Molecular Forces which regulate the Constitution of the Luminiferous Ether," *Transactions of the Cambridge Philosophical Society*, vol. 7, pp. 97–112, 1842, Read March 18, 1839. Vol. VII, Part I. [Online]. Available: https://www.mit.edu/~kardar/research/seminars/Casimir2010/pdf/EarnshawPaper.pdf.

[93] W. Braunbeck, "Free suspension of bodies in electric and magnetic fields," *Zeitschrift fur Physik*, vol. 112, 753–763W, 1939.

[94] W. Braunbeck, "Electrically and magnetically freely suspended bodies," *Umshau 53 (3)*, pp. 68–70, 1953.

[95] M. G. Latorre, "Chip-based magnetic levitation of superconducting microparticles," PhD Thesis, Chalmers University of Technology, Sweden, Jan. 2023. [Online]. Available: `https://research.chalmers.se/publication/533897/file/533897_Fulltext.pdf`.

[96] M. Gutierrez Latorre, J. Hofer, M. Rudolph, and W. Wieczorek, "Chip-based superconducting traps for levitation of micrometer-sized particles in the meissner state," *Superconductor Science and Technology*, vol. 33, no. 10, p. 105 002, 2020. DOI: `10.1088/1361-6668/aba6e1`.

[97] J. D. Jackson, *Classical Electrodynamics*, 3rd. New York: Wiley, 1999, ISBN: 978-0-471-30932-1.

[98] M. Gutierrez Latorre, A. Paradkar, D. Hambraeus, G. Higgins, and W. Wieczorek, "A chip-based superconducting magnetic trap for levitating superconducting microparticles," *IEEE Transactions on Applied Superconductivity*, vol. 32, no. 4, p. 1 800 305, 2022. DOI: `10.1109/TASC.2022.3147730`.

[99] B. Josephson, "Possible new effects in superconductive tunnelling," *Physics Letters*, vol. 1, no. 7, pp. 251–253, Jul. 1962. DOI: `10.1016/0031-9163(62)91369-0`.

[100] C. D. Tesche and J. Clarke, "Dc squid: Noise and optimization," *Journal of Low Temperature Physics*, vol. 29, no. 3–4, pp. 301–331, Nov. 1977, ISSN: 1573-7357. DOI: `10.1007/bf00655097`.

[101] L. F. Deeg, "Inductively coupled electromechanics by utilizing a nonlinear cavity," PhD Thesis, Institute of Experimental Physics, Leopold-Franzens University of Innsbruck, Dec. 2025.

[102] A. Paradkar et al., *Efficient flip-chip and on-chip-based modulation of flux-tunable superconducting resonators*, 2025. DOI: `10.1063/5.0235266`. arXiv: `2512.23119 [quant-ph]`.

[103] K. K. Likharev, *Dynamics of Josephson Junctions and Circuits*. Gordon and Breach, 1986.

[104] V. Ambegaokar and A. Baratoff, "Tunneling between superconductors," *Physical Review Letters*, vol. 10, no. 11, pp. 486–489, Jun. 1963. DOI: `10.1103/physrevlett.10.486`.

[105] A. A. Golubov, M. Y. Kupriyanov, and E. Il'ichev, "The current-phase relation in josephson junctions," *Reviews of Modern Physics*, vol. 76, no. 2, pp. 411–469, 2004. DOI: 10.1103/RevModPhys.76.411.

[106] W. C. Stewart, "Current-voltage characteristics of josephson junctions," *Applied Physics Letters*, vol. 12, pp. 277–280, 1968. DOI: 10.1063/1.1651991.

[107] D. E. McCumber, "Effect of ac impedance on dc voltage-current characteristics of superconductor weak-link junctions," *Journal of Applied Physics*, vol. 39, pp. 3113–3118, 1968. DOI: 10.1063/1.1656743.

[108] R. N. Simons, *Coplanar Waveguide Circuits, Components, and Systems.* New York: Wiley-IEEE Press, 2001, ISBN: 978-0-471-16121-9. DOI: 10.1002/0471224758.

[109] D. M. Pozar, *Microwave Engineering*, 4th. Hoboken, NJ: John Wiley & Sons, 2011, ISBN: 978-0-470-63155-3.

[110] J. M. Gambetta et al., "Investigating surface loss effects in superconducting transmon qubits," *IEEE Trans. Appl. Supercond.*, vol. 27, no. 1, p. 1 700 205, 2017. DOI: 10.1109/TASC.2016.2629670.

[111] C. E. Murray, "Analytical modeling of participation reduction in superconducting coplanar resonator and qubit designs through substrate trenching," *IEEE Trans. Microw. Theory Techn.*, vol. 68, no. 10, pp. 3263–3270, 2020. DOI: 10.1109/TMTT.2020.2998257.

[112] J. Krupka, J. Breeze, A. Centeno, N. Alford, T. Claussen, and L. Jensen, "Measurements of permittivity, dielectric loss tangent, and resistivity of float-zone silicon at microwave frequencies," *IEEE Trans. Microw. Theory Techn.*, vol. 54, no. 11, pp. 3995–4001, 2006. DOI: 10.1109/TMTT.2006.883655.

[113] J. Krupka, P. Kamiński, R. Kozłowski, B. Surma, A. Dierlamm, and M. Kwestarz, "Dielectric properties of semi-insulating silicon at microwave frequencies," *Appl. Phys. Lett.*, vol. 107, no. 8, p. 082 105, 2015. DOI: 10.1063/1.4929503.

[114] C. Wen, "Coplanar waveguide, a surface strip transmission line suitable for nonreciprocal gyromagnetic device applications," in *1969 G-MTT International Microwave Symposium*, 1969, pp. 110–115. DOI: 10.1109/GMTT.1969.1122668.

[115] S. Gevorgian, L. J. P. Linnér, and E. L. Kollberg, "CAD models for shielded multilayered CPW," *IEEE Transactions on Microwave Theory and Techniques*, vol. 43, no. 4, pp. 772–779, Apr. 1995. DOI: 10.1109/22.375223.

[116] J. Gao, "The physics of superconducting microwave resonators," Ph.D. dissertation, California Institute of Technology, Pasadena, CA, 2008. [Online]. Available: https://thesis.library.caltech.edu/2530/.

[117] K. Watanabe, K. Yoshida, and T. A. Kohjiro, "Kinetic inductance of superconducting coplanar waveguides," *Japanese Journal of Applied Physics*, vol. 33, no. 10R, p. 5708, Oct. 1994. DOI: 10.1143/jjap.33.5708.

[118] J. M. Martinis, R. Barends, and A. N. Korotkov, *Calculation of coupling capacitance in planar electrodes*, 2014. arXiv: 1410.3458. [Online]. Available: https://arxiv.org/abs/1410.3458.

[119] M. Göppl et al., "Coplanar waveguide resonators for circuit quantum electrodynamics," *Journal of Applied Physics*, vol. 104, no. 11, p. 113 904, Dec. 2008. DOI: 10.1063/1.3010859.

[120] I. Besedin and A. P. Menushenkov, "Quality factor of a transmission line coupled coplanar waveguide resonator," *EPJ Quantum Technology*, vol. 5, no. 1, Jan. 2018, ISSN: 2196-0763. DOI: 10.1140/epjqt/s40507-018-0066-3. [Online]. Available: http://dx.doi.org/10.1140/epjqt/s40507-018-0066-3.

[121] P. W. Anderson, B. I. Halperin, and C. M. Varma, "Anomalous low-temperature thermal properties of glasses and spin glasses," *The Philosophical Magazine: A Journal of Theoretical Experimental and Applied Physics*, vol. 25, no. 1, pp. 1–9, 1972. DOI: 10.1080/14786437208229210. eprint: https://doi.org/10.1080/14786437208229210. [Online]. Available: https://doi.org/10.1080/14786437208229210.

[122] W. A. Phillips, "Tunneling states in amorphous solids," *J. Low Temp. Phys.*, vol. 7, no. 3-4, pp. 351–360, May 1972.

[123] W. A. Phillips, "Two-level states in glasses," *Rep. Prog. Phys.*, vol. 50, no. 12, pp. 1657–1708, 1987. DOI: 10.1088/0034-4885/50/12/003.

[124] J. Gao et al., "Experimental evidence for a surface distribution of two-level systems in superconducting lithographed microwave resonators," *Applied Physics Letters*, vol. 92, no. 15, Apr. 2008. DOI: 10.1063/1.2906373.

[125] C. Müller, J. H. Cole, and J. Lisenfeld, "Towards understanding two-level-systems in amorphous solids: Insights from quantum circuits," *Rep. Prog. Phys.*, vol. 82, no. 12, p. 124 501, Nov. 2019. DOI: 10.1088/1361-6633/ab3a7e.

[126] D. Niepce, J. J. Burnett, M. G. Latorre, and J. Bylander, "Geometric scaling of two-level-system loss in superconducting resonators," *Superconductor Science and Technology*, vol. 33, no. 2, p. 025 013, Jan. 2020, ISSN: 13616668. DOI: 10.1088/1361-6668/ab6179.

[127] J. Burnett, A. Bengtsson, D. Niepce, and J. Bylander, "Noise and loss of superconducting aluminium resonators at single photon energies," *Journal of Physics: Conference Series*, vol. 969, p. 012 131, Mar. 2018. DOI: 10.1088/1742-6596/969/1/012131.

[128] P. J. de Visser, J. J. A. Baselmans, P. Diener, S. J. C. Yates, A. Endo, and T. M. Klapwijk, "Number fluctuations of sparse quasiparticles in a superconductor," *Phys. Rev. Lett.*, vol. 106, p. 167 004, 2011. DOI: 10.1103/PhysRevLett.106.167004.

[129] C. Wang et al., "Measurement and control of quasiparticle dynamics in a superconducting qubit," *Nat. Commun.*, vol. 5, p. 5836, 2014. DOI: 10.1038/ncomms6836.

[130] A. P. Vepsäläinen et al., "Impact of ionizing radiation on superconducting qubit coherence," *Nature*, vol. 584, pp. 551–556, 2020. DOI: 10.1038/s41586-020-2619-8.

[131] M. Wallquist, V. S. Shumeiko, and G. Wendin, "Selective coupling of superconducting charge qubits mediated by a tunable stripline cavity," *Phys. Rev. B*, vol. 74, p. 224 506, 22 Dec. 2006. DOI: 10.1103/PhysRevB.74.224506. [Online]. Available: https://link.aps.org/doi/10.1103/PhysRevB.74.224506.

[132] W. Wustmann and V. Shumeiko, "Parametric resonance in tunable superconducting cavities," *Phys. Rev. B*, vol. 87, p. 184 501, 2013. DOI: 10.1103/PhysRevB.87.184501.

[133] P. E. Schmidt, "Nanomechanical quantum systems," PhD Thesis, Walther-Meißner-Institut für Tieftemperaturforschung der Bayerischen Akademie der Wissenschaften, Feb. 2020. [Online]. Available: https://www.wmi.badw.de/fileadmin/WMI/Publications/Schmidt_Philip_Doktorarbeit_2020.pdf.

[134] I. C. Corveira Rodrigues, "Coupling harmonic oscillators to superconducting quantum interference cavities," PhD Thesis, Delft University of Technology, Aug. 2021. [Online]. Available: https://doi.org/10.4233/uuid:90c588b1-ebef-4ab8-b51f-b3221d8ad6cc.

[135] I. Siddiqi et al., "Direct observation of dynamical bifurcation between two driven oscillation states of a josephson junction," *Phys. Rev. Lett.*, vol. 94, no. 2, p. 027 005, Jan. 2005. DOI: 10.1103/PhysRevLett.94.027005. [Online]. Available: https://doi.org/10.1103/PhysRevLett.94.027005.

[136] V. E. Manucharyan, E. Boaknin, M. Metcalfe, R. Vijay, I. Siddiqi, and M. Devoret, "Microwave bifurcation of a josephson junction: Embedding-circuit requirements," *Phys. Rev. B*, vol. 76, p. 014 524, 1 Jul. 2007. DOI: 10.1103/PhysRevB.76.014524. [Online]. Available: https://link.aps.org/doi/10.1103/PhysRevB.76.014524.

[137] L. F. Deeg, D. Zoepfl, N. Diaz-Naufal, M. L. Juan, A. Metelmann, and G. Kirchmair, "Optomechanical backaction in the bistable regime," *Phys. Rev. Appl.*, vol. 23, p. 014 082, 1 Jan. 2025. DOI: 10.1103/PhysRevApplied.23.014082.

[138] N. Diaz-Naufal et al., "Kerr-enhanced optomechanical cooling in the unresolved-sideband regime," *Phys. Rev. A*, vol. 111, p. 053 505, 5 May 2025. DOI: 10.1103/PhysRevA.111.053505. [Online]. Available: https://link.aps.org/doi/10.1103/PhysRevA.111.053505.

[139] S. Probst, F. B. Song, P. A. Bushev, A. V. Ustinov, and M. Weides, "Efficient and robust analysis of complex scattering data under noise in microwave resonators," *Review of Scientific Instruments*, vol. 86, no. 2, p. 024 706, Feb. 2015. DOI: 10.1063/1.4907935.

[140] M. S. Khalil, M. J. Stoutimore, F. C. Wellstood, and K. D. Osborn, "An analysis method for asymmetric resonator transmission applied to superconducting devices," *Journal of Applied Physics*, vol. 111, no. 5, Mar. 2012. DOI: 10.1063/1.3692073.

[141] C. W. Gardiner and M. J. Collett, "Input and output in damped quantum systems: Quantum stochastic differential equations and the master equation," *Physical Review A*, vol. 31, pp. 3761–3774, 1985. DOI: 10.1103/PhysRevA.31.3761.

[142] D. F. Walls and G. J. Milburn, *Quantum Optics*, 2nd. Berlin: Springer, 2008, ISBN: 978-3-540-28573-1. DOI: 10.1007/978-3-540-28574-8.

[143] R. H. Koch, D. P. DiVincenzo, and J. Clarke, "Model for $1/f$ flux noise in squids and qubits," *Physical Review Letters*, vol. 97, no. 26, p. 267 003, Dec. 2007. DOI: 10.1103/physrevlett.97.267003.

[144] S. M. Anton et al., "Magnetic flux noise in dc squids: Temperature and geometry dependence," *Phys. Rev. Lett.*, vol. 110, p. 147 002, 14 Apr. 2013. DOI: 10.1103/PhysRevLett.110.147002.

[145] S. E. de Graaf et al., "Two-level systems in superconducting quantum devices due to trapped quasiparticles," *Sci. Adv.*, vol. 6, no. 51, eabc5055, Dec. 2020. DOI: 10.1126/sciadv.abc5055.

[146] J. J. Olivero and R. L. Longbothum, "Empirical fits to the voigt line width: A brief review," *J. Quant. Spectrosc. Radiat. Transf.*, vol. 17, no. 2, pp. 233–236, 1977. DOI: 10.1016/0022-4073(77)90161-3.

[147] C. R. Paul, *Inductance loop and partial Clayton R. Paul*. John Wiley & Sons, 2011, p. 126.

[148] D. Griffiths, *Introduction to Electrodynamics*. Pearson Education, 2014, ISBN: 9780321972101. [Online]. Available: https://books.google.co.in/books?id=J9ygBwAAQBAJ.

[149] H. Li, "Flip-chip integrated superconducting quantum processors," PhD Thesis, Chalmers University of Technology, Sweden, Jan. 2025. [Online]. Available: https://research.chalmers.se/publication/544309/file/544309_Fulltext.pdf.

[150] J. Wenner et al., "Wirebond crosstalk and cavity modes in large chip mounts for superconducting qubits," *Superconductor Science and Technology*, vol. 24, no. 6, p. 065 001, Mar. 2011. DOI: 10.1088/0953-2048/24/6/065001.

[151] S. Huang et al., "Microwave package design for superconducting quantum processors," *PRX Quantum*, vol. 2, p. 020 306, 2 Apr. 2021. DOI: 10.1103/PRXQuantum.2.020306.

[152] J. Biznarova, "Development of high-coherence superconducting devices for quantum computing: Fabrication process development, materials analysis, and device characterization," PhD Thesis, Chalmers University of Technology, Sweden, Aug. 2024. [Online]. Available: https://research.chalmers.se/publication/542528/file/542528_Fulltext.pdf.

[153] J. Biznárová et al., "Mitigation of interfacial dielectric loss in aluminum-on-silicon superconducting qubits," *npj Quantum Information*, vol. 10, no. 1, Aug. 2024. DOI: 10.1038/s41534-024-00868-z.

[154] S. Simbierowicz, V. Y. Monarkha, M. von Soosten, S. Andresen, and R. E. Lake, "Calibrated transmission and reflection from a multi-qubit microwave package," *Rev. Sci. Instrum.*, vol. 94, no. 5, p. 054 713, May 2023. DOI: 10.1063/5.0144840. [Online]. Available: https://doi.org/10.1063/5.0144840.

[155] C.-Y. Lee, Y. Liu, and T. Itoh, "The effects of the coupled slotline mode and air-bridges on cpw and nlc waveguide discontinuities," *IEEE Transactions on Microwave Theory and Techniques*, vol. 43, no. 12, pp. 2759–2765, 1995. DOI: 10.1109/22.475632.

[156] J. Wenner et al., "Surface loss simulations of superconducting coplanar waveguide resonators," *Appl. Phys. Lett.*, vol. 99, no. 11, p. 113 513, Sep. 2011. DOI: 10.1063/1.3637047. [Online]. Available: https://doi.org/10.1063/1.3637047.

[157] G. Ponchak, J. Papapolymerou, and M. Tentzeris, "Excitation of coupled slotline mode in finite-ground cpw with unequal ground-plane widths," *IEEE Transactions on Microwave Theory and Techniques*, vol. 53, no. 2, pp. 713–717, Feb. 2005. DOI: 10.1109/tmtt.2004.840571.

[158] A. Dunsworth et al., "Characterization and reduction of capacitive loss induced by sub-micron josephson junction fabrication in superconducting qubits," *Applied Physics Letters*, vol. 111, no. 2, Jul. 2017. DOI: 10.1063/1.4993577.

[159] A. Osman, "Scaling superconducting quantum processors: Coherence, frequency targeting and crosstalk," PhD Thesis, Chalmers University of Technology, Sweden, Nov. 2024. [Online]. Available: https://research.chalmers.se/publication/543784/file/543784_Fulltext.pdf.

[160] C. Song et al., "Microwave response of vortices in superconducting thin films of re and al," *Phys. Rev. B*, vol. 79, no. 17, p. 174 512, May 2009. DOI: 10.1103/PhysRevB.79.174512. [Online]. Available: https://doi.org/10.1103/PhysRevB.79.174512.

[161] D. Bothner et al., "Reducing vortex losses in superconducting microwave resonators with microsphere patterned antidot arrays," *Applied Physics Letters*, vol. 100, no. 1, p. 012 601, 2012. DOI: 10.1063/1.3673869. arXiv: 1110.6332 [cond-mat.supr-con].

[162] I. Nsanzineza and B. L. T. Plourde, "Trapping a single vortex and reducing quasiparticles in a superconducting resonator," *Physical Review Letters*, vol. 113, p. 117 002, 2014. DOI: 10.1103/PhysRevLett.113.117002. arXiv: 1405.0256 [cond-mat.supr-con].

[163] G. Stan, S. B. Field, and J. M. Martinis, "Critical field for complete vortex expulsion from narrow superconducting strips," *Phys. Rev. Lett.*, vol. 92, no. 9, p. 097 003, Mar. 2004. DOI: 10.1103/PhysRevLett.92.097003. [Online]. Available: https://doi.org/10.1103/PhysRevLett.92.097003.

[164] B. Chiaro et al., "Dielectric surface loss in superconducting resonators with flux-trapping holes," *Superconductor Science and Technology*, vol. 29, no. 10, p. 104 006, Aug. 2016. DOI: 10.1088/0953-2048/29/10/104006. [Online]. Available: https://doi.org/10.1088/0953-2048/29/10/104006.

[165] J. M. Sage, V. Bolkhovsky, W. D. Oliver, B. Turek, and P. B. Welander, "Study of loss in superconducting coplanar waveguide resonators," *Journal of Applied Physics*, vol. 109, no. 6, Mar. 2011. DOI: 10.1063/1.3552890.

[166] D. P. Pappas, M. R. Vissers, D. S. Wisbey, J. S. Kline, and J. Gao, "Two level system loss in superconducting microwave resonators," *IEEE Transactions on Applied Superconductivity*, vol. 21, no. 3, pp. 871–874, Jun. 2011. DOI: 10.1109/tasc.2010.2097578.

[167] K. Wade and A. Banister, *The Chemistry of Aluminium, Gallium, Indium and Thallium* (Pergamon Texts in Inorganic Chemistry), 1st. Oxford, UK: Pergamon Press, 1973, vol. 12, p. 107, ISBN: 9780080187983. [Online]. Available: https://books.google.se/books?id=QwNPDAAAQBAJ.

[168] R. G. Gordon, X. Liu, R. N. Broomhall-Dillard, and Y. Shi, "Highly conformal diffusion barriers of amorphous niobium nitride," *MRS Proceedings*, vol. 564, p. 335, 1999. DOI: 10.1557/proc-564-335.

[169] S. Kosen et al., "Building blocks of a flip-chip integrated superconducting quantum processor," *Quantum Science and Technology*, vol. 7, no. 3, p. 035 018, Jun. 2022. DOI: 10.1088/2058-9565/ac734b.

[170] R. Das et al., "Interconnect scheme for die-to-die and die-to-wafer-level heterogeneous integration for high-performance computing," in *2019 IEEE 69th Electronic Components and Technology Conference (ECTC)*, 2019, pp. 1611–1621. DOI: 10.1109/ECTC.2019.00248.

[171] C. Thomas et al., "Superconducting routing platform for large-scale integration of quantum technologies," *Materials for Quantum Technology*, vol. 2, no. 3, p. 035 001, Aug. 2022. DOI: 10.1088/2633-4356/ac88ae.

[172] K. S. Il'in, A. Stockhausen, M. Siegel, A. D. Semenov, H. Richter, and H.-W. Hübers, "Nb HEB for THz radiation: Technological issues and proximity effect," in *Proceedings of the 19th International Symposium on Space Terahertz Technology, ISSTT 2008*, 2008, pp. 367–372. [Online]. Available: http://www.nrao.edu/meetings/isstt/papers/2008/2008403408.pdf.

[173] R. N. Das et al., "Cryogenic qubit integration for quantum computing," in *2018 IEEE 68th Electronic Components and Technology Conference (ECTC)*, 2018, pp. 504–514. DOI: 10.1109/ECTC.2018.00080.

[174] D. Hamilton, C. Raub, B. Matthias, E. Corenzwit, and G. Hull, "Some new superconducting compounds," *Journal of Physics and Chemistry of Solids*, vol. 26, no. 3, pp. 665–667, Mar. 1965. DOI: 10.1016/0022-3697(65)90144-7.

[175] S. Leith, M. Vogel, J. Fan, E. Seiler, R. Ries, and X. Jiang, "Superconducting NbN thin films for use in superconducting radio frequency cavities," *Supercond. Sci. Technol.*, vol. 34, no. 2, p. 025 006, Jan. 2021. DOI: 10.1088/1361-6668/abc73b.

[176] S. Kalal, S. Nayak, A. Tayal, J. Birch, R. Rawat, and M. Gupta, "Effect of disorder on superconductivity of NbN thin films studied using x-ray absorption spectroscopy," *J. Phys.: Condens. Matter*, vol. 33, no. 30, p. 305 401, Jun. 2021. DOI: 10.1088/1361-648X/ac00dc.

[177] V. A. Matylitskaya, O. Brunkahl, G. Kothleitner, W. Bock, and B. O. Kolbesen, "Annealing of evaporated and sputtered niobium films in oxygen and nitrogen rich atmospheres by rapid thermal processing (rtp)," *Phys. Status Solidi C*, vol. 4, no. 6, pp. 1802–1816, May 2007. DOI: 10.1002/pssc.200675231.

[178] M. Lucci et al., "Anodization-based process for the fabrication of all niobium nitride Josephson junction structures," *Beilstein J. Nanotechnol.*, vol. 8, pp. 539–546, Mar. 2017. DOI: 10.3762/bjnano.8.58.

[179] F. Lecocq et al., "Junction fabrication by shadow evaporation without a suspended bridge," *Nanotechnology*, vol. 22, no. 31, p. 315 302, Jul. 2011. DOI: 10.1088/0957-4484/22/31/315302.

[180] G. J. Dolan, "Offset masks for lift-off photoprocessing," *Applied Physics Letters*, vol. 31, no. 5, pp. 337–339, Sep. 1977. DOI: 10.1063/1.89690.

[181] J. J. Raftery, "Nonequilibrium quantum simulation in circuit qed," Ph.D. dissertation, Princeton University, Princeton, NJ, 2017. [Online]. Available: http://arks.princeton.edu/ark:/88435/dsp019593tx73k.

[182] R. Simmonds, K. Lang, D. Hite, S. Nam, D. Pappas, and J. Martinis, "Decoherence in josephson phase qubits from junction resonators," *Physical Review Letters*, vol. 93, no. 7, Aug. 2004. DOI: 10.1103/physrevlett.93.077003.

[183] J. M. Martinis et al., "Decoherence in josephson qubits from dielectric loss," *Physical Review Letters*, vol. 95, no. 21, Nov. 2005. DOI: 10.1103/physrevlett.95.210503.

[184] A. Osman et al., "Simplified josephson-junction fabrication process for reproducibly high-performance superconducting qubits," *Applied Physics Letters*, vol. 118, no. 6, Feb. 2021. DOI: 10.1063/5.0037093.

[185] F. Resare, S. Islam Soke, and W. Wieczorek, "Modification of adhesion between microparticles and engineered silicon surfaces," *Journal of Applied Physics*, vol. 138, no. 22, Dec. 2025, ISSN: 1089-7550. DOI: 10.1063/5.0297664. [Online]. Available: http://dx.doi.org/10.1063/5.0297664.

[186] D. J. Inman, *Engineering Vibrations*, 4th. Pearson, 2014, ISBN: 978-0-273-76844-9.

[187] A. Söderqvist, "Cryogenic vibration isolation for low frequency levitation experiments," Individual Project ENG5041. Internal supervisors: Andrea Cammarano, Martin Weides. External supervisors: Witlef Wieczorek, Achintya Paradkar, Master's Thesis, University of Glasgow, James Watt School of Engineering, Glasgow, UK, Jan. 2023.

[188] J. W. Ekin, *Experimental Techniques for Low-Temperature Measurements: Cryostat Design, Material Properties and Superconductor Critical-Current Testing*. Oxford University Press, 2006, ISBN: 978-0-19-857054-7. DOI: 10.1093/acprof:oso/9780198570547.001.0001.

[189] S. Pirro et al., "Vibrational and thermal noise reduction for cryogenic detectors," *Nuclear Instruments and Methods in Physics Research Section A*, vol. 444, no. 1-2, pp. 331–335, 2000. DOI: 10.1016/S0168-9002(99)01376-5.

[190] B. Foxen et al., "Qubit compatible superconducting interconnects," *Quantum Science and Technology*, vol. 3, no. 1, p. 014 005, Nov. 2017. DOI: 10.1088/2058-9565/aa94fc.

[191] D. Rosenberg et al., "3d integrated superconducting qubits," *npj Quantum Information*, vol. 3, no. 1, Oct. 2017. DOI: 10.1038/s41534-017-0044-0.

[192] C. R. Conner et al., "Superconducting qubits in a flip-chip architecture," *Applied Physics Letters*, vol. 118, no. 23, Jun. 2021. DOI: 10.1063/5.0050173.

[193] G. J. Norris et al., "Improved parameter targeting in 3D-integrated superconducting circuits through a polymer spacer process," *EPJ Quantum Technology*, vol. 11, no. 1, p. 5, Jan. 2024. DOI: 10.1140/epjqt/s40507-023-00213-x.

[194] N. S. DeNigris et al., "Fabrication of flexible superconducting wiring with high current-carrying capacity indium interconnects," *Journal of Low Temperature Physics*, vol. 193, no. 5–6, pp. 687–694, Jul. 2018. DOI: 10.1007/s10909-018-2019-8.

[195] T. J. Lucas et al., "Indium bump process for low-temperature detectors and readout," *Journal of Low Temperature Physics*, vol. 209, no. 3–4, pp. 293–298, May 2022. DOI: 10.1007/s10909-022-02728-6.

[196] Q. Huang, G. Xu, Y. Yuan, X. Cheng, and L. Luo, "Development of indium bumping technology through az9260 resist electroplating," *Journal of Micromechanics and Microengineering*, vol. 20, no. 5, p. 055 035, Apr. 2010. DOI: 10.1088/0960-1317/20/5/055035.

[197] M. Plötner, G. Sadowski, S. Rzepka, and G. Blasek, "Aspects of indium solder bumping and indium bump bonding useful for assembling cooled mosaic sensors," *Microelectronics International*, vol. 8, no. 2, pp. 27–30, Feb. 1991. DOI: 10.1108/eb044447.

[198] M. Volpert, L. Roulet, J.-F. Boronat, I. Borel, S. Pocas, and H. Ribot, "Indium deposition processes for ultra fine pitch 3D interconnections," *2010 Proceedings 60th Electronic Components and Technology Conference (ECTC)*, pp. 1739–1745, 2010. DOI: 10.1109/ECTC.2010.5490736.

[199] P. Kozłowski et al., "Indium-based micro-bump array fabrication technology with added pre-reflow wet etching and annealing," *Materials*, vol. 14, no. 21, p. 6269, Oct. 2021. DOI: 10.3390/ma14216269.

[200] CAPLINQ, *In100 pure indium solder spheres*. [Online]. Available: https://www.caplinq.com/solder-spheres.html.

[201] H. Schoeller and J. Cho, "Oxidation and reduction behavior of pure indium," *Journal of Materials Research*, vol. 24, no. 2, pp. 386–393, 2009. DOI: 10.1557/JMR.2009.0040.

[202] Q. Zhao, T. Wang, Y. K. Ryu, R. Frisenda, and A. Castellanos-Gomez, "An inexpensive system for the deterministic transfer of 2d materials," *Journal of Physics: Materials*, vol. 3, no. 1, p. 016 001, Jan. 2020. DOI: 10.1088/2515-7639/ab6a72.

[203] S. Krinner et al., "Engineering cryogenic setups for 100-qubit scale superconducting circuit systems," *EPJ Quantum Technology*, vol. 6, p. 2, May 2019. DOI: 10.1140/epjqt/s40507-019-0072-0.

[204] P. Krantz, M. Kjaergaard, F. Yan, T. P. Orlando, S. Gustavsson, and W. D. Oliver, "A quantum engineer's guide to superconducting qubits," *Applied Physics Reviews*, vol. 6, no. 2, p. 021 318, Jun. 2019. DOI: 10.1063/1.5089550.

[205] M. A. Castellanos-Beltran and K. W. Lehnert, "Widely tunable parametric amplifier based on a superconducting quantum interference device array resonator," *Applied Physics Letters*, vol. 91, no. 8, p. 083 509, Aug. 2007. DOI: 10.1063/1.2773988. [Online]. Available: https://doi.org/10.1063/1.2773988.

[206] G. Ventura, A. Bonetti, L. Lanzi, I. Peroni, A. Peruzzi, and G. Ponti, "Thermal conductivity of the normal and superconducting Al/Si 1% alloy," *Nucl. Phys. B Proc. Suppl.*, vol. 61, no. 3, pp. 576–581, Feb. 1998. DOI: 10.1016/S0920-5632(97)00623-9. [Online]. Available: https://doi.org/10.1016/S0920-5632(97)00623-9.

[207] C. Hickman et al., "Superconducting properties of commercially available solders for low-field applications," *Cryogenics*, vol. 153, p. 104 219, Jan. 2026. DOI: 10.1016/j.cryogenics.2025.104219.

[208] S. Danilin et al., "Engineering the microwave to infrared noise photon flux for superconducting quantum systems," *EPJ Quantum Technol.*, vol. 9, no. 1, p. 1, Jan. 2022. DOI: 10.1140/epjqt/s40507-022-00121-6. [Online]. Available: https://doi.org/10.1140/epjqt/s40507-022-00121-6.

[209] Y. Iwashita, Y. Kuriyama, Y. Fuwa, and H. Tongu, "Magnetic field shield for SC-cavity with thin Nb sheet," in *Proceedings of the 13th International Particle Accelerator Conference*, Geneva, Switzerland: JACoW Publishing, Jun. 2022, pp. 3090–3092, ISBN: 978-3-95450-227-1. DOI: 10.18429/JACoW-IPAC2022-THPOMS052. [Online]. Available: https://doi.org/10.18429/JACoW-IPAC2022-THPOMS052.

[210] R. Benaroya and H. P. Mogensen, "Magnetic shielding by superconducting niobium tin plates," *Journal of Applied Physics*, vol. 37, no. 5, pp. 2162–2166, Apr. 1966. DOI: 10.1063/1.1708752. [Online]. Available: https://doi.org/10.1063/1.1708752.

[211] H. P. Quach and T. C. P. Chui, "Low temperature magnetic properties of metglas 2714A and its potential use as core material for EMI filters," *Cryogenics*, vol. 44, no. 6-8, pp. 445–449, Jun. 2004. DOI: 10.1016/j.cryogenics.2004.01.006. [Online]. Available: https://doi.org/10.1016/j.cryogenics.2004.01.006.

[212] T. J. Sumner, J. M. Pendlebury, and K. F. Smith, "Conventional magnetic shielding," *J. Phys. D: Appl. Phys.*, vol. 20, no. 9, pp. 1095–1101, Sep. 1987. DOI: 10.1088/0022-3727/20/9/001. [Online]. Available: https://doi.org/10.1088/0022-3727/20/9/001.

[213] Z.-Z. Zhou et al., "Magnetic shield design and simulation optimization of metallic magnetic calorimeter in ultra-low temperature working state," *Journal of Low Temperature Physics*, vol. 215, no. 1–2, pp. 46–63, Mar. 2024. DOI: 10.1007/s10909-024-03060-x.

[214] J. Koch et al., "Charge-insensitive qubit design derived from the cooper pair box," *Physical Review A*, vol. 76, no. 4, Oct. 2007. DOI: 10.1103/physreva.76.042319.

[215] H. Nyquist, "Thermal agitation of electric charge in conductors," *Phys. Rev.*, vol. 32, no. 1, pp. 110–113, Jul. 1928. DOI: 10.1103/PhysRev.32.110.

[216] J.-H. Yeh, J. LeFebvre, S. Premaratne, F. C. Wellstood, and B. S. Palmer, "Microwave attenuators for use with quantum devices below 100 mk," *J. Appl. Phys.*, vol. 121, no. 22, p. 224 501, Jun. 2017. DOI: 10.1063/1.4984894. [Online]. Available: https://doi.org/10.1063/1.4984894.

[217] T. Luschmann, "Interfacing microwaves, mechanical vibrations, and sound waves through superconducting quantum circuits," PhD Thesis, Technische Universität München TUM School of Natural Sciences, May 2024. [Online]. Available: https://www.wmi.badw.de/fileadmin/WMI/Publications/Luschmann_Thomas_Doktorarbeit_2024.pdf.

[218] D. M. Zöpfl, "Demonstration of nonlinear enhanced backaction cooling in microwave magnetomechanics," PhD Thesis, Institute of Experimental Physics, Leopold-Franzens University of Innsbruck, Sep. 2022. [Online]. Available: https://ulb-dok.uibk.ac.at/ulbtirolhs/content/titleinfo/8072572.

[219] F. Yan et al., "Spectroscopy of low-frequency noise and its temperature dependence in a superconducting qubit," *Phys. Rev. B*, vol. 85, no. 17, p. 174 521, May 2012. DOI: 10.1103/PhysRevB.85.174521. [Online]. Available: https://doi.org/10.1103/PhysRevB.85.174521.

[220] J. Thomasson and D. Ginsberg, "Magnetic field shielding by a superconducting cylindrical tube of finite length," *Review of Scientific Instruments*, vol. 47, no. 3, pp. 387–388, Mar. 1976. DOI: 10.1063/1.1134637.

[221] A. Zehnder, P. Lerch, S. P. Zhao, T. Nussbaumer, E. C. Kirk, and H. R. Ott, "Proximity effects in Nb/Al–AlO_x–Al/Nb superconducting tunneling junctions," *Physical Review B*, vol. 59, no. 13, pp. 8875–8886, Apr. 1999. DOI: 10.1103/physrevb.59.8875.

[222] M. C. de Ory, D. Rodriguez, M. T. Magaz, V. Rollano, D. Granados, and A. Gomez, "Low loss hybrid Nb/Au superconducting resonators for quantum circuit applications," *arXiv*, no. arXiv:2401.14764, 2024. DOI: 10.48550/arXiv.2401.14764.

[223] L. Sun et al., "The electrical resistivities of nanostructured aluminium films at low temperatures," *Journal of Physics D: Applied Physics*, vol. 50, no. 41, p. 415 302, Sep. 2017. DOI: 10.1088/1361-6463/aa8736.

[224] R. Janninck and D. Whitmore, "Electrical conductivity and thermoelectric power of niobium dioxide," *Journal of Physics and Chemistry of Solids*, vol. 27, no. 6–7, pp. 1183–1187, Jun. 1966. DOI: 10.1016/0022-3697(66)90094-1.

[225] S. Krause et al., "Ambient temperature growth of mono- and polycrystalline NbN nanofilms and their surface and composition analysis," *IEEE Transactions on Applied Superconductivity*, vol. 26, no. 3, pp. 1–5, 2016. DOI: 10.1109/TASC.2016.2529432.

[226] R. F. Averill, L. S. Straus, and W. D. Gregory, "Tunneling measurements of the superconducting energy gap of bulk polycrystalline indium," *Applied Physics Letters*, vol. 20, no. 2, pp. 55–56, Jan. 1972. DOI: 10.1063/1.1654043.

[227] D. Golubev and L. Kuzmin, "Nonequilibrium theory of a hot-electron bolometer with normal metal-insulator-superconductor tunnel junction," *Journal of Applied Physics*, vol. 89, no. 11, pp. 6464–6472, Jun. 2001. DOI: 10.1063/1.1351002.

[228] F. Giazotto, T. T. Heikkilä, A. Luukanen, A. M. Savin, and J. P. Pekola, "Opportunities for mesoscopics in thermometry and refrigeration: Physics and applications," *Reviews of Modern Physics*, vol. 78, no. 1, pp. 217–274, Mar. 2006. DOI: 10.1103/revmodphys.78.217.

[229] B. Karimi, Y.-C. Chang, and J. P. Pekola, "Low temperature characteristics of the metal–superconductor nis tunneling thermometer," *Journal of Low Temperature Physics*, vol. 207, no. 3–4, pp. 220–225, Apr. 2022. DOI: 10.1007/s10909-022-02713-z.

[230] R. A. Anderson and D. M. Ginsberg, "Penetration depth and flux creep in thin superconducting indium films," *Phys. Rev. B*, vol. 5, pp. 4421–4434, 11 Jun. 1972. DOI: 10.1103/PhysRevB.5.4421.

[231] E. Maxwell and O. S. Lutes, "Threshold field properties of some superconductors," *Phys. Rev.*, vol. 95, pp. 333–338, 2 Jul. 1954. DOI: 10.1103/PhysRev.95.333.

[232] L. A. Hall, "Survey of electrical resistivity measurements on 16 pure metals in the temperature range 0 to 273 k," National Bureau of Standards, technical report, 1968. DOI: 10.6028/nbs.tn.365.

[233] A. Megrant et al., "Planar superconducting resonators with internal quality factors above one million," *Applied Physics Letters*, vol. 100, p. 113 510, 2012. DOI: 10.1063/1.3693409.

[234] Y. Zheng, S. Li, Z. Ding, K. Xiong, J. Feng, and H. Yang, "Fabrication of Al/AlOx/Al junctions with high uniformity and stability on sapphire substrates," *Scientific Reports*, vol. 13, no. 1, p. 11 874, Jul. 2023. DOI: 10.1038/s41598-023-39052-2.

[235] M. Watanabe, K. Inomata, T. Yamamoto, and J.-S. Tsai, "Power-dependent internal loss in josephson bifurcation amplifiers," *Physical Review B*, vol. 80, no. 17, p. 174 502, Nov. 2009. DOI: 10.1103/physrevb.80.174502.

[236] K. Uhl, D. Hackenbeck, C. Füger, R. Kleiner, D. Koelle, and D. Bothner, "A flux-tunable yba2cu3o7 quantum interference microwave circuit," *Applied Physics Letters*, vol. 122, no. 18, p. 182 603, May 2023, ISSN: 1077-3118. DOI: 10.1063/5.0146524.

[237] M. F. Gely, A. Sanz Mora, S. Yanai, R. van der Spek, D. Bothner, and G. A. Steele, "Apparent nonlinear damping triggered by quantum fluctuations," *Nature Communications*, vol. 14, no. 1, Nov. 2023, ISSN: 2041-1723. DOI: 10.1038/s41467-023-43128-y. [Online]. Available: http://dx.doi.org/10.1038/s41467-023-43128-y.

[238] J. van Soest, C. Potts, S. Peiter, A. Sanz Mora, and G. Steele, "Multitone microwave frequency locking to a noisy cavity via real-time feedback," *Phys. Rev. Appl.*, vol. 20, p. 034 007, 3 Sep. 2023. DOI: 10.1103/PhysRevApplied.20.034007. [Online]. Available: https://link.aps.org/doi/10.1103/PhysRevApplied.20.034007.

[239] N. E. Frattini, U. Vool, S. Shankar, A. Narla, K. M. Sliwa, and M. H. Devoret, "3-wave mixing josephson dipole element," *Applied Physics Letters*, vol. 110, no. 22, p. 222 603, May 2017. DOI: 10.1063/1.4984142.

[240] N. E. Frattini, V. V. Sivak, A. Lingenfelter, S. Shankar, and M. H. Devoret, "Optimizing the nonlinearity and dissipation of a snail parametric amplifier for dynamic range," *Phys. Rev. Appl.*, vol. 10, p. 054 020, 5 Nov. 2018. DOI: 10.1103/PhysRevApplied.10.054020.

[241] V. Sivak, N. Frattini, V. Joshi, A. Lingenfelter, S. Shankar, and M. Devoret, "Kerr-free three-wave mixing in superconducting quantum circuits," *Phys. Rev. Appl.*, vol. 11, p. 054 060, 5 May 2019. DOI: 10.1103/PhysRevApplied.11.054060.

[242] L. Magrini et al., "Real-time optimal quantum control of mechanical motion at room temperature," *Nature*, vol. 595, no. 7867, pp. 373–377, 2021. DOI: 10.1038/s41586-021-03602-3.

[243] J. Gao, J. Zmuidzinas, B. A. Mazin, H. G. LeDuc, and P. K. Day, "Noise properties of superconducting coplanar waveguide microwave resonators," *Appl. Phys. Lett.*, vol. 90, p. 102 507, 10 Mar. 2007. DOI: 10.1063/1.2711770. [Online]. Available: https://doi.org/10.1063/1.2711770.

[244] A. Paradkar, P. Nicaise, K. Dakroury, F. Resare, and W. Wieczorek, "Superconducting flip-chip devices using indium microspheres on au-passivated nb or NbN as under-bump metallization layer," *Applied Physics Letters*, vol. 126, no. 2, p. 022 601, 2025, ISSN: 0003-6951. DOI: 10.1063/5.0235266.

PAPER A

A Chip-Based Superconducting Magnetic Trap for Levitating Superconducting Microparticles

Martí Gutierrez Latorre, Achintya Paradkar, David Hambraeus, Gerard Higgins, Witlef Wieczorek

IEEE Transactions on Applied Superconductivity **32**, no. 4, 1800305 (2022).
© DOI: 10.1109/TASC.2022.3147730

A Chip-Based Superconducting Magnetic Trap for Levitating Superconducting Microparticles

Martí Gutierrez Latorre, Achintya Paradkar, David Hambraeus, Gerard Higgins, and Witlef Wieczorek

***Abstract*—Magnetically-levitated superconducting microparticles have been recently proposed as a promising platform for performing quantum experiments with particles in the picogram regime. Here, we demonstrate the superconducting technology to achieve chip-based magnetic levitation of superconducting microparticles. We simulate and fabricate a chip-based magnetic trap capable of levitating superconducting particles with diameters from 0.5 μm to 200 μm. The trap consists of two stacked silicon chips, each patterned with a planar multi-winding superconducting coil made of niobium. The two coils generate a magnetic field resembling a quadrupole near the trap center, in which we demonstrate trapping of a spherical 50 μm diameter SnPb microparticle at temperatures of 4 K and 40 mK.**

***Index Terms*—Magnetic levitation, superconducting coils, superconducting devices, quantum technology, integrated devices, finite element method (FEM).**

I. Introduction

SUPERCONDUCTING levitation is a well known phenomenon and allows levitation of objects of vastly different masses [1]. In the context of quantum experiments with macroscopic objects [2], superconducting levitation can enable a novel experimental platform combining ultra-low mechanical dissipation of levitated particles [3]–[6] with the capability to stably trap micrometer-sized objects [7], [8]. Theoretical proposals to realize macroscopic quantum superposition states [9], as well as novel ultra-sensitive force and acceleration sensors [10], [11], have recently been put forward that exploit these unique features.

Manuscript received September 29, 2021; revised January 18, 2022; accepted January 24, 2022. Date of publication February 1, 2022; date of current version March 1, 2022. This work was supported in part by Knut and Alice Wallenberg Foundation through the Wallenberg Academy Fellowship (W.W.), in part by the Wallenberg Center for Quantum Technology (WACQT, A.P.), and in part by Chalmers Excellence Initiative Nano. The work of Gerard Higgins was supported by the Swedish Research Council under Grant 2020-00381. Sample fabrication was performed in the Myfab Nanofabrication Laboratory at Chalmers. Simulations were performed on resources provided by the Swedish National Infrastructure for Computing (SNIC) at Tetralith, Linkping University, partially funded by the Swedish Research Council under Grant 2018-05973. *(Corresponding author: Witlef Wieczorek.)*

Martí Gutierrez Latorre, Achintya Paradkar, David Hambraeus, and Witlef Wieczorek are with the Department of Microtechnology and Nanoscience (MC2), Chalmers University of Technology, 41296 Gothenburg, Sweden (e-mail: gmart@chalmers.se; achintya@chalmers.se; witlef.wieczorek@chalmers.se).

Gerard Higgins is with the Department of Microtechnology and Nanoscience (MC2), Chalmers University of Technology, 41296 Gothenburg, Sweden, and also with the Institute for Quantum Optics and Quantum Information (IQOQI), Austrian Academy of Sciences, 1090 Vienna, Austria (e-mail: higgins@chalmers.se).

Color versions of one or more figures in this article are available at https://doi.org/10.1109/TASC.2022.3147730.

Digital Object Identifier 10.1109/TASC.2022.3147730

Recent experiments have shown initial steps in this direction by levitating micro-magnets on top of superconductors [12]–[16], diamagnetic particles in strong magnetic fields [4], [17], [18], and superconducting microparticles in millimeter-sized superconducting magnetic traps [19], [20]. Levitating a superconducting particle in a fully chip-based, microfabricated trap is advantageous as it enables high magnetic field gradients through miniaturization [21], [22] and a straightforward integration of precisely positioned superconducting circuits for read-out and quantum control of the particle's motion [7]–[10].

In our work, we demonstrate a fully chip-based superconducting levitation platform. We discuss the design, simulation, and fabrication of our trap, and we use this trap in a proof-of-principle demonstration of levitating a 50 μm-diameter superconducting particle. We base the design of our trap on recent theoretical work in which different magnetic trap architectures were analyzed [7], [8], [23]–[25].

II. Chip-Based Superconducting Magnetic Trap

A. Levitation Requirements

In order to stably levitate a diamagnetic particle, first, a three-dimensional magnetic field minimum is required to confine it [24], [26]. The magnetic field distribution used to achieve such a confinement resembles that of an anti-Helmholtz coil configuration. At the levitation point, the magnetic force balances Earth's gravity. Second, to initially lift the particle off the substrate, the magnetic lift force must also overcome adhesive forces between the particle and the substrate. From a simulation of our trap, we expect a lift force of 19 nN on a 50 μm-diameter superconducting sphere in the Meissner state when we apply a current of 0.5 A through the coils. This force greatly exceeds the particle's weight (0.5 nN) and is, for certain particle-substrate interfaces, sufficient to overcome adhesive forces in our experiments. Note that these forces can be as large as 2 μN for a 50 μm metal sphere separated by 0.3 nm from a flat surface [27].

B. Design and Simulation of the Magnetic Trap

The chip-based trap (see Fig. 1) consists of two multi-winding planar superconducting coils microfabricated on two silicon chips, which are stacked on top of each other. The coil separation is given by the 280 μm thickness of one silicon chip. Each coil has ten windings with 2 μm spacing, and each winding has a rectangular cross-section with 30 μm width and 1 μm thickness. The coils are made of niobium and can carry a maximal current of 0.9 A at 4 K, limited by the critical current density of niobium

This work is licensed under a Creative Commons Attribution-NonCommercial-NoDerivatives 4.0 License. For more information, see https://creativecommons.org/licenses/by-nc-nd/4.0/

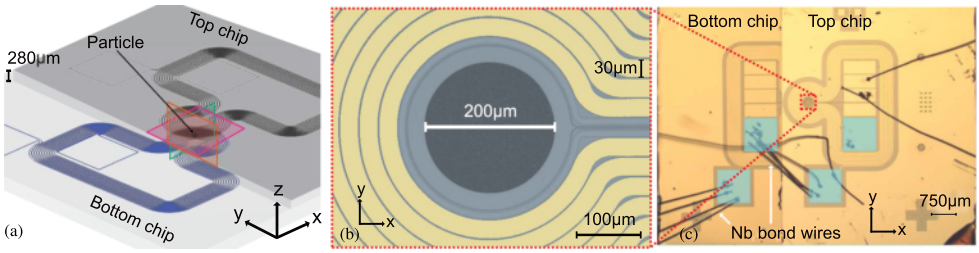

Fig. 1. Chip-based magnetic trap. (a) Schematic of the trap assembly, showing two 280 μm thick silicon chips (top and bottom). The trap coils are colored in blue (bottom) and black (top), and the particle is shown between the coils. The colored rectangles indicate the orthogonal plane cuts used in Fig. 2. (b) False-color scanning electron microscope image of the top chip. The dark gray region is the hole where a particle is placed, the light gray region is the surface of the top silicon chip, and the yellow lines show the windings of the top coil. (c) Assembled two-chip magnetic trap. The bond pads on the chip (light blue) are wire-bonded using 25 μm diameter niobium wires (black lines). The crosses are alignment markers used for etching the hole in panel (b).

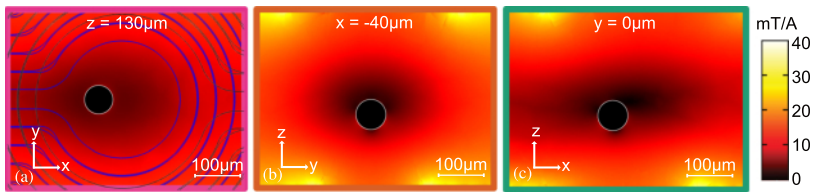

Fig. 2. Simulated magnetic field strength in the trap scaled by the current in the coils, along the (a) xy, (b) yz, and (c) xz planes. The center of the bottom coil defines the origin of the coordinate system. The displacement of each cut plane from the origin is given at the top of each panel. The equilibrium position of the levitated 50 μm-diameter particle (black circle) is displaced from the origin along z due to gravity and along x due to the openings of the superconducting coils. Blue and black lines in (a) mark the projection of the bottom and top coil windings onto the xy slice, respectively.

($3{\cdot}10^{10}$ A/m^2 [28]). The coil dimensions are chosen as a trade-off between the magnetic field strength and the microfabrication yield: Narrower windings with smaller spacing can allow for a stronger magnetic field, due to the dependence of critical current density [28] and current uniformity [29], [30] on cross-section. However, millimeter-long narrow wires frequently detach from the substrate or break during assembly when their height to width ratio exceeds about 0.5.

To simulate the particle in the trap, we account for the three-dimensional geometry of the coils and the particle. We do this because the sample is not symmetric, thus, planar or rotationally symmetric two-dimensional models fail to capture its behavior, and also because the particle perturbs the trap field due to field expulsion [23], [24], [31]. We calculate the magnetic field distribution from finite element method simulations using COMSOL Multiphysics [32]. The simulations operate in the static regime and are based on the A-V formulation of the Maxwell-London equations [33], for details see Ref. [24]. The simulations yield the magnetic field (shown in Fig. 2), magnetic force and supercurrents. We assume that the particle is in the Meissner state and model it via the Maxwell-London equations in A-V formulation [24]. This situation holds when the particle is cooled below its critical temperature in zero field, and if the field near the particle stays below the first critical field of the material that the particle is made of, as is the case in our experiment. The coils are made of a type-II superconductor; we capture this in the model assuming a nearly-perfectly diamagnetic material (relative permeability 0.001) with a high electrical conductivity for the coils, as described in Ref. [30]. Hence, our model assumes that (i) the particle is in the Meissner state, and (ii) that there is no trapped flux in the levitated particle, inside the coil wire or inside the coil windings. Trapped flux would affect the levitation height, trap frequencies and mechanical dissipation.

Fig. 2 shows the trapping magnetic field, with a three-dimensional field minimum between the coils. The particle's equilibrium position is slightly shifted along the z axis due to gravity, and along the x axis due to the openings of the coils.

The simulated magnetic field allows us to estimate the trapped particle's centre-of-mass (COM) motional frequencies: We calculate the restoring force acting on the particle when it is shifted by a small distance from its equilibrium position [24]. In this way, we obtain motional frequencies for a 50 μm particle, $(\omega_x, \omega_y, \omega_z) = 2\pi \times (43 \pm 4, 64 \pm 19, 125 \pm 3)$ Hz when 0.5 A current is passed through the coils (error is simulation uncertainty, see Ref. [24]). These frequencies are much lower than the frequencies of typical micro- and nanomechanical resonators used in quantum experiments [34]. As a consequence, if the motional modes are in thermal states they will have around 10^9 (10^7) phonons at 4 K (10 mK). Thus, in order for the levitated particle to be in its COM motional ground state additional cooling techniques, such as feedback [5], [6] or sideband cooling [35], [36], are required.

The magnetic trap can be used to levitate particles of a huge range of diameters; the lower limit depends on the London penetration depth, λ_L, and the upper limit depends on the first critical field strength of the particle, B_{c_1}, or is given by the

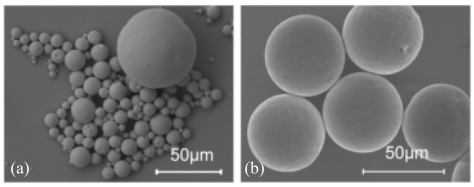

Fig. 3. Scanning electron microscope images of superconducting microspheres used in the experiments. (a) Lead microspheres produced by ultrasonic cavitation. (b) Commercially-available tin-lead microspheres.

geometry of the trap. For example, SnPb particles with diameters from 500 nm to 220 μm could be levitated in our chip-based trap (assuming $\lambda_L = 100$ nm and $B_{c_1} = 40$ mT [37], [38], when using a trap current of 0.5 A).

C. Fabrication

The chip trap is fabricated using conventional microfabrication techniques: The substrate is a double-side-polished, 280 μm-thick, two-inch undoped silicon wafer with (100) orientation. A 1 μm-thick Nb layer is deposited on the wafer by DC magnetron sputtering. The wafer is then diced into 7 mm $\times$ 7 mm chips with a Loadpoint Microace 3+ saw. The design for the magnetic trap is transferred to the Nb layer using electron beam lithography (Raith EBPG 5200) and reactive ion etching (Oxford Plasmalab 100). We etch a cylindrical hole into the top chip using the Bosch process with an STS ICP deep silicon etch system. The two chips are manually aligned using an optical microscope, and glued together using cryogenic GE-varnish. The top and bottom coils are electrically connected by wire bonding with a 25 μm diameter niobium wire as described in Ref. [39]; this ensures a superconducting connection between the coils at temperatures below 9 K. Finally, a single particle is placed within the etched hole using a Signatone SE-10 T tungsten tip attached to a xyz translation stage.

III. Superconducting Microparticles

We use spherical microparticles made of lead (Pb) or a tin-lead alloy (Sn63Pb37), shown in Fig. 3, since lead and tin-lead have critical temperatures higher than 4 K (6.4 K and 7.0 K, respectively). Additionally, they have relatively high first critical field strengths (40 mT and 80 mT respectively [40]). We determined all these values, except for the critical field of lead, using AC magnetic susceptibility measurements.

The Pb microparticles are made in-house using ultrasonic cavitation [41], which yields near-spherical particles with a distribution of diameters between 0.5 μm and 200 μm. The tin-lead microspheres of 50 μm diameter are commercially available (EasySpheres).

IV. Experimental Setup

The chip trap is placed in a dilution refrigerator, which has a viewport that provides optical access to the sample stage. We use a custom-made microscope employing Köhler illumination to monitor the particle on a CMOS camera.

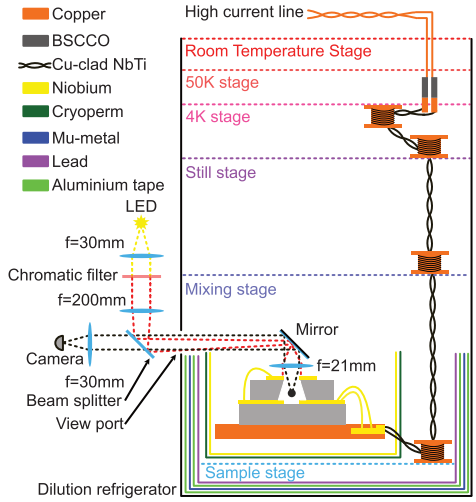

Fig. 4. Schematic of the setup in the dilution refrigerator. The particle (black circle) levitates in the two-chip trap (not to scale) and is imaged using a custom-made microscope with Köhler illumination. The current supplied to the trap coils passes through superconducting wiring from the 50 K stage down to the sample stage. The wires are thermalized at each stage using copper bobbins. The two-chip trap is glued to a copper holder that sits within a multi-layer magnetic shield.

The trap current is supplied by an external current source, that passes through both pre-installed and custom-made wiring, as shown in Fig. 4. It is crucial to thermalize the wiring at each stage, to minimize the heat load at the sample stage. Pre-installed copper wires transport the current from room temperature to the 50 K stage, then a pre-installed superconducting BSCCO tape transports the current to the 4 K stage. At the 4 K stage the BSCCO tape terminates in gold-plated copper connectors, to which we clamp a copper-clad, formvar insulated, 190 μm twisted NbTi wire pair, which transports the current to the sample stage. At the sample stage, the NbTi wire is clamped to bulky Nb bond pads on the sample holder. At either end where the NbTi cable is clamped, the insulation and the cladding are removed to ensure a superconducting connection. The NbTi wire is wound and glued with GE-varnish around copper bobbins, which are attached to different stages for thermalization, as shown in Fig. 4. The chip trap contains microfabricated Nb bond pads [see Fig. 1(c)], which are electrically connected to the bulky Nb bond pads on the sample holder via 25 μm-diameter Nb wire bonds.

The sample is magnetically shielded (Fig. 4) by two open-top baskets made of layers of superconducting and ferromagnetic material: the sample holder lies within a shield made of niobium and Cryoperm, and the entire sample stage lies within a shield made of lead, aluminium and mu-metal.

V. Demonstration of Magnetic Levitation

In Fig. 5 we show images of a SnPb particle in the magnetic trap at a temperature of 4 K (see also video material [42]). When we apply sufficient current to the trap, the particle levitates. This

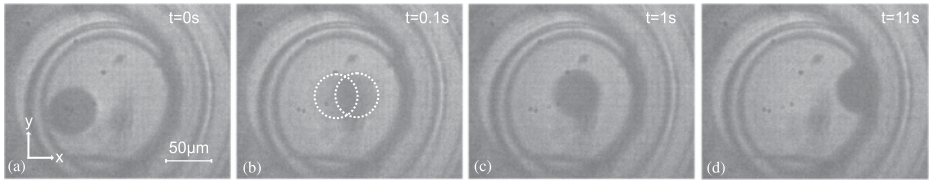

Fig. 5. Top view of a single 50 μm diameter microsphere in the chip trap before (a), during (b, c) and after (d) levitation. The time t is the time after current is applied to the trap coils. (a) The particle rests on the substrate when no current is applied to the trap. (b) The particle levitates and has a large oscillation amplitude when a current of 0.5 A runs through the magnetic trap. The particle is seen as a blur because the oscillation period of the particle's motion is shorter than the camera's exposure time. The white dotted lines are a guide to the eye to identify the particle. (c) The amplitude of the particle motion decreases until it is not resolved. The equilibrium position in (b) and (c) are the same. (d) Particle position after levitation has ceased.

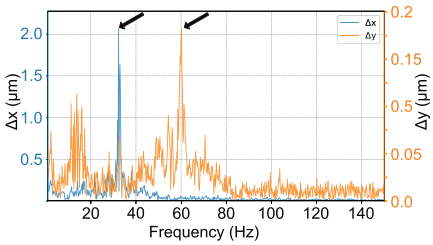

Fig. 6. Frequency spectrum of the particle's motion at a trap current of 0.5 A, along the x and y directions, extracted from analyzing the camera videos.

is evidenced by a sudden change of the particle position from its initial rest position [Fig. 5(a)], additionally the particle becomes blurred because of its oscillatory motion about the trap center [Fig. 5(b)]. The motional amplitude is strongly damped after 1 s [Fig. 5(c)]. After about 10 s the continuous illumination causes superconductivity to break and as a result the particle falls down [Fig. 5(d)]. When we do not shine light on the particle, we can levitate it for several days. We observe similar levitation results when using pure lead microparticles and also when the trap is operated at 40 mK (see also video material [42]).

We extract the particle's motional frequencies from an analysis of the levitation video. To this end, we determine the time-dependent particle center by fitting an ellipse to the particle images and identify the center position of the ellipse with the position of the particle in the xy plane. A Fourier transform of this time-dependent position yields the data in Fig. 6. We can clearly identify two dominant frequency components and attribute these to the COM motional modes along the x and y direction, $(\omega_x, \omega_y) = 2\pi \times (32 \pm 1.6, 60 \pm 1.8)$ Hz, respectively. The frequencies are in good agreement with the simulation results of $(\omega_x, \omega_y) = 2\pi \times (43 \pm 4, 64 \pm 19)$ Hz. We attribute the small discrepancy to the spatial misalignment between the bottom and top coils, as is visible in Fig. 5.

VI. Conclusion and Outlook

We have presented the design, simulation and fabrication of a chip-based superconducting magnetic trap for levitating superconducting microparticles of diameters between 0.5 μm and 200 μm. We have demonstrated stable levitation of 50 μm-diameter superconducting particles in this trap at temperatures of 4 K and 40 mK. In the future, we will lower the particle's motional dissipation rate by using a DC-SQUID magnetometer to detect the particle motion non-invasively and by improving the magnetic field shielding. These are crucial steps to eventually bring the particle's COM motion into the quantum regime.

Note that in an independent recent experiment, chip-based superconducting magnetic levitation of a superconducting microparticle has also been realized [43].

Acknowledgment

The authors would like to thank the Thilo Bauch and Avgust Yurgens for insightful discussions. They acknowledge fruitful exchange with Joachim Hofer, Philip Schmidt, Stefan Minniberger, Michael Trupke, Markus Aspelmeyer, and the other members of the EU Horizon 2020 project MaQSens. They are thankful for initial microfabrication support from David Niepce.

References

[1] F. Moon and P. Chang, *Superconducting Levitation: Applications to Bearings and Magnetic Transportation (A Wiley Interscience Publication Series)*. Hoboken, NJ, USA: Wiley, 1994. [Online]. Available: https://books.google.at/books?id=ARdRAAAAMAAJ

[2] M. Arndt and K. Hornberger, "Testing the limits of quantum mechanical superpositions," *Nat. Phys.*, vol. 10, no. 4, pp. 271–277, 2014. [Online]. Available: http://www.nature.com/doifinder/10.1038/nphys2863

[3] U. Delić *et al.*, "Cooling of a levitated nanoparticle to the motional quantum ground state," *Science*, vol. 367, no. 6480, pp. 892–895, 2020. [Online]. Available: https://science.sciencemag.org/content/367/6480/892

[4] Y. Leng *et al.*, "Mechanical dissipation below 1 μHz with a cryogenic diamagnetic levitated micro-oscillator," *Phys. Rev. Appl.*, vol. 15, no. 2, Feb. 2021, Art. no. 24061.

[5] F. Tebbenjohanns, M. L. Mattana, M. Rossi, M. Frimmer, and L. Novotny, "Quantum control of a nanoparticle optically levitated in cryogenic free space," *Nature*, vol. 595, no. 7867, pp. 378–382, 2021.

[6] L. Magrini *et al.*, "Real-time optimal quantum control of mechanical motion at room temperature," *Nature*, vol. 595, no. 7867, pp. 373–377, 2021.

[7] O. L. Romero-Isart, C. Clemente, A. N. Sanchez, and J. I. Cirac, "Quantum magnetomechanics with levitating superconducting microspheres," *Phys. Rev. Lett.*, vol. 109, Oct. 2012, Art. no. 147205. [Online]. Available: https://link.aps.org/doi/10.1103/PhysRevLett.109.147205

[8] M. G. K. C. Brennen and J. Twamley, "Quantum magnetomechanics: Ultrahigh- Q -Levitated mechanical oscillators," *Phys. Rev. Lett.*, vol. 109, no. 14, 2012, Art. no. 147206. [Online]. Available: http://link.aps.org/doi/10.1103/PhysRevLett.109.147206

[9] H. J. Pino, K. Prat-Camps, B. P. S. Venkatesh, and O. Romero-Isart, "On-chip quantum interference of a superconducting microsphere," *Quantum Sci. Technol.*, vol. 3, no. 2, Jan. 2018, Art. no. 25001, doi: 10.1088/2058-9565/aa9d15

[10] M. T. Johnsson, G. K. Brennen, and J. Twamley, "Macroscopic superpositions and gravimetry with quantum magnetomechanics," *Sci. Rep.*, vol. 6, no. 1, Nov. 2016, Art. no. 37495.

[11] J. Prat-Camps, C. Teo, C. Rusconi, W. Wieczorek, and O. Romero-Isart, "Ultrasensitive inertial and force sensors with diamagnetically levitated magnets," *Phys. Rev. Appl.*, vol. 8, no. 3, Sep. 2017, Art. no. 34002.

[12] M. W. Niemetz, J. T. S. Simola, and J. T. Tuoriniemi, "The oscillating magnetic microsphere: A tool for investigating vorticity in superconductors and superfluids," *Physica B, Condens. Matter*, vol. 280, pp. 559–560, 2000. [Online]. Available: http://www.sciencedirect.com/science/article/pii/S0921452699018645

[13] T. Wang *et al.*, "Dynamics of a ferromagnetic particle levitated over a superconductor," *Phys. Rev. Appl.*, vol. 11, no. 4, Apr. 2019, Art. no. 44041.

[14] C. Timberlake, G. Gasbarri, A. Vinante, A. Setter, and H. Ulbricht, "Acceleration sensing with magnetically levitated oscillators above a superconductor," *Appl. Phys. Lett.*, vol. 115, no. 22, 2019, Art. no. 224101. [Online]. Available: https://aip.scitation.org/doi/10.1063/1.5129145

[15] A. Vinante, P. Falferi, G. Gasbarri, A. Setter, C. Timberlake, and H. Ulbricht, "Ultralow mechanical damping with Meissner-levitated ferromagnetic microparticles," *Phys. Rev. Appl.*, vol. 13, no. 6, Jun. 2020, Art. no. 64027.

[16] J. Gieseler *et al.*, "Single-spin magnetomechanics with levitated micromagnets," *Phys. Rev. Lett.*, vol. 124, Apr. 2020, Art. no. 163604. [Online]. Available: https://link.aps.org/doi/10.1103/PhysRevLett.124.163604

[17] B. R. Slezak, C. W. Lewandowski, J.-F. Hsu, and B. D'Urso, "Cooling the motion of a silica microsphere in a magneto-gravitational trap in ultra-high vacuum," *New J. Phys.*, vol. 20, no. 6, Jun. 2018, Art. no. 63028.

[18] D. Zheng *et al.*, "Room temperature test of the continuous spontaneous localization model using a levitated micro-oscillator," *Phys. Rev. Res.*, vol. 2, 2020, Art. no. 13057. [Online]. Available: https://link.aps.org/doi/10.1103/PhysRevResearch.2.013057

[19] B. van Waarde, "The Lead Zeppelin - A force sensor without a handle," Ph.D. dissertation, Universiteit Leiden, The Netherlands, 2016.

[20] J. Hofer and M. Aspelmeyer *et al.*, 2022, unpublished.

[21] J. Fortágh and C. Zimmermann, "Magnetic microtraps for ultracold atoms," *Rev. Modern Phys.*, vol. 79, pp. 235–289, 2007. [Online]. Available: http://link.aps.org/doi/10.1103/RevModPhys.79.235

[22] V. V. Dikovsky, B. Sokolovsky, C. Z. Henkel, and R. Folman, "Superconducting atom chips: Advantages and challenges," *Eur. Phys. J. D*, vol. 51, pp. 247–259, 2009. [Online]. Available: http://dx.doi.org/10.1140/epjd/e2008-00261-5

[23] J. Hofer and M. Aspelmeyer, "Analytic solutions to the Maxwell–London equations and levitation force for a superconducting sphere in a quadrupole field," *Physica Scripta*, vol. 94, no. 12, Dec. 2019, Art. no. 125508.

[24] M. G. Latorre, J. Hofer, M. Rudolph, and W. Wieczorek, "Chip-based superconducting traps for levitation of micrometer-sized particles in the meissner state," *Supercond. Sci. Technol.*, vol. 33, no. 10, Aug. 2020, Art. no. 105002. [Online]. Available: https://doi.org/10.1088/1361-6668/aba6e1

[25] C. Navau, S. Minniberger, M. Trupke, and A. Sanchez, "Levitation of superconducting microrings for quantum magnetomechanics," *Phys. Rev. B*, vol. 103, no. 17, May 2021, Art. no. 174436.

[26] M. D. Simon and A. K. Geim, "Diamagnetic levitation: Flying frogs and floating magnets (invited)," *J. Appl. Phys.*, vol. 87, no. 9, pp. 6200–6204, 2000. [Online]. Available: http://scitation.aip.org/content/aip/journal/jap/87/9/10.1063/1.372654

[27] S. P. Alvo, M. L. Gauthier, and S. Régnier, "A van der Waals force-based adhesion model for micromanipulation," *J. Adhesion Sci. Technol.*, vol. 24, no. 15/16, pp. 2415–2428, 2010. [Online]. Available: https://hal.archives-ouvertes.fr/hal-00545519

[28] W. R. Hudson and R. J. Jirberg, *Superconducting Properties of Niobium Films*, vol. 6380. Nat. Aeronau. Space Admin., Albuquerque, NM, USA: Tech Library Kafb, 1971. [Online]. Available: https://ntrs.nasa.gov/citations/19710018646

[29] K. Il'in *et al.*, "Influence of thickness, width and temperature on critical current density of Nb thin film structures," *Physica C, Supercond.*, vol. 470, no. 19, pp. 953–956, Oct. 2010. [Online]. Available: https://linkinghub.elsevier.com/retrieve/pii/S0921453410001498

[30] E. F. A. E. Talantsev, W. P. P. Crump, and J. L. Tallon, "Current distribution across type II superconducting films: A new vortex-free critical state," *Sci. Rep.*, vol. 8, pp. 1–9, 2018. [Online]. Available: https://www.nature.com/articles/s41598-018-20279-3

[31] Q.-G. Lin, "Theoretical development of the image method for a general magnetic source in the presence of a superconducting sphere or a long superconducting cylinder," *Phys. Rev. B*, vol. 74, no. 2, 2006, Art. no. 24510. [Online]. Available: http://link.aps.org/doi/10.1103/PhysRevB.74.024510

[32] COMSOL AB, "Comsol multiphysics 5.4," Stockholm, Sweden, 2019. [Online]. Available: www.comsol.com

[33] A. M. Campbell, "An introduction to numerical methods in superconductors," *J. Supercond. Novel Magnetism*, vol. 24, no. 1, pp. 27–33, Jan. 2011.

[34] M. Aspelmeyer, T. J. Kippenberg, and F. Marquardt, "Cavity optomechanics," *Rev. Modern Phys.*, vol. 86, no. 4, pp. 1391–1452, Dec. 2014.

[35] J. Chan *et al.*, "Laser cooling of a nanomechanical oscillator into its quantum ground state," *Nature*, vol. 478, no. 7367, pp. 89–92, 2011. [Online]. Available: http://www.nature.com/doifinder/10.1038/nature10461

[36] J. D. Teufel *et al.*, "Sideband cooling of micromechanical motion to the quantum ground state," *Nature*, vol. 475, no. 7356, pp. 359–363, 2011. [Online]. Available: http://www.nature.com/doifinder/10.1038/nature10261

[37] Y. Tsui, R. Mahmoud, E. Surrey, and D. Hampshire, "Superconducting and mechanical properties of low-temperature solders for joints," *IEEE Trans. Appl. Supercond.*, vol. 26, no. 3, Apr. 2016, Art. no. 6900204, doi: 10.1109/TASC.2016.2536806.

[38] J. M. Lock, "Penetration of magnetic fields into superconductors III. Measurements on thin films of tin, lead and indium," *Proc. Roy. Soc. London. Ser. A. Math. Phys. Sci.*, 1951, vol. 208, pp. 391–408. [Online]. Available: https://royalsocietypublishing.org/doi/10.1098/rspa.1951.0169

[39] W. Jaszczuk, H. J. M. ter Brake, J. Flokstra, D. Veldhuis, R. Stammis, and H. Rogalla, "Bonding of a niobium wire to a niobium thin film," *Meas. Sci. Technol.*, vol. 2, no. 11, pp. 1121–1122, Nov. 1991.

[40] G. Chanin and J. P. Torre, "Critical-field curve of superconducting lead," *Phys. Rev. B*, vol. 5, pp. 4357–4364, Jun. 1972. [Online]. Available: https://link.aps.org/doi/10.1103/PhysRevB.5.4357

[41] H. Friedman, Z. Porat, I. Halevy, and S. Reich, "Formation of metal microspheres by ultrasonic cavitation," *J. Mater. Res.*, vol. 25, no. 4, pp. 633–636, Apr. 2010.

[42] M. G. Latorre, A. Paradkar, D. Hambraeus, G. Higgins, and W. Wieczorek, "Video material and plot data at 10.5281/zenodo.5911190 for: A chip-based superconducting magnetic trap for levitating superconducting microparticles," 2022. [Online]. Available: https://zenodo.org/record/5911190

[43] S. Minniberger and M. Trupke, private communication, 2021.

PAPER B

Superconducting flip-chip devices using indium microspheres on Au-passivated Nb or NbN as under-bump metallization layer

Achintya Paradkar, Paul Nicaise, Karim Dakroury, Fabian Resare, Witlef Wieczorek

Applied Physics Letters **126**, 022601 (2025).
© DOI: 10.1063/5.0235266

Applied Physics Letters

RESEARCH ARTICLE | JANUARY 13 2025

Superconducting flip-chip devices using indium microspheres on Au-passivated Nb or NbN as under-bump metallization layer

Achintya Paradkar ; Paul Nicaise ; Karim Dakroury; Fabian Resare ; Witlef Wieczorek

Check for updates

Appl. Phys. Lett. 126, 022601 (2025)
https://doi.org/10.1063/5.0235266

View Online
Export Citation

Articles You May Be Interested In

Plasma treatment methods to improve indium bump bonding via indium oxide removal

J. Vac. Sci. Technol. B (August 2009)

Au–Sn solder bumps with tungsten silicide based barrier metallization schemes

Appl. Phys. Lett. (October 1995)

First level interconnection based on optimization of Cu stud bump for chip to chip package

AIP Conf. Proc. (December 2018)

10 January 2026 19:02:15

AIP Publishing
Applied Physics Letters
Special Topics Open for Submissions
Learn More

AIP Publishing

Applied Physics Letters ARTICLE pubs.aip.org/aip/apl

Superconducting flip-chip devices using indium microspheres on Au-passivated Nb or NbN as under-bump metallization layer

Cite as: Appl. Phys. Lett. **126**, 022601 (2025); doi: 10.1063/5.0235266
Submitted: 26 August 2024 · Accepted: 3 December 2024 ·
Published Online: 13 January 2025

View Online Export Citation CrossMark

Achintya Paradkar, Paul Nicaise, Karim Dakroury, Fabian Resare, and Witlef Wieczorek[a)]

AFFILIATIONS

Department of Microtechnology and Nanoscience (MC2), Chalmers University of Technology, SE-412 96 Gothenburg, Sweden

[a)]Author to whom correspondence should be addressed: witlef.wieczorek@chalmers.se

ABSTRACT

Superconducting flip-chip interconnects are crucial for the three-dimensional integration of superconducting circuits in sensing and quantum technology applications. We demonstrate a simplified approach for a superconducting flip-chip device using commercially available indium microspheres and an in-house-built transfer stage for bonding two chips patterned with superconducting thin films. We use a gold-passivated niobium or niobium nitride layer as an under-bump metallization (UBM) layer between an aluminum-based superconducting wiring layer and the indium interconnect. At millikelvin temperatures, our flip-chip assembly can transport a supercurrent with tens of milliamperes, limited by the smallest geometric feature size and critical current density of the UBM layer and not by the indium interconnect. We show that the pressed indium interconnect itself can carry a supercurrent exceeding 1 A due to its large size of about 500 μm diameter. Our flip-chip assembly does require neither electroplating nor patterning of indium. The assembly process does not need a flip-chip bonder and can be realized with a transfer stage using a top chip with transparency or through-vias for alignment. These flip-chip devices can be utilized in applications that require few superconducting interconnects carrying large currents at millikelvin temperatures.

© 2025 Author(s). All article content, except where otherwise noted, is licensed under a Creative Commons Attribution (CC BY) license (https://creativecommons.org/licenses/by/4.0/). https://doi.org/10.1063/5.0235266

10 January 2026 19:02:15

Superconducting flip-chip interconnects are pivotal in the integration of superconducting circuits for quantum computing[1–5] and sensing applications.[6,7] A commonly used method employs indium (In) bump bonding as In is superconducting below 3.4 K, ductile,[8] mechanically stable at cryogenic temperatures,[1,2,7] and resilient to thermal cycling[1] and reduces thermal stress between the top and bottom chips.[8,9] However, indium as a bonding material may diffuse into certain superconducting thin films, potentially degrading their superconducting properties. This issue arises when indium is bonded to aluminum (Al), which results in an intermetallic compound that exhibits non-superconducting behavior.[10] Therefore, a commonly used method is to add an under-bump metallization (UBM) layer between the In and Al layers to prevent this diffusion. The UBM layer is usually made with superconductors such as niobium nitride[4,11] or titanium nitride.[1,12] The UBM layer can potentially have a native oxide that must be removed before indium microbumps are deposited to make galvanic contact.

Indium microbumps are typically grown via electroplating[9,13] or evaporation[1,4,5,13] and face-to-face compression bonded using a flip-chip bonder.[1,4,5,14,15] This technique is used in high-density three-dimensional packaging of integrated superconducting qubit processors with small In bumps to accommodate a large number of connections and a small (spacing ≤ 10 μm) and uniform (tilt ≤ 100 μrad) chip separation for scalability.[4,5] However, this approach requires an elaborate fabrication process and a high-precision flip-chip bonder. Alternative flip-chip bonding techniques have been developed to mitigate this problem,[3,16] but they do not provide a galvanic contact necessary for DC transport.

In our work, we present a simplified fabrication and assembly process for making a superconducting flip-chip connection between a superconducting Al wiring layer, which is a commonly used material for superconducting quantum circuits,[1,2,4,5] and a superconducting niobium nitride (NbN) or niobium (Nb) layer as the UBM layer. At temperatures in the range of a few tens of millikelvin to 1.2 K, i.e., the superconducting transition of Al, our flip-chip assembly using passivated UBM layers can carry a supercurrent of tens of mA, which is limited by the geometry of the patterned thin films and the current density of the utilized materials. Our approach targets applications

© Author(s) 2025

that require only a few superconducting connections, allowing for a larger indium bump size. We demonstrate that superconducting flip-chip devices can be assembled using commercially available 300 μm diameter indium microspheres[17] as the bond connection, which, when pressed to a flat cylinder of about 500 μm diameter, can carry a supercurrent of more than 1 A. The microspheres are placed manually on a bottom chip before pressing the bottom and a top chip together using a simple transfer stage,[18] provided that the top chip is made of a transparent substrate (e.g., sapphire used in this work) or contains through-vias for alignment.

Our flip-chip assembly approach uses indium microspheres, eliminating the need to grow and pattern indium microbumps. To connect to a superconducting Al thin film, we demonstrate flip-chip assemblies with the commonly used NbN.[4,11] Importantly, we also show that Nb can be used as a UBM layer, provided that it is capped with a thin Au layer to prevent oxidization. We choose Nb specifically because it exhibits a higher critical current density, which enables high-current devices such as on-chip magnetic traps[19,20] or on-chip solenoids,[21] and its lower intrinsic microwave losses are promising for high-Q superconducting resonators.[22,23] Au is chosen as the passivation layer because it mechanically strengthens the flip-chip bond,[24] and if an Au–In intermetallic compound is formed, it would also be superconducting at millikelvin temperatures.[25]

An overview of the flip-chip device is shown in Fig. 1. It consists of a bottom chip made from silicon and a top chip made from sapphire that allows for *in situ* alignment during assembly due to its transparency. The two chips are galvanically connected through indium microspheres of 300 μm diameter, which, after bonding, give a separation of below 50 μm, see Fig. 1(a). The bottom chip contains an Al wiring layer [Fig. 1(b)], which can be used, for example, to pattern a superconducting circuit. This chip contains large areas ($1.5 \times 2\,\mathrm{mm}^2$) for wire bonding to make external electrical connections to the chip. To make flip-chip interconnects, we pattern and deposit UBM pads on top of the Al layer, upon which we place indium microspheres that connect galvanically to the top chip. The top chip [Fig. 1(b)] consists of a superconducting layer, which can, for example, be shaped as a loop [see Fig. 1(d)] or other geometry. A completed flip-chip device is shown in Fig. 1(c). The fabrication process for thin films of Al (150 nm), Nb (50 nm), NbN (50 nm), and Au (5 nm) is described in detail in the supplementary material S1.

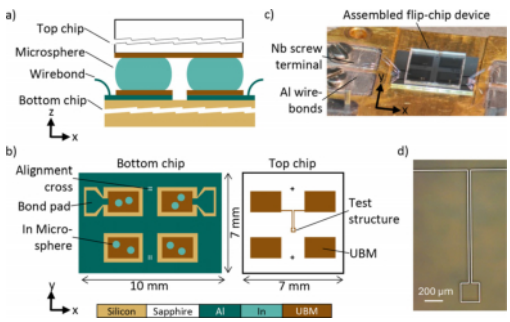

FIG. 1. Schematic representation of a flip-chip device, showing (a) the side view after assembly and (b) the top view before assembly. (c) Photograph of an assembled flip-chip device wire bonded to a copper sample holder. (d) Optical image of a fabricated test structure on a sapphire substrate.

We assembled our flip-chip devices using two different methods: an in-house-built transfer stage [Fig. 2(a)] and a commercial flip-chip bonder [Fig. 2(b)]. The former method is commonly used for the transfer of two-dimensional materials.[18] Both tools create a mechanically sturdy bond with a lateral alignment accuracy of a few micrometers. Details of the assembly procedure are described in the supplementary material S2.

To make a galvanic and robust connection between the chips, we use commercially available 99.99% pure indium microspheres[17] [Fig. 2(c), right panel]. The microspheres have a diameter of $300 \pm 5\,\mu$m and a spheroid tolerance of 1.5%. Although In possesses a native oxide, it normally passivates at a few nanometers.[26] This oxide layer is easily broken during bonding, as In is malleable and deforms significantly when pressed. We typically use two microspheres per pad, but, in principle, a single microsphere per pad would suffice, which would then also allow the UBM pad size to be reduced, enabling us to realize more connections per chip. The applied pressure during the flip-chip bonding process flattens each 300 μm-diameter microspheres into a flat cylinder with a diameter of around 500 μm.

In general, the transfer stage achieved alignment accuracy (5 μm) similar to that of the flip-chip bonder (3 μm). However, the flip-chip bonder achieved a closer chip separation (20 μm) compared to the transfer stage (50 μm). The chip separation can be reduced in future devices using smaller indium microspheres. In addition, an average tilt of 2–3 mrad was obtained with both methods. The results presented in

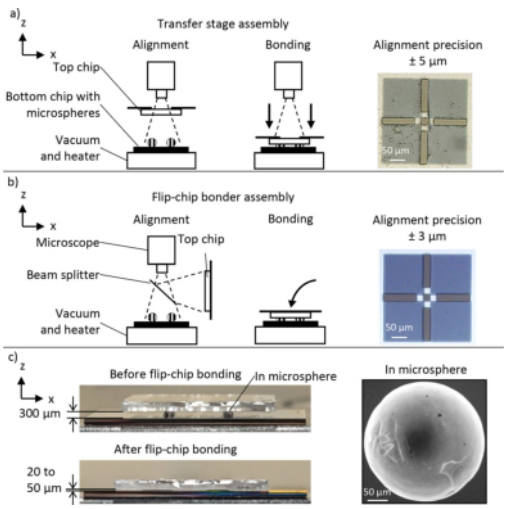

FIG. 2. Schematic of the flip-chip assembly method and picture of the alignment crosses after bonding for (a) the transfer stage and (b) the flip-chip bonder. (c) The flip-chip device before and after bonding. Note that the colors on the bottom panel are light reflections of the surroundings. The close-up is an SEM image of an indium microsphere used for flip-chip bonding.

10 January 2026 19:02:15

© Author(s) 2025

the remainder of this work were obtained using the commercial flip-chip bonder unless otherwise stated.

It is crucial to characterize the material composition and superconducting properties of the utilized UBM thin films in order to realize functioning superconducting flip-chip devices. To this end, we show measurements of the material composition of the UBM thin films using time-of-flight secondary ion mass spectrometry (TOF-SIMS) in order to analyze the potential oxidization of the non-passivated UBM thin films. Figure 3 presents TOF-SIMS depth-profiles of the UBM films, in the case of Nb/Au, NbN, and NbN/Au sputtered on the Al layer of the bottom chip and in the case of Nb sputtered directly on the sapphire substrate of the top chip. The films were analyzed a few weeks after exposure to air. The obtained SIMS data allow us to make qualitative statements about the material composition of the films (for more details, see the supplementary material S4).

We observe that non-passivated Nb and NbN films [Figs. 3(b) and 3(h)] exhibit native Nb oxides of different stoichiometry (NbO, NbO_2, and Nb_2O_5) in the surface region and rapidly decreasing in the bulk region. In contrast, Au-passivated films [Figs. 3(d) and 3(j)] show strong Au signals at the surface with minimal oxide presence [Figs. 3(e) and 3(k)], demonstrating effective passivation. The Nb and NbN layers in all samples demonstrate stable signals throughout the respective UBM film thickness [Figs. 3(a), 3(d), 3(g), and 3(j)]. A sharp increase in the Al signals marks the UBM-Al interface for the Nb/Au, NbN, and NbN/Au thin films and the UBM/sapphire interface for the Nb thin film.

To then characterize the superconducting properties of the UBM thin films, we patterned a test structure to determine the transition temperature T_c and the critical current I_c of the patterned passivated and non-passivated UBM thin films. The test structure is a long wire of 10 μm width and 4740 μm length with a loop of 200 μm diameter in its middle [see Fig. 1(d)]. We performed electrical measurements inside a dilution refrigerator, allowing us to characterize samples down to millikelvin temperature. The details of the measurement setup and procedure are explained in the supplementary material S3.

Figure 4(a) shows the measured voltage and calculated resistance of the test structure as a function of temperature, measured with a bias current of 10 μA. The thin films exhibit a normal-state resistance that is similar to values reported in the literature (see the supplementary material S5). A sharp transition in resistance is observed at the respective T_c (taken as the temperature at which the resistance is at least tenfold the residual resistance), indicating the onset of superconductivity. The respective T_c for the Nb and NbN thin films is 8.0 and 10.4 K, respectively, similar to the values reported in Refs. 27–29. However, T_c of our Nb film is lower than the bulk value of 9.3 K that was also observed in unpatterned thin Nb films.[30] We believe that this could be due to disorder in our film,[31] the presence of native oxides[32] [see Fig. 3(b)], or the geometric constrictions[28] in our test structure. The Au-passivated thin films show a T_c for Nb/Au and NbN/Au of 7.7 and 9.9 K, respectively, slightly lower than their non-passivated counterparts. We attribute this small reduction in T_c to the proximity effect[33] induced by the Au capping layer on Nb[34] or NbN.[27]

Figure 4(b) shows the dependence of the thin film's critical current on the sample temperature. We obtain a similar T_c as in the resistance measurements [Fig. 4(a)]. At temperatures approaching T_c, I_c drops drastically, as expected. We fit the data assuming the simple two-fluid model[35] as ($t = T/T_c$)

$$I_c = I_{c0}(1 - t^4). \tag{1}$$

This fit agrees well with the data, as seen in Fig. 4(b). At a temperature of ~ 100 mK, we determine j_c of the thin films to be 9.26 and 2.5 MA cm^{-2} for Nb and NbN, respectively, similar to other works[28,36] (see the supplementary material S5). The determined j_c of Nb/Au (6.3 MA cm^{-2}) and NbN/Au (3.2 MA cm^{-2}) is close to their non-passivated counterparts. Note that we calculate the critical current density j_c of the thin films considering the relevant geometric feature size of the superconductor, and we assume bulk transport for Nb and NbN and screening transport for Al and In. For simplicity, we neglect the

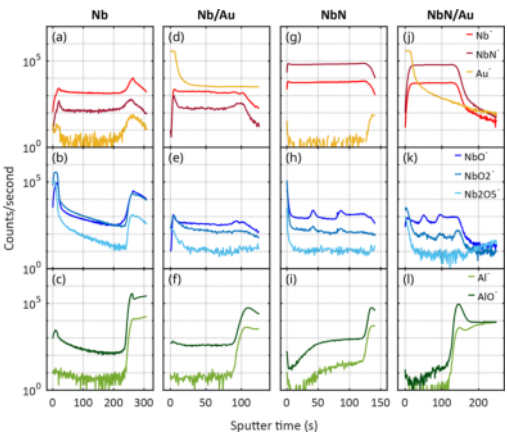

FIG. 3. TOF-SIMS profiles of Nb, Nb/Au, NbN, and NbN/Au thin films acquired with 1 s intervals using Cs^+ primary ions. The plots show the secondary ion rate as a function of sputtering time for key elements and compounds present in the samples. Top panels: UBM metallic ions; middle panels: native Nb oxide ions; bottom panels: Al ions from Al ground plane (for Nb/Au, NbN, and NbN/Au) or sapphire substrate (for Nb).

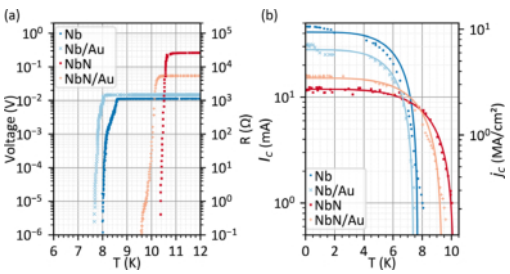

FIG. 4. Measurements of superconducting thin films. (a) Voltage and resistance as a function of temperature at 10 μA bias current. Below the T_c of the respective material, the measured voltage drops to the noise floor, which has been subtracted from the shown data. (b) Critical current and critical current density as a function of temperature. The solid line is a fit using Eq. (1).

10 January 2026 19:02:15

© Author(s) 2025

influence of the proximitization from the metal layer on the current distribution in the UBM layer. Furthermore, we overlook the possibility of sheath transport that could occur in Nb thin films.

Having characterized the UBM thin films, we then assembled flip-chip devices as described earlier. Figure 5(a) shows the measured voltage and calculated resistance of the flip-chip devices as a function of temperature. The flip-chip devices that we patterned with NbN, NbN/Au, or Nb/Au as the UBM layer were fully superconducting at millikelvin temperatures and are, thus, useful devices for making superconducting flip-chip-based interconnects. In contrast, the non-passivated Nb-based flip-chip device showed a finite resistance of some Ohm at millikelvin temperatures. Thus, in the following, we will focus on discussing the functioning NbN, NbN/Au, and Nb/Au-based flip-chip devices.

In Fig. 5(a), we observe transitions at the T_c of the respective superconducting materials. At 1.25 K, all three flip-chip devices show a sharp increase in resistance, which marks the T_c of Al. We estimate a normal-state resistivity of Al to be between 0.68 and 1.6 $\mu\Omega \cdot$ cm, which is comparable to that reported in Ref. 37. The resistance of flip-chip devices that use Au-passivated UBM layers remains constant between the T_c of Al and another sharp transition in resistance at 7.4 K for the Nb/Au and 10.0 K for the NbN/Au flip-chip device. These temperatures mark the respective T_c of the utilized UBM thin films and are similar to those determined for the thin films only. Above their respective T_c, all flip-chip devices exhibit resistance values corresponding to their normal-state resistances, as observed for their respective thin films (see the supplementary material S5).

The non-passivated NbN flip-chip device shows an additional sharp increase in resistance at 3.5 K, which corresponds to the T_c of In. Given the geometry of our In microspheres, we expect their normal-state resistance to be some nΩ, which is well below the observed resistance change. Instead, we attribute the finite resistance to the thin native oxide layer that forms on the surface of the non-passivated NbN film due to exposure to air. Figure 3(h) shows the presence of the NbO_x oxides NbO, NbO_2, and Nb_2O_5 in the non-passivated NbN film. In contrast, oxide growth is effectively prevented in the Au-passivated NbN thin film [see Fig. 3(k)]. We assume that the NbO_x oxide layer acts as an insulator and estimate its resistivity to be of the order of $10^6\ \Omega \cdot$ cm (see the supplementary material S6), which is reasonable for NbO_2 oxide.[38] NbO_2 was also identified in Ref. 39 as a relevant oxide of superconducting NbN thin films. We assume that below the T_c of In, the NbN/NbO_x/In interface forms a superconductor-insulator-superconductor (SIS) connection and, thus, can transport a superconducting current below the critical current of the SIS connection. Using the Ambegaonkar–Baratoff equation, we estimate this critical current to be around 2 mA (see the supplementary material S6). Close to this value, we also observe a finite resistance step in a current-dependent measurement of the NbN flip-chip device (see the supplementary material S6). Above the T_c of In, the interface should behave as a metal-insulator-superconductor (NIS) connection. We then observe that the voltage decreases with an increase in temperature, which is similar to other NIS connections.[40–42] However, to support our interpretation, additional measurements would be required to clearly identify the non-linear behavior of the SIS or NIS junction via determining the current- and voltage-bias characteristics at different temperatures. This we leave to future work.

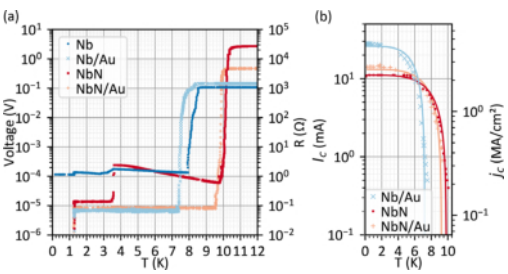

FIG. 5. Measurements of flip-chip devices. (a) Voltage and resistance as a function of temperature at 100 μA bias current. Note that the voltage noise floor has been subtracted from the shown data. (b) Critical current and critical current density as a function of temperature.

Figure 5(b) shows the temperature dependence of the critical current of the functioning flip-chip devices. The critical current behavior of the flip-chip devices is governed by the smallest superconducting structure on the flip-chip device, which, in our case, was the test structure on the top chip's UBM layer [see Fig. 1(d)]. The data are well described by Eq. (1), and the observed T_c values agree well with those determined from the data of Fig. 5(a). The flip-chip devices exhibit slightly lower T_c than their thin-film counterparts, which we attribute to the proximity effect due to the Al layer[43] below the respective UBM layer on each bottom chip. We infer a maximum I_c (j_c) at $\sim$100 mK of 28 mA (5.6 MA cm^{-2}) and 15 mA (3.0 MA cm^{-2}) for the Nb/Au and NbN/Au flip-chip devices, respectively, similar to their thin-film counterparts (see the supplementary material S5).

We also determined the critical current of the indium microsphere-based interconnects (for details, see the supplementary material S7). To this end, we assembled a simplified flip-chip device using the transfer stage, with unpatterned chips of Nb/Au film chosen for its high critical current and absence of oxidation. Two In microspheres were placed on each bottom chip, while a third chip was pressed on top to establish a galvanic connection between the two bottom chips. We used 24 aluminum wire bonds per bond pad to allow the transport of large supercurrents. With this flip-chip device, we could run a supercurrent of up to 2 A (see the supplementary material S7) limited by the maximum output of the current source.

To conclude, we have presented a simple approach for superconducting flip-chip devices using 300 μm diameter indium microspheres for bonding on Au-passivated Nb- or NbN-based UBM layers. Our assembly method achieves chip separations of 20–50 μm with a transversal alignment accuracy of better than 5 μm and a tilt of 2–3 mrad using either a transfer stage or a conventional flip-chip bonder. Smaller chip separations may be achieved using smaller indium microspheres, which would require a smaller pad size. This would also allow for patterning a larger number of pads, thus resulting in more superconducting interconnects per chip.

Our flip-chip assembly is suitable for high-current applications. The indium interconnects, with a pressed diameter of about 500 μm, can carry currents exceeding 1 A at millikelvin temperatures. With patterned superconducting thin films, we have demonstrated that our flip-chip devices could run tens of mA at temperatures below the superconducting transition of Al, which was used as a wiring layer in the bottom chip. We found that although native oxides were present in

10 January 2026 19:02:15

© Author(s) 2025

both non-passivated Nb and NbN flip-chip devices, only the latter were superconducting at millikelvin temperatures. An Au passivation layer enabled functioning Nb flip-chip devices, opening up the possibility for high-current applications since the critical current density of Nb is larger than that of NbN or Al.

The presented flip-chip devices are suitable for various superconducting devices, such as chip-based high-current magnetic traps[19,20] or solenoids,[21] efficient flux readout in SQUID-based sensors,[20,44,45] or transport of supercurrent to flux-tunable superconducting couplers.[46,47] Thus, our flip-chip devices can find applications in superconducting-based sensors[6,7] or superconducting quantum technologies.[1–5,45]

See the supplementary material for details on the microfabrication of flip-chip devices, their assembly, the measurement setup and procedure, additional TOF-SIMS data, collected data, and additional measurements and calculations.

The authors thank Marcus Rommel and Henrik Frederiksen for their support in microfabrication, Hanlin Fang and Thilo Bauch for technical support, and Per Malmberg for performing TOF-SIMS measurements. This work was supported in part by the Horizon Europe 2021-2027 framework program of the European Union under Grant Agreement No. 101080143 (SuperMeQ), the European Research Council under Grant No. 101087847 (ERC Consolidator SuperQLev), the Knut and Alice Wallenberg (KAW) Foundation through a Wallenberg Academy Fellowship (WW), and the Wallenberg Center for Quantum Technology (WACQT, AP). The devices were fabricated at Chalmers Myfab Nanofabrication Laboratory and analyzed in part at Chalmers Materials Analysis Laboratory (CMAL).

AUTHOR DECLARATIONS

Conflict of Interest

The authors have no conflicts to disclose.

Author Contributions

Achintya Paradkar: Conceptualization (equal); Formal analysis (lead); Methodology (equal); Writing – original draft (equal); Writing – review & editing (equal). **Paul Nicaise:** Methodology (equal); Writing – original draft (equal); Writing – review & editing (supporting). **Karim Dakroury:** Methodology (equal); Writing – original draft (equal); Writing – review & editing (supporting). **Fabian Resare:** Methodology (supporting); Writing – original draft (supporting); Writing – review & editing (supporting). **Witlef Wieczorek:** Conceptualization (equal); Supervision (lead); Writing – original draft (equal); Writing – review & editing (equal).

DATA AVAILABILITY

The data that support the findings of this study are openly available in Zenodo at https://doi.org/10.5281/zenodo.13377108 (Ref. 48).

REFERENCES

[1] B. Foxen, J. Y. Mutus, E. Lucero, R. Graff, A. Megrant, Y. Chen, C. Quintana, B. Burkett, J. Kelly, E. Jeffrey *et al.*, "Qubit compatible superconducting interconnects," Quantum Sci. Technol. **3**, 014005 (2018).
[2] D. Rosenberg, D. Kim, R. Das, D. Yost, S. Gustavsson, D. Hover, P. Krantz, A. Melville, L. Racz, G. O. Samach *et al.*, "3D integrated superconducting qubits," npj Quantum Inf. **3**, 42 (2017).
[3] C. R. Conner, A. Bienfait, H.-S. Chang, M.-H. Chou, É. Dumur, J. Grebel, G. A. Peairs, R. G. Povey, H. Yan, Y. P. Zhong *et al.*, "Superconducting qubits in a flip-chip architecture," Appl. Phys. Lett. **118**, 232602 (2021).
[4] S. Kosen, H.-X. Li, M. Rommel, D. Shiri, C. Warren, L. Grönberg, J. Salonen, T. Abad, J. Biznárová, M. Caputo *et al.*, "Building blocks of a flip-chip integrated superconducting quantum processor," Quantum Sci. Technol. **7**, 035018 (2022).
[5] G. J. Norris, L. Michaud, D. Pahl, M. Kerschbaum, C. Eichler, J.-C. Besse, and A. Wallraff, "Improved parameter targeting in 3D-integrated superconducting circuits through a polymer spacer process," EPJ Quantum Technol. **11**, 5 (2024).
[6] N. S. DeNigris, J. A. Chervenak, S. R. Bandler, M. P. Chang, N. P. Costen, M. E. Eckart, J. Y. Ha, C. A. Kilbourne, and S. J. Smith, "Fabrication of flexible superconducting wiring with high current-carrying capacity indium interconnects," J. Low Temp. Phys. **193**, 687–694 (2018).
[7] T. J. Lucas, J. P. Biesecker, W. B. Doriese, S. M. Duff, G. C. Hilton, J. N. Ullom, M. R. Vissers, and D. R. Schmidt, "Indium bump process for low-temperature detectors and readout," J. Low Temp. Phys. **209**, 293–298 (2022).
[8] M. Plötner, G. Sadowski, S. Rzepka, and G. Blasek, "Aspects of indium solder bumping and indium bump bonding useful for assembling cooled mosaic sensors," Microelectron. Int. **8**, 27–30 (1991).
[9] Q. Huang, G. Xu, Y. Yuan, X. Cheng, and L. Luo, "Development of indium bumping technology through AZ9260 resist electroplating," J. Micromech. Microeng. **20**, 055035 (2010).
[10] K. Wade and A. Banister, *The Chemistry of Aluminium, Gallium, Indium and Thallium*, 1st ed., Pergamon Texts in Inorganic Chemistry Vol. 12 (Pergamon Press, Oxford, UK, 1973), p. 107.
[11] R. G. Gordon, X. Liu, R. N. Broomhall-Dillard, and Y. Shi, "Highly conformal diffusion barriers of amorphous niobium nitride," MRS Proc. **564**, 335 (1999).
[12] C. Thomas, J.-P. Michel, E. Deschaseaux, J. Charbonnier, R. Souil, E. Vermande, A. Campo, T. Farjot, G. Rodriguez, G. Romano *et al.*, "Superconducting routing platform for large-scale integration of quantum technologies," Mater. Quantum Technol. **2**, 035001 (2022).
[13] M. Volpert, L. Roulet, J.-F. Boronat, I. Borel, S. Pocas, and H. Ribot, "Indium deposition processes for ultra fine pitch 3D interconnections," in *Proceedings 60th Electronic Components and Technology Conference (ECTC)* (IEEE, 2010), pp. 1739–1745.
[14] P. Kozłowski, K. Czuba, K. Chmielewski, J. Ratajczak, J. Branas, A. Korczyc, K. Regiński, and A. Jasik, "Indium-based micro-bump array fabrication technology with added pre-reflow wet etching and annealing," Materials **14**, 6269 (2021).
[15] R. Das, V. Bolkhovsky, C. Galbraith, D. Oates, J. Plant, R. Lambert, S. Zarr, R. Rastogi, D. Shapiro, M. Docanto, T. Weir, and L. Johnson, "Interconnect scheme for die-to-die and die-to-wafer-level heterogeneous integration for high-performance computing," in *IEEE 69th Electronic Components and Technology Conference (ECTC)* (IEEE, 2019), pp. 1611–1621.
[16] K. J. Satzinger, C. R. Conner, A. Bienfait, H.-S. Chang, M.-H. Chou, A. Y. Cleland, É. Dumur, J. Grebel, G. A. Peairs, R. G. Povey *et al.*, "Simple non-galvanic flip-chip integration method for hybrid quantum systems," Appl. Phys. Lett. **114**, 173501 (2019).
[17] CAPLINQ, see https://www.caplinq.com/solder-spheres.html for "In 100 pure indium solder spheres."
[18] Q. Zhao, T. Wang, Y. K. Ryu, R. Frisenda, and A. Castellanos-Gomez, "An inexpensive system for the deterministic transfer of 2D materials," J. Phys. Mater. **3**, 016001 (2020).
[19] M. G. Latorre, A. Paradkar, D. Hambraeus, G. Higgins, and W. Wieczorek, "A chip-based superconducting magnetic trap for levitating superconducting microparticles," IEEE Trans. Appl. Supercond. **32**, 1–5 (2022).
[20] M. G. Latorre, G. Higgins, A. Paradkar, T. Bauch, and W. Wieczorek, "Superconducting microsphere magnetically levitated in an anharmonic potential with integrated magnetic readout," Phys. Rev. Appl. **19**, 054047 (2023).
[21] A. L. Graninger, M. R. Longo, M. Rennie, R. Shiskowski, K. Mercurio, M. Lilly, and C. H. Smith, "Superconducting on-chip solenoid for Josephson junction characterization," Appl. Phys. Lett. **115**, 032601 (2019).
[22] J. Verjauw, A. Potocnik, M. Mongillo, R. Acharya, F. Mohiyaddin, G. Simion, A. Pacco, T. Ivanov, D. Wan, A. Vanleenhove, L. Souriau, J. Jussot, A. Thiam,

10 January 2026 19:02:15

© Author(s) 2025

J. Swerts, X. Piao, S. Couet, M. Heyns, B. Govoreanu, and I. Radu, "Investigation of microwave loss induced by oxide regrowth in high-Q niobium resonators," Phys. Rev. Appl. **16**, 014018 (2021).
[23]M. V. P. Altoé, A. Banerjee, C. Berk, A. Hajr, A. Schwartzberg, C. Song, M. Alghadeer, S. Aloni, M. J. Elowson, J. M. Kreikebaum, E. K. Wong, S. M. Griffin, S. Rao, A. Weber-Bargioni, A. M. Minor, D. I. Santiago, S. Cabrini, I. Siddiqi, and D. F. Ogletree, "Localization and mitigation of loss in niobium superconducting circuits," PRX Quantum **3**, 020312 (2022).
[24]R. N. Das, J. Yoder, D. Rosenberg, D. Kim, D. Yost, J. Mallek, D. Hover, V. Bolkhovsky, A. Kerman, and W. Oliver, "Cryogenic qubit integration for quantum computing," in *IEEE 68th Electronic Components and Technology Conference (ECTC)* (IEEE, 2018), pp. 504–514.
[25]D. Hamilton, C. Raub, B. Matthias, E. Corenzwit, and G. Hull, "Some new superconducting compounds," J. Phys. Chem. Solids **26**, 665–667 (1965).
[26]H. Schoeller and J. Cho, "Oxidation and reduction behavior of pure indium," J. Mater. Res. **24**, 386–393 (2009).
[27]K. S. Il'in, A. Stockhausen, M. Siegel, A. D. Semenov, H. Richter, and H.-W. Hübers, "Nb HEB for THz radiation: Technological issues and proximity effect," in *Proceedings of the 19th International Symposium on Space Terahertz Technology (ISSTT 2008)* (NRAO library, 2008), pp. 367–372, see https://www.nrao.edu/meetings/isstt/2008.shtml.
[28]Y. W. Kim, Y. H. Kahng, J.-H. Choi, and S.-G. Lee, "Critical properties of submicrometer-patterned Nb thin film," IEEE Trans. Appl. Supercond. **19**, 2649–2652 (2009).
[29]D. Niepce, "Superinductance and fluctuating two-level systems loss and noise in disordered and non-disordered superconducting quantum devices," Ph.D. thesis (Chalmers University of Technology, 2020).
[30]K. R. Joshi, S. Ghimire, M. A. Tanatar, A. Datta, J.-S. Oh, L. Zhou, C. J. Kopas, J. Marshall, J. Y. Mutus, J. Slaughter *et al.*, "Quasiparticle spectroscopy, transport, and magnetic properties of Nb films used in superconducting transmon qubits," Phys. Rev. Appl. **20**, 024031 (2023).
[31]T. Freitas, J. Gonzalez, V. Nascimento, A. Takeuchi, and E. Passamani, "Negative magnetoresistance in sputtered niobium thin films grown on silicon substrates," Curr. Appl. Phys. **17**, 1532–1538 (2017).
[32]M. David Henry, S. Wolfley, T. Monson, B. G. Clark, E. Shaner, and R. Jarecki, "Stress dependent oxidation of sputtered niobium and effects on superconductivity," J. Appl. Phys. **115**, 083903 (2014).
[33]G. Deutscher and P. G. de Gennes, "Proximity effects," in *Superconductivity*, edited by R. D. Parks (Marcel Dekker, Inc., New York, 1969), Vol. 1.
[34]M. C. de Ory, D. Rodriguez, M. T. Magaz, V. Rollano, D. Granados, and A. Gomez, "Low loss hybrid Nb/Au superconducting resonators for quantum circuit applications," arXiv:2401.14764 (2024).
[35]M. Tinkham, *Introduction to Superconductivity*, 2nd ed. (Dover Publications, Mineola, NY, 2004).
[36]K. Il'in, M. Siegel, A. Semenov, A. Engel, and H. Hubers, "Critical current of Nb and NbN thin-film structures: The cross-section dependence," Phys. Status Solidi C **2**, 1680–1687 (2005).
[37]L. Sun, F. Dai, J. Zhang, J. Luo, C. Xie, J. Li, and H. Lei, "The electrical resistivities of nanostructured aluminium films at low temperatures," J. Phys. D **50**, 415302 (2017).
[38]R. Janninck and D. Whitmore, "Electrical conductivity and thermoelectric power of niobium dioxide," J. Phys. Chem. Solids **27**, 1183–1187 (1966).
[39]S. Krause, V. Afanas'ev, V. Desmaris, D. Meledin, A. Pavolotsky, V. Belitsky, A. Lubenschenko, A. Batrakov, M. Rudziński, and E. Pippel, "Ambient temperature growth of mono- and polycrystalline NbN nanofilms and their surface and composition analysis," IEEE Trans. Appl. Supercond. **26**, 1–5 (2016).
[40]D. Golubev and L. Kuzmin, "Nonequilibrium theory of a hot-electron bolometer with normal metal-insulator-superconductor tunnel junction," J. Appl. Phys. **89**, 6464–6472 (2001).
[41]F. Giazotto, T. T. Heikkilä, A. Luukanen, A. M. Savin, and J. P. Pekola, "Opportunities for mesoscopics in thermometry and refrigeration: Physics and applications," Rev. Mod. Phys. **78**, 217–274 (2006).
[42]B. Karimi, Y.-C. Chang, and J. P. Pekola, "Low temperature characteristics of the metal–superconductor nis tunneling thermometer," J. Low Temp. Phys. **207**, 220–225 (2022).
[43]A. Zehnder, P. Lerch, S. P. Zhao, T. Nussbaumer, E. C. Kirk, and H. R. Ott, "Proximity effects in Nb/Al–AlO_x–Al/Nb superconducting tunneling junctions," Phys. Rev. B **59**, 8875–8886 (1999).
[44]M. G. Latorre, J. Hofer, M. Rudolph, and W. Wieczorek, "Chip-based superconducting traps for levitation of micrometer-sized particles in the Meissner state," Supercond. Sci. Technol. **33**, 105002 (2020).
[45]P. Schmidt, R. Claessen, G. Higgins, J. Hofer, J. J. Hansen, P. Asenbaum, M. Zemlicka, K. Uhl, R. Kleiner, R. Gross, H. Huebl, M. Trupke, and M. Aspelmeyer, "Remote sensing of a levitated superconductor with a flux-tunable microwave cavity," Phys. Rev. Appl. **22**, 014078 (2024).
[46]Y. Chen, C. Neill, P. Roushan, N. Leung, M. Fang, R. Barends, J. Kelly, B. Campbell, Z. Chen, B. Chiaro *et al.*, "Qubit architecture with high coherence and fast tunable coupling," Phys. Rev. Lett. **113**, 220502 (2014).
[47]Z. Niu, W. Gao, X. He, Y. Wang, Z. Wang, and Z.-R. Lin, "DC flux crosstalk reduction with dual flux line," Appl. Phys. Lett. **124**, 254002 (2024).
[48]A. Paradkar, P. Nicaise, K. Dakroury, F. Resare, and W. Wieczorek (2024). "Superconducting flip-chip devices using indium microspheres on Au-passivated Nb or NbN as under-bump metallization layer (v1.0)," Zenodo. https://doi.org/10.5281/zenodo.13377108

10 January 2026 19:02:15

© Author(s) 2025

Supplementary Material: Superconducting flip-chip devices using indium microspheres on Au-passivated Nb or NbN as under-bump metallization layer

Achintya Paradkar,[1] Paul Nicaise,[1] Karim Dakroury,[1] Fabian Resare,[1] and Witlef Wieczorek[1,*]

[1] *Department of Microtechnology and Nanoscience (MC2), Chalmers University of Technology, SE-412 96 Gothenburg, Sweden*

This Supplementary Material contains details on the microfabrication of flip-chip devices, their assembly, the measurement setup and procedure, additional TOF-SIMS data, collected data, and additional measurements and calculations.

S1. FABRICATION

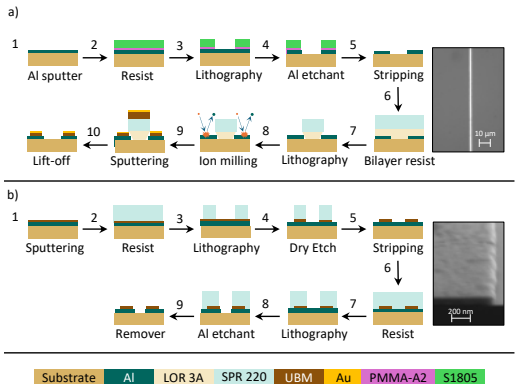

FIG. S1. (a) Schematic of the liftoff process. Right: an optical image of a 2 µm wide test structure. (b) Schematic of the etching process. Right: SEM image of a 100 nm thick UBM film.

In the following, we describe the fabrication of the layers on the bottom chip since it contains the UBM layer and the additional Al wiring layer. We present two approaches for patterning the UBM layer: a liftoff process and an etching process. The top chip consists of only the UBM layer patterned with pads and the test structure, and thus, the fabrication procedure is the same as that for the bottom chip without the process steps of the Al layer. Before any film is deposited, the wafers are cleaned in an ultrasonic bath with acetone, followed by isopropyl alcohol (IPA).

The liftoff process (Fig. S1(a)) begins with the fabrication of an Al wiring layer. First, 150 nm of Al is sputtered on a 2" Si wafer using a DC magnetron sputtering tool (step 1). The deposition is followed by the spin coating of resists PMMA-A2 (to protect Al against developer MF-319) and S1805 (step 2), exposing the pattern with optical lithography and developing the resist in MF-319 (first part of step 3). The PMMA-A2 in the developed area is then ashed in O_2 plasma at 40 W for 90 s (second part of step 3). The Al layer is then etched in Transene Etchant A at 40 °C for 90 s and rinsed with water (step 4). Finally, the resist is stripped with Remover 1165 (step 5), and the wafer is cleaned as mentioned above. The UBM layer is fabricated by spin-coating the wafer with a bilayer resist (LOR 3A (0.4 µm) & SPR 220 (3 µm)) to create an undercut and avoid sidewall deposition for easier liftoff (step 6). The pattern is then exposed using optical lithography and developed in MF-24A. The wafer is flood-exposed using a UV lamp to prevent bubble formation during sputtering due to trapped N_2, followed by descumming in O_2 plasma as before (step 7). To deposit the UBM layer, we use a magnetron sputtering system with an Nb DC source at a base pressure of $\sim 10^{-8}$ mbar. Before sputtering, we ion-milled the surface (step 8) with an Ar flow of 2 sccm and a beam current of 10 mA for 50 s to remove native Al oxide for galvanic contact between the wiring layer and the UBM pads. The DC power source is set at 200 W during the deposition of Nb and NbN (first part of step 9) and sputtered in steps of 17 nm to avoid excessive heating and therefore bubbling of the resist during deposition. Additionally, for depositing NbN, the N_2 flow is set at 8 sccm and the Ar flow to 60 sccm for a stoichiometry of approximately 1:1. Surface profilometry shows that the thickness uniformity of the Nb or NbN film is precise to within 10 percent of the desired thickness. A thin layer of 5 nm Au is sputtered in the same vacuum for devices with passivation (second part of step 9). Finally, the wafer is soaked overnight in Remover 1165 for liftoff of the UBM layer (along with the Au layer, if present) (step 10) and then cleaned with acetone and IPA.

In the etching process (Fig. S1(b)), the Al wiring layer and the UBM layer (Nb or NbN) are sputtered in the same vacuum (step 1), one after the other, on a pre-cleaned bare wafer. The UBM resist mask (step 2) is then patterned on top of the thin film using SPR220 and optical lithography. After the resist is developed (step 3), the wafer is placed in a reactive ion etching chamber. The UBM layer is selectively etched with NF_3 gas (step 4), which does not attack the Al layer beneath. The resist is dissolved in Remover 1165 (step 5), and a second resist mask of SPR220 (step 6) is patterned to define the wiring layer. After development and ashing (step 7), the wafer is submerged in a Transene etchant bath to etch

* witlef.wieczorek@chalmers.se

the Al layer (step 8). Finally, the resist mask is dissolved in Remover 1165 (step 9), and the wafer is cleaned as stated above.

Both processes are suitable alternatives for fabricating the desired material stacks. In some devices, the adhesion of Au to Nb was inadequate. Future processes could mitigate this issue by incorporating an additional 5 nm layer of Ti as an adhesion promoter [1]. With liftoff, we have reliably patterned long and narrow features with widths as small as 2 µm using optical lithography (Fig. S1(a)) and can, in principle, pattern sub-µm features using e-beam lithography. Patterning such features via etching requires a high degree of control over selectivity, anisotropy, and etch rate. Therefore, the liftoff process is preferred to pattern narrow and long coil features [2, 3], coplanar waveguides [4], or microbridges [5, 6]. However, liftoff is viable only up to a certain film thickness, beyond which the resist may harden during deposition and become insoluble, or the resist may not be thick enough. Thus, an etching-based process is preferred for layers thicker than 100 nm (Fig. S1(b)). Certain deposition tools lack ion milling capability but can deposit multiple materials within the same vacuum environment. In that case, the etching process can be used to pattern each film successively with suitable selective etching processes.

S2. FLIP-CHIP ASSEMBLY

In our first approach to flip-chip bonding (manuscript Fig. 2(a)), we use an xyz micro-manipulator stage. The bottom chip is held via vacuum, and the indium microspheres are placed on the UBM pads with tweezers. The top chip is attached to the glass slide with polydimethylsiloxane (PDMS) tape and is positioned above the bottom chip. The two chips are aligned with respect to each other via alignment markers, which can be seen through the transparent sapphire substrate of the top chip in a microscope. Alternatively, non-transparent substrates could also be used if they have through-vias for alignment. The bottom chip can be heated to 110 °C if reflow of indium is desired; otherwise, it can be kept at room temperature. The reflow temperature must remain well below 156 °C to avoid melting of indium, and also low enough to prevent oxide growth that can hinder galvanic contact with the UBM layers [7]. Finally, the top chip is brought down and pressed against the indium microspheres using the manipulator stage. Since the applied force is unknown, the pressing is stopped if any relative lateral motion between the two chips is observed. Additionally, the x-y alignment is continuously monitored and corrected during the bonding procedure.

We have also used a commercial flip-chip bonder (Fineplacer 96 Lambda from Finetech GmbH), manuscript Fig. 2(b), to bond the chips and compare performance with the manual transfer stage. The top chip is held with a vacuum on a pick-up tool that stands vertically next to the bottom chip. A beam splitter in the optical path enables both chips to be seen simultaneously. Once alignment is achieved, the microscope is retracted, and a precalibrated lever presses the top chip onto the bottom chip with a calibrated force (bonding pressure) between 50 to 65 N (60 to 80 MPa) at room temperature. The alignment cannot be monitored or corrected during bonding.

S3. EXPERIMENTAL SETUP AND MEASUREMENT PROCEDURE

We performed electrical measurements inside a dilution refrigerator (see Fig. S2), allowing us to characterize samples to millikelvin temperature. The chips are glued with BF-6 glue to a copper sample holder, as shown in manuscript Fig. 1(c). The test structure bond pads are connected to Nb screw terminals on a sample holder with Al wirebonds (25 µm diameter).

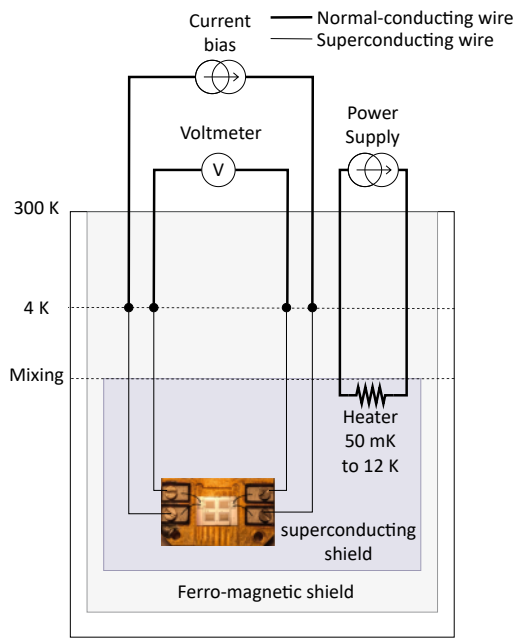

FIG. S2. Schematic of the four-wire measurement setup inside the dilution refrigerator. The sample is wire-bonded to the Nb screw terminals of the copper holder. The screw terminals clamp superconducting NbTi wires that terminate at the 4 K plate, where the normal-conducting wires make connections to the instruments. A controlled resistive heater is located on the mixing chamber plate (base plate) to vary the temperature of the sample.

Below the T_c of Al, each Al bond wire can carry a supercurrent of up to 85 mA. The screw terminals are used to clamp twisted niobium-titanium (Nb-Ti) wires that are soldered to a DC breakout on the 4 K plate of the cryostat. Thus, the entire line is superconducting below the 4 K plate.

Electrical characterization is performed by measuring the resistance of a four-wire connection to the device under test, which excludes the wire bonds and other connections to the sample. The bias current is provided with a Keithley 2450 source, and voltage is measured by a Rohde & Schwarz HMC8012. We subtracted a systematic nonzero voltage offset of the voltmeter from the data presented in manuscript Fig. 4(a) and manuscript Fig. 5(a). The HMC8012 has a systematic voltage offset uncertainty of $\pm 8\,\mu\mathrm{V}$, which translates to $\pm 0.8\,\Omega$ ($\pm 0.08\,\Omega$) for a bias current of $10\,\mu\mathrm{A}$ ($100\,\mu\mathrm{A}$).

We controlled the temperature of the samples by varying the power to an inbuilt heater on the base plate of the dilution refrigerator in the range of 50 µW to 1 mW while circulating the He-3/He-4 mixture, and further up to 0.8 W with only pre-cooling turned on.

For the measurements to determine the critical current at various temperatures, we infer the I_c at each temperature from individual measurements, in which we increase the current in steps of 0.1 µA until the measured resistance increases sharply as a result of the transition from the superconducting state to the normal conducting state. An increase in the temperature of the cryostat accompanies this increase in resistance. Before taking the next measurement, we set the power to a built-in heater on the base plate of the dilution refrigerator and wait a sufficient amount of time for the cryostat to thermalize to the desired temperature.

The contribution of Al bond pads to the resistance and the critical current values is negligible due to their large cross-sectional area (1 mm × 150 nm) and surface sheath area (determined by $\lambda_L = 54\,\mathrm{nm}$ [8]) compared to the test structure patterned in the UBM layer.

S4. TOF-SIMS

Time-of-flight secondary ion mass spectrometry (TOF-SIMS) measurements were performed using Cs^+ primary ions that sputter the material with an energy of 1 keV over a 300 µm × 300 µm area for Nb thin film and 250 µm × 250 µm area for the remaining thin films. The created secondary ions are sputtered at varying rates depending on the secondary ion's mass and ionization potential. The SIMS analyzer measures the secondary ions, recording counts as a function of sputtering time.

When examining the NbN UBM oxide data in manuscript Fig. 3(h,k), we observe peaks in the Nb oxide signals. It is important that the height of these peaks is small compared to the background Nb oxide signal and much smaller than the initial Nb oxide signal close to the surface. We hypothesize that these peaks could result from changes in the interfacial layer that cause localized oxygen enrichment at specific depths. Residual oxygen from sample exposure to air and trace amounts in the vacuum system during sputtering may also contribute to the observation of such peaks.

Furthermore, we observe a decrease in the Nb oxide signal in manuscript Fig. 3(b). We thereby distinguish two behaviors: a rapid decrease of the signal at the surface and a slow decrease within the film. The former rapid decrease we attribute to surface oxidation of the Nb film, which we explain in the main text. The slow decrease within the film is not so clear to us. This could be due to variations in film homogeneity or sample preparation artifacts, such as grains or pores, which can affect oxygen distribution and lead to different signal behaviors.

S5. COLLECTED DATA: RESISTANCE, TRANSITION TEMPERATURE, CRITICAL CURRENT DENSITY

A. UBM materials and flip-chip devices

We summarize the measured resistance R, the calculated resistivity ρ (both determined at 12 K and 300 K), and the calculated residual resistance ratio $RRR = R_{300\,\mathrm{K}}/R_{12\,\mathrm{K}}$ for the UBM thin films in Tab. S1 and for the flip-chip devices in Tab. S2.

The $\rho_{300\,\mathrm{K}}$ and RRR of the non-passivated thin films align with Refs. [4, 9]. The Au-passivated films exhibit lower $\rho_{300\,\mathrm{K}}$ values compared to their non-passivated counterparts due to the parallel conductance of the Au layer.

To verify the effect of the Au film, we estimate $\rho_{300\,\mathrm{K}}$ of 5 nm Au to be $11\,\mu\Omega\cdot\mathrm{cm}$ [15], and obtain $\rho_{300\,\mathrm{K}}$ of $15\,\mu\Omega\cdot\mathrm{cm}$ for Nb and $69\,\mu\Omega\cdot\mathrm{cm}$ for NbN, close to our measured values. Similarly, using $\rho_{12\,\mathrm{K}}$ of Au to be $2.6\,\mu\Omega\cdot\mathrm{cm}$ [16], we calculate $\rho_{12\,\mathrm{K}}$ of $9\,\mu\Omega\cdot\mathrm{cm}$ for Nb and $26\,\mu\Omega\cdot\mathrm{cm}$ for NbN.

The corresponding values of the flip-chip devices are very close to those of their thin-film counterparts, with slightly lower R, and therefore ρ, due to the parallel resistance of the Si substrate at room temperature.

Tab. S3 and Tab. S4 summarize the determined T_c and j_c for the UBM thin films and the flip-chip devices, respectively, and compare our values to the values in the literature.

B. Aluminum thin film

The resistance of the Al film is obtained from the resistance step observed at the T_c of Al (manuscript Fig. 5(a)) to be about 0.08 to $0.2\,\Omega$. Considering the smallest cross-sectional area in the Al layer (300 µm × 150 nm of length 400 µm), we estimate that the normal-state resistivity of Al lies between $0.68\,\mu\Omega\cdot\mathrm{cm}$ and $1.6\,\mu\Omega\cdot\mathrm{cm}$, which is comparable to that reported in Ref. [17].

Thin film material [thickness]	$R_{12\,\mathrm{K}}$ (kΩ)	$R_{300\,\mathrm{K}}$ (kΩ)	$\rho_{12\,\mathrm{K}}$ (μΩ · cm)	$\rho_{300\,\mathrm{K}}$ (μΩ · cm)		RRR	
				Exp.	Lit.	Exp.	Lit.
Nb[50 nm]	1.13	2.89	11.9	30.5	19.4 [4]	2.6	6.5 [4]
Nb[50 nm] / Au[5 nm]	1.47	2.54	17.1	29.5	-	1.73	-
NbN[50 nm]	26.1	21.9	278	233	∼250 [9]	0.84	∼0.8 [9]
NbN[50 nm] / Au[5 nm]	5.41	6.50	62.9	75.6	-	1.2	-

TABLE S1. Electrical properties of the sputtered UBM layers patterned independently on a sapphire substrate. The literature values are taken from works that use similar deposition techniques and film thicknesses.

UBM material [thickness]	$R_{12\,\mathrm{K}}$ (kΩ)	$R_{300\,\mathrm{K}}$ (kΩ)	$\rho_{12\,\mathrm{K}}$ (μΩ · cm)	$\rho_{300\,\mathrm{K}}$ (μΩ · cm)	RRR
Nb[50 nm] / Au[5 nm]	1.42	2.66	16.52	30.86	1.87
NbN[50 nm]	27.2	21.7	286.7	228.9	0.81
NbN[50 nm] / Au[5 nm]	4.69	5.80	54.5	67.3	1.23

TABLE S2. Electrical properties of the flip-chip devices with different UBM materials.

Thin film material [thickness]	j_c (MA/cm^2)		T_c (K)	
	Exp.	Lit.	Exp.	Lit.
Nb[50 nm]	9.3	4 [10]	8.0	8.1 [10]
Nb[50 nm] / Au[5 nm]	6.3	-	7.7	7.3 [11]
NbN[50 nm]	2.5	2.5 [12]	10.4	10.6 [13]
NbN[50 nm] / Au[5 nm]	3.2	-	9.9	10.2 [14]

TABLE S3. Superconducting properties of the sputtered UBM layers patterned independently on a sapphire substrate. The literature values are taken from works that use similar deposition techniques and film thicknesses.

UBM material [thickness]	j_c (MA/cm^2)	T_c (K)
Nb[50 nm] / Au[5 nm]	5.6	7.4
NbN[50 nm]	0.4*	10.0
NbN[50 nm] / Au[5 nm]	3.0	9.7

TABLE S4. Superconducting properties of the flip-chip devices with different UBM materials. *The NbN flip-chip device exhibits 2.2 MA/cm^2 limited by the NbN test structure, and 0.4 MA/cm^2 limited by Nb oxide in the flip-chip interconnects.

C. Indium microsphere

Bulk indium exhibits an electrical resistivity of 1.2 nΩ · cm at 4 K [18]. Approximating a pressed indium microsphere as a cylinder with 500 μm diameter and 50 μm height yields an estimated normal-state resistance of 30 nΩ.

S6. NON-PASSIVATED NBN FLIP-CHIP DEVICE

A. Critical current of the SIS junction

In the non-passivated NbN flip-chip device, we observe a resistance step of 2.5 Ω at the transition temperature of In (see manuscript Fig. 5(a)). We assume that this resistance comes from the oxide on top of NbN. Considering a contact area with a diameter of about 500 μm (for pressed microspheres) and an oxide thickness of 0.5 nm (estimated from the SIMS data, manuscript Fig. 3(g), assuming a sputtering rate of 3.6 nm/min [19]) we obtain a resistivity of the order of 10^6 Ω · cm, which is expected for NbO_2 at such low temperatures [20].

The total resistance $R = 2.5\,\Omega$ is assumed to be evenly distributed at each oxide interface of the entire flip-chip device. Since the In microsphere is pressed with NbN on top and bottom, we consider two oxide interfaces in series per microsphere. Considering two microspheres per pad implies that the normal-state resistance at each interface is $R_N = R/2 = 1.25\,\Omega$.

Using the Ambegaonkar-Baratoff equation [21], we can then estimate the critical current of the SIS junction

formed by the NbN/NbO_x/In interface as

$$I_{c0} = \frac{\pi\sqrt{\Delta_{In}\Delta_{NbN}}}{2eR_N}\tanh\left(\frac{\sqrt{\Delta_{In}\Delta_{NbN}}}{2k_{\mathrm{B}}T}\right), \qquad \text{(S1)}$$

where k_{B} is Boltzmann's constant, e electric charge, T temperature (100 mK), the superconducting energy gaps of NbN $\Delta_{NbN} = 4.16$ meV [22] and In $\Delta_{In} = 1.05$ meV [23]. We obtain $I_{c0} = 2.6$ mA.

B. Current measurement

Fig. S3 shows resistance vs. current measurements of the non-passivated NbN and Au-passivated NbN flip-chip devices. For both flip-chip devices, we observe a sharp increase in resistance above a current of 12 mA, which indicates the critical current through the test structure of the NbN thin film. For the non-passivated NbN flip-chip device (Fig. S3(a)), we observe an additional resistance step of about 1 Ω starting at a current close to 2 mA. We attribute this additional resistance step to the presence of the interface oxide in the flip-chip interconnect, which forms an SIS junction with about this critical current, which is close to the estimated 2.6 mA from the Ambegaonkar-Baratoff equation.

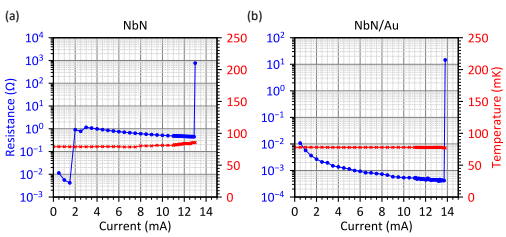

FIG. S3. Current-dependent measurements of (a) non-passivated NbN and (b) Au-passivated NbN flip-chip devices. The plots show resistance (blue circles) and temperature at the mixing chamber (red crosses) as a function of current. Lines are a guide to the eye.

S7. CRITICAL CURRENT OF INDIUM MICROSPHERE

We assembled a simplified flip-chip device using the transfer stage, with unpatterned chips of Nb/Au film chosen for its high critical current and absence of oxidation. Two In microspheres were placed on each bottom chip, while a third chip was pressed on top to establish a galvanic connection between the two bottom chips Fig. S4(c). We used 24 aluminum wire bonds per bond pad (Fig. S4(b)) to allow the transport of large supercurrents.

The critical current of two Indium microspheres is measured to be above 2 A (see Fig. S4(a)). In our measurement, we were limited by the maximum output of our current source, which was 2 A. Assuming a diameter (d) of the contact area of the pressed In microsphere of 500 µm and the current to be flowing only within the London penetration depth of 40 nm [24] we estimate the j_c of In to be greater than 1.6 MA/cm^2. Considering a critical field (H_c) of 2.75×10^{-2} T [25] for pure bulk In, we estimate the critical current (I_c) using the Silsbee criterion ($I_c = \pi d H_c$ [21]) to be about 34 A, which is higher than the value we can measure with the available current source. The observed heating in the cryostat for currents larger than about 1.2 A is the result of Joule heating at the 4 K stage, where the superconducting NbTi connection terminates in a normal copper connection. During measurement, this connection heats up, which is seen as a rise in temperature at the 4 K stage in Fig. S4(a). This heat propagates down to the sample, which is seen as an increase in the base temperature at the mixing chamber.

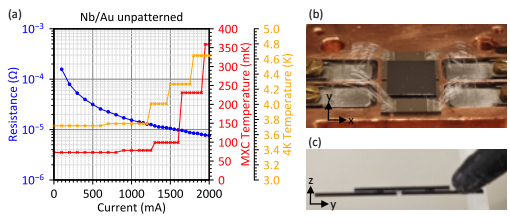

FIG. S4. (a) Current measurement of an unpatterned Nb/Au flip-chip device using In microsphere interconnects. The plot shows resistance (blue curve) as well as the temperature at the base plate (red curve) and 4 K stage (orange curve) in dependence on current. Image of (b) the assembled Nb/Au flip-chip device and (c) a close-up of its cross-section. The flip-chip device was wire bonded with 24 Al bonds per pad.

[1] R. N. Das, J. Yoder, D. Rosenberg, D. Kim, D. Yost, J. Mallek, D. Hover, V. Bolkhovsky, A. Kerman, and W. Oliver, Cryogenic qubit integration for quantum computing, in *2018 IEEE 68th Electronic Components and Technology Conference (ECTC)* (2018) pp. 504–514.

[2] M. G. Latorre, A. Paradkar, D. Hambraeus, G. Higgins, and W. Wieczorek, A chip-based superconducting magnetic trap for levitating superconducting microparticles,

IEEE Transactions on Applied Superconductivity **32**, 1 (2022).

[3] M. G. Latorre, G. Higgins, A. Paradkar, T. Bauch, and W. Wieczorek, Superconducting microsphere magnetically levitated in an anharmonic potential with integrated magnetic readout, Phys. Rev. Appl. **19**, 054047 (2023).

[4] J. Verjauw, A. Potocnik, M. Mongillo, R. Acharya, F. Mohiyaddin, G. Simion, A. Pacco, T. Ivanov, D. Wan, A. Vanleenhove, L. Souriau, J. Jussot, A. Thiam, J. Swerts, X. Piao, S. Couet, M. Heyns, B. Govoreanu, and I. Radu, Investigation of microwave loss induced by oxide regrowth in high-Q niobium resonators, Phys. Rev. Appl. **16**, 014018 (2021).

[5] N. Haberkorn, Y. Lee, C. Lee, J. Yun, F. Verón Lagger, M. Sirena, and J. Kim, Probing the quasiparticle relaxation time in ultrathin NbN microbridges via larkin–ovchinnikov instability near tc, ACS Applied Electronic Materials **6**, 5077 (2024).

[6] H. Du, Z. Xu, P. Zhang, D. Li, Z. Wei, Z. Wang, S. Hou, B. Chen, T. Liu, R. Liu, and et al., High-energy electron injection in top-gated niobium microbridges for enhanced power efficiency and localized control, Applied Physics Letters **124**, 112601 (2024).

[7] H. Schoeller and J. Cho, Oxidation and reduction behavior of pure indium, Journal of Materials Research **24**, 386–393 (2009).

[8] D. López-Núñez, Q. P. Montserrat, G. Rius, E. Bertoldo, A. Torras-Coloma, M. Martínez, and P. Forn-Díaz, Magnetic penetration depth of aluminum thin films, arXiv 10.48550/arXiv.2311.14119 (2023).

[9] D. M. Glowacka, D. J. Goldie, S. Withington, H. Muhammad, G. Yassin, and B. K. Tan, Development of a NbN deposition process for superconducting quantum sensors, arXiv 10.48550/arXiv.1401.2292 (2014).

[10] Y. W. Kim, Y. H. Kahng, J.-H. Choi, and S.-G. Lee, Critical properties of submicrometer-patterned Nb thin film, IEEE Transactions on Applied Superconductivity **19**, 2649 (2009).

[11] M. C. de Ory, D. Rodriguez, M. T. Magaz, V. Rollano, D. Granados, and A. Gomez, Low loss hybrid Nb/Au superconducting resonators for quantum circuit applications, arXiv 10.48550/arXiv.2401.14764 (2024).

[12] K. Il'in, M. Siegel, A. Semenov, A. Engel, and H. Hubers, Critical current of Nb and NbN thin-film structures: The cross-section dependence, Physica Status Solidi (c) **2**, 1680–1687 (2005).

[13] D. Niepce, *Superinductance and fluctuating two-level systems loss and noise in disordered and non-disordered superconducting quantum devices*, Ph.D. thesis, Chalmers University of Technology (2020).

[14] K. S. Il'in, A. Stockhausen, M. Siegel, A. D. Semenov, H. Richter, and H.-W. Hübers, Nb HEB for THz radiation: Technological issues and proximity effect, in *Proceedings of the 19th International Symposium on Space Terahertz Technology, ISSTT 2008* (2008) pp. 367–372.

[15] M. C. Salvadori, A. R. Vaz, R. J. Farias, and M. Cattani, Electrical resistivity of nanostructured platinum and gold thin films, Surface Review and Letters **11**, 223–227 (2004).

[16] J. R. Sambles, K. C. Elsom, and D. J. Jarvis, The electrical resistivity of gold films, Philosophical Transactions of the Royal Society of London. Series A, Mathematical and Physical Sciences **304**, 365–396 (1982).

[17] N. Joshi, A. Debnath, D. Aswal, K. Muthe, M. Senthil Kumar, S. Gupta, and J. Yakhmi, Morphology and resistivity of Al thin films grown on Si (111) by molecular beam epitaxy, Vacuum **79**, 178–185 (2005).

[18] L. A. Hall, *Survey of electrical resistivity measurements on 16 pure metals in the temperature range 0 to 273 K*, technical report (National Bureau of Standards, 1968).

[19] A. He, S. Xu, A. Foroughi-Abari, and D. Karpuzov, Depth profiling of Nb_xO/W multilayers: Effect of primary ion beam species (O_2^+, Ar^+ and Cs^+), Surface and Interface Analysis **44**, 934–937 (2012).

[20] R. Janninck and D. Whitmore, Electrical conductivity and thermoelectric power of niobium dioxide, Journal of Physics and Chemistry of Solids **27**, 1183–1187 (1966).

[21] M. Tinkham, *Introduction to Superconductivity*, 2nd ed. (Dover Publications, Mineola, New York, 2004).

[22] K. Komenou, T. Yamashita, and Y. Onodera, Energy gap measurement of niobium nitride, Physics Letters A **28**, 335–336 (1968).

[23] R. F. Averill, L. S. Straus, and W. D. Gregory, Tunneling measurements of the superconducting energy gap of bulk polycrystalline indium, Applied Physics Letters **20**, 55–56 (1972).

[24] R. A. Anderson and D. M. Ginsberg, Penetration depth and flux creep in thin superconducting indium films, Phys. Rev. B **5**, 4421 (1972).

[25] E. Maxwell and O. S. Lutes, Threshold field properties of some superconductors, Phys. Rev. **95**, 333 (1954).

PAPER C

Efficient flip-chip and on-chip-based modulation of flux-tunable superconducting resonators

Achintya Paradkar, Paul Nicaise, Karim Dakroury, Fabian Resare, Christian Dejaco, Lukas Deeg, Gerhard Kirchmair, and Witlef Wieczorek

arXiv preprint arXiv:2512.23119 (2025).
© DOI: 10.48550/arXiv.2512.23119

arXiv:2512.23119v1 [quant-ph] 28 Dec 2025

Efficient flip-chip and on-chip-based modulation of flux-tunable superconducting resonators

Achintya Paradkar,[1] Paul Nicaise,[1] Karim Dakroury,[1] Fabian Resare,[1] Christian Dejaco,[2,3] Lukas Deeg,[2,3] Gerhard Kirchmair,[2,3] and Witlef Wieczorek[1,*]

[1] *Department of Microtechnology and Nanoscience (MC2), Chalmers University of Technology, Kemivägen 9, Gothenburg, SE-41296, Sweden*

[2] *Institute for Quantum Optics and Quantum Information, Austrian Academy of Sciences, 6020 Innsbruck, Austria*

[3] *University of Innsbruck, Institute for Experimental Physics, 6020 Innsbruck Austria*

We demonstrate the efficient modulation of flux-tunable superconducting resonators (FTRs) using flip-chip or on-chip-based input coils. The FTRs we use are aluminum-based quarter-wave coplanar waveguide resonators terminated with 100 µm or 200 µm-wide square loop dc superconducting quantum interference devices (SQUIDs) employing 1 µm-sized Josephson junctions. We employ SQUIDs with a geometric loop inductance of up to 0.7 nH to increase the flux transfer efficiency. The geometric inductance of the SQUID results in a non-zero screening parameter β_{L}, whose branch switching effect is mitigated by using asymmetric junctions. We achieve flux modulation of the FTRs by more than one GHz and flux responsivities of up to tens of GHz/Φ_0 with µA-scale on-chip currents. We compare flip-chip with on-chip input-coil-based flux modulation, where the former is realized through galvanically connected and closely spaced chips, while the latter is achieved through superconducting air-bridge connections. We achieve a flux-transfer efficiency from the input coil to the SQUID loop of up to 20%. Our work paves the way for efficient low current flux modulation of FTRs and sensitive measurement of flux signals.

I. INTRODUCTION

Superconducting quantum circuits are widely employed in quantum technologies due to their high coherence, controllability, coupling strength, and potential for scalability [1–4]. Flux-tunable superconducting elements are crucial components in superconducting quantum circuits, enabling flux-tunable transmon-like qubits [5–7], flux-tunable couplers [8–10], Josephson parametric amplifiers [11–14], or flux-tunable resonators (FTRs) [15–19]. FTRs are typically implemented as coplanar waveguide (CPW) or lumped element resonators that are terminated by a dc superconducting quantum interference device (SQUID) [15]. The flux modulation of the FTR exhibits a tunable response that can be as large as tens of GHz/Φ_0, making the FTR a suitable device for sensing of magnetic flux.

FTRs have been employed, for example, for flux-based detection of the motion of micromechanical resonators [20–28], for detecting the electronic state of spin ensembles [29], for photon–pressure coupling of superconducting resonators [30, 31], for intra-cavity photon generation [32], qubit read-out [33], or for dark-matter searches [34]. For flux sensing using FTRs, it is crucial to transport the flux signal efficiently from the source to the SQUID loop of the FTR. This is challenging when the SQUID loop cannot be placed near the source for readout, for example, due to limits imposed by the critical field of the superconducting material employed in the FTR. In such cases, the flux can be transported to the FTR via a flux transformer [35–39], in which a pick-up coil is located at the source and connected to an input coil located at the FTR. It is crucial that the input coil transports the flux efficiently into the SQUID loop without affecting the coherence of the FTR. For certain applications, it may be necessary to increase the geometric inductance of the SQUID loop for optimal flux-transfer efficiency. This can then lead to a non-zero screening parameter β_{L}, which can result in branch switching behavior of the resonance frequency of the FTR [14, 18, 19, 40–42].

In our work, we demonstrate two efficient

* witlef.wieczorek@chalmers.se

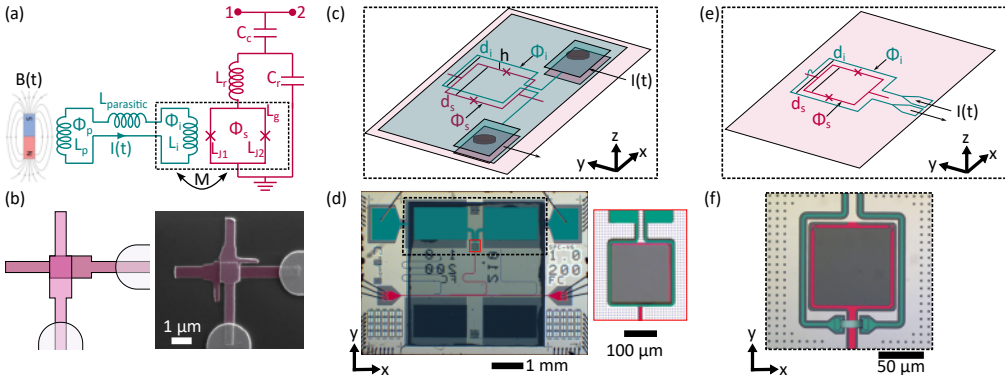

Figure 1. Chip-based modulation of a flux-tunable resonator (FTR) using integrated input coils. (a) Equivalent lumped element circuit model: the FTR (red) is inductively coupled via a flux transformer (green) to an external magnetic source. (b) Left: design of a 1 µm-wide Josephson junction. Right: false-colored SEM image of the fabricated junction where the dark electrode is patterned first; the thin appendages on either side are artifacts of the shadow evaporation technique. (c) Schematic of a flip-chip input coil (green) concentric with the SQUID (red) and galvanically connected to the bottom chip via superconducting indium bumps [43]. (d) Device based on schematic shown in (c): 200 µm-wide SQUID-loop FTR on a silicon bottom chip with a NbN input coil on a sapphire top chip (false-colored). (e) Schematic of an on-chip input coil (green) patterned concentrically around the SQUID loop (red). (f) Device based on schematic shown in (e): optical image (false-colored) of a 100 µm-wide SQUID-loop FTR; the input coil is routed over the CPW via an aluminum air bridge [44, 45].

methods to modulate FTRs using chip-based input coils. The first method involves positioning the input coil on a separate chip above the SQUID loop and galvanically connecting it through superconducting interconnects in a simple flip-chip assembly [43]. The second method involves placing the input coil concentrically with the SQUID loop on the same chip, made possible through air-bridge interconnects [44, 45]. Our FTRs use large-loop dc SQUIDs with asymmetric Josephson junctions (JJs). The large loop increases flux-transfer efficiency, while the asymmetry mitigates the branch switching effect [46–52]. We account for the large loop inductance in our FTR model through a finite screening parameter β_L and for the junction asymmetry through an asymmetry parameter α [40, 41]. We analyze the efficiency of our flux-transfer methods and their effect on the intrinsic quality factor of the FTR. Finally, we employ a flux transformer to couple a source magnetic field to the FTR via the input coil while keeping the source and FTR physically separated.

II. RESULTS

Fig. 1(a) shows the lumped-element circuit representation of the FTR, which is a quarter-wave CPW terminated by a dc SQUID at the grounded end, i.e., at the current anti-node. The FTR is capacitively coupled to a transmission line for readout at the voltage anti-node. A magnetic field $B(t)$ is measured through a pick-up loop, whose flux Φ_p is transported to an input coil at the SQUID via a flux transformer. The resonance frequency of the FTR depends on the flux Φ_s through the SQUID approximately as [14, 15, 25, 53, 54] (a detailed derivation can be found in App. B)

$$\omega_r(\Phi_s) \simeq \frac{\omega_0}{1+\gamma(\Phi_s)}, \tag{1}$$

with $\omega_0 = A\sqrt{1/(L_r C_r)}$ the resonance frequency of the bare CPW (with inductance L_r, capacitance C_r, and a scaling factor A) and the inductance participation ratio γ, which quantifies the

nonlinearity of the FTR via

$$\gamma(\Phi_s) = \frac{L_S(\Phi_s)}{lL_l}, \tag{2}$$

i.e., the ratio of total SQUID inductance $L_S(\Phi_s)$, which includes contributions from the Josephson inductances ($L_{Ji}(\Phi_s)$) of each JJ and the loop's geometric inductance (L_g), to the linear inductance per unit length (L_l) and total CPW length (l); we provide the full equation in App. A.

The FTRs we employ have a large geometric inductance of up to $L_g = 750\,\mathrm{pH}$, which gives rise to a non-negligible screening current. As a result, the flux Φ_s threading the SQUID loop differs from the externally applied flux Φ_e set by the coil. Following Ref. [40], these quantities are related by (see App. A)

$$\Phi_e = \Phi_s \pm \Phi_0 \frac{\beta_\mathrm{L}}{2} \frac{(1-\alpha^2)\sin\left(\pi\frac{\Phi_s}{\Phi_0}\right)}{\sqrt{1+\alpha^2\tan^2\left(\pi\frac{\Phi_s}{\Phi_0}\right)}}, \tag{3}$$

where $\beta_\mathrm{L} = 2L_g I_0/\Phi_0$ is the screening parameter, $I_0 \sim 375\,\mathrm{nA}$ is the average critical current of our Josephson junctions, and α is the junction asymmetry defined as

$$\alpha = (I_{\mathrm{c}1} - I_{\mathrm{c}2})/(I_{\mathrm{c}1} + I_{\mathrm{c}2}), \tag{4}$$

with $I_{\mathrm{c}i}$ being the critical current of the ith junction. In our devices, we expect $\beta_\mathrm{L} \sim 0.3$ for the 200 µm-wide dc SQUID. We use the simplifying assumption that the SQUID perturbs the FTR boundary only locally at its grounded end. However, as our SQUID loops are rather large, i.e., up to 12% of the CPW length, we expect a deviation from this assumption and introduce a phenomenological scaling factor A in Eq. (1).

We fabricate the wiring layer and ground plane of the FTR by patterning a 150 nm thick Al film on a high-resistivity ⟨111⟩ silicon substrate. The JJs are Manhattan-style [55] Al/AlO$_x$/Al junctions deposited using the shadow evaporation technique [45]. We realized 1 µm-sized JJs, as shown in Fig. 1(b) (for fabrication details, see App. D), to reduce the nonlinearity of the FTR, i.e., its Kerr coefficient $\mathcal{K}$, which, among other factors, is reduced for larger junction sizes. Our Manhattan-style junction design, combined with the shadow evaporation process, allows us to pattern one junction smaller than the other due to resist shadowing effects (see App. D 1). We determine the critical current of the JJs from the normal-state resistance (R_N) above the critical temperature using the Ambegaokar–Baratoff relation $I_\mathrm{c} = \pi\Delta/(2\mathrm{e}R_N)$ [56], where Δ is the superconducting gap with $\Delta \sim 180\,\mu\mathrm{eV}$ for Al. R_N is estimated by measuring the junctions at room temperature and accounting for a 10% increase at 4 K [57]. We obtain $I_{\mathrm{c}1} \approx 500\,\mathrm{nA}$ and $I_{\mathrm{c}2} \approx 250\,\mathrm{nA}$, with corresponding inductances of $L_{J1} \approx 650\,\mathrm{pH}$ and $L_{J2} \approx 1300\,\mathrm{pH}$, respectively, leading to $\alpha \sim 0.3$.

Fig. 1(c) shows a schematic of the flip-chip-based input coil on the FTR, and Fig. 1(d) shows its implementation. The top chip of the flip-chip assembly contains a 215 µm-wide input coil, patterned on a sapphire substrate, and placed above a 200 µm-wide SQUID, both of square geometry. We galvanically connect the top and bottom chips using indium bumps and achieve a chip separation of approximately 50 µm; for details, see Ref. [43]. Note that the separation can, in principle, be made smaller by using smaller indium bumps. Our second integrated modulation technique relies on a 125 µm-wide on-chip input coil patterned around a 100 µm-wide square SQUID loop (Fig. 1(e,f)). The input coil needs to bridge the FTR central line, which is achieved through the use of a superconducting air bridge; for fabrication details, see Refs. [44, 45]. Note that the on-chip input coil could, in principle, also be located within the SQUID loop using two air bridge connections.

Fig. 2(a) shows the expected flux transfer efficiency $\eta_2 = \Phi_e/\Phi_i$ from the input coil of width d_i to the SQUID loop of width d_s, for the flip-chip case (axial coil separation $h = 50\,\mu\mathrm{m}$) and for the on-chip case ($h = 0\,\mu\mathrm{m}$), with Φ_i being the flux in the input coil; for details, see App. C. Note that one can obtain the mutual inductance M between the SQUID loop and the input coil via $M = L_i \cdot \eta_2$, where L_i is the inductance of the input coil. The simulated input coil inductance for the flip-chip coil loop is 567 pH and 348 pH for the on-chip coil loop. As expected, η_2 is maximum when the loop widths are the same, i.e., $d_i/d_s = 1$. Our implemen-

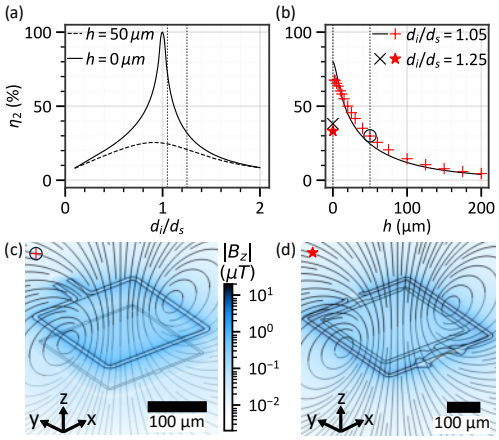

Figure 2. Flux transfer efficiency η_2 between the input coil and the SQUID loop. Efficiency as a function of (a) the ratio of input coil loop width to SQUID loop width d_i/d_s and (b) axial loop separation h. The black lines represent analytic results assuming one-dimensional square loops, while the red markers are results from FEM simulations of realistic geometries of the on-chip (star) and flip-chip (cross) configurations. The dotted vertical lines in (a) are at d_i/d_s of 1.05 and 1.25 and in (b) at h of 0 µm and 50 µm. FEM-simulated magnetic field distribution for (c) flip-chip and (d) on-chip configurations assuming an input coil current of 100 µA.

tation achieves loop ratios close to this optimal value, i.e., $d_i/d_s = 1.05$ for the flip-chip case, whereas for the on-chip case, we have to compromise to $d_i/d_s = 1.25$, as the input coil must be slightly larger than the SQUID loop it surrounds. We place the input coil outside the SQUID loop. Placing it inside instead would require an additional air-bridge, which would increase the parasitic coupling loss of the FTR. Fig. 2(b) shows η_2 as a function of loop distance h. We compare analytic results for η_2, assuming an idealized geometry of one-dimensional square loops, to FEM simulations of the real geometries of the flip-chip and on-chip cases; see Fig. 2(c,d). The simulated results follow the trend of the analytical calculation but are slightly lower at smaller separations; see Fig. 2(b). The reason is that the analytical model assumes a one-dimensional geometry with no coil openings, while the simulations are performed for the actual geometry. The simulation results of both the flip-chip and on-chip methods yield similar efficiencies of about 30%. In the flip-chip method, the efficiency is mainly limited by the axial loop separation ($h = 50$ µm), while in the on-chip method, it is limited by the constraint $d_i > d_s$ imposed by routing the input coil around the SQUID loop.

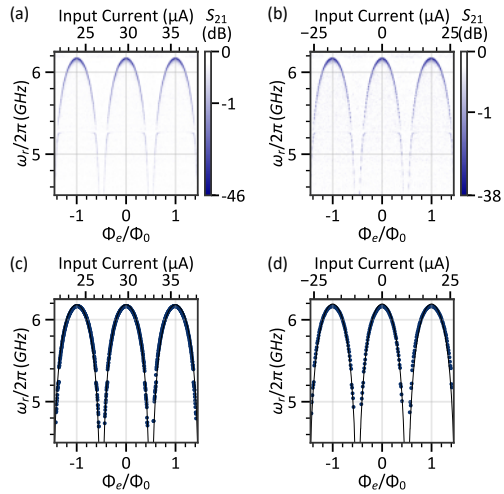

Figure 3. Multiple Φ_0 modulations of an FTR with a 200 µm-wide SQUID modulated at 0.33 intra-cavity photons via (a,c) an external bias coil and (b,d) via a flip-chip-based input coil. (a,b) show the background-subtracted FTR modulation in dependence of coil current and applied flux. (c,d) show the extracted resonance frequency of the FTR (dots), the solid line is the model accounting for finite screening and junction asymmetry.

We turn now to the characterization of the FTRs. Figs. 3(a) and (b) compare external-coil-based and input-coil-based modulation of an FTR with a 200 µm-wide SQUID, respectively. We observe the expected periodic dependence of the resonator frequency over multiple Φ_0 modulations achieved via the external multi-winding bias coil (Fig. 3(a)) as well as with the flip-chip-based input coil (Fig. 3(b)). We see no discernible difference between the two modulation types. We observe an avoided crossing close to 5.3 GHz, which we attribute to the hybridization of the FTR with a parasitic slotline mode on the chip. Note that we obtain the primary x-axis by converting the applied current I_{in} to the external

flux seen by the SQUID $\Phi_e = \Phi_0 \cdot (I_{\text{in}} - I_{\text{off}})/I_{\Phi_0}$, where I_{off} is the current at which Φ_e/Φ_0 takes an integer value, and I_{Φ_0} is the current required for modulation by one Φ_0 [40].

Figs. 3(c) and (d) show the resonance frequencies of the FTRs extracted as the minima of the scattering parameter $|S_{21}|$ near resonance, after background subtraction. The solid curve shows the model according to Eq. (1) with the circuit parameters extracted from high-resolution measurements shown in Fig. 4; see also Table I. We account for the finite screening current and junction asymmetry using Eq. (3) and Eq. (4), respectively. The model shows good agreement with the data. The FTR does not exhibit branch switching behavior due to the use of the asymmetric dc SQUID, similar to previous work using asymmetric SQUID-like elements [5, 7, 47, 58].

Figs. 4(a) and (b) show high-resolution measurements of the FTR modulation achieved through the flip-chip and the on-chip input coil, respectively. We use these measurements to extract the parameters of our devices. We observe that we require only tens of µA of current via the chip-based coils to realize a modulation of one flux quantum. Figs. 4(c) and (d) show the resonance frequencies of the FTRs determined from a circle-fit routine [24, 27, 59] (see App. E). We use the expected device parameters as input to the model fit according to Eq. (1) and obtain fitted parameters that are close to our design values (see Table I) with a fit result that shows good agreement with the data. Independently, we modulated the FTRs using the external bias coil only (see Figs. 10(a) and (b)) and fitted their tuning behavior (see Figs. 10(c) and (d)). The corresponding fitted parameters (see Table I) are in good agreement with those determined from the chip-based input coil modulations. Hence, both the chip-based and external-coil-based modulation methods tune the FTR in a similar way. The FTRs reach a flux responsivity $\partial\omega_r/\partial\Phi$ of up to $2\pi \cdot 20\,\text{GHz}/\Phi_0$, making them suitable devices as sensitive flux detectors.

We use the observed modulation by one flux quantum to determine the flux transfer efficiency η_2 from its relation to the mutual inductance $\eta_2 = M/L_i$; see App. C. From Figs. 4(a) and (b), we extract the input coil current I_{Φ_0} required for one period of resonance modulation, corresponding to a change of Φ_e by one flux quantum. With $M = \Phi_0/I_{\Phi_0}$ and using the previously mentioned simulated input coil inductances, we obtain experimental efficiencies of 21% and 19%, respectively. These values are lower than the simulated efficiencies of 30% and 33%, respectively, which do not account for flux screening in the SQUID loop. The finite SQUID loop inductance causes partial screening of the applied flux, reducing the experimentally determined flux transfer efficiency.

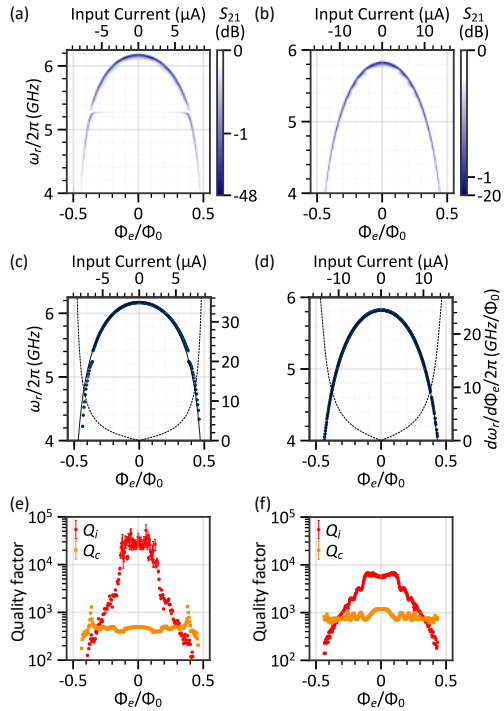

Figure 4. Modulation of FTRs via flip-chip-based (a,c,e) and on-chip-based (b,d,f) input coil measured at 0.33 and 0.83 intra-cavity photons, respectively. (a,b) show background-subtracted plots of the FTR modulation in dependence of input coil current and input flux. (c,d) show the resonance frequency (dots), extracted via a circle-fit routine, as a function of input flux. The solid line and the dotted line are the fit result for the model according to Eq. (1) and its derivative, respectively. (e,f) show the intrinsic and coupling quality factors of the FTRs as a function of input flux.

Next, we study the quality factors of the FTRs as a function of chip-based flux biasing. Figs. 4(e) and (f) show the intrinsic (Q_i) and coupling (Q_c) quality factors as a function of input flux. Note that our FTRs are overcoupled near zero flux bias, which may lead to a systematic uncertainty when determining Q_i [60, 61]. We observe a maximum Q_i of about $3 \cdot 10^4$ and $0.7 \cdot 10^4$ for flip-chip and on-chip devices, respectively, near the zero flux bias point, comparable to previous works [15, 27] (see Table II). These values are similar to those obtained using external coil modulation only (Fig. 10), i.e., $3 \cdot 10^4$ and $0.8 \cdot 10^4$. Hence, we observe that driving current on-chip is not detrimental to the intrinsic quality factor of the FTRs. Note that we attribute the slightly lower Q_i of the on-chip device to parasitic capacitive coupling between the resonator and the nearby input coil. This effect is suppressed in the flip-chip geometry due to the vertical separation of 50 µm between the input coil and the FTR.

We observe a decrease in the effective Q_i with increasing flux bias, which is consistent with previous works [15, 16, 25, 27, 28]. We attribute this primarily to flux noise-induced linewidth broadening due to the increased flux responsivity away from the zero-flux bias point. The coupling quality factors Q_c at the zero-flux bias point are 490 and 1170 for the flip-chip and on-chip devices, which are close to their design values of 470 and 1250, respectively. The slight variations in Q_c with flux bias arise from flux-dependent changes in the characteristic impedance and resonance frequency of the FTR.

We also briefly study the nonlinear behavior of the FTR, which is inherited from the nonlinearity of the JJs [15]. To this end, we performed power sweeps at the zero-flux bias point. Figs. 5(a) and (b) show the resonance frequency of the FTR for increasing intra-cavity photon numbers. The frequency pulling to lower frequencies, observed at higher powers, is due to the negative Kerr nonlinearity of the FTR. We can model this behavior as [20, 62]

$$\omega_r(n_c) = \omega_r(0) - \mathcal{K} n_c, \tag{5}$$

where $\omega_r(n_c)$ is the resonance frequency for n_c intra-cavity photons with the flux-dependent

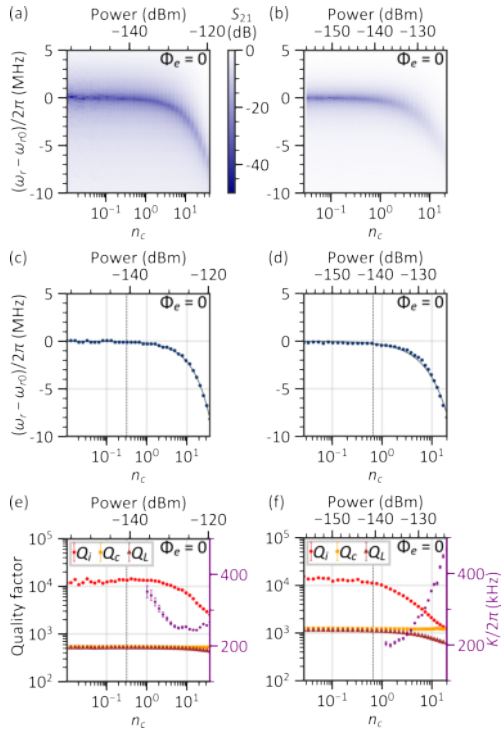

Figure 5. Kerr nonlinearity of FTRs. (a) and (b) show the lowering of the resonance frequency as a function of intra-cavity photon number due to the Kerr coefficient for the flip-chip and on-chip modulated FTRs, respectively. (c,d) Circle fit results obtained from power sweep measurements at the zero-flux-bias point of the FTRs with flip-chip-based input coil (c) and on-chip-based input coil (d). The data is fit using Eq. (5) to obtain the Kerr coefficients. (e) and (f) show the intrinsic, coupling, and loaded quality factors ($Q_L^{-1} = Q_i^{-1} + Q_c^{-1}$), and the Kerr coefficient as a function of intra-cavity photons. The dashed lines in both plots show the power at which the flux modulation measurements, shown in Fig. 4, were taken for the respective devices.

Kerr coefficient $\mathcal{K}(\Phi_s)$. From our data shown in Figs. 5(c) and (d), we determine $\mathcal{K}/2\pi = 216\,\mathrm{kHz/n_c}$ and $\mathcal{K}/2\pi = 381\,\mathrm{kHz/n_c}$ for the flip-chip device and the on-chip device, respectively. These values are similar to their respective predicted values of $184\,\mathrm{kHz/n_c}$ and $371\,\mathrm{kHz/n_c}$, calculated at zero flux bias.

Figs. 5(e) and (f) show the quality factors for

varying intra-cavity photon numbers. While Q_c remains constant, as expected, Q_i decreases with larger drive power, similar to Ref. [63].

Finally, we employed an FTR in a proof-of-principle experiment as a flux detector. To this end, we used an FTR with a 200 µm on-chip input coil to detect a magnetic source via the scheme depicted in Fig. 1(a). The magnetic source field was generated on an independent chip, which contained a multi-winding coil for creating a magnetic field as well as a pick-up coil; for details of a similar device, see Refs. [64, 65]. By injecting a current into the multi-winding coil, a magnetic field was generated, which was detected through the pick-up coil with a current-to-flux transduction of $0.27\,\Phi_0\,\mu\mathrm{A}^{-1}$. The pick-up coil was connected through Al wire bonds to off-chip 5 mm long superconducting Al leads, whose ends were wire-bonded to the input coil connections on the FTR chip. A dc current sweep of 230 µA through the multi-winding coil resulted in a modulation by one flux quantum of the FTR; see App. E. This yields a total flux transfer efficiency of 1.6%, close to the estimate of 1.5% based on the inductances involved in the circuit. Our efficiency is an order of magnitude larger than that achieved in Ref. [28], which employed a similar flux transfer architecture.

III. CONCLUSION

We have demonstrated on-chip and flip-chip-based modulation of flux-tunable superconducting resonators. We achieved flux tuning by one flux quantum with tens of µA of current and flux transfer efficiencies from the input coil to the SQUID loop of up to 20%. This flux transfer efficiency can be further improved by using washer-type SQUIDs [66–68], which allow for a decrease in loop geometric inductance while keeping the effective area similar [69–71]. Furthermore, the use of multiwinding input coils [71, 72] would decrease the contribution of parasitic inductance to the total flux transfer efficiency. Some applications may require a reduction in the nonlinearity of the FTR, which could be realized by operating the nonlinear resonator at a Kerr-free point via the use of superconducting nonlinear asymmetric inductive elements (SNAILs) [47, 48, 51, 52] or asymmetrically threaded SQUIDs [49, 50]. Efficient on-chip modulation of flux-tunable superconducting resonators is key for measuring small magnetic flux signals and for precise and low-current tuning of resonators, as required in quantum sensing and computing applications.

ACKNOWLEDGMENTS

We gratefully acknowledge support from Amr Osman, Anita Fadavi, and Jonas Bylander in device microfabrication, and Irshad Ahmad in SEM imaging. We acknowledge fruitful discussions with the entire team of the SuperMeQ EU project. This work was supported in part by the Horizon Europe 2021-2027 framework program of the European Union under Grant Agreement No. 101080143 (SuperMeQ), the European Research Council under Grant No. 101087847 (ERC Consolidator SuperQLev), the Knut and Alice Wallenberg (KAW) Foundation through a Wallenberg Academy Fellowship and Scholar (WW), and the Wallenberg Center for Quantum Technology (WACQT). Samples were fabricated at the Chalmers Myfab Nanofabrication Laboratory.

DATA AVAILABILITY

Data underlying the results presented in this paper are available in the open-access Zenodo database: 10.5281/zenodo.18079253.

Appendix A: Asymmetric dc SQUID

We treat the dc SQUID core as a lumped, lossless, quasi-static termination at the CPW end $x = l$ with asymmetric JJs, similar to Ref. [40]; see Fig. 6. The junction capacitance and shunt are neglected for the static relations, and we assume small-signal operation so that the SQUID behaves as an inductive load. The loop geometry is symmetric, with total geometric inductance L_g split equally between the two arms, so that each arm has geometric inductance $L_{\rm arm} = L_g/2$. A general nonzero transport current $I \equiv I_1 + I_2$ can be supplied by the CPW ground termination.

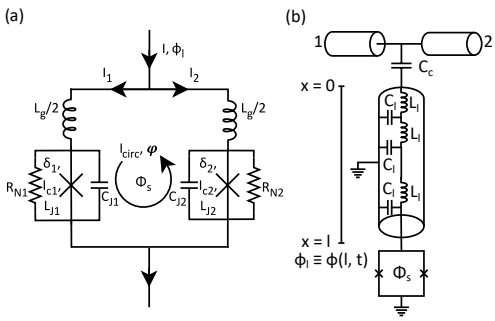

Figure 6. (a) Schematic of a dc SQUID with asymmetric Josephson junctions. (b) Transmission line model of a $\lambda/4$ flux-tunable resonator (FTR) capacitively coupled to a transmission feedline in notch-type configuration.

1. Transport and circulating current, screening relation

a. Definitions. We use the terminal phase (common mode) $\phi_l(t) \equiv \phi(l,t)$ and the loop phase (differential mode) $\varphi(t)$, expressed via the gauge-invariant phase drops across the two Josephson junctions (JJs)

$$\delta_1 = \phi_l + \varphi, \qquad \delta_2 = \phi_l - \varphi. \tag{A1}$$

The current across each JJ is given by the Josephson relation

$$I_k = I_{ck} \sin \delta_k, \tag{A2}$$

with $k = 1, 2$. We introduce an asymmetry in the critical current of the JJs with the parameter α while keeping the loop geometry symmetric:

$$\alpha = (I_{c1} - I_{c2})/(I_{c1} + I_{c2}) \tag{A3}$$

and define the mean critical current I_0 as

$$I_0 = (I_{c1} + I_{c2})/2. \tag{A4}$$

From I_0 and α, it follows that

$$I_{c1} = I_0(1+\alpha), \qquad I_{c2} = I_0(1-\alpha). \tag{A5}$$

Finally, we use the screening parameter $\beta_{\rm L}$ and the reduced external flux ϕ_e defined as

$$\beta_{\rm L} \equiv \frac{2L_g I_0}{\Phi_0}, \qquad \phi_e \equiv \frac{\Phi_e}{\Phi_0}. \tag{A6}$$

b. Josephson junction RCSJ model. We are interested in the small-signal input inductance of the dc SQUID as seen by the CPW node. We treat the SQUID as a linear termination with a small ac perturbation around a chosen static bias

$$\delta_{1,2}(t) = \delta_{1,2} + \delta_{1,2}^{\rm ac}(t), \qquad |\delta_{1,2}^{\rm ac}| \ll 1.$$

In the resistively and capacitively shunted junction (RCSJ) model, the small-signal admittance is

$$Y_J(\omega) = \frac{1}{i\omega L_J} + i\omega C_J + \frac{1}{R},$$

with $Z_J(\omega) = Y_J(\omega)^{-1}$. In the quasistatic limit with negligible C_J and $R \to \infty$, $Z_J(\omega) \approx i\omega L_J$.

For each junction, we use the small-signal Josephson inductance at the chosen static bias as

$$L_{Jk}(\delta_k) = \frac{\Phi_0}{2\pi\, I_{ck} \cos \delta_k}, \qquad k = 1, 2, \tag{A7}$$

evaluated at the operating point $(\bar{\phi}_l, \bar{\varphi})$ determined by the external flux and bias current.

c. Input inductance. The inductance of each SQUID arm is given as

$$L_{\rm arm,1} \equiv L_{J1} + \frac{L_g}{2}, \qquad L_{\rm arm,2} \equiv L_{J2} + \frac{L_g}{2}. \tag{A8}$$

The total SQUID inductance seen by the CPW node is then

$$L_S = \frac{L_{\mathrm{arm},1} L_{\mathrm{arm},2}}{L_{\mathrm{arm},1} + L_{\mathrm{arm},2}} = \frac{\big(L_{J1} + L_g/2\big)\big(L_{J2} + L_g/2\big)}{L_{J1} + L_{J2} + L_g}. \tag{A9}$$

The small-signal input inductance $L_S(\bar{\varphi}, \alpha)$ is then evaluated at the operating point $(\bar{\phi}_l, \bar{\varphi})$ of the SQUID.

d. Transport current. The transport current through the SQUID is given as

$$\begin{aligned} I &= I_1 + I_2 \\ &= I_{c1} \sin(\phi_l + \varphi) + I_{c2} \sin(\phi_l - \varphi) \\ &= 2I_0 \cos\varphi \, \sin\phi_l \; + \; 2\alpha I_0 \sin\varphi \, \cos\phi_l. \end{aligned} \tag{A10}$$

We can rewrite this equation by defining

$$R(\varphi) = 2I_0 \sqrt{\cos^2\varphi + \alpha^2 \sin^2\varphi}, \tag{A11}$$

$$\psi_0(\varphi) = \mathrm{atan2}\big(\alpha \sin\varphi, \; \cos\varphi\big), \tag{A12}$$

so that we obtain

$$I \; = \; R(\varphi) \, \sin\big(\phi_l + \psi_0(\varphi)\big), \; |I| \le R(\varphi). \tag{A13}$$

This equation can be regarded as the Josephson relation of an effective JJ, whose critical current $R(\varphi)$ is phase dependent. Resolving this equation for ϕ_l yields

$$\phi_l = -\psi_0(\varphi) + (-1)^n \arcsin\Big(\frac{I}{R(\varphi)}\Big) + n\pi, \tag{A14}$$

$$\text{with } \arcsin\Big(\frac{I}{R(\varphi)}\Big) \in [-\pi/2, \pi/2],$$
$$n \in \{0, 1\} \text{ and } |I| \le R(\varphi).$$

These two solutions for ϕ_l result in two screening branches, as we will see later.

e. Circulating current. The circulating current is given as

$$\begin{aligned} I_{\mathrm{circ}} &= \frac{I_1 - I_2}{2} \\ &= I_0 \left(\alpha \sin\phi_l \cos\varphi + \cos\phi_l \sin\varphi\right). \end{aligned} \tag{A15}$$

Rewriting this equation by using Eq. (A14) for ϕ_l and defining $D(\varphi) = R(\varphi)/(2I_0)$, we get

$$I_{\mathrm{circ}}(\varphi) = \pm I_0 \frac{(1-\alpha^2)\, \cos\varphi \, \sin\varphi}{D(\varphi)} \sqrt{1 - \Big(\frac{I}{2I_0 D(\varphi)}\Big)^2} \; + \; \frac{\alpha}{2} \frac{I}{D(\varphi)^2}. \tag{A16}$$

For $I = 0$, this reduces to

$$I_{\mathrm{circ}}(\varphi) = \pm \, I_0 (1-\alpha^2) \frac{\sin\varphi}{\sqrt{1 + \alpha^2 \tan^2\varphi}}. \tag{A17}$$

f. Fluxoid constraint. Applying the gauge-invariant fluxoid quantization around the SQUID loop, we obtain

$$\oint \Big(\nabla\phi - \frac{2\pi}{\Phi_0}\mathbf{A}\Big) \cdot d\boldsymbol{\ell} \; = \; 2\pi m, \; m \in \mathbb{Z}. \tag{A18}$$

The phase jumps across the junctions are δ_1 and $-\delta_2$, and the arm contributions provide the self-flux from the circulating current. With external flux Φ_e and symmetric arms of total inductance L_g carrying a circulating current I_{circ}, one obtains [40, 41]

$$\begin{aligned} &\delta_1 - \delta_2 + \frac{2\pi}{\Phi_0} L_g I_{\mathrm{circ}}(\varphi) = 2\pi \frac{\Phi_e}{\Phi_0} + 2\pi m \\ &\iff 2\varphi + \pi \, \beta_{\mathrm{L}} \frac{I_{\mathrm{circ}}(\varphi)}{I_0} = 2\pi(\phi_e + m), \end{aligned} \tag{A19}$$

where $\delta_{1,2} = \phi_l \pm \varphi$. In the limit $L_g \to 0$ (that is, $\beta_{\mathrm{L}} \to 0$), this reduces to $\varphi = \pi(\phi_e + m)$.

Using

$$\varphi = \pi\Big(\frac{\Phi_s}{\Phi_0} + m\Big), \tag{A20}$$

with the screened flux Φ_s, we can write

$$\Phi_s \equiv \Phi_e - L_g I_{\mathrm{circ}}(\varphi). \tag{A21}$$

Eq. (A16) and Eq. (A21) give the implicit $\Phi_s(\Phi_e)$ at finite I.

For $I = 0$, representative screening characteristics $\Phi_s(\Phi_e)$ for symmetric ($\alpha = 0$) and asymmetric ($\alpha = 0.3$) SQUIDs at $\beta_{\rm L} = 0$ and $\beta_{\rm L} = 0.3$ are plotted in Figs. 7(a) and (b).

For sufficiently large screening, Eq. (A19) becomes multivalued in $\varphi(\phi_e)$ over finite intervals, leading to a switching between the two screening branches. In the symmetric and zero-transport limit, the onset occurs at $\beta_{\rm L} \geq 2/\pi$.

2. Potential energy

For static operation (zero voltage), the potential energy of the dc SQUID biased by external flux Φ_e and transport current I is [14, 40, 41]

$$U(\phi_l, \varphi) = -\frac{\Phi_0}{2\pi}[I_{c1}\cos(\phi_l + \varphi) + I_{c2}\cos(\phi_l - \varphi)] + \frac{1}{2L_g}\left[\Phi_0 \cdot \left(\frac{\varphi}{\pi} - m\right) - \Phi_e\right]^2 - \frac{\Phi_0}{2\pi} I\,\phi_l. \quad \text{(A22)}$$

The three terms are, respectively, the Josephson energy of the two junctions, the magnetic energy of the loop, and the tilt of the potential washboard due to current bias at the node. The magnetic-energy term in Eq. (A22) accounts for screening through the circulating current (differential mode). Using $\Phi_s = \Phi_0 \cdot (\varphi/\pi - m)$ and $E_0 = \Phi_0 I_0/2\pi$, $i = I/I_0$, we can rewrite Eq. (A22) as

$$u(\phi_l, \varphi) \equiv \frac{U}{E_0} = -\big(1+\alpha\big)\cos(\phi_l + \varphi) - \big(1-\alpha\big)\cos(\phi_l - \varphi) + \frac{2\pi}{\beta_{\rm L}}\left(\frac{\varphi}{\pi} - m - \phi_e\right)^2 - i\,\phi_l. \quad \text{(A23)}$$

Representative landscapes of $u(\phi_l, \varphi)$ for $\beta_{\rm L} = 0$ and $\beta_{\rm L} = 0.3$, and for symmetric ($\alpha = 0$) and asymmetric ($\alpha = 0.3$) junctions at $\Phi_e = 0.5\Phi_0$, are shown in Fig. 7(e)-(h).

a. Branch switching criterion. Differentiating with respect to ϕ_l and φ gives

$$\frac{\partial U}{\partial \phi_l} = \frac{\Phi_0}{2\pi}[I_{c1}\sin(\phi_l + \varphi) + I_{c2}\sin(\phi_l - \varphi) - I]\,, \quad \text{(A24)}$$

$$\frac{\partial U}{\partial \varphi} = \frac{\Phi_0}{2\pi}[I_{c1}\sin(\phi_l + \varphi) - I_{c2}\sin(\phi_l - \varphi)] + \frac{\Phi_0}{\pi L_g}\left[\Phi_0 \cdot \left(\frac{\varphi}{\pi} - m\right) - \Phi_e\right]. \quad \text{(A25)}$$

When setting each derivative to zero, Eq. (A24) gives the transport-current relation for I, while Eq. (A25) reduces to the fluxoid constraint Eq. (A21). A given state (ϕ_l, φ) is a stable operating point if the Hessian matrix $H(\phi_l, \varphi)$ of U is positive definite (i.e., $\det H > 0$).

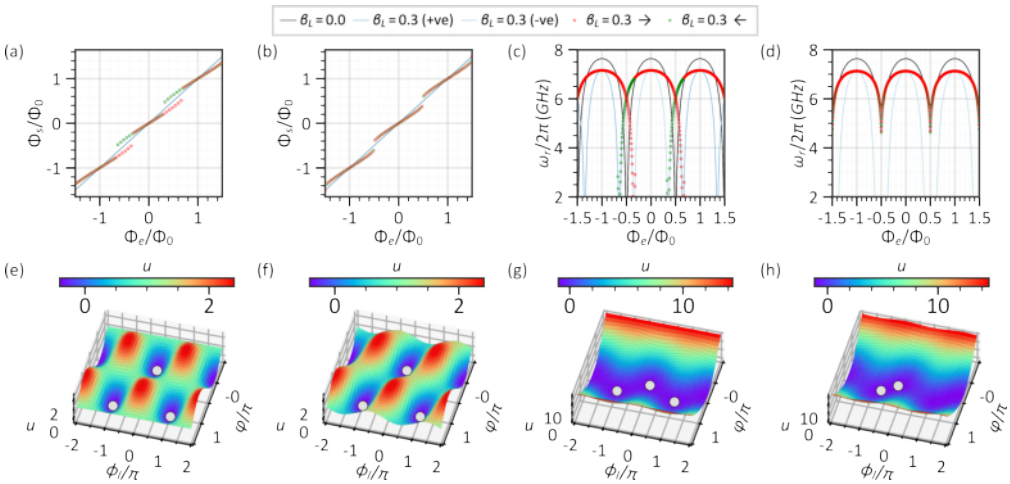

Figure 7. Symmetric vs. asymmetric dc SQUID. (a,b) Loop flux vs. applied flux for $\beta_{\rm L} = 0$ and $\beta_{\rm L} = 0.3$ with symmetric ($\alpha = 0$) and asymmetric ($\alpha = 0.3$) junctions. (c,d) Corresponding FTR resonance frequency vs. applied flux. (e-h) Normalized dc SQUID potential $U(\phi_l, \varphi)/E_0$ for $\beta_{\rm L} \to 0$ (e,f) and 0.3 (g,h), symmetric ($\alpha = 0$) and asymmetric ($\alpha = 0.3$), at external flux bias $\Phi_e = 0.5\Phi_0$.

$$H(\phi_l, \varphi) = \begin{pmatrix} U_{\phi\phi} & U_{\phi\varphi} \\ U_{\phi\varphi} & U_{\varphi\varphi} \end{pmatrix}$$
$$= \frac{\Phi_0}{2\pi} \begin{pmatrix} I_{c1}\cos(\phi_l+\varphi) + I_{c2}\cos(\phi_l-\varphi) & I_{c1}\cos(\phi_l+\varphi) - I_{c2}\cos(\phi_l-\varphi) \\ I_{c1}\cos(\phi_l+\varphi) - I_{c2}\cos(\phi_l-\varphi) & I_{c1}\cos(\phi_l+\varphi) + I_{c2}\cos(\phi_l-\varphi) + \frac{2\Phi_0}{\pi L_g} \end{pmatrix}. \quad \text{(A26)}$$

Here, the derivatives are evaluated at the stationary point $(\bar{\phi}_l, \bar{\varphi})$ that satisfies Eq. (A24) and Eq. (A25) when set to zero. Branch switching occurs when

$$\det H \;=\; U_{\phi\phi}U_{\varphi\varphi} - U_{\phi\varphi}^2 \;=\; 0, \qquad \text{(A27)}$$

This simplifies to

$$I_{c1}\cos(\phi_l+\varphi) + I_{c2}\cos(\phi_l-\varphi) \quad \text{(A28)}$$
$$+\pi\beta_{\rm L} I_0\,(1-\alpha^2)\,\cos(\phi_l+\varphi)\cos(\phi_l-\varphi) = 0.$$

For example, for $\alpha = 0$ and $I = 0$, the transport equation forces $\sin\phi_l = 0$, so $\phi_l = 0$. Then Eq. (A28) reduces to

$$\cos\varphi \cdot \big(2 + \pi\beta_{\rm L}\cos\varphi\big) = 0.$$

A nontrivial turning point is obtained when $\cos\varphi = -2/(\pi\beta_{\rm L})$, which exists when $\beta_{\rm L} \geq 2/\pi$. In Fig. 7(e)-(h), this onset of hysteresis corresponds to the appearance of multiple minima and saddle points in the potential landscape as $\beta_{\rm L}$ is increased from 0 to 0.3 and asymmetry is introduced.

Appendix B: Theory of a flux-tunable resonator

Our FTR consists of a $\lambda/4$ CPW of length l with distributed capacitance C_l and inductance L_l per unit length, and the CPW is terminated with a dc SQUID at the grounded end; see Fig. 6(b). We represent the SQUID termination by a total junction capacitance C_S and by a small-signal termination inductance: in the quasistatic dc limit this is the one-port input induc-

tance $L_S(\bar{\varphi}, \alpha)$. Shunt resistances and parasitic capacitances are ignored. We now derive how this SQUID inductance modifies the resonator modes and obtain a transcendental equation for the eigenfrequencies, see also Ref. [53, 54]. We fix coordinates such that the open end of the CPW is at $x = 0$ and the grounded end is at $x = l$, where the dc SQUID provides a lumped shunt termination to the ground. We denote the terminal phase at the SQUID end by $\phi_l(t) \equiv \phi(l, t)$.

1. Resonance frequency

a. Lagrangian. The Lagrangian of a CPW of length l with distributed capacitance C_l and inductance L_l per unit length is [53, 54]

$$\mathcal{L}_{\rm cpw} = \int_0^l \left[\frac{C_l}{2}\, \dot{\Phi}^{\,2} - \frac{1}{2L_l}\, (\partial_x \Phi)^2 \right] dx. \tag{B1}$$

Substituting the node flux $\Phi(x,t) = \left(\frac{\Phi_0}{2\pi}\right) \phi(x,t)$, where $\phi(x,t)$ is the dimensionless phase, we obtain

$$\mathcal{L}_{\rm cpw}[\phi] = \left(\frac{\Phi_0}{2\pi}\right)^2 \int_0^l \frac{C_l}{2} \left[\dot{\phi}^2 - v^2 (\phi')^2 \right] dx\,, \tag{B2}$$

with the wave speed $v = 1/\sqrt{L_l C_l}$. At the grounded end $x = l$, the dc SQUID is treated as a lumped, flux-dependent termination obtained by choosing a static operating point $(\bar{\phi}_l, \bar{\varphi})$ set by the external flux and bias current, and then considering only small ac perturbations around this point.

In this small-signal regime, the internal loop phase (φ) adjusts quasi-statically to the terminal phase (ϕ_l), so that the SQUID can be represented, as seen from the CPW node, by a single effective capacitance C_S and a small-signal input inductance $L_S(\bar{\varphi}, \alpha)$. For the asymmetric SQUID defined in App. A, these parameters are

$$\begin{aligned} C_S &= C_{J1} + C_{J2}, \\ L_S(\bar{\varphi}, \alpha) &= \frac{L_{\rm arm,1} L_{\rm arm,2}}{L_{\rm arm,1} + L_{\rm arm,2}}, \end{aligned} \tag{B3}$$

with $L_{\rm arm,1}$ and $L_{\rm arm,2}$, evaluated at the operating point $(\bar{\phi}_l, \bar{\varphi})$, as given in Eq. (A8). The small-signal SQUID Lagrangian, written solely in terms of $\phi_l(t)$, is

$$\mathcal{L}_S[\phi_l] = \left(\frac{\Phi_0}{2\pi}\right)^2 \left[\frac{C_S}{2}\, \dot{\phi}_l^{\,2} - \frac{\phi_l^2}{2L_S(\bar{\varphi}, \alpha)} \right]. \tag{B4}$$

This is a lumped shunt termination at $x = l$ which modifies only the boundary conditions. The total Lagrangian is then

$$\mathcal{L}_{\rm FTR}[\phi, \phi_l] = \mathcal{L}_{\rm cpw}[\phi] + \mathcal{L}_S[\phi_l]. \tag{B5}$$

Varying the field in the interior of the line yields the one-dimensional wave equation,

$$\ddot{\phi}(x,t) - v^2\, \phi''(x,t) = 0. \tag{B6}$$

Since the SQUID acts as a lumped termination at $x = l$, it only modifies the endpoint condition.

In the perfect short-termination limit at $x = l$, the bare $\lambda/4$ fundamental mode has a mode shape

$$u_0(x) = \cos(kx)\,,$$

with wave vector $k = \pi/2l$. We write the distributed phase as consisting of a time-dependent part multiplied by the spatial profile $u_0(x)$:

$$\phi(x,t) = \phi_0(t)\, u_0(x).$$

Using $u_0'(x) = -k \sin(kx)$ and

$$\int_0^l u_0(x)^2\, dx = \frac{l}{2}, \int_0^l [u_0'(x)]^2\, dx = \frac{k^2 l}{2} = \frac{\pi^2}{8l},$$

yields then for Eq. (B2)

$$\mathcal{L}_{\rm cpw}[\phi] = \left(\frac{\Phi_0}{2\pi}\right)^2 \left[\frac{C_l}{2}\, \frac{l}{2}\, \dot{\phi}_0^2 - \frac{1}{2L_l}\, \frac{\pi^2}{8l}\, \phi_0^2 \right].$$

We compare this result to a single-degree-of-freedom LC Lagrangian,

$$\mathcal{L}_{\rm mode} = \left(\frac{\Phi_0}{2\pi}\right)^2 \left[\frac{C_r}{2}\, \dot{\phi}_0^2 - \frac{\phi_0^2}{2L_r} \right],$$

and read off the modal lumped parameters

$$C_r = \frac{1}{2}\, C_l\, l\,, \qquad L_r = \frac{8}{\pi^2}\, L_l\, l\,.$$

b. Boundary condition. We now derive the boundary condition for $\phi(x,t)$ at the time-dependent SQUID termination. Using Eq. (B2) and keeping the endpoint terms, the boundary variation gives the CPW contribution:

$$\left.\frac{\partial \mathcal{L}_{\rm cpw}}{\partial \phi'}\right|_x = -\left(\frac{\Phi_0}{2\pi}\right)^2 \frac{1}{L_l}\,\phi'(x,t). \tag{B7}$$

At the open end $x=0$, the current must vanish. Hence,

$$\phi'(0,t) = 0. \tag{B8}$$

At the SQUID end $x = l$, the variation of Eq. (B4) gives

$$\frac{\partial \mathcal{L}_S}{\partial \phi_l} = -\left(\frac{\Phi_0}{2\pi}\right)^2 \frac{\phi_l}{L_S},\ \frac{\partial \mathcal{L}_S}{\partial \dot{\phi}_l} = \left(\frac{\Phi_0}{2\pi}\right)^2 C_S\,\dot{\phi}_l. \tag{B9}$$

The endpoint condition reads as follows:

$$\left.\frac{\partial \mathcal{L}_{\rm cpw}}{\partial \phi'}\right|_{x=l} + \frac{\partial \mathcal{L}_S}{\partial \phi_l} - \frac{d}{dt}\left(\frac{\partial \mathcal{L}_S}{\partial \dot{\phi}_l}\right) = 0, \tag{B10}$$

and yields the lumped load boundary

$$\phi'(l,t) = -L_l\left[\frac{\phi_l(t)}{L_S} + C_S\,\ddot{\phi}_l(t)\right]. \tag{B11}$$

In the quasistatic-load limit $C_S \to 0$, this reduces to the purely inductive condition

$$\phi'(l,t) = -\frac{L_l}{L_S}\,\phi_l(t). \tag{B12}$$

This inductive boundary condition assumes $\omega \ll 1/\sqrt{L_S\,C_S}$ evaluated near $\omega \approx \omega_r$ (typically $\sim 2\pi\cdot 26\,\mathrm{GHz}$ in our devices with $L_S \sim 600\,\mathrm{pH}$ and $C_S \sim 60\,\mathrm{fF}$). This expression provides the flux-dependent boundary condition of the FTR.

c. Transcendental equation of an FTR. Assuming a harmonic solution $\phi(x,t) = \psi(x)\,e^{-i\omega t}$ with $k = \omega\sqrt{L_l C_l}$ and inserting this ansatz into Eq. (B6), the spatial amplitude satisfies

$$\psi''(x) + k^2\psi(x) = 0. \tag{B13}$$

Applying the open-end boundary Eq. (B8) to the ansatz $\psi(x) = A\cos(kx) + B\sin(kx)$ imposes $\psi'(0) = 0$, which gives $B = 0$ and thus $\psi(x) = A\cos(kx)$. At $x = l$,

$$\psi(l) = A\cos(kl), \qquad \psi'(l) = -Ak\sin(kl).$$

Using Eq. (B11) in the frequency domain ($\ddot{\phi}_l \to -\omega^2\phi_l$), we obtain

$$\tan(kl) = \frac{L_l}{kL_S}\big(1 - \omega^2 C_S L_S\big). \tag{B14}$$

Solutions exist for frequencies well below the junction plasma frequency, $\omega \ll \omega_p$, with $\omega_p = 1/\sqrt{L_J(\bar{\varphi})\,C_J} \approx 2\pi\cdot 32\,\mathrm{GHz}$ for $L_J \approx 800\,\mathrm{pH}$ and $C_J \approx 30\,\mathrm{fF}$, and below the series LC resonance associated with the shunt capacitance, $\omega \ll 1/\sqrt{L_S\,C_S}$ evaluated near $\omega \approx \omega_r$. In the purely inductive limit, i.e., $C_S \to 0$, this reduces to

$$\tan(kl) = \frac{L_l}{kL_S}. \tag{B15}$$

For later normalization, we consider the bare quarter-wave limit of the FTR boundary. Taking $L_S \to 0$ in Eq. (B15) forces $\tan(kl) \to \infty$; hence,

$$\cos(kl) = 0 \Rightarrow kl = \frac{(2n+1)\pi}{2},\ n = 0, 1, 2, \ldots$$

With $k = \omega\sqrt{L_l C_l}$, this gives the bare quarter-wave modes

$$\omega_n = \frac{(2n+1)\pi}{2l\sqrt{L_l C_l}}, \tag{B16}$$

and for $n = 0$:

$$\omega_0 = \frac{\pi}{2l\sqrt{L_l C_l}}. \tag{B17}$$

d. Solution of the transcendental equation. We now solve Eq. (B15) approximately. We define θ as

$$\theta = kl = \omega\, l\sqrt{L_l C_l} = \frac{\pi}{2}\frac{\omega}{\omega_0},$$

and introduce

$$\gamma(\omega) \equiv \frac{L_S}{lL_l}, \tag{B18}$$

which is the SQUID termination inductance participation ratio. With this, we can write the transcendental equation as

$$\tan\theta = \frac{1}{\gamma\,\theta}. \tag{B19}$$

For the fundamental mode, θ lies close to $\pi/2$. We set $\theta = \pi/2 - \epsilon$ with $|\epsilon| \ll 1$:

$$\tan\theta = \cot\epsilon = \frac{1}{\epsilon} + O(\epsilon).$$

Thus, we can write

$$\theta\tan\theta = \frac{1}{\gamma} \;\Rightarrow\; \left(\frac{\pi}{2} - \epsilon\right)\frac{1}{\epsilon} + O(\epsilon) = \frac{1}{\gamma}.$$

To leading order, this yields

$$\frac{\pi}{2\epsilon} - 1 \approx \frac{1}{\gamma} \;\Rightarrow\; \epsilon \approx \frac{\pi}{2}\frac{\gamma}{1+\gamma}.$$

Hence

$$\theta = \frac{\pi}{2} - \epsilon \approx \frac{\pi}{2}\frac{1}{1+\gamma} \quad\Rightarrow\quad \frac{\omega}{\omega_0} \approx \frac{1}{1+\gamma},$$

so that

$$\omega \approx \frac{\omega_0}{1+\gamma(\omega)}, \qquad \gamma(\omega) = \frac{L_S}{lL_l}. \tag{B20}$$

The resulting flux dependence of the fundamental FTR resonance frequency for symmetric ($\alpha = 0$) and asymmetric ($\alpha = 0.3$) SQUID parameters is shown in Figs. 7(c) and (d), respectively.

2. Evaluation of FTR resonance frequency

To obtain $\omega_r(\Phi)$ for non-zero JJ asymmetry α and a finite screening parameter β_{L}, we use the following steps.

We determine the static dc SQUID operating point: For the eigenmode analysis, we assume a transport current $I = 0$. We solve the fluxoid constraint Eq. (A19) together with the circulating-current expression Eq. (A16) to obtain $\bar{\varphi}(\Phi_e)$ on the desired screening branch, and obtain $\phi_l(\Phi_e)$ from Eq. (A14). Then, we compute the screened flux from Eq. (A21).

We determine the flux-dependent SQUID inductance: We compute the junction phase drops via Eq. (A1) and the Josephson inductances via Eq. (A7). We insert these into Eq. (A9) to obtain $L_S(\Phi_s)$.

We determine the participation ratio and resonance frequency: We evaluate $\gamma(\Phi_s)$ using Eq. (B18). Then, we compute $\omega_r(\Phi_s)$ using Eq. (B20) with ω_0 as defined in Eq. (B17).

Appendix C: Flux transfer efficiency

When a current I_{in} flows through the closed loop contour C_i of the input coil, it generates a magnetic vector potential $\mathbf{A}$ at any point in space $\mathbf{r}$. In the Coulomb gauge, this vector potential is given by the Biot–Savart law:

$$\mathbf{A}(\mathbf{r}) = \frac{\mu_0 I_{in}}{4\pi}\oint_{C_i}\frac{d\boldsymbol{\ell}'}{|\mathbf{r}-\mathbf{r}'|}, \tag{C1}$$

where $|\mathbf{r}-\mathbf{r}'|$ is the distance between the source point $\mathbf{r}'$ on the input coil and $\mathbf{r}$.

Ignoring the screening flux due to finite loop inductance, the external flux coupled into the SQUID loop as Φ_e is defined as the line integral of $\mathbf{A}$ along the SQUID loop contour C_s:

$$\Phi_e = \oint_{C_s}\mathbf{A}(\mathbf{r})\cdot d\boldsymbol{\ell}, \tag{C2}$$

Substituting Eq. (C1) into Eq. (C2) yields:

$$\Phi_e = \frac{\mu_0 I_{in}}{4\pi}\oint_{C_s}\oint_{C_i}\frac{d\boldsymbol{\ell}_s\cdot d\boldsymbol{\ell}_i}{|\mathbf{r}_s-\mathbf{r}_i|}. \tag{C3}$$

This double line integral represents the Neumann formula for mutual inductance between the SQUID loop and the input coil [73]. The mutual inductance M relates the current in the input coil to the flux in the SQUID loop through $\Phi_e = M\cdot I_{in}$. From Eq. (C3), we can express M as:

$$M = \frac{\mu_0}{4\pi}\oint_{C_s}\oint_{C_i}\frac{d\boldsymbol{\ell}_s\cdot d\boldsymbol{\ell}_i}{|\mathbf{r}_s-\mathbf{r}_i|}. \tag{C4}$$

The self-inductance of the input coil follows a similar formula, but with both path integrals taken over the same contour C_i:

$$L_i = \frac{\mu_0}{4\pi}\oint_{C_i}\oint_{C_i}\frac{d\boldsymbol{\ell}_i\cdot d\boldsymbol{\ell}_i'}{|\mathbf{r}_i-\mathbf{r}_i'|}. \tag{C5}$$

The self-flux in the input coil is then $\Phi_i = L_i\cdot I_{in}$, and the flux efficiency is re-written as:

$$\eta_2 = \Phi_e/\Phi_i = M/L_i. \tag{C6}$$

Appendix D: Experimental methods

This section describes the microfabrication of devices, as well as the measurement setup and characterization techniques utilized.

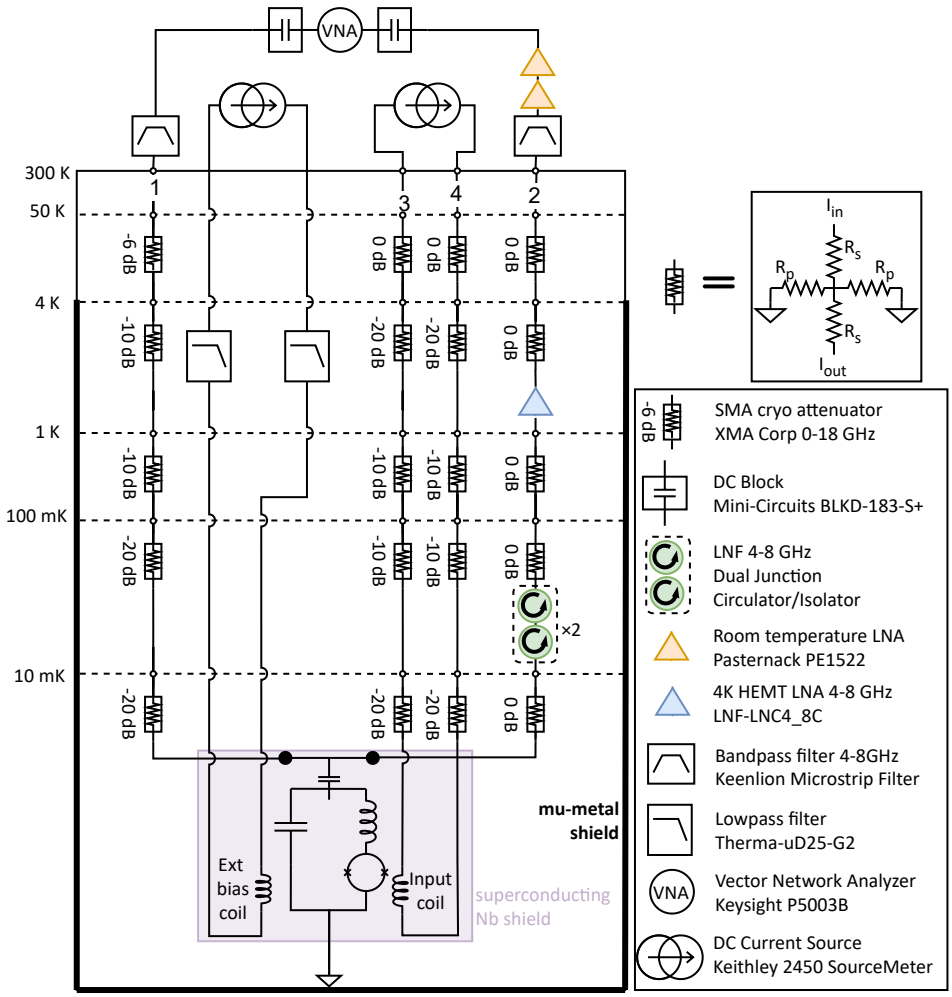

Figure 8. Wiring diagram illustrating the electrical connections and signal paths in the experimental setup.

1. Device fabrication and assembly

The flux-tunable resonators are patterned on a ⟨111⟩ silicon chip that is glued to an OFHC copper sample holder using BF-6 glue. The chip contains a bare CPW resonator, an FTR with a 10 µm-wide SQUID loop, and an FTR with a 100 µm or 200 µm-wide SQUID loop that is coupled to an integrated input coil placed either on-chip or via flip chip. The ground plane, junction electrodes, patch layer, and air-bridges are all made of aluminum. To galvanically connect to the flip-chip via indium microspheres, we require an under-bump metallization layer on the connecting pads, which prevents the diffusion of In from the microsphere into the Al layer, forming a non-superconducting intermetallic compound [74]; for details of fabrication and thin film properties, see Ref. [43]. This UBM layer is 50 nm thick NbN. The UBM layer is only patterned on the four flip-chip bonding pads; see Fig. 1(d). The JJ oxidation parameters are 2 mbar pres-

sure in a 100 sccm static MFC environment for 20 minutes, which is expected to yield a thin oxide layer of approximately 2 nm. The first and second aluminum junction electrodes are 50 nm and 100 nm thick, respectively, while the patch layer is 200 nm thick.

The width of our Manhattan-style JJ fabricated via the shadow evaporation process cannot reliably exceed 750 nm, as it is limited by the total resist height and the length of the undercut region. Therefore, we fabricated our 1 µm JJs by designing the electrodes to be 500 nm-wide and making only the junction area 1 µm-wide, with an additional 1 µm offset on each electrode to compensate for the resist shadow (see inset of Fig. 1(b)). This increases the effective overlapping area of the junction, despite some appendages created as an artifact of the shadow evaporation and resist undercut. In our design, one junction was patterned smaller than the other junction, resulting in an asymmetric dc SQUID.

The sample holder has a machined recess below the chip that leaves an air gap between the substrate and the metallic base. This prevents the chip from forming a large parallel plate capacitor with the ground of the sample holder and reduces parasitic coupling to box modes. The chip ground plane is tied to the sample holder in a controlled manner using aluminum wire bonds distributed along all edges of the chip to provide uniform grounding. The CPW feedline is wire bonded to the exposed, milled center pin of an SMA connector. The dc flux bias lines for the on-chip input coil are wire bonded to a PTFE insulated beryllium copper pin that is soldered to a twisted pair of NbTi wires. An additional external flux bias coil, made from Niobium Titanium (NbTi) wire and wound with more than 1000 turns on a 10 mm bobbin glued to the top of the sample holder, is connected to the cryostat dc wiring via pin headers.

2. Experimental setup

An overview of the setup is shown in Fig. 8. The sample is mounted to the mixing chamber plate of a BlueFors LD250 dilution refrigerator. It is placed inside a Niobium shield that is wrapped with a mu-metal (annealed soft ferromagnet) sheet. Additional shielding is provided by a tin-plated copper shield fixed to the mixing chamber plate and a mu-metal shield in the vacuum can. The microwave feedlines and the input coil lines are driven via standard microwave wiring of the fridge, with a total of 66 dB and 60 dB, respectively. Fig. 8 also shows the circuit of the attenuators, which reduce the current applied to the chip-based input coils. All measurements in this work were obtained at a base temperature of 20 mK. The FTR feedline is driven using a Keysight P5003B Vector Network Analyzer (VNA) in transmission (to measure the scattering parameter S_{21}), while both the input coil and the external biasing coil are driven using a Keithley 2450 sourcemeter current source.

3. Circle fitting technique

We analyze resonator traces using the circle-fitting routine from Ref. [75]. We use the model of a single notch-type microwave resonator in transmission.

a. *Linear circle fitting*

In the linear regime, we model the complex transmission of a single-mode notch resonator as

$$S_{21}(\omega) = 1 - \frac{Q_L}{Q_c^{\text{complex}}} \frac{1}{1 + 2iQ_L\left(\frac{\omega-\omega_r}{\omega_r}\right)}, \quad \text{(D1)}$$

with a resonance frequency ω_r, a loaded quality factor Q_L, and a complex coupling $Q_c^{\text{complex}} \equiv Q_c e^{i\phi}$ that accounts for small impedance mismatches. The quality factors are related to the decay rates via

$$\frac{1}{Q_L} = \frac{1}{Q_i} + \frac{1}{Q_c}, \qquad Q_L = \frac{\omega_r}{\kappa}, \quad Q_c = \frac{\omega_r}{\kappa_c}, \quad \text{(D2)}$$

where $\kappa = \kappa_i + \kappa_c$ is the total linewidth. From the complex fit, we extract the effective real coupling

$$\frac{1}{Q_c^{\text{eff}}} = \Re\left(\frac{1}{Q_c^{\text{complex}}}\right), \qquad \frac{1}{Q_L} = \frac{1}{Q_i} + \frac{1}{Q_c^{\text{eff}}}. \quad \text{(D3)}$$

Before fitting, the raw VNA data are corrected for a smooth complex background: we remove a linear phase ramp and a weak linear tilt in $|S_{21}|$ taken from off-resonant data, which is equivalent to dividing by a complex baseline $S_{\rm bg}(\omega)$ over the narrow bandwidth of each resonance.

In the complex plane, the background-corrected response traces an approximately circular arc as the probe frequency is swept. For each trace, we fit a circle to the complex data points $S_{21}(f_i)$ using a standard algebraic least-squares procedure to obtain the circle center z_c and radius r_0. We then map the off-resonant point on this circle to $1+0i$ by a global complex normalization, and finally remove the effect of the complex coupling $Q_c^{\rm complex} = Q_c^{\rm abs} e^{i\phi}$ by rotating the normalized circle around $1+0i$ by the angle ϕ and scaling radial distances from this point by $\cos\phi$. This yields the matched-circle representation, in which the circle center lies on the real axis and the radius $r_0^{\rm (matched)}$ obeys

$$r_0^{\rm (matched)} = \frac{Q_L}{2\,Q_c^{\rm eff}} = \frac{\kappa_c}{2\,\kappa}. \tag{D4}$$

In the fit, this identity is included as a soft constraint in addition to the complex residuals of Eq. (D1), ensuring that the extracted circle parameters remain consistent with the underlying resonator model.

b. *Nonlinear circle fitting*

For power-dependent traces, we apply the same preprocessing and circle-fitting routine to each trace but interpret the fitted resonance frequency as a Kerr-shifted effective resonance $\omega_r - \mathcal{K}n$ with an intracavity photon number n.

At higher drive, the mode behaves as a driven Duffing oscillator with a Kerr coefficient $\mathcal{K}$. The steady state satisfies

$$a = \frac{\sqrt{\kappa_c}\, s_{\rm in}}{\frac{\kappa}{2} - i\big[\Delta - \mathcal{K}n\big]}, \qquad n = |a|^2, \tag{D5}$$

with detuning $\Delta = \omega - \omega_r$ and input amplitude $s_{\rm in}$, such that $|s_{\rm in}|^2$ is the incident photon flux. We obtain a real cubic equation for n [75],

$$\mathcal{K}^2 n^3 - 2\Delta\mathcal{K}n^2 + \Big(\Delta^2 + \frac{\kappa^2}{4}\Big)n - \kappa_c\,|s_{\rm in}|^2 = 0. \tag{D6}$$

The power at the device P_g determines $|s_{\rm in}|^2$ via $|s_{\rm in}|^2 = P_g/(\hbar\omega)$. In the bistable regime, Eq. (D6) has three real roots; the smallest and largest dynamically stable roots define the low and high photon number branches.

The nonlinear transmission follows from evaluating the linear response at the Kerr-shifted resonance,

$$S_{21}^{\rm (nl)}(\omega, n) = 1 - \frac{\kappa_c}{\frac{\kappa}{2} - i\big[\omega - (\omega_r - \mathcal{K}n)\big]}. \tag{D7}$$

This can be written in terms of quality factors and in the matched-circle representation, where $Q_c^{\rm eff}$ is real, as

$$S_{21}^{\rm (nl)}(f, n) = 1 - \frac{Q_L}{Q_c^{\rm eff}}\,\frac{1}{1 + 2iQ_L\Big(\frac{f-(f_r-\frac{\mathcal{K}}{2\pi}n)}{f_r}\Big)}, \tag{D8}$$

with $f = \omega/2\pi$. Thus, for each power, the circle fit provides $\omega_r(P)$ and $Q_L(P)$, while the power dependence of $\omega_r(P)$ is evaluated through the Kerr model as a function of the intracavity photon number.

Appendix E: Supplementary data

1. Bare CPW resonator

The CPW resonator is 10 µm-wide with a 2 µm gap from the ground on either side. One end is shorted to ground, while the other end is left open and capacitively coupled to the transmission line for readout, realizing a $\lambda/4$ notch-type resonator with an electric-field antinode at the coupling capacitor. The corresponding lumped-element circuit in Fig. 9(a) shows that the resonance is probed as a dip in transmission, and the internal and coupling losses are obtained from the complex S_{21} response. The optical micrograph in Fig. 9(b) shows the fabricated aluminum CPW with air bridges across the gaps, which suppress odd (slotline-like) modes and equalize the electric field on both sides of

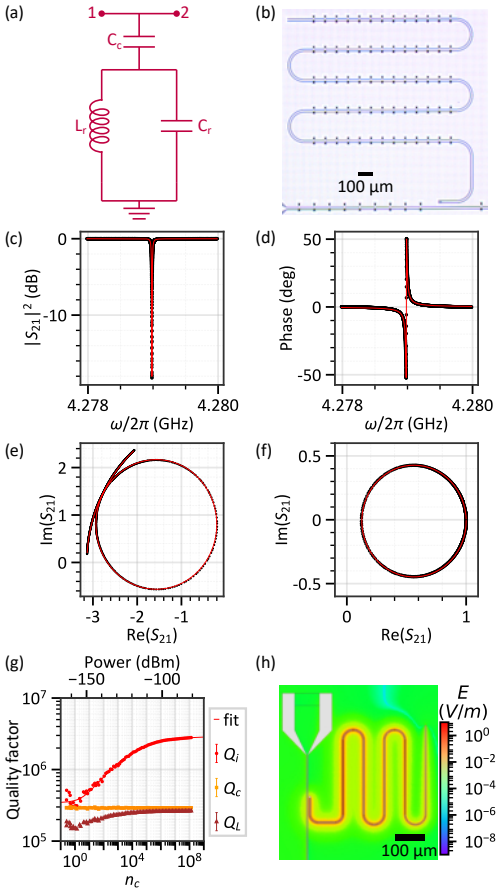

Figure 9. Bare CPW resonator. (a) Lumped-element circuit of a $\lambda/4$ CPW resonator capacitively coupled to a transmission line in notch-type configuration. (b) Optical micrograph of the aluminum CPW with air bridges across the gaps that suppress odd (slotline-like) modes and equalize the electric potential of the ground planes on either side of the center conductor. (c) Magnitude and (d) phase of the transmission coefficient S_{21} around the fundamental resonance. (e) Complex S_{21} data at $-114\,\mathrm{dBm}$ input power and (f) corresponding normalized circle used for parameter extraction. (g) Internal (Q_i), coupling (Q_c), and loaded (Q_L) quality factors versus intracavity photon number n_c, together with a two-level system (TLS) saturation fit for $Q_i(n_c)$. (h) HFSS eigenmode simulation showing the electric field distribution of the CPW resonator.

the center conductor, thereby allowing a well-defined quasi-TEM fundamental mode [76, 77]. The simulated eigenmode in Fig. 9(h) confirms that the electric field is concentrated in the CPW gaps and closely follows the expected $\lambda/4$ profile, validating the use of a single-mode description in App. B.

We characterize the resonator by measuring the complex transmission parameter S_{21} around the fundamental mode. The magnitude and phase traces in Figs. 9(c) and (d) exhibit the characteristic notch and dispersive phase swing of an overcoupled CPW resonator, indicating that the coupling loss dominates over the internal loss above single-photon powers. To extract reliable quality factors in the presence of cable delays and impedance mismatches, we apply the linear circle-fit procedure described in App. D to the complex S_{21} data. Figs. 9(e) and (f) illustrate how the raw complex response at $-40\,\mathrm{dBm}$ is mapped onto a normalized circle, from which we obtain the internal, coupling, and loaded quality factors Q_i, Q_c, and Q_L, respectively. The power dependence of these quantities, shown in Fig. 9(g), reveals that Q_i increases with the intra-cavity photon number while Q_c remains essentially constant.

The observed behavior of Q_i is well described by a standard two-level system (TLS) saturation model [78] of the form

$$Q_i^{-1}(n_c) = \delta_0 + \frac{\delta_{\mathrm{TLS}}}{1 + \left(n_c/n_c^*\right)^{\beta'}},$$

where δ_0 is a residual loss term unrelated to TLS, δ_{TLS} is the low-power TLS loss contribution, β' is the saturation exponent, and n_c^* is the characteristic photon number at which the TLS contribution begins to saturate. For the bare CPW resonator, we obtain

$$\begin{aligned} \delta_0 &= 3.4 \times 10^{-7}, \\ \delta_{\mathrm{TLS}} &= 2.6 \times 10^{-6}, \\ \beta' &= 0.295, \\ n_c^* &= 3.30, \end{aligned}$$

which correspond to a low-power quality factor $Q_{i,0} = 1/(\delta_0 + \delta_{\mathrm{TLS}}) \approx 3.5 \times 10^5$ and a high-power saturation value $Q_{i,\infty} = 1/\delta_0 \approx 2.9 \times 10^6$.

The extracted parameters are consistent with loss dominated by TLS [78]. An n_c^* of order a few photons, together with $\beta' \simeq 0.3$, indicates that the TLS bath begins to saturate close to the single-photon regime, consistent with observations on aluminum CPW resonators fabricated using a similar process [79].

2. FTR parameters

Table I shows the FTR parameters determined from fitting our experimental data.

Fig. 10 shows the modulation using an external bias coil of the flip-chip and on-chip FTR devices.

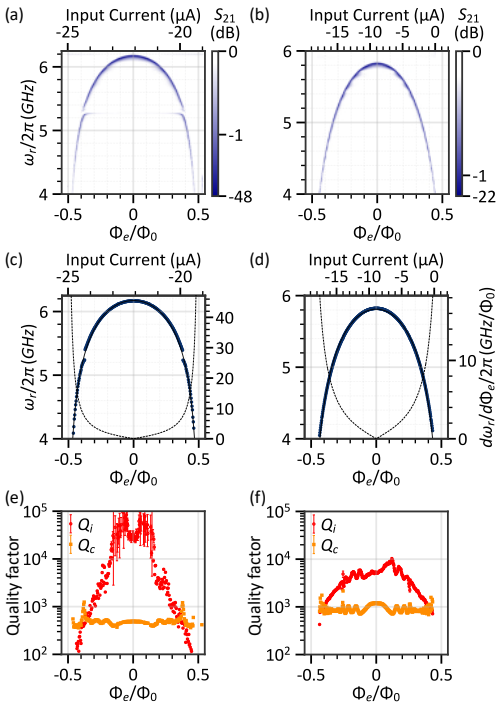

Figure 10. Flux modulation using external bias coil of the flip-chip-based (a,c,e) and on-chip-based (b,d,f) FTRs measured at 0.33 and 0.83 intra-cavity photons, respectively.

3. 10-µm-wide loop FTR characterization

Our chip design also contained a smaller-loop FTR with a 10 µm-wide SQUID loop and 1 µm-wide JJs. This device has no input coil and is modulated solely by the external bias coil. We use it as a fabrication reference. For input-coil-based modulation of the large-loop FTRs, the external bias coil detunes the 10 µm-loop reference FTR, thereby avoiding mode hybridization (see App. E).

Fig. 11 shows the flux tuning behavior of the reference FTR. We first take a coarse measurement with multiple modulations to obtain the current required for one flux quantum. Then we take a high-resolution measurement to obtain the FTR's parameters through circle fitting as summarized in Table I. Fig. 12 shows a power sweep of the reference FTR. With circle-fit determined Q_i limited by overcoupling, we obtain Q_i close to 10^5, comparable to state-of-the-art results [80]; see Table II.

4. Flux transfer efficiency

Table III shows the collected values for the flux transfer efficiency between the input coil and the SQUID loop. We determine the inductance for the square coil geometry of length l and wire width w via [81]

$$L_{\mathrm{coil2}}(l,w) = \frac{2\mu_0\, l}{\pi}\left[\sqrt{2} - 2 + \ln\left(\frac{4l}{w\,(1+\sqrt{2})}\right)\right]. \tag{E1}$$

To obtain the total flux transfer efficiency, we use a pickup coil concentrically placed around an on-chip magnetic field generating coil [64, 65]. From a FEM simulation of the coils, we determine the current-to-flux transduction to be $0.27\,\Phi_0\,\mu\mathrm{A}^{-1}$. In our experiment (see Fig. 13), a current of 230 µA provides modulation of the FTR by one Φ_0. This implies $\Phi_p = 62\,\Phi_0$ and $\Phi_e = 1\,\Phi_0$, which yield $\eta = \Phi_e/\Phi_p = 1.6\%$. We can compare this value to the expected efficiency determined from the involved inductances as

$$\eta = \frac{\Phi_e}{\Phi_p} = \frac{M}{L_p + L_{\mathrm{wire}} + L_i} = 1.5\%, \tag{E2}$$

Table I. Fitted parameters for three FTRs all with 1 µm-wide Josephson junction: one with a 200 µm-wide SQUID loop modulated via a flip-chip input coil, one with a 100 µm-wide SQUID loop modulated via an on-chip input coil, and a reference device with a 10 µm-wide SQUID loop.

Parameter	Symbol	Unit	200 µm loop FTR			100 µm loop FTR			10 µm loop FTR	
CPW parameters										
CPW length	l_r	µm	3259			3440			3320	
CPW inductance	L_r	pH	881.2			930.1			897.7	
CPW capacitance	C_r	fF	354.2			373.9			360.9	
CPW frequency	ω_0	GHz	9.008			8.534			8.843	
SQUID parameters			Flip-chip device			On-chip device			Reference device	
			Analytic	Input	Ext	Analytic	Input	Ext	Analytic	Ext
Current per Φ_0	I_{Φ_0}	µA/Φ_0	-	17.8	5.8	-	30.8	20	-	83.0
Scaling factor	A	-	-	1.1	1.06	-	0.98	0.98	-	0.98
Junction asymmetry	α	-	0.33	0.3	0.35	0.33	0.35	0.33	0.33	0.35
Avg critical current	I_0	nA	400	361	405	400	394	400	452	444
Avg JJ inductance	L_J	pH	823	913	812	823	836	823	727	740
SQUID inductance	L_S	pH	600	663	605	492	509	502	364	380
Loop inductance	L_g	pH	697	776	723	331	331	332	10.8	13.0
Screening parameter	β_L	-	0.27	0.27	0.28	0.11	0.13	0.13	0.005	0.006
Participation ratio	γ	-	0.55	0.61	0.56	0.43	0.44	0.44	0.33	0.34

Table II. FTR parameters of similar devices.

Reference	JJ material	$\omega_0/2\pi$ (GHz)	Q_i ($\Phi_s = 0$)	L_g (pH)	loop area (µm^2)	L_J (pH)	γ	β_L
Chalmers I [16]	Al/AlOx/Al	4.77	10×10^3	-	30	274	-	-
Chalmers II [80]	Al/AlOx/Al	5.46	400×10^3	-	100	350	0.1	-
Innsbruck [27]	Nb/Al/Nb	8.18	7.2×10^3	56	216	17	0.004	1.03
TU Delft [23]	Al/AlOx/Al	5.22	19×10^3	150	90	13	0.02	3.7
WMI [26]	Al/AlOx/Al	7.96	6×10^3	19	45	360	0.23	0.013
IQOQI [28]	Al/AlOx/Al	4.44	0.9×10^3	120	3000	360	0.19	0.06
This Work	Al/AlOx/Al	6.18	10×10^3	750	40 000	800	0.6	0.28

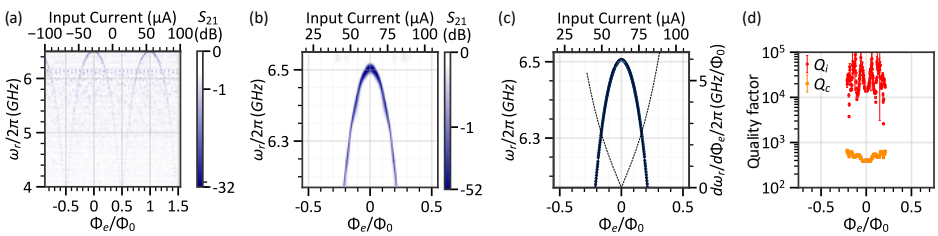

Figure 11. Flux modulation using external bias coil of an FTR with 10 µm-wide SQUID loop and 1 µm-wide Josephson junctions. (a) Multiple Φ_0 modulations showing the 10 µm loop FTR up to a frequency of 6.5 GHz and the 200 µm loop FTR up to a frequency of 6.2 GHz. (b) High-resolution measurement of the 10 µm loop FTR. (c) Resonance frequency and (d) quality factors as a function of flux, extracted via circle fitting, taken at 0.76 intra-cavity photons.

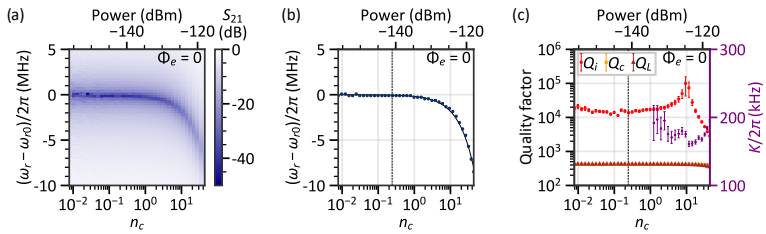

Figure 12. Power sweep of an uncoupled FTR with 10 µm-wide SQUID loop and 1 µm-wide Josephson junctions. We determine a Kerr coefficient of $\mathcal{K}/2\pi = 187\,\mathrm{kHz}/\mathrm{n_c}$ by fitting to Eq. (5).

Table III. Comparison of flux transfer parameters for flip-chip and on-chip approaches.

		Flip-chip device			On-chip device		
Parameter	Unit	Cal.	Sim.	Exp.	Cal.	Sim.	Exp.
L_i	pH	565	567	-	315	348	-
$M = \Phi_0/I_{\Phi_0}$	pH	153	169	116	121	116	67
η_2	%	29.3	29.8	20.8	38.4	33.1	19.3

with a mutual inductance of $M = 469\,\mathrm{pH}$ between the 210 µm-wide input coil and the 200 µm-wide SQUID loop, a simulated pickup coil inductance of $L_p = 2.02\,\mathrm{nH}$, a simulated input coil inductance of $L_i = 485\,\mathrm{pH}$, and an analytically estimated parasitic inductance of $L_p \approx 28.7\,\mathrm{nH}$. This parasitic inductance is given by two dc pins made of superconducting aluminum that connect the pickup coil to the input coil via bond wires. The single bond wire inductance is $L_{\mathrm{bondwire}} = 1.65\,\mathrm{nH}$ (in total, four have been used), and the single dc pin inductance is $L_{\mathrm{DCpin}} = 11.0\,\mathrm{nH}$, both estimated for a cylindrical geometry of length l and radius r using [82]

$$L = \frac{\mu_0 l}{2\pi}\left(\log\frac{2l}{r} - 0.75\right). \tag{E3}$$

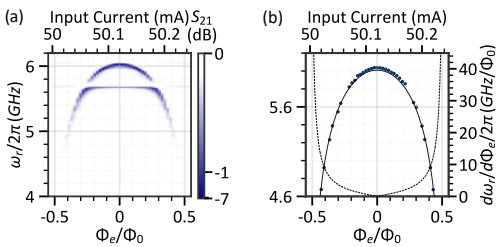

Figure 13. Modulation of a 200 µm-SQUID FTR coupled to an on-chip input coil by running current through a magnetic coil placed concentrically around a pickup coil. Measurements performed at 1.45 intracavity photons.

Appendix F: Symbols and parameters

Table IV: Symbols and parameters used.

Symbol	Description	Unit
Geometry and material parameters		
l	length of coplanar waveguide	m
$x \in [0, l]$	Longitudinal coordinate; $x = 0$ open, $x = l$ SQUID end	m
d_s	SQUID loop width (linear size)	m
d_i	Input coil loop width	m
h	Axial separation between input coil and SQUID loop	m
C_l	CPW capacitance per unit length	$\mathrm{F\,m^{-1}}$
L_l	CPW inductance per unit length	$\mathrm{H\,m^{-1}}$
C_r	Effective quarter-wave modal capacitance	F
L_r	Effective quarter-wave modal inductance	H
L_g	SQUID loop geometric inductance	H
L_i	Self inductance of the input coil	H
M	Mutual inductance (input coil to SQUID loop)	H
Fields, fluxes, and phases		
$\Phi(x, t)$	Node flux along the CPW	Wb
$\phi(x, t)$	Dimensionless phase, $\Phi = (\Phi_0/2\pi)\phi$	-
$\Phi_l(t)$	Node flux at the SQUID termination ($x = l$)	Wb
$\phi_l(t)$	Terminal phase at $x = l$, $\phi_l \equiv \phi(l, t)$	-
$\varphi(t)$	Loop (differential) SQUID phase	-
$\bar{\varphi}$	Static bias value of the loop phase	-
I_1, I_2	Currents through junctions 1 and 2	A
I	Transport current supplied by the CPW	A
I_{circ}	Circulating current in the SQUID loop	A
Φ_e	External flux threading the SQUID loop	Wb
Φ_s	Screened (internal) SQUID loop flux	Wb
Φ_p	Flux in the pickup coil	Wb
Φ_i	Self flux of the input coil	Wb
ϕ_{e}	Reduced external flux, $\phi_{\mathrm{e}} = \Phi_e/\Phi_0$	-
Φ_0	Flux quantum, $\Phi_0 = h/2e$	Wb
$\mathbf{A}(\mathbf{r})$	Magnetic vector potential at position $\mathbf{r}$	$\mathrm{Wb\,m^{-1}}$
Spectral and mode quantities		
v	Wave speed on the CPW, $v = 1/\sqrt{L_l C_l}$	$\mathrm{m\,s^{-1}}$
k	Wavenumber, $k = \omega\sqrt{L_l C_l} = \omega/v$	$\mathrm{m^{-1}}$
$\psi(x)$	Mode profile in $\phi(x, t) = \psi(x)e^{-i\omega t}$	-
$u_0(x)$	Bare quarter-wave mode shape, $u_0(x) = \cos(kx)$	-
ω	Angular drive frequency	$\mathrm{rad\,s^{-1}}$
ω_r	Angular resonance frequency of the FTR	$\mathrm{rad\,s^{-1}}$
$\omega_r(\Phi_s)$	Flux dependent resonance frequency	$\mathrm{rad\,s^{-1}}$
ω_0	Bare quarter-wave fundamental CPW frequency	$\mathrm{rad\,s^{-1}}$
θ	Electrical length, $\theta = kl = (\pi/2)(\omega/\omega_0)$	-
γ	SQUID inductance participation ratio $\gamma = L_S/(lL_l)$	-
Lagrangians and effective circuit parameters		
$\mathcal{L}_{\mathrm{cpw}}$	Lagrangian of the distributed CPW	J
$\mathcal{L}_S$	Effective SQUID Lagrangian	J
$\mathcal{L}_{\mathrm{FTR}}$	Total Lagrangian (CPW plus SQUID termination)	J
C_S	Effective SQUID capacitance	F
$L_J(\bar{\varphi})$	Average Josephson inductance at loop bias $\bar{\varphi}$	H

Table IV – continued from previous page

Symbol	Description	Unit
$L_S(\bar{\varphi})$	Effective SQUID inductance seen by the CPW	H
$L_{\mathrm{arm},1}, L_{\mathrm{arm},2}$	Series inductances of the two SQUID arms	H
dc SQUID parameters and screening		
δ_1, δ_2	Junction phase drops across junctions 1 and 2	-
I_{ck}	Critical current of a single k^{th} junction	A
$I_{\mathrm{c}1}, I_{\mathrm{c}2}$	Critical currents of junctions 1 and 2	A
I_0	Average junction critical current $(I_{\mathrm{c}1} + I_{\mathrm{c}2})/2$	A
α	Junction asymmetry $(I_{\mathrm{c}1} - I_{\mathrm{c}2})/(I_{\mathrm{c}1} + I_{\mathrm{c}2})$	-
β_{L}	Screening parameter, $\beta_{\mathrm{L}} = 2L_g I_0/\Phi_0$	-
L_{J1}, L_{J2}	Josephson inductances of junctions 1 and 2	H
C_J	Junction capacitance	F
$L_S(\bar{\varphi}, \alpha)$	Small-signal input inductance of the SQUID at bias $(\bar{\varphi}, \alpha)$	H
ω_p	Junction plasma frequency, $\omega_p = 1/\sqrt{L_J(\bar{\varphi})\, C_J}$	$\mathrm{rad\,s^{-1}}$
$R(\varphi)$	Amplitude in $I = R(\varphi)\sin(\phi_l + \psi_0)$	A
$\psi_0(\varphi)$	Phase offset in transport relation	-
$U(\phi_l, \varphi)$	SQUID potential energy	J
$u(\phi_l, \varphi)$	Dimensionless potential, $u = U/E_0$	-
Mode quantization and nonlinearity		
Φ_r	Generalized mode flux at the open end	Wb
Q_r	Conjugate charge of the mode	C
Φ_{zpf}	Zero-point flux fluctuation of the mode	Wb
$\lambda(\Phi_s)$	Termination factor, $\lambda = \phi_l/\phi_0 = \cos\theta(\Phi_s)$	-
Flux transfer and transformer parameters		
η_2	Flux transfer efficiency, $\eta_2 = \Phi_e/\Phi_i = M/L_i$	-
η	Total pickup to SQUID flux efficiency, $\eta = \Phi_e/\Phi_p$	-
I_{in}	Input coil current	A
I_{off}	Coil current corresponding to $\Phi_e = 0$	A
I_{Φ_0}	Coil current needed to change Φ_e by one Φ_0	A
Quality factors and Kerr nonlinearity		
Q_i	Internal quality factor	-
Q_c	Coupling quality factor	-
Q_L	Loaded quality factor, $1/Q_L = 1/Q_i + 1/Q_c$	-
n_c	Intra cavity photon number	-
$\mathcal{K}$	Kerr coefficient in angular frequency units	$\mathrm{rad\,s^{-1}}$
Input-output and circle fit		
a	Intracavity field amplitude	-
κ	Total decay rate, $\kappa = \kappa_i + \kappa_c$	$\mathrm{rad\,s^{-1}}$
Δ	Detuning, $\Delta = \omega - \omega_r$	$\mathrm{rad\,s^{-1}}$
S_{21}	Complex transmission coefficient	-
ϕ	Phase offset from impedance mismatch	-
τ	Electrical delay of the microwave line	s

[1] M. H. Devoret and R. J. Schoelkopf, Science **339**, 1169–1174 (2013).

[2] G. Wendin, Reports on Progress in Physics **80**, 106001 (2017).

[3] P. Krantz, M. Kjaergaard, F. Yan, T. P. Orlando, S. Gustavsson, and W. D. Oliver, Applied Physics Reviews **6**, 021318 (2019).

[4] A. Blais, A. L. Grimsmo, S. Girvin, and A. Wallraff, Reviews of Modern Physics **93**, 025005 (2021).

[5] M. D. Hutchings, J. B. Hertzberg, Y. Liu, N. T. Bronn, G. A. Keefe, M. Brink, J. M. Chow, and B. L. T. Plourde, Phys. Rev. Appl. **8**, 044003 (2017).

[6] M. Mergenthaler, C. Müller, M. Ganzhorn, S. Paredes, P. Müller, G. Salis, V. P. Adiga, M. Brink, M. Sandberg, J. B. Hertzberg, and et al., npj Quantum Information **7**, 157 (2021).

[7] J. M. Chávez-Garcia, F. Solgun, J. B. Hertzberg, O. Jinka, M. Brink, and B. Abdo, Phys. Rev. Appl. **18**, 034057 (2022).

[8] M. Pierre, I.-M. Svensson, S. Raman Sathyamoorthy, G. Johansson, and P. Delsing, Applied Physics Letters **104**, 232604 (2014).

[9] D. Kafri, C. Quintana, Y. Chen, A. Shabani, J. M. Martinis, and H. Neven, Phys. Rev. A **95**, 052333 (2017).

[10] T. Menke, W. P. Banner, T. R. Bergamaschi, A. Di Paolo, A. Vepsäläinen, S. J. Weber, R. Winik, A. Melville, B. M. Niedzielski, D. Rosenberg, and et al., Physical Review Letters **129**, 220501 (2022).

[11] T. Yamamoto, K. Inomata, M. Watanabe, K. Matsuba, T. Miyazaki, W. D. Oliver, Y. Nakamura, and J. S. Tsai, Applied Physics Letters **93**, 042510 (2008).

[12] N. Roch, E. Flurin, F. Nguyen, P. Morfin, P. Campagne-Ibarcq, M. H. Devoret, and B. Huard, Physical Review Letters **108**, 147701 (2012).

[13] M. Simoen, C. W. Chang, P. Krantz, J. Bylander, W. Wustmann, V. Shumeiko, P. Delsing, and C. M. Wilson, Journal of Applied Physics **118**, 154501 (2015).

[14] S. Pogorzalek, K. G. Fedorov, L. Zhong, J. Goetz, F. Wulschner, M. Fischer, P. Eder, E. Xie, K. Inomata, T. Yamamoto, and et al., Physical Review Applied **8**, 024012 (2017).

[15] A. Palacios-Laloy, F. Nguyen, F. Mallet, P. Bertet, D. Vion, and D. Esteve, Journal of Low Temperature Physics **151**, 1034– (2008).

[16] M. Sandberg, C. M. Wilson, F. Persson, T. Bauch, G. Johansson, V. Shumeiko, T. Duty, and P. Delsing, Applied Physics Letters **92**, 203501 (2008).

[17] P. Krantz, Y. Reshitnyk, W. Wustmann, J. Bylander, S. Gustavsson, W. D. Oliver, T. Duty, V. Shumeiko, and P. Delsing, New Journal of Physics **15**, 105002 (2013).

[18] O. Kennedy, J. Burnett, J. Fenton, N. Constantino, P. Warburton, J. Morton, and E. Dupont-Ferrier, Phys. Rev. Appl. **11**, 014006 (2019).

[19] K. Uhl, D. Hackenbeck, C. Füger, R. Kleiner, D. Koelle, and D. Bothner, Applied Physics Letters **122**, 182603 (2023).

[20] P. D. Nation, M. P. Blencowe, and E. Buks, Phys. Rev. B **78**, 104516 (2008).

[21] S. Etaki, M. Poot, I. Mahboob, K. Onomitsu, H. Yamaguchi, and H. S. van der Zant, Nature Physics **4**, 785–788 (2008).

[22] M. Poot, S. Etaki, I. Mahboob, K. Onomitsu, H. Yamaguchi, Y. M. Blanter, and H. S. J. van der Zant, Phys. Rev. Lett. **105**, 207203 (2010).

[23] I. C. Rodrigues, D. Bothner, and G. A. Steele, Nat. Commun. **10**, 1 (2019).

[24] D. Zoepfl, M. L. Juan, C. M. Schneider, and G. Kirchmair, Phys. Rev. Lett. **125**, 023601 (2020).

[25] P. Schmidt, M. T. Amawi, S. Pogorzalek, F. Deppe, A. Marx, R. Gross, and H. Huebl, Communications Physics **3**, 233 (2020).

[26] T. Luschmann, P. Schmidt, F. Deppe, A. Marx, A. Sanchez, R. Gross, and H. Huebl, Sci. Rep. **12**, 1 (2022).

[27] D. Zoepfl, M. L. Juan, N. Diaz-Naufal, C. M. F. Schneider, L. F. Deeg, A. Sharafiev, A. Metelmann, and G. Kirchmair, Phys. Rev. Lett. **130**, 033601 (2023).

[28] P. Schmidt, R. Claessen, G. Higgins, J. Hofer, J. J. Hansen, P. Asenbaum, M. Zemlicka, K. Uhl, R. Kleiner, R. Gross, H. Huebl, M. Trupke, and M. Aspelmeyer, Phys. Rev. Appl. **22**, 014078 (2024).

[29] Y. Kubo, F. R. Ong, P. Bertet, D. Vion, V. Jacques, D. Zheng, A. Dréau, J.-F. Roch, A. Auffeves, F. Jelezko, and et al., Physical Review Letters **105**, 140502 (2010).

[30] C. Eichler and J. R. Petta, Phys. Rev. Lett. **120**, 227702 (2018).

[31] D. Bothner, I. C. Rodrigues, and G. A. Steele, Nature Physics **17**, 85–91 (2020).

[32] C. M. Wilson, T. Duty, M. Sandberg, F. Persson, V. Shumeiko, and P. Delsing, Phys. Rev. Lett. **105**, 233907 (2010).

[33] P. Krantz, A. Bengtsson, M. Simoen, S. Gustavsson, V. Shumeiko, W. D. Oliver, C. M. Wilson, P. Delsing, and J. Bylander, Nature Communications **7**, 11417 (2016).

[34] F. Zhao, Z. Li, A. V. Dixit, T. Roy, A. Vrajitoarea, R. Banerjee, A. Anferov, K.-H. Lee, D. I. Schuster, and A. Chou, Phys. Rev. Lett. **135**,

201002 (2025).
[35] D. Duret and P. Karp, Journal of Applied Physics **56**, 1762–1768 (1984).
[36] J. Knuutila, M. Kajola, H. Seppä, R. Mutikainen, and J. Salmi, Journal of Low Temperature Physics **71**, 369–392 (1988).
[37] H. R. Yi, Y. Zhang, J. Schubert, W. Zander, X. H. Zeng, and N. Klein, Journal of Applied Physics **88**, 5966–5974 (2000).
[38] C. Granata, A. Vettoliere, and M. Russo, Review of Scientific Instruments **82**, 013901 (2011).
[39] M. Chukharkin, A. Kalabukhov, J. F. Schneiderman, F. Öisjöen, O. Snigirev, Z. Lai, and D. Winkler, Applied Physics Letters **101**, 042602 (2012).
[40] C. D. Tesche and J. Clarke, Journal of Low Temperature Physics **29**, 301–331 (1977).
[41] V. Lefevre-Seguin, E. Turlot, C. Urbina, D. Esteve, and M. H. Devoret, Physical Review B **46**, 5507–5522 (1992).
[42] P. Bhupathi, P. Groszkowski, M. DeFeo, M. Ware, F. K. Wilhelm, and B. Plourde, Physical Review Applied **5**, 024002 (2016).
[43] A. Paradkar, P. Nicaise, K. Dakroury, F. Resare, and W. Wieczorek, Applied Physics Letters **126**, 022601 (2025).
[44] A. Osman, J. Simon, A. Bengtsson, S. Kosen, P. Krantz, D. P. Lozano, M. Scigliuzzo, P. Delsing, J. Bylander, and A. Fadavi Roudsari, Applied Physics Letters **118**, 064002 (2021).
[45] A. Osman, *Scaling superconducting quantum processors: Coherence, frequency targeting and Crosstalk*, Ph.D. thesis, Chalmers University of Technology (2024).
[46] O. Shevchuk, G. A. Steele, and Y. M. Blanter, Phys. Rev. B **96**, 014508 (2017).
[47] N. E. Frattini, U. Vool, S. Shankar, A. Narla, K. M. Sliwa, and M. H. Devoret, Applied Physics Letters **110**, 222603 (2017).
[48] N. E. Frattini, V. V. Sivak, A. Lingenfelter, S. Shankar, and M. H. Devoret, Phys. Rev. Appl. **10**, 054020 (2018).
[49] R. Lescanne, M. Villiers, T. Peronnin, A. Sarlette, M. Delbecq, B. Huard, T. Kontos, M. Mirrahimi, and Z. Leghtas, Nature Physics **16**, 509–513 (2020).
[50] T. Hillmann and F. Quijandría, Phys. Rev. Appl. **17**, 064018 (2022).
[51] Y. Lu, M. Kudra, T. Hillmann, J. Yang, H.-X. Li, F. Quijandría, and P. Delsing, npj Quantum Information **9**, 1 (2023).
[52] A. M. Eriksson, T. Sépulcre, M. Kervinen, T. Hillmann, M. Kudra, S. Dupouy, Y. Lu, M. Khanahmadi, J. Yang, C. Castillo-Moreno, and et al., Nature Communications **15**, 1 (2024).
[53] M. Wallquist, V. S. Shumeiko, and G. Wendin, Phys. Rev. B **74**, 224506 (2006).
[54] W. Wustmann and V. Shumeiko, Phys. Rev. B **87**, 184501 (2013).
[55] A. Potts, P. R. Routley, G. J. Parker, J. J. Baumberg, and P. A. de Groot, Journal of Materials Science: Materials in Electronics **12**, 289–293 (2001).
[56] M. Tinkham, *Introduction to Superconductivity*, 2nd ed. (Dover Publications, Mineola, New York, 2004).
[57] Y. Zheng, S. Li, Z. Ding, K. Xiong, J. Feng, and H. Yang, Scientific Reports **13**, 11874 (2023).
[58] V. Sivak, N. Frattini, V. Joshi, A. Lingenfelter, S. Shankar, and M. Devoret, Phys. Rev. Appl. **11**, 054060 (2019).
[59] S. Probst, F. B. Song, P. A. Bushev, A. V. Ustinov, and M. Weides, Review of Scientific Instruments **86**, 024706 (2015).
[60] D. Rieger, S. Günzler, M. Spiecker, A. Nambisan, W. Wernsdorfer, and I. Pop, Phys. Rev. Appl. **20**, 014059 (2023).
[61] P. G. Baity, C. Maclean, V. Seferai, J. Bronstein, Y. Shu, T. Hemakumara, and M. Weides, Phys. Rev. Res. **6**, 013329 (2024).
[62] N. Diaz-Naufal, L. Deeg, D. Zoepfl, C. M. F. Schneider, M. L. Juan, G. Kirchmair, and A. Metelmann, Phys. Rev. A **111**, 053505 (2025).
[63] M. Watanabe, K. Inomata, T. Yamamoto, and J.-S. Tsai, Physical Review B **80**, 174502 (2009).
[64] M. G. Latorre, A. Paradkar, D. Hambraeus, G. Higgins, and W. Wieczorek, IEEE Transactions on Applied Superconductivity **32**, 1800305 (2022).
[65] M. G. Latorre, G. Higgins, A. Paradkar, T. Bauch, and W. Wieczorek, Phys. Rev. Appl. **19**, 054047 (2023).
[66] J. Jaycox and M. Ketchen, IEEE Transactions on Magnetics **17**, 400 (1981).
[67] M. B. Ketchen and J. M. Jaycox, Applied Physics Letters **40**, 736–738 (1982).
[68] R. Gross, P. Chaudhari, M. Kawasaki, M. B. Ketchen, and A. Gupta, Applied Physics Letters **57**, 727–729 (1990).
[69] D. Drung, C. Abmann, J. Beyer, A. Kirste, M. Peters, F. Ruede, and T. Schurig, IEEE Transactions on Applied Superconductivity **17**, 699 (2007).
[70] C. Granata and A. Vettoliere, Physics Reports **614**, 1–69 (2016).
[71] M. Xie, M. L. Chukharkin, S. Ruffieux, J. F. Schneiderman, A. Kalabukhov, M. Arzeo, T. Bauch, F. Lombardi, and D. Winkler, Superconductor Science and Technology **30**, 115014

(2017).

[72] E. Dantsker, S. Tanaka, and J. Clarke, Applied Physics Letters **70**, 2037–2039 (1997).

[73] E. B. Rosa, *The self and mutual inductances of linear conductors*, 80 (US Department of Commerce and Labor, Bureau of Standards, 1908).

[74] K. Wade and A. Banister, *The Chemistry of Aluminium, Gallium, Indium and Thallium*, 1st ed., Pergamon Texts in Inorganic Chemistry, Vol. 12 (Pergamon Press, Oxford, UK, 1973) p. 107.

[75] L. F. Deeg, D. Zoepfl, N. Diaz-Naufal, M. L. Juan, A. Metelmann, and G. Kirchmair, Phys. Rev. Appl. **23**, 014082 (2025).

[76] C.-Y. Lee, Y. Liu, and T. Itoh, IEEE Transactions on Microwave Theory and Techniques **43**, 2759 (1995).

[77] Z. Chen, A. Megrant, J. Kelly, R. Barends, J. Bochmann, Y. Chen, B. Chiaro, A. Dunsworth, E. Jeffrey, J. Y. Mutus, and et al., Applied Physics Letters **104**, 052602 (2014).

[78] J. Burnett, A. Bengtsson, D. Niepce, and J. Bylander, Journal of Physics: Conference Series **969**, 012131 (2018).

[79] J. Biznárová, J. Rivera Hernández, D. Forchheimer, J. Bylander, D. B. Haviland, and G. Andersson, Phys. Rev. Appl. **22**, 014063 (2024).

[80] I.-M. Svensson, M. Pierre, M. Simoen, W. Wustmann, P. Krantz, A. Bengtsson, G. Johansson, J. Bylander, V. Shumeiko, and P. Delsing, Journal of Physics: Conference Series **969**, 012146 (2018).

[81] C. R. Paul, *Inductance loop and partial Clayton R. Paul* (John Wiley & Sons, 2011) p. 126.

[82] X. Qi, *High-frequency characterization and modeling of on-chip interconnects and RF IC Wire bonds*, Ph.D. thesis, Stanford University (2001).